JOTCS A
Journal of the Turkish Chemical Society
Section: A
Chemistry
TURKISH CHEMICAL SOCIETY

The Biological Potential and Synthetic Diversity of 1,3,4-Oxadiazole Multiplexed with Various Heterocyclic Compounds

Rahul K[1], Deevan Paul A[1]*, Hariraj N[2], and Adhya Das[2]

[1]Chettinad School of Pharmaceutical Sciences, Chettinad Hospital and Research Institute, Chettinad Academy of Research and Education, Kelambakkam- 603103, Tamil Nadu, India.
[2]Department of Pharmaceutical Sciences, Government Medical College Kannur, 670503, Kerala, India
* E-mail address: deevan4@gmail.com Tel: + 919000105599

Abstract: Countless bioactive compounds are having the oxadiazole nucleus showing clinical and biological applications. Oxadiazole is a heterocyclic compound of the azole family that has gained increasing attention due to its wide therapeutic potential. Many significant synthetic medicinal compounds have the oxadiazole scaffold, which provided a good treatment idea and binds with high affinity to a variety of receptors to aid in the development of novel beneficial derivatives. Numerous researchers have worked to create novel oxadiazole compounds and evaluate them for how they affect inflammation, tumor, epilepsy, microbial infections, and analgesic properties. The present review article summarizes some of the oxadiazole derivatives synthesized and their biological activities and can be a useful guide for researchers working on this scaffold.

Keywords: Heterocyclic scaffolds, 1,3,4-oxadiazole, anticonvulsant, anti-inflammatory, antimicrobial, anticholinesterase.

Submitted: November 11, 2022. **Accepted:** January 10, 2023.

Cite this: Rahul K, Deevan Paul A, Hariraj N, Adhya D. The Biological Potential and Synthetic Diversity of 1,3,4-Oxadiazole Multiplexed with Various Heterocyclic Compounds. JOTCSA. 2023;10(2):267–76.

DOI: https://doi.org/10.18596/jotcsa.1202640.

***Corresponding author. E-mail:** rahulkcpspariyaram@gmail.com.

1. INTRODUCTION

Heterocyclic compounds are a class of organic substance that has a closed ring structure and contains heteroatom. These substances have numerous medical, veterinary, and agrochemical applications. Modern drug design now places a greater emphasis on these compounds' physiological and pharmacological activity(1). Oxadiazole has a chemical formula of $C_2H_2ON_2$, an aromatic heterocyclic molecule, unsaturated, unstable, nonbenzenoid, heteroaromatic with oxygen and a couple of nitrogens in a closed cyclopentane ring and has 12 electrons (eight from lone pairs and four electrons from double bonds) (2). Because of the electronegativities of nitrogen and oxygen, Oxadiazoles show hydrogen bond acceptor properties, in this, nitrogen is a stronger hydrogen bond acceptor than oxygen(3). Additional names for the ring system include azoximes, oxybiazole, biazole, diazoxole, furadiazole, and furoxans. In 1965, Ainsworth created oxadiazole for the first time by thermolyzing hydrazine(2). Oxadiazole has the characteristics of a conjugated diene since it contains two nitrogens of the pyridine type. Depending on where the two nitrogens are situated, oxadiazole can take one of four possible isomers (Figure 1)(2).

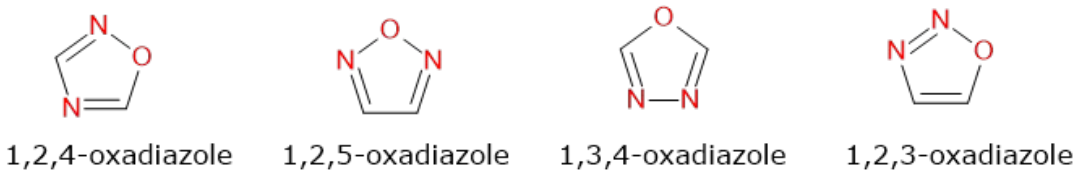

Figure 1: Four possible isomers of Oxadiazoles.

The isomer 1,3,4-oxadiazole exhibits an extensive range of therapeutic effects. The antiviral drug Raltegravir, the anti-arrhythmic medication Nesapidil, the antihypertensive medication Tiodazosin, and others are some of the 1,3,4-oxadiazole-ringed medications (Figure 2) that are commercially accessible(3). 1,3,4-oxadiazole ring changes the kinetic properties of the compounds(4). It is additionally utilized as a key component of pharmacophore that can bind to the ligand. It can also act as a linker in other circumstances to ensure optimal structural orientation. Here, we have made an effort to condense the significant pharmacological actions of oxadiazole derivatives.

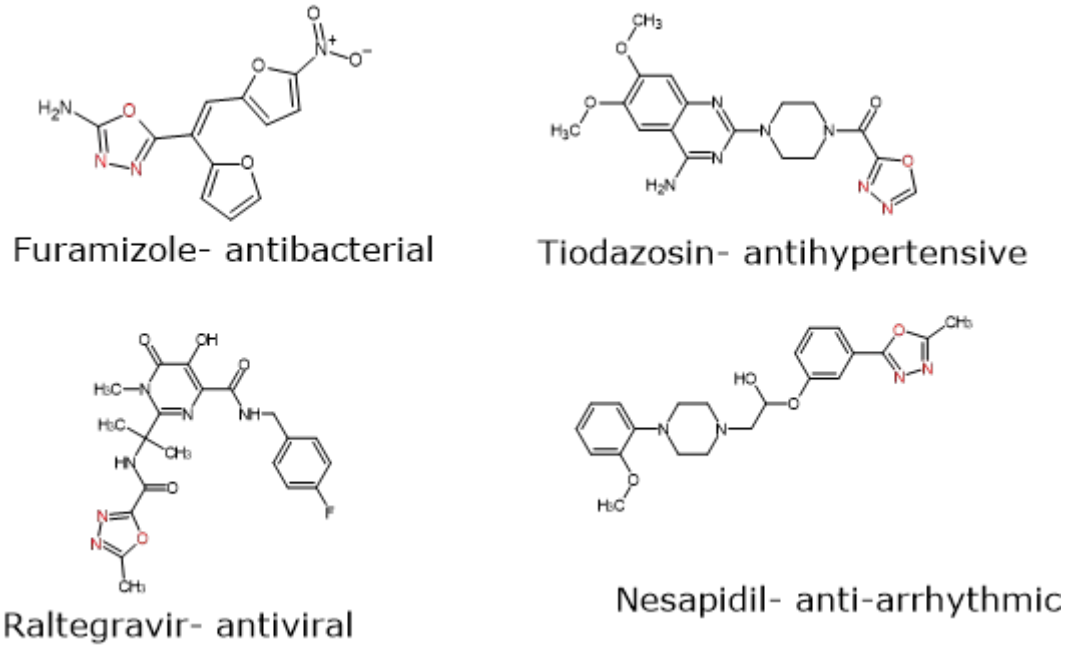

Figure 2: Chemical structure of commercial drugs.

2. BIOLOGICAL ACTIVITIES OF OXADIAZOLES

1,3,4-oxadiazole is recognized as a valuable pharmacophore for anti-infective including "antifungal, anti-bacterial, anti-trypanosomal, anti-malarial, anti-tubercular and anti-viral activities"(6,7,8).

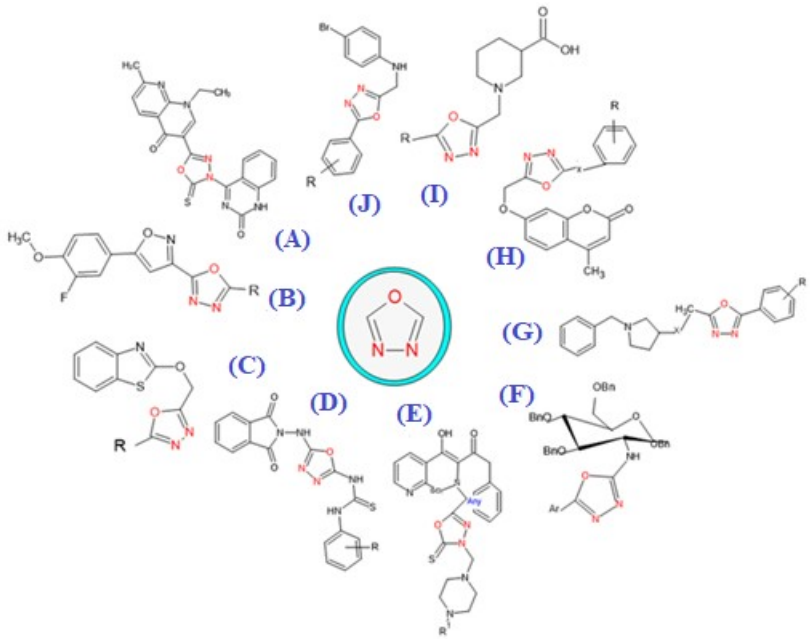

Figure 3: Structures of 1,3,4-oxadiazole with other scaffolds.

2.1. Antimicrobial Activity

Newer variants of nalidixic acid (Figure 4) were developed by Ramalingam Peraman, Reghu Veer Varma, and Y. Padmanabha Reddy. Designing novel compounds with anti-bacterial and anti-tubercular activity has made use of the COOH group of nalidixic acid. Agar plate disk diffusion and microdilution method were performed against various species for anti-bacterial screening. The compound 1-ethyl-7-methyl-3-(4-(3-oxo-3,4-dihydro quinoxaline-2-yl)-5-thioxo-4,5-dihydro-1,3,4-oxadiazol-2-yl)-1,8-naphthyridin-4(1H)-one(6) was found to potent (<6.25 µg/mL) than the reference drug ciprofloxacin against *S. aureus.* Student t-test showed 5% critical difference proves the activity significantly(6).

4-Bromo [(N-5-substituted [1,3,4-oxadiazole-2yl) methyl] aniline derivatives (Figure 5)(7) were synthesized and reported as anti-inflammatory and anti-microbial agent by KI Bhat *et al*. In all these screened compound 4-methoxy substituted one showed better antibacterial activity (zone of inhibition: 18mmin *S.aureus* and *B.subtilis*,19mm in *E.coli*, 15mm in *P.aeruginosa*) using amoxicillin as standard. Additionally, they were tested against various organism like *Candida albicans* and *Aspergillus niger* for anti-fungal activity (using ketoconazole standard)(7).

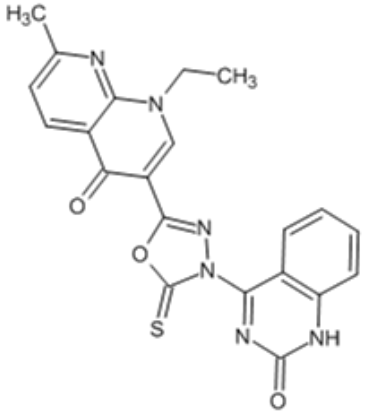

Figure 4: Oxadiazole with Nalidixic acid .

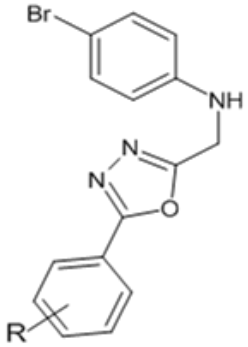

Figure 5: 1,3,4- oxadiazol with aniline derivatives.

By reacting 5-(3-fluoro-4-methoxyphenyl) isoxazole-3-carbohydrazide with pyridinyl /indoyl/benzoic acid derivatives using $POCl_3$, Ramesh Shingare, Yogesh Patil, and others were able to synthesize and assess a variety of 1,3,4-oxadiazole derivatives (Figure 6). Ampicillin was used as the reference medicine to test the antibacterial activity of this oxadiazole series(8). The results of the investigation indicated that the halogenated phenyl ring is essential for antibacterial action. Comparatively to the standard, the compounds having 4-chlorophenyl, 3,4-dichlorophenyl, 4-pyridinyl and 2-fluorophenyl groups were found to be good antibacterial activity. These compounds were also try out for anti-TB activity using isoniazid as the reference(8). It was discovered that compounds 2-methoxyphenyl and 4-fluorophenyl were effective against *M. tuberculosis*. The inhibition of the MurD ligase enzyme was also studied and was supported by molecular docking studies(8).Alghamdi, *et al*. synthesized fifteen 2- hydroxyl benzthiazole-linked 1,3,4- oxadoazoles and confirmed their anti-bacterial properties using an in-vitro susceptibility test (disc diffusion method) (Figure 7). Compounds with 2-chlorophenyl, p-methylphenyl, m-chlorophenyl, 2-methylphenyl, p-nitrophenyl and 2,4-dichlorophenyl are the best active derivatives against the bacterial strains(9). Compounds having –SH group(10) showed equivalent MIC 6.25 ±0.2 µg/disc to the amoxicillin (standard drug) against the Gram-positive bacteria and these have potent antiviral properties. The IC_{50} ranges from 0.4 to 2.1 µg/mL.(9). Insilico pharmacokinetic and drug-likeness properties of these derivatives were studied and were found to be excellent.

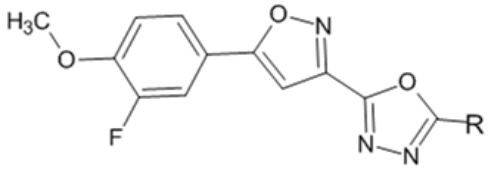

Figure 6: Isoxazole with 1,3,4-oxadiazole.

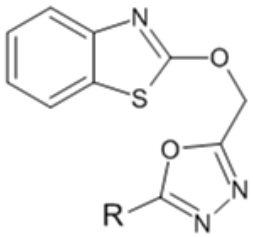

Figure 7: Benzothiazole-linked oxadiazole.

2.2. Anti-Alzheimer Activity As a potential multi-target directed ligand, George *et al*. developed and synthesized two series of ligands containing Coumarin with oxadiazole (Figure 8) and in-vitro anti-cholinesterase activity, anti-oxidant, and anti-inflammatory effects are evaluated. To ascertain the AChE and BuChE binding mechanism, molecular docking studies, as well as colorimetric assay (modified Ellman's method) were conducted,

and galantamine was used as standard. Cheminformatics software was also used to analyze the pharmacokinetic profile of all produced compounds. Based on the results they conclude that the methoxy linker between these two scaffolds has a very important role in AChE inhibition. The synthesized compounds' IC_{50} value ranges from 28.7 to 159.7 µM. Among these, three hydroxyl groups containing phenyl substitution at the 3,4,5 position of 1,3,4-oxadiazole were reported as the best AChE inhibitor(11). Docking results show that derivatives with three hydroxyl groups have dock scores of 9.7 Kcal/mol. Decreasing the -OH groups from 3,4,5 trihydroxy to 3,4 dihydroxy showed a better binding score (10.1 Kcal/Mol) but showed a slight decrease in in-vitro activity. DPPH free radical assay was performed to determine in-vitro antioxidant potential, and the compounds with phenolic hydroxyl group exhibited better performance. Based on these invitro and insilico studies it was concluded that Coumarin-1,3,4-oxadiazole scaffolds act as a multi-targeted hybrid for anti-Alzheimer's drugs(11).

Choubey *et al*. Synthesized and evaluated N-benzylpyrrolidine and 1,3,4-oxadiazole hybrid (Figure 9) for Alzheimer's treatment. All the hybrids were tested with different in-vitro parameters such as Cholinesterase and BACE-1 inhibition assay, enzyme kinetics study, PI displacement assay, BBB penetration assay, Thioflavin T assay, and neuroprotective assay(12). Invivo behavioral studies were also performed on the Scopolamine-induced amnesia model. In these, compounds having fluoro substitution on the phenyl ring showed potential inhibition against hAChE, BuChE, and BACE-1. Among these trifluoromethyl substituted derivatives showed significant permeability and prominently disaggregate Aβ fibrils. The compound was also found to reverse scopolamine-induced connective dysfunction and ameliorate cognitive dysfunction. An Ex-vivo study was also conducted to ascertain AChE inhibitory and antioxidant potential. The binding affinity was predicted by docking studies. The study concluded that the compounds with CF_3 on phenyl and amino or methyl amino spacer can be potential candidates [IC_{50}=0.091 ± 0.008 (AChE), 0.106 ± 0.013(hBChE) for amino spacer and 0.064 ± 0.006(AChE), 0.074 ± 0.016(hBChE) for methylamino spacer] for the treatment of Alzheimer's disease(13).

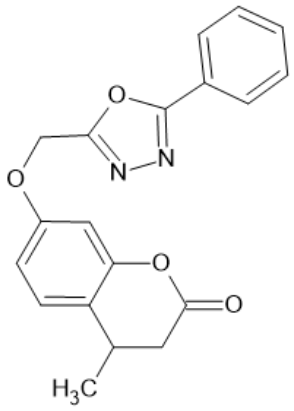

Figure 8: Coumarin-linked oxadiazole.

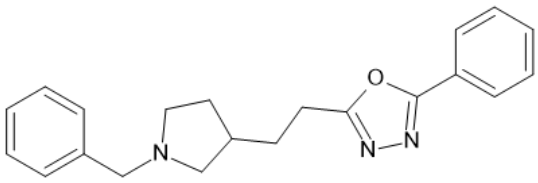

Figure 9: Oxadiazole with pyrrolidine.

A variety of C2-Glycosyl oxadiazole compounds were produced by base-catalyzed reactions by Wang *et al*. (Figure 10)**.** For acetylcholinesterase inhibition assay Ellman's method (reference: galantamine and tacrine) were used(14). Among the synthesized compound methoxy group in the fifth position possess the best one (IC_{50}2.03 ± 0.26) (13).

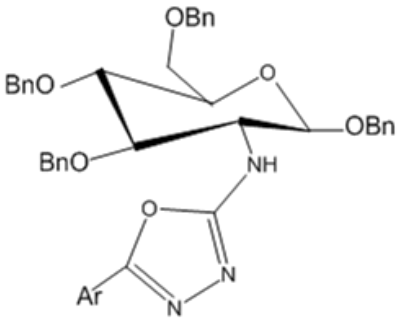

Figure 10: Glycosyloxadiazole.

Pyridine containing oxadiazole derivatives as (Figure 11) potential acetylcholinesterase inhibitory agents narrated by Puja Mishra *et al*. 4-hydroxyl substituted compound showed maximum inhibition with the IC_{50} value 1.098 µM and value of K_i = 0.960 µM. This derivative also inhibited acetylcholinesterase-induced Aβ aggregation (38.2–65.9%) determined by thioflavin T assay(15). 4-hydroxyl substituted compound and donepezil (standard) produced similar interaction (glide score reported as -10.6 kcal/mol) at the same binding site of acetylcholine esterase.

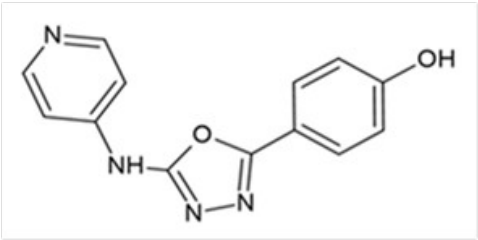

Figure 11: Oxadiazole with Pyridine.

2.3. Anti-inflammatory Activity

By reacting benzoyl chloride with different chloro-nitro-benzoyl chlorides and semi-carbazides, Singh *et al*. were able to create a variety of five-membered heterocyclic rings (Figure 12). The NMR, IR, and mass spectra were used to characterize and identify each of the synthesized oxadiazole derivatives. The anti-inflammatory activities were determined by the edema model (Carrageenan-induced rat- paw) using standard indomethacin(16). It was concluded that the entire compound has good anti-inflammatory activity. The compounds with 4-chloro-benzoic acid substitution on 2, 5-position showed improved activity than that of 3-chloro and 2-chloro substitution(16).

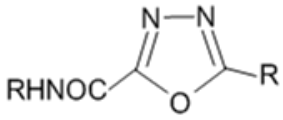

Figure 12: Oxadiazole derivatives(16).

Novel 1,3,4-oxadiazole with pyridothiazine-1,1-dioxide derived compounds (Figure 13) as inhibitors of COX-1 and 2 reported by Glomb *et al*. The final product was designed as an N-Mannich base, to obtain a synergistic effect on anti-inflammatory activity. These abilities were tested by a colorimetric inhibitor screening technique(17). On typical NHDF fibroblasts, the antioxidant and cytotoxic effects were also investigated. Multiple-criteria decision analysis discloses that 4-nitro phenyl, 2-pyridyl, and 2-pyramidal substituted compounds showed better activity (reference-Meloxicam)(17).

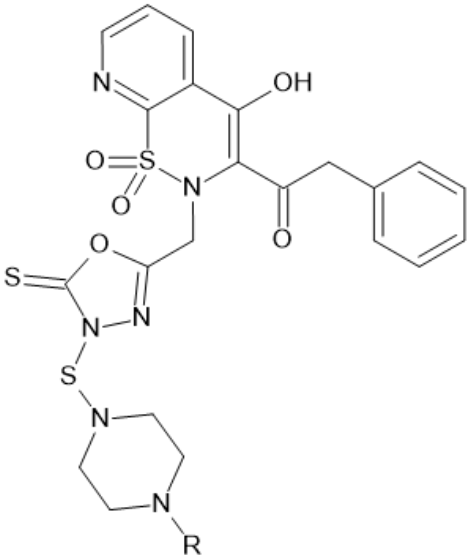

Figure 13: Oxadiazole with pyridothiazine-1,1-dioxide(17).

A new set of 2,5-biaryl-1,3,4-oxadiazoles (Figure 14) were synthesized and analyzed as possible cyclooxygenase-2 inhibitors by J. Grover *et al*. Chloro and nitro group on one of the aryl ring as well as the acetyl substitution at one of the nitrogen of oxadiazole found to be best inhibitors of COX-2 (IC_{50} = 0.48-0.89 µM)(18). Such derivatives showed superior inhibitory activity than the standard-celecoxib (carrageenan-induced model). Compounds having methylsulfonyl moieties show more selective cyclooxygenase-2 inhibition, confirmed through computational study(18).

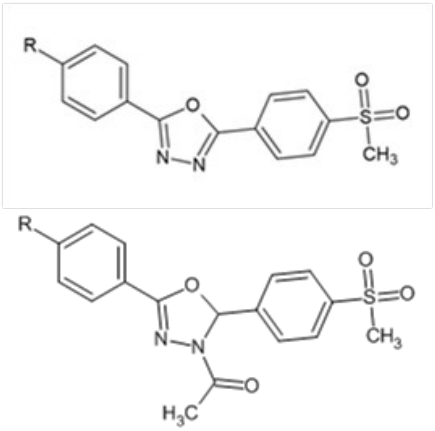

Figure 14: 1,3,4-Oxadiazole with different phenyl scaffolds.

"2,5-disubstitution at 1,3,4-oxadiazoles becomes an important strategy to generate novel heterocyclic compounds with a wide range of pharmacological activities"(19). Sudhir Bhardwaj *et al*. reported a new structural sequence of 2,5-disubstituted oxadiazoles (Figure 15) which has anti-inflammatory activity. The derivatives with hydroxyl, methoxy and tri-methyl amino group exhibited good anti-inflammatory (carrageenan-

induced paw edema, standard- diclofenac sodium; 44.45– 83.34 %) and analgesic activity (52 to 82 %)(19).

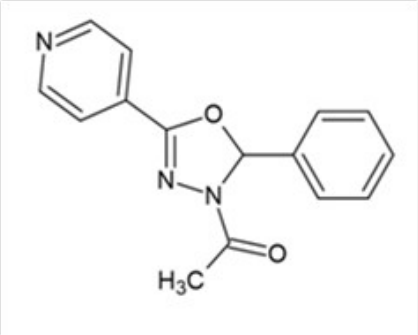

Figure 15: 1,3,4-Oxadiazole with pyridine.

Various Schiff bases of 1,3,4-oxadiazole (Figure 16) were introduced by Sahoo *et al*. microwave heating technology was applied for the synthesis. The anti-inflammatory activity is mainly influenced by substituents on the aromatic ring. In these, the compound with para substitution showed more activity than ortho and meta-substituted compounds. The para-hydroxy substitution showed maximum activity than halogens, $-OCH_3$, $-NO_2$ group(20).

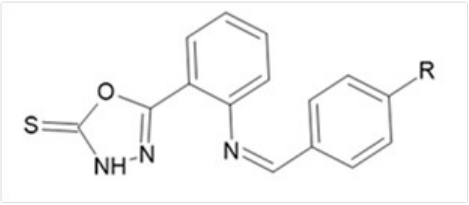

Figure 16: 1,3,4-Oxadiazole with Schiff base.

2.4. Anti-convulsant activity

For their anti-convulsant and neurotoxicity activity, Bhat *et al*. produced and assessed some phthalimide derivatives of 1,3,4-oxadiazole (Figure 17). The maximal electric shock method was used to test all of the compounds. The compound's neurotoxicity was also tested using the rotarod method, and it was discovered to be lower than phenytoin. Actophotometer was used to conduct a behavioral test, and all of the compounds except 13d displayed increased motor activity. The basic structure of the compounds had all the pharmacophoric structural requirements. The presence of constituents like $-OCH_3$ at the para position of the phenyl ring and the alkyl group at the distant aryl ring has potent activity(21). To increase the lipophilicity of the molecule, thioureido moiety was introduced into the structure. The study concluded by revealing that the phthalimide derivatives exhibit anticonvulsant activity comparable to phenytoin(7).

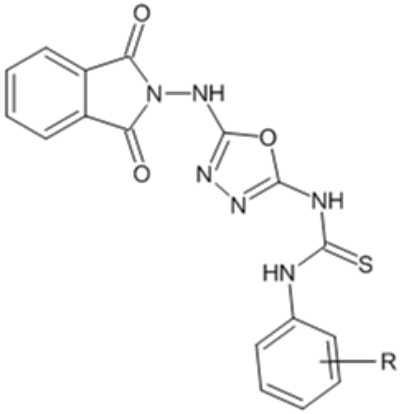

Figure 17: Phthalimide-1,3,4-Oxadiazole derivative(7).

The anticonvulsant activity of oxadiazole with nipecotic acid (Figure 18) was elaborated by Singh *et al*. Oxadiazole was attached to the secondary amine of nipecotic acid through a methylene bridge. The hybridized molecule was tested for its ability to treat epilepsy (PTZ-induced model) and depression (standard: Tiagabine (dose: 100 mg/kg), imipramine (dose: 50 mg/kg)). The homology model of the GAT_1 GABA transporter was developed and docking studies are also conducted(22). The 2,4-Dihydroxyphenyl derivative showed hydrogen bond interactions with Glycine65, Tyrosine140, and Aspartic acid451 residues (glide score -6.2) which is similar to the standard Tiagabin(22). It was concluded that the compounds 14d, 14e, 14g, 14m, and 14o showed an anti-epileptic effect comparable to Tiagabine. All the potential compounds were found to be devoid of toxicity and have a good safety profile. They concluded that derivatives with 3-Cyanophenyl, 2,4-Dihydroxyphenyl, 3-Methoxyphenyl, 3,5-Dinitrophenyl, and 2-Amino-4,5-dimethoxy phenyl substitution can be used as a lead for safer anti-epileptic agents (22).

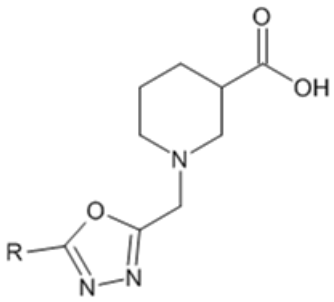

Figure 18: Nipecotic acid with oxadiazole.

Oxadiazole derivatives with dihydroquinolin and 1,2,4-triazole (Figure 19) were designed and synthesized by Shiben Wang *et al*. The anticonvulsant activity of these was tested by subcutaneous pentylenetetrazole and maximal electroshock models. In that, 4-dihydroquinolin-2-one derivative showed the best activity (maximal electroshock seizure model- ED_{50} = 8.9 mg/kg;

subcutaneous Pentylenetetrazole model- ED_{50} = 10.2 mg/kg), which showed greater activities than the ethosuximide and carbamazepine(23). Elevated plus maze experiments results conclude that these derivatives showed similar activity to that of diazepam. The radioreceptor binding assay of 4- dihydroquinolin-2-one divulges that it has a high binding affinity toward GABAA receptors (IC_{50} of 0.11 µM)(23).

Harish Rajak *et al*. designed and synthesized a set of semicarbazones containing 2, 5- disubstituted 1,3,4-oxadiazoles (Figure 20). All of them were screened for anticonvulsant activity through maximal electroshock seizure and subcutaneous Pentylenetetrazole models. Compounds having nitro or hydroxy on the phenyl ring possess high potency, but they can be replaced with methoxy and chloro substitution showed a decrease in activity(24). This study reveals that the hydroxyl-substituted compounds are more active than nitro, chloro and methoxy substituted ones.

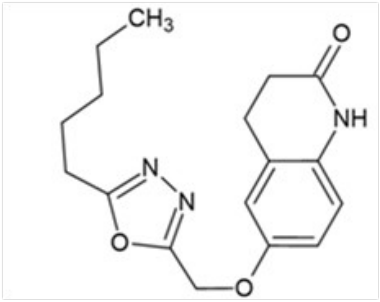

Figure 19: Dihydroquinolin with oxadiazole.

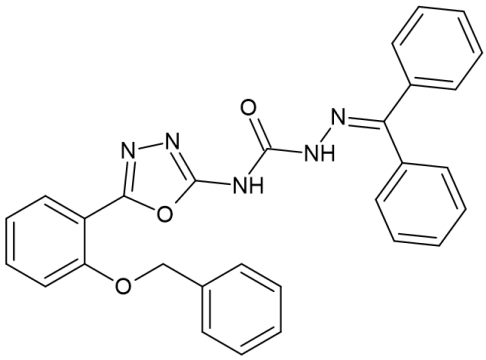

Figure 20: Oxadiazole with semicarbazone.

2.5. Commonly used synthetic strategies of 1,3,4-oxadizoles.

The 1,3,4-oxadiazole scaffolds were synthesized by various strategies (Figure 21) including the use of different hydrazides with carbon disulfide in DMF(Route A)(25), aromatic acids with POCl3(Route B)(26), and cyanogens bromide in ethanol (Route C)(27). The current review paper also focuses on synthetic methods that use all of these approaches A through C.

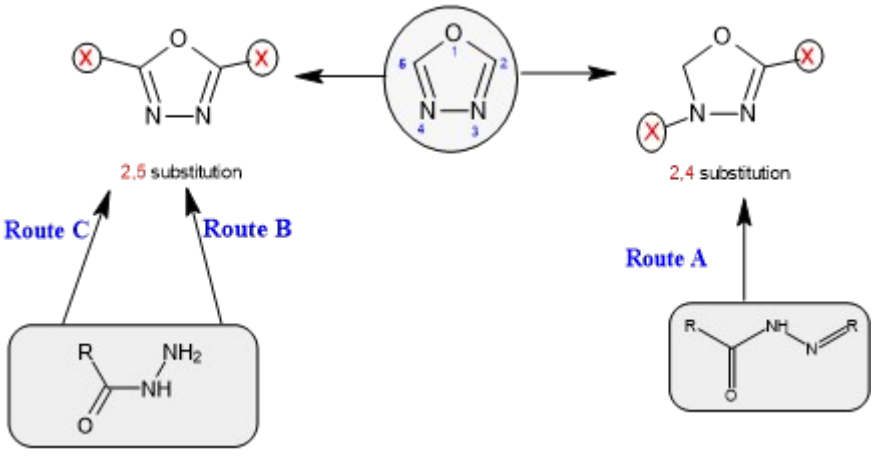

Figure 21: General strategy for the synthesis of 1,3,4-oxadiazoles.

Peraman *et al*. reported carbon disulfide-mediated synthesis of oxadiazole was achieved by cyclization in DMF. This was achieved by equimolar carbohydrazide treated with Quinoxalin-2,3(1H,4H)–dione (reflux) to give the corresponding carbohydrazide (Route A)(28). Then it was subjected to cyclization by using carbon disulfide in dimethyl formamide(Scheme 1)(6).

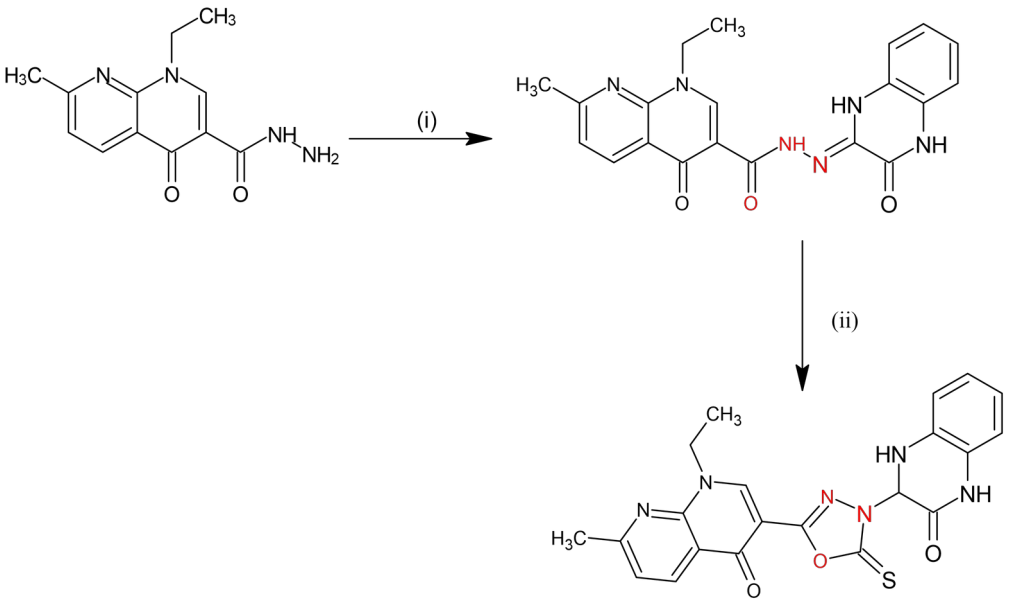

Scheme 1: Synthesis of 1,3,4-oxadiazole derivatives (i) Quinoxaline-2,3(1H, 4H)-dione, (ii) CS_2/DM.

M.A.Bhat *et al*. Reported the synthesis of 1,3,4-oxadiazole containing phthalimide by phosphorous oxychloridemediated reaction of hydrazinecarboxamide derivatives (Route B). This can be done by adding an ethanolic solution of an equimolar amount of hydrazine carboxamide (0.01 mol) to cyanogen bromide (0.01 mol) and warming at 55-60°C for one and half hours (7)(29). Then the solution was neutralized using $NaHCO_3$ (Scheme 2) (30). The same type of reaction is followed by Shingare *et al*. synthesized 1,3,4-oxadiazoles with the help of Phosphorus oxychloride and aromatic carboxylic acid by refluxing at 70ºC for 6-8 hours (Route C; Scheme 3)(8).

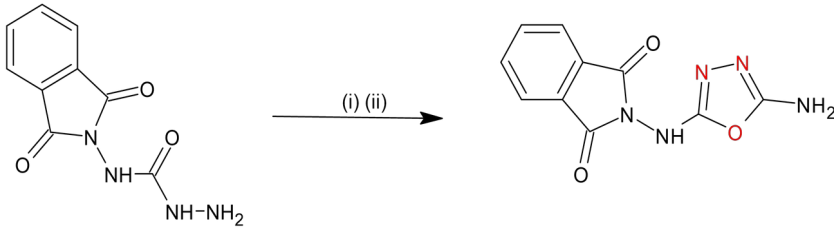

Scheme 2: Synthesis of 1,3,4-oxadiazole derivatives. (i): ethanolic solution of cyanogen bromide, (ii) $NaHCO_3$.

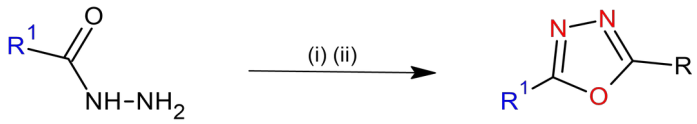

Scheme 3: Synthesis of 1,3,4-oxadiazole derivatives. (i): $POCl_3$, (ii): RCOOH, reflux, 6-8 h.

Sudhir Bhardwaj *et al*. applied a green chemistry approach for the synthesis (microwave-assisted) of Oxadiazoles (Scheme 4). This synthesis can be done by adding Silica gel to the different isonicotinohydrazide (0.01 mol) and acetic anhydride (10 mL) at room temperature(31). This mixture was mixed thoroughly and dried in air and irradiated in the microwave at 400W at 30s intervals. Methanol was used for extraction, and diluting the methanol solution with ice water gave the crude product(19).

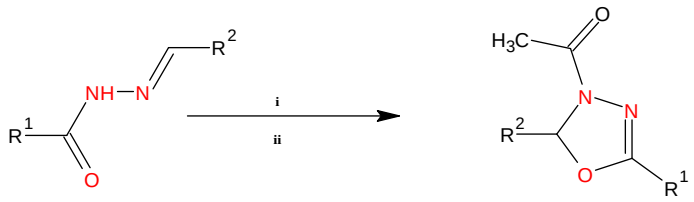

Scheme 4: Synthesis of 1,3,4-oxadiazole derivatives. (i): Acetic anhydride, (ii): silica gel, M.W.

4. CONCLUSION

Derivatives with a 1,3,4-oxadiazole core exhibit different biological activities. Various synthetic leads contain an oxadiazole core as part of the pharmacophore structure, facilitating the binding of these leads to binding site residues of the desired target. These initiatives have made oxadiazole a focus of research for the identification of new chemical entities.

As a summary of the literature findings mentioned above, we can state that 1,3,4-oxadiazole exhibits a wide range of biological activities. These are generally synthesized from different hydrazides with carbon disulfide, aromatic acids with $POCl_3$, cyanogens bromide in ethanol, or by green chemistry approach like microwave irradiation. The chemistry of the 1,3,4-oxadiazole derivatives discussed in this study will aid researchers all around the world in the design and synthesis of innovative pharmaceuticals that will be helpful in the mitigation of a variety of illnesses.

5. CONFLICT OF INTEREST

No potential conflicts of interest exist between the authors' authorship and the publishing, they disclose.

6. ACKNOWLEDGMENTS

Authors are thankful to Chettinad Academy of Research and Education for infrastructure support and CARE seed money research grant (Ref.No.004/Regr./AR-Research/2022-02)

7. REFERENCES

1. Qadir T, Amin A, Sharma PK, Jeelani I, Abe H. A Review on Medicinally Important Heterocyclic Compounds. Open Med Chem J. 2022;16(1):1–34.

2. Siwach A, Verma PK. Therapeutic potential of oxadiazole or furadiazole containing compounds. BMC Chem [Internet]. 2020;14(1):1–40. Available from: https://doi.org/10.1186/s13065-020-00721-2

3. Shukla C, Srivastav S. Biologically Active Oxadiazole. Asian J Res Pharm Sci. 2015;5(4):227.

4. Khalilullah H, J. Ahsan M, Hedaitullah M, Khan S, Ahmed B. 1,3,4-Oxadiazole: A Biologically Active Scaffold. Mini-Reviews Med Chem. 2012;12(8):789–801.

5. Xie Y, Yang W, Chen X, Xiao J. Inhibition of flavonoids on acetylcholine esterase: Binding and structure–activity relationship. Food Funct. 2014 Sep 24;5(10):2582–9.

6. Chawla G, Naaz B, Siddiqui AA. Exploring 1,3,4-Oxadiazole Scaffold for Anti-inflammatory and Analgesic Activities: A Review of Literature From 2005-2016. Mini-Reviews Med Chem. 2017 Feb 23;18(3).

7. Peraman R, Varma RV, Reddy YP. Re-engineering nalidixic acid's chemical scaffold: A step towards the development of novel anti-tubercular and anti-bacterial leads for resistant pathogens. Bioorganic Med Chem Lett. 2015 Oct 1;25(19):4314–9.

8. Jang C, Yadav DK, Subedi L, Venkatesan R, Venkanna A, Afzal S, *et al*. Identification of novel acetylcholinesterase inhibitors designed by pharmacophore-based virtual screening, molecular docking and bioassay. Sci Rep. 2018 Dec 1;8(1).

9. Bhat MA, Al-Omar MA, Siddiqui N. Synthesis, anticonvulsant and neurotoxicity of some novel 1,3,4-oxadiazole derivatives of phthalimide. Der Pharma Chem [Internet]. 2010;2(2):1–10. Available from: www.derpharmachemica.com

10. Shingare RM, Patil YS, Sangshetti JN, Patil RB, Rajani DP, Madje BR. Synthesis, biological evaluation and docking study of some novel isoxazole clubbed 1,3,4-oxadiazoles derivatives. Med Chem Res [Internet]. 2018;27(4):1283–91. Available from: http://dx.doi.org/10.1007/s00044-018-2148-2

11. Alghamdi AA, Alam MM, Nazreen S. In silico ADME predictions and in vitro antibacterial evaluation of 2-hydroxy benzothiazole-based 1,3,4-oxadiazole derivatives. Turkish J Chem. 2020;44(4):1068–84.

12. George N, Sabahi B Al, AbuKhader M, Balushi K Al, Akhtar MJ, Khan SA. Design, synthesis and in vitro biological activities of coumarin linked 1,3,4-oxadiazole hybrids as potential multi-target directed anti-Alzheimer agents. J King Saud Univ - Sci. 2022 Jun 1;34(4).

13. Colovic MB, Krstic DZ, Lazarevic-Pasti TD, Bondzic AM, Vasic VM. Acetylcholinesterase Inhibitors: Pharmacology and Toxicology. Curr Neuropharmacol. 2013;11(3):315–35.

14. Kumari P, Tripathi A, Kumar M, Seth A, Kumar S. Bioorganic Chemistry diazole as multitargeted hybrids for the treatment of Alzheimer ' s disease. 2021;111(April).

15. Dhanjal JK, Sharma S, Grover A, Das A. Use of ligand-based pharmacophore modeling and docking approach to find novel acetylcholinesterase inhibitors for treating Alzheimer's. Biomed Pharmacother. 2015 Apr 1;71:146–52.

16. Mishra P, Sharma P, Tripathi PN, Gupta SK, Srivastava P, Seth A, *et al*. Design and development of 1,3,4-oxadiazole derivatives as potential inhibitors of acetylcholinesterase to ameliorate scopolamine-induced

cognitive dysfunctions. Bioorg Chem [Internet]. 2019;89:103025. Available from: https://doi.org/10.1016/j.bioorg.2019.103025

17. Kumar Singh A, Lohani M, Parthsarthy R. Synthesis , Characterization and Anti-Inflammatory Activity of Various Isatin Derivatives. Iran J Pharm Res [Internet]. 2013;12(2):319–23. Available from: https://www.ncbi.nlm.nih.gov/pmc/articles/PMC3813233/

18. Tomasz G. New 1 , 3 , 4-Oxadiazole Derivatives of Pyridothiazine- 1 , 1-Dioxide with Anti-Inflammatory Activity. Int J Mol Sci. 2020;21:1–22.

19. Grover J, Bhatt N, Kumar V, Patel NK, Gondaliya BJ, Elizabeth Sobhia M, *et al*. 2,5-Diaryl-1,3,4-oxadiazoles as selective COX-2 inhibitors and anti-inflammatory agents. RSC Adv [Internet]. 2015;5(56):45535–44. Available from: http://dx.doi.org/10.1039/C5RA01428J

20. Bhardwaj S, Parashar B, Parashar N, Sharma VK. Microwave assisted synthesis and pharmacological evaluation of. Arch Appl Sci Res [Internet]. 2011;3(2):558–67. Available from: www.scholarsresearchlibrary.com

21. Banik BK, Sahoo BM, Kumar BVVR, Panda KC, Jena J, Mahapatra MK, *et al*. Green synthetic approach: An efficient eco-friendly tool for synthesis of biologically active oxadiazole derivatives. Molecules. 2021;26(4).

22. Singh RB, Singh GK, Chaturvedi K, Kumar D, Singh SK, Zaman MK. Design, synthesis, characterization, and molecular modeling studies of novel oxadiazole derivatives of nipecotic acid as potential anticonvulsant and antidepressant agents. Med Chem Res [Internet]. 2018;27(1):137–52. Available from: http://dx.doi.org/10.1007/s00044-017-2047-y

23. Wang S, Liu H, Wang X, Lei K, Li G, Li J, *et al*. Synthesis of 1,3,4-oxadiazole derivatives with anticonvulsant activity and their binding to the GABAA receptor. Eur J Med Chem [Internet]. 2020;206:112672. Available from: https://doi.org/10.1016/j.ejmech.2020.112672

24. Rajak H, Singour P, Kharya MD, Mishra P. A Novel Series of 2,5-Disubstituted 1,3,4-oxadiazoles: Synthesis and SAR Study for their Anticonvulsant Activity. Vol. 77, Chemical Biology and Drug Design. 2011. p. 152–8.

25. Mickevičius V, Vaickelionienė R, Sapijanskaitė B. Synthesis of substituted 1,3,4-oxadiazole derivatives. Chem Heterocycl Compd. 2009;45(2):215–8.

26. Nazari M, Rezaee E, Hariri R, Akbarzadeh T, Tabatabai SA. Novel 1,2,4-oxadiazole derivatives as selective butyrylcholinesterase inhibitors: Design, synthesis, and biological evaluation. EXCLI J. 2021;20:907–21.

27. Pflégr V, Štěpánková Š, Svrčková K, Švarcová M, Vinšová J, Krátký M. 5-Aryl-1,3,4-Oxadiazol-2-Amines Decorated with Long Alkyl and Their Analogues: Synthesis, Acetyl-and Butyrylcholinesterase Inhibition and Docking Study. Pharmaceuticals. 2022;15(4):1–21.

28. Ergenç N, Çapan G, Demirdamar R. Synthesis, characterization and analgesic activity of new 4-arylhydrazono-3-methoxymethyl-2-pyrazolin-5-ones. Arzneimittel-Forschung/Drug Res. 2001;51(2):118–24.

29. Vaidya A, Pathak D, Shah K. 1,3,4-oxadiazole and its derivatives: A review on recent progress in anticancer activities. Chem Biol Drug Des. 2021 Mar 1;97(3):572–91.

30. Parikh PK, Marvaniya HM, Sen DJ. Synthesis and biological evaluation of 1,3,4-oxadiazole derivatives as potential antibacterial and antifungal agents. Int J Drug Dev Res [Internet]. 2011;3(2):248–55. Available from: http://www.ijddr.in

31. Misra HK. Synthesis of Some New Substituted 1,3,4-Oxadiazoles as Potential Insecticidal, Antibacterial and Anti-acetylcholine Esterase Agents. Arch Pharm (Weinheim). 1983;316(6):487–93.

JOTCS A
Journal of the Turkish Chemical Society
Section: A
Chemistry

TURKISH
CHEMICAL SOCIETY

Synthesis of Imino Stabilized Iron Oxide Nanosensor for Selective Detection of Lead Ions

Erum Hasan[1], Syed Nawazish Ali[1]*, Ambreen Zia[1], Sabira Begum[2], Salman Tariq Khan[3], and Syeda Farah Bukhari[1]

[1]University of Karachi, Department of Chemistry, 75270, Karachi, Pakistan.
[2]University of Karachi, Department of Chemistry, 75270, Karachi, Pakistan.
[3]Pharmaceutical Research Centre, PCSIR Laboratories Complex, Karachi, 75280, Pakistan.

Abstract: The present work describes the successful preparation of iron oxide nanoparticles (NSB1) stabilized with 4-((2-hydroxybenzylidene)amino)benzoic acid. The characterization has been achieved through ultraviolet visible (UV-Vis), fourier transform infra-red (FTIR) spectroscopy and scanning electron microscopy (SEM) with electron dispersive X-ray elemental analysis (EDX). These magnetic nanoparticles have exhibited significant chemosensing properties in the aqueous media to screen Cr^{3+}, Cd^{2+}, Li^{+}, Co^{2+}, Al^{3+}, Pb^{2+}, Ni^{2+} and Sr^{2+} ions. However, lead (Pb^{2+}) ions have shown the highest selectivity as compared to other metal ions without any interference in the competitive ion study. The detection limit of Pb^{2+} ions was found to be 1.7 µM by this nanosensor. The binding ratio and stoichiometry was found to be 1:1 as measured by Job's plot. The binding strength was also computed through Benesei-Hildebrand equation.

Keywords: Iron oxide nanoparticles, p-aminobenzoic acid, Job's plot, chemosensors, Schiff base, lead ions detection.

Submitted: April 18, 2022. **Accepted:** January 26, 2023.

Cite this: Hasan E, Ali SN, Zia A, Begum S, Khan ST, Bukhari SF. Synthesis of Imino Stabilized Iron Oxide Nanosensor for Selective Detection of Lead Ions. JOTCSA. 2023;(2):277–86.

DOI: https://doi.org/10.18596/jotcsa.1097197.

***Corresponding author. E-mail:** syed.nawazish@gmail.com.

1. INTRODUCTION

Lead ions (Pb^{2+}) are responsible for the contamination of water, food and soil due to their nonbiodegradable nature and accumulation in the environment (1-3). However, trace amount of lead is potent as toxicant (4) and pigment (5). It acts as enzyme inhibitor when it coheres with SH group in proteineous enzyme. Tetramethyl lead , an organic compound of lead, is also exceptionally toxic because it is prone to absorb by the body through mucus membrane and skin (4). Prolong accumulation of Pb^{2+} is lethal for peripheral and central nervous system as it causes numerous life threatening diseases including memory loss, nervous muscles paralysis, hypertension, kidney failure, abnormality in reproductive system, lungs and liver damages (1-4, 6, 7). Lead pollution is also inevitable due to excessive use of lead containing products in our daily life such as coal combustion, gasoline, usage of paint in water supply system and lead acid batteries. Thereby, development of sensitive and reliable methods for lead detection is of great interest across the world.

Normally, lead analysis has been done through various spectrophotometric methods such as liquid phase micro-extraction with atomic absorption spectroscopy (8), inductively coupled plasma mass spectrometry (ICP-MS) (9, 10), dynamic light scattering technique (11, 12), functional nucleic acids (*e.g.* DNA enzymes, aptamers)-based sensors (13), electrochemical (14-16), and optical methods including fluorimetric (17-22), UV-Vis spectrophotometry (23), chemiluminescence (24), visual detection (25), and photonic crystal optrode (26). In present studies, we report ~~the~~ a rapid synthesis of magnetic nanoparticles under mild reaction conditions. These particles are utilized for selective detection of lead ion in the presence of other metal ions resulted in the development of a new chemosensor.

2. EXPERIMENTAL SECTION

2.1. Material

Para aminobenzoic acid (PABA), lead acetate, ferrous sulfate, ferric chloride, and ammonium hydroxide were purchased from Sigma Aldrich.

2.2. Instrumentation

UV-Visible spectra were recorded on Shimadzu UV-240 spectrophotometer in the range of 200-800 nm with 1 cm path length in quartz cell whereas pH was measured by PHS-3B microprocessor pH meter. Infrared spectra have been monitored through FTIR spectrophotometer (Shimadzu IR-Prestige-21) using KBr pellet. EIMS (Mass spectrometry, JEOL JMS600H-1) was performed to confirm the molecular mass of NSB (iminobase). SEM (Scanning electron microscopy, JEOL from Japan, JSM-6380A; Sample coater model#JFC-1500) was used to examine the size and morphological characterization of nanoparticle. Moreover, the elemental composition was obtained by the help of EDX (Energy-dispersive X-ray spectroscopy, Model No: EX-54175IMU, JEOL Japan, the sample was coated up to 300 µA with gold).

2.3. Synthesis of Schiff base

The formation of 4-((2-hydroxybenzylidene)amino)benzoic acid (NSB) was done by the addition of salicylaldehyde (10.0 mmol, 1.06 mL) into a methanolic solution of PABA (10.0 mmol, 1.37 g) in a 100mL round bottom flask for 30 minutes stirring using a magnetic stirrer (Scheme 1). The obtained yellow precipitates of NSB were filtered and washed with methanol (27).

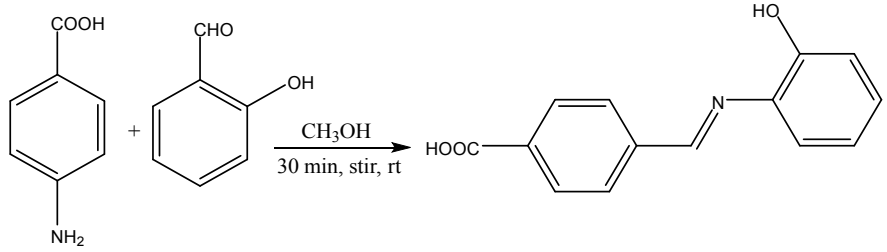

Scheme 1: Synthesis of 4-((2-hydroxybenzylidene)amino)benzoic acid (NSB).

4-((2-hydroxybenzylidene)amino)benzoic acid: Color yellow, Yield: 1.68 g (70%); m.p: 268 °C; FT-IR ($\bar{\upsilon}_{max}$, cm^{-1}): (Stretch, OH) 3426, (sp^2 C–H stretch) 2985, (COO, asymmetric) 1651, (C=C, aromatic) 1593, 1435, (HC=N) 1583, (COO, symmetric) 1377, (C–N) 1288; UV (λ_{max}, nm) 387 π-π* and 321 n-π* transition (azomethine linkage), 245 π-π* transition (aromatic ring); ^{1}H NMR (DMSO-d_6) δ : 11.14 (s, 1H, COOH), 8.26 (d, 2H, J = 8.2 Hz, Ar), 8.18 (d, 2H, J = 8.2 Hz, Ar), 8.16 (s, 1H, HC=N), 7.68 (d, 2H, J = 8.1 Hz, Ar), 7.10 (t, 1H, J = 8.0 Hz, Ar), 6.84 (t, 1H, J = 8.0 Hz, Ar); EIMS (70 eV): m/z 241.

2.4. Preparation of iron oxide nanoparticles (NSB1)

NSB (0.62 g, 4.5 mmol) was dissolved in deionized water (75 mL) at 80 ℃ in a conical flask. An aqueous solution of $FeCl_3.6H_2O$ (1.17 g in 5 mL, 4.3 mmol) was dropwise added into the flask with stirring time of 30 minutes. The aqueous solution of $FeSO_4{\cdot}7H_2O$ (0.94 g in 2 mL, 3.3 mmol) was also added followed by continuous stirring for 30 minutes. Then, NH_4OH (10 mL) was poured and continued to stir for 60 minutes until the brown suspension of NSB1 was obtained (Scheme 2). Washing of nanoparticles was done with deionized water and methanol.

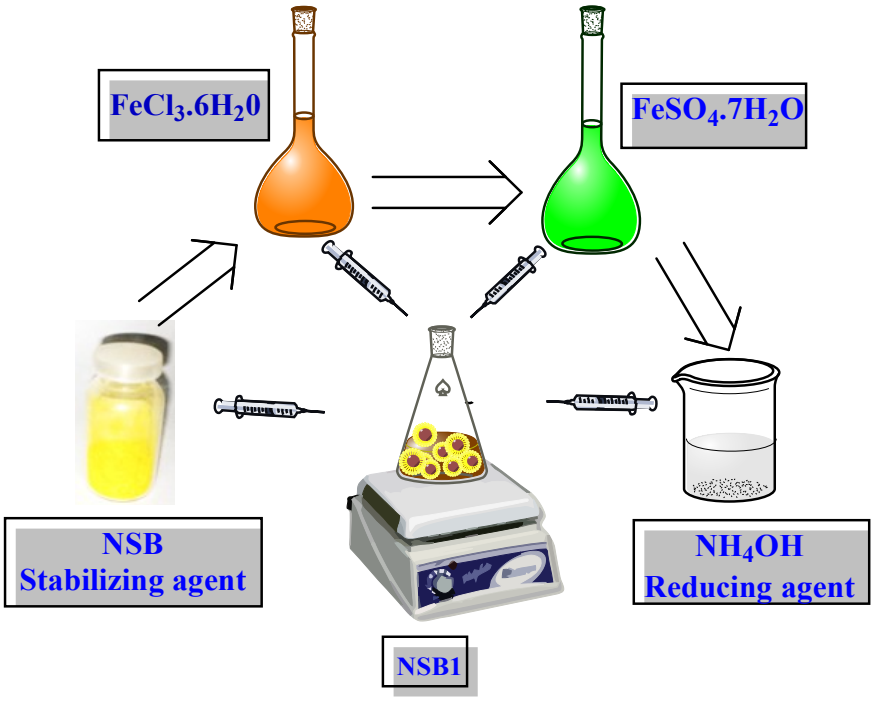

Scheme 2: Synthesis of Iron nanoparticles (NSB1).

3. RESULTS AND DISCUSSION

3.1. NSB and NSB1 comparative FTIR and UV spectra

The FTIR spectrum of NSB and NSB1 were comparatively studied. The absorption band at 3426 cm^{-1} attributes to -OH group whereas the stretching frequencies at 1593 and 1435 cm^{-1} confirms the presence of aromatic C=C functionality. The absorption frequency peak at about 1583 cm^{-1} accredites to HC=N (imine) functional group. The shifting, broadening, and disappearance of certain functional groups show their interaction with nanoparticles for stabilization. The absence of carboxylate stretching frequencies, broadening of aromatic hydrogen peaks (1651 and 1377 cm^{-1}) and weakening of imine group intensity shows the participation of these functionalities (Figure 1). Hence it is anticipated that imine and carbonyl groups work for stabilization of iron nanoparticles.

Ultraviolet visible spectra showed maximum absorbance at 387 and 321 nm due to π-π* and n-π* electronic transition (28) for imine group. On the other hand the absorption maxima at 244 nm was assigned to aromatic acid (Figure 2). The absorption maxima at 260 nm is also in accordance to the reported value of O^{2-}/Fe^{3+} ligand to metal charge transfer transitions to confirm the formation of iron oxide nanoparticles (29). The shifting of absorption maxima also confirmed the involvement of certain functional groups as capping and stabilizing agents.

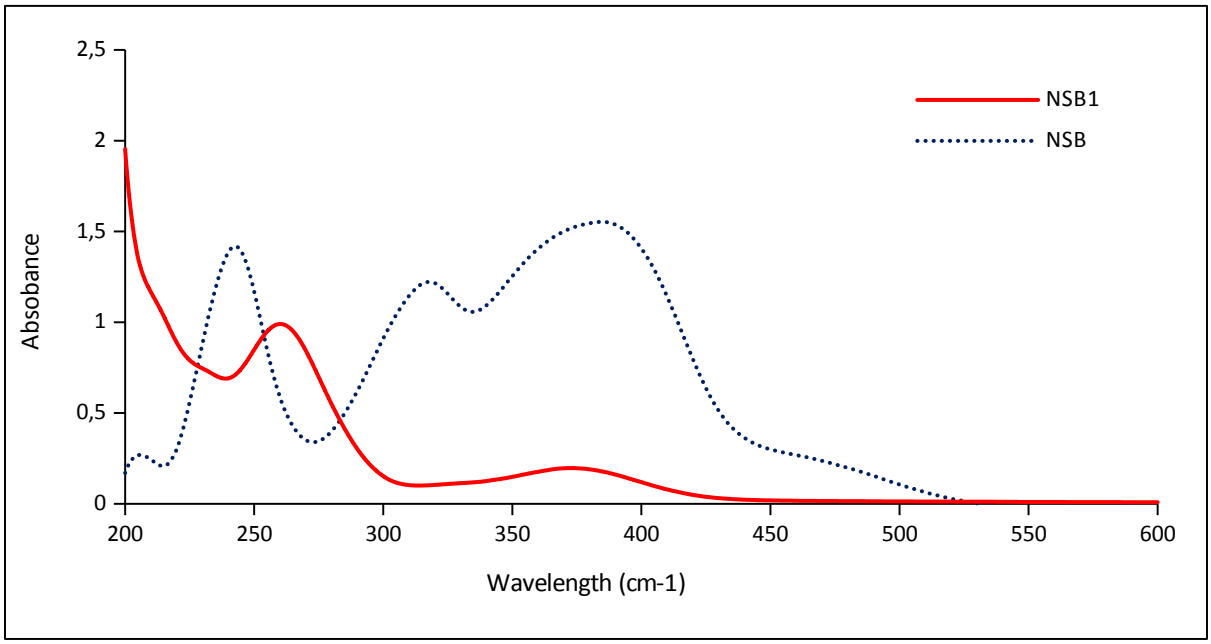

Figure 1: FTIR Spectra of NSB and NSB1.

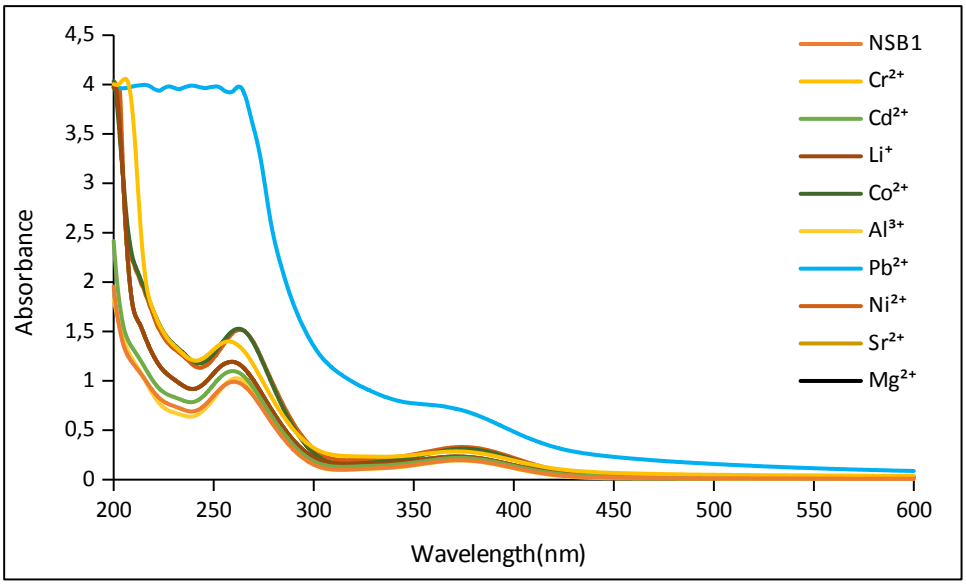

Figure 2: UV-visible spectra of NSB and NSB1.

3.2. SEM and EDX analysis of NSB1

The morphology of iron oxide nanoparticles was analyzed by SEM technique. The obtained results clearly showed the spherically shaped nanoparticles (NSB1) with average size of 87-97 nm (Figure 3).

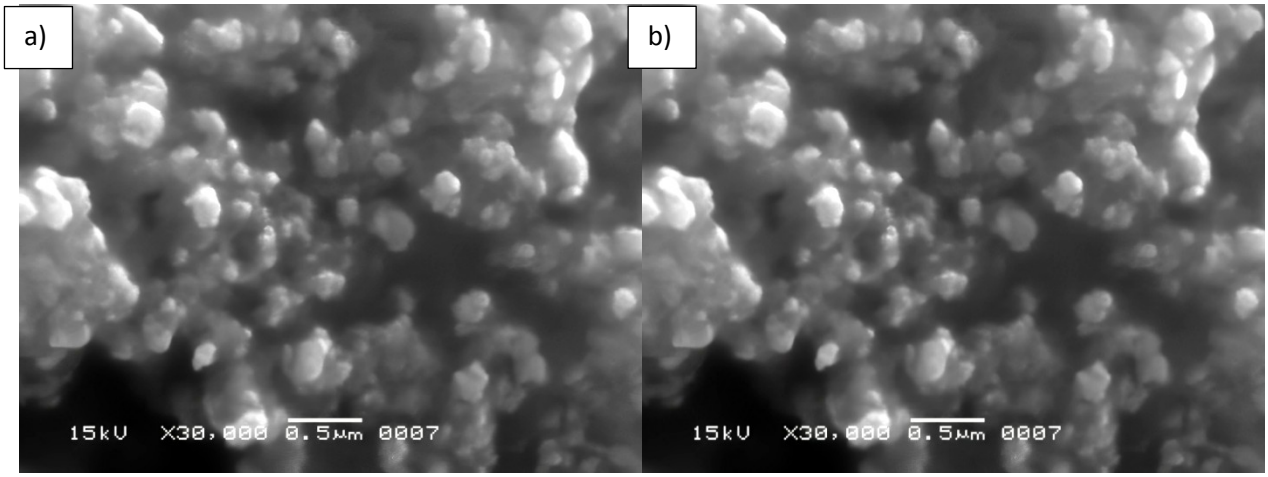

Figure 3: SEM images of NSB1.

EDX analysis also indicates the presence of elements with their mass percentage. However there is slight difference in calculated values due to the presence of other elements. In addition to iron and oxygen, carbon was also appeared due to the interactions of nanoparticles with organic compounds whereas minor quantity of chloride was also observed from other source (Figure 4). Elemental analysis % calculated (observed): Fe 69.94 (74.72), O 30.06 (21.26)

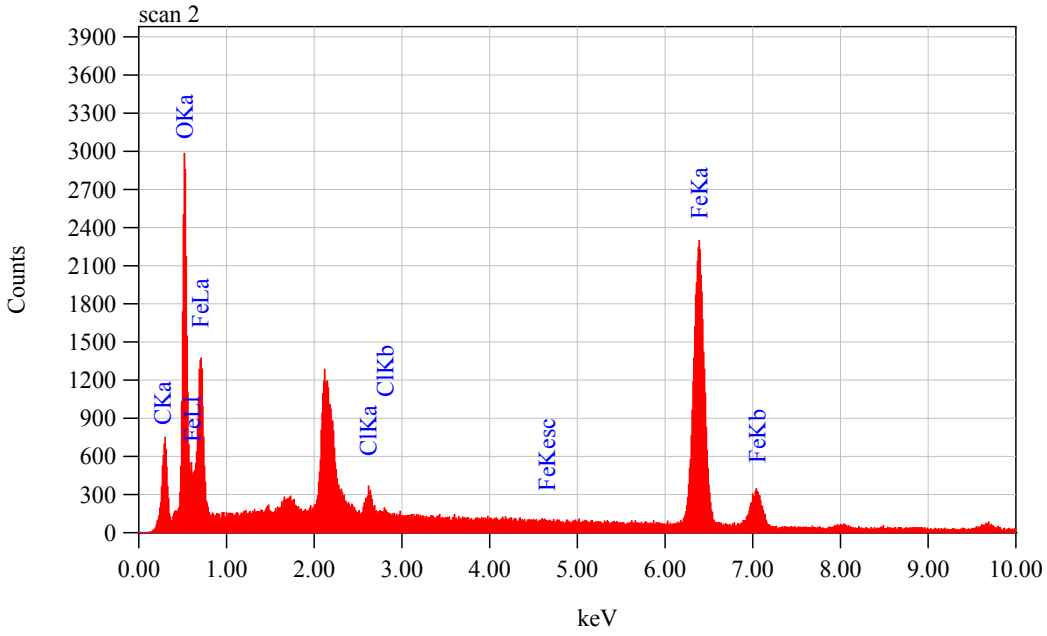

Figure 4: EDX spectrum of chemical elements on iron oxide nanparticles.

3.3. Screening of metal ions

Various metals Cr^{3+}, Cd^{2+}, Li^{+}, Co^{2+}, Al^{3+}, Pb^{2+}, Ni^{2+} and Sr^{2+} were investigated through UV-Vis spectrophotometric method as shown in Figure 5. NSB1 showed highest absorbance at 260 nm. Presently synthesized magnetic nanoparticles are found highly selective for lead because a prominent enhancement was observed with Pb^{2+} whereas other ions were remained unaffected.

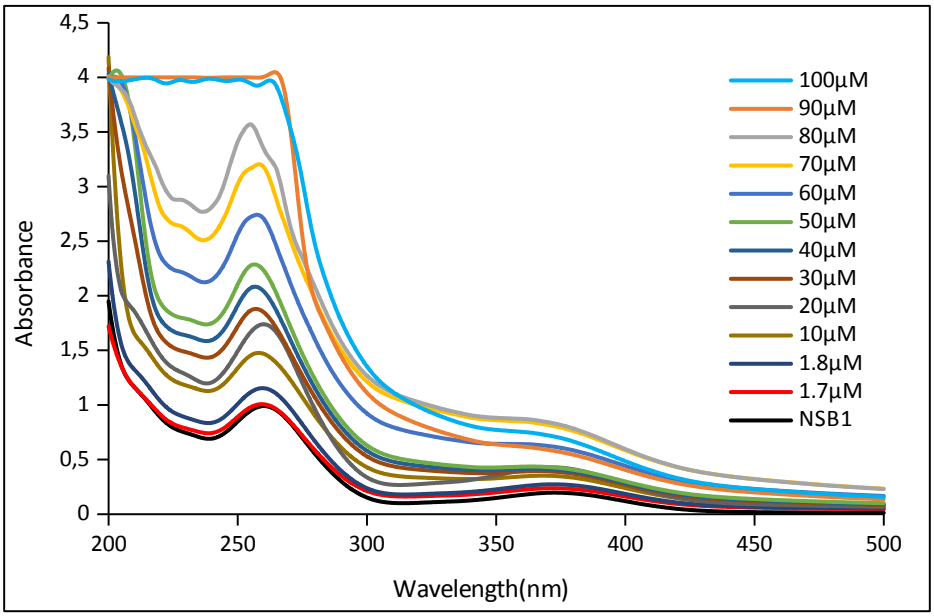

Figure 4: Screening of metals by using mixture of NSB1 and metalsalts solution (1:1).

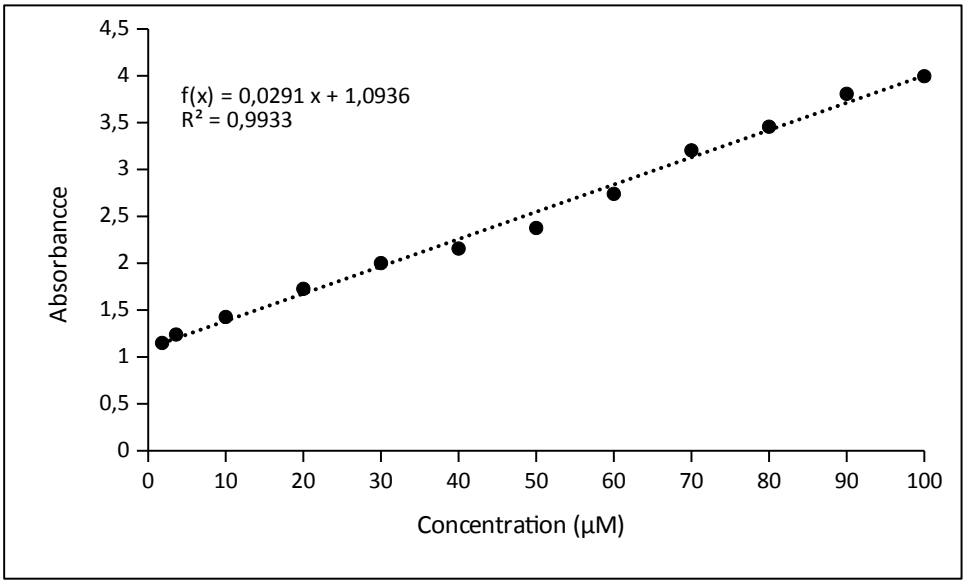

Figure 5a: Limit of detection was measured by the gradual decreasing in concentration of Pb^{2+} salt solution.

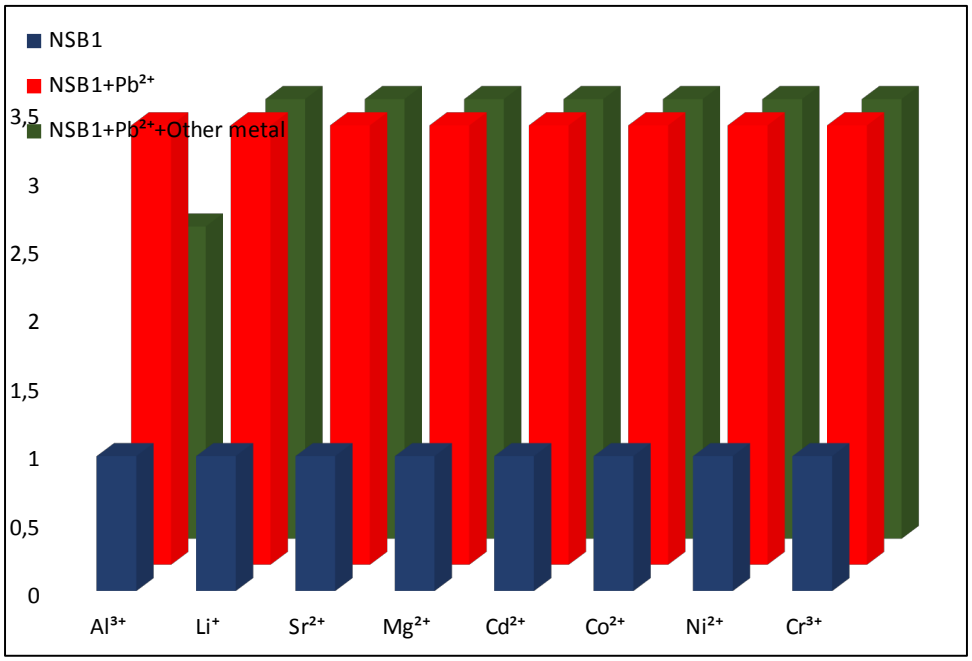

Figure 5b: Regression curve was plotted to determine uniform absorbance reduction with gradual decreasing of concentration of metal ion.

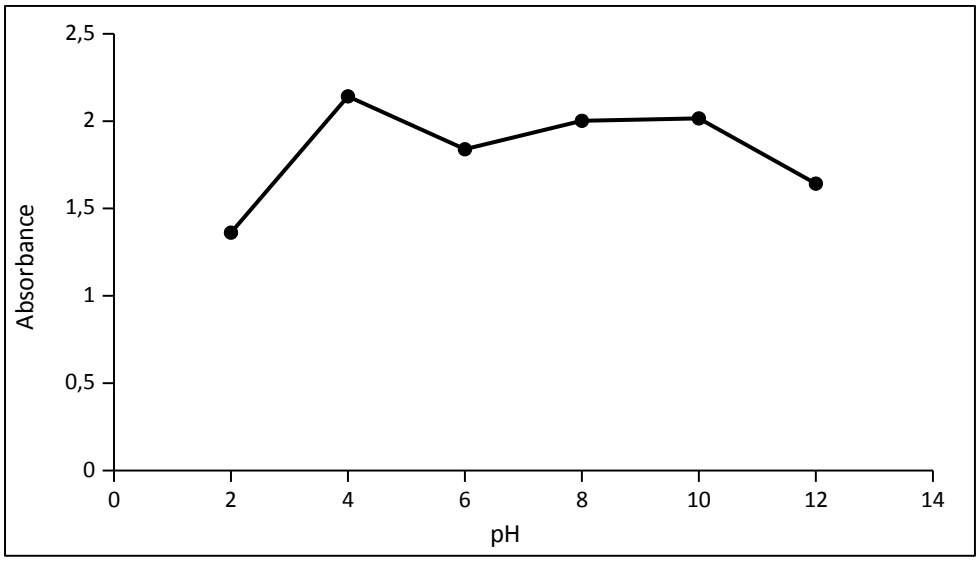

Figure 6: Competitive study of NSB1 to determine its selectivity in prevalence of other metal ions.

The binding detection limit for Pb^{2+} ions with NSB1 is shown in Figure 6a. The absorbance was recorded by successive decrease in concentration of lead while keeping the concentration of NSB1 constant. The highest selectivity for lead and NSB1 is observed in the presence of multiple metal ions (100 µM) in the recognition study as shown in Figure 7. The iron nanoparticles showed great affinity towards lead ions and this association remained undisturbed in the presence of other metal ions.

Behaviour of NSB1 towards lead ions has been evaluated at various pH (2, 4, 6, 8, 10, and 12) as presented in Figure 8. The Aqueous solutions of NaOH and HCl were used to adjust the pH values. The absorbance was decreased by addition of acid due to protonation of imine group which may destabilize nanoparticle. However the absorbance was found nearly unchanged , on increasing the pH. It may be due to the presence of free imine group which eventually stabilizes the NSB1.

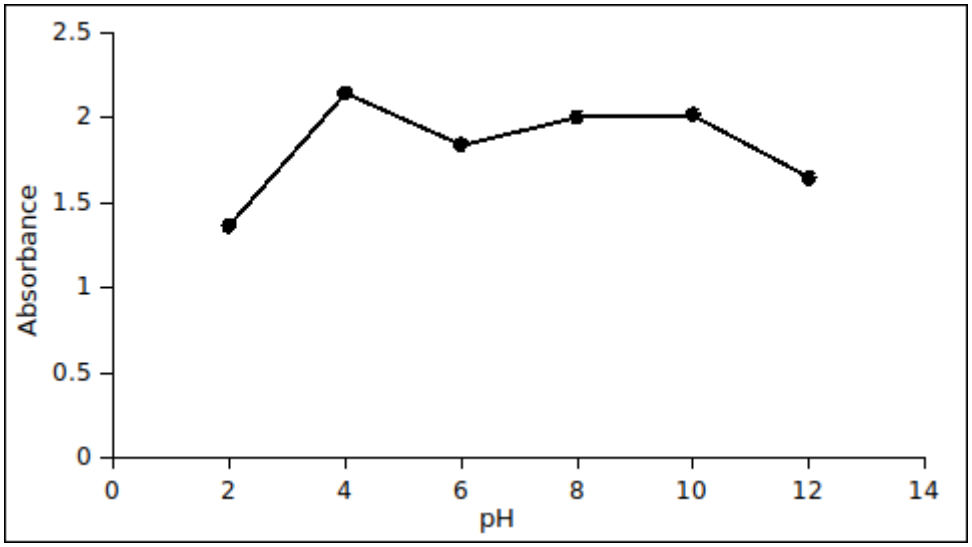

Figure 7: Binding of NSB1 with Pb^{2+} ion at different pH.

The binding ratio of complexation was measured by Job's plot in which absorbance was plotted against mole fraction of lead ions at gradual variation of mole fractions as shown in Figure 9. The favorable binding stoichiometry between NSB1 and lead ions was observed to be 1:1.

The binding constant (Ka) for NSB1 and metal complex was determined by using absorbance titration data (Figure 10). This value was computed through Benesie-Hildebrand equation (Eq. 1) and found to be 16.66×10^3 M^{-1} (30).

$$\frac{1}{A-A_0}=\frac{1}{A_1-A_0}+\frac{1}{A_1-A_0 Ka[Pb^{2+}]} \quad \text{(Eq.1)}$$

Where A_0 is the absorbance of NSB1, A is the absorbance in the presence of Pb^{2+}, A1 is the absorbance upon saturation with lead ion and Ka is the binding constant of the complex.

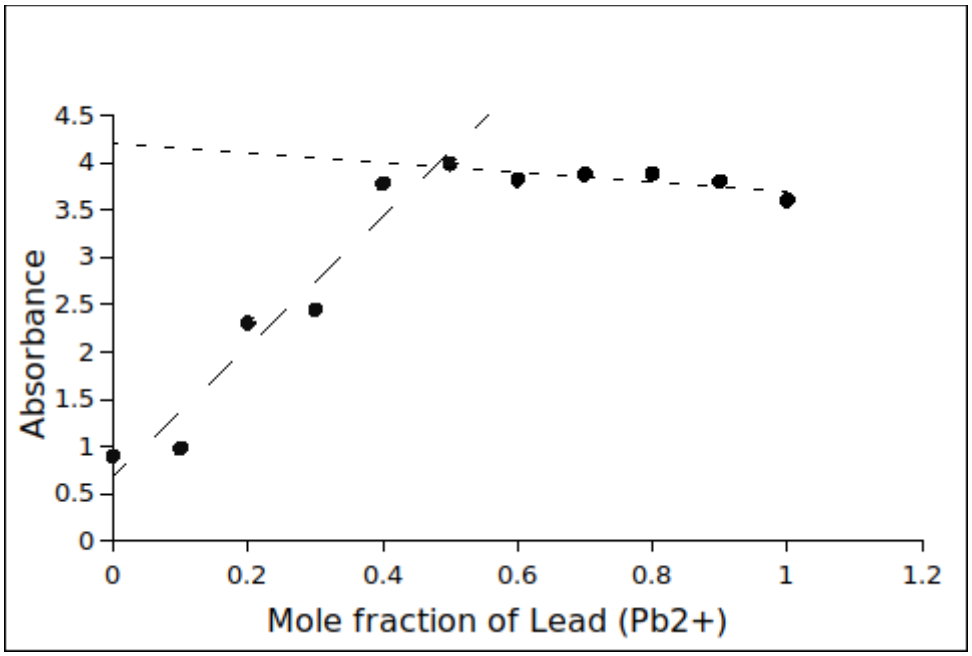

Figure 8: Job's plot of the complexation of NSB1 along with lead.

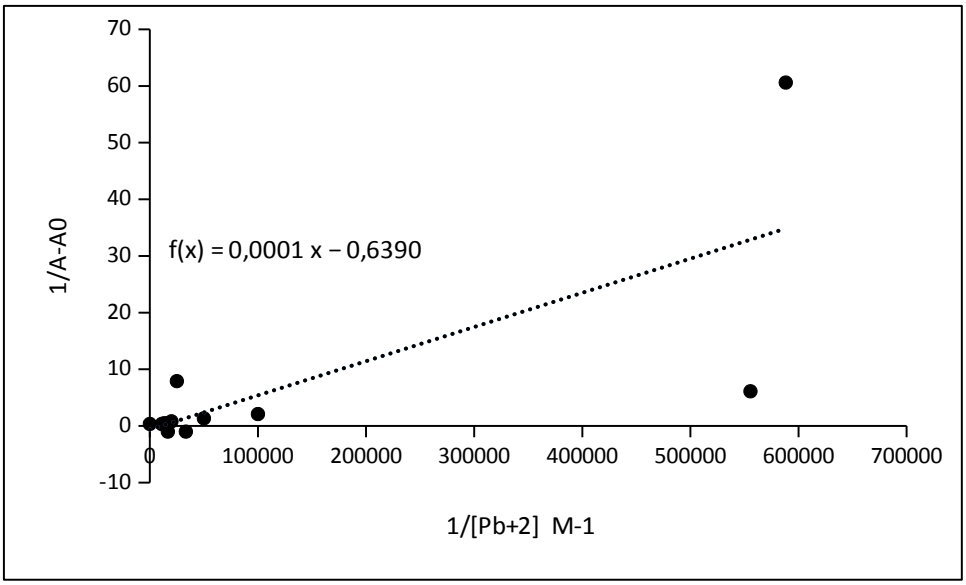

Figure 9: Stability constant of complexation measure by applying Benesi Hildebrand equation.

4. CONCLUSION

A selective magnetic nanosensor stabilized by Schiff base was prepared for rapid detection of lead ions through UV-Visible spectrophotometer. The detection of lead ions has been carried out by considering its toxic effects on environment and human. This nanosensor is cost effective very compitable to human body due to the presence of iron. The obtained nanoparticle revealed the limit of detection upto 1.7 µM for lead ions and its selectivity in the presence of other metal ions. The binding ratio and stoichiometry was found to be 1:1 as measured by Job's plot. The binding strength was also computed through Benesei-Hildebrand equation.

5. REFERENCES

1. Zhu G, Zhang C yang. Functional nucleic acid-based sensors for heavy metal ion assays. Analyst. 2014 Sep 25;139(24):6326–42. Available from: <URL>.

2. Kim HN, Ren WX, Kim JS, Yoon J. Fluorescent and colorimetric sensors for detection of lead, cadmium, and mercury ions. Chem Soc Rev. 2012;41(8):3210–44. Available from: <URL>.

3. Lin YW, Huang CC, Chang HT. Gold nanoparticle probes for the detection of mercury, lead and copper ions. Analyst. 2011;136(5):863–71. Available from: <URL>.

4. Khan H, Jamaluddin Ahmed M, Iqbal Bhanger M. A simple spectrophotometric method for the determination of trace level lead in biological samples in the presence of aqueous micellar solutions. Spectroscopy. 2006;20(5–6):285–97. Available from: <URL>.

5. Clayton GD, Clayton FE. Patty's industrial hygiene and toxicology. Vol. 2A. Toxicology. John Wiley & Sons, Inc., Baffins Lane, Chichester, Sussex PO19 1DU; 1981. ISBN: 978-0-471-16042-7.

6. Steenland K, Boffetta P. Lead and cancer in humans: Where are we now? Am J Ind Med. 2000 Sep;38(3):295–9. Available from: <URL>.

7. Aragay G, Pons J, Merkoçi A. Recent Trends in Macro-, Micro-, and Nanomaterial-Based Tools and Strategies for Heavy-Metal Detection. Chem Rev. 2011 May 11;111(5):3433–58. Available from: <URL>.

8. Rivas RE, López-García I, Hernández-Córdoba M. Microextraction based on solidification of a floating organic drop followed by electrothermal atomic absorption spectrometry for the determination of ultratraces of lead and cadmium in waters. Anal Methods. 2010;2(3):225. Available from: <URL>.

9. Grindlay G, Mora J, Gras L, de Loos-Vollebregt MTC. Ultratrace determination of Pb, Se and As in wine samples by electrothermal vaporization inductively coupled plasma mass spectrometry. Analytica Chimica Acta. 2009 Oct;652(1–2):154–60. Available from: <URL>.

10. Hsieh HF, Chang WS, Hsieh YK, Wang CF. Lead determination in whole blood by laser ablation coupled with inductively coupled plasma mass spectrometry. Talanta. 2009 Jul 15;79(2):183–8. Available from: <URL>.

11. Miao X, Ling L, Shuai X. Ultrasensitive detection of lead(ii) with DNAzyme and gold nanoparticles probes by using a dynamic light scattering technique. Chem Commun. 2011;47(14):4192. Available from: <URL>.

12. Beqa L, Singh AK, Khan SA, Senapati D, Arumugam SR, Ray PC. Gold Nanoparticle-Based Simple Colorimetric and Ultrasensitive Dynamic Light Scattering Assay for the Selective Detection of Pb(II) from Paints, Plastics, and Water Samples. ACS Appl Mater Interfaces. 2011 Mar 23;3(3):668–73. Available from: <URL>.

13. Nie D, Wu H, Zheng Q, Guo L, Ye P, Hao Y, et al. A sensitive and selective DNAzyme-based flow cytometric method for detecting Pb^{2+} ions. Chem Commun. 2012;48(8):1150–2. Available from: <URL>.

14. Wang B, Luo B, Liang M, Wang A, Wang J, Fang Y, et al. Chemical amination of graphene oxides and their

extraordinary properties in the detection of lead ions. Nanoscale. 2011;3(12):5059. Available from: <URL>.

15. Lin CH, Wu HL, Huang YL. Combining high-performance liquid chromatography with on-line microdialysis sampling for the simultaneous determination of ascorbyl glucoside, kojic acid, and niacinamide in bleaching cosmetics. Analytica Chimica Acta. 2007 Jan;581(1):102–7. Available from: <URL>.

16. Hou R, Niu X, Cui F. A label-free biosensor for selective detection of DNA and Pb $^{2+}$ based on a G-quadruplex. RSC Adv. 2016;6(10):7765–71. Available from: <URL>.

17. Zhao XH, Kong RM, Zhang XB, Meng HM, Liu WN, Tan W, et al. Graphene–DNAzyme Based Biosensor for Amplified Fluorescence "Turn-On" Detection of Pb $^{2+}$ with a High Selectivity. Anal Chem. 2011 Jul 1;83(13):5062–6. Available from: <URL>.

18. Wang X, Guo X. Ultrasensitive Pb2+ detection based on fluorescence resonance energy transfer (FRET) between quantum dots and gold nanoparticles. Analyst. 2009;134(7):1348. Available from: <URL>.

19. Hu ZQ, Lin C sheng, Wang XM, Ding L, Cui CL, Liu SF, et al. Highly sensitive and selective turn-on fluorescent chemosensor for Pb2+ and Hg2+ based on a rhodamine–phenylurea conjugate. Chem Commun. 2010;46(21):3765. Available from: <URL>.

20. Li T, Dong S, Wang E. A Lead(II)-Driven DNA Molecular Device for Turn-On Fluorescence Detection of Lead(II) Ion with High Selectivity and Sensitivity. J Am Chem Soc. 2010 Sep 29;132(38):13156–7. Available from: <URL>.

21. Wu J, Qin Y. Polymeric optodes based on upconverting nanorods for fluorescence measurements of Pb2+ in complex samples. Sensors and Actuators B: Chemical. 2014 Mar;192:51–5. Available from: <URL>.

22. Tümay SO, Şanko V, Şenocak A, Demirbas E. A hybrid nanosensor based on novel fluorescent iron oxide nanoparticles for highly selective determination of Hg $^{2+}$ ions in environmental samples. New J Chem. 2021;45(32):14495–507. Available from: <URL>.

23. Ge L, Liu H. Engineering Grey Nanosystem as Activatable Ratio-colorimetric Probe for Detection of Lead Ions in Preserved Egg. ANAL SCI. 2020 Nov;36(11):1407–13. Available from: <URL>.

24. Elbaz J, Shlyahovsky B, Willner I. A DNAzyme cascade for the amplified detection of Pb2+ ions or l-histidine. Chem Commun. 2008;(13):1569. Available from: <URL>.

25. Liu XH, Zheng H, Zhong L, Huang S, Karki K, Zhang LQ, et al. Anisotropic Swelling and Fracture of Silicon Nanowires during Lithiation. Nano Lett. 2011 Aug 10;11(8):3312–8. Available from: <URL>.

26. Reese CE, Asher SA. Photonic Crystal Optrode Sensor for Detection of Pb $^{2+}$ in High Ionic Strength Environments. Anal Chem. 2003 Aug 1;75(15):3915–8. Available from: <URL>.

27. Hamid A, Aamer S, Farukh J, Abdul B, Irfan ZQ, Abdul A, et al. Synthesis, Characterization, Biological and Docking Simulations of 4-(Benzylideneamino) Benzoic Acids ((1)). CHINESE JOURNAL OF STRUCTURAL CHEMISTRY. 2021;40(3):291–300.

28. Valarmathy G, Subbalakshmi R, Sabarika B, Nisha C. Schiff bases derived from 4-amino-N-substituted benzenesulfonamide: synthesis, spectral characterisation and MIC evaluation. Bull Chem Soc Eth. 2021 Oct 24;35(2):435–48. Available from: <URL>.

29. Ferroudj N, Nzimoto J, Davidson A, Talbot D, Briot E, Dupuis V, et al. Maghemite nanoparticles and maghemite/silica nanocomposite microspheres as magnetic Fenton catalysts for the removal of water pollutants. Applied Catalysis B: Environmental. 2013 Jun;136–137:9–18. Available from: <URL>.

30. Shah K, Hassan E, Ahmed F, Anis I, Rabnawaz M, Shah MR. Novel fluorene-based supramolecular sensor for selective detection of amoxicillin in water and blood. Ecotoxicology and Environmental Safety. 2017 Jul;141:25–9. Available from: <URL>.

JOTCS A Journal of the Turkish Chemical Society Section: A Chemistry

TURKISH CHEMICAL SOCIETY

Synthesis of Graphene Nanoplatelet-Alginate Composite Beads and Removal of Methylene Blue from Aqueous Solutions

Ferda CİVAN ÇAVUŞOĞLU[1,*]

[1]İstanbul Beykent University, Faculty of Engineering and Architecture, Department of Chemical Engineering, İstanbul, 34396, Turkey

Abstract: The discharge of various types of wastewater into natural streams leads to significant problems by increasing the toxicity of the wastewater. For this reason, methods and materials are being developed by researchers in line with effective, economic, and environmental principles. In this study, the removal of methylene blue, a toxic dyestuff, from aqueous solutions was investigated by synthesizing sodium alginate (SA) and graphene nanoplatelet-sodium alginate composite (SA-GNP) beads. The structural characteristics of the materials were analyzed using FTIR, TGA, optical microscope, and SEM methods. All parameters determining the efficiency of the methylene blue adsorption system were optimized in a batch system. The effects of various factors, such as adsorbent amount, contact time, adsorption temperature, dye concentration, solution pH, pHzpc values of SA and SA-GNP beads, presence of different ions, and beads swelling, on the adsorption process, were investigated. To investigate the mechanism of the adsorption system, the adsorption data were fitted to a non-linear form of the Langmuir, Freundlich, and Temkin equilibrium isotherm models, as well as the Pseudo-first-order (PFO), Pseudo-second-order (PSO), and Bangham kinetic models. High regression coefficients were achieved in the studied kinetic and isotherm models ($0.86 \leq R^2 \leq 0.99$), and the experimental data were found to be compatible with the model parameters. Maximum adsorption capacities (q_m) of 167.52 mg/g and 290.36 mg/g were obtained for the SA and SA-GNP adsorbents, respectively, at 308 K. The optimum temperature for both adsorption systems was found to be 308 K. The efficiency of methylene blue dyestuff removal was improved with graphene nanoplatelet-based adsorbents.

Keywords: Adsorption, alginate, graphene nanoplatelet, isotherm, kinetics, methylene blue.

Submitted: October 29, 2022. **Accepted:** February 20, 2023.

Cite this: Civan Çavuşoğlu F. Synthesis of Graphene Nanoplatelet-Alginate Composite Beads and Removal of Methylene Blue from Aqueous Solutions. JOTCSA. 2023;10(2):287–302.

DOI: https://doi.org/10.18596/jotcsa.1196282.

***Corresponding author. E-mails:** ferda.cvn@gmail.com; ferdacavusoglu@beykent.edu.tr.

1. INTRODUCTION

Ground and surface waters are polluted by wastewater from industrial, urban and agricultural sources. Due to rapid population growth and industrialization, the demand for clean water is increasing day by day (1). Synthetic dyes are pigments used in industries to color various products. It is widely used in many industries such as textile, plastic, paint, food, paper, cosmetics, medicine, and leather, and the wastewater of these sectors contains significant amounts of dyestuffs (2–4). The textile industry is the primary source of dyes, and today more than 10,000 dyes and pigments are used for this purpose (5,6). The discharge of colored wastewater, which has a toxic effect and is resistant to degradation in the aquatic environment, into natural streams causes many serious problems by increasing the toxicity of the wastewater and the chemical oxygen demand (COD) (4,6).

Methylene blue (MB), which is in the cationic dye class, has many industrial applications (6–8). It is considered an important harmful organic pollutant in the aquatic environment due to its toxicity, carcinogenicity, mutagenicity, and non-biodegradability (7). Exposure can cause respiratory

complications, increased heart rate, nausea, profuse sweating, jaundice, and tissue necrosis (1,6,8). Various biological and physicochemical methods such as ultrafiltration, nanofiltration, coagulation, precipitation, membrane processes, ion exchange, electrolysis, biological processes, chemical oxidation, and adsorption are used in the removal of dyestuffs from wastewater (2,5,9).

The adsorption process is considered a versatile method for the removal of environmental pollutants from aqueous solutions with its low cost, simple and easy separation method, fast and environmentally friendly features (7,8). It also does not require sludge formation; adsorbents can be regenerated and reused (2). In recent years, various studies have been carried out to develop materials that can be used as low-cost and environmentally friendly adsorbents in wastewater treatment applications. Natural resource-based adsorbents such as activated carbon, zeolite, clay, and synthetic polymers are the materials used for this purpose. Among the biopolymers of interest, alginate and its cross-linked derivatives are well-known polysaccharide-based materials (9,10). It is an environmentally friendly natural carbohydrate polymer composed of sodium alginate (SA), mannuronic acid, and guluronic acid (7). Adsorbents derived from natural polymers are widely used in the removal of dyes from wastewater due to their abundance, low cost, non-toxicity, biocompatibility, biodegradability, abundant carboxyl and hydroxyl groups, hydrophilicity and recyclability (1,7,9). Due to its negative charge, alginate is seen as a suitable polymer that can be used in the removal of heavy metals and cationic dyestuffs. Studies have shown that using alginate in the form of nanocomposites with materials such as graphene, Fe_3O_4, and montmorillonite contributes to the improvement of both the mechanical properties of alginate and its adsorption properties (4). Compositing graphene with polymeric materials increases the possibility of adding new functional groups to the surface, as well as increasing the number of active sites to fix a large number of organic and inorganic contaminants (11).

Recently, many studies have used graphene-based materials for the adsorption of different pollutant components from water (12,13). Graphene, which is a two-dimensional allotrope of carbon, is used in many fields due to its large specific surface area and biocompatibility, electronic, chemical, and thermal properties, removal of drugs and organic pollutants, and its suitability for use in composite material production. Having a good strength structure and being environmentally compatible, graphene-derived composite materials (graphene oxide, graphene nanoplatelets-GNPs, etc.) are preferred in environmental technologies of the removal of pollutants from water (13–15).

In recent studies, many graphene-polymer composites have been synthesized and used in the removal of various pollutants by the adsorption method (7,10,11,16–21). In this study, SA and SA-GNP beads were synthesized and used as an adsorbent for the removal of methylene blue from aqueous solutions by the adsorption method. In order to improve the adsorption properties, an SA-GNP composite was prepared by adding GNP to the bead formulation. The characterizations of the synthesized adsorbents were conducted by FTIR, TGA, optical microscope and SEM methods. The effects of different parameters such as adsorbent amount, dyestuff concentration, solution pH, pHzpc values, presence of different ions (NaCl), contact time, and adsorption temperature on the adsorption system were investigated, and optimum conditions were determined. In addition, the effect of swelling of the beads on the adsorption capacity was investigated by looking at the swelling behavior of the adsorbent beads. Langmuir, Freundlich, and Temkin isotherm equilibrium models and PFO, PSO, and Bangham kinetic models were fitted with experimental data, and the mechanism of the adsorption system was examined and interpreted.

2. MATERIALS AND METHODS

2.1. Materials

GNP (thickness 1–20 nm, width: 1–50 µm) from XG Science (xGnP®-C-750), sodium alginate from Sigma-Aldrich, $CaCl_2$, methylene blue (MB) ($C_{16}H_{18}ClN_3SxH_2O$ (x=2-3)), HCl (36.5%), NaOH (≥99) and NaCl were obtained from Merck. High-purity water obtained from the Millipore Direct-Q3 water treatment system was used in all experimental stages.

2.2. Synthesis of Materials

To synthesize materials, 2% (w/v) sodium alginate solution was mixed thoroughly in a magnetic stirrer and prepared separately for SA and SA-GNP composite beads. In synthesizing GNP-based composite material (SA-GNP), 50 mg GNP was added to the prepared 2% sodium alginate solution and mixed again in the magnetic stirrer until a homogeneous mixture was obtained. This suspension mixture was slowly added to the 2% $CaCl_2$ solution prepared in a volume of 100 mL with the help of a dropper to form beads in a spherical shape. After being kept in solution for gelatinization for 24 hours, the obtained materials were filtered off and washed several times with distilled water to separate them from $CaCl_2$. Then, the prepared beads were kept in a vacuum oven at 30°C for 3 hours to allow them to dry. It has been seen in the literature that partial drying of the prepared materials reduces the porosity of the beads, while complete dehydration can cause surface cracking, which can facilitate the surface erosion of the material upon rehydration. Temperature is important as it can affect the swelling behavior of

the beads (22). Synthesis of SA adsorbent without GNP additive was carried out similarly. Prepared SA and SA-GNP materials were stored in a desiccator for use in studies. The preparation of SA and SA-GNP beads is schematically presented in Figure 1.

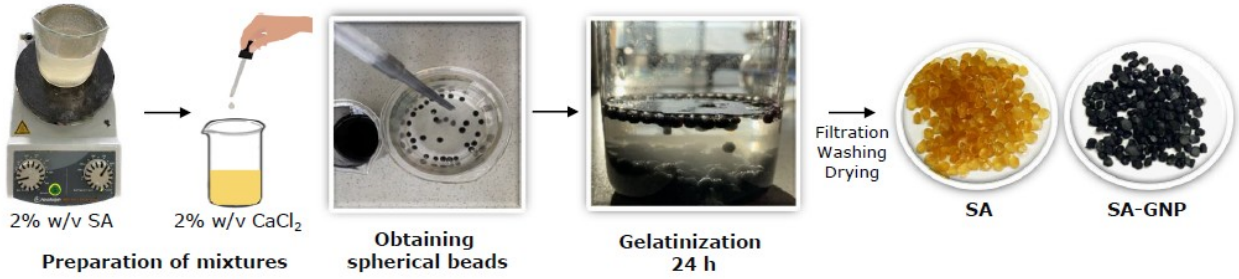

Figure 1: Preparation of SA and SA-GNP beads.

2.3. Characterization of Materials

Surface characterizations of SA and SA-GNP adsorbents were performed using Fourier transform infrared spectroscopy (FTIR), thermogravimetric analysis (TGA), optical microscope, and Scanning electron microscopy (SEM) methods. FTIR analysis (Bruker Alpha) was performed to determine the structural properties; the KBr method was used by recording the IR spectra between 400-4000 cm^{-1}. TGA (Hitachi STA-7200) measurements were carried out by taking samples in the range of 5-10 mg and heating them at a rate of 10°C/min under a nitrogen atmosphere (200 mL/min) in the temperature range of 25°C-1000°C. The morphology of the beads was observed with a scanning electron microscope (TESCAN VEGA 3) at 10 kV and 100x magnification. Before analysis, the surface of the samples was sputter coated with a gold-palladium layer for SEM visualization.

Additionally, The morphology of the beads was visually examined using an OLYMPUS microscope (CKX53, Japan), and digital images were obtained. Information about the color, shape, and texture of the surface of the beads was obtained, and the diameter of the beads was measured. Besides, a swelling test was applied to the prepared adsorbent beads, and its effect on the adsorption process was investigated.

2.4. Adsorption Studies

Adsorption studies were carried out batch-wise in an incubator shaker. To determine the optimum adsorption conditions, the effects of different process variables such as adsorbent amount, contact time, dyestuff concentration, temperature, pH and foreign ion effect (NaCl) on adsorption were investigated. Different parameter ranges (adsorbent amount 0.1-1 g/L, contact time 0-180 min, dyestuff concentration 1-25 mg/L, temperature 298-318 K, pH value 3-11, NaCl molar concentration 0.005-0.1 M) based experiments were carried out. The MB dyestuff solution volume was kept constant at 10 mL in all experiments. In experimental studies, all concentrations of adsorbate solutions were measured at 665 nm with a UV–Vis spectrophotometer (Jasco V-730, Japan). Adsorption capacities (q_e, mg/g) and removal efficiencies (%) are respectively calculated using Equation 1 and Equation 2. In equations, Co (mg/L) dyestuff initial concentration, Ce (mg/L) equilibrium concentration, m (g) adsorbent amount, and V (L) solution volume.

$$q_e = \frac{(Co - Ce).V}{m} \quad \text{(Eq. 1)}$$

$$\%\, Percentage\ of\ removal = \frac{(Co - Ce)}{Co} x\, 100 \quad \text{(Eq. 2)}$$

The point of zero charge (pH_{PZC}) values of the adsorbent materials were determined by the pH drift method. The pH of 0.01 M NaCl solution was adjusted to different pH values (4, 6, 8, 10, and 12) with 0.1 M NaOH and 0.1 M HCl solutions. Mixtures of approximately 1.5 mg of SA and SA-GNP beads and 20 mL of NaCl solution were kept in a shaking incubator at 25°C for 24 hours. After this process, the final pH values of samples were measured by pH meter, and a graph was drawn between the initial and final pH values, and the diagonal intersection point was accepted as pHzpc (23,24).

3. RESULTS AND DISCUSSIONS

3.1. Characterization Results

FTIR, TGA, and SEM methods were applied to characterize the prepared alginate-based adsorbent beads, and their morphology was examined by obtaining digital images with an optical microscope. The FTIR spectra of SA and SA-GNP adsorbents measured in the 400-4000 cm^{-1} range before and after adsorption are shown in Figure 2. FTIR spectra of alginate-based adsorbents show similar peaks before and after adsorption for both adsorbents. Specified wavelengths indicate the presence of

groups at 1028 and 1037 cm^{-1} (C–O–C stretching frequency), 1410, 1430 $cm^{-1,}$ and 1637 cm^{-1} (symmetric and asymmetric stretching COO^-), 2922 and 2926 cm^{-1} (C-H stretching vibration), 3445 and 3450 cm^{-1} (–OH stretching vibration) (25–28). It was observed that the intensity of these peaks after adsorption decreased compared to before adsorption. It is thought that the MB dyestuff attaches to the functional groups herein.

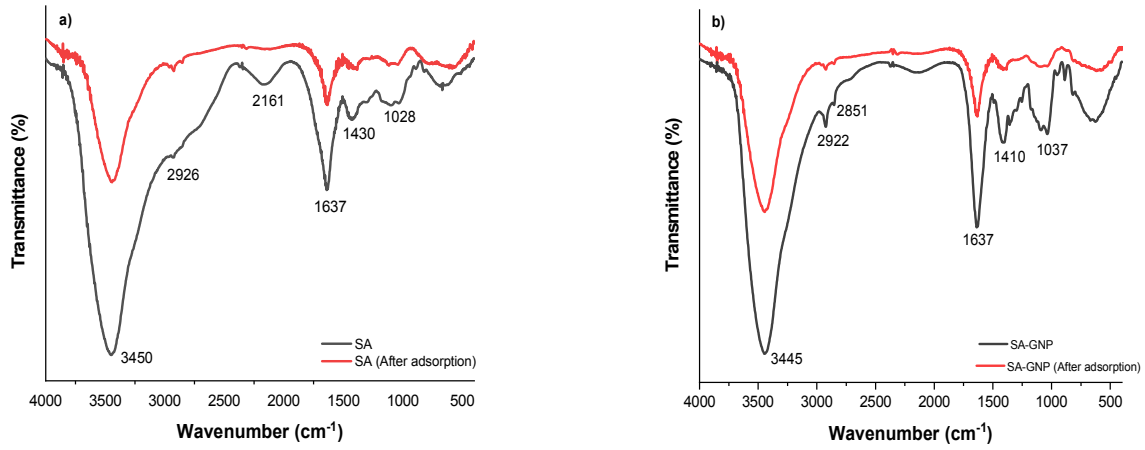

Figure 2: FTIR plots of SA (a) and SA-GNP (b) before and after adsorption.

TGA plots of SA and SA-GNP are shown in Figure 3. The thermal behavior of adsorbents is similar, and their thermal decomposition takes place in the temperature region of 200°C to 500°C. The weight loss in the first stage is attributed to the removal of volatile products such as physically adsorbed water (29,30). The decomposition temperature at 10% weight loss was calculated as 189°C and 197°C for SA and SA-GNP adsorbents, respectively.

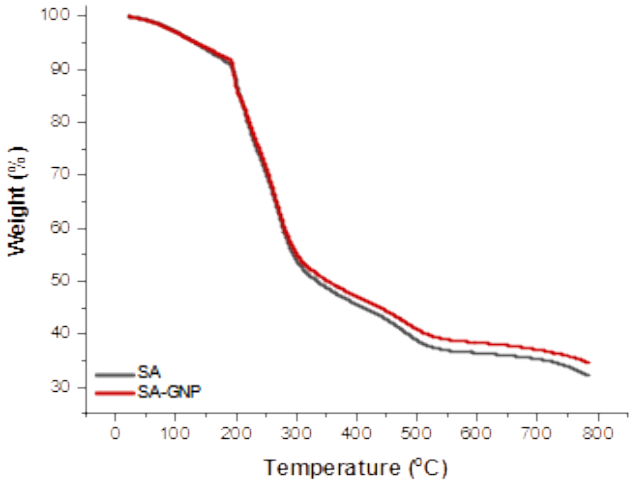

Figure 3: TGA curves of SA and SA-GNP.

Weight loss in the second stage is attributed to the decrosslinking of the polymer networks (29). The region responsible for the large weight loss shows the degradation of the carboxylic groups in the sodium alginate structure (in the temperature range of 178-190 °C). The thermal stability of the materials is determined by the large loss of mass at which thermal decomposition begins, large changes are observed after exceeding 200 °C (31). From the data obtained at 800 °C, it is seen that the remaining material contents for SA and SA-GNP are 31% and 35% by weight (total weight),

respectively. According to the final thermal oxidative decomposition temperatures, it can be said that SA-GNP composite material has slightly higher thermal stability than SA. In this direction, it can be said that the GNP additive slightly increases the thermal stability of the material.

The morphological characterization of beads was observed using SEM. The obtained topographic images of SA and SA-GNP are shown in Figure 4. The surfaces and sections of SA and SA-GNP showed a smooth and homogeneous morphology. GNP did not appear to cause any roughness or heterogeneity in the beads. It shows that the GNP is successfully dispersed by sonication and does not form agglomeration.

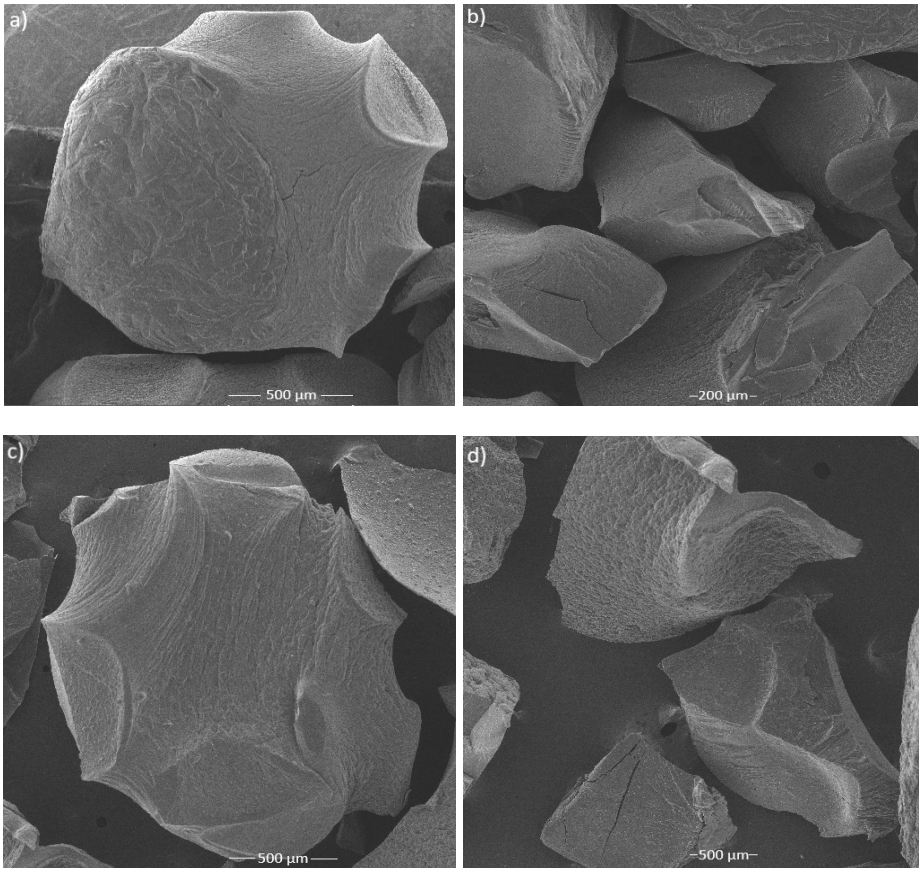

Figure 4: SEM images of SA (a,b) and SA-GNP (c,d) beads.

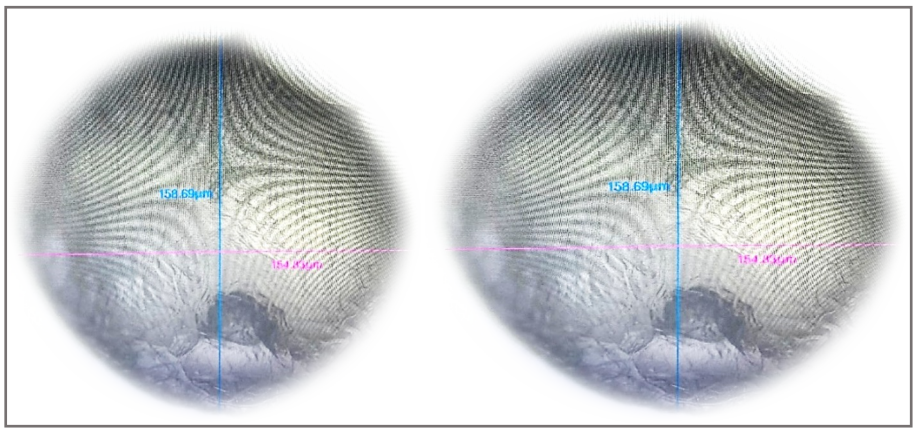

Figure 5: Digital images of SA and SA-GNP beads.

Additionally, the morphology of the beads was visually examined using an optical microscope, and their digital images were obtained as in Figure 5. Information about the color, shape, and texture of

the surface of the beads was obtained, and the diameter of the beads was measured. The beads have a spherical shape and measure approximately 150 µm in diameter on average. SA beads are light yellow in color, while SA-GNP beads are black due to the color of the GNP.

The swelling behavior of adsorbent beads was determined gravimetrically in MB solution (pH=5.5) at 25°C. The percent swelling was calculated using Equation 3:

$$\%\,Swelling = \frac{(Ws - Wd)}{Wd}\,x\,100 \qquad \text{(Eq. 3)}$$

Ws is the weight of the swollen beads, and Wd is the weight of the dried beads. Swelling measurement continued until the swollen beads were adequately weighed. Although the beads had swelling properties, there was no change in the percentage of dye removal of the swollen beads compared to the dry ones (32,33).

3.2. Adsorption Studies

3.2.1. Adsorption process variables

To investigate the effect of the amount of adsorbent, mixtures of adsorbents in 0.1, 0.25, 0.5, 0.75, and 1 g/L amounts and stock MB solution with an initial dye concentration of 10 mg/L were left to shake for 120 minutes, based on previous preliminary experiments. The calculated adsorption capacities of the experiments with different amounts of SA and SA-GNP adsorbents are shown in Figure 6. According to the experimental results, the highest removal efficiencies (%) of SA and SA-GNP were obtained as 71.55% and 74.59%, respectively. As the amount of adsorbent increased, the removal efficiency of the dyestuff increased. This is due to the grown surface area resulting from the rise in adsorbent mass and the increased number of active sites (34,35).

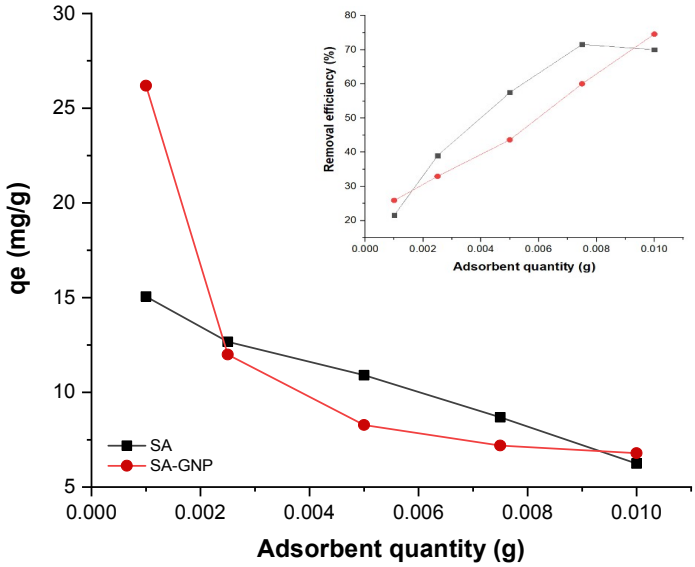

Figure 6: Effect of adsorbent dose on adsorption capacity and removal efficiency (inset).

As seen in Figure 6, the adsorption capacity decreased as the amount of adsorbent increased. The adsorption capacity values vary between 6.25–15.06 mg/g for SA, and 6.79–26.19 mg/g for SA-GNP. As the adsorbent dose decreased, the amount of MB solution per gram of adsorbent increased. This may be because all active sites in the adsorbent are fully exposed to MB and utilized at a lower adsorbent dose, and only some of the active sites are exposed and occupied by MB at a higher adsorbent dose (35). The highest adsorption capacity was obtained at 0.1 g/L adsorbent concentration as 15.06 mg/g for SA and 26.19 mg/g for SA-GNP. Based on these data, the optimum amount of adsorbent was chosen as 0.1 g/L.

To determine the equilibrium time of the adsorbents, experiments were carried out with MB solution for 1, 5, 10, 15, 30, 45, 60, 90, 120, and 180 minutes. Equilibrium times were determined, and the obtained data were also used for kinetic modeling calculations. The calculated adsorption capacities of the experiments performed with SA and SA-GNP adsorbents at different times are shown in Figure 7.

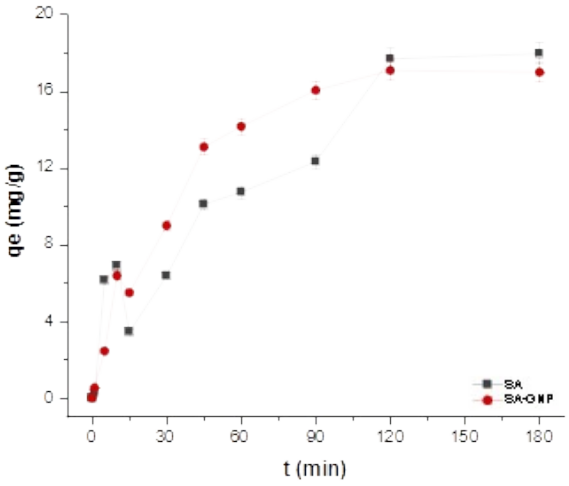

Figure 7: Effect of contact time on adsorption capacity.

Equilibrium times of the adsorption systems were determined at room temperature. The fast adsorption in the first stage can be explained by the high driving force that provides rapid mass transfer of MB ions to the adsorbent surface, as well as the high number and availability of active sites in the adsorbent (36). Both adsorption systems reached equilibrium after approximately 120 minutes, and it was observed that there were no major changes in adsorption capacity after this point. Based on these data, 120 minutes was chosen as the optimum contact time, and the q_e values for SA and SA-GNP adsorbents were obtained as 17.97 mg/g and 17.00 mg/g, respectively.

The effect of MB solution at different pH values on adsorption was investigated by adjusting the pH values to 3, 5, 7, 9, and 11 with 0.1 M HCl and 0.1 M NaOH solutions. Calculated adsorption capacities of the experiments with SA and SA-GNP adsorbents at different pH values are shown in Figure 8 (a). The q_e values ranged from 48.16 – 67.52 mg/g for SA and 50.95–97.29 mg/g for SA-GNP; that is, the amount of MB solution per gram adsorbent decreased as pH increased. These results show that an acidic solution is more suitable for the MB adsorption system. Since the surface of sodium alginate is negatively charged up to pH 7, the presence of H^+ ions at low pH values increased the adsorption capacity value (37). According to the literature, this shows that the cationic dyestuff can be better ionized at low pH values and is based on the interaction of more dye molecules with the adsorbent (38). The highest adsorption capacities were obtained at pH 3, 67.52 mg/g for SA and 97.29 mg/g for SA-GNP.

The surface charge properties of adsorbents at different pH values significantly affect their adsorption capacity. Additionally, the pHpzc was determined to evaluate the surface electrification of adsorbents in the solution. As seen in Figure 8 (b), experimental pHzpc values of SA and SA-GNP were obtained as 5.26 and 5.11, respectively. In the pH range of 3-10, an increase in the negative charge of the adsorbent surface due to deprotonation of the carboxyl group increased the electrostatic attraction between the cationic MB, thereby increasing the adsorption capacity of SA and SA-GNP beads (24). In the study, SA and SA-GNP beads showed efficient adsorption on MB from an aqueous solution in the initial pH range of 4-7. The normal pH of the MB solution is also about 6.06 (T=27.5°C), so no pH adjustment was required for the other experiments, and the MB initial pH value is in optimum conditions for the study.

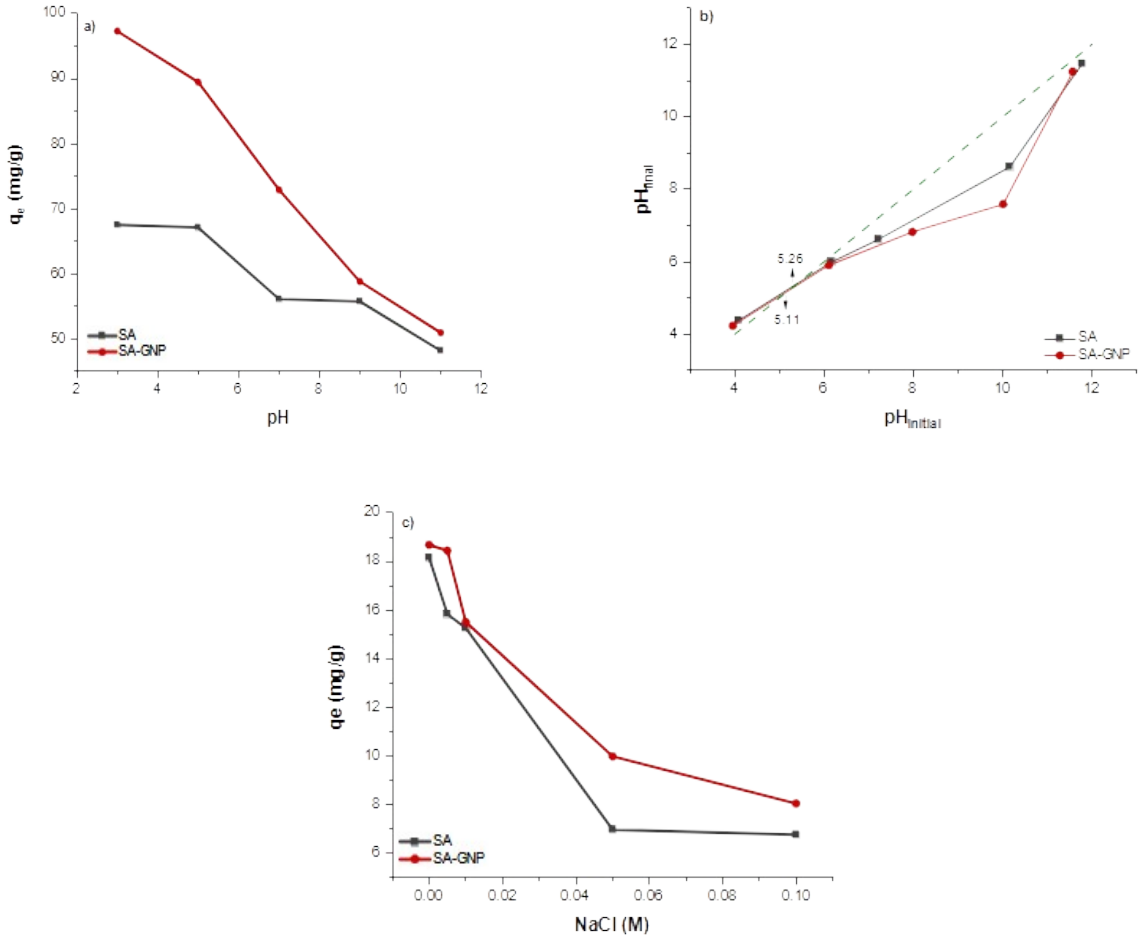

Figure 8: Effect of pH (a) on adsorption capacity, pH_{ZPC} plots of SA and SA-GNP (b), and foreign ion-NaCl (c) on adsorption capacity.

It is known that different polluting ions present with MB dyestuff in adsorption processes also affect adsorption. In this study, NaCl was chosen as a different foreign ion, and its effect on adsorption capacity with MB was investigated. While MB concentration was 10 mg/L, NaCl concentrations were prepared as 0.005, 0.01, 0.05, and 0.1 M. The graph of Figure 8 (c) shows the adsorption capacity values obtained at different NaCl concentrations of SA and SA-GNP adsorbents. As the molar concentration of NaCl increased, the adsorption capacity values decreased. The adsorption capacity of SA decreased from 15.83 mg/g (0.005 M) to 6.76 mg/g (0.1 M). The adsorption capacity of SA-GNP decreased from 18.43 mg/g (0.005 M) to 8.05 mg/g (0.1 M). This result is thought to be related to the competition of cation ions and Na^+ of MB for adsorption sites (34).

3.2.2. Adsorption kinetic models

Adsorption kinetics were investigated by using experimental data obtained at different times in the adsorption of SA and SA-GNP adsorbents and MB dyestuff. The adsorption data were fitted to a non-linear form of PFO (Equation 4), PSO (Equation 5), and Bangham (Equation 6) (23) kinetic models. The graphs of all adsorption systems are shown in Figure 9, and the calculated model parameters are presented in Table 1.

In equations, q_t (mg/g) adsorption capacity at time t, k_1 (min^{-1}) PFO kinetic model rate constant, k_2 (g/mg.min) PSO kinetic model rate constant, k Bangham constant, u Bangham parameter and t (min) is the contact time.

$$q_t = q_e.\left(1 - e^{-k_1.t}\right) \quad \text{(Eq. 4)}$$

$$q_t = \frac{q_e^2.k_2.t}{1 + k_2.q_e.t} \quad \text{(Eq. 5)}$$

$$q_t = k.t^{\upsilon} \quad \text{(Eq .6)}$$

According to the parameters and R^2 values of the models, the kinetic models for both adsorption

systems fit well with the experimental data (SA; $R^2 \geq 0.87$, SA-GNP; $R^2 \geq 0.92$), which are consistent with previous studies (36,39). The R^2 values of the PFO and PSO kinetic models show that both adsorption systems fit the PSO kinetic model better. The reaction mechanisms between adsorbent and adsorbate depend on chemical adsorption, including the sharing or exchanging of electrons as covalent forces and valence forces via ion exchange (40). The kinetic model rate (k_1, k_2) obtained from the models showed that the adsorption process performed with SA-GNP/MB was faster than the SA/MB adsorption system (SA: k_1=0.0168 min^{-1} k_2=0.0007 g/mg.min; SA-GNP: k_1=0.0417 min^{-1}, k_2=0.0028 g/mg.min). Experimental data and model parameters of adsorption capacity were found to be compatible with each other.

Bangham model is a generalization of the Weber-Morris model and can be used to explain pore diffusion mechanisms. R^2 values (≥0.92) are high for both adsorption systems. The Bangham model shows that rate-controlled step adsorption of MB on SA and SA-GNP is pore diffusion (23).

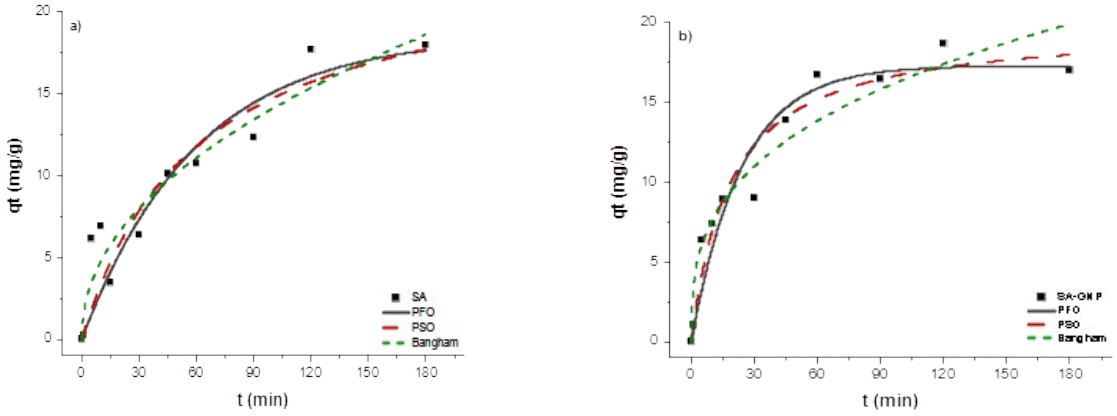

Figure 9: PFO, PSO, and Bangham kinetic models of SA (a) and SA-GNP (b).

Table 1: Kinetic model parameters of SA and SA-GNP.

MB Adsorption	SA	SA-GNP
PFO		
$\mathbf{q_e}$ (mg/g)	18.58	17.302
$\mathbf{k_1}$ (min^{-1})	0.0168	0.0417
$\mathbf{R^2}$	0.87	0.93
PSO		
$\mathbf{q_e}$ (mg/g)	23.60	19.815
$\mathbf{k_2}$ (g/mg.min)	0.0007	0.0028
$\mathbf{R^2}$	0.88	0.95
Bangham		
k	1.617	3.569
u	0.4705	0.3311
$\mathbf{R^2}$	0.92	0.93

MB concentration: mg/L

3.2.3. Adsorption equilibrium models

The effects of MB concentration and temperature on the adsorption process were investigated. Adsorption mechanisms and equilibrium conditions were examined using experimental data obtained at different temperatures for the adsorption of SA and SA-GNP adsorbents and MB dyestuff. Optimum adsorption temperatures were determined, and maximum adsorption capacities were calculated using the data obtained for isotherm model calculations. The adsorption data were fitted to a non-linear form of Langmuir (Equation 7), Freundlich (Equation 8) (23), and Temkin (Equation 9) (41) equilibrium isotherm models. The graphs of all adsorption systems are shown in Figures 10 and 11, and the calculated model parameters are presented in Table 2.

In equations, q_m (mg/g) maximum adsorption capacity, K_L (L/mg) Langmuir isotherm constant, K_F $(mg/g).(L/mg)^{1/n}$ Freundlich isotherm constant, heterogeneity factor showing 1/n adsorption density, A_T Temkin isotherm equilibrium binding

constant, b_T isotherm constant, R (J/mol.K) gas constant, T (K) absolute temperature.

$$q_e = \frac{K_L q_m C_e}{1 + K_L C_e} \quad \text{(Eq. 7)}$$

$$q_e = K_F C_e^{1/n} \quad \text{(Eq. 8)}$$

$$q_e = \frac{R \times T}{b_T} \times \ln\left(A_T \times C_e\right) \quad \text{(Eq. 9)}$$

According to the parameters and R^2 values of Langmuir and Freundlich models, the isotherm models for both adsorbent-MB adsorption systems fitted very well with the experimental data ($R^2 \geq 0.98$). Maximum adsorption capacities (q_m) for SA and SA-GNP were obtained in the range of 39.05-167.52 mg/g and 63.67-290.36 mg/g, respectively. While the q_m value for the SA-MB adsorption system was 167.52 mg/g at 308 K, the q_m for the SA-GNP-MB adsorption system was calculated as 290.36 mg/g at 308 K.

The maximum adsorption capacities obtained in similar studies in the literature are presented in Table 3. Compared to the literature, very efficient results were obtained in MB removal. Freundlich isotherm generally represents heterogeneous adsorption systems, and it is known that the adsorption process is suitable when the n parameter is between 1 and 10. MB removal is successful in applied adsorption processes since n values for both adsorption systems vary between 1.11-1.86. In other words, 1/n<1 indicates that the adsorption mechanism depends on chemisorption. It is known that the heterogeneity of the systems increases as the 1/n value approaches zero (40), and the highest heterogeneity in the investigated adsorption systems was obtained at 308 K for both adsorbents. The optimum temperature of the adsorption systems is 308 K, and the maximum adsorption capacities were obtained at this temperature value. The Temkin isotherm model indirectly describes the effects of adsorbent/adsorbate interactions. In this model, it is assumed that the heat of adsorption of all molecules decreases linearly with increasing coverage of the adsorbent (42). The Temkin model shows that the adsorption of MB dyestuff with SA and SA-GNP adsorbents is based on a chemisorption process.

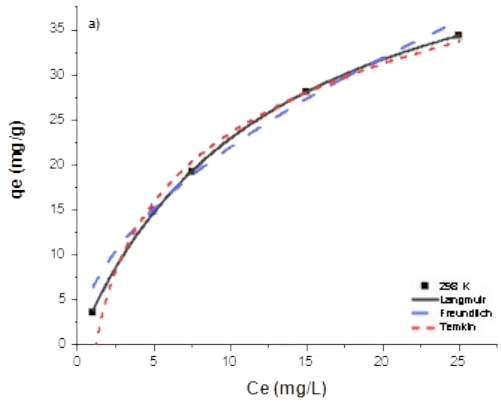

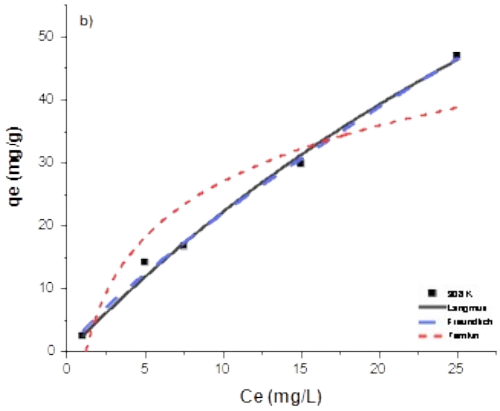

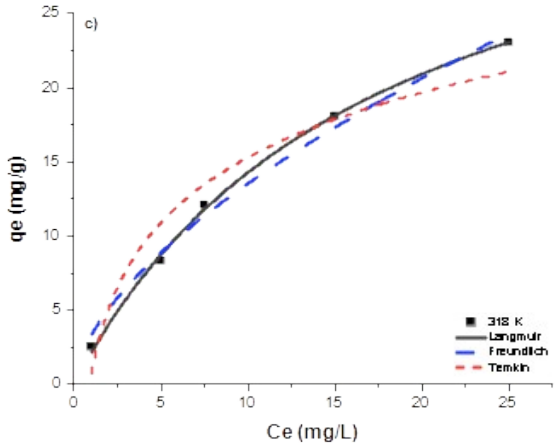

Figure 10: Langmuir, Freundlich, and Temkin isotherm models of SA, 298 K (a), 308 K (b), 318 K (c).

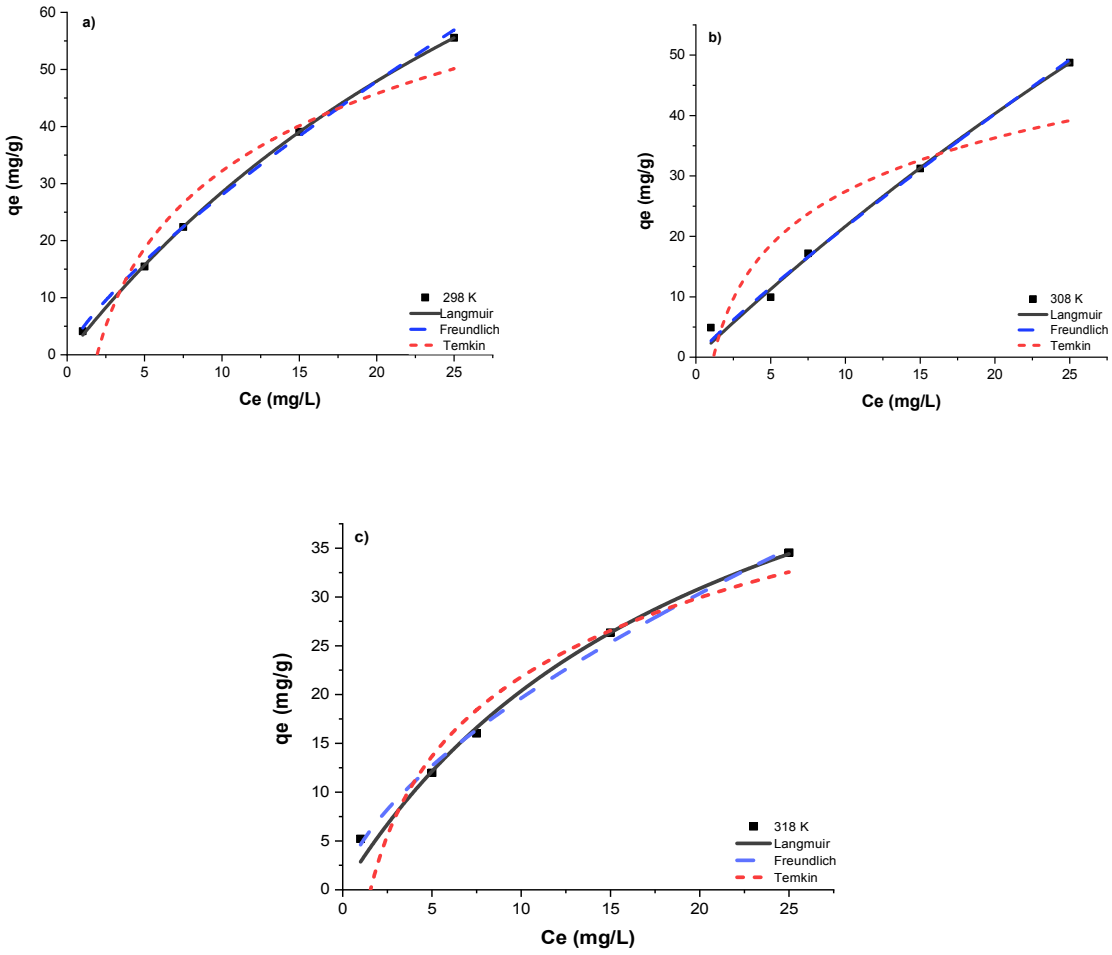

Figure 11: Langmuir, Freundlich, and Temkin isotherm models of SA-GNP**,** 298 K (a), 308 K (b), 318 K (c).

Tablo 2: Langmuir, Freundlich, and Temkin isotherm parameters.

MB Adsorption	SA			SA-GNP		
	298 K	**308 K**	**318 K**	**298 K**	**308 K**	**318 K**
Langmuir						
q_m (mg/g)	51.52	167.52	39.05	151.79	290.36	63.67
K_L	0.080	0.015	0.058	0.023	0.008	0.047
R^2	0.99	0.99	0.99	0.99	0.99	0.99
Freundlich						
K_F	6.36	3.34	3.33	4.71	2.70	4.62
n	1.86	1.22	1.64	1.29	1.11	1.59
R^2	0.98	0.99	0.99	0.99	0.99	0.99
Temkin						
A_T	0.837	0.833	1.12	0.518	0.851	0.641
b_T	223.7	200.4	418.2	126.6	199.9	225.2
R^2	0.98	0.86	0.94	0.94	0.79	0.97

Table 3: Summary of similar studies in the literature on methylene blue removal with composite alginate materials.

Adsorbents/Composite materials	Maximum adsorption capacities, q_m	References
Activated carbon-alginate beads	230 mg/g	(2)
Activated carbon, copper ferrite and alginate composites	400 mg/g	(9)
Activated carbon-alginate beads	769.23 mg/g	(43)
Bentonite-encapsulated alginate beads	2041 mg/g	(44)
Graphene oxide-magnetite nanocomposite	172.6 mg/g	(3)
Graphene oxide-montmorillonite/sodium alginate aerogel beads	150.66 mg/g	(7)
Graphene oxide/alginate quasi-cryogel beads	122.26 mg/g	(10)
Magnetic sodium alginate-modified zeolite adsorbent	181.85 mg/g	(24)
Magnetic alginate beads	38.9 mmol/g	(45)
Magnetic microspheres with sodium alginate and activated carbon	222.3 mg/g	(46)
Metal-organic framework (MOF)-based alginate composite beads	490.72 mg/g	(47)
Sodium alginate beads, SA	167.52 mg/g	This work
Graphene nanoplatelet composite beads, SA-GNP	290.36 mg/g	

4. CONCLUSIONS

SA and SA-GNP composite beads were synthesized as adsorbent material, and studies were carried out on the removal of MB from aqueous solutions by the adsorption method. Structural characterizations of the synthesized adsorbents are compatible with the literature. Optimum conditions for the adsorption system were determined by investigating the effects of different parameters such as adsorbent dose, MB dyestuff concentration, solution pH, presence of different ions (NaCl), beads swelling, contact time, and adsorption temperature. According to the results:

- An adsorbent dose of 0.1 g/L was determined as the optimum amount of adsorbent. At the end of the adsorption period of 120 minutes, the system reached equilibrium, and the optimum contact time for the experiments was determined as 120 minutes.
- In different pH experiments, high adsorption capacities were obtained at low pH (≤7) values, so the pH value of the MB solution (pH=6.06; T=27°C) is suitable for adsorption studies, and no pH adjustment has been made. In addition, in order to see the effect of pH, the pH_{ZPC} values of SA and SA-GNP beads were obtained as 5.26 and 5.11, respectively, by using the drift method. The effect of the presence of a different ion, NaCl, on the adsorption process was investigated, and the

adsorption capacity values decreased as the NaCl concentration increased.

- The mechanism of the adsorption system was investigated and interpreted. The adsorption data were fitted to a non-linear form of Langmuir, Freundlich, and Temkin equilibrium isotherm models and PFO, PSO, and Bangham kinetic models. High regression coefficients ($0.86 \leq R^2 \leq 0.99$) were obtained with the studied kinetic and isotherm models, and the experimental data were found to be compatible with the model parameters.
- The maximum adsorption capacities (q_m) of SA and SA-GNP adsorbents were obtained as 167.52 and 290.36 mg/g at 308 K, respectively, and the optimum temperature was 308 K for both adsorption systems.
- Despite the very low amount of GNP in SA-GNP adsorbent, it significantly increased the adsorption capacity and improved the adsorption process. Also, the addition of GNP slightly increased the thermal stability of SA-GNP.
- The spherical shape of the adsorbents did not require extra filtration and allowed them to be easily separated from the adsorbates. In this direction, simple operating convenience is provided to the adsorption process.

In conclusion, SA and SA-GNP were found to be economical, effective, and environmentally friendly adsorbents that can be used for the removal of MB from aqueous solutions.

5. CONFLICT OF INTEREST

The author declares no conflict of interest.

6. REFERENCES

1. Balçık Canbolat Ç, Özbey B. Production of cellulose nanocrystalline additive alginate adsorbent for the removal of organic dyes from aqueous solutions and investigation of dye removal efficiency. Düzce University J of Science and Techn. 2021;10:300–8. Available from: <DOI>.

2. Nasrullah A, Bhat AH, Naeem A, Isa MH, Danish M. High surface area mesoporous activated carbon-alginate beads for efficient removal of methylene blue. Int J Biol Macromol. 2018;107:1792–9. Available from: <DOI>.

3. Meral K, Metin Ö. Graphene oxide{magnetite nanocomposite as an effcient and magnetically separable adsorbent for methylene blue removal from aqueous solution. Turkish J Chem. 2014;38(5):775–82. Available from: <DOI>.

4. Okur M, Aktı F, Çetintaş A. Use of Polyaniline/Alginate Composite Material in the Adsorption of Acid Violet 90 Dye:Kinetics and Isotherm Evaluation. Gazi University J of Science Part C: Design and Techn. 2018;6(4):729–40. Available from: <DOI>.

5. Khan IA, Hassan MIU, Hussain H, Shah SM, Yasin T. Fabrication and characterization of amidoxime-functionalized silica decorated with copper: A catalytic assembly for rapid reduction of dyes. Turkish J Chem. 2021;45(2):410–9. Available from: <DOI>.

6. Hameed BH, Ahmad AA. Batch adsorption of methylene blue from aqueous solution by garlic peel, an agricultural waste biomass. J Hazard Mater. 2009;164(2–3):870–5. Available from: <DOI>.

7. E T, Ma D, Yang S, Hao X. Graphene oxide-montmorillonite/sodium alginate aerogel beads for selective adsorption of methylene blue in wastewater. J Alloys Compd. 2020;832:154833. Available from: <DOI>.

8. Borghei SA, Zare MH, Ahmadi M, Sadeghi MH, Marjani A, Shirazian S, et al. Synthesis of multi-application activated carbon from oak seeds by KOH activation for methylene blue adsorption and electrochemical supercapacitor electrode. Arab J Chem. 2021;14(2):102958. Available from: <DOI>.

9. Othman I, Abu Haija M, Kannan P, Banat F. Adsorptive removal of methylene blue from water using high-performance alginate-based beads. Water Air Soil Pollut. 2020;231(8). Available from: <DOI>.

10. Balkız G, Pingo E, Kahya N, Kaygusuz H, Bedia Erim F. Graphene oxide/alginate quasi-cryogels for removal of methylene blue. Water Air Soil Pollut. 2018;229(4). Available from: <DOI>.

11. Faysal Hossain MD, Akther N, Zhou Y. Recent advancements in graphene adsorbents for wastewater treatment: Current status and challenges. Chinese Chem Lett. 2020;31(10):2525–38. Available from: <DOI>.

12. Nigiz FU. Synthesis of a novel graphene–kaolin–alginate adsorbent for dye removal, and optimization of the adsorption by response surface methodology. Res Chem Intermed. 2019;45(7):3739–53. Available from: <DOI>.

13. Yusuf M, Elfghi FM, Zaidi SA, Abdullah EC, Khan MA. Applications of graphene and its derivatives as an adsorbent for heavy metal and dye removal: a systematic and comprehensive overview. RSC Adv. 2015;5(62):50392–420. Available from: <DOI>.

14. Madenli Ö, Deveci EU, Gönen Ç. Graphene Applications in Heavy Metal Removal: Adsorption Technology. Fırat University J of Engineering Science. 2021;33(1):151–9. Available from: <DOI>.

15. Zhang C, Chen Z, Guo W, Zhu C, Zou Y. Simple fabrication of Chitosan/Graphene nanoplates composite spheres for efficient adsorption of acid dyes from aqueous solution. Int J Biol Macromol. 2018;112:1048–54. Available from: <DOI>.

16. Bai C, Wang L, Zhu Z. Adsorption of Cr(III) and Pb(II) by graphene oxide/alginate hydrogel membrane: Characterization, adsorption kinetics, isotherm and thermodynamics studies. Int J Biol Macromol. 2020;147:898–910. Available from: <DOI>.

17. Wang Y, Pan J, Li Y, Zhang P, Li M, Zheng H, et al. Methylene blue adsorption by activated carbon, nickel alginate/activated carbon aerogel, and nickel alginate/graphene oxide aerogel: A comparison study. J Mater Res Technol. 2020;9(6):12443–60. Available from: <DOI>.

18. González-López ME, Laureano-Anzaldo CM, Pérez-Fonseca AA, Gómez C, Robledo-Ortíz JR. Congo red adsorption with cellulose-graphene nanoplatelets beads by differential column batch reactor. J Environ Chem Eng. 2021;9(2). Available from: <DOI>.

19. Ma J, Jiang Z, Cao J, Yu F. Enhanced adsorption for the removal of antibiotics by carbon nanotubes/graphene oxide/sodium alginate triple-network nanocomposite hydrogels in aqueous solutions. Chemosphere. 2020;242:125188. Available from: <DOI>.

20. Politaeva N, Yakovlev A, Yakovleva E, Chelysheva V, Tarantseva K, Efremova S, et al. Graphene oxide-chitosan composites for water treatment from copper cations. Water. 2022 Apr 29;14(9):1430. Available from: <DOI>.

21. Wang M, Li Y, Cui M, Li M, Xu W, Li L, et al. Barium alginate as a skeleton coating graphene oxide and bentonite-derived composites: Excellent adsorbent based on predictive design for the enhanced adsorption of methylene blue. J Colloid Interface Sci. 2022;611:629–43. Available from: <DOI>.

22. Bajpai SK, Sharma S. Investigation of swelling/degradation behaviour of alginate beads crosslinked with Ca^{2+} and Ba^{2+} ions. React Funct Polym. 2004;59(2):129–40. Available from: <DOI>.

23. Özçelik G, Civan Çavuşoğlu F, Özkara-Aydınoğlu Ş, Bayazit ŞS. Enhanced & effective phosphate recovery from water by indium fumarate & zirconium fumarate metal-organic frameworks: Synthesis, characterization, adsorption, kinetic and isotherm studies. Surfaces and Interfaces. 2022;29(December 2021). Available from: <DOI>.

24. Liu F, Li W, Zhou Y. Preparation and characterization of magnetic sodium alginate-modified zeolite for the efficient removal of methylene blue. Colloids Surfaces A Physicochem Eng Asp. 2021;629(May):127403. Available from: <DOI>.

25. Lacerda L, Parize AL, Fávere V, Laranjeira MCM, Stulzer HK. Development and evaluation of pH-sensitive sodium alginate/chitosan microparticles containing the antituberculosis drug rifampicin. Mater Sci Eng C. 2014;39(1):161–7. Available from: <DOI>.

26. Boddu A, Obireddy SR, Subbarao SMC, Rao KM, Venkata KRKS. Encapsulation of 5-Fluorouracil treated reduced graphene oxide in sodium alginate matrix for controlled and pH-responsive drug delivery. ChemistrySelect. 2021;6(25):6533–40. Available from: <DOI>.

27. Fan L, Du Y, Huang R, Wang Q, Wang X, Zhang L. Preparation and characterization of alginate/gelatin blend fibers. J Appl Polym Sci. 2005;96(5):1625–9. Available from: <DOI>.

28. Urzedo AL, Bernardes JS, Pedron T, Batista BL, Akiba N, Gaubeur I, et al. Synthesis and characterization of calcium alginate and cellulose nanocrystal films for lead removal. J Phys Conf Ser. 2019;1323(1). Available from: <DOI>.

29. Siddaramaiah, Swamy TMM, Ramaraj B, Lee JH. Sodium alginate and its blends with starch: Thermal and morphological properties. J Appl Polym Sci. 2008 Sep 15;109(6):4075–81. Available from: <DOI>.

30. Lu T, Xiang T, Huang XL, Li C, Zhao WF, Zhang Q, et al. Post-crosslinking towards stimuli-responsive sodium alginate beads for the removal of dye and heavy metals. Carbohydr Polym. 2015;133:587–95. Available from: <DOI>.

31. Kulig D, Zimoch-Korzycka A, Jarmoluk A, Marycz K. Study on alginate-chitosan complex formed with different polymers ratio. Polymers. 2016; 8(5): 167. Available from: <DOI>.

32. Li L, Zhao J, Sun Y, Yu F, Ma J. Ionically cross-linked sodium alginate/κ-carrageenan double-network gel beads with low-swelling, enhanced mechanical properties, and excellent adsorption performance. Chem Eng J. 2019;372(February):1091–103. Available from: <DOI>.

33. Abd El-Latif MM, El-Kady MF, Ibrahim AM, Ossman ME. Alginate/polyvinyl alcohol - kaolin composite for removal of methylene blue from aqueous solution in a batch stirred tank reactor. J Am Sci. 2010;6(December 2014):280–92. Available

from: <URL>.

34. Lafi R, ben Fradj A, Hafiane A, Hameed BH. Coffee waste as potential adsorbent for the removal of basic dyes from aqueous solution. Korean J Chem Eng. 2014 Nov 28;31(12):2198–206. Available from: <DOI>.

35. Liu T, Li Y, Du Q, Sun J, Jiao Y, Yang G, et al. Adsorption of methylene blue from aqueous solution by graphene. Colloids Surfaces B Biointerfaces. 2012;90(1):197–203. Available from: <DOI>.

36. Yürekli Y. Determination of adsorption capacities of NaX Nano-particles against heavy metals and dyestuff. J Fac Eng Archit Gazi Univ. 2019;34(4):2113–24. Available from: <DOI>.

37. Polat H, Zeybek N, Polat M. Tissue engineering applications of marine-based materials. Marine Biomaterials. 2022;205–54. Available from: <DOI>.

38. Günay A, Dikmen S, Ersoy B, Evcin A. Adsorption of Basic Blue-16 Dye onto Clay. Environ Eng Manag J. 2014;13(2):395–405. Available from: <URL>.

39. Xu J, Tian Y, Li Z, Tan BH, Tang KY, Tam KC. β-Cyclodextrin functionalized magnetic nanoparticles for the removal of pharmaceutical residues in drinking water. J Ind Eng Chem. 2022;109:461–74. Available from: <DOI>.

40. Civan Çavuşoğlu F, Akan S, Arı EA, Çetinkaya E, Çolak E, Daştan GN, et al. Preparation of magnetic activated carbon-chitosan nanocomposite for crystal violet adsorption. Korean J Chem Eng. 2019;36(11):1915–21. Available from: <DOI>.

41. Dada A.O, Olalekan A.P, Olatunya, A.M, Dada O. Langmuir, Freundlich, Temkin and Dubinin–Radushkevich Isotherms Studies of Equilibrium Sorption of Zn^{2+} Unto Phosphoric Acid Modified Rice Husk. IOSR J Appl Chem. 2012;3(1):38–45. Available from: <DOI>.

42. Pormazar SM, Dalvand A. Adsorption of Reactive Black 5 azo dye from aqueous solution by using amine-functioned Fe_3O_4 nanoparticles with L-arginine: Process optimisation using RSM. Int J Environ Anal Chem. 2022 Jun 21;102(8):1764–83. Available from: <DOI>.

43. Alamin NU, Khan AS, Nasrullah A, Iqbal J, Ullah Z, Din IU, et al. Activated carbon-alginate beads impregnated with surfactant as sustainable adsorbent for efficient removal of methylene blue. Int J Biol Macromol. 2021;176:233–43. Available from: <DOI>.

44. Ravi, Pandey LM. Enhanced adsorption capacity of designed bentonite and alginate beads for the effective removal of methylene blue. Appl Clay Sci. 2019;169(October 2018):102–11. Available from: <DOI>.

45. Rocher V, Siaugue JM, Cabuil V, Bee A. Removal of organic dyes by magnetic alginate beads. Water Res. 2008;42(4–5):1290–8. Available from: <DOI>.

46. Li C, Lu J, Li S, Tong Y, Ye B. Synthesis of Magnetic Microspheres with Sodium Alginate and Activated Carbon for Removal of Methylene Blue. Materials (Basel). 2017 Jan 20;10(1):84. Available from: <DOI>.

47. Eltaweil AS, Mamdouh IM, Abd El-Monaem EM, El-Subruiti GM. Highly efficient removal for methylene blue and Cu^{2+} onto UiO-66 metal–organic framework/carboxylated graphene oxide-incorporated sodium alginate beads. ACS Omega. 2021 Sep 14;6(36):23528–41. Available from: <DOI>.

JOTCS A
Journal of the Turkish Chemical Society
Section: A
Chemistry
TURKISH CHEMICAL SOCIETY

Investigation on the Quality of Prolonged Storage of Packaged Water Commonly Produced in North Central, Nigeria

Fatai Olayiwola OKEOLA[1], Taofiqat Omotayo ABU[1], Aminat Aderonke MOHAMMED[1]*, Muyiwa Michael OROSUN[2], Abdullahi BABA[1], Mariam Bolanle ADEBOJE[1]

[1]University of Ilorin, Department of Industrial Chemistry, Kwara State, Nigeria.
[2]University of Ilorin, Department of Physics, Kwara State, Nigeria.

Abstract: This study investigated the effects of prolonged storage conditions on the physicochemical parameter, toxic metals, microbial loads, and health risks assessment of randomly selected three brands of sachet and bottled water in North Central, Nigeria. One hundred eighty samples of water brands (sachet and bottled) were collected from 10 different factories and were grouped into three. They were analyzed immediately (initial), being exposed to mild sunlight (stored with a container) and exposed to intense sunlight (stored without a container) conditions for six weeks. The results of the physicochemical parameters (sachet and bottle) were within the limits set by the World Health Organization (WHO) and the Standard Organization of Nigeria (SON). While the results of heavy metals analysis for both sachet and bottled water recorded 0.15 - 0.51 mg/L (0.10 mg/L , 0.05 mg/L), 0.13 - 0.38 mg/L (0.015 mg/L, 0.01 mg/L) and 0.55 - 1.11 mg/L (0.03 mg/L, 0.3 mg/L) for Chromium (Cr), Lead (Pb) and Iron (Fe) respectively, as compared to the permissible limits (values in the bracket for each heavy metals) set by WHO and SON. The microbial analysis results ranged between 6.58 - 124.51 Cfu/100 mL, 0.52 - 37.56 Cfu/100 mL, 0.07 - 5.00 Cfu/100 mL, 0 - 2.07 Cfu/100 mL for Total Bacteria Count (TBC), Total Coliform Count (TCC), Faecal Coliform Count (FCC) and Total Fungal Count (TFC) respectively, which showed no effective quality control system. Incremental lifetime cancer risk (ILCR) assessment revealed a carcinogenic health risk to the populace drinking this water. The study concludes that water stored under sunlight for a long period is not good for human consumption and therefore adequate monitoring by the appropriate agencies is emphasized.

Keywords: Sunlight, Ilorin, sachet water, storage condition, microbial analysis.

Submitted: May 16, 2022. **Accepted:** January 26, 2023.

Cite this: OKEOLA FO, ABU TO, MOHAMMED AA, OROSUN MM, BABA A, ADEBOJE MB. Investigation on the Quality of Prolonged Storage of Packaged Water Commonly Produced in North Central, Nigeria. JOTCSA. 2023;10(2):303–14.

DOI: https://doi.org/10.18596/jotcsa.1116034.

***Corresponding author. E-mail:** mohammed.aa@unilorin.edu.ng.

1. INTRODUCTION

Water is an essential liquid for human day-to-day activities. It is a basic need for human existence required to maintain personal hygiene, prevention of diseases, and food production (1-3). Waterfalls such as rain can be found in lakes and rivers which are the primary sources of fresh water for agriculture, human consumption, and industrial uses (4, 5). Portable water is a source of water that is properly treated and showed a minute amount of contaminants such as toxic metals, microorganisms, nitrates, sulfates among others (5, 6, 7). Various natural processes (such as wind deposition, weathering of rocks, soil leaching, and biological processes) and anthropogenic activities (such as agricultural run-off, mining, recreational activities, industrial and domestic sewage) all contribute to the release of contaminants into water bodies, which poses serious health risks like malnutrition, gastrointestinal diseases, slowing nutrient absorption, and disrupting the endocrine system, among others (5, 8, 9).

According to WHO/UNICEF (10), over 844 million people in most developing countries lack adequate

good water supply as a result of an increase in population and urbanization, and this paves way for packaged water as a fast-growing business in most developing countries. The water business is very lucrative due to the rate at which consumers buy this packaged water (sachet and bottled). Sachet and bottled water can come from a variety of sources, including well, water from a protected spring, or water from a public water supply. However, there is a great risk associated with water produced in an unsafe and unhygienic environment (11, 12). Many scholars have reported that sachet and bottled water are the major drivers for the transmission of pathogens and toxic metals into the body (13, 14, 15, 16), and these often resulted in several health challenges among children and infants, with noticeable effects including water-borne diseases like diarrhea, typhoid, cholera, hepatitis, and dysentery among others (17, 18, 19, 20).

Similarly, several researchers reported that the main problems associated with the production of sachet and bottled water in Nigeria include the way they were handled during the production process, ways in which distributors and vendors transported the packaged water, and how the packaged water was stored for several weeks before they were sold (21, 22). In most of the cities and towns in Nigeria, sachet and bottled water are often stored and exposed to direct sunlight without adequate knowledge of the effect of the quality of this packaged water on the populace buying them. To the best of our knowledge, the rate at which packaged water (sachet and bottled) production increases in the Ilorin metropolis (North Central, Nigeria) is becoming so alarming. However, there is a need for a routine investigation on the quality of prolonged storage of both sachet and bottled water exposed to sunlight under different storage conditions.

This research aimed to determine the physicochemical, heavy metal concentrations, microbial analysis, and human health risk assessment of some sachet and bottled water sold within North Central, Nigeria, and compared the results obtained with the permissible limits of the Standard Organization of Nigeria (SON) and World Health Organization (WHO).

2. MATERIAL AND METHODS

2.1. Description of the Study Area

The Kwara State of Nigeria belongs to North Central Nigeria. There are sixteen Local Government Areas in Kwara State, with the capital city at Ilorin. The Local Government Area in Kwara State includes Ilorin East, Ilorin South, Ilorin West, Moro, Kaima, Asa, Offa, Ekiti, and Edu among others. The Ilorin West Local Government lies between latitude 4° 28 E, 8° 34 N and longitude 4° 35 E, 8° 24 as shown in Figure 1. According to National Population Census 2006, the population of Ilorin West People is 364,666 with a total landscape of 105 square kilometers.

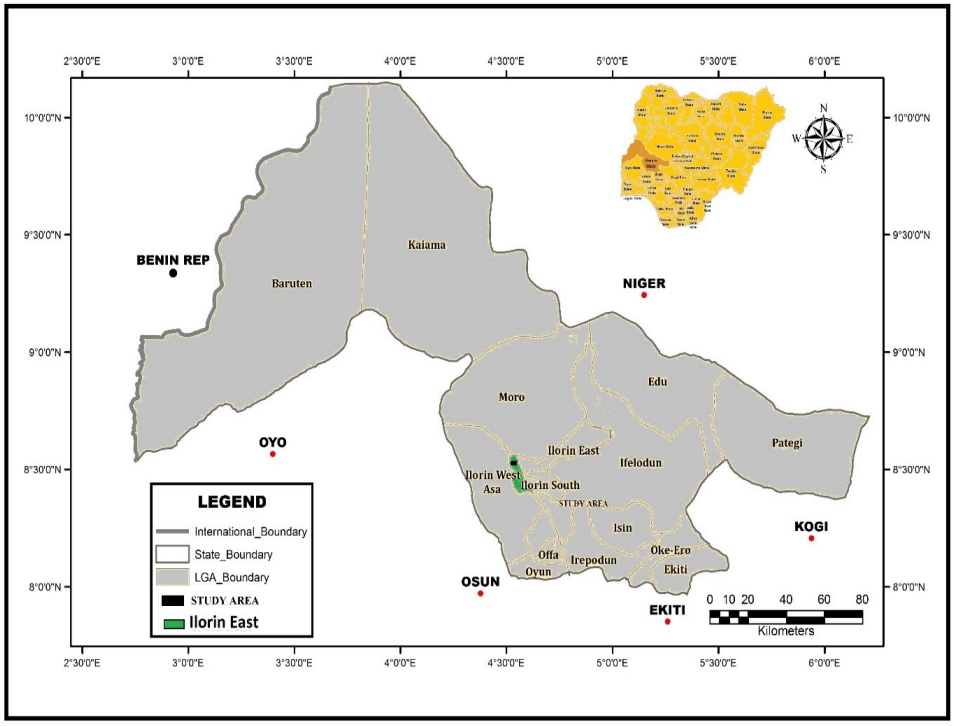

Figure 1: Showing Map of Ilorin West Local Government Area, Kwara State, Nigeria.

2.2. Sample Collection and Preparation

Three brands of sachet and bottled water were collected from three factories. Thirty samples each of sachet and bottled were procured from each factory amounting to a total of 180 samples (90 sachets and 90 bottled water). For each brand, the samples were divided into groups A, B, and C. Group A represents 20 water samples (10 sachet and 10 bottles) analyzed immediately (initial) after being purchased from the factories. Group B represents 20 water samples stored in a container and exposed to sunlight for six weeks (mild condition) before analysis. And Group C represents 20 water samples stored and exposed directly to the sunlight without a container for six weeks (intense condition) before analysis.

2.3. Reagents and Pretreatment

Milli-Q water, HNO_3 (65%), and HCl (37%) analytical grades were purchased from Merck Darmstadt, Germany. All glassware used for this study was soaked in 1M HNO_3 for 24 hours and rinsed severally with distilled water.

2.4. Physico-chemical Parameters

The pH was measured using a pH meter Ino Lab Tech 7310 digital multimeter, which gives a direct value of pH, and it was calibrated with buffer solutions (pH 4 and 7). A thermometer was used to measure the temperature of the water samples in situ. Electrical conductivity (EC) and total dissolved solids (TDS) were determined by the HANNA Digital multimeter and it was calibrated with potassium chloride solution. Alkalinity, hardness, chloride, and calcium contents were determined titrimetrically. The concentration of magnesium contents was determined by subtracting the concentrations of calcium from total hardness. sulfate contents were determined turbidimetrically and Nitrate contents were determined by the Brucine method (23). Water samples were taken from each brand in triplicates for the analysis.

2.5. Determination of Toxic Metals

A 50 mL of each water sample (sachet and bottled) was digested by aqua regia method of digestion using HNO_3/HCl in 1:3 ratio and was later analyzed for the presence of toxic metals, namely chromium (Cr), lead (Pb), and iron (Fe) in triplicates using Atomic Absorption Spectrophotometer (AAS-Buck Scientific Model 210 VGP, USA).

2.6. Quality Control Determination

Calibration curves were plotted for all analyzed elements (Cr, Pb, and Fe) which were used to measure the absorbance value for the blank and working standard solution (which was prepared from a stock standard of each metal using Milli- Q water) to determine the concentrations of toxic metals in the digested samples. The detection limits of the instrument range from 0.005 – 0.040 mg/L as shown in Table 1. Blank determination was done by weighing 2 mL of HNO_3 in a beaker with 6 mL of HCl added, and the mixture was heated in the water bath for 40 minutes and cooled. The mixture was transferred to a 50 mL standard flask and make-up to the mark with distilled water. The experiment was repeated three times and then analyzed using Atomic Absorption Spectrophotometer. A recovery study was done by spiking 10 mL of heavy metal standards (Cr, Pb, and Fe) to already analyzed water samples and re-analyzed (A). A known amount of water samples (sachet and bottled) was left un-spiked (Z) and analyzed using AAS. The percentage recovery study (R.S%) was evaluated using the equation 1 (24)

$$R.S\% = \frac{A - Z}{10} \quad (1)$$

Table 1: Detection limits of the instrument.

Elements	Instrument detection limits (mg/L)
Cr	0.005
Pb	0.040
Fe	0.007

2.7. Microbiological Parameters

Total bacterial count (TBC), total coliform count (TCC), and total fungal count were also determined in each of the water samples using multiple tube fermentation and membrane filtration methods described by (25).

2.8. Human Health Risk Assessment

The association between the concentration of the toxic metals and their apparent risk to human health is generally appraised by the human health risk assessment models established by the USEPA (26, 27, 28) and UNC (29). This technique is accessible using the risk assessment information system (RAIS) USEPA (26) and the toxicological profiles presented by the United State Environmental Protection Agency's Integrated Risk Information System (IRIS) (30, 31, 32), in collaboration with the United State Agency for Toxic Substances and Disease Registry – Toxicological profiles (33). In this current research, the risk evaluation of the toxic elements (Cr, Pb and Fe) was initiated by primarily evaluating the chronic daily intake (CDI) of each of the metals through the possible exposure pathways (in this case, ingestion pathway).

For the ingestion pathway of exposure, the chronic daily intake (CDI) (mg/L/day) was evaluated by the following equation 2 USEPA (34).

$$ADI_{\text{ing-water}} = \frac{Cw \times Ing Rw \times EF \times ED}{BW \times AT} \quad (2)$$

Where C_w is the concentration of the given heavy metal in the sampled drinking water, BW is bodyweight of the exposed person (70 kg), ED is

the lifetime exposure period (average life expectancy of Nigerians is 55 years), EF is the exposure frequency (365 days/year), AT is the period through which the dose is averaged (ED x 365 days) and $IngR_w$ is the ingestion rate of the drinking waters (2 L/day).

2.9. The Carcinogenic and Non-Carcinogenic Risk Assessment

The calculated chronic daily intake (CDI) in proportion to oral reference dose (RfD_{oral}) of the selected toxic metals branded as target Hazard Quotient (HQ), is generally utilized to highlight the severity of the non-carcinogenic risks. The hazard quotient is called by the formula in equation 3 as described by USEPA (26);

$$HQ = \frac{ADI}{RfD} \quad (3)$$

where CDI is the chronic daily intake of a given toxic constituent and RfD is the persistent reference dose for the element i.e. for the Cr, Fe, and Pb, we have 3.0E-03, 9.0E-02, 3.5E-03 mg/L-day (34). If the HQ > 1, however, there is an increased probability of unfavorable health effects to the exposed populace. Conversely, if HQ < 1 subsequently there is no possibility of negative health effects (35).

The hazard index (HI) is the sum of the HQ calculated using Equation 4

$$HI = \sum HQ \quad (4)$$

According to the risk classification system assembled by the International Agency for Research on Cancer (IARC) and WHO, among the toxic metals analyzed in this study, Pb and Cr were human carcinogens, and their carcinogenic slope factors are 8.5E-03 and 0.5 $(mg/L/day)^{-1}$ respectively (30). The carcinogenic risk estimation gives an index of risk or possibility of an aimed people developing cancer of several types as a result of the ingestion of the carcinogens in the drinking water over a projected lifetime. Incremental Lifetime Cancer Risk (ILCR**)** presents the carcinogenic risk calculated using equation 5 (30, 36).

$$ILCR = ADI \times SF \quad (5)$$

Where CDI (mg/L/day) and SF $(mg/L/day)^{-1}$ are the mean daily consumption of the toxic metals and the carcinogenic gradient factor. Cancer risk higher than 1E-04 is considered high as they pose a higher cancer threat while values below 1E-06 are assumed not to cause any cancer risk to the populace; the suitable range is flanked by 1E-04 and 1E-06.

3. RESULTS AND DISCUSSION

The recovery study (R.S%) was done to ascertain the analytical method employed in the determination of toxic metals in the water samples (sachet and bottled water). The R.S% estimated ranges between 85.2 - 102.8% as illustrated in Table 2.

Table 2: Recovery study of toxic metals in the water samples.

Water Samples	Toxic metals Analyzed	Amount Spiked	Amount Un-spiked	R.S%
Sachet	Cr	62.55	54.03	85.2
	Pb	34.39	25.06	93.3
	Fe	58.50	48.22	102.8
Bottled	Cr	48.73	39.02	97.1
	Pb	74.95	65.31	96.4
	Fe	29.54	20.65	88.9

The physicochemical parameters, toxic metals, and microbiological analysis examined show considerable variations in the sachet and bottled water samples analyzed as shown in Figures 2 - 6. The pH value of all the brands of water analyzed ranged from 6.56 - 8.22. The pH of the water sample was recorded between 6.65 - 7.28 and 7.78 - 8.22 for bottled and sachet water respectively (Figure 2a & b). This is similar to the report by previous researchers (37, 38, 39). Water samples stored at mild sunlight exposure (Group 2) ranged from 6.79 - 8.01 and 6.62 - 8.00 for intense sunlight exposure (Group 3). Water samples in Brand 3 recorded the highest pH value of 8.22 and 7.28 (Group 1) for sachet and bottled water respectively. An increase in the pH values of water can lead to an increase in the bacteria population (10). An increase in the pH values could be due to the different modes of storage as shown in Figure 2. The pH values of all the water brands were within the recommended pH range WHO (40), SON (41), and WHO (42) as shown in Table 3. The mean temperature value ranged from 28.61 - 30.64 ^{0}C for all brand samples analyzed (Figure 2). Samples of water analyzed immediately (initial) after being purchased from the factories ranged between 28.70 - 29.03 ^{0}C (Group 1). While samples of water stored and exposed to mild and intense sunlight exposure ranged between 29.82 - 30.64 ^{0}C (Group 2 and 3) as shown in Figure 2. This is similar to the previous report elsewhere (43). An increase in the warmness of an

environment favours the growth of microorganisms and this can affect the taste and odour of the water samples (44). Turbidity values in all the brands of water samples analyzed (bottled and sachet) were found to be less than 5 NTU for all the water samples exposed to different storage conditions. The turbidity values recorded were all within acceptable limits of 5 NTU (41, 42) as shown in Table 3. Conductivity values in all the brands of water samples (sachet and bottled) ranged from 45.33 - 160.12 µS/cm. Water samples analyzed immediately (Group 1) ranged from 89.9 - 146.90 µS/cm, while water samples exposed to mild (Group 2) and intense sunlight (Group 3) ranged from 49.55 - 131.30 µS/cm and 53.94 - 147.20 µS/cm respectively. This is similar to the previous study reported in the literature (45, 46). Brands 1 and 3 (Group 1) recorded the lowest results in both sachet and bottled water. The TDS concentrations of the water samples in all the brands ranged from 22.03 - 81.00 mg/L as shown in Figure 2. Water samples analyzed immediately (Group 1) recorded 30.00 - 81.00 mg/L for both sachet and bottled water brands. A similar result was reported elsewhere (46). While water samples (sachet and bottled) stored under mild (Group 2) and intense sunlight exposure (Group 3) ranged from 22.03 - 65.76 mg/L and 23.51 - 73.60 mg/L respectively (Figure 2). TDS was found to be within the permissible limit of 500 mg/L as shown in Table 3.

The total hardness concentration (TH) ranged from 20.05 - 80.40 mg/L for all brands of water analyzed. The hardness values recorded were all within WHO-acceptable limits (100 mg/L). TH of the water samples (sachet and bottled) stored under mild sunlight exposure (Group 2) ranged from 20.05 - 76.11 mg/L (Figure 3). While those stored under intense sunlight conditions (Group 3) ranged from 24.13 - 80.40 mg/L. A similar result was obtained elsewhere (44). The results obtained in this study showed an increase in the value of hardness when subjected to both mild and intense sunlight conditions. Chloride concentration ranged from 0.43 - 41.83 mg/L for all brands of water stored under different conditions. The highest chloride concentration value of 41.83 mg/L was recorded in Brand 3 for sachet water analyzed (Figure 3a), and the least was recorded in the bottled water in Brand 1 (1.03 mg/L), (Figure 3b). The Calcium (Ca) concentration ranged from 11.33 - 54.08 mg/L for all the brands of water samples (initial, mild, and intense) for both sachet and bottled water. This result followed a similar trend to the previous study (46). The highest value of calcium was recorded in Brand 3 (54.08 mg/L) and the lowest was recorded in Brand 2 (11.33 mg/L) for mild and initial sunlight exposure respectively. The concentration of calcium was found to be lower than the permissible limit set by WHO as indicated in Table 3. The concentration of magnesium in all the water samples analyzed ranged from 6.02 - 30.22 mg/L in all brands of water used for this study. The results obtained were found to be higher than the previous reports elsewhere (47, 48). A higher concentration of magnesium is known to cause water hardness, and cathartic and diuretic effects in the human body (49). The concentration of sulfate was found to be lower in bottled water (0.01 - 0.03 mg/L) than the values obtained in sachet water (0.01 - 0.15 mg/L). The concentration of sulfate reported in this study is lower than the values obtained in previous literature (50, 51). The concentration of sulfate was found to be lower than the permissible limit (100 mg). Alkalinity values ranged from 2.16 - 8.32 mg/L for all the water brand samples investigated. It was observed that there is a variation in the concentration of the water samples exposed to various storage conditions (mild and intense sunlight exposure). High values of Alkalinity were reported in similar work (50, 51). The values of Nitrate obtained in water samples ranged from 2.11 - 8.47 mg/L. The Nitrate value recorded ranged from 3.9 - 7.0 mg/L and 2.11 - 8.47 mg/L in sachet (Figure 3a) and bottled (Figure 3b) water respectively. This is similar to the previous literature (50, 51). The Nitrate contents in all the brands of water investigated were below the permissible limits by WHO (40), SON (41) and WHO (42) as shown in Table 3.

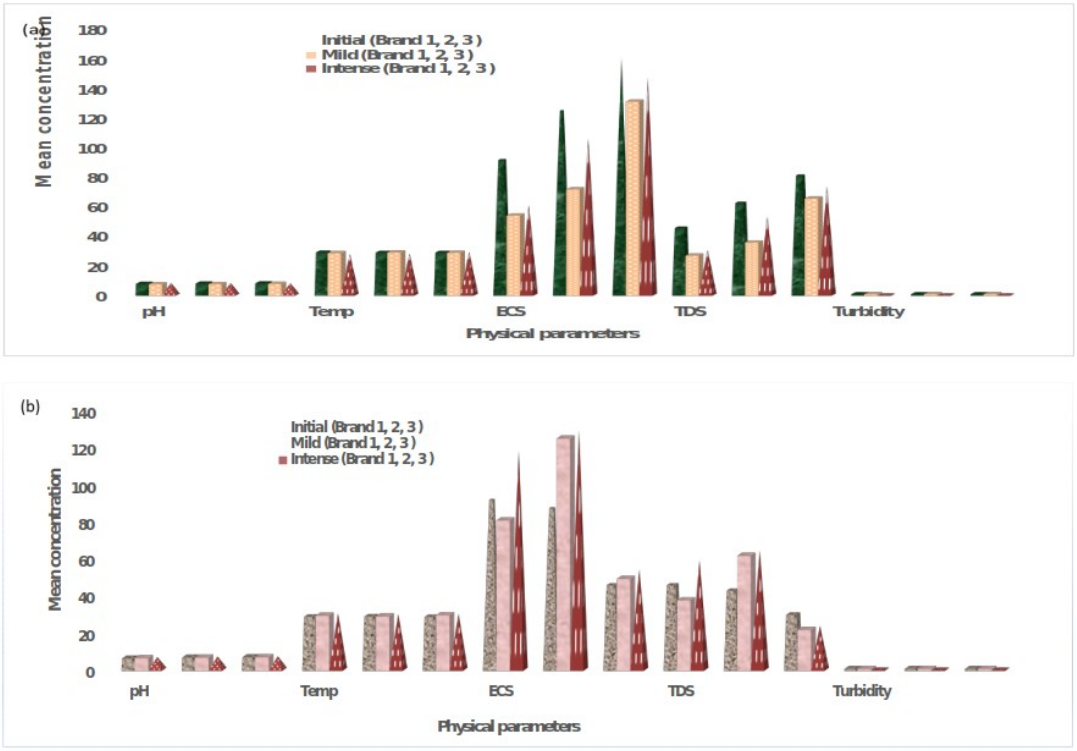

Figure 2: Showing Variation of Physical Parameters in (a) sachet water and (b) bottled water groups.

Table 3: Permissible limits set by WHO and SON.

Parameter	Maximum Permissible limits WHO[a]	SON[b]
pH	6.5-8.5	6.5-8.5
Temperature	35-40 °C	Ambient
Electrical Conductivity	1.0 ms/cm	1000 µs/cm
Total Dissolved Solids	500 mg/L	500 mg/L
Turbidity	5 NTU	5 NTU
Total Hardness	100 mg/L	150 mg/L
Calcium	200 mg/L	
Magnesium	150 mg/L	-
Chloride	100 mg/L	250 mg/L
Sulfate	250 mg/L	100 mg/L
Nitrate	10 mg/L	50 mg/L
Alkalinity	200 mg/L	NA
Chromium	0.10 mg/L	0.05 mg/L
Lead	0.015 mg/L	0.01 mg/L
Iron	0.03 mg/L	0.3 mg/L
Total bacterial count	100 cfu/mL	NA
Total Coliform Count	NA	NA
Faecal Coliform Count	Negative	NA
Total Fungal Count	1-130 cfu/L	NA

* WHO[a] (2006, 2011) *SON[b] (2007) *NA= Not available *NA=Not Available

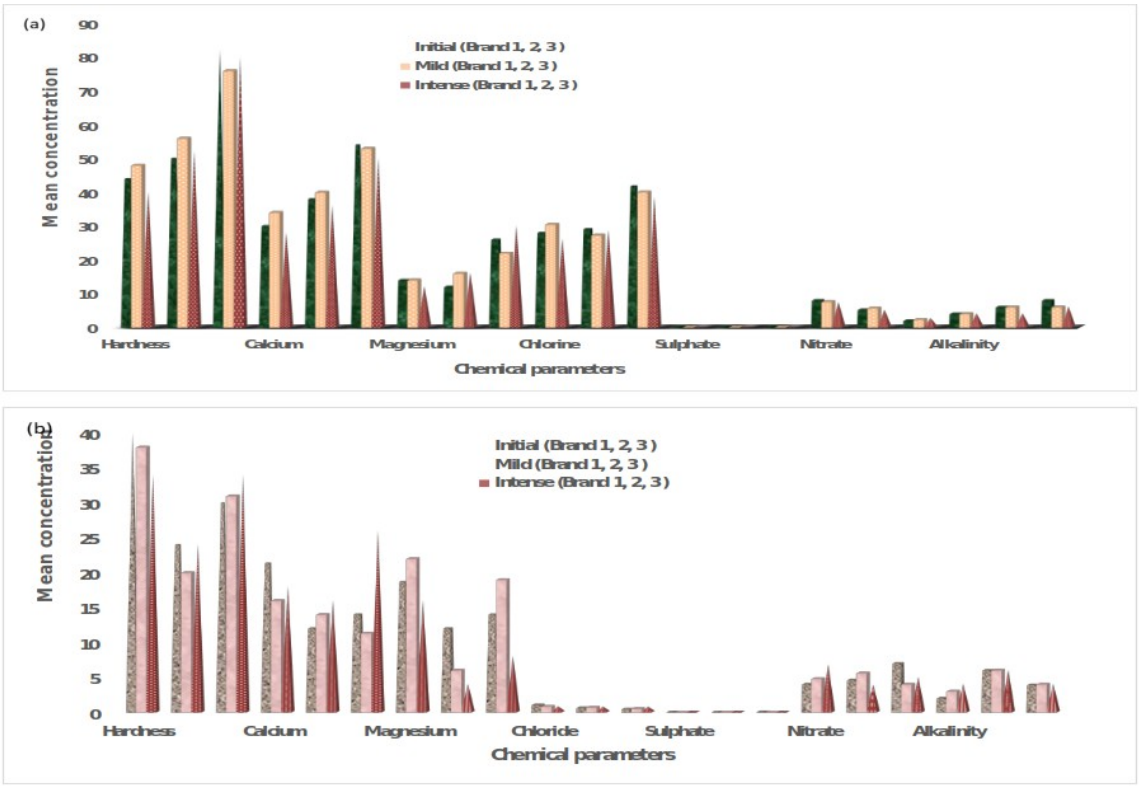

Figure 3: Showing Variation of Chemical Parameters in (a) sachet water and (b) bottled water groups.

Chromium (Cr) value ranged from 0.15 - 0.51 mg/L for all the water samples analyzed under different conditions of storage which was found to be higher than the permissible limit set by both SON and WHO (Table 3). Cr contents ranged from 0.14 - 0.22 mg/L and 0.16 - 0.51 mg/L) in both sachet (Figure 4a) and bottled water samples (Figure 4b) respectively. This result is well corroborated by the previous researcher (52). Cr at a very high concentration is known to be toxic to humans and can cause cancer. Lead (Pb) value ranged from 0.13 - 0.38 mg/L for all the brands of water samples. The presence of Lead in high concentrations can damage nervous connections (especially in young children), cause blood, and brain disorders. Pb is also known to be a possible human carcinogen (53). The concentration of Pb in all samples from the different brands was found to be higher than the acceptable limits of 0.015 mg/L and 0.01 mg/L set by WHO (40) and SON (41) as shown in Table 2. The mean concentrations of Iron (Fe) obtained in all the water samples ranged from 0.55 - 1.11 mg/L. The results obtained in this study are similar to the results earlier reported in the literature (44, 54). The highest concentration of Fe was recorded in Brand 2 (sachet) and the least concentration in Brand 1 (bottled) for intense and mild sunlight exposure respectively. The Fe concentrations ranged from 0.55 - 1.06 mg/L and 0.69 - 1.11 mg/L for water samples stored under mild and intense sunlight conditions respectively (Figure 4). There is a variation in the values of all the parameters checked on all the brands of water samples stored under different conditions (mild and intense sunlight exposure). This could be a result of the geochemistry of the soil in which water is drilled, water treatment methods employed, ways of handling and transportation of the packaged water (sachet and bottled) from the vendors to final consumers.

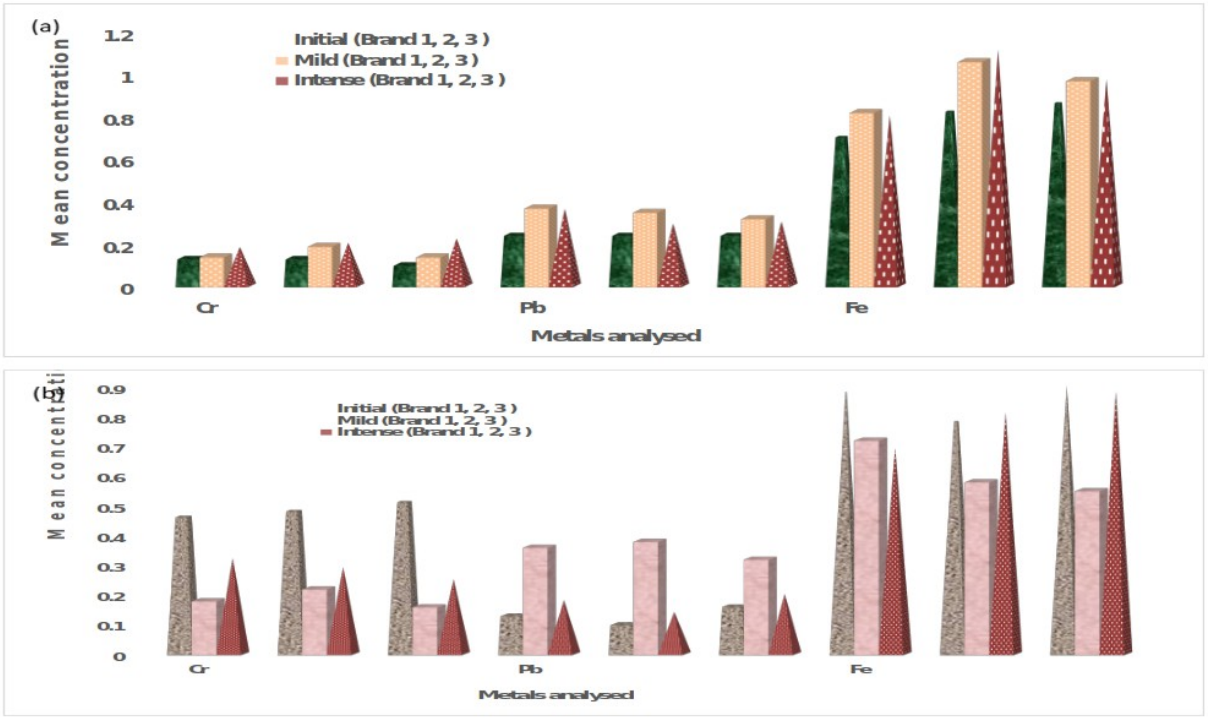

Figure 4: Showing variation of metals analyzed in (a) sachet water and (b) bottled water groups.

The value of Total bacteria count (TBC) ranged from 6.58 - 124.51 Cfu/100 mL for all the water samples (Figure 5). TBC values recorded for water samples stored under mild and intense sunlight condition ranged from 14.51 - 124.51 Cfu/100 mL and 21.55 - 84.05 Cfu/100 mL, respectively. This follows a similar trend to the previous reports elsewhere (46, 55). This is because a warm environment favors the growth of bacteria. The TBC found in all the water samples was found to be higher than permissible limits by WHO (40), SON (41), and WHO (42) as shown in Table 3. The value of Total coliform count (TCC) ranged from 0.52 - 37.56 Cfu/100 mL for all the water samples (Figure 5). The TCC values ranged from 0.52 - 5.0 Cfu/100 mL and 1.05 - 37.5 Cfu/100 mL in both bottled and sachet water, respectively. The result obtained in this study is higher than the previous report in the assessment of the quality of water before and after storage in the Nyankpala Community of the Tolon-Kumbungu District, Ghana (46) and lower than the previously reported research from different scholars (56, 57, 58). Brand A water sample showed no TCC value in bottled water as compared to other brands of water samples which were above the limits set by WHO (33) and (34). Water samples analyzed immediately recorded Faecal coliform count (FCC) that ranged between 0.09 - 0.27 Cfu/100 mL. The FCC values ranged from 0.53 - 5.10 Cfu/100 mL and 0.51 - 1.08 Cfu/100 mL in both sachet (Figure 5a) and bottled water (Figure 5b) respectively for mild and intense storage conditions. Total fungi count (TFC) found in all the sachet water samples ranged from 0 - 2.07 Cfu/100 mL which are lower than the permissible limit by WHO and SON. TFC analysis showed that water analyzed at zero-day (initial) has 0 Cfu/100 mL for all the brands. While those exposed to mild sunlight exposure recorded 0.64 - 2.07 Cfu/100 mL and samples stored under intense sunlight exposure recorded 0.52 - 1.11 Cfu/100 mL which are below the limits set by WHO (40) and SON (41). The results obtained in this study showed that as the temperature increases, microbial loads (TBC, TCC, FCC and TFC) also increase for water samples exposed to mild and intense storage conditions.

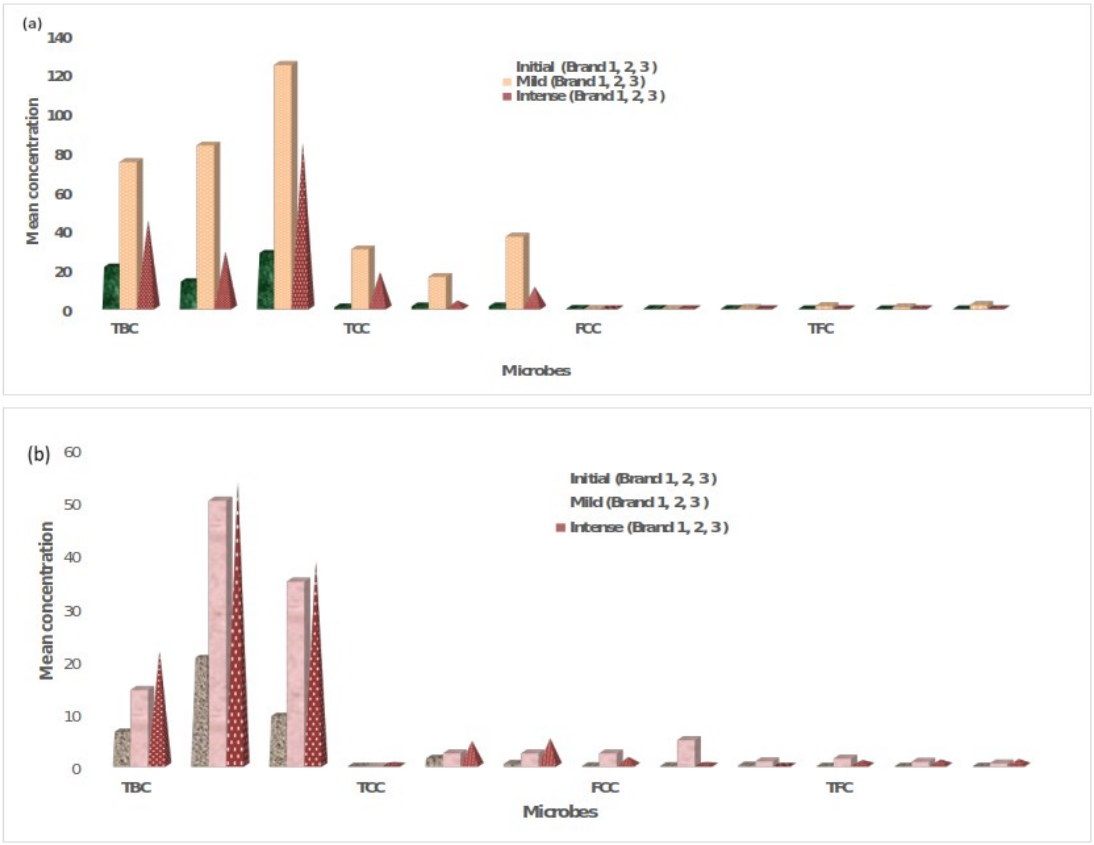

Figure 5: Showing the variation of (a) microbial analysis in sachet water and (b) bottled water groups.

The Hazard Quotient (HQ) estimated for all the toxic metals in all the three (3) water groups (i.e. initial, mild and intense conditions) are within the recommended safe limit (<1)) set by USEPA (34). The total Hazard Index (HI) for the initial, mild, and intense condition groups are 0.8373, 0.6620, and 0.6664 respectively for bottled water and 0.1874, 0.2446, and 0.2512 respectively for sachet water (Figure 6). The results obtained in this study imply that the general populaces are not in any danger of non-carcinogenic health effects of these toxic metals. While the mean HI value for the initial conditioning appears to be greater than the mild and intense conditioning category for the bottled water, the reverse is the case with sachet water where the mean HI value for the intense conditioning is greatest.

The Incremental Lifetime Cancer Risk (ILCR) was estimated and the mean values for the initial, mild and intense condition groups are 8.86E-4, 1.16E-3, and 1.47E-3 respectively for the sachet water (Figure 6a), 6.94E-03, 2.75E-03, and 4.14E-03 respectively for the bottled water (Figure 6b), and with Cr contributing most to the cancer risk in both cases. Because cancer risks greater than 1.00E-4 are considered high since they pose a higher cancer risk, and values below 1.00E-6 are considered not to pose any cancer risk to humans, it follows that the cancer risks are high for the three (3) water groups (i.e. initial, mild and intense condition) for both sachet and bottled water. Since the result reveals values of ILCR that are 100% higher than the recommended limit, the general populace is in danger of carcinogenic health effects. However, it is noteworthy that the reported carcinogenic and non-carcinogenic risk values in this study may be undervalued because the appraisals did not capture intakes from other metals like arsenic, cadmium, and nickel, among others, and the exposure parameters (i.e. EF, AT, BW and ED) used were adopted from USEPA (28), so might not ineludibly represent a typical Nigerian case.

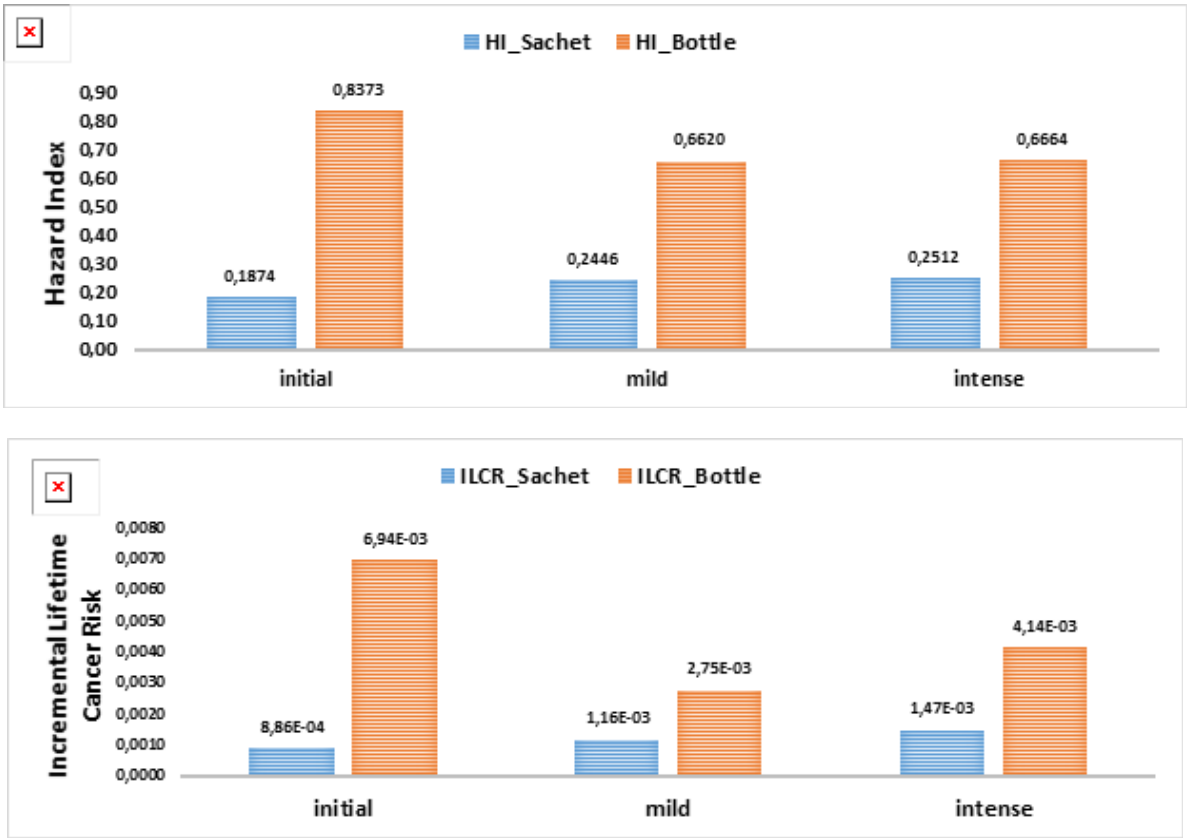

Figure 6: Showing (a) Hazard Index and (b) Incremental Lifetime Cancer Risk for all the water groups

4. CONCLUSION

Water is a liquid needed at all times for several human activities. This study revealed that the samples taken to the laboratory were operating within the WHO limits for physicochemical guidelines for drinking water regardless of the mode of storage. Heavy metal concentrations were found to be above the limits set by WHO/SON in all the water samples analyzed. While the corresponding carcinogenic risks revealed values that are higher than the recommended safety range, the non-carcinogenic risk assessment reveals values within the acceptable limits. Thus, the study reveals that the general populace is in danger of carcinogenic health effects. The appearance of microbial loads (TBC, TCC, FCC, and TFC) in all the water analyzed revealed prolonged storage of water has led to an increase in microbial growth. Therefore, this study concluded that water samples exposed to prolong sunlight are not safe for human consumption. However, proper monitoring and compliance with drinking water standards are adequately required by various agencies.

5. CONFLICT OF INTEREST

No conflict of interest was declared by the authors.

6. ACKNOWLEDGMENTS

All authors appreciate the support given to us by the Department of Industrial Chemistry, University of Ilorin, Ilorin, Nigeria for providing laboratory facilities for this research.

7. REFERENCES

1. Oparaocha E, Iroegbu O, Obi R, others. Assessment of quality of drinking water sources in the Federal University of Technology, Owerri, Imo state, Nigeria. J Appl Biosci. 2010;32:1964–76.

2. Edema M, Atayese A, Bankole M. Pure water syndrome: Bacteriological quality of Sachet- packed drinking water sold in Nigeria. African Journal of Food, Agriculture, Nutrition and Development [Internet]. 2011 Apr 29 [cited 2023 Mar 11];11(1). Available from: <URL>

3. Adegoke O, Bamigbowu E, Oni E, Ugbaja K. Microbiological examination of sachet water sold in Aba, Abia State, Nigeria. Global Research Journal of Microbiology. 2012;2(1):62–6.

4. Hoekstra AY, Chapagain AK. Water footprints of nations: Water use by people as a function of their consumption pattern. Water Resour Manage. 2006 Dec 27;21(1):35–48. Available from: <URL>.

5. Khatri N, Tyagi S. Influences of natural and anthropogenic factors on surface and groundwater quality in rural and urban areas. Frontiers in Life Science. 2015 Jan 2;8(1):23–39. Available from: <URL>.

6. Singh S, Mosley LM. Trace metal levels in drinking water on Viti Levu, Fiji Islands. S Pac J Nat App Sci. 2003;21(1):31. Available from: <URL>.

7. Sharma S, Bhattacharya A. Drinking water contamination and treatment techniques. Appl Water Sci. 2017 Jun;7(3):1043–67. Available from: <URL>.

8. Kim KH, Jahan SA, Kabir E, Brown RJC. A review of airborne polycyclic aromatic hydrocarbons (PAHs) and their human health effects. Environment International. 2013 Oct;60:71–80. Available from: <URL>.

9. Lin L, Yang H, Xu X. Effects of Water Pollution on Human Health and Disease Heterogeneity: A Review. Front Environ Sci. 2022 Jun 30;10:880246. Available from: <URL>.

10. WHO/UNICEF. World Health Organization/United Nations children's fund (WHO/UNICEF). Progress on Drinking Water, Sanitation and Hygiene: 2017 Update and SDG Baselines. 2017 [Internet]. Progress on Drinking Water, Sanitation and Hygiene: 2017 Update and SDG Baselines. 2017 [cited 2021 Dec 14]. Available from: <URL>.

11. Pal M, Ayele Y, Hadush M, Panigrahi S, Jadhav V. Public health hazards due to unsafe drinking water. Air Water Borne Dis. 2018;7(1000138):2.

12. Haack SK, Fogarty LR, Wright C. *Escherichia coli* and Enterococci at Beaches in the Grand Traverse Bay, Lake Michigan: Sources, Characteristics, and Environmental Pathways. Environ Sci Technol. 2003 Aug 1;37(15):3275–82. Available from: <URL>.

13. Love MR. Production and Vendor Practices that Compromise the Quality of "Sachet" Water in the Central Region, Ghana. IJSTS. 2013;1(3):64. Available from: <URL>.

14. Dafae F, Bopp C, Kargbo D, Stroika S, Kamara A, Ayers T, et al. Cholera Epidemic Associated with Consumption of Unsafe Drinking Water and Street-Vended Water—Eastern Freetown, Sierra Leone, 2012. The American Journal of Tropical Medicine and Hygiene. 2014 Mar 5;90(3):518–23. Available from: <URL>.

15. Emenike PC, Tenebe TI, Omeje M, Osinubi DS. Health risk assessment of heavy metal variability in sachet water sold in Ado-Odo Ota, South-Western Nigeria. Environ Monit Assess. 2017 Sep;189(9):480. Available from: <URL>.

16. Manjaya, Tilley, Marks. Informally Vended Sachet Water: Handling Practices and Microbial Water Quality. Water. 2019 Apr 17;11(4):800. Available from: <URL>.

17. Yusuff AS, John W, Oloruntoba AC. Review on prevalence of waterborne diseases in Nigeria. Journal of Advancement in Medical and life sciences. 2014;1(2):1–3.

18. Nwabor OF, Nnamonu E, Martins P, Ani O. Water and waterborne diseases: a review. Int J Trop Dis Health. 2016;12(4):1–14.

19. Quah SR, editor. International encyclopedia of public health. Second edition. Kidlington, Oxford: Elsevier; 2017. ISBN: 978-0-12-803708-9.

20. Daud MK, Nafees M, Ali S, Rizwan M, Bajwa RA, Shakoor MB, et al. Drinking Water Quality Status and Contamination in Pakistan. BioMed Research International. 2017;2017:1–18. Available from: <URL>.

21. Wright J, Dzodzomenyo M, Wardrop N, Johnston R, Hill A, Aryeetey G, et al. Effects of Sachet Water Consumption on Exposure to Microbe-Contaminated Drinking Water: Household Survey Evidence from Ghana. IJERPH. 2016 Mar 9;13(3):303. Available from: <URL>.

22. Ajala OJ, Ighalo JO, Adeniyi AG, Ogunniyi S, Adeyanju CA. Contamination issues in sachet and bottled water in Nigeria: a mini-review. Sustain Water Resour Manag. 2020 Dec;6(6):112. Available from: <URL>.

23. Clesceri LS, Greenberg AE, Eaton AD. Standard Methods for the Examination of Water and Wastewater, 20th Edition [Internet]. APHA American Public Health Association; 1998. Available from: <URL>

24. Oyekunle JAO, Yussuf NA, Durodola SS, Adekunle AS, Adenuga AA, Ayinuola O, et al. Determination of polycyclic aromatic hydrocarbons and potentially toxic metals in commonly consumed beef sausage roll products in Nigeria. Heliyon. 2019 Aug;5(8):e02345. Available from: <URL>.

25. Means B. Risk-assessment guidance for Superfund. Volume 1. Human Health Evaluation Manual. Part A. Interim report (Final). 1989 Dec; Available from: <URL>.

26. Mundy P, Bascietto J. Risk-assessment guidance for Superfund. Volume 2. Environmental evaluation manual. Interim report (Final). 1989 Mar; Available from: <URL>,

27. USEPA. Drinking Water Requirements for States and Public Water Systems [Internet]. United State Environmental Protection Agency (USEPA); 2011 [cited 2022 Jan 24]. Available from: <URL>.

28. UNC. Updated Baseline Human Health Risk Assessment [Internet]. United Nuclear Corporation (UNC); 2011. Available from: <URL>.

29. Orosun MM, Adewuyi AD, Salawu NB, Isinkaye MO, Orosun OR, Oniku AS. Monte Carlo approach to risks assessment of heavy metals at automobile spare part and recycling market in Ilorin, Nigeria. Sci Rep. 2020 Dec 16;10(1):22084. Available from: <URL>.

30. Orosun MM. Assessment of arsenic and its associated health risks due to mining activities in parts of North-central Nigeria: Probabilistic approach using Monte Carlo. Journal of Hazardous Materials. 2021 Jun;412:125262. Available from: <URL>.

31. Singh A, Maichle R, Singh AK, Lee SE, Armbya N. ProUCL Version 4.00.02 User Guide [Internet]. U.S. Environmental Protection Agency; 2007. Available from: <URL>.

32. Agency for Toxic Substances and Disease Registry (ATSDR) [Internet]. Agency for Toxic Substances and Disease Registry (ATSDR); 2007. Available from: <URL>.

33. USEPA. Guidance for Characterizing Background Chemicals in Soil at Superfund Sites [Internet]. United State Environmental Protection Agency (USEPA); 2001. Available from: <URL>.

34. Rinklebe J, Antoniadis V, Shaheen SM, Rosche O, Altermann M. Health risk assessment of potentially toxic elements in soils along the Central Elbe River, Germany. Environment International. 2019 May;126:76–88. Available from: <URL>.

35. Isinkaye OM. Distribution and Multivariate Pollution Risks Assessment of Heavy Metals and Natural Radionuclides Around Abandoned Iron-Ore Mines in North

Central Nigeria. Earth Syst Environ. 2018 Oct;2(2):331–43. Available from: <URL>.

36. Lawson SD, Ibiene AA, Amadi V, Enyinnaya SO, Nnodim LC, Uzah GA. Assessment of Physicochemical and Microbiological Quality of Table Water Sold in School Campuses of the University of Port Harcourt, Nigeria. JAMB. 2021 Jan 11;22–33. Available from: <URL>.

37. E. I. U, W. R. B, A. S. Physicochemical and Bacteriological Analyses of Sachets Water Samples in Kano Metropolis, Nigeria. IOSRJAC. 2014;6(6):52–6. Available from: <URL>.

38. Duru CE, Amadi US, Enyoh CE. Storage and its effect on chemical quality indicators in sachet water brands sold in Owerri Municipal, Imo State, Nigeria. World news of natural sciences. 2017;12.

39. World Health Organization. Guidelines for drinking-water quality [electronic resource]: incorporating 1st and 2nd addenda,Vol.1, recommendations [Internet]. 3rd ed. Geneva: World Health Organization; 2008 [cited 2023 Mar 11]. Available from: <URL>.

40. Nigerian Standard for Drinking Water Quality. Nigerian Standard for Drinking Water Quality [Internet]. STANDARDS ORGANISATION OF NIGERIA; 2015. Available from: <URL>.

41. World Health Organization. Guidelines for drinking-water quality: fourth edition incorporating first addendum [Internet]. 4th ed + 1st add. Geneva: World Health Organization; 2017 [cited 2023 Mar 11]. 541 p. Available from: <URL>.

42. Anake W, Siyanbola T, Ehi-Eromosele C, Edobor-Osoh A, Adeniyi I, Taiwo O. Physico-chemical and microbial assessment of different water sources in Ota, Ogun state, Nigeria. International Journal of Current Research. 2013;5(7):1797–801.

43. Sheshe M, Magashi A. Assessment of physicochemical quality of sachet water produced in selected local government areas of Kano Metropolis, Kano State - Nigeria. Bayero J Pure App Sci. 2015 Jan 14;7(2):31. Available from: <URL>.

44. Chinedu SN, Nwinyi O, Oluwadamisi AY, Eze VN. Assessment of water quality in Canaanland, Ota, southwest Nigeria. Agriculture and Biology Journal of North America. 2011;2(4):577–83.

45. Afolabi T, Ogbuneke C, Ogunkunle O, Bamiro F. Comparative assessment of the potable quality of water from industrial, urban and rural parts of Lagos, Nigeria. Ife Journal of Science. 2012;14(2):221–32.

46. Orosun MM, Tchokossa P, Nwankwo LI, Lawal TO, Bello SA, Ige SO. Assessment of heavy metal pollution in drinking water due to mining and smelting activities in Ajaokuta, Nigeria. Nig J Technol Dev. 2016 Sep 26;13(1):31. Available from: <URL>.

47. Association APH, others. American Public Health Association (APHA). Standard Methods for the Examination of Water and Wastewater. Apha, WEF and AWWA; Greenberg, AE, Clesceri, LS, Eaton, AD, Eds. 1992;1134.

48. Okunola OJ, Oba DO, Oranusi SU, Okagbue HI. Data on microbial assessment and physicochemical characteristics of sachet water samples obtained from three factories in Ota, Ogun state, Nigeria. Data in Brief. 2018 Aug;19:2445–51. Available from: <URL>.

49. Ajekunle Z, Ojekunle V, Eruola A, Oyebanji F, Olatunde K, Amujo B, et al. The Effects of Storage on Sachet Water Quality in Ogun State, Nigeria. Journal of Applied Sciences and Environmental Management. 2015 Jul 24;19(2):183. Available from: <URL>.

50. Alhassan MM, Ujoh F. Assessment of the chemical quality of potable water sources in Abuja, Nigeria. British Journal of Applied Science & Technology. 2012;2(2):146.

51. Wani AL, Ara A, Usmani JA. Lead toxicity: a review. Interdisciplinary Toxicology. 2015 Jun 1;8(2):55–64. Available from: <URL>.

52. Akuffo I, Cobbina S, Alhassan E, Nkoom M. Assessment of the quality of water before and after storage in the Nyankpala community of the Tolon-Kumbungu District, Ghana. INTERNATIONAL JOURNAL OF SCIENTIFIC & TECHNOLOGY RESEARCH. 2013;2(2):221–7.

53. Joy Chinenye I. Effect of Storage and Exposure to Sunlight on the Quality of Sachet Water Sold in Ibadan Metropolis. SJPH. 2017;5(4):321. Available from: <URL>.

54. Garkuwa NA, Mustapha SS, Ibrahim SA, Yusha'u M, Abdulrasheed M, Garkuwa UA. Enumeration of total and <I>Feacal coliform</I> bacteria of some borehole water in Gombe, Gombe State, Nigeria. Bayero J Pure App Sci. 2020 Apr 15;12(1):221–6. Available from: <URL>.

55. AKINNIBOSUN FI, Ugbawa L. Comparative analysis of bottled and sachet water sold in urban and rural areas of Edo State, Nigeria. Sierra Leone Journal of Biomedical Research. 2017;9(2):19–27.

56. Kgopa PM, Mashela PW, Manyevere A. Microbial Quality of Treated Wastewater and Borehole Water Used for Irrigation in a Semi-Arid Area. IJERPH. 2021 Aug 23;18(16):8861. Available from: <URL>.

JOTCS A
Journal of the Turkish Chemical Society
Section: A
Chemistry
TURKISH CHEMICAL SOCIETY

Synthesis and Characterization of New Anderson-Type Polyoxometalates: $[M((1,10\text{-phen})(OH)_x]_3[Cr(OH)_6Mo_6O_{18}]\cdot 16H_2O$ (M=Cr, Mn, Co, Ni, Cu; x=1,2)

Hülya AVCI ÖZBEK[1*]

[1]Manisa Celal Bayar University, Faculty of Sciences & Liberal Arts, Department of Chemistry, 45140, Muradiye-Manisa, Turkey.

Abstract: Five new Anderson-type polyoxometalate compounds $[M((1,10\text{-phen})(OH)_x]_3[Cr(OH)_6Mo_6O_{18}]\cdot 16H_2O$ (M=Cr(**1**), Mn(**2**), Co(**3**), Ni(**4**), Cu(**5**); x=1,2) were obtained from $Na_2MoO_4{\cdot}2H_2O$ and $CrCl_3{\cdot}6H_2O$ within acidic aqueous medium (pH=2-3). The compounds are characterized by means of FT-IR, TGA, ICP-MS, and elemental analysis techniques. The structural analysis show that compounds (**1-5**) consist of a Anderson-type polyanion $[Cr(OH)_6Mo_6O_{18}]^{3-}$.

Keywords: Molybdenum, Chromium, Polyoxometalate, Anderson-Evans.

Submitted: December 6, 2022. **Accepted:** February 25, 2023.

Cite this: Avcı Özbek, H. Synthesis and Characterization of New Anderson-Type Polyoxometalates: $[M((1,10\text{-phen})(OH)_x]_3[Cr(OH)_6Mo_6O_{18}]\cdot 16H_2O$ (M=Cr, Mn, Co, Ni, Cu; x=1,2). JOTCSA. 2023;10(2):315-24.

DOI: https://doi.org/10.18596/jotcsa.1215066.

***Corresponding author. E-mail:** hulya.avci@cbu.edu.tr.

1. INTRODUCTION

Polyoxometalates (POMs) as a family of metal-oxo clusters have attracted extensive attention due to their various structural characteristics, highly negative charges, excellent redox ability, and potential applications in catalysis, medicine, materials science, protein crystallography, nanotechnology and photochemistry (1-12). POMs are classified different categories such as Anderson, Lindqvist, Keggin, Waugh, Dawson, and Silverton. The Anderson-type heteropolyanions with the general formula $[Hy(XO_6)M_6O_{18}]^{n-}$ (X: Co, Ni, Cr or Mn and M=Mo(VI) or W(VI)) are an essential subfamily of POMs and have been of great importance due to their attractive magnetic and electronic properties. These POMs are ideal inorganic building blocks for creating hybrid materials since their easily get at covalent modification (13). In addition, chromium-containing POMs have interesting physicochemical properties (14). In recent years, interest in chromium derivatives of Anderson-type POMs have been increasing (15-17). $[(Gly)_2Cu][Na(H_2O)_4Cr(OH)_6Mo_6O_{18}]\cdot 9.5H_2O$ (Gly=glycine), has been synthesized and structurally characterized by An and co-workers (18). The luminescent properties of $(NH_4)_3[Cr(OH)_6Mo_6O_{18}]\cdot nH_2O$ have been investigated for the first time (19). $[Cr(OH)_6Mo_6O_{18}\{Cu(phen)(H_2O)_2\}_2]$ $[Cr(OH)_6Mo_6O_{18}\{Cu(phen)(H_2O)Cl\}_2](H_2O)\cdot 5H_2O$ has been reported by Shivaiah and Das (20). Shi and co-workers have been successfully synthesized compounds based on the $[Cr(OH)_6Mo_6O_{18}]^{3-}$ and lanthanide ions (21-22). $[Cu(phen)]_2[CrMo_6H_5O_{24}]$ has been hydrothermally synthesized (23). $(H_3O)[(3\text{-}C_5H_7N_2)_2(Cr(OH)_6Mo_6O_{18})]\cdot 3H_2O$ was also hydrothermally synthesized and showed high catalytic activity for oxidation of acetone (24). $Na_4[Ni(OH)_6Mo_6O_{18}]\cdot 16H_2O$ has been reported by Gumerova and co-workers (25). Liu and co-workers have reported chromium-centered Anderson-Evans type polytungstate $Na_6[H_3Cr^{III}W_6O_{24}]\cdot 22H_2O$ (14). Tewari and co-workers have synthesized a series of Anderson-type clusters coordinated with lanthanides $[Ln(H_2O)_7\{Cr(OH)_6Mo_6O_{18}\}]\cdot 4H_2O$ (Ln = La, Ce, Pr, Nd, Sm, Eu, Gd, Tb, Dy, Ho, Er, Tm, Yb, Lu, and Y) (26). $(NH_4)_3[CrMo_6O_{18}(OH)_6]$ have been efficient in the direct oxidation of a variety of alcohols (27).

In the current work, the new chromium-containing Anderson-type POM compounds $[M((1,10\text{-phen})(OH)_x]_3[Cr(OH)_6Mo_6O_{18}]\cdot 16H_2O$ (M=Cr(**1**), Mn(**2**), Co(**3**), Ni(**4**), Cu(**5**); x=1,2) have been synthesized and characterized by FT-IR, TGA, ICP-MS, and elemental analysis.

2. MATERIAL AND METHOD

2.1. General Methods

All reagents were purchased from commercial sources and used as received. FT-IR spectrum was recorded in 400–4000 cm^{-1} with a Perkin Elmer LR 64912 C spectrometer using KBr pellets. Elemental analyses (i.e., for C, H, and N) were performed on a LECO-932 CHNS model analyzer. ICP-MS analyses were performed on ICP-MS Agilent Technologie 7700. TGA analysis was carried out on Hitachi Exstar TG/DTA 7300.

2.2. Synthesis of Compounds

A mixture of $Na_2MoO_4{\cdot}2H_2O$ (157 mg, 0.65 mmol) and $CrCl_3{\cdot}6H_2O$ (69 mg, 025 mmol) was dissolved in distilled water (5 mL). Glacial acetic acid (1 mL) was then added to the mixture with by stirring at room temperature for about 30 min. Afterward, 1,10-phenanthroline monohydrate (155 mg, 0.78 mmol) and metal chloride salts (0.78 mmol) ($CrCl_3{\cdot}6H_2O$, $MnCl_2{\cdot}4H_2O$, $CoCl_2{\cdot}6H_2O$, $NiCl_2{\cdot}6H_2O$, $CuCl_2{\cdot}2H_2O$) dissolved in a mixture of water (2 mL) were added to the resulting reaction mixture, stirred for 2 hours. The product was filtered off, washed with water, and dried under a vacuum at 50 °C.

$[Cr(1,10\text{-phen})(OH)_2]_3[Cr(OH)_6Mo_6O_{18}]16H_2O$ (1):

Yield: 122 mg, 22%. FT-IR (KBr pellets): υ= 3067 (w), 1623 (s), 1597 (s), 1544 (s), 1519 (m), 1469 (m), 1451 (m), 1427 (s), 1338 (m), 1316 (m), 1225 (s), 1146 (s), 1107 (m), 1036 (m), 936 (m), 911 (m), 846 (m), 774 (m), 717 (m), 649 (m), 496 (m), 463 (m), 426 (m), 410 (m) cm^{-1}. Elem. Anal. Calcd. $Cr_4Mo_6C_{36}H_{68}N_6O_{46}$ (2104.56 g/mol): C, 20.55, H, 3.26, N, 3.99, Mo, 27.35, Cr, 9,88. found: C, 20.59, H, 3.11, N, 4.09, Mo, 29.35 (ICP-MS), Cr, 9.77 (ICP-MS). TGA (loss of $16H_2O$): calcd. 13.69%, found 13.16%; (loss of $[Cr(1,10\text{-phen})(OH)_2]_3$): calcd. 37.95%, found 38.07%.

$[Mn(1,10\text{-phen})(OH)]_3[Cr(OH)_6Mo_6O_{18}]{\cdot}16H_2O$ (2):

Yield: 118 mg, 22%. FT-IR (KBr pellets): υ= 3369 (w), 1623 (s), 1585 (s), 1579 (m), 1517 (s), 1425 (s), 1342 (s), 1224 (s), 1144 (s), 1103 (s), 941 (m), 913 (m), 888 (m), 849 (m), 781 (m), 724 (m), 648 (m), 496 (m), 421 (m) cm^{-1}. Elem. Anal. Calcd. $CrMn_3Mo_6C_{36}H_{65}N_6O_{43}{\cdot}$(2062.36 g/mol): C, 20.97, H, 3.18, N, 4.07, Mo, 27.91, Cr, 2,52, Mn, 7,99. found: C, 20.87, H, 2.80, N, 5.42, Mo, 23.41 (ICP-MS), Cr, 2.13 (ICP-MS), Mn, 7.15 (ICP-MS). TGA (loss of $16H_2O$): calcd. 13.97%, found 12.35%; (loss of $[Mn(1,10\text{-phen})(OH)_2]_3$): calcd. 36.68%, found 35.80%.

$[Co(1,10\text{-phen})(OH)]_3[Cr(OH)_6Mo_6O_{18}]{\cdot}16H_2O$ (3):

Yield: 131 mg, 24%. FT-IR (KBr pellets): υ= 3205 (w), 1622 (s), 1579 (m), 1514 (s), 1424 (s),1344 (m), 1223 (m), 1144 (s), 1104 (s), 944 (s), 913 (m), 849 (m), 776 (m), 727 (m), 642 (m), 565 (m), 413 (m) cm^{-1}. Elem. Anal. Calcd. $CoMn_3Mo_6C_{36}H_{65}N_6O_{43}$ (2074.35 g/mol): C, 20.84, H, 3.16, N, 4.05, Mo, 27.75, Cr, 2,51, Co, 8,52. found: C, 21.94, H, 3.15, N, 4.71, Mo, 24.69 (ICP-MS), Cr, 2.48 (ICP-MS), Co, 8.33 (ICP-MS). TGA (loss of $16H_2O$): calcd. 13.89%, found 12.77%; (loss of $[Co(1,10\text{-phen})(OH)_2]_3$): calcd. 37.04%, found 36.03%.

$[Ni(1,10\text{-phen})(OH)]_3[Cr(OH)_6Mo_6O_{18}]{\cdot}16H_2O$ (4):

Yield: 108 mg, 20%. FT-IR (KBr pellets): υ= 3065 (w), 1625 (s), 1585 (s), 1517 (s), 1425 (s), 1341 (s), 1225 (s), 1146 (s), 1105 (s), 941 (m), 914 (m), 847 (m), 725 (m), 643 (m), 567 (m), 531 (m), 425 (m) cm^{-1}. Elem. Anal. Calcd. $NiMn_3Mo_6C_{36}H_{65}N_6O_{43}$ (2073.63 g/mol): C, 20.85, H, 3.16, N, 4.05, Mo, 27.76, Cr, 2.51, Ni, 8.49. found: C, 20.35, H, 2.74, N, 4.83, Mo, 26.36 (ICP-MS), Cr, 1.89 (ICP-MS), Ni, 8.34 (ICP-MS). TGA (loss of $16H_2O$): calcd. 13.90%, found 12.35%; (loss of $[Ni(1,10\text{-phen})(OH)_2]_3$): calcd. 37.02%, found 36.00%.

$[Cu(1,10\text{-phen})(OH)]_3[Cr(OH)_6Mo_6O_{18}]{\cdot}16H_2O$ (5):

Yield: 95 mg, 18%. FT-IR (KBr pellets): υ= 3054 (w), 1622 (s), 1518 (s), 1427 (s), 1342 (m), 1309 (m), 1225 (m), 1146 (s), 1107 (s), 915 (s), 890 (m), 842 (m), 772 (m), 722 (m), 643 (m), 496 (m), 427 (m) cm^{-1}. Elem. Anal. Calcd. $CuMn_3Mo_6C_{36}H_{65}N_6O_{43}$ (2088.19 g/mol): C, 20.71, H, 3.14, N, 4.02, Mo, 27.57, Cr, 2,49, Cu, 9,13. found: C, 21.42, H, 2.85, N, 5.32, Mo, 26.89 (ICP-MS), Cr, 2,07 (ICP-MS), Cu, 8,99 (ICP-MS). TGA (loss of $16H_2O$): calcd. 13.80%, found 13.94%; (loss of $[Cu(1,10\text{-phen})(OH)_2]_3$): calcd. 37.46%, found 30.69%.

3. RESULT AND DISCUSSION

A series of new Anderson-type POM compounds $[M((1,10\text{-phen})(OH)_x]_3[Cr(OH)_6Mo_6O_{18}]{\cdot}16H_2O$ (M=Cr(**1**), Mn(**2**), Co(**3**), Ni(**4**), Cu(**5**); x=1,2) were obtained from of $Na_2MoO_4{\cdot}2H_2O$ and $CrCl_3{\cdot}6H_2O$ acidic aqueous medium (Figure 1). It is well known that the stability of polyoxoanions in an aqueous solution depends on the pH. Stability range of $[Cr(OH)_6Mo_6O_{18}]^{3-}$ is 2<pH<3 (20). To obtain this anion it is important to maintain the pH of the solution between 2 and 3 during the addition of the counterion.

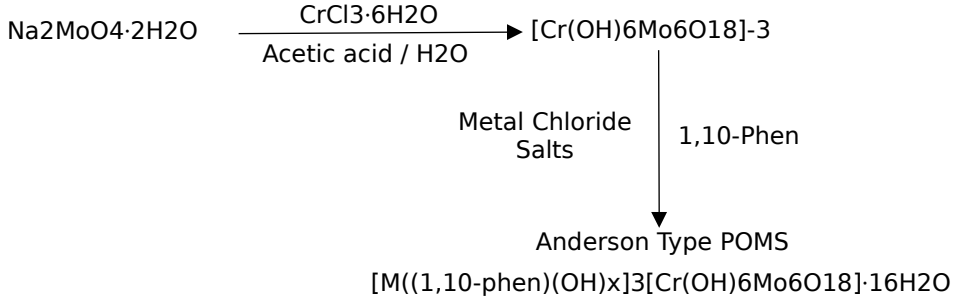

Metal	X	Compound No
Cr	2	**1**
Mn	1	**2**
Co	1	**3**
Ni	1	**4**
Cu	1	**5**

Figure 1. Synthesis of new compounds (**1-5**).

The color of the compounds are white (**1**), yellow (**2**), orange (**3**), beige (**4**), and green (**5**). The observed elemental analyses (C, H, N) and ICP-MS (Mo, Cr, Mn, Co, Ni, Cu) data of the new compounds (**1-5**) are in good agreement with the calculated values. Furthermore, experimentally obtained elemental analyses results and other spectroscopic data (FT-IR, ICP-MS, and TGA) support the compounds (**1-5**) formulated as $[M((1,10\text{-phen})(OH)_x]_3[Cr(OH)_6Mo_6O_{18}]\cdot 16H_2O$ (M=Cr(**1**), Mn(**2**), Co(**3**), Ni(**4**), Cu(**5**); x=1,2). Thus, it was determined that the structures of these newly synthesized compounds were similar to the previously reported compounds. (21,22,25,26).

The FT-IR spectra of compounds **1-5** (Supplementary Information Figure S1-S5.) confirms their isostructural nature. The broad bands, respectively 3067 (**1**), 3369 (**2**), 3205 (**3**), 3065 (**4**), and 3054 (**5**) cm^{-1} in the FT-IR spectra of the compounds could be ascribed to O–H bonds, and the bands at 1623,1622 cm^{-1} are attributed to the characteristic of the deformation vibrations of H–O–H of coordinated and lattice-water molecules. The vibrations of compounds **1-5**, ranging from 1107 to 1597 cm^{-1}, are assigned to the 1,10-phenanthroline molecules (20). The vibrations in the range 960-400 cm^{-1} well confirm the Anderson-type cluster $[Cr(OH)_6Mo_6O_{18}]^{3-}$. The bands at 410-940 cm^{-1} are attributed to the vibration modes ($Mo\text{-}O_t$), ($Mo\text{-}O_b$), and ($Mo\text{-}O_c$) of the Anderson anion $[Cr(OH)_6Mo_6O_{18}]^{3-}$. The absorption band at 410-422 cm^{-1} is attributed to the Cr–O. FT-IR results are in agreement with those from previous studies (20-22,25-26).

Thermogravimetric measurements were carried out under a flowing nitrogen atmosphere with a heating rate of 10 °C min^{-1} in 40-800 °C. TGA thermograms of **1** in Figure 2, **2-5** in Supplementary Information Figure S6-S9. As expected, the thermal behavior of compounds **1-5** hasn't been different. The TGA curve of **1** shows (Figure 3), the total weight loss of 16 H_2O (13.16%) in the range of 25–178 °C is attributed to the loss of adsorbed, lattice, coordinated water molecules, and hydroxyls. The second weight loss of 38.07% in the range of 178–704 °C possibly corresponds to the loss of $[Cr(1,10\text{-phen})(OH)_2]_3$ group. Table 1 shows the results of the TGA analysis. TGA results are in agreement with those from previous studies (20-22,25-26).

Table 1. Results of the TGA analysis.

Compound	Losses Part	Calc. (%)	Exp. (%)	Losses Part	Calc. (%)	Exp. (%)
1	$16H_2O$	13.69	13.16	$[Cr(1,10\text{-phen})(OH)_2]_3$	37.95	38.07
2	$16H_2O$	13.97	12.35	$[Mn(1,10\text{-phen})(OH)]_3$	36.68	35.80
3	$16H_2O$	13.89	12.77	$[Co(1,10\text{-phen})(OH)]_3$	37.04	36.03
4	$16H_2O$	13.90	12.35	$[Ni(1,10\text{-phen})(OH)]_3$	37.02	36.00
5	$16H_2O$	13.80	13.94	$[Cu(1,10\text{-phen})(OH)]_3$	37.46	30.69

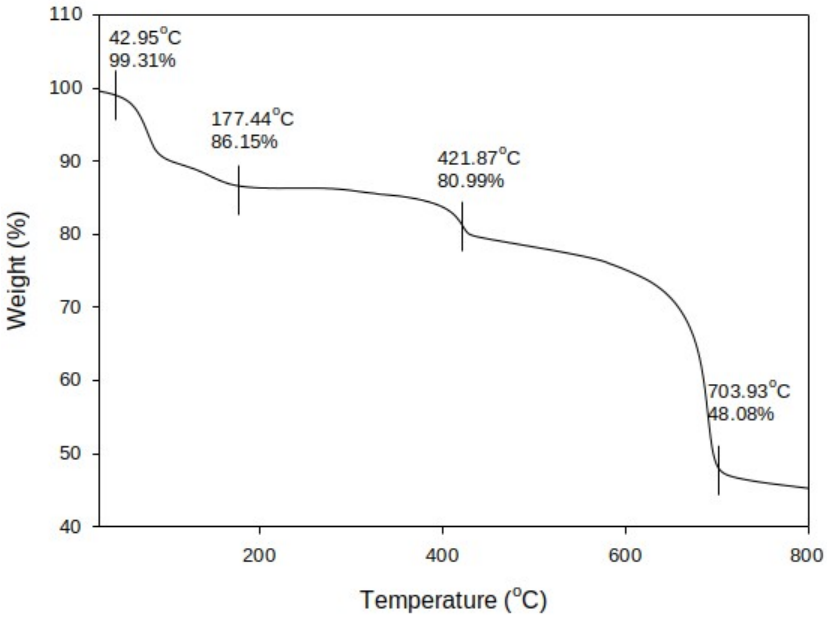

Figure 2. TGA spectrum of **1**.

4. CONCLUSION

In this paper, the structural characterization of newly synthesized Anderson-type POMs: [M((1,10-phen)$(OH)_x]_3[Cr(OH)_6Mo_6O_{18}]\cdot 16H_2O$ (M=Cr(**1**), Mn(**2**), Co(**3**), Ni(**4**), Cu(**5**); x=1,2) were carried out using FT-IR, elemental analysis, ICP-MS, and TGA methods. Since the low solubility of the compounds in organic solvents and insoluble in water, other spectroscopic methods (NMR, ESI) could not be used in structural characterization and crystal suitable for X-Ray analysis could not be obtained.

5. CONFLICT OF INTEREST

There is no conflict of interest.

6. ACKNOWLEDGMENTS

The Manisa Celal Bayar University Scientific Research Projects Coordination Unit supported this study. Project Number: 2022-091.

7. REFERENCES

1. Wang S-S, Yang G-Y. Recent Advances in Polyoxometalate-Catalyzed Reactions. Chem Rev [Internet]. 2015 Jun 10;115(11):4893-962. Available from: <URL>.

2. Cherevan AS, Nandan SP, Roger I, Liu R, Streb C, Eder D. Polyoxometalates on Functional Substrates: Concepts, Synergies, and Future Perspectives. Adv Sci [Internet]. 2020 Apr 6;7(8):1903511. Available from: <URL>.

3. Ramezani-Aliakbari M, Varshosaz J, Sadeghi-aliabadi H, Hassanzadeh F, Rostami M. Biotin-Targeted Nanomicellar Formulation of an Anderson-Type Polyoxomolybdate: Synthesis and In Vitro Cytotoxicity Evaluations. Langmuir [Internet]. 2021 Jun 1;37(21):6475-89. Available from: <URL>.

4. Streb C, Kastner K, Tucher J. Polyoxometalates in photocatalysis. Phys Sci Rev [Internet]. 2019 May 27;4(6):20170177. Available from: <URL> .

5. Shen Y, Jiang P, Wai P, Gu Q, Zhang W. Recent Progress in Application of Molybdenum-Based Catalysts for Epoxidation of Alkenes. Catalysts [Internet]. 2019 Jan 2;9(1):31. Available from: <URL>.

6. Rhule JT, Hill CL, Judd DA, Schinazi RF. Polyoxometalates in Medicine. Chem Rev [Internet]. 1998 Feb 1;98(1):327-58. Available from: <URL>.

7. Bijelic A, Rompel A. The use of polyoxometalates in protein crystallography – An attempt to widen a well-known bottleneck. Coord Chem Rev [Internet]. 2015 Sep 1;299:22-38. Available from: <URL>.

8. Bijelic A, Rompel A. Ten Good Reasons for the Use of the Tellurium-Centered Anderson–Evans Polyoxotungstate in Protein Crystallography. Acc Chem Res [Internet]. 2017 Jun 20;50(6):1441-8. Available from: <URL>.

9. Proust A, Thouvenot R, Gouzerh P. Functionalization of polyoxometalates: towards advanced applications in catalysis and materials science. Chem Commun [Internet]. 2008;(16):1837. Available from: <URL>.

10. Tucher J, Wu Y, Nye LC, Ivanovic-Burmazovic I, Khusniyarov MM, Streb C. Metal substitution in a Lindqvist polyoxometalate leads to improved photocatalytic performance. Dalt Trans [Internet]. 2012 Jul 31;41(33):9938-43. Available from: <URL>.

11. Tucher J, Schlicht S, Kollhoff F, Streb C. Photocatalytic reactivity tuning by heterometal and addenda metal variation in Lindqvist polyoxometalates. Dalt Trans [Internet]. 2014 Oct 29;43(45):17029-33. Available from: <URL>.

12. Jin P, Wei H, Zhou L, Wei D, Wen Y, Zhao B, et al. Anderson-type polyoxometalate as excellent catalyst for green synthesis of adipic acid with hydrogen peroxide. Mol Catal [Internet]. 2021 Jun 1;510:111705. Available from: <URL>.

13. Wu P, Wang Y, Huang B, Xiao Z. Anderson-type polyoxometalates: from structures to functions. Nanoscale [Internet]. 2021 Apr 23;13(15):7119-33. Available from: <URL> .

14. Liu W, Lin Z, Bassil BS, Al-Oweini R, Kortz U. Synthesis and Structure of Hexatungstochromate(III), $[H_3Cr^{III}W_6O_{24}]^{6-}$. Chima [Internet]. 2015 Sep 30;69(9):537-40. Available from: <URL>.

15. Ouahab L, Golhen S, Yoshida Y, Saito G. One Dimensional Face-to-Face Stacking of Anderson–Evans $[Cr(OH)_6Mo_6O_{18}]^{3-}$ Polyoxometalate Anion: Synthesis, Structure, and Physical Properties of (BEDT-TTF) 4 $[Cr(OH)_6Mo_6O_{18}]$ $2H_2O$. J Clust Sci [Internet]. 2003 Sep;14(3):193-204. Available from: <URL>.

16. Li Q, Wei Y. A series of unprecedented triol-stabilized $[H_3MW_6O_{24}]^{n-}$: the missing piece between A- and B-type Anderson–Evans polyoxometalates. Chem Commun [Internet]. 2018 Feb 1;54(11):1375-8. Available from: <URL>.

17. Gumerova NI, Caldera Fraile T, Roller A, Giester G, Pascual-Borras M, Ohlin CA, et al. Direct Single- and Double-Side Triol-Functionalization of the Mixed Type Anderson Polyoxotungstate $[Cr(OH)_3W_6O_{21}]^{6-}$. Inorg Chem [Internet]. 2019 Jan 7;58(1):106-13. Available from: <URL>.

18. An H, Guo Y, Li Y, Wang E, Lü J, Xu L, et al. A novel organic-inorganic hybrid with Anderson type polyanions as building blocks: $[(Gly)_2Cu][Na(H_2O)_4Cr(OH)_6Mo_6O_{18}]\cdot 9.5H_2O$ (Gly=glycine). Inorg Chem Commun [Internet]. 2004 Apr 1;7(4):521-3. Available from: <URL>.

19. Yin M, Yusov AB, Fedosseev AM, Krupa J-C. Optical evidence of Cr^{3+} ion pairs in $(NH_4)_3[Cr(OH)_6Mo_6O_{18}]\cdot nH_2O$. J Alloys Compd [Internet]. 2004 Sep 8;377(1-2):43-6. Available from: <URL>.

20. Shivaiah V, Das SK. Polyoxometalate-Supported Transition Metal Complexes and Their Charge Complementarity: Synthesis and Characterization of $[M(OH)_6Mo_6O_{18}\{Cu(Phen)(H_2O)_2\}_2][M(OH)_6Mo_6O_{18}$ $\{Cu(Phen)(H_2O)Cl\}_2]\cdot 5H_2O$ (M=Al^{3+}, Cr^{3+}). Inorg Chem [Internet]. 2005 Nov 1;44(24):8846-54. Available from: <URL>.

21. Shi D-M, Ma F-X, Zhang C-J, Lu S, Chen Y-G. Self-Assembly of Polyoxometalate-Supported Ln-H nydroxo/Oxo Clusters with 1D Extended Structure: $[Ln^{III}(H_2O)_7Cr(OH)_6Mo_6O_{18}]_n\cdot 4nH_2O$ (Ln= Ce, Sm, Eu). Z. Anorg. Allg. Chem. [Internet]. 2008 Apr 1;634(4):758-63. Available from: <URL>.

22. Shi D, Hu M, Zhang C, Li J, Chen Y. Synthesis and Structure of a Novel Polyoxomolybdate Lanthanide Complex: $[Er_2(H_2O)_{14}Cr(OH)_6Mo_6O_{18}][Cr(OH)_6Mo_6O_{18}]\cdot 14H_2O$. J Chem Crystallogr [Internet]. 2008 Sep 9;38(9):695-700. Available from: <URL>.

23. Ma H, Wu L, Pang H, Meng X, Peng J. Hydrothermal synthesis of two Anderson POM-supported transition metal organic-inorganic compounds. J Mol Struct [Internet]. 2010 Apr 1;967(1-3):15-9. Available from: <URL>.

24. Peng Z-S, Zhang C-L, Shen X-M, Deng Q, Cai T-J. A novel Anderson-type polyoxometalate: hydrothermal synthesis, crystal structure, and catalytic performance of $(H_3O)[(3\text{-}C_5H_7N_2)_2$ $(Cr(OH)_6Mo_6O_{18})]\cdot 3H_2O$. J Coord Chem [Internet]. 2011 Aug 20;64(16):2848-58. Available from: <URL>.

25. Gumerova NI, Melnik NA, Rozantsev GM, Baumer VN, Radio S V. Sodium heteropolyhexamolybdenumnickelate (II) $Na_4[Ni(OH)_6Mo_6O_{18}]\cdot 16H_2O$ with an anderson anion: Synthesis and crystal structure. J Struct Chem [Internet]. 2015 Sep 16;56(5):926-33. Available from: <URL>.

26. Tewari S, Adnan M, Balendra, Kumar V, Jangra G, Prakash GV, et al. Photoluminescence Properties of Two Closely Related Isostructural Series Based on Anderson-Evans Cluster Coordinated With Lanthanides $[Ln(H_2O)_7\{X(OH)_6Mo_6O_{18}\}]\cdot yH_2O$, X = Al, Cr. Front Chem [Internet]. 2019 Jan 7;6:631. Available from: <URL>.

27. Wang Y, Wu Z, Yu H, Han S, Wei Y. Highly efficient oxidation of alcohols to carboxylic acids using a polyoxometalate-supported chromium(III) catalyst and CO_2. Green Chem [Internet]. 2020 May 26;22(10):3150-4. Available from: <URL>.

SUPPLEMENTARY INFORMATION

Synthesis and Characterization of New Anderson-Type Polyoxometalates: $[M((1,10\text{-phen})(OH)_x]_3[Cr(OH)_6Mo_6O_{18}]\cdot 16H_2O$ (M=Cr, Mn, Co, Ni, Cu; x=1,2)

Hülya AVCI ÖZBEK[1*]

[1]Manisa Celal Bayar University, Faculty of Sciences & Liberal Arts, Department of Chemistry, 45140, Muradiye-Manisa, Turkey.

FT-IR Spectrum

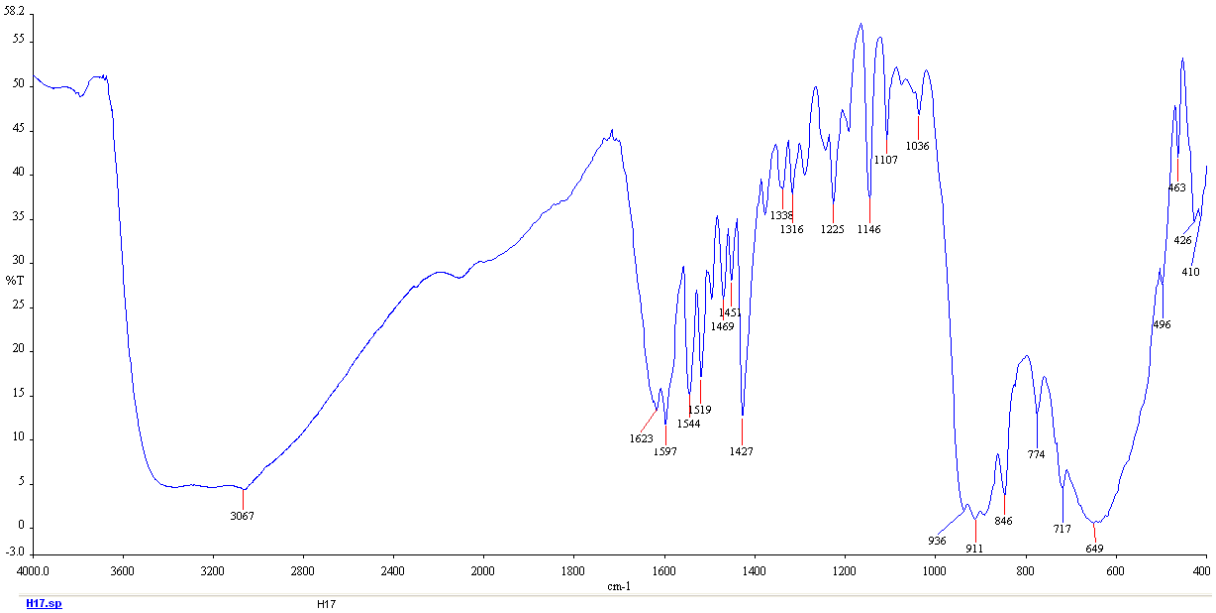

Figure S 1. FT-IR Spectrum of **1**

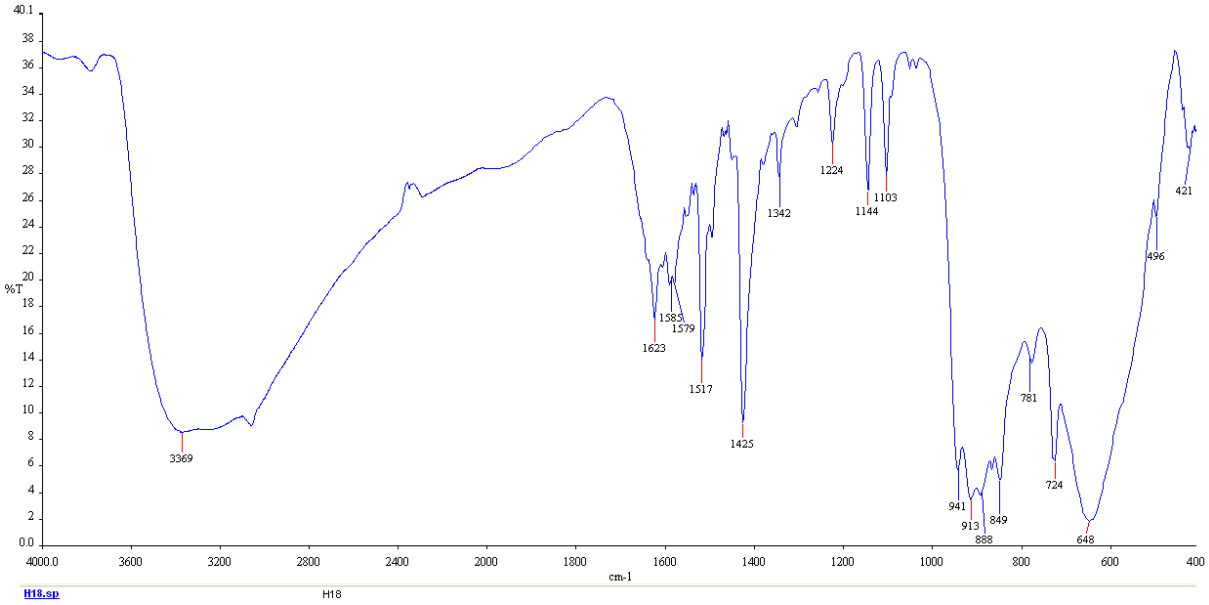

Figure S 2. FT-IR Spectrum of **2**

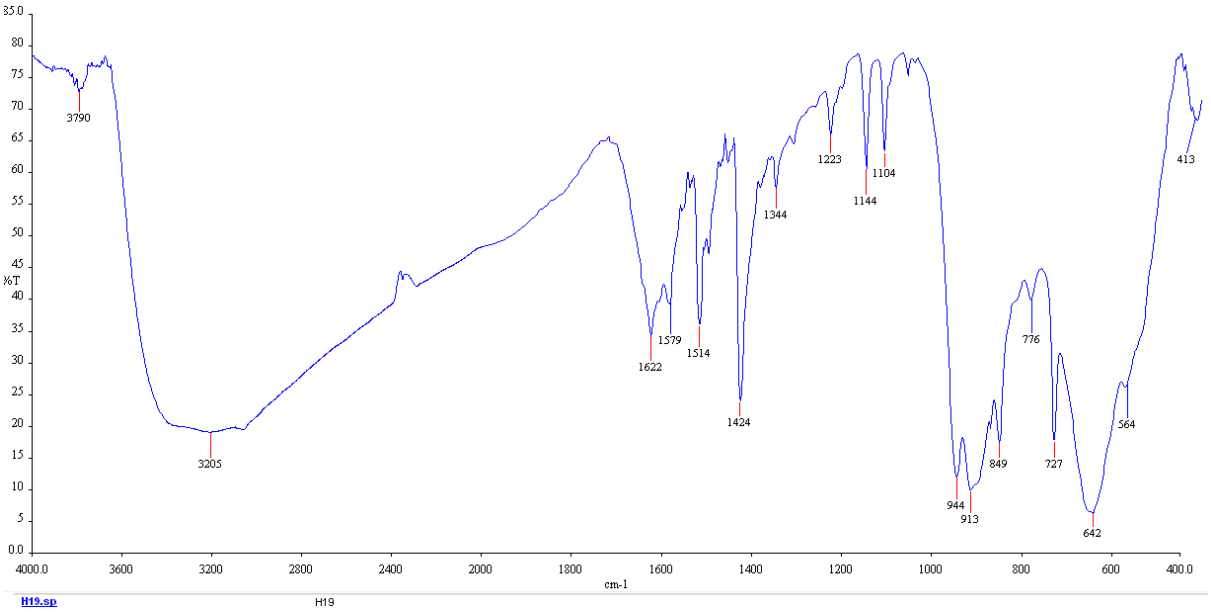

Figure S 3. FT-IR Spectrum of **3**

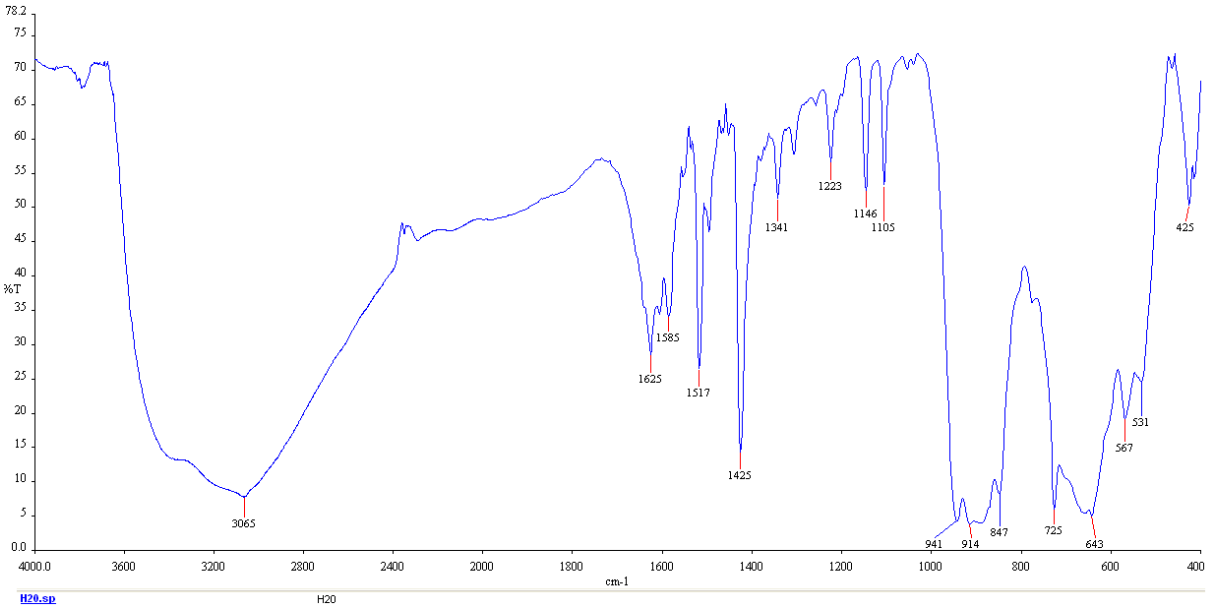

Figure S 4. FT-IR Spectrum of **4**

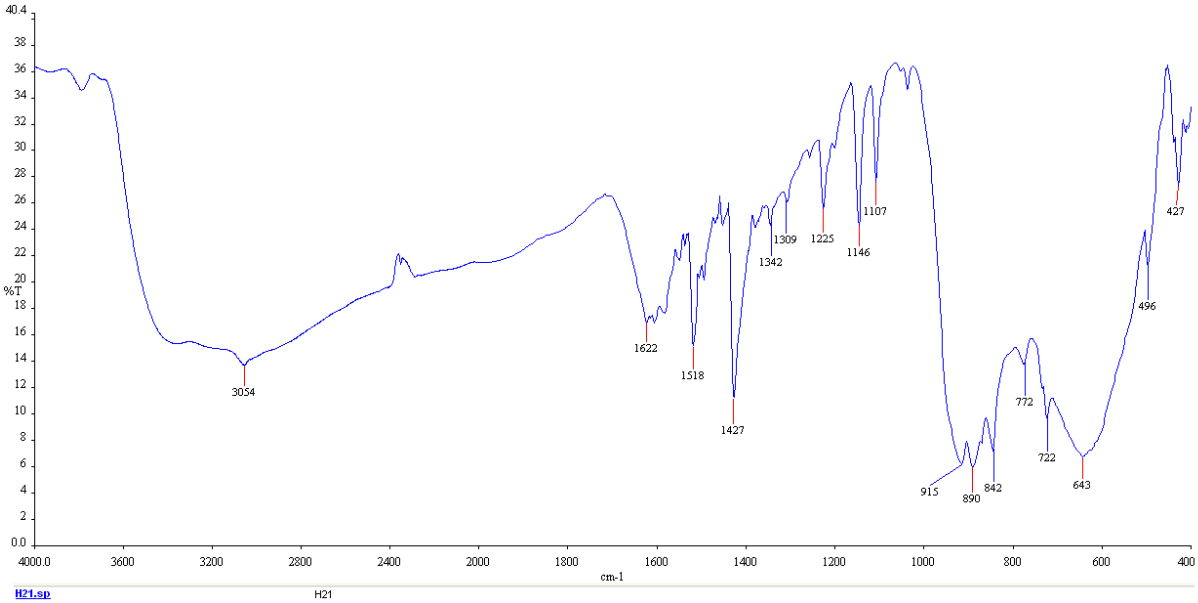

Figure S 5. FT-IR Spectrum of **5**

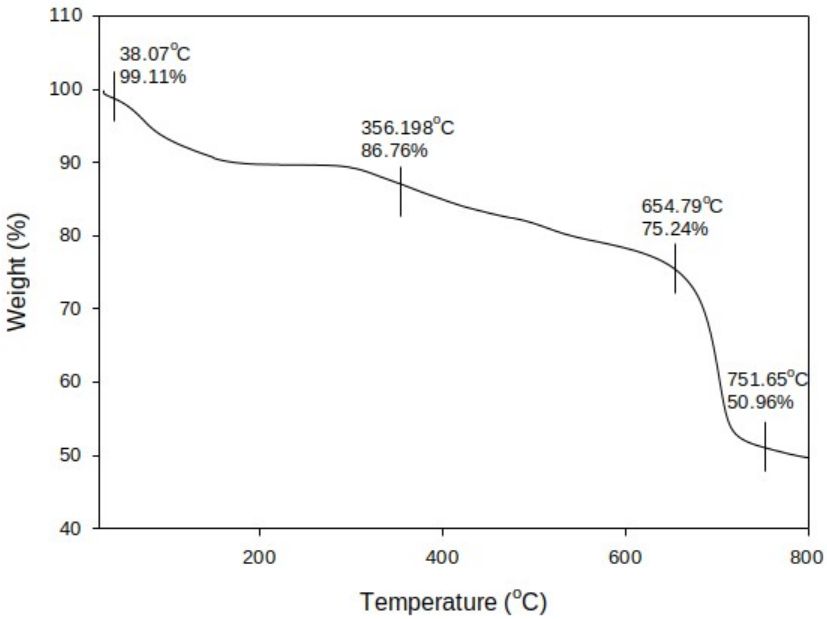

Figure S 6. TGA spectrum of **2**

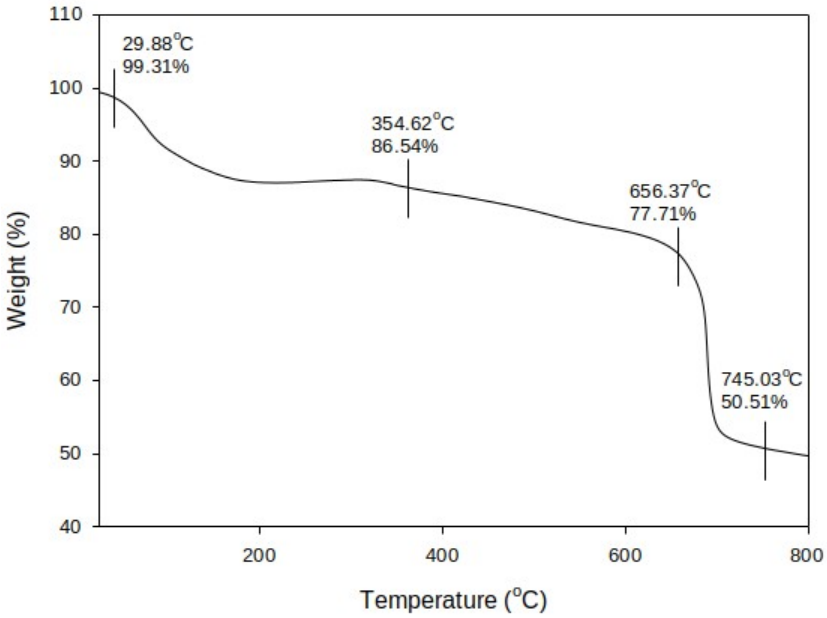

Figure S 7. TGA spectrum of **3**

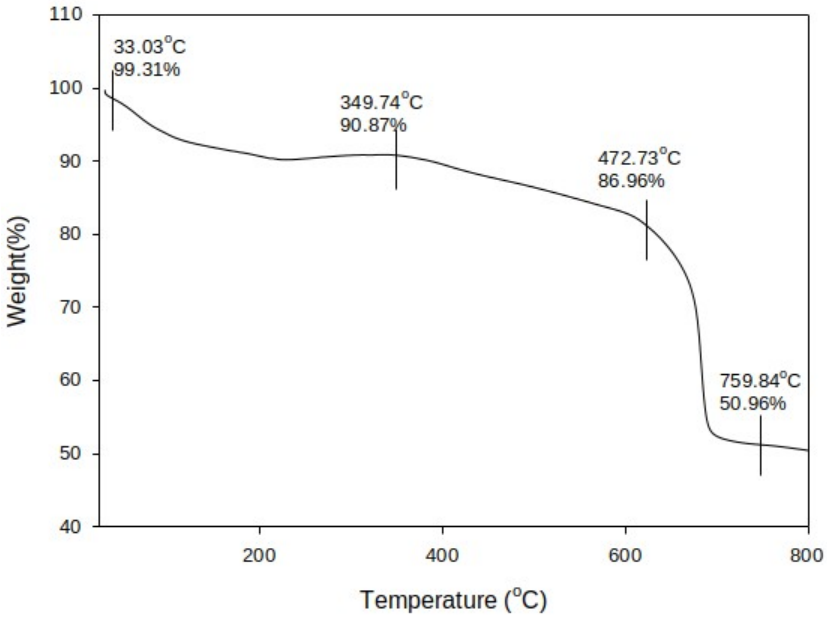

Figure S 8. TGA spectrum of **4**

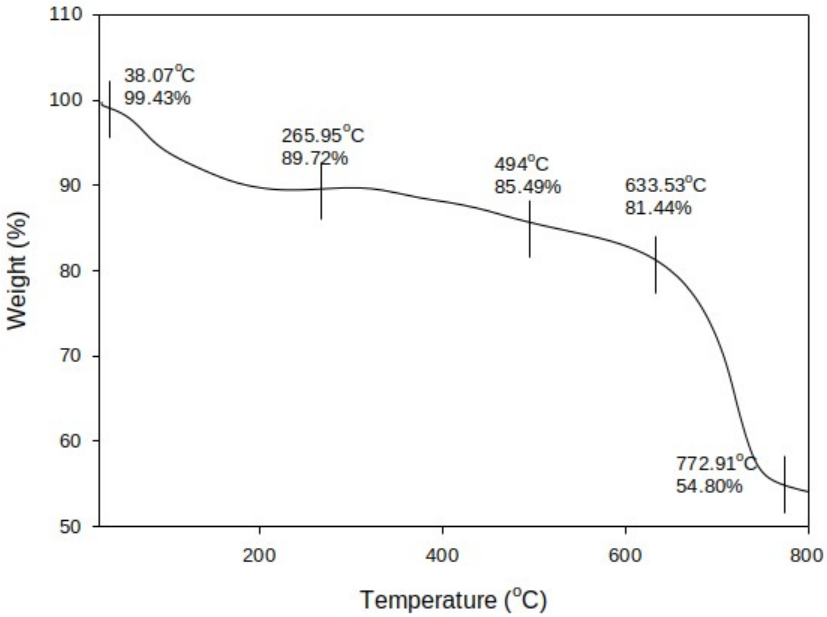

Figure S 9. TGA spectrum of **5**

JOTCS A
Journal of the Turkish Chemical Society
Section: A
Chemistry
TURKISH CHEMICAL SOCIETY

Potentiometric Studies on Binary and Ternary Complexes of Ni(II) and Cu(II) Ions with L-Valine and Paracetamol

Aisha Al-Abbasi[1]*, Nouria Ali Belkher[1], Khadija Ahmida[1], Mohamed Zidan[1]
[1]Sebha University, Department of Chemistry, Sebha, Libya

Abstract: The protonation constants of the free ligands and the stability constants of binary and ternary complexes of bivalent metal ions of Ni(II) and Cu(II) with a biologically important amino acid of L-valine, *Val*, and paracetamol, *Para*, were studied potentiometrically in aqueous solutions at 313.15 ± 0.1 K and a fixed ionic strength of I = 0.10 M NaCl. The complexation model for each system was established using the Irving-Rossotti equation. The formation of the 1:2 or 1:1 binary complexes and 1:1:1 ternary complexes in which the amino acid *Val* was used as the primary ligand and *Para* as the secondary ligand, as inferred from the corresponding potentiometric pH-metric titration curves, and their relative stabilities compared to the corresponding ML and ML_2 binary complexes are expressed in terms of statistical parameters ΔlogK, $\log K_1$ and $\log K_2$. The complex stability was found to follow the order of Cu(II) > Ni(II). Through these diagnostic studies, it was possible to give the general formula of compounds prepared from amino acids and paracetamol. Amino acid binds to the central ion through oxygen in the hydroxyl group and nitrogen atom in the amine group ($-NH_2$), whereas paracetamol forms a unipolar bond by binding to the concentrated ion through the oxygen atom in the hydroxyl group. Most of the nickel complexes had octahedral symmetry with valine and paracetamol ligands, while the copper complexes had square or hierarchical to square base symmetry.

Keywords: Binary complexes; L-Valine; Paracetamol; Potentiometric method; Stability constant; Ternary complexes

Submitted: July 3, 2022. **Accepted:** February 2, 2023.

Cite this: Al-Abbasi A, Belkher NA, Ahmida K, Zidan M. Potentiometric Studies on Binary and Ternary Complexes of Ni(II) and Cu(II) Ions with L-Valine and Paracetamol. JOTCSA. 2023;10(2):325-338

DOI: https://doi.org/10.18596/jotcsa.1140039.

***Corresponding author. E-mail:** ais.alabbasi@sebhau.edu.ly

1. INTRODUCTION

Mixed-ligand metal complexes are a branch of biological inorganic chemistry and have important implications for many other sciences, ranging from medicine to environmental science. Studies on the roles of metal ions in biological systems often involve the development of relevant chemistry (1-3). Metal-ligand complexes consist of a central metal, known as Lewis acid, that is bound to ligands, commonly known as Lewis bases, which can either be ions, atoms, or neutral molecules (1-3). When a ligand contains two or more donor atoms close to each other, the formed metal complex is said to be a chelate, and the process is referred to as chelating. Cu(II), among essential transition metals, is important for many enzymes, particularly those catalyzing physiologically important reactions. Copper has a strong ability to form complexes with proteins, peptides, and enzymes in living organisms (4, 5). Examples of copper-containing compounds are tyrosinase, ferroxidase and haemocyanin (4). Ni(II) is important because of its ability to replace other metal ions in enzymes and proteins, as well as to bind to cellular compounds containing O, S and N atoms, such as enzymes and nucleic acids. Nickel is essential for the healthy life of humans and animals, and its deprivation profoundly impairs intestinal absorption of iron and thus causes anaemia. It has been reported that 90% of both glucose and glycogen concentrations in the liver and serum were reduced by nickel depletion (6).

Among various bioactive ligands, amino acids have special importance compared to other chemical compounds because they are regarded as the foundation stones of living organisms. Therefore, it is necessary to study their chemical properties to explain their behavior and potential applications. Among these properties are the stability constants and the thermodynamics of complexes they form with various metals (7, 8). Amino acids can act as coordinating agents through their amino (NH_2) and carboxyl (COO^-) groups. These groups provide a

more diverse coordination activity towards heavy metal ions and thus can be used to isolate heavy metal ions and obtain safer drugs or antidotes against metal poisoning.

L-Val (Fig. 1) is an α-amino acid used in the biosynthesis of proteins (9). Because L-*Val* is an essential amino acid that is not synthesized by the body, it must be obtained from food or supplements. *L-Val* plays an important role in synthesis and maintenance of muscles, stress management, growth in children, and support of the immune system as well as the functioning of the nervous system. Earlier studies have shown that *L-Val* may help to manage nervousness and insomnia because it has a role in forming the myelin sheaths that cover nerve cells. Valine, like other branched-chain amino acids, is associated with insulin resistance; higher levels of valine are observed in the blood of diabetic humans (9-11).

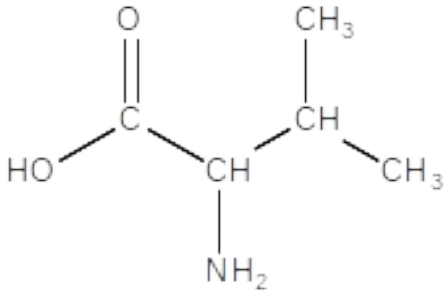

Figure 1: Structure of *L-Val* (2-amino-3-methylbutanoic acid).

Paracetamol *(Para)* (Fig. 2) is most widely used in the world today and leads the list of the World Health Organization (WHO) as the most important, safe, and effective medicine for the health care system (1, 2, 12-20). It is used as a treatment for headache, toothache, migraine attacks, moderate strength cases of arthritis, as well as to reduce postvaccination fever in children (1, 2, 12-21). In addition, it is used instead of aspirin, especially in patients with infectious diseases such as gastric ulcers (13, 14). Although *Para* is used to treat inflammatory pain, it is not generally classified as a nonsteroidal anti-inflammatory drug (NSAID) because it exhibits only weak anti-inflammatory activity (1, 2, 12-22).

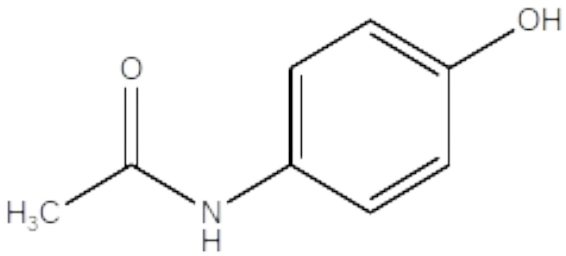

Figure 2: Structure of para(N-(4-hydroxyphenyl)acetamide)

Singh and coworkers studied the interaction of transition metal ions with N-benzoyl-*Val*, N–benzoyl, glycol-*Val,* and isovaleric acid (23). They adopted the pH titration technique to evaluate stability constants at 25, 35 and 45 °C and an ionic strength of 0.15 M (KNO_3) in 50 % (v/v) water-dioxane medium. Their study reported that only 1:1 metal complexes were formed with stability.

Enamullah and coworkers determined the proton-ligand and metal-ligand formation constants of phthalamic acid with transition metal ions such as Zn(II), Ni(II), and Cd(II) (1, 2, 24). It has been found that the metal ions Zn(II) and Cd(II) formed complexes at low ionic strength, I = 0.1 M. At higher ionic strengths, such as I = 0.15 M, these ions seem to be inactive towards the ligand. Some chelates of penicillamine with different metal ions have been studied (25-27). Chakravarti et al. studied the formation of biological chelates of divalent metal ions with a cephalosporin by the pH-metric method (1, 2, 28). In their study, it was found that the stability constants follow the order Cu(II) > Zn(II) > Co(II) > Ni(II) > Cd(II) > Mg(II) > Mn(II). In addition, the logK values are less negative than -0.6, suggesting favored formation of ternary complexes.

As part of our interest in studying the coordination chemistry of transition metal (29-35), this paper addresses the determination of the stability constants of new ternary complexes formed by Ni(II) and Cu(II) with *Val* and *Para* (first report), using a potentiometric pH method in the presence of 0.1 M (NaCl) ionic strength at the bodily temperature of 313.15 ± 0.1 K. The method of Calvin-Bjerrum (36, 37) as adopted by Irving and Rossotti (38, 39) was used to determine logK values.

2. MATERIALS AND METHODS

2.1 Materials

All chemicals utilized in this investigation were of analytical reagent grade (AR) quality and highest purity. *Val* (>99%) and *Para* (99.5%) were purchased from Fluka and CCM (Malaysia), respectively. Metal salts, including $CuCl_2.2H_2O$ (≥ 99.99%), were obtained from T-Baker lab chemicals, and $NiCl_2.6H_2O$ (98%) was obtained from Surechem Products. Sodium hydroxide (98.8%) was purchased from Shandong, hydrochloric acid (36%) from Scharlau-chemise and sodium chloride (99.7%) from BDH Chemicals. The most of metal cation-EDTA complexes have a relatively high formation constant, which is the main factor driving the widespread use of EDTA in the standardization of metal cation solutions. A complexometric indicator is needed to identify the endpoint of metal cation titrations carried out with EDTA. The most common indication for this use is a blue dye called Eriochrome Black T (Erio-T). When complexed with metal ions, Erio-T is utilized in EDTA titration, which results in a color change from blue to pink at the endpoint. In the complexometric titration, an ammoniacal buffer solution of pH 10 (mixture of ammonium chloride and ammonium hydroxide) is used because all metal–EDTA reactions are pH-dependent.

2.2 Solutions

A hydrochloric acid stock solution was prepared and titrated against standardized sodium hydroxide. The stock solution of 0.004 M *Val* was freshly prepared before use by accurately dissolving 0.04686 g of *Val* powder with a minimum quantity of deionized distilled water. A fresh stock solution of 0.02 M *Para* was prepared daily by dissolving 0.30234 g of *Para*

in deionized distilled water. Carbonate-free sodium hydroxide solution was prepared and standardized against standard oxalic acid solution before starting an experiment. The stock solution of each metal salt was prepared by dissolving the required quantities (0.47542 g of Ni(II) and 0.34096 g of Cu(II)) in deionized distilled water. The stock solution of metal salt was standardized by ethylenediaminetetraacetic acid (EDTA) titrations.

2.3 Apparatus

Potentiometric titration was performed using a Thermo Electron Corporation Orion 3-Star pH Benchtop (accuracy ± 0.002) instrument with a glass and calomel electrode assembly. The pH-meter was standardized before each titration with a buffer solution of pH 4.01, 7 and 10. The temperature was constantly maintained (± 0.1 K) by Gant Instruments (Cambridge) Ltd. Thermostated Water Bath: Model SUB28.

2.4 Procedure

The experimental procedure involved the potentiometric titration of the following sets of solutions:

1) Acid titration: HCl (0.1 M, 10 mL)
2) Ligand titration: HCl (0.1 M, 10 mL) + *Val* (0.004 M, 10 mL).
3) Metal(II) + ligand titration: HCl (0.1 M, 10 mL) + *Val* (0.004 M, 10 mL) + metal(II) (0.004 M, 10 mL).
4) Metal(II) + ligand titration: HCl (0.1 M, 10 mL) + *Para* (0.004 M, 10 mL) + metal(II) (0.004 M, 10 mL).
5) Metal(II) + mixed ligand titration: HCl (0.1 M, 10 mL) + *Val* (0.004 M, 10 mL) + metal(II) (0.004 M, 10 mL) + *Para* (0.004 M, 10 mL).

The total volume used in each cell was 50 mL in the absence and presence of 0.1 M NaCl for the ionic strength study and at a temperature of 313.15 ± 0.1 K. Titration curves were obtained from the plots of pH versus volume of alkali required, and the four curves are referred to as (i) acid, (ii) ligand, (iii) complex, and (iv) mixed ligand complex (Fig. 3).

3. RESULTS AND DISCUSSION

3.1 Collection of Literature Data

The protonation constants and stability constant of the binary complexes of the drugs paracetamol and the amino acid L-Valine had previously been determined and are reported in various literature reports. According to the temperature and the type of solvent, it was observed that the values of these constants varied (see Tables 1 and 2).

Moreover, there was also a variety of salts (KNO_3, $NaNO_3$, NaCl and $NaClO_4$) that were added to the aqueous medium as an ionic force. Furthermore, the values of these constants were affected by the ionic strengths of several salts (KNO_3, $NaNO_3$, NaCl, and $NaClO_4$). Since these values will be utilized to determine the stability constants of the ternary complexes, it was necessary to re-determine these constants.

3.2 Protonation Constants of Paracetamol and L-Valine Ligands

A critical study of the literature data was conducted because there are various studies dealing with the protonation constant of the L-Valine amino acids and paracetamol ligands. The most relevant references are those shown in Table 1, the values are in good agreement (40). L-Valine exists as zwitterions in aqueous solution, the carboxyl group is deprotonated in acidic media at pH 2 to 3, whereas the amino group is protonated in basic solutions at pH 9 to 10. The two dissociation mechanisms are thus entirely distinct from one another. In the case of paracetamol, its pK_a is 9.38, at this pH, the paracetamol molecules are in the protonated form, while the deprotonated form will be mostly present when pH > 9.24 (41).

Stability constants for the nickel and copper complexes of L-Valine amino acid can readily be obtained with pH-metry. Tentative values of the stability constants for the nickel and copper binary system are listed in Table 2. The values obtained are in agreement, and they are given as recommended values.

Many authors have reported the study of stability constant of L-Valine with Cu and Ni metal complexes as seen in Table 2. However, few data on the stability constant of binary paracetamol–Cu(II) or binary paracetamol-Ni(II) complexes have been reported in literature and for the mixed ligands complexes have not been reported elsewhere in literature, to the best of our knowledge. Therefore, the present study is aimed at determining the stability constant of ternary para-L-Val-Cu(II) para-L-Val-Ni(II)and complexes using pH-metry method.

3.3 Potentiometric Measurements of Binary and Ternary Complexes

3.3.1 Binary Complexes

The proton dissociation constants of *Para* and *L*-Valine and their complexes with Ni(II) and Cu(I) were determined in aqueous medium at 313.15 K in the absence of I = 0.1 mol/L NaCl. The formation constants of binary complexes were obtained using Irving - Rossotti equations by calculating the values of the average number of ligand molecules attached per metal ion (ñ) and free ligand exponent (pL) (Irving and Rossotti, 1953, 1954). The titration curves (Fig. 3) indicate that the ligand curves are slightly shifted to the high pH value of the acid titration curve.

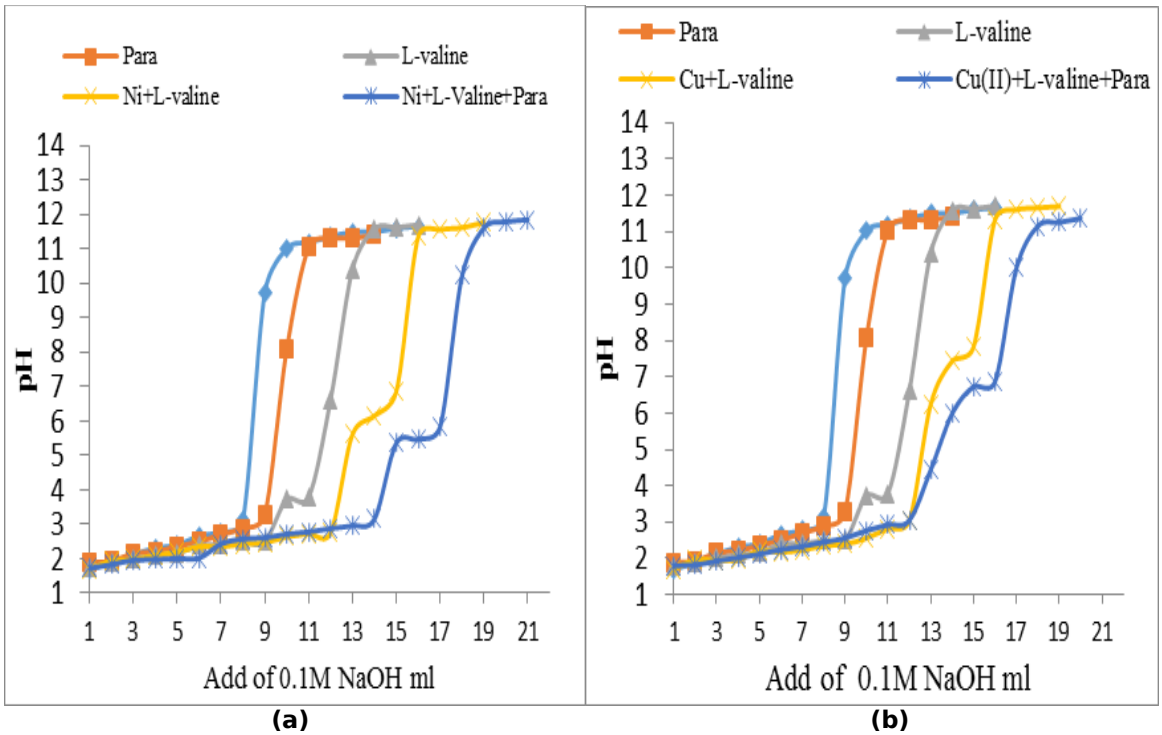

Figure 3: Potentiometric titration curves of **(a)** *Val - Para* - Ni(II) complexes and **(b)** *Val-Para* - Cu(II) complexes at 313.15 K.

Table 1: Protonation constants (logK^H) of free ligands (Literature Values)

ligand	$\log K_1^H$	$\log K_2^H$	Condition	Ref.
L-Valine	9.41	2.95	25 °C, $NaNO_3$ (0.1 M), 40% ethanol-water	(42)
	9.62	2.32	25 °C, aq, KNO_3(0.1M)	(43)
	9.50	2.36	25 °C, aq, $NaClO_4$(0.1M)	(44)
	9.405	2.292	37 °C, aq,	(45)
	9.805	2.298	37 °C, aq, (NaCl 0.1 M)	(46)
	9.47	2.25	25 °C, aq, (KNO_3 0.11M)	(47)
	9.49	2.26	30 °C, aq, ($NaClO_4$ 0.1M)	(48)
	9.60	2.31	30 °C, aq, ($NaClO_4$ 0.2M)	(49)
Paracetamol	9.24	-	37 °C, aq, ($NaNO_3$ 0.1M)	(50)
	9.50	-	25 °C, aq	(51)
	9.47	-	37 °C, aq,	(46)
	9.67	-	37 °C,(KNO_3 0.1 M), 40% Ethanol-water	(52)

Table 2: Stability constants of Cu and Ni binary metal complexes of L-Valine amino acids and paracetamol ligands (Literature Values)

Complexes	$\log K_1$	Condition	Ref.
Ni(II)-Para	5.59	25 °C, aq, $NaClO_4$(0.1 M)	(53)
	3.30	KNO_3 (0.1),40%ethanol-water	(52)
Cu(II)-Para	1.54	37 °C, aq, $NaNO_3$ (0.1 M)	(50)
Ni(II)-L-Val	9.71	30 °C, aq, $NaClO_4$ (0.1 M)	(48)
	8.98	30 °C, aq, $NaClO_4$ (0.2 M)	(49)
	9.72	25 °C, aq,	(54)
	9.53	25 °C, aq, KNO_3 (0.15 M)	(55)
	9.02	40 °C, aq, KNO_3 (0.15 M)	(55)
Cu(II)-L-Val	11.54	25 °C, aq, $NaNO_3$ (0.1 M), 40%ethanol-water	(42)
	14. 76	25 °C, aq, KNO_3 (0.15 M)	(55)
	14.28	35 °C, aq, KNO_3 (0.15 M)	(55)

The shift is due to the interaction of protons with the ligand and subsequently with the metal ion. The values of n_A (the degree of formation of the proton complex) were calculated using the following equation:

$$n_A = Y + \frac{\left[(V' - V'') \times (N + E^0)\right]}{\left[(V^0 + V') \times T_L^0\right]} \quad \text{(Eq. 1)}$$

where Y = number of replaceable hydrogen ions, V°

= total volume (50 mL), V' = volume of alkali required by the acid, V" = volume of alkali used by acid and ligand, N = concentration of alkali, E° = total strength of acid and T_{L° = total concentration of ligand (37, 39).

The proton ligand formation curve was obtained by plotting the degree of formation (n_A) of the proton complex against pH values. The values of $\log K_1^H$ and $\log K_2^H$ were determined from the curves corresponding to n_A values of 0.5 and 1.5 (Fig. 4). The protonation constants at 313.15 ± 0.1 K were calculated (39, 56) and are summarized in Table 3.

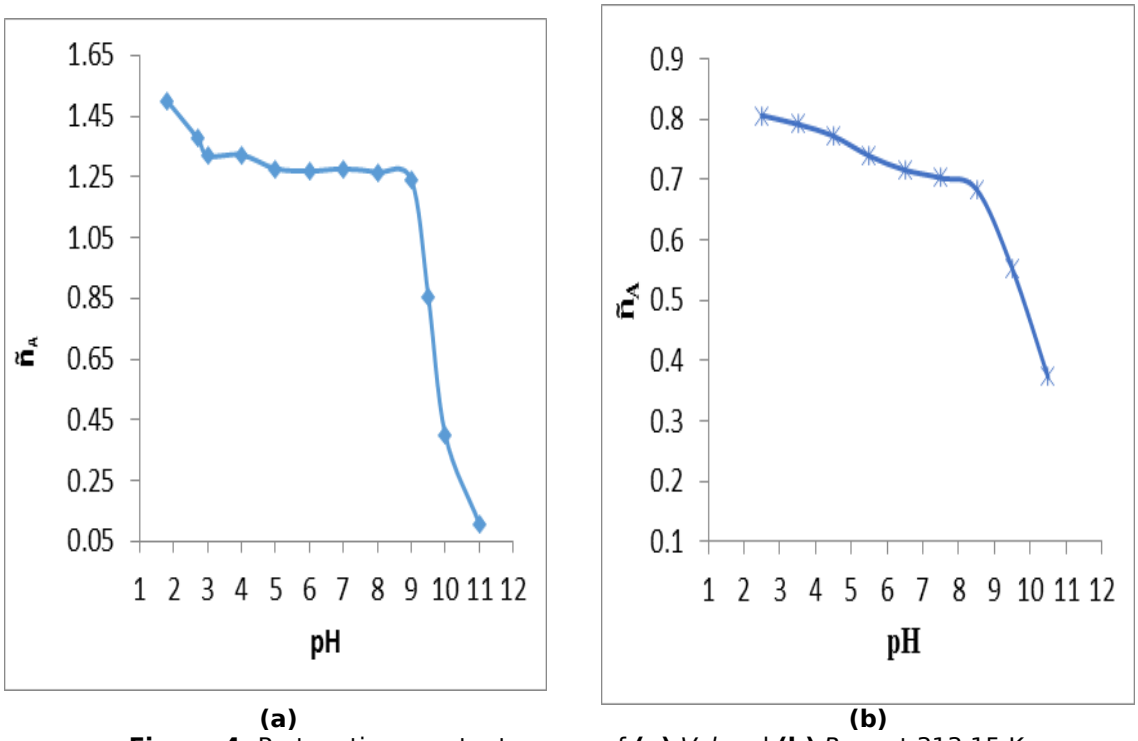

(a) **(b)**

Figure 4: Protonation constant curves of **(a)** *Val* and **(b)** *Para* at 313.15 K.

Table 3: Protonation constants of *Val* and *Para* and stability constants of their complexes in the absence of 0.1 M NaCl (ionic strength) at 313.15 K.

Metal ions	M(*Val*)	M(*Val*)	M(*Para*)	$\log K^{M(L-Val)}_{M(L-Val)(Para)}$	Δ log*K*
	$\log K_1^H$	$\log K_2^H$	$\log K_1^H$		
H⁺	10.123	2.314	9.8773	------	------
Ni(II)	8.856	2.866	3.8250	5.9594	+ 2.1345
Cu(II)	9.342	2.995	4.0767	6.3943	+ 2.3176

The values of ñ (average number of ligand molecules attached per metal ion) were calculated using Equation 2:

$$\tilde{n} = \frac{\left[(V''' - V'') \times (N + E^0)\right]}{\left[(V^0 + V'') \times n_A \times T^0_M\right]} \qquad \text{(Eq. 2)}$$

where V"' = volume of alkali used for acid + ligand + metal ion, T_{M° = total concentration of the metal ion, while the other terms are defined as in Equation 1. The free ligand exponent, pL, was calculated using Equations 3a and 3b as given below:

$$pL = \log_{10}\left\{\sum_{j=0}^{j=J} {}^0\beta_j^H \frac{[H]^j}{(T_L - n T_M)}\right\} \qquad \text{(3a)}$$

$$pL = \log\left[\frac{1 + pK_1^H(1/anti\log B) + pK_1^H \times pK_2^H(1/anti\log B)^2}{T_L - \tilde{n} T_M} \times \frac{V + V'''}{V}\right] \qquad \text{(3b)}$$

where β_j^H = proton ligand stability constant and the rest of the terms are similarly defined as in Equations 1 and 2 (38, 39). Values of $\log K_1$ and $\log K_2$ were obtained using the Bjerrum half-integral

method (37, 39) and interpolation at half n values calculation method using the following equations:

$$\log K_1 = pL \quad (4a)$$

$$\log K_2 = pL \quad (4b)$$

By plotting a graph of ñ against pL and determining the corresponding values of pL at ñ equal to 0.5 and 1.5, the respective values of $\log K_1$ and $\log K_2$ were obtained. The values of n obtained for the metal-ligand system indicate the formation of either 1:1 or 1:2 complexes (Fig. 5). The overall order of stability (logβ) is Cu(II)>Ni(II) and is in good agreement with the Irving-Williams order of stability (38). The values listed in Table 3 are related to the following equilibrium:

$$HL \leftrightarrow H^+ + L^- \qquad K_1=[H^+][L^-]/[HL] \quad (5a)$$

$$H_2L \leftrightarrow H^+ + HL^- \qquad K_2=[H^+][HL^-]/[H_2L] \quad (5b)$$

The attachment of a proton to the NH_2-group (A is the primary ligand) is associated with the $\log K_1$ value in *Val*, and the protonation of an α-carboxylate group (L is the second ligand) corresponds to the $\log K_2$ value in *Val* and the $\log K_1$ value in *Para*.

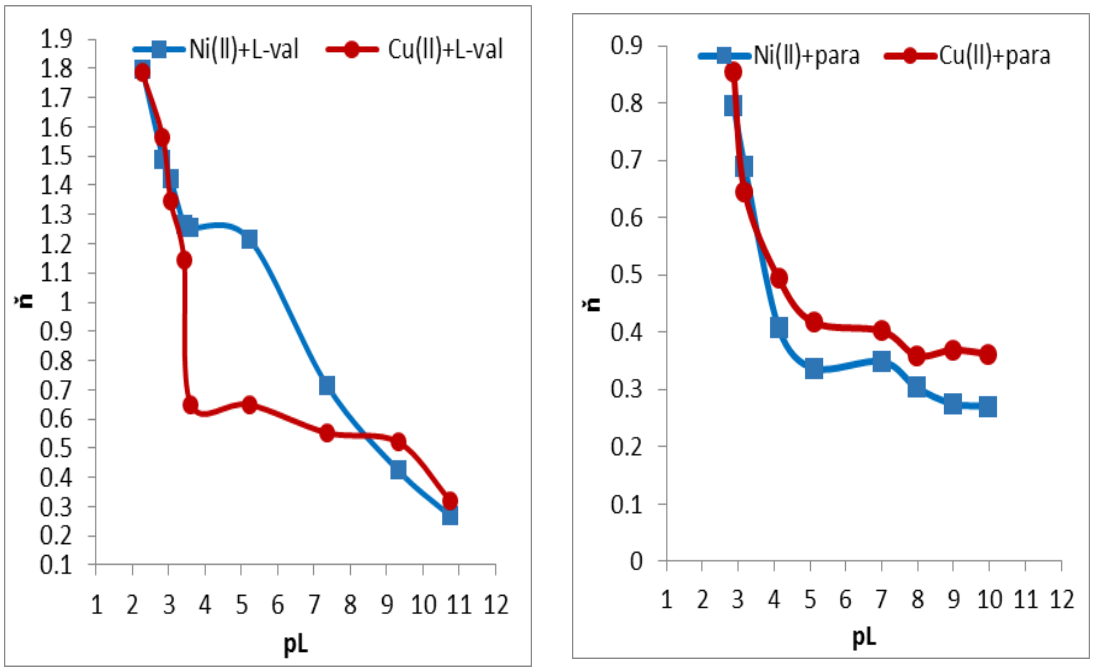

(a) **(b)**

Figure 5: Formation curves of binary metal ion complexes with **(a)** M(II) + *Val* and **(b)** M(II) + *Para* at 313.15 K

The obtained results show the same logarithm to the formation constants for all types of complexes, which have been identified using potentiometric titration as given by the following equilibria:

$$M+L \leftrightarrow ML \qquad K_1=[ML]/[M][L] \quad (6a)$$

$$\text{or } M+2L \leftrightarrow ML_2 \qquad K_2=[ML2]/[M][L]^2 \quad (6b)$$

3.3.2 Ternary Complexes

The potentiometric titration curves for ternary complexes (metal–*Val*-*Para*), representing typical titration curves for the metal–*Val*–*Para* system, studied in a 1:1:1 molar ratio at 313.15 K and in the absence of 0.1 M NaCl are shown in Fig. 3. The primary complex curve (free acid + M(II) + *Val*) and mixed ligand curve (free acid + M(II) + *Val* + *Para*) overlap with each other up to pH 3. This result indicates that within this pH range, the combination of secondary ligands does not take place when the primary ligand combines with the metal. Above pH 3, the two curves start to diverge from each other, signifying the starting point of occurrence for the combination of the secondary ligand with the primary complex (1, 2, 57-61).

In the calculation, ternary complexes were assumed to form in two steps. Initially, the primary ligand (A), with a higher formation constant in the binary complex, reacts with the metal ion to form a binary complex with formula MA. The binary ligand then coordinates to the second ligand (L) to form a mixed ligand complex in the form of MAL. The primary ligand can also be determined by comparing the titration curves of binary systems.

The complex that reached the highest pH before precipitation of the metal hydroxide was considered to be the first complex formed in mixed ligand systems, and the corresponding ligand was the primary ligand in a ternary complex. The formation of a ternary complex can be represented by the stepwise equilibrium below:

$$M + A \Leftrightarrow MA \qquad K_{MA}^{M} = \frac{[MA]}{[M][A]} \quad (7a)$$

$$MA + L \Leftrightarrow MAL \qquad K_{MAL}^{MA} = \frac{[MAL]}{[MA][L]} \quad (7b)$$

The values of ň (average number of secondary ligand molecules attached to the primary complex (M-*Val*)) were calculated from the following equation:

$$\tilde{n} = \frac{(V''' - V'') \times (N + E)}{(V - V'') \times T_M \times \tilde{n}_A} \quad \text{(Eq. 8)}$$

where T_M° = initial total metal ion concentration, V''' = the differences in the volume of alkali added between the (free acid + metal+ *Val* + *Para*) curve and (free acid + metal + *Val*) curve, and V'' = the differences in the volume of alkali added between the (free acid) curve and (free acid + *Para*) curve (1, 2, 57-61). The free secondary ligand exponent, pL, was calculated using Equation 3b and is shown in Fig. 6. The horizontal distance between the (free acid) curve and (free acid + *Para*) curve, V'', indicates the protons released as a result of self-dissociation of the secondary ligand, whereas the difference between the (free acid + M(II) + *Val*) curve and (free acid + M(II) + *Val* + *Para*) curve, V''', indicates the sum of protons released due to the self-dissociation of secondary ligand and protons released due to the formation of mixed ligand complex. Thus, (V''-V'') accounts for the total protons released due to the formation of the mixed ligand complex. The formation of the ternary complex M-(*Val*)-(*Para*) shifts the buffer region of the ligands to lower pH values, which indicates that the ternary complex is more stable than the binary complex.

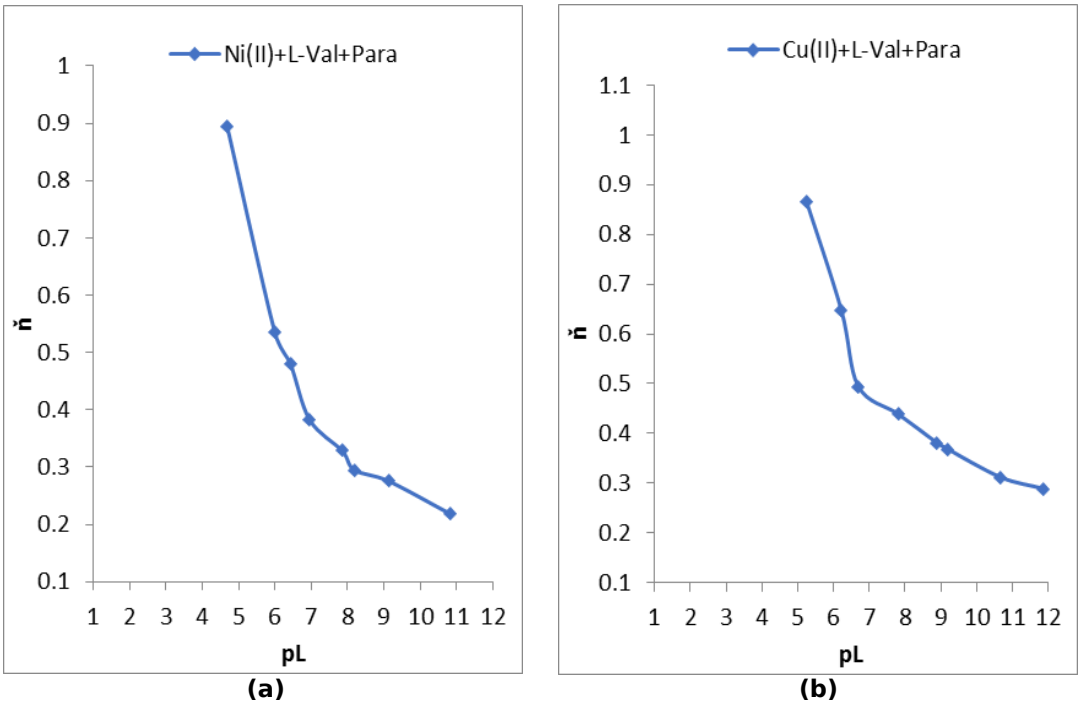

(a) **(b)**

Figure 6: Formation curves of **(a)** Cu(II)-*Val*-*Para* and **(b)** Ni(II)-*Val*-*Para* complexes at 313.15 K.

To compare the stabilities of the ternary complex species with those of the parent binary complexes, the difference between the stabilities of the binary and ternary complexes values, Δlog*K*, were determined using Equation 9 and are summarized in Table 3.

$$\Delta \log K = \log K^{M(L-Val)}_{M(L-Val)(Para)} - \log K^{M}_{M} \quad (9)$$

It was determined that the Δlog *K* values were positive in terms of stability, and a statistical increase is shown in the value of stability constants of the mixed ligand complex. Based on the results in Table 3, the values of the ternary stability constants are found to decrease in the order of Cu(II) > Ni(II).

The complex formation equilibrium of the ternary metal ion complexes and the overall stability constants were calculated using the equations below:

$$M + (Val) + Para \leftrightarrow M(Val)(Para) \quad (10a)$$

$$K^{M}_{M(Val)(Para)} = \frac{[M(Val)(Para)]}{[M][Val][Para]} = K^{M(Val)}_{M(Val)(Para)} \times K^{M}_{M(Val)} \quad (10b)$$

3.4 Effect of Ionic Strength on Binary and Ternary Complex Formation

The interfering effects of ionic strength on the strength of metal ions, *Val*, and *Para* were studied in the presence and absence of ionic strength (0.1 M NaCl) at 313.15 K and 0.004 M of metal ions.

The titration curves of metal complexes in the presence of 0.1 M NaCl (Fig. 7) indicated that there was no precipitate formed in the solutions. This implies that there was no tendency to form hydroxo complexes either because the number of moles of

NaOH consumed was equivalent to the number of moles of HCl or because the interfering effects of hydroxo complexes are negligible. Based on Fig. 8, it can be concluded that metal ions with *Val* or *Para* form a 1:1 or 1:2 ratio of metal-ligand complexes.

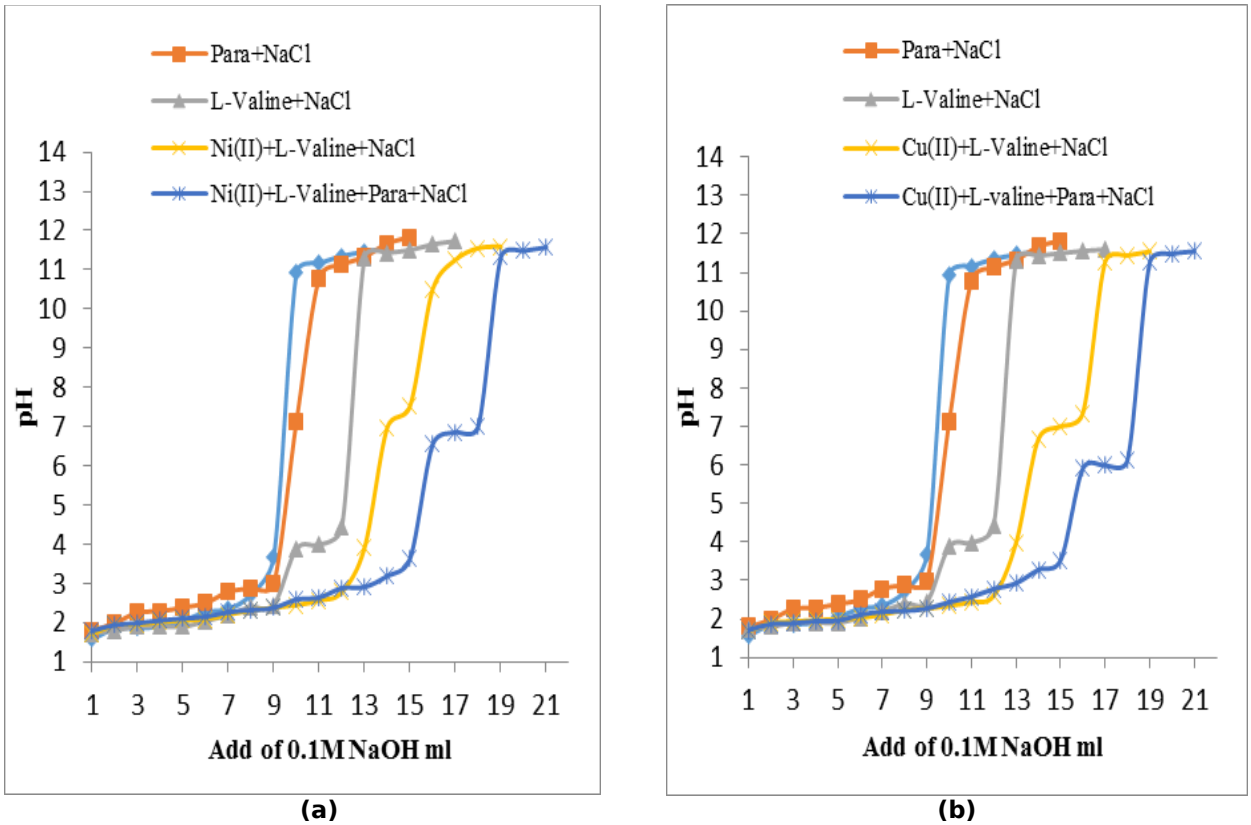

Figure 7: Potentiometric titration curves of **(a)** *Val*-*Para*-Ni(II) complexes and **(b)** *Val*-*Para*-Cu(II) complexes at 313.15 K and 0.1 M NaCl ionic strength.

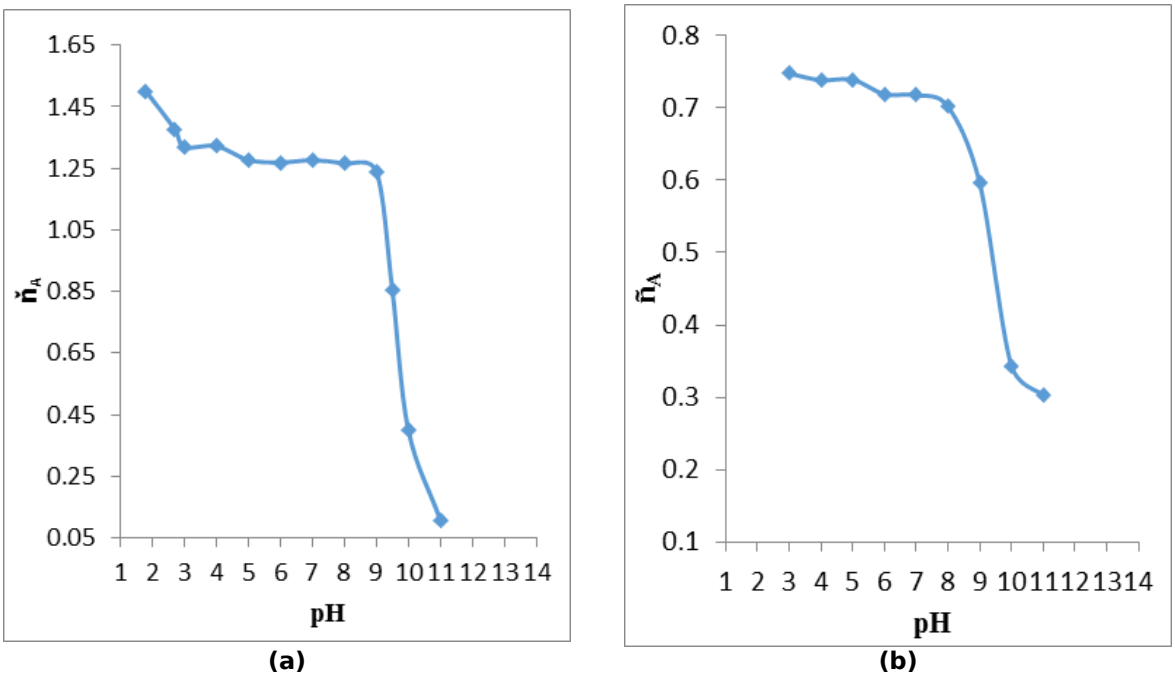

Figure 8: Protonation constant curves of **(a)** *Val* and **(b)** *Para* at 313.15 K.

It was also noted that the presence of NaCl during the complexation reaction causes an increase in pH (Fig. 9) as a result of the decrease in the protonation constant of *Val* for configuring the binary complex (M-*Val*) and the decrease in the protonation constant of *Para* for configuring the ternary complex (M-*Val*-*Para*), as shown in Fig. 8 and Table 4.

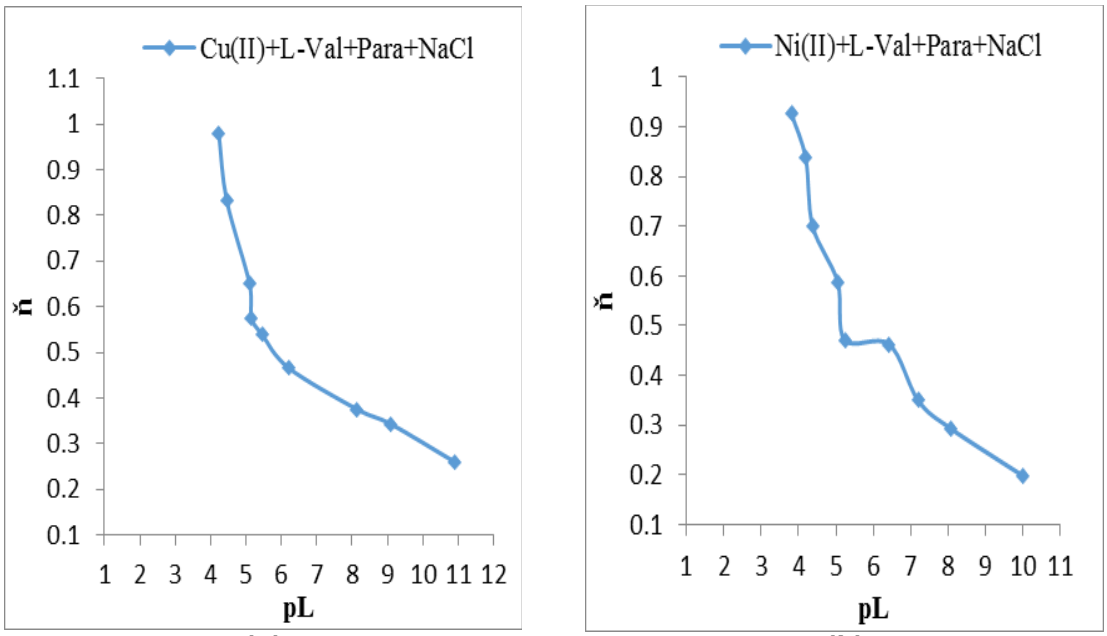

(a) **(b)**

Figure 9: Formation curves of ternary M(II)–Val-*Para* complexes at 313.15 K in the presence of 0.1 M NaCl and 0.004 M of **(a)** Cu(II) and **(b)** Ni(II).

Table 4: Protonation constants of *Val* and stability constants of its complexes at 313.15 K in the presence of 0.1 M NaCl (ionic strength).

Metal ions	M(*Val*)	M(*Val*)	M(*Para*)	$\log K^{M(Val)}_{M(Val)(Para)}$	Δ log *K*
	$\log K_1^H$	$\log K_2^H$	$\log K_1^H$		
H⁺	9.914	2.151	9.4058	-----	------
Ni(II)	8.683	2.811	3.0561	5.1567	+ 2.1006
Cu(II)	9.166	2.900	3.6011	5.7567	+ 2.1556

Moreover, it is noted that the values of stability constants of the formed complexes in the presence of NaCl are lower than the corresponding values in the absence of NaCl. The order of stability constants of the metal-para complexes formed (Table 4) shows a good agreement with the Irving–Williams order of Cu(II) > Ni(II) (62).

3.5 Effect of Ni(II) & Cu(II) Metal Ions on the Structure of Used Ligands

3.5.1 L-Valine

In order to comprehend how metals and proteins interact in biological systems, it is important to study metal complexes of physiologically active ligands such as amino acids. The stability constants of these complexes will also aid in identifying the atoms or groups that are in charge of forming the bonds with the metal ions. Metal ions have a number of distinguishing characteristics that make them able to perform out a wide variety of biofunctions as their small size, positive charge, and electron spin configuration (63, 64). Due to their acidic-basic nature, amino acids function as bidentate ligands to bind through (N, O) donor atoms. Amino acids are regarded as zwitterions, in which they include the positively charged NH_3^+ group or the negatively charged COO^- group (64).

The main goals of this investigation are to report the stability constants of the Cu(II) and Ni(II) complexes of *L-Val* along with to investigate the method in which *L-Val* interacts with the respective metal cations in aqueous environment. A copper(II) complex that exhibits a broad affinity for L-amino acids was described by Leach and Angelici (65). With L-leucine, L-phenylalanine, alanine, L-serine, and valine, copper(II) forms stronger complexes than with the corresponding antipodes, according to a set of stability constants determined using potentiometry. Noori et al. (66) had synthesized complexes of Mn(II), Fe(II), Co(II), Ni(II), Cu(II), and Cd(II) ions with L-Valine as a primary ligand and 1,10-phenanthroline as a secondary ligand. The work indicated that nickel has an octahedral geometry. Fayad et al. (67) reported the synthesis of six novel mixed ligand complexes of metals (II), using saccharin and L-Valine as primary and secondary ligands, respectively (67). The complexes with the formulas $[M(Val)_2(Sac)_2]$, M(II) = Mn(II), Fe(II), Co(II), Ni(II), Cu(II), Zn(II), and Cd(II) were obtained. Based on the results, it could be concluded that L-Valine coordinated to metal ions as a bidentate ligand through the nitrogen of the amine group and the oxygen of the carboxylate group (See Fig. 10).

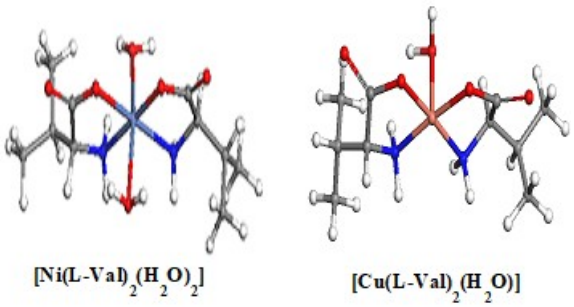

Figure 10: Suggested geometric structures of L-Valine complex.

3.5.2 Paracetamol Complexes

Metal complexes are playing a bigger role in the development of pharmaceuticals. This has prompted extensive research on metal drug complexes, in which pharmaceutical substances function through chelation to understand how metal binding affects the behaviors of biological processes in the human body (1, 2). Since paracetamol has two functional groups (NH amide and OH phenol), it is bound to metal ions once it enters the body. Refat et al. (68, 69) synthesized paracetamol complexes with Mn(II), Co(II), Fe(III), Zn(II), and Cu(II). Paracetamol behaves as a monobasic bidentate ligand in these complexes, and the structures of those complexes have been validated by elemental analysis, FT-IR spectroscopy, and thermal analysis. Obaleye et al. prepared and investigated complexes of Co(II), Ni(II), and Fe(III) with paracetamol (70, 71). According to research, paracetamol ligand acts as a bidentate chelating agent in which the oxygen of the hydroxyl and amide groups are coordinated (Fig. 11). Babamale et al. synthesized mixed metal complexes of aspirin and ascorbic acid involving the ions Fe(II), Co(II), Ni(II), Cu(II), and Zn(II) (72). According to the physical and spectroscopic studies, paracetamol's amide nitrogen and carbonyl oxygen were responsible for the metal's coordination. Based on the results, it could be concluded that paracetamol coordinated as a monodentate through the nitrogen atom (See Fig. 11).

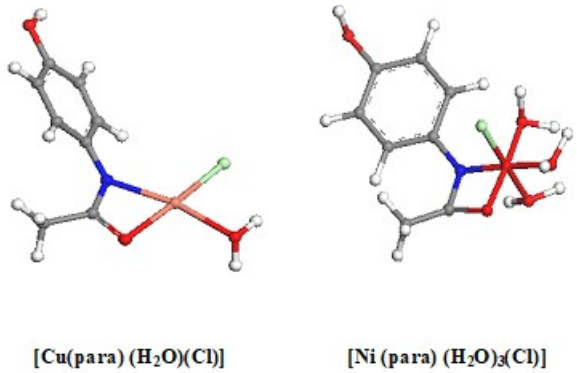

Figure 11: Suggested geometric structures of paracetamol complexes.

4. CONCLUSION

The stability constants for the ternary metal complexes of *Val* and *Para* with Ni(II) and Cu(II), formed with *Val* as the primary ligand and *Para* as the secondary ligand with metal ions, were computed from potentiometric titrations. The concentration of metal ions was kept constant at 0.004 M, and the ratio of metal ions: *Val*: *Para* was kept at 1:1:1. The stability constants in the absence of 0.1 M NaCl ionic strength were found to be higher than the stability constants in the presence of 0.1 M NaCl ionic strength. The order of stability is in accordance with the Irving-Williams order of stability: Cu(II) > Ni(II). The calculated values of the ΔlogK parameters showed the effect of the bound primary ligand on an incoming secondary ligand. The positive values of ΔlogK parameters indicate the higher stability of ternary complexes than the corresponding binary ones.

5. ACKNOWLEDGMENTS

The authors wish to acknowledge the Chemistry Department and Sebha University for providing the necessary facilities to perform the studies.

6. REFERENCES

1. Myers R. The basics of chemistry. Greenwood Publishing Group; 2003.

2. Crabb E, Moore E. Metals and Life Chapter 9. RSC Publishing; 2010.

3. Jones C, Thornback JR. Medicinal Applications of Coordination Chemistry. RSC Publishing; 2007.

4. Alexandrova R, Rasshkova G, Alexandrov I, Tsenova W, Tudose R, Costisor O. Briefly about copper. Exp Pathol Parasitol. 2003;1311:6851.

5. Malmström BG, Leckner J. The chemical biology of copper. Curr Opin Chem Biol [Internet]. 1998 Apr 1;2(2):286–92. Available from: <URL>

6. Coleman N, Castrejon A, Blaine C, Chemmachel T. The toxicology of essential and nonessential metals. 2017.

7. Smith RM, Motekaitis RJ, Martell AE. Prediction of stability constants. II. Metal chelates of natural alkyl amino acids and their synthetic analogs. Inorganica Chim Acta [Internet]. 1985 Sep 2;103(1):73–82. Available from: <URL>

8. Gergely A, Nagypál I, Farkas E. Thermodynamic relations of parent and mixed complexes of asparagine and glutamine with copper(II). J Inorg Nucl Chem [Internet]. 1975 Feb 1;37(2):551–5. Available from: <URL>

9. IUPAC-IUB Joint Commission on Biochemical Nomenclature (JCBN). Nomenclature and symbolism for amino acids and peptides. Recommendations 1983. Biochem J [Internet]. 1984 Apr 15;219(2):345–73. Available from: <URL>

10. Lynch CJ, Adams SH. Branched-chain amino acids in metabolic signalling and insulin resistance. Nat Rev Endocrinol [Internet]. 2014 Dec 7;10(12):723–36. Available from: <URL>

11. Belkher NA, Al-Abbas AA, Zidan M. Potentiometric Studies on Stability Constant of the Complexes of Some Essential Transition Metal Ions with L-Valine. J Pure Appl Sci [Internet]. 2019 May 1;18(3):59–63. Available from: <URL>

12. Sigel A, Sigel H, Sigel, Roland KO. Nickel and its surprising impact in nature. Metal Ions in Life Sciences, Volume 2 [Internet]. England: Wiley; 2007. 728pp p. Available from: <URL>

13. Wieser ME, Holden N, Coplen TB, Böhlke JK, Berglund

M, Brand WA, et al. Atomic weights of the elements 2011 (IUPAC Technical Report). Pure Appl Chem [Internet]. 2013 Apr 30;85(5):1047–78. Available from: <URL>

14. Wiberg E, Wiberg N, Holleman A. Inorganic chemistry. Academic Press; 2001. 1665 p.

15. Harris ED. Copper Homeostasis: The Role of Cellular Transporters. Nutr Rev [Internet]. 2001 Apr 27;59(9):281–5. Available from: <URL>

16. Groff JL, Gropper SS, Hunt SM. Advanced nutrition and human metabolism. St. Paul Minneapolis: West Publishing Company. 1995.

17. Araya M, Pizarro F, Olivares M, Arredondo M, Gonzalez M, Mendez M. Understanding copper homeostasis in humans and copper effects on health. Biol Res [Internet]. 2006;39(1):183–7. Available from: <URL>

18. Bowman WC, Rand MJ. Textbook of pharmacology. Blackwell Scientific Publications; 1980.

19. Negwer M. Organic-chemical drugs and their synonyms: (an international survey). Wiley-VCH; 2001. 4880 p.

20. Alhalib A. Spectrophotometric determination of acetaminophen content of different brands of paracetamol tablets from Zliten. J Alasmarya Univ [Internet]. 2017;2(2):134–40. Available from: <URL>

21. Van Boxtel CJ, Santoso B, Edwards IR. Drug benefits and risks: International textbook of clinical pharmacology-revised 2nd edition. Ios Press; 2008.

22. Goodman LS. Goodman and Gilman's The Pharmacological Basis of Therapeutics. New York: Mcgraw-Hill; 1996.

23. Singh Sandhu R, Kumar Kalia R. Complexation reaction of metal ions with peptide systems. VII. Equilibrium studies of N-benzoyl-L-valine, N-benzoyl-glycyl-L-valine and isovaleric acid with metal(II) ion systems. Thermochim Acta [Internet]. 1980 Sep 15;40(2):305–9. Available from: <URL>

24. Enamullah M, Ahmed MG, Akhtar F. Meters of Divalent Zinc, Nickel, Cobalt and Cadmium Complexes of Phthalic Acid. J Bangladesh Chem Soc. 1991;4(2):129–36.

25. Mendes J, de Almeida KJ, Neto JL, Ramalho TC, Duarte HA. Theoretical spectroscopic insights of tautomers and enantiomers of penicillamine. Spectrochim Acta Part A Mol Biomol Spectrosc [Internet]. 2017 Sep 5;184:308–17. Available from: <URL>

26. Mackay D. The reaction of thiol amino acids with pyridoxal 5′-phosphate in the absence and in the presence of l-glutamic acid. Biochim Biophys Acta - Spec Sect Enzymol Subj [Internet]. 1963 Jul 9;73(3):445–53. Available from: <URL>

27. Ash T, Debnath T, Ghosh A, Das AK. Comprehensive understanding of multiple binding of D-penicillamine with Cu2+-hexa aqua complex: a DFT approach. Struct Chem [Internet]. 2020 Feb 4;31(1):155–69. Available from: <URL>

28. Chakrawarti PB, Chakrawarti M, Maini P. Equilibrium studies of ternary chelates of some divalent metal ions with cephalosporins and α-alanine. J Indian Chem Soc. 2000 Mar 15;77(5):217–9.

29. Suhud K, Heng LY, Rezayi M, Al-abbasi AA, Hasbullah SA, Ahmad M, et al. Conductometric Studies of the Thermodynamics for Complexation of 1,1-Diethyl-3-(4-methoxybenzoyl)thiourea and Cobalt(II) Cation in Aqueous Binary Mixtures of Polar Organic Solvents. J Solution Chem [Internet]. 2015 Feb 22;44(2):181–92. Available from: <URL>

30. Tan SS, Al-abbasi AA, Mohamed Tahir MI, Kassim MB. Synthesis, structure and spectroscopic properties of cobalt(III) complexes with 1-benzoyl-(3,3-disubstituted)thiourea. Polyhedron [Internet]. 2014 Jan 28;68:287–94. Available from: <URL>

31. Al-abbasi AA, Mohamed Tahir MI, Kassim MB. 1,1-Diethyl-3-(4-methoxybenzoyl)thiourea. Acta Crystallogr Sect E [Internet]. 2011 Dec 15;E67:o3414. Available from: <URL>

32. Al-abbasi AA, Kassim MB. 1-Ethyl-1-methyl-3-(2-nitrobenzoyl)thiourea. Acta Crystallogr Sect E [Internet]. 2011 Jul 15;E67:o1840. Available from: <URL>

33. Al-abbasi AA, Tan SS, Kassim MB. 1-Benzoyl-3-(4-hydroxyphenyl)thiourea. Acta Crystallogr Sect E Struct Reports Online [Internet]. 2010 Dec 15;E66:o3181. Available from: <URL>

34. Al-abbasi AA, Tahir MIM, Kayed SF, Kassim MB. Synthesis, characterisation and biological activities of mixed ligand oxovanadium (IV) complexes derived from N , N -diethyl- N ′- para -substituted-benzoylthiourea and hydrotris(3,5-dimethylpyrazolyl)borate. Appl Organomet Chem [Internet]. 2022 Apr 1;36(4):e6607. Available from: <URL>

35. Almutaleb AAA, Alabbasi AA. Synthesis, characterization and computational studies for (2′ S *,3 R *,3′ S *,8a′ R *)-2′,3′-bis(ethoxycarbonyl)-2-oxo-2′,3′-dihydro-8a′H-spiro[indoline-3,1′-indolizine]-6′-carboxylic acid and some derivatives. J Phys Org Chem [Internet]. 2023 Feb 27;36(2):e4452. Available from: <URL>

36. Bjerrum J. Metal ammine formation in aqueous solution: Theory of the reversible step reactions. 1957. 296 p.

37. Bjerrum J. Stability Constants of Metal-Ion Complexes with Solubility Products of Inorganic Substances. Stability Constants of Metal-Ion Complexes. Section I: Inorganic Ligands. Compiled by Lars Gunnar Sillén. Section II: Organic Ligands. Compiled by Arthur E. Marte [Internet]. London : Chemical society; 1964. Available from: <URL>

38. Irving H, Williams RJP. The stability of transition-metal complexes. J Chem Soc [Internet]. 1953 Jan 1;3192–210. Available from: <URL>

39. Irving HM, Rossotti HS. The calculation of formation curves of metal complexes from pH titration curves in mixed solvents. J Chem Soc [Internet]. 1954 Jan 1;2904–10. Available from: <URL>

40. Bretti C, Giuffrè O, Lando G, Sammartano S. Modeling solubility and acid–base properties of some amino acids in aqueous NaCl and (CH3)4NCl aqueous solutions at different ionic strengths and temperatures. Springerplus [Internet]. 2016 Dec 30;5(1):928. Available from: <URL>

41. Juela DM. Comparison of the adsorption capacity of acetaminophen on sugarcane bagasse and corn cob by dynamic simulation. Sustain Environ Res [Internet]. 2020 Dec 1;30(1):23. Available from: <URL>

42. Doğan A, Kılıç E. Potentiometric studies on the stability constants of some-amino acid-copper (II) and nickel (II) systems in ethanol-water mixture. Indian J Chem - Sect A Inorganic, Phys Theor Anal Chem. 2003;42(7):1632–5.

43. Snyder RV. A Study of Stereoselective Amino Acid Complexes of Copper(II) and Nickel(II) [Internet]. Doctoral Theses. [United States -- Iowa]: Iowa State University; 1972. Available from: <URL>

44. Zine AM. Ni(II)-Mercaptosuccinic Acid/2-Mercaptopropionyl Glycine-Amino Acids Ternary Complexes-A potentiometric Study. Int J Chem Sci. 2005;3(2):295–300.

45. Smith PK, Taylor AC, Smith ERB. Thermodynamic properties of solutions of amino acids and related substances. J Biol Chem [Internet]. 1937 Dec;122(1):109–23. Available from: <URL>

46. Belkher NA, Al-Abbas AA, Zidan M. Potentiometric Studies on Stability Constant of the Complexes of Some Essential Transition Metal Ions with L-Valine. J Pure Appl Sci [Internet]. 2019;18(3):59–63. Available from: <URL>

47. Angelici RJ, Allison JW. Stability constants for amino acid coordination by substituted diethylenetriamine complexes of copper(II) and the kinetics of amino acid ester hydrolysis. Inorg Chem [Internet]. 1971 Oct 1;10(10):2238–43. Available from: <URL>

48. Magare BK, Ubale MB. Equilibrium Studies on Ternary Metal Complexes of Drug Ethambutol Hydrochloride with Nickel and Cobalt Metal Ions and Four Amino Acids. Int Res J Eng Technol [Internet]. 2008;6(8):1280–4. Available from: <URL>

49. Rajarajan G, Dhineshkumar E, Amala S, Seenivasan M, Paramasivan A. Determination of Stability constants Nickel binary and ternary complexes in aquesous DMSO by Pontentiometric method. J Phys Conf Ser [Internet]. 2021 Jan 1;1724(1):012005. Available from: <URL>

50. Chandrathilaka A, Ileperuma O, Hettiarachchi C. Spectrophotometric and pH-metric studies on Pb(II), Cd(II), Al(III) and Cu(II) complexes of paracetamol and ascorbic acid. J Natl Sci Found Sri Lanka [Internet]. 2013 Dec 12;41(4):337–44. Available from: <URL>

51. O'Neil MJ, Heckelman PE, Koch CB, Roman KJ. The Merck Index, 14th edition. Merck, John Wiley & Sons, Inc.; 2006.

52. Patil A. Stability constants of binary and ternery complexes of ibuprofen and paracetamol. Rasayan J Chem [Internet]. 2013;6(3):168–71. Available from: <URL>

53. Kaur H, Singla A. Comparative study of stability constants and thermodynamic properties of complexation of Aspirin and Paracetamol with divalent metal ions by potentiometry. Int J Theor Appl Sci. 2010;2(1):14–7. <URL>

54. Sovago I, Kiss T, Gergely A. Critical survey of the stability constants of complexes of aliphatic amino acids (Technical Report). Pure Appl Chem [Internet]. 1993 Jan 1;65(5):1029–80. Available from: <URL>

55. Li NC, White JM, Yoest RL. Some Metal Complexes of Glycine and Valine 1. J Am Chem Soc [Internet]. 1956 Oct 1;78(20):5218–22. Available from: <URL>

56. Irving H, Rossotti HS. Methods for computing successive stability constants from experimental formation curves. J Chem Soc [Internet]. 1953 Jan 1;3397–405. Available from: <URL>

57. Thanavelan R, Ramalingam G, Manikandan G, Thanikachalam V. Stability constants of mixed ligand complexes of lead(II) with 1-(aminomethyl) cyclohexane acetic acid and α-amino acids. J Saudi Chem Soc [Internet]. 2014 Jul 1;18(3):227–33. Available from: <URL>

58. Chandrathilaka AMDS, Ileperuma OA, Hettiarachchi CV. Spectrophotometric and pH-metric studies on Pb(II), Cd(II), Al(III) and Cu(II) complexes of paracetamol and ascorbic acid. J Natl Sci Found Sri Lanka [Internet]. 2013 Dec 12;41(4):337–44. Available from: <URL>

59. Rawate GD. pH metric and thermodynamic studies of binary complexes of Co(II), Rh(II), Pd(II), Pt(II), Ag(I), Zn(II), and Cd(II) with Ibuprofen and Paracetamol. 2014-2016;47-671/13.

60. Kemp HR. The effect of temperature and pressure on equilibria: A derivation of the van't Hoff rules. J Chem Educ [Internet]. 1987 Jun 1;64(6):482. Available from: <URL>

61. Helmy ET, Gomaa EA, Elleef EMA, Negm A. Conductometric, Spectrophotometric and In vivo Investigation of the Interaction of Ca(II) Ion with Oxytetracycline Hydrochloride. Int J Pharma Med Biol Sci [Internet]. 2015;4(3):197–203. Available from: <URL>

62. Miličević A, Branica G, Raos N. Irving-Williams Order in the Framework of Connectivity Index 3χv Enables Simultaneous Prediction of Stability Constants of Bivalent Transition Metal Complexes. Molecules [Internet]. 2011 Jan 26;16(2):1103–12. Available from: <URL>

63. Mandal S, Das G, Askari H. Physicochemical investigations of the metal complexes of L-valine with doubly charged ions of nickel, copper and zinc: a combined experimental and computational approach. RSC Adv [Internet]. 2014 Jun 9;4(47):24796–809. Available from: <URL>

64. Dudev T, Lim C. Metal Binding Affinity and Selectivity in Metalloproteins: Insights from Computational Studies. Annu Rev Biophys [Internet]. 2008 Jun 7;37(1):97–116. Available from: <URL>

65. Leach BE, Angelici RJ. Stereoselective interaction of optically active amino acids and esters with (L;valine-N-monoacetato) Copper(II). J Am Chem Soc [Internet]. 1969 Nov 1;91(23):6296–300. Available from: <URL>

66. Fayad NK, Al-Noor TH, Mahmood AA, Malih IK. Synthesis, Characterization, and Antibacterial Studies of Mn(II), Fe(II), Co(II), Ni(II), Cu(II) and Cd(II) Mixed-Ligand Complexes Containing Amino Acid (L-Valine) And (1,10-phenanthroline). Chem Mater Res [Internet]. 2013;3(5):66–73. Available from: <URL>

67. Fayad NK, Al-Noor TH, Ghanim FH. Synthesis, Characterization, And Antibacterial Activities Of Manganese (II), Cobalt(II), Iron (II), Nickel (II) , zinc (II) And Cadmium(II) Mixed-Ligand Complexes Containing Amino Acid(L-Valine) And Saccharin. Adv Phys Theor Appl [Internet]. 2012;9:1–13. Available from: <URL>

68. Refat MS, El-Korashy SA, Hussien MA. Ligational, Spectroscopic (Infrared and Electronic) and Thermal Studies on the Mn(II), Co(II), Fe(II) and Cu(II) Complexes with Analgesic Drugs. Can Chem Trans [Internet]. 2014;2(1):24–35. Available from: <URL>

69. Refat MS, Mohamed GG, El-Sayed MY, Killa HMA, Fetooh H. Spectroscopic and thermal degradation behavior of Mg(II), Ca(II), Ba(II) and Sr(II) complexes with paracetamol drug. Arab J Chem [Internet]. 2017 May 1;10:S2376–87. Available from: <URL>

70. Amolegbe SA, Adewuyi S, Akinremi CA, Adediji JF, Lawal A, Atayese AO, et al. Iron(III) and copper(II) complexes bearing 8-quinolinol with amino-acids mixed ligands: Synthesis, characterization and antibacterial investigation. Arab J Chem [Internet]. 2015 Sep 1;8(5):742–7. Available from: <URL>

71. Lawal A, Obaleye J. Synthesis, characterization and antibacterial activity of aspirin and paracetamolmetal complexes. Biokemistri [Internet]. 2007 Jul 12;19(1):9–15. Available from: <URL>

72. Babamale HF, Lawal A, Rajee OA, Oloyede EA. Synthesis, characterization and biological activity studies

of mixed paracetamol- ascorbic acid metal complexes. J Appl Sci Environ Manag [Internet]. 2017 Feb 2;20(4):1157–61. Available from: <URL>

JOTCS A
Journal of the Turkish Chemical Society
Section: A
Chemistry
TURKISH CHEMICAL SOCIETY

Adsorptive Elimination of Methyl Orange Dye over the Activated Carbon Derived from Bitter Almond Shells: An Isothermal, Thermodynamic, and Kinetic Study

Rana H. Al-Hyali[1], Wael A. Alqazzaz[1], Duaa H. Altamer[2,*]

[1]Department of Chemistry, College of Science, Mosul University, Mosul, Iraq
[2]Department of New and Renewable Energies, College of Science, Mosul University, Mosul, Iraq

Abstract: Bitter almond shells (BAS) were inspected as a cheap source for the creation of activated carbon (AC) through the optimized $ZnCl_2$-activation approach. The raw BAS were impregnated with $ZnCl_2$ at multiple ratios (1:1 - 3:1 $ZnCl_2$:BAS), followed by carbonization at various temperatures (400 – 800 °C) for different durations (30 – 120 minutes) in a tubular reactor. The typical AC sample was produced with a yield of 23.46% using a 1:1 $ZnCl_2$:BAS impregnation ratio at 500 °C for 60 minutes. The ideal AC sample was identified by BET surface area (SA_{BET}), Boehm titration method, point of zero charges (pH_{PZC}), FESEM, XRD, FTIR, and EDX. The identification consequences revealed that this sample is mesoporous with SA_{BET}, iodine number, total pore volume, and average pore width of 1221.60 m^2/g, 1444.23 mg/g,1.50 cm^3/g, and 4.98 nm, respectively. The adsorptive removal (AR) of methyl orange (MO) dye from its aqueous phase by this AC was accomplished at various solution pH (2–10), diverse mass of the AC (0.05-0.4 g), multiple initial concentrations (50–400 mg/L), variable temperature (30-50 °C) and diverse contact periods (0–420 min) in a batch- mode operation. The maximum monolayer adsorption capacity of 224.71 mg/g was obtained at 323 K, pH= 2.0, 400 mg/L initial concentration of MO, 0.25 g AC dose, and 420 minutes contact period. The kinetic outcomes best fitted to the pseudo-2^{nd} -order kinetics model, while the MO equilibrium capacity obeyed the Langmuir model rather than other models. Thermodynamic studies of the MO adsorption by the BAS-derived AC disclosed that the adsorption was spontaneous and endothermic. The adsorption mechanism of MO by the declared AC primarily involved electrostatic attractions and hydrogen bonding interaction. This work demonstrates that BAS is an excellent raw material for producing low-cost and effectual mesoporous AC carbon with substantive surface area.

Keywords: Activated carbon; Bitter almond shells; Adsorption isotherms and kinetics ; Methyl Orange Dye.

Submitted: November 10, 2022. **Accepted:** January 30, 2023.

Cite this: Al-Hyali RH, Alqazzaz WA, Altamer DH. Adsorptive Elimination of Methyl Orange Dye over the Activated Carbon Derived from Bitter Almond Shells: An Isothermal, Thermodynamic, and Kinetic Study. JOTCSA. 2023;10(2):339–58.

DOI: https://doi.org/10.18596/jotcsa.1177543.

***Corresponding author. E-mail:** duaaaaltamer@uomosul.edu.iq.

1. INTRODUCTION

The production of colored and fashioned clothes is based on utilizing organic dyes (ODs) (1). Multiple industries, including dyeing, textile, food processing, printing, papermaking, and electroplating, are based on the utilization of ODs (2). Nonetheless, ejecting the leftover dyes as per textile discharges as a wastewater causes a huge environmental hazard to both the surface and underground water sources (3). Also, because of their slow biodegradability, the occurrence of ODs in wastewater will affect human health (4). Several effective and profitable procedures have been followed to treat wastewater ejected by the textile industry (5). Membrane separation (6), oxidation (3), precipitation (7), ion-exchange (8), coagulation (9), flocculation (10), and adsorption

(11-13) are the most traditional routes utilized to solve problems associated with ODs effluents. Nevertheless, adsorption is the most efficient approach for ODs removal because it is cheap, eco-friendly, and possesses high elimination ability (14).

Numerous effective adsorbents, including biowastes (15), modified biowastes (16), zeolites (17), fly ash (18), biochar (19), polymeric materials (20), modified biochar (21), AC (22), and AC composites (23) were utilized in the adsorptive elimination of diverse ODs from their aqueous medium. Amongst the most effective adsorbents that have employed in the adsorptive removal (AR) of ODs from polluted wasters is AC. This adsorbent owns an elevated surface area, in the range of 500 m^2/g and 2000 m^2/g, besides its low-density, high adsorptive capacity, high chemical stability, and high porosity. Also, one of the most attractive features of the AC is its surface, which contains numerous functional groups, particularly oxygen groups (24, 25). The primary feedstocks employed in AC production at the commercial scale are wood, coal, and lignite. These raw materials are relatively expensive, which raises the production cost of AC, besides making the utilization of AC in controlling water pollution unwelcomed (25). The selection of low-cost feedstocks for creating AC has become an important issue. In this regard, agricultural wastes have been proposed as a significant feedstock for AC production due to their renewability and low cost. Consequently, recent investigations focused on AC production from such cheap organic-wastes (26).

Methyl orange (MO) is a carcinogenic dye that belongs to the azo class of dyes. It is an anionic dye and a chemically water-stable dye. Thus, its removal from wastewater via conventional routes of purification is hard. Its presence in water affects the aquatic plants' response to photosynthesis, as it lessens the ability of light to penetrate water (27). Adsorption was widely implemented in the adsorptive elimination of MO from wastewater. Multiple bio-wastes were employed in AC preparation to eliminate MO dye from its aqueous medium. As reported by Abdullah et al., the corn con-derived AC was utilized in the adsorptive elimination of MO dye (27). Pomelo peel wastes derived biochar was activated with H_3PO_4 and then applied to eliminate MO from wastewater (28). The AR of MO dye from wastewater was conducted using the Mahagoni Bark-derived AC established by Chakraborty et al. (29). Sea mango-derived AC was prepared via the H_3PO_4 activation method and activated using microwave radiation to be implemented in MO removal from its aqueous solution (30). However, to the authors' knowledge, the creation of AC using bitter almond shells (BAS) as a precursor by the $ZnCl_2$-activation method, with exploring the impact of the preparation conditions on the yield and iodine number (IN) of the created AC has not been established yet. Moreover, employing the typical AC sample in the AR of MO dye from its aqueous phase has not been reported yet, which encouraged us to conduct this work.

This study focuses on using BAS as a raw material to create AC using the $ZnCl_2$ activation approach through optimizing the impact of the impregnation ratio (IR) of $ZnCl_2$ besides the activation temperature and duration, on the AC yield and IN. The typical sample of the AC was further identified by numerous techniques to assess its structure and adsorptive capacity. Factors affecting the adsorption of MO by the as-prepared AC were optimized as well. The AC's adsorption kinetics, isotherms, and thermodynamics of MO elimination were also inspected.

2. EXPERIMENTAL

2.1 Chemicals and Feedstock

Fresh bitter almond fruit was purchased from markets situated in Dohuk Governorate, north of Iraq. Preparation and analysis of the prepared AC needed multiple chemicals, such as iodine solution (0.05 mol/L (0.1 N)), $ZnCl_2$ (98.0 – 100.5 %), HCl (36.5 – 38.0 %), $Na_2S_2O_3.5H_2O$ (99.0 – 100.5 %), and NaOH, pellets (98.50 %) were acquired from Scharlab (Scharlab, Barcelona, Spain). They were employed as received. The MO dye, which possesses an MW of 327.33 g/mol and a chemical formula of $C_{14}H_{14}N_3NaO_3S$, was provided by Merck. Figure 1 shows the chemical structure of Eriochrome Black T (Erio-T) dye.

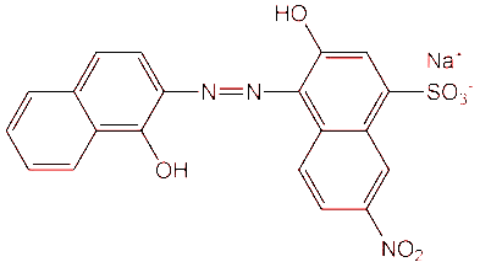

Figure 1: Chemical structure of Erio-T dye.

2.2 Analysis of BAS

Shells were stripped from the bitter almond fruit and used as a feed in AC synthesis. The BAS was rinsed with tap water, followed by DW to remove dust and foreign impurities. After heating to dryness in an oven at 110 °C for a day so as to guarantee the entire removal of washing water. To pulverize the dry BAS, an industrial electrical grinder was employed. The obtained powder was sieved to produce 60 mesh-sized particles. The ultimate analysis of the dried BAS was accomplished to recognize its C, H, N, S, and O content. The ASTM 3174 and ASTM 3175 were followed to specify the proximate analysis of the BAS, namely fixed carbon humidity, volatiles, and

ash. Finally, the BAS component analysis was accomplished per the method established by Mansor et al. (31) to recognize their contents of cellulose, hemicellulose, and lignin.

2.3 Preparation of AC from BAS

The $ZnCl_2$ activation method was employed in creating the AC from the dried BAS. The dried BAS was immersed in solutions containing multiple mass ratios of $ZnCl_2$: BAS (1:1,1-2, and 3:1) and magnetically stirred for 12 h. The attained mixtures were then dried at 80 °C until dryness. Later, the dried mixtures were heated at numerous temperatures (400 °C to 700 °C) for different durations (0.5 h- 2.0 h) in a tubular furnace at a 10 °C/min heating rate. After activation, the activated samples were treated with a solution of 0.50 N HCl with stirring to eliminate the excess of $ZnCl_2$. The samples were then carefully washed with DW until a neutral pH was reached. After being oven-dried at 105 °C for 10 h, the activated samples were then maintained in a tight container (32). Calculating the yield of the AC was done as follows:

$$AC\ Yield(\%) = \frac{Weight\ of\ AC}{Weight\ of\ BAS\ used} \times 100 \quad \text{(Eq. 1)}$$

2.4 Identification of the AC

The typical AC sample was characterized by multiple techniques, including Field Emission-Scanning Electron Microscope (FESEM) on an instrument (A TESCAN MIRA FESEM, Czech Republic) attached to an energy-dispersive analysis X-ray (EDX) to determine the AC surface morphology and elemental analysis, respectively. The BET surface area (SA_{BET}) of the AC, besides its pore volume, was measured on a BELSORP MINI II, Japan, surface area and porosimetry analyzer. A Malvern Panalytical X-ray diffractometer, UK, was used to inspect the amorphous and crystal structure of the created AC. Surface functional groups containing oxygen on the AC surface were determined through the titration method (33). A Fourier transform infrared (FTIR) (JASCO V-630, USA) was utilized in identifying the surface functional groups and chemical bonds. The ASTM D4607-14 was followed in determining the iodine number (IN) of the so-created AC samples.

2.5 Adsorption Equilibrium Studies

The MO adsorption experiments by the so-synthesized AC were accomplished via a batch process. Firstly, a 500 mg/L stock solution of MO was prepared. Next, solutions of various concentrations of MO were prepared from the stock solution through dilution to prepare the standardization curve. A known weight of the AC was mixed with a given volume of MO solution at the optimized pH value, and the mixtures were shaken at room temperature (30 °C) for a specified period. After attaining the equilibrium, the mixture was separated by centrifugation at 6000 rpm for 5 minutes. The concentration of the residual dye in the solution was spectrophotometrically determined using a UV–Vis spectrophotometer at the maximum wavelength (λ_{max}=464 nm). The amount of adsorbed dye, q_e (mg/g), was calculated as per the following equations:

$$MO(\%) = \frac{(C_0 - C_e)}{C_0} \times 100 \quad \text{(Eq. 2)}$$

$$q_e = \frac{(C_o - C_e)V}{W} \quad \text{(Eq. 3)}$$

where, C_0 and C_e are the MO initial and equilibrium concentrations (mg/L), respectively, while V (L) and W (g) are the volume of MO solution employed and the AC mass utilized in the AR process.

2.6 Equilibrium Models of Adsorption Isotherms

The adsorption isotherm describes the equilibrium between the adsorbent and the adsorbate in the solution. It can be employed to express the adsorbent capacity at equilibrium by describing the distribution of the adsorbate molecules between the solution phase and the solid phase equilibrium. It is also imperative to explain the solute's interactions with adsorbents and optimize its usage (33). Three famous isotherms of adsorption, namely the Langmuir, Freundlich, and Temkin, were compared to clarify the adsorption mechanism that will describe the adsorption data at equilibrium. The Langmuir model adopts monolayer adsorption onto the adsorbent surface, and its linearized form can be expressed as follows:

$$\frac{C_e}{q_e} = \frac{1}{q_m K_L} + \frac{C_e}{q_m} \quad \text{(Eq. 4)}$$

where, q_m (mg/g) and K_L (L/mg) express the maximum quantity of the contaminant adsorbed per unit mass of adsorbent and the Langmuir constant, respectively. K_L relates to the affinity of the binding sites, and its higher value means that the adsorption of the solute by the adsorbent is easier. The Freundlich isotherm, which refers to the multilayer adsorption of solute onto the adsorbent surface, is an empirical equation. The linearized form is this isotherm can be given as follows:

$$\ln q_e = \ln K_F + \frac{1}{n} \ln C_e \quad \text{(Eq. 5)}$$

where, K_F (mg/g) and n express respectively the Freundlich adsorption capacity and intensity. According to the Temkin isotherm, whose linear equation is shown in equation (6), a decrease in

adsorption heat occurs as a function of temperature (33).

$$q_e = \frac{RT}{B} \ln KT + \frac{RT}{B} \ln C_e \qquad \text{(Eq. 6)}$$

where, R is the universal gas constant (8.314 J/(mol), K_T is the equilibrium binding constant (L/g) and B (J/mol) represents the heat of adsorption heat.

2.7 Adsorption models of kinetics

The pseudo-1st-order and pseudo-2nd-order kinetic models, whose equations are respectively provided in Eqs. (7) and (8), were used to examine the adsorption kinetics.

$$\ln\left(q_e - q_t\right) = \ln\left(q_e\right) - k.t \qquad \text{(Eq. 7)}$$

$$\frac{t}{q_t} = \frac{1}{k_2 q_e^{\,2}} + \frac{t}{q_e} \qquad \text{(Eq. 8)}$$

where, q_t (mg/g) and q_e (mg/g) are the quantity of the solute adsorbed at time t (minute) at equilibrium, while k (min^{-1}) and k_2 (g/(mg min) are respectively the pseudo-first-order and pseudo-second-order rate constants.

2.8 Intraparticle Diffusion Model

This model of diffusion is usually used to recognize the mechanism of the contaminant adsorption for design purposes. This model suggests that in most adsorption processes, the adsorption changes almost proportionally with $t^{½}$ more than with the contact time (34). This model of diffusion is represented in the following equation:

$$q_t = K_{id} t^{0.5} + C \qquad \text{(Eq. 9)}$$

where, q_t is the quantity of contaminant adsorbed at time t, while $t^{0.5}$ is the square root of the time, C is the intercept, and K_{id} (mg g^{-1} $min^{-0.5}$) is the intraparticle diffusion rate constant.

2.9 Reusability Studies

The reusability tests of the MO by the prepared AC were investigated similarly to the batch adsorption studies. The typical mass of the AC was mixed with 100 mL of MO solution. The mixture was shaken for a specified period. After filtration, the MO concentration remained after the adsorption process was measured employing a UV-Vis spectrophotometer, while the AC was treated with a solution of 0.1 M HCl for 5h. After washing until neutral water was obtained, the AC was dried at 110 °C to ensure the complete dryness of the sample and then implemented in the AR of MO for 5 cycles (34).

3. RESULTS AND DISCUSSION

3.1 Analysis of the Raw BAS

The ultimate analysis results of the raw BAS exhibited that its content of C, H, S, N, and O is 49.97%, 4.88%, 0.61%, 0.10%, and 44.44 %, respectively. The high C % for the BAS suggests its suitability as an AC precursor. The proximate analysis outcomes of the authentic BAS were moisture = 2.23%, volatile matters = 74.02 %, ash = 1.21 %, and fixed carbon = 22.54 %. The high fixed carbon % of BAS recommends its utilization in the synthesis of AC. Also, a minimum ash % precursor could create low-ash content AC (35). The component analysis of the BAS showed that it contains 4.0 % extractives, lignin = 22.12 %, hemicellulose =25.55 %, and Cellulose = 48.22 %. The lignin, cellulose, and hemicellulose contents, of AC have an impact on its porosity. Lignin may withstand the damaging reactions of the activation process due to its high stability and low reactivity. Since lignin is primarily responsible for developing the AC carbon skeletons and giving it its porous structure, the fixed carbon percentage in the implemented precursor is related to its lignin content (36). The contents of hemicellulose and cellulose in the source material are vital for releasing volatile matters besides their responsibility to create a meso and macro porous AC (37). The obtained ultimate, proximate, and component analysis outcomes of the BAS utilized in this work were comparable to those established by Li et al. (38).

3.2 Optimization of AC Synthesis

The impact of the IR of $ZnCl_2$ besides the activation temperature and duration, on the AC yield and IN were investigated. Selecting the proper IR of the activating agent has a practical impact on the AC features, as it affects its porous structure and enlarges the forming pores (39). The AC yield dropped with rising the activator IR from 1:1 to 3:1, as presented in **Table 1**. This outcome suggests that the activator makes the impregnated samples in evolving more volatile materials from its lingo-cellulosic structure as aldehydes, H_2O, tar, CH_4, CO, and CO_2. This removal of volatiles accounts for the carbon content of the pristine feedstock. Increasing the activator IR: feedstock will promote the evolution of more volatiles from the feed skeleton, thereby decreasing the AC yield (40). Preparation of AC samples from soybean straw (41), Fox nutshell (42), wild mustard stems (43) via $ZnCl_2$ activation displayed the same conclusions. The IN of the AC samples declined as the amount of $ZnCl_2$ increased. The best IN was obtained at 1:1 $ZnCl_2$: feed IR indicating that this ratio created an AC with a microporous structure. Above the best ratio of impregnation, the IN dropped because of the widening of micropores into mesopores besides further burn-off of the carbon (40). Hussein and Fadhil (40) and Fadhil and Kareem (44) declared similar findings upon creating AC from mixed biowastes and mixed date pits and olive stones, respectively.

The activation temperature dramatically influences the textural structures as well as the physical and chemical properties of AC. The AC yield diminished progressively as the temperature of activation raised from 400 °C to 800 °C, as displayed in Table 1, because of the extra devolatilization and dehydration of the impregnated samples (43). Demiral et al. (45) also announced comparable consequences upon transforming pumpkin seed shells into AC via the $ZnCl_2$ activation. Table 1 shows a rise in the IN from 1244.5 mg/g to 1442.33 mg/g as the temperature of activation increased from 400 °C to 500 °C. This finding is originated because of further elimination of the volatiles besides extra dehydration of the impregnated samples, leading to create an AC with a more micro-porous structure (43). Beyond 500 °C, the IN due to the possibility of the degradation of the walls of micro-pores walls in addition to the creation of meso and macro-pores at the expanse of micro-pores. $ZnCl_2$ activation of mixed date pits and olive stones (44) and pumpkin seed shell (45) for AC preparation have been observed previously.

Table 1: Effect of preparation conditions on the AC yield and IN.

$ZnCl_2$: feedstock	**Yield (wt.%)**	**IN (mg/g)**
1.0	29.57 ± 1.50	1350.55 ±2.0
2.0	25.31 ± 1.0	1235.28±1.50
3.0	23.11 ± 1.0	1127.50 ±1.50
Temperature = 600 °C; Time of activation= 90 minutes; Size of particle = 0.40 mm		
Temperature (°C)	**Yield (wt.%)**	**IN (mg/g)**
400	28.88 ± 1.50	1244.55 ±1.50
500	23.46 ± 1.50	1443.23 ±1.25
600	21.01± 2.0	1350.12 ±1.50
700	20.55 ± 1.0	1155.34 ±1.50
$ZnCl_2$:feedstock =1:1; Time of activation = 90 minutes; Size of particle = 0.40 mm		
Time (minutes)	**Yield (wt.%)**	**IN (mg/g)**
30	30.55 ± 1.25	1122.35 ± 1.50
60	23.46 ± 1.50	1443.23 ± 1.25
90	21.23± 1.50	1375.77 ± 1.25
120	20.55 ± 2.0	1188.65 ± 2.00
$ZnCl_2$:feedstock=1:1; Temperature= 500 °C; Size of particle = 0.40 mm		

It can be seen in Table 1, which offers the activation period influence on the yield and IN of the created samples. The AC yield was diminished when the activation period expanded from 30 minutes to 120 minutes due to the further dehydration of the impregnated samples, leading to a decline in the AC yield. At the same time, an enhancement in the IN was seen with extending the period of activation from 30 minutes to 60 minutes. This consequence could be ascribed to the creation of more micropores of new microporous structure. Duration above 60 minutes diminished the IN due to the distortion or expansion of the micro-pores into mesopores (43). Mohammed-Taib and Fadhil (43) and Fadhil and Kareem (44) declared the same consequences upon the $ZnCl_2$ activation of wild mustard stems and mixed date pits and olive stones for AC synthesis, respectively.

3.3 Characterization of the AC from BAS

The FESEM image of the AC synthesized from BAS via $ZnCl_2$ activation, depicted in Figure 2, exhibited that its surface contains a porous structure. The FE-SEM image demonstarted that the AC surface is rough with the occurrence of multiple pores of various sizes on it. These pores are expected to play a vital role in trapping the MO molecules as well as help in diffusing them into the porous structure of the AC. The occurrence of pores of various sizes on the AC surface will also help in the deep diffusion of the MO molecules. Besides, the FE-SEM image affirmed that BAS activation by $ZnCl_2$ at 500 °C creates many micropores, significantly enhancing the AC surface area. The formation of micropores attributes the activating agent's activity to the evolution of most organic volatiles from the original BAS structure, leaving behind a well-developed micro-porous surface.

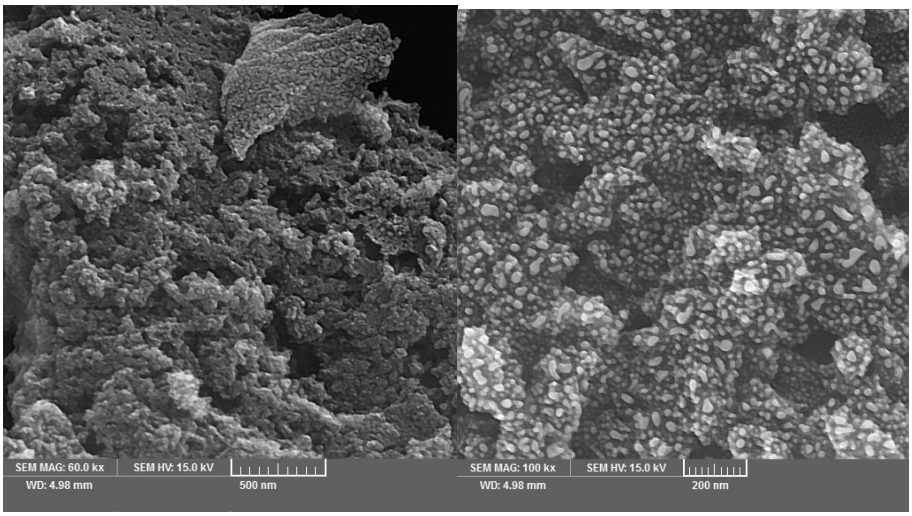

Figure 2: FE-SEM images of the typical AC sample.

The outcomes deduced from the EDS (Figure 3) disclosed an increase in the C content and a decrease in the O content after the activation process. This consequence ascribes to the pyrolytic action of the activator ($ZnCl_2$), which causes the devolatilization of the organic ingredients in the form of gaseous products and liquid tar, leaving a material with a high content of C and a low content of O (46). Additionally, Zn was observed after the activation carbonization, which is expected due to using $ZnCl_2$ in the activation process (47).

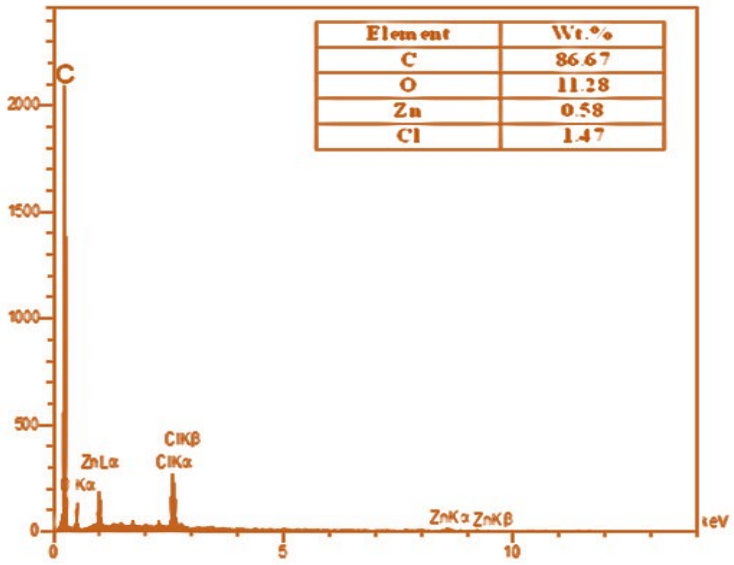

Figure 3: The EDS analysis results of the typical AC sample.

The N_2 adsorption/desorption isotherm (Figure 4) of the so-prepared AC indicates that the AC from BAS disclosed the characterization of type I adsorption isotherms. At the same time, its hysteresis belongs to IV types as per the IUPAC classification. This isotherm mainly indicated considerable development of mesoporous AC.

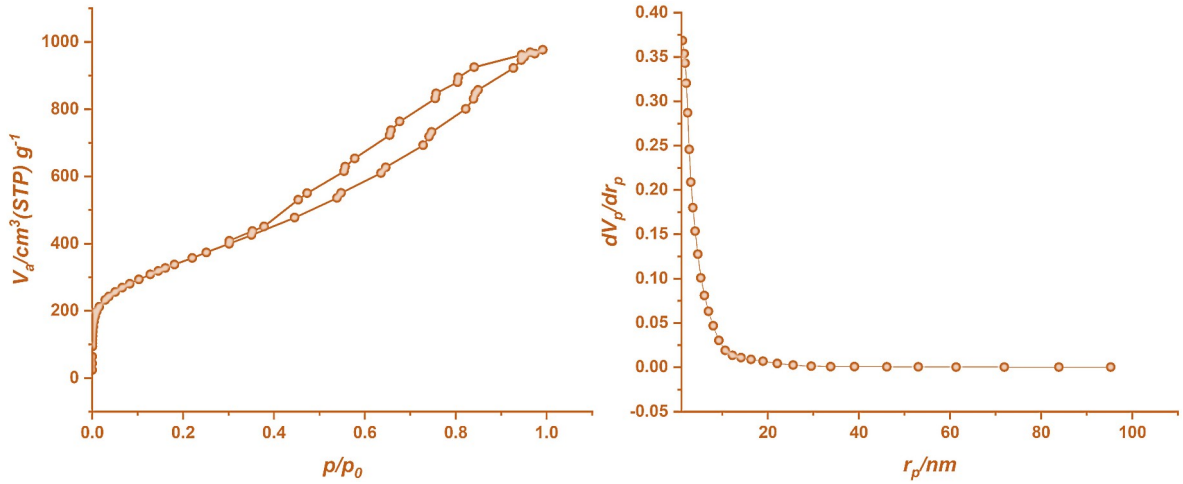

Figure 4: The N_2 adsorption/desorption isotherm and pore volume of the AC at 77 K.

At P/P_0 0.1, the adsorption showed a fast developing trend, then slowed but continued to grow clearly, confirming the possibility of the molecular monolayer adsorption phenomenon or microporous adsorption of multilayer. After P/P_0 > 0.4, a hysteresis loop was discovered, indicating that capillary condensation and inhomogeneous adsorption had occurred, demonstrating the presence of mesoporous particles (47). The so-synthesized AC possessed a SA_{BET} of 1221.60 m^2/g. A the same time, this sample showed its mesoporosity due to its average pore size, which was 2.10 nm.

The AC prepared via the $ZnCl_2$ activation of BAS exhibited a SA_{BET} greater than that established for the AC prepared through $ZnCl_2$ activation of date pits, which was 1061.3457 m^2/g(48). Table 2 lists the texture, amounts of the total acid and basic sites, and pH_{PZC} of this AC.

Table 2: Surface area, pore volume, surface functional groups amounts, and pH_{PZC} of the AC derived from BAS.

Property	AC
BET surface area (m^2/g)	1221.60
Langmuir surface area (m^2/g)	942.82
t-Plot micropore area (m^2/g)	1246.70
V_{total} ($cm^3\ g_{-1}$)	1.5091
Mean Pore Diameter width (nm)	4.98
Iodine adsorption number (mg/g)	1443.23 ±1.0
Total acid sites (mmol/g)	0.5225 ±0.001
Total basic sites (mmol/g)	0.2422 ±0.001
pH_{PZC}	4.40

Diverse functional groups could occur on the AC surface depending on the precursor implanted in its preparation and the preparation route. These groups are significant to the AC as they specify its quality as well as surface features (46).

Figure 5: The FTIR spectrum of the BAS-derived AC.

The FTIR spectrum of the AC, which is demonstrated in Figure 5, disclosed the occurrence of multiple functional groups. The Boehm titrations results showed that the chemical activation of the BAS by $ZnCl_2$ provided the surface of the attained AC with oxygenated acidic groups rather than basic groups. The value of pH_{PZC}, which was 4.40, also confirmed this conclusion. These findings were consistent with those found in the literature (40,46). The strong, broad peak around 3435 cm^{-1} belongs to the O-H stretching group of phenol, alcohol, or carboxylic acid. The bands around 2926 cm^{-1} and 2858 cm^{-1} are respectively related to asymmetric and symmetric C-H stretching vibrations (49). The absorption band observed at 1655 cm^{-1} represents the stretching carboxylate bonds. The bands from 1565 to 1471 cm^{-1} are attributed to the aromatic ring modes. The O-H bending bonds are represented by the band seen at 1384 cm^{-1} (50). Bands between 877 cm^{-1} and 750 cm^{-1} relate to the C-H aromatic out-of-plane (50). Lastly, the Zn-O stretch for the AC could be identified at 625 cm^{-1} (51).

The XRD pattern of the prepared AC is shown in Figure 6. This pattern revealed two broad phases at 2θ ranging from 20° to 30°. This pattern belongs to (002) phase, while the (100) is repserented by the broad peak in the range 40° and 50°. The occurance of these two phases in the XRD pattern assured that previously mentioned AC owns an amorphous structure (43).

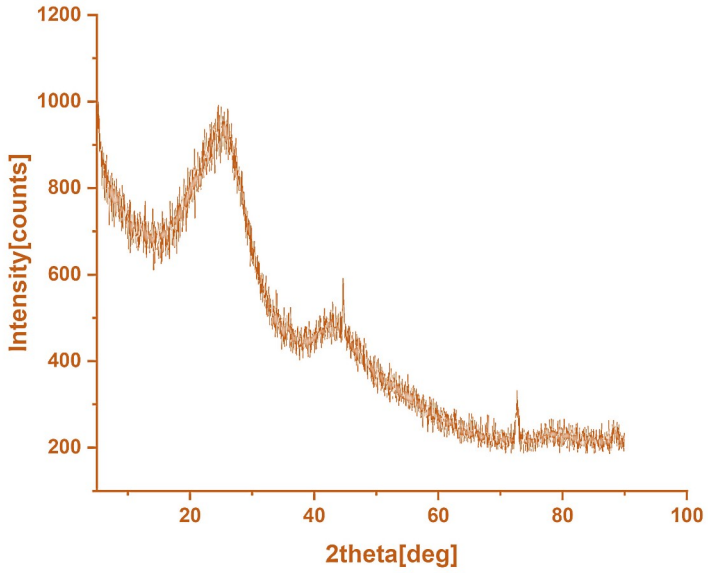

Figure 6: The XRD pattern of the BAS- derived AC.

3.4 Optimization of MO Adsorption

The influence of many variables on the adsorptive elimination (AE) of MO using BAS derived AC was investigated, as follows:

3.4.1 Influence of the initial pH

The initial pH of the working solution greatly influences the adsorption process of any pollutant. This factor affects both the functional groups existing on the AC surface besides molecular ionization of the dye, which in turn affects the interactions between both phases (24). Therefore, several adsorption experiments were accomplished between the AC and MO solutions at various values of pH (2, 3, 4, 6, 7, 8 and 10) by adding NaOH or HCl. The MO adsorption dependence on pH is presented in Figure 7, which disclosed that a pH value of 2.0 exhibited the maximum MO% removal. In contrast, the MO% removal declined with raising the solution pH over 2.0. The obtained findings assure that the acidic pH is the best for MO elimination by the as-prepared AC, which is in line with conclusions established in the literature (48,49). This outcome can be explained as follows: In an aqueous solution, MO will dissociate to give the dye ions ($R\text{-}SO_3^-$) and (Na^+). In the acidic pH, the AC surface will be protonated, making its surface to be a positive charge, which in turn increases MO's adsorption by the AC due to the increment of the electrostatic interactions, namely dipole-dipole or hydrogen bonding between the AC surface (+ve) and the MO anions (-ve). In contrast, in the basic pH, the surface of the created AC will become negatively charged due to high numbers of OH^- ions on its surface, which causes the repulsion between the negatively charged surface of the AC and the dye anions, leading to lower adsorption.

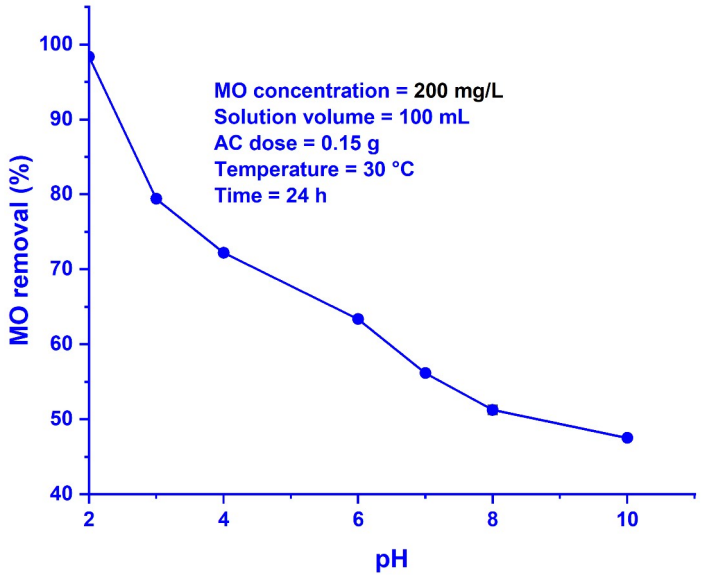

Figure 7: pH influence on MO elimination by the AC.

The pH_{PZC} of BAS-derived AC was 4.30, suggesting that the AC surface is positively charged due to the pH of the solution, which exhibited the maximum removal of MO was 2.0, which is lower than pH_{PZC} (52,53). Determining the quantity of the acidic and basic functional groups present on the AC surface was accomplished as per the Boehm titration method. The results revealed that the amount of acidic effective groups on the AC surface was nearly twice that of basic groups (Table 2), suggesting the acidic nature of the surface of the AC originated from BAS. Figure 8 illustrates the pH_{PZC} of the as-created AC.

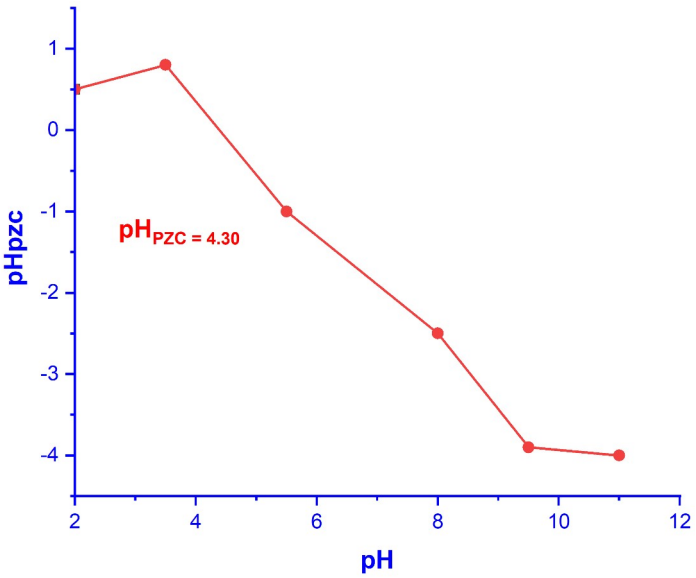

Figure 7: pH_{PZC} of the AC originated from BAS.

3.4.2 Influence of the MO initial concentration

The influence of the MO initial concentration on its adsorption capacity (q_e, mg/g) and removal efficiency (%) is given in Figure 9, which implies that by increasing the MO initial concentration from 50 mg/L to 400 mg/L, the q_e value raised from 23.0 mg/g to 194.0 mg/g due to raising the MO initial concentration increases the number of MO species per mass unit of AC, resulting in an improved interaction between the MO molecules and the AC particles.

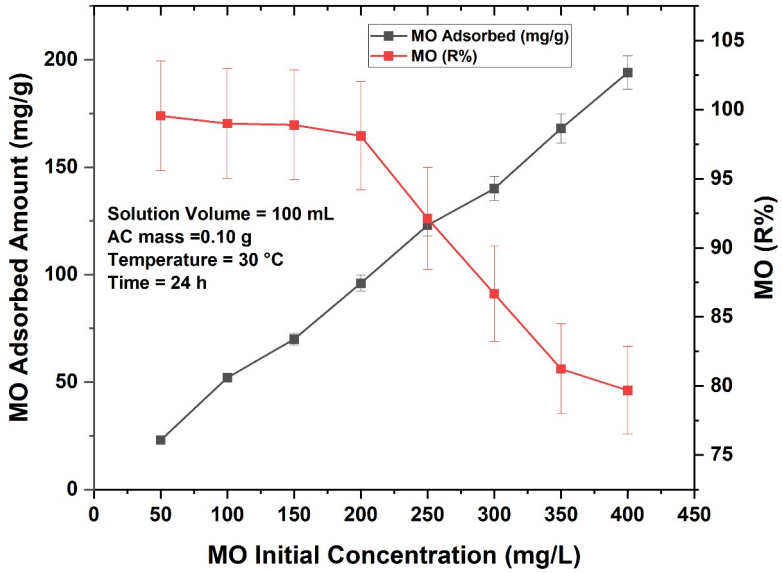

Figure 9: The initial concentration influence on the adsorptive capacity and efficiency by the AC.

In addition, increasing the sorbate initial concentration will supply the necessary driving force required to alleviate the resistance between the MO liquid phase and the AC solid phase (52). It is evident from Figure 9 that MO % removal declined with increasing the MO initial concentration. This phenomenon is explained by the fact that the number of active sites available for MO adsorption is fixed, but the number of MO molecules increases with rising MO concentration. As a result, the active sites will be rapidly depleted, resulting in a decrease in the MO R% (53).

3.4.3 Influence of the AC dosage

Because of the positive impact of AC dosage on MO R%, the effect of this parameter was investigated by attempting multiple doses of AC ranging from 0.05 g to 0.40 g.

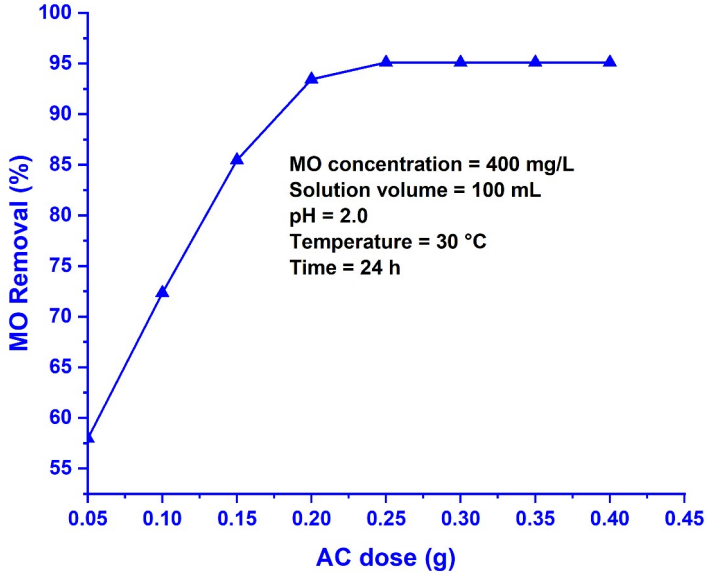

Figure 10: Influence of the AC dose on the adsorptive removal of MO.

The experiments were carried out under the conditions specified in Figure 10's legend, which implies that the MO % removal enhanced from 57.97 % to 95.11% when the AC dose increased from 0.05 g to 0.25 g. The high uptake of MO with increasing AC dose could be attributed to the fact that increasing the AC dose provides a greater number of AC particles, which means higher SA and more active sites available to adsorb the MO molecule in the solution (28). Further increasing the AC dosage had no effect on the MO R%, indicating that the equilibrium between MO-free molecules and the AC particles in the solution was attained. Other researchers have announed similar consequences(55).

3.4.4 Influence of temperature and contact time

The effect of temperature on the MO uptake of the prepared AC was investigated by conducting experiments at three different temperatures, 303, 313, and 323 K. The trials were completed using the conditions fixed in the legend for Figure 11. The MO uptake increases with rising temperature due to increasing the adsorption temperature is accompanied by a rise in the system entropy, which enhances the collisions among the AC particles and MO species. This will enhance the activity at the interface between the adsorbent and adsorbate (52). Additionally, the solution viscosity declines as the system temperature increases, leading to a better collisions among the two phases. Consequently, the MO % becomes better (53). In addition, the improvement of MO elimination with rising temperature reflects the endothermic nature of MO adsorption.

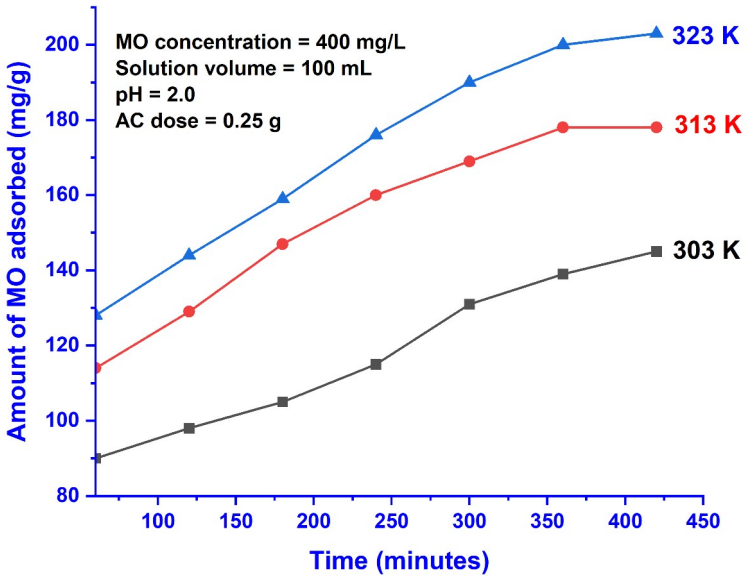

Figure 11: The impact of temperature and time on MO adsorption by the BAS-derived AC.

The contact time impact the MO elimination by the AC was inspected at various time intervals in the range of 60 –540 minutes, which is also presented in Figure 11. The adsorption experiments were done utilizing the ideal conditions obtained earlier. The consequences illustrated in Figure 11 imply that the AR of MO by BAS-derived AC enhanced when the contact period between the two phases increased. It can be seen that after 60 minutes of the process, high uptake of the MO was noticed, indicating the spontaneity of the process. This outcome attributes to the rapid adsorption in the initial steps due to the larger surface area of the adsorbent accessible to adsorb the MO molecules. The equilibrium was attained after 420 minutes. When the balance is reached, the MO molecules will occupy the most active sites, and the active positions will be unreachable. This may generate a repulsive force between the adsorbate on the adsorbent surface and in the bulk phase (49).

3.5. Adsorption Isotherms and Kinetics of MO on BAS-Derived AC

The adsorption mechanism can better be recognized by analyzing the adsorption isotherms of MO on the so-synthesized AC. As such, namely the Langmuir (Figure 12a), Freundlich (Figure 12b), and Temkin (Figure 12c) isotherms, were applied to inspect the MO adsorption data by the BAS-derived AC at multiple adsorption temperatures (303 K, 313 K, and 323 K).

From the theoretical point of view, the Langmuir model suggests monolayer adsorption onto the solid surface. It also indicates the effectiveness of the active sites toward the adsorption of the pollutant species because of the diminish of interactions among the pollutant species (24). The Langmuir constants q_m and K_L can be calculated from the plot slope and intercept, respectively, while the dimensionless separation factor (R_L) was calculated using the following equation :

$$R_L = \frac{1}{1 + C_0 K_L} \quad \text{(Eq. 10)}$$

This factor can express the favorability of adsorbate adsorption onto the adsorbent surface. Also, this factor suggests many cases of the adsorption process, e.g. the reaction is irreversible if the value of R_L = 0, while the reaction is linear if the value of R_L = 1 (40). Relating to adsorption, the latter will be favorable if 0 < R_L < 1, while the adsorption will be unfavorable when R_L > 1. The Freundlich model suggests multilayer adsorption on the solid surface. It also proposes that the solid surface is heterogeneous with the occurrence of different-affinity active sites onto the material surface (43). The the slope and the intercept of the Freundlich linear plot will provide its constants, namely *n* and K_F. The favorability of the adsorption onto the solid surface can be determined by the value of n, which suggests the adsorption favorability when its value is greater than 1.0. Because n > 1.0, the MO adsorption by the BAS-derived AC is preferable (40). The Temkin constants B and K_T can be respectively obtained from the plot's slope and intercept. As per the outcomes offered in Table 3, the Langmuir model exhibited higher R^2 values than those related to the Freundlich and Temkin models. Moreover, the q_m values for the Langmuir model were above than those observed for K_F and B, suggesting that the MO adsorption by BAS-derived AC can better be expressed by the Langmuir model than the Freundlich and Temkin models, indicating that the MO adsorption onto the surface of the obtained AC happens in monolayer so that the interactions among the MO molecules is inhibited due to the adsorption happens onto active sites with the same energy (40,44).

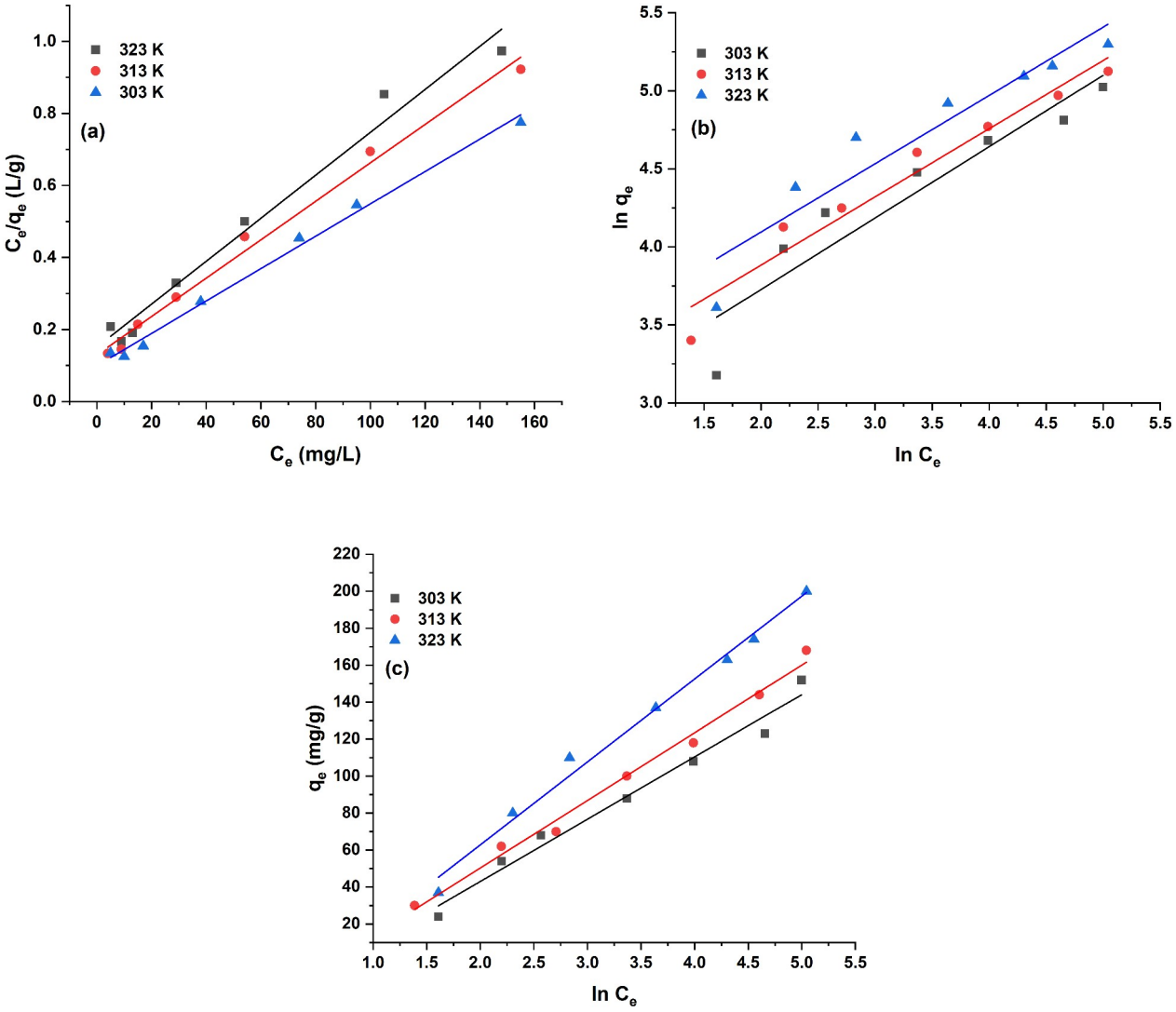

Figure 12: The adsorption isotherms of (a) Langmuir, (b) Freundlich, (c) Temkin for MO adsorption by the BAS derived AC at multiple temperatures.

Table 3: The constants of the Langmuir, Freundlich, and Temkin for the MO adsorption by the BAS derived AC.

T = 303 K									
Langmuir constants				**Freundlich constants**			**Temkin constants**		
R^2	**q_m (mg/g)**	**K_L**	**R_L**	**R^2**	**n (mg/g)**	**K_F**	**R^2**	**B (mg/g)**	**K_T (kJ/mol)**
0.9852	163.93	0.0411	0.0583	0.8825	0.45	2.82	0.8529	32.88	0.7256
T = 313 K									
Langmuir constants				**Freundlich constants**			**Temkin constants**		
R^2	**q_m (mg/g)**	**K_L**	**R_L**	**R^2**	**n (mg/g)**	**K_F**	**R^2**	**B (mg/g)**	**K_T (kJ/mol)**
0.9920	185.52	0.0421	0.0417	0.9507	0.4350	3.41	0.9919	36.26	0.6944
T = 323 K									
Langmuir constants				**Freundlich constants**			**Temkin constants**		
R^2	**q_m (mg/g)**	**K_L**	**R_L**	**R^2**	**n (mg/g)**	**K_F**	**R^2**	**B (mg/g)**	**K_T (kJ/mol)**
0.9940	224.71	0.0448	0.0528	0.8959	0.4358	3.22	0.9889	44.70	0.6655

Besides the equilibrium time, the adsorption process's efficiency can be controlled by recognizing the adsorption kinetics. The latter can also describe the adsorbate uptake rate onto the AC (33). So, three famous models, namely the pseudo-1st-order model (Figure 13a), pseudo-2nd-order model (Figure 13b), and Intra-particle diffusion model (Figure 13c) were fit to the adsorption data of MO on the BAS-derived AC so as to recognize steps controlling the MO adsorption by the said AC. The MO adsorption on the aforesaid AC was accomplished at multiple temperatures (303, 313, and 323 K). The obtained data were analyzed by applying the linear forms of those models.

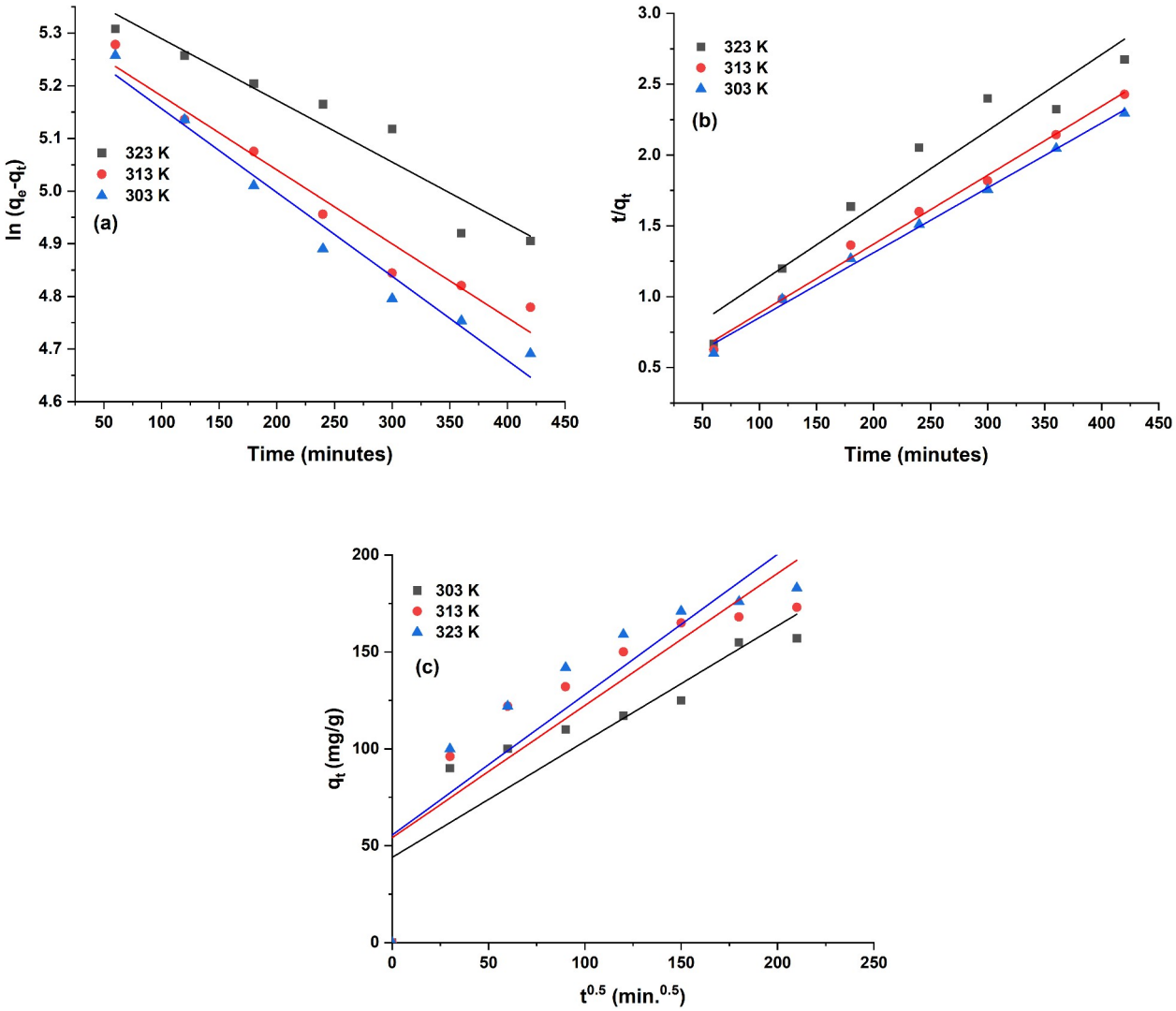

T = 313 K								
Pseudo-1st-order			**Pseudo-2nd-order**			**Intra-particle diffusion**		
R^2	**q_e (mg/g)**	**k_1**	**R^2**	**q_e (mg/g)**	**k_2**	**R^2**	**C**	**K_{id}**
0.9602	1.71	0.0020	.99438	212.76	0.00049	0.7673	54.16	0.6817
T = 323 K								
Pseudo-1st -order			**Pseudo-2nd -order**			**Intra-particle diffusion**		
R^2	**q_e (mg/g)**	**k_1**	**R^2**	**q_e (mg/g)**	**k_2**	**R^2**	**C**	**K_{id}**
0.9717	1.67	0.0015	0.9954	222.20	0.00048	0.7618	58.20	0.7178

The intra-particle diffusion model of Weber was also used to examine the MO experimental adsorption data. This model can suggest mechanisms and rate-controlling steps that affect

the kinetics of MO adsorption (57). It is clear from Figure 15, which depicts Weber's intra-particle diffusion model, that this model cannot be used solely to describe the rate-limiting step of MO adsorption by the BAS-derived AC because none of the regression plots pass through the origin, suggesting that another mechanism could have occurred (58).

3.6 Adsorption Thermodynamics

As per the adsorption outcomes, thermodynamic parameters viz. ΔH°, ΔS°, and ΔG°, were calculated. These functions, in addition to spontaneity, can provide information about the adsorption process, such as exothermicity or endothermicity, potential rise or decline in randomness at the solid/liquid interface (59). The explanation of the adsorption mechanism can be deduced from these functions as well (59). The calculation of these functions for MO adsorption by the AC originated from the BAS was accomplished at multiple temperatures, namely 303, 313, and 323 K. The following equations were utilized in the calculation of ΔH°, ΔS°, and ΔG° (51-53,59):

$$\ln\left(K_c\right)=\frac{\Delta S_o}{R}-\frac{\Delta H_o}{RT} \quad \text{(Eq. 11)}$$

$$\left(\frac{q_e}{C_e}\right)=K_c \quad \text{(Eq. 12)}$$

$$\Delta G_o=-RT\ln K \quad \text{(Eq. 13)}$$

where, K_c represents the equilibrium constant. Plotting ln K_c vs 1/T yields a straight line with a slope of ΔH° and an intercept of ΔS°, according to the van't Hoff equation. Table 5 shows the ΔH°, ΔS°, and ΔG° values, and the result reveals that the MO adsorption by the so-synthesized AC was endothermic. This conclusion was drawn from the ΔH° value, which was 9.51 kJ/mole, indicating that the MO adsorption by this AC is temperature-dependent and endothermic. This was expected because the adsorption of MO by the AC from BAS increased as the temperature rose from 303 K to 323 K. Furthermore, because of the negative values of ΔG° at different temperatures, the MO adsorption by the BAS-derived AC was spontaneous.

It was reported that when the values of ΔG° are in the range of (–20 to 0.0 kJ/mol); the adsorption is physical, while the values in the range of (– 400 to – 80 kJ/mol) suggest chemisorption (60).

The (+ve) value of ΔS° indicates an increase in the adsorption's entropy due to the adsorption and desorption phenomenon that could be involved during the solid-liquid adsorption process. This will reduce the randomness of the MO adsorption and raises it during the desorption of water molecules from the adsorbent's superficial layer (59). Similar observations were also announced by Hussain et al. (59) during the MO adsorption over chitosan composite films. The values of ΔG° for MO adsorption by the so-prepared AC were between – 2.56 to – 3.46 kJ/mol, offering that the adsorptive removal of MO by the AC surface is physical. It is accomplished through electrostatic attraction and H-bonding, as demonstrated by FTIR analysis and batch adsorption studies (60).

Table 5: Thermodynamic parameters for eliminating MO by the AC from BAS.

Temperature (K)	ΔG° (kJ/mol)	ΔH° (kJ/mol)	ΔS° (kJ/mol.K)
303	–2.56	9.51	31.42
313	–2.86	-	**-**
323	–3.46	-	**-**

3.7 Comparison of the Adsorptive Capacity

The adsorptive capacity of MO by AC prepared from BAS was compared to those of other AC samples reported in the literature, as well as other adsorbents, as tabulated in Table 6. The aforesaid created AC possessed an adsorptive capacity for MO comparable to those established for other adsorbents in the literature and, in most cases, better. The variances in the adsorptive capacity of BAS-derived AC to MO compared to the adsorbents may be ascribed to many factors, including the SA_{BET} of the adsorbent implemented besides its pore width, total pore volume, and the amount of the acidic or basic groups onto its surface. Also, the volume of the MO solution implemented, the typical pH value, and the type of mechanism involved in the adsorption process, can also affect the MO removal by any given adsorbent.

3.8 Reusability Experiments

Besides the amount of solid waste remaining, the adsorbent cost specifies the efficiency of the adsorption method used in wastewater treatment. Here, the regeneration trials of the so-prepared AC were done in an acidic medium promoting MO desorption. Outcomes from the reusability trails, which are demonstrated in Figure 14, showed a successive decline in the AR of MO by the regenerated AC. This decline is due to the loss of some active sites due to the adsorption of MO species deeply in the AC pores (67). Besides, the number of functional groups available for the adsorption procrss will be reduced as an outcome of their leaching because of the successive washing by the acid. However, the AC performance remains good even after the 5th cycle.

Table 6: The adsorptive capacity of the AC from BAS to MO compared to other adsorbents.

Adsorbent	pH	Temperature (°C)	q_{max} (mg/g)	Reference
AC from aloe vera	3.0	25.0	196.10	(61)
AC from sugarcane mills boiler residue	5.0	25.0	161.80	(62)
Biochar from hazelnut shell	-	-	181.80	(63)
Biochar from glucose	-	-	147.10	(63)
Activated biochar from pomelo peel waste	3.0	25.0	163.10	(28)
Mesoporous carbon material	2.50	20	294.10	(64)
AC from phragmites australis	-	-	217.0	(65)
Nano-adsorbent	-	-	46.0	(66)
AC from BAS	**2.0**	**50.0**	**224.21**	**This study**

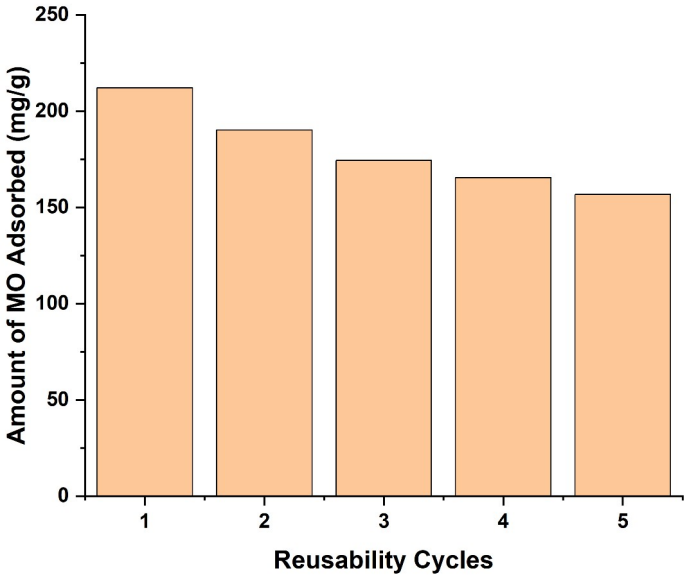

Figure 14: Reusability trails of the AC.

4. CONCLUSIONS

The BAS proved its suitability as an influential precursor in the synthesis of AC. The optimized $ZnCl_2$-activation of the BAS at an impregnation ratio of 1:1 $ZnCl_2$: BAS and 500 °C activation temperature for 60 minutes produced an AC with high SA_{BET} (1221.60 m^2/g). This AC was effective toward the adsorptive elimination of MO dye from its aqueous phase. The highest adsorptive capacity of MO by the said AC amounted to 224.71 mg/g using 0.25 g of the AC at 323 K for 420 minutes and a pH of 2.0. The Langmuir model with a maximum monolayer adsorption capacity as well as the pseudo-2nd-order kinetics best described the adsorption outcome of MO by the AC compared to other models. The thermodynamic functions of the MO adsorption by the BAS-derived AC disclosed the spontaneity and endothermic nature of MO adsorption by the said AC. Also, the adsorption of MO on the AC described above was spontaneous due to the (-ve) values of ΔG° at multiple temperatures. The mechanism of adsorption included mainly electrostatic attractions and hydrogen bonding interaction.

5. ACKNOWLEDGEMENTS

Thank is due to the Mosul University, College of Science, Chemistry Department for supporting this research work.

6. REFERENCES

1. Hasan M, Rashid MM, Hossain MM, Al Mesfer MK, Arshad M, Danish M, et al. Fabrication of polyaniline/activated carbon composite and its testing for methyl orange removal: Optimization, equilibrium, isotherm and kinetic study. Polymer Testing. 2019 Aug;77:105909. Available from: <URL>.

2. Jawad AH, Mamat NFH, Hameed BH, Ismail K. Biofilm of cross-linked Chitosan-Ethylene Glycol Diglycidyl Ether for removal of Reactive Red 120 and Methyl Orange: Adsorption and mechanism studies. Journal of Environmental Chemical Engineering. 2019 Apr;7(2):102965. Available from: <URL>.

3. Muslim M, Ali A, Neogi I, Dege N, Shahid M, Ahmad M. Facile synthesis, topological study, and adsorption properties of a novel Co (II)-based coordination polymer for adsorptive removal of methylene blue and methyl orange dyes. Polyhedron. 2021 Dec;210:115519. Available from: <URL>.

4. He W, Li N, Wang X, Hu T, Bu X. A cationic metal-organic framework based on {Zn4} cluster for rapid and selective adsorption of dyes. Chinese Chemical Letters. 2018 Jun;29(6):857–60. Available from: <URL>.

5. Bera R, Ansari M, Mondal S, Das N. Selective CO2 capture and versatile dye adsorption using a microporous polymer with triptycene and 1,2,3-triazole motifs. European Polymer Journal. 2018 Feb;99:259–67. Available from: <URL>.

6. Thamaraiselvan C, Noel M. Membrane Processes for Dye Wastewater Treatment: Recent Progress in Fouling Control. Critical Reviews in Environmental Science and Technology. 2015 May 19;45(10):1007–40. <URL>.

7. Piaskowski K, Świderska-Dąbrowska R, Zarzycki PK. Dye Removal from Water and Wastewater Using Various Physical, Chemical, and Biological Processes. Journal of AOAC INTERNATIONAL. 2018 Sep 1;101(5):1371–84. Available from: <URL>.

8. Hassan MM, Carr CM. A critical review on recent advancements of the removal of reactive dyes from dyehouse effluent by ion-exchange adsorbents. Chemosphere. 2018 Oct;209:201–19. Available from: <URL>.

9. Gadekar MR, Ahammed MM. Coagulation/flocculation process for dye removal using water treatment residuals: modelling through artificial neural networks. Desalination and Water Treatment. 2016 Nov 25;57(55):26392–400. Available from: <URL>.

10. Nourmoradi H, Zabihollahi S, Pourzamani HR. Removal of a common textile dye, navy blue (NB), from aqueous solutions by combined process of coagulation–flocculation followed by adsorption. Desalination and Water Treatment. 2016 Mar 2;57(11):5200–11. Available from: <URL>.

11. Veksha A, Pandya P, Hill JM. The removal of methyl orange from aqueous solution by biochar and activated carbon under microwave irradiation and in the presence of hydrogen peroxide. Journal of Environmental Chemical Engineering. 2015 Sep;3(3):1452–8. Available from: <URL>.

12. Mohamed EA, Selim AQ, Ahmed SA, Sellaoui L, Bonilla-Petriciolet A, Erto A, et al. H2O2-activated anthracite impregnated with chitosan as a novel composite for Cr(VI) and methyl orange adsorption in single-compound and binary systems: Modeling and mechanism interpretation. Chemical Engineering Journal. 2020 Jan;380:122445. Available from: <URL>.

13. Siyasukh A, Chimupala Y, Tonanon N. Preparation of magnetic hierarchical porous carbon spheres with graphitic features for high methyl orange adsorption capacity. Carbon. 2018 Aug;134:207–21. <URL>.

14. Kaykhaii M, Sasani M, Marghzari S. Removal of dyes from the environment by adsorption process. Chem Mater Eng. 2018;6(2):31–5.

15. Iqbal M, Saeed A, Kalim I. Characterization of Adsorptive Capacity and Investigation of Mechanism of Cu $^{2+}$, Ni $^{2+}$ and Zn $^{2+}$ Adsorption on Mango Peel Waste from Constituted Metal Solution and Genuine Electroplating Effluent. Separation Science and Technology. 2009 Oct 30;44(15):3770–91. Available from: <URL>.

16. Mekhalif T, Guediri K, Reffas A, Chebli D, Bouguettoucha A, Amrane A. Effect of acid and alkali treatments of a forest waste, *Pinus brutia* cones, on adsorption efficiency of methyl green. Journal of Dispersion Science and Technology. 2017 Apr 3;38(4):463–71. Available from: <URL>.

17. Kiwaan HA, Mohamed FSh, El-Ghamaz NA, Beshry NM, El-Bindary AA. Experimental and electrical studies of Na-X zeolite for the adsorption of different dyes. Journal of Molecular Liquids. 2021 Jun;332:115877. Available from: <URL>.

18. Aigbe UO, Ukhurebor KE, Onyancha RB, Osibote OA, Darmokoesoemo H, Kusuma HS. Fly ash-based adsorbent for adsorption of heavy metals and dyes from aqueous solution: a review. Journal of Materials Research and Technology. 2021 Sep;14:2751–74. Available from: <URL>.

19. Aichour A, Zaghouane-Boudiaf H, Djafer Khodja H. Highly removal of anionic dye from aqueous medium using a promising biochar derived from date palm petioles: Characterization, adsorption properties and reuse studies. Arabian Journal of Chemistry. 2022 Jan;15(1):103542. Available from: <URL>.

20. Hu X, Li Z, Ge Y, Liu S, Shi C. Enhanced π – π stacks of aromatic ring-rich polymer adsorbent for the rapid adsorption of organic dyes. Colloids and Surfaces A: Physicochemical and Engineering Aspects. 2022 Jun;643:128782. Available from: <URL>.

21. Xie J, Lin R, Liang Z, Zhao Z, Yang C, Cui F. Effect of cations on the enhanced adsorption of cationic dye in Fe3O4-loaded biochar and mechanism. Journal of Environmental Chemical Engineering. 2021 Aug;9(4):105744. Available from: <URL>.

22. Wang C, Yang Q, Ren N, Zhao Z, Wei W, Qin G. Preparation of loofah vine-based hierarchical porous activated carbon for methylene blue adsorption. Chemical Engineering Communications. 2022 Jan 2;209(1):62–8. Available from: <URL>.

23. Agbor Tabi G, Ngouateu Rene Blaise L, Daouda K, Naphtali Odogu A, Aime Victoire A, Nsami Julius N, et al. Non-linear modelling of the adsorption of Indigo Carmine dye from wastewater onto characterized activated carbon/volcanic ash composite. Arabian Journal of Chemistry. 2022 Jan;15(1):103515. Available from: <URL>.

24. Martini BK, Daniel TG, Corazza MZ, de Carvalho AE. Methyl orange and tartrazine yellow adsorption on activated carbon prepared from boiler residue: Kinetics, isotherms, thermodynamics studies and material characterization. Journal of Environmental Chemical Engineering. 2018 Oct;6(5):6669–79. Available from: <URL>.

25. Jiang T, Liang Y dong, He Y jun, Wang Q. Activated carbon/NiFe2O4 magnetic composite: A magnetic

adsorbent for the adsorption of methyl orange. Journal of Environmental Chemical Engineering. 2015 Sep;3(3):1740–51. Available from: <URL>.

26. Singh S, Sidhu GK, Singh H. Removal of methylene blue dye using activated carbon prepared from biowaste precursor. Indian Chemical Engineer. 2017 Dec 11;1–12. Available from: <URL>.

27. Abdullah NH, Ghani NAA, Razab MKAA, Noor AM, Halim AZA, Rasat MSM, et al. Methyl orange adsorption from aqueous solution by corn cob based activated carbon. In Kelantan, Malaysia; 2019 [cited 2023 Mar 12]. p. 020036. Available from: <URL>.

28. Zhang B, Wu Y, Cha L. Removal of methyl orange dye using activated biochar derived from pomelo peel wastes: performance, isotherm, and kinetic studies. Journal of Dispersion Science and Technology. 2020 Jan 2;41(1):125–36. Available from: <URL>.

29. Ghosh GC, Chakraborty TK, Zaman S, Nahar MN, Kabir AHME. Removal of Methyl Orange Dye from Aqueous Solution by a Low-Cost Activated Carbon Prepared from Mahagoni (Swietenia mahagoni) Bark. Pollution [Internet]. 2020 Jan [cited 2023 Mar 12];6(1). Available from: <URL>.

30. Azmi NH, Ali UFMd, Muhammad Ridwan F, Isa KM, Zulkurnai NZ, Aroua MK. Preparation of activated carbon using sea mango (*Cerbera odollam*) with microwave-assisted technique for the removal of methyl orange from textile wastewater. Desalination and Water Treatment. 2016 Dec 25;57(60):29143–52. Available from: <URL>.

31. Dai F, Muhammad Y, Gong X, Li C, Li Z, Zhang S. Low-temperature and low-pressure fuel hydrodesulfurization by solid catalyst coupling with ionic liquids. Fuel. 2014 Oct;134:74–80. Available from: <URL>.

32. Zyoud A, Nassar HNI, El-Hamouz A, Hilal HS. Solid olive waste in environmental cleanup: Enhanced nitrite ion removal by ZnCl2-activated carbon. Journal of Environmental Management. 2015 Apr;152:27–35. Available from: <URL>.

33. León G, García F, Miguel B, Bayo J. Equilibrium, kinetic and thermodynamic studies of methyl orange removal by adsorption onto granular activated carbon. Desalination and Water Treatment. 2015 Jul 25;1–14. Available from: <URL>.

34. Bilal M, Ali J, Bibi K, Khan SB, Saqib M, Saeed R, et al. Remediation of different dyes from textile effluent using activated carbon synthesized from Buxus Wallichiana. Industrial Crops and Products. 2022 Nov;187:115267. Available from: <URL>.

35. Macías-García A, Cuerda-Correa EM, Olivares-Marín M, Díaz-Paralejo A, Díaz-Díez MÁ. Development and characterization of carbon-honeycomb monoliths from kenaf natural fibers: A preliminary study. Industrial Crops and Products. 2012 Jan;35(1):105–10. Available from: <URL>.

36. Rodríguez Correa C, Stollovsky M, Hehr T, Rauscher Y, Rolli B, Kruse A. Influence of the Carbonization Process on Activated Carbon Properties from Lignin and Lignin-Rich Biomasses. ACS Sustainable Chem Eng. 2017 Sep 5;5(9):8222–33. Available from: <URL>.

37. Hong D, Zhou J, Hu C, Zhou Q, Mao J, Qin Q. Mercury removal mechanism of AC prepared by one-step activation with ZnCl2. Fuel. 2019 Jan;235:326–35. Available from: <URL>.

38. Li K, Chen H, Yu H, Zhu H, Mao Q, Ma X, et al. Study on the comprehensive utilization of bitter almond shell. BioResources. 2014;9(3):4993–5006.

39. Li Y, Li Y, Zang H, Chen L, Meng Z, Li H, et al. ZnCl $_2$ -activated carbon from soybean dregs as a high efficiency adsorbent for cationic dye removal: isotherm, kinetic, and thermodynamic studies. Environmental Technology. 2020 Jul 2;41(15):2013–23. Available from: <URL>.

40. Hussein AA, Fadhil AB. Kinetics and isothermal evaluations of adsorptive desulfurization of dibenzothiophene over mixed bio-wastes derived activated carbon. Energy Sources, Part A: Recovery, Utilization, and Environmental Effects. 2021 Mar 8;1–20. Available from: <URL>.

41. Miao Q, Tang Y, Xu J, Liu X, Xiao L, Chen Q. Activated carbon prepared from soybean straw for phenol adsorption. Journal of the Taiwan Institute of Chemical Engineers. 2013 May;44(3):458–65. Available from: <URL>.

42. Singh PK, Banerjee S, Srivastava AL, Sharma YC. Kinetic and equilibrium modeling for removal of nitrate from aqueous solutions and drinking water by a potential adsorbent, hydrous bismuth oxide. RSC Adv. 2015;5(45):35365–76. Available from: <URL>.

43. Mohammed-Taib BM, Fadhil AB. Dibenzothiophene capture from model fuel by wild mustard stems derived activated carbon: kinetics and isothermal evaluations. International Journal of Environmental Analytical Chemistry. 2021 May 26;1–23. Available from: <URL>.

44. Fadhil AB, Kareem BA. Co-pyrolysis of mixed date pits and olive stones: Identification of bio-oil and the production of activated carbon from bio-char. Journal of Analytical and Applied Pyrolysis. 2021 Sep;158:105249. Available from: <URL>.

45. Demiral İ, Aydın Şamdan C, Demiral H. Production and characterization of activated carbons from pumpkin seed shell by chemical activation with $ZnCl_2$. Desalination and Water Treatment. 2016 Feb;57(6):2446–54. Available from: <URL>.

46. Mbarki F, Selmi T, Kesraoui A, Seffen M. Low-cost activated carbon preparation from Corn stigmata fibers chemically activated using H3PO4, ZnCl2 and KOH: Study of methylene blue adsorption, stochastic isotherm and fractal kinetic. Industrial Crops and Prod ucts. 2022 Apr;178:114546. Available from: <URL>.

47. Li C, Zhang L, Xia H, Peng J, Zhang S, Cheng S, et al. Kinetics and isotherms studies for congo red adsorption on mesoporous Eupatorium adenophorum-based activated carbon via microwave-induced H3PO4 activation. Journal of Molecular Liquids. 2016 Dec;224:737–44. Available from: <URL>.

48. Cherik D, Louhab K. Preparation of microporous activated carbon from date stones by chemical activation using zinc chloride. Energy Sources, Part A: Recovery, Utilization, and Environmental Effects. 2017 Sep 17;39(18):1935–41. Available from: <URL>.

49. Georgin J, de O. Salomón YL, Franco DSP, Netto MS, Piccilli DGA, Perondi D, et al. Development of highly porous activated carbon from Jacaranda mimosifolia seed pods for remarkable removal of aqueous-phase ketoprofen. Journal of Environmental Chemical Engineering. 2021 Aug;9(4):105676. Available from: <URL>.

50. Cruz GJF, Pirilä M, Matějová L, Ainassaari K, Solis JL, Fajgar R, et al. Two Unconventional Precursors to Produce ZnCl 2 -Based Activated Carbon for Water Treatment Applications. Chem Eng Technol. 2018 Aug;41(8):1649–59. Available from: <URL>.

51. Lazarotto JS, da Boit Martinello K, Georgin J, Franco DSP, Netto MS, Piccilli DGA, et al. Preparation of activated carbon from the residues of the mushroom (Agaricus bisporus) production chain for the adsorption of the 2,4-dichlorophenoxyacetic herbicide. Journal of Environmental Chemical Engineering. 2021 Dec;9(6):106843. Available from: <URL>.

52. Yönten V, Sanyürek NK, Kivanç MR. A thermodynamic and kinetic approach to adsorption of methyl orange from aqueous solution using a low cost activated carbon prepared from Vitis vinifera L. Surfaces and Interfaces. 2020 Sep;20:100529. Available from: <URL>.

53. Mohammadi N, Khani H, Gupta VK, Amereh E, Agarwal S. Adsorption process of methyl orange dye onto mesoporous carbon material–kinetic and thermodynamic studies. Journal of Colloid and Interface Science. 2011 Oct;362(2):457–62. Available from: <URL>.

54. Zhang B, Wu Y, Cha L. Removal of methyl orange dye using activated biochar derived from pomelo peel wastes: performance, isotherm, and kinetic studies. Journal of Dispersion Science and Technology. 2020 Jan 2;41(1):125–36. Available from: <URL>.

55. Azam K, Raza R, Shezad N, Shabir M, Yang W, Ahmad N, et al. Development of recoverable magnetic mesoporous carbon adsorbent for removal of methyl blue and methyl orange from wastewater. Journal of Environmental Chemical Engineering. 2020 Oct;8(5):104220. Available from: <URL>.

56. Vali SI, Sirisha U, Poiba VR, Vangalapati M, King P. Synthesis and characterization of Titanium doped activated carbon nanoparticles and its application for the removal of dicofol. Materials Today: Proceedings. 2021;44:2290–5. Available from: <URL>.

57. Safari M, Khataee A, Darvishi Cheshmeh Soltani R, Rezaee R. Ultrasonically facilitated adsorption of an azo dye onto nanostructures obtained from cellulosic wastes of broom and cooler straw. Journal of Colloid and Interface Science. 2018 Jul;522:228–41. Available from: <URL>.

58. Dong Z, Du J, Wang A, Yang X, Zhao L. Removal of methyl orange and acid fuschin from aqueous solution by guanidinium functionalized cellulose prepared by radiation grafting. Radiation Physics and Chemistry. 2022 Sep;198:110290. Available from: <URL>.

59. Hussain S, Kamran M, Khan SA, Shaheen K, Shah Z, Suo H, et al. Adsorption, kinetics and thermodynamics studies of methyl orange dye sequestration through chitosan composites films. International Journal of Biological Macromolecules. 2021 Jan;168:383–94. Available from: <URL>.

60. Dutta SK, Amin MK, Ahmed J, Elias Md, Mahiuddin Md. Removal of toxic methyl orange by a cost-free and eco-friendly adsorbent: Mechanism, phytotoxicity, thermodynamics, and kinetics. South African Journal of Chemical Engineering. 2022 Apr;40:195–208. Available from: <URL>.

61. Khaniabadi YO, Heydari R, Nourmoradi H, Basiri H, Basiri H. Low-cost sorbent for the removal of aniline and methyl orange from liquid-phase: Aloe Vera leaves wastes. Journal of the Taiwan Institute of Chemical Engineers. 2016 Nov;68:90–8. Available from: <URL>.

62. Martini BK, Daniel TG, Corazza MZ, de Carvalho AE. Methyl orange and tartrazine yellow adsorption on activated carbon prepared from boiler residue: Kinetics, isotherms, thermodynamics studies and material characterization. Journal of Environmental Chemical Engineering. 2018 Oct;6(5):6669–79. Available from: <URL>.

63. Çağlar E, Donar YO, Sinağ A, BiRoğlu İ, BiLge S, Aydincak K, et al. Adsorption of anionic and cationic dyes on biochars, produced by hydrothermal carbonization of waste biomass: effect of surface functionalization and ionic strength. Turk J Chem. 2018;42:86–99. Available from: <URL>.

64. Mohammadi N, Khani H, Gupta VK, Amereh E, Agarwal S. Adsorption process of methyl orange dye onto mesoporous carbon material–kinetic and thermodynamic studies. Journal of Colloid and Interface Science. 2011 Oct;362(2):457–62. Available from: <URL>.

65. Chen S, Zhang J, Zhang C, Yue Q, Li Y, Li C. Equilibrium and kinetic studies of methyl orange and methyl violet adsorption on activated carbon derived from Phragmites australis. Desalination. 2010 Mar;252(1–3):149–56. Available from: <URL>.

66. Baig U, Uddin MK, Gondal MA. Removal of hazardous azo dye from water using synthetic nano adsorbent: Facile synthesis, characterization, adsorption, regeneration and design of experiments. Colloids and Surfaces A: Physicochemical and Engineering Aspects. 2020 Jan;584:124031. Available from: <URL>.

67. Fadhil AB, Saeed HN, Saeed LI. Polyethylene terephthalate waste-derived activated carbon for adsorptive desulfurization of dibenzothiophene from model gasoline: Kinetics and isotherms evaluation. Asia-Pac J Chem Eng [Internet]. 2021 Mar [cited 2023 Mar 12];16(2). Available from: <URL>.

JOTCS A
Journal of the Turkish Chemical Society
Section: A
Chemistry
TURKISH CHEMICAL SOCIETY

Molecularly Imprinted Polymers Based on Konjac for Selective Caffeine Adsorption in Aqueous Solution

Saranya Wattananon[1], Samroeng Narakaew[2], Aphiruk Chaisena[2*]

[1]Department of Food Science and Technology, Faculty of Agricultural Technology, Lampang Rajabhat University, Lampang 52100, Thailand
[2]Department of Applied Chemistry and Center of Excellence for Innovation in Chemistry, Faculty of Science, Lampang Rajabhat University, Lampang 52100, Thailand

Abstract: A number of caffeine extraction methods have been developed, such as microwave assisted extraction and ultrasonic-assisted extraction. The disadvantages of these methods are low selectivity, inconvenience, and inefficiency. Among the existing technologies, molecularly imprinted polymers (MIPs) are one of the most efficient and economical methods for the removal of caffeine contaminants. In this study, the objective was to prepare MIPs for the removal of complicated samples. The obtained materials were used as a sorbent for the extraction of caffeine from coffee brewed in an espresso. The MIPs were prepared using konjac/acrylic acid as a functional monomer, N, N′-methylenebisacrylamide as a cross-linker, and caffeine as a template. The chemical structures of MIPs were characterized by Fourier transform infrared spectroscopy. MIPs exhibited a higher maximum adsorption capacity (87.72 mg/g). The equilibrium adsorption data fit well with the Langmuir adsorption isotherm models, which confirm the monolayer adsorption behaviour of caffeine molecules on the surfaces of the MIPs samples. According to the experimental results of the adsorption capacity of caffeine from aqueous solution, the MIPs showed a higher percentage removal of caffeine (75.66%). Our findings suggest that MIPs are useful adsorbents for the decaffeination of coffee brewed in an espresso.

Keywords: adsorption, molecularly imprinted polymer, konjac, caffeine, sorbent

Submitted: October 25, 2022. **Accepted:** February 14, 2023.

Cite this: Wattananon S, Narakaew S, Chaisena A. Molecularly Imprinted Polymers Based on Konjac for Selective Caffeine Adsorption in Aqueous Solution. JOTCSA. 2023;10(2):359–70.

DOI: https://doi.org/10.18596/jotcsa.1194200.

***Corresponding author. E-mail:** aphiruk@lpru.ac.th.

1. INTRODUCTION

Caffeine (1,3,7-trimethylxanthine) is a widely known compound found in numerous plants and beverages such as cocoa, coffee, tea, and cola. Caffeine alleviates fatigue by activating the central nervous system and stimulating metabolism. However, consumption for an extended period or in large quantities results in unpleasant effects, including addiction, neuroticism, muscular twitching, and anxiety (1, 2). Limiting caffeine intake from coffee is recommended, depending on the time zone and other conditions. Decaffeinated coffee was first advocated in the early 1900s; by the early 2000s, decaffeinated coffee accounted for approximately 10% of the entire coffee consumption (3). Coffee beans were heavily decaffeinated before roasting. Organic solvents such as chloroform, dichloromethane (4), supercritical carbon dioxide (5, 6), and water were utilized in the initial part of the decaffeination process (7). Following the extraction procedure, further decaffeination was performed. This method of adsorbing caffeine from coffee extracts utilizes adsorbents such as activated carbon (AC) (8), which can reduce the levels of other desirable substances in coffee, such as polyphenols (9, 10).

Molecularly Imprinted Polymers (MIPs) demonstrate a considerably higher affinity towards molecules employed as templates than similar molecules, including closely related isomers. MIPs have

received significant attention in recent years because of their unique benefits, such as predetermined recognition ability, stability, relative ease, low cost of synthesis, and possible application to a wide range of target molecules (11-17). MIPs are distinctly more advantageous than typical solid-phase extraction packing materials in terms of specificity (18). As an adsorbent, caffeine MIP was used to extract caffeine from green tea after four hours of solvent extraction (19). A large quantity of chlorinated solvent is used in the conventional method to obtain caffeine from a sample, which is time-consuming (20). In contrast to traditional sorbents, MIPs are better at concentrating and separating target analytes from mixtures. MIPs are based on synthetic and natural polymers, depending on their primary components. To synthesize MIPs, cross-linking agents, such as N, N′-methylenebisacrylamide and ethylene glycol dimethacrylate, copolymerize functional monomers of acrylic acid (AA) and acrylamide. The resulting copolymers are expensive. Additionally, they exhibit poor biocompatibility and biodegrade slowly in the environment (21, 22). However, MIPs derived from natural polysaccharides, such as cyclodextrin (23,24) and chitosan (25-27), offer the following advantages: they are biocompatible and biodegradable, and particularly well suited for use in biology and medicine. MIPs are cost-effective due to their abundance and biodegradability. Therefore, polysaccharide-based MIPs have gained considerable attention recently. According to Lin et al., MIPs used for protein recognition are based on agarose (28). According to Zhao et al., alginate is used to make MIPs for protein separation (29). Konjac (K), which is a water-soluble polysaccharide with a large molecular mass, is composed of □-1, 4 connected D-glucose and D-mannose units in a 1:1.6 molar ratio. It is prepared from the tubers of the Amorphophallus konjac plant, which is an important crop in mountainous areas. Due to its high water solubility as well as its film and gel properties, konjac has several applications in medicine, biology, chemical engineering, and other fields (30-34). However, research on MIPs based on konjac is limited (35).

MIPs based on konjac were prepared for caffeine extraction using a graft copolymer of konjac and acrylic acid (K-g-PAA) as the functional monomer, N, N′-methylenebisacrylamide as the cross-linker, and caffeine as the template. The adsorption capabilities of the MIPs were tested for caffeine adsorption properties in aqueous solutions. In this study, MIPs were used as sorbents for decaffeinated coffee solutions to find out how well they could remove caffeine from coffee brewed in an espresso.

2. EXPERIMENTAL SECTION

2.1. Chemicals and Materials

Standard caffeine (≥99%), ammonium ceric nitrate (CAN), and acrylic acid (AA) were sourced from Loba Chemie Pvt. Ltd. (India). AA was distilled via CuCl at low pressure prior to use. Theophylline, anhydrous (□99%), and N, N′-methylenebisacrylamide (NMBA, □99%) were purchased from Sigma–Aldrich (USA). Konjac was obtained from Bkkchemi (Thailand) and used as received. Fresh coffee samples were obtained from local markets. All the other reagents were of analytical grade and were used untreated. Deionized water was used throughout the experiments.

2.2. Preparation of Molecularly Imprinted Polymers (MIPs) and Nonimprinted Polymers (NIPs)

Konjac (1.5 g) in 70 mL of deionized water, 1.0 g of caffeine, and 0.14 g of CAN were added and stirred in a three-necked flask. A solution of 935.9 mL of AA and 15.4 g of NMBA was prepared by dissolving them in deionized water; it was poured into the three-necked flask through a pressure equalizing dropping funnel. The filtrate was washed with deionized water, methanol, and acetic acid/methanol, respectively, until no UV absorption was detected at 275 nm. After removing the acetic acid with methanol, it was dried under vacuum for 24 h to obtain MIPs. NIPs were prepared and processed in a similar manner as MIPs, except that caffeine was not used as a template.

2.3. Fourier Transform Infrared Spectroscopy Analysis (FTIR)

FTIR spectra of the samples were obtained using a Shimadzu (FTIR 8900) at wavenumber range from 4000 to 400 cm^{-1} using the KBr pellet technique.

2.4. Determination of Caffeine in Coffee Samples by UV–vis Spectrophotometry

The absorbance of caffeine was measured at 275 nm using a UV-vis spectrophotometer with double-beam optical system (Agilent Cary 60). A calibration curve was constructed each day before the analysis of the samples. Deionized water was used as a blank. Calibration standards from the caffeine stock solution (2 mg/mL) were prepared by dissolving 200.00 mg of pure caffeine in 100 mL of distilled water. Working solutions of 0.014, 0.020, 0.026, 0.032, and 0.038 mg/mL (14, 20, 26, 32, 38 mg/L) caffeine were prepared by serial dilution of the stock in 25 mL volumetric flasks with deionized water.

2.5. Adsorption Experiment

MIPs or NIPs weighing 0.1 g were added to the solution of caffeine (2 mg /mL, pH 7) in a volume of 5 mL. The concentration of caffeine in the filtrate solution was measured using UV-vis spectrophotometer at a wavelength of 275 nm; the adsorption capacity was calculated, and a plot between the adsorption capacity and time was created. The adsorption capacity (Q, mg/g) was primarily determined by the variance in caffeine concentration, which was computed using the following formula:

$$Q=\frac{(C_0-C_t)}{m\times V} \quad \text{(Eq. 1)}$$

where C_0 (mg/mL) is caffeine's initial concentration, C_t (mg/mL) is the caffeine concentration in filtrate at t min, V (mg/mL) is the starting solution volume, and m (mg) is the mass of the MIPs or NIPs.

2.6. Modelling of Experimental Isotherms

The modeling of the experimental data of the isotherms is used to determine the adsorption capacity of MIPs and NIPs adsorbent materials and to evaluate the mechanisms applied in the adsorption process. The Langmuir and Freundlich isotherm models were applied to fit the experimental data. The Langmuir isotherm model justifies a monolayer and homogeneous adsorption.

$$Q_e=\frac{Q_m\times K_L\times C_e}{1+K_L\times C_e} \quad \text{(Eq. 2)}$$

where Q_m (mg/g) and K_L are the Langmuir maximum adsorption capacity of the adsorbent material and Langmuir's constant; Q_e (mg/g) represents the amount of caffeine adsorbed, and C_e represents the equilibrium concentration (mg/mL). According to the Freundlich isotherm model, the adsorption is multilayer and heterogeneous in nature.

$$logQ_e=\frac{1}{n}logC_e+logK_F \quad \text{(Eq. 3)}$$

where K_F and n are the Freundlich adsorption and exponential coefficients, respectively.

2.7. Selectivity Test of MIPs and NIPs

Theophylline was used as a control molecule to determine the selectivity of the MIPs and NIPs. The adsorption test was performed, as previously described, using 0.1 g of MIPs or NIPs in 5 mL of caffeine or theophylline (0.1 mg/mL, pH 7). The selectivity of the MIPs was demonstrated using static distribution coefficient (K_D), separation factor (α), and relative separation factor (β). The values are determined by the following formulas (25, 36):

$$K_D=\frac{Q_e}{C_0} \quad \text{(Eq. 4)}$$

where C_0 (mg/mL) represents the initial precursor concentration and Q_e (mg/g) is the equilibrium adsorption capacity; K_D represents the binding capacity between the MIPs and the precursor (the higher the K_D, the stronger the rebinding capacity).

$$\alpha=\frac{K_{Di}}{K_{Dj}} \quad \text{(Eq. 5)}$$

where K_{Di} and K_{Dj} are the static distribution coefficients of MIPs and control polymers, respectively; α demonstrates the selectivity of MIPs (the higher of the value of α, the better the selectivity).

$$\beta=\frac{\alpha_M}{\alpha_N} \quad \text{(Eq. 6)}$$

where α_M is the separation factor of MIPs, and α_N is the separation factor for control polymers. β demonstrates the difference between molecular selectivity of MIPs and control polymers.

2.8. Caffeine Adsorption Capability of MIPs in Coffee Brewed in an Espresso

A liquid–liquid decantation using dichloromethane was performed for decaffeinating coffee brewed in espresso solutions (37, 38). The coffee solution (Espresso 2 oz, 60 mL) was mixed with MIPs according to the best conditions obtained from the above study. Next, 2 g of sodium carbonate (Na_2CO_3) and 4 mL of dichloromethane (CH_2Cl_2) were added to the mixed samples in a separating funnel and shaken for 20 min. The residual water was separated from dichloromethane by draining dichloromethane through a separating funnel. The extraction was repeated by adding 4 mL of dichloromethane. The extracted solution was evaporated by heating, and the sample was adjusted to the required volume with deionized water before UV–vis analysis, where the absorbance was measured at a wavelength of 275 nm.

3. RESULTS AND DISCUSSION

3.1. Preparation of MIPs (K-g-PAA) and NIPs

Figure 1 illustrates the method of producing MIPs using caffeine as a template. Acrylic acid and konjac are initially bound together by hydrogen bonds surrounding caffeine molecules. Graft copolymers are prepared by graft polymerization using NMBA as the cross-linker and ammonium ceric nitrate as an initiator. Noncovalent linkages were used to imprint the caffeine molecules into the cross-linked graft polymer. When caffeine molecules are removed by the eluent, molecular recognition units are formed, which have equivalent structures and sizes to caffeine molecules (35, 39). Subsequently, the MIPs obtained can selectively recognize caffeine molecules. Typical photographs of MIPs are shown in Figure 2. The sample of dry MIPs resembles a flaky white powder.

3.2. FTIR Analysis of the Samples

The spectra of the samples are illustrated in Figure 3. Caffeine, konjac, MIPs before extraction, MIPs

after extraction, and NIPs are represented by Figure 3(a) – 3(e), respectively. The band at 1657 cm^{-1} is attributed to the stretching modes of the C=O group of caffeine, as illustrated in Figure 3(a). The band at 3109 cm^{-1} is the C–H stretching vibration of caffeine's aromatic rings. Additionally, at 748 cm^{-1}, deformation vibrations are observed.

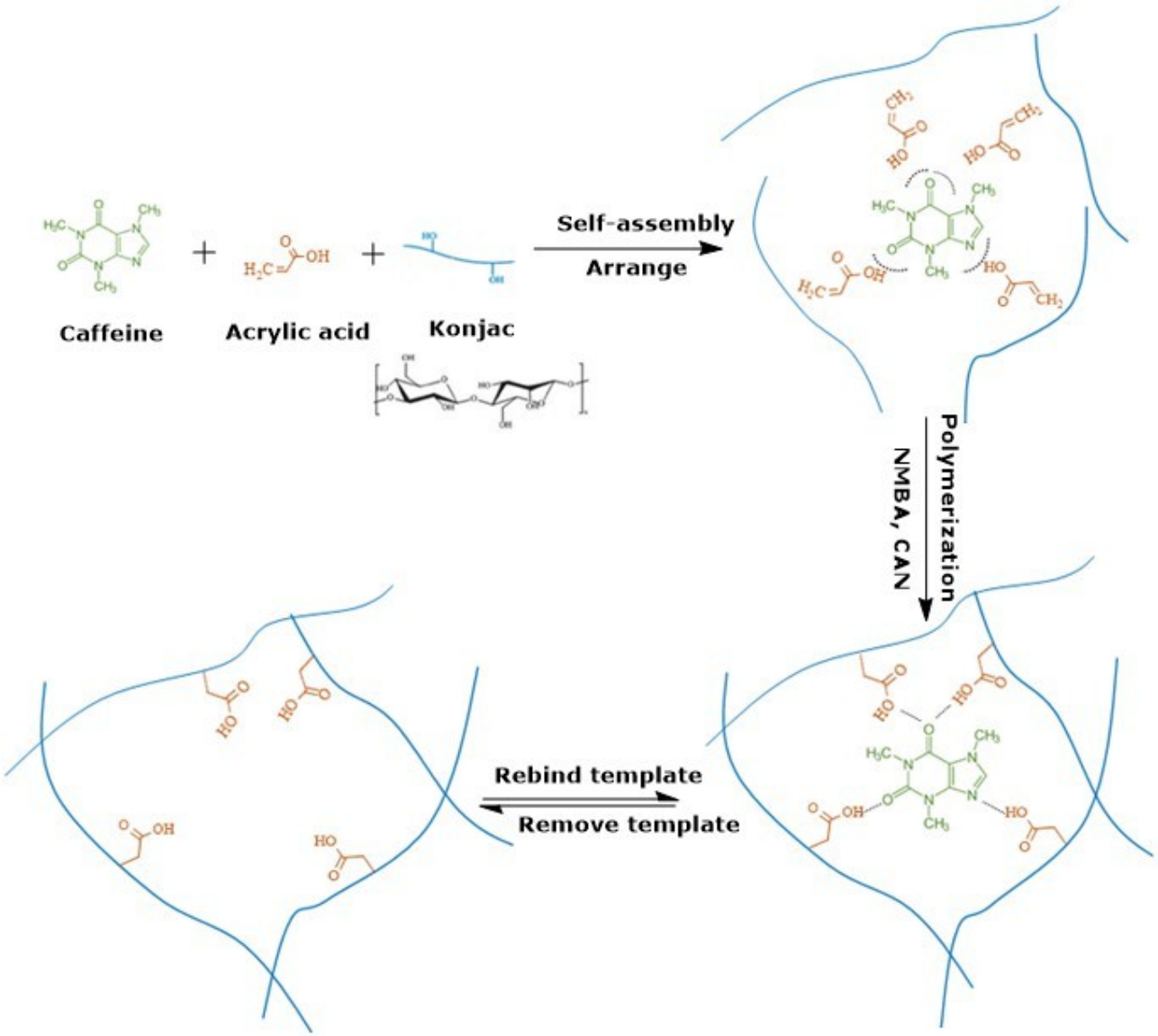

Figure 1: Preparation process of MIPs (K-g-PAA).

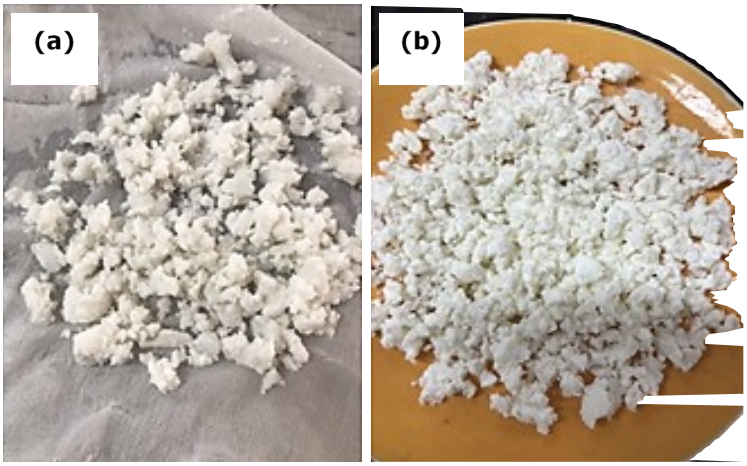

Figure 2: MIPs (K-g-PAA) wet (a) and dry composite (b).

The infrared spectrum of konjac is shown in Figure 3(b). The O–H groups' stretching mode produces a broad band at 3398 cm^{-1}. Sharp bands at 1741 and 1638 cm^{-1} indicated minor C=O groups in konjac and intramolecular hydrogen interactions, respectively. The C–O–C stretching vibrations are attributed to the sharp band at 1020 cm^{-1}. Figure 3(c) illustrates the MIPs' infrared spectrum prior to extraction. In addition to the bands mentioned above for caffeine, there remain the characteristic bands of K-g-PAA. The overlap of O–H groups gives the broad band at 3398 cm^{-1} in both konjac and PAA. The C–O–C stretching and C–H vibrations of konjac are attributed to a sharp band at 1020 cm^{-1} and the band at 2924 cm^{-1}, respectively. For PAA, symmetric and asymmetric stretching of COO^- appear at 1532 and 1407 cm^{-1}, respectively. The carbonyl stretch C=O of a carboxylic acid indicates the presence of a new sharp band at 1659 cm^{-1} . According to the results, caffeine molecules are the template molecules for the graft copolymers (35). The distinctive bands of caffeine disappear in Figure 3(d) (MIPs after extraction), indicating that caffeine had been removed from the MIPs. These differences can be considered as providing evidence that MIPs retained caffeine within their structures, possibly through weak noncovalent interactions like hydrogen bonding. For NIPs, the wave number of 1657 cm^{-1} does not appear in Figure 3(e).

3.3. Adsorption Rate and Adsorption Isotherm of MIPs and NIPs

The adsorption kinetic curves for MIPs and NIPs are shown in Figure 4 (a). Both NIPs and MIPs are capable of adsorbing caffeine. At 80 min, the adsorption capacity increases significantly and gradually decreases until adsorption equilibrium is reached at 120 min. This phenomenon can be explained as follows: In the first stage, adsorption of gels occurs on the surface, resulting in a high adsorption rate. However, as adsorption occurs within the gel network, adsorption equilibrium is subsequently reached on the gels' surfaces. The rate of adsorption is controlled by the rate of caffeine diffusion through the gel network.

Caffeine diffusion into the gels must overcome resistance from the gels' surface and hole wall. As a result, caffeine's diffusion rate is slow, resulting in a slow adsorption rate (40). In addition, the caffeine concentration in the outside solution gradually drops during the adsorption process, but the concentration of caffeine inside the gels rises. Particularly, the concentration gradient between the interior and exterior of the gels reduces, resulting in a low adsorption rate (41). MIPs demonstrate a higher adsorption rate and capacity than NIPs, according to their adsorption curves. This is because template molecules build a large number of recognition units in gel networks during the process, and the adsorption "channels" established by template extraction result in a high adsorption rate.

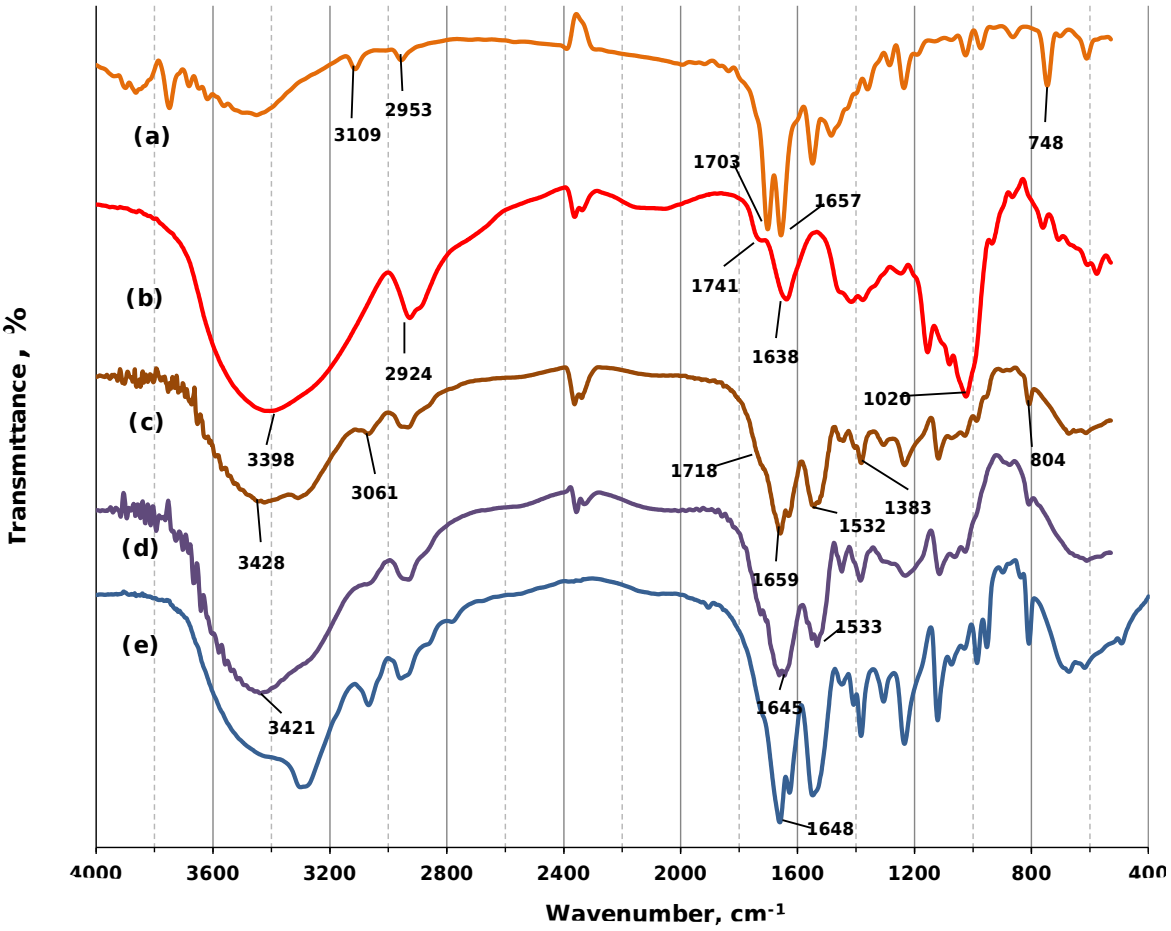

Figure 3: FTIR spectra of MIPs and NIPs ((a), caffeine; (b), Konjac; (c), MIPs before extraction; (d), MIPs after extraction (e) NIPs.)

The adsorption isotherm models for the MIP and NIPs at various caffeine concentrations are depicted in Figure 4 (b). The equilibrium adsorption capacities of both MIPs and NIPs increase with increasing caffeine concentration and then stabilize at a certain level of caffeine concentration. When the interaction between recognition units and caffeine approaches saturation, the gel networks keep a constant number of recognition units, and the adsorption capacity does not increase with increasing caffeine concentration (42). The adsorption isotherms are fitted by Langmuir and Freundlich equations to understand the behaviour of adsorption (26, 43). Figure 5 shows the fitted straight lines for the Langmuir (a) and Freundlich (b) equations, where Q_m of the Langmuir equation and n of the Freundlich equation are calculated from the corresponding slopes; K_L of the Langmuir equation and K_F of the Freundlich equation are calculated from the corresponding intercepts, respectively (Table 1). With the Langmuir model, the linear correlation coefficients for MIPs and NIPs are 0.9978 and 0.9950, respectively. They are greater than the correlation coefficients for MIPs and NIPs with the Freundlich model, which are 0.9757 and 0.9646, respectively. Therefore, the adsorption behaviour of both MIPs and NIPs for caffeine can be expressed in terms of the Langmuir equation; the adsorption behaviour indicates monolayer adsorption (1). Based on the intercept, the Q_m values of MIPs and NIPs are 87.72 and 70.92 mg/g, respectively; the K_L values are 5.18 and 4.02, respectively. Higher Q_m values result in higher adsorption capacities. Similarly, higher K_F values result in higher adsorption rates.

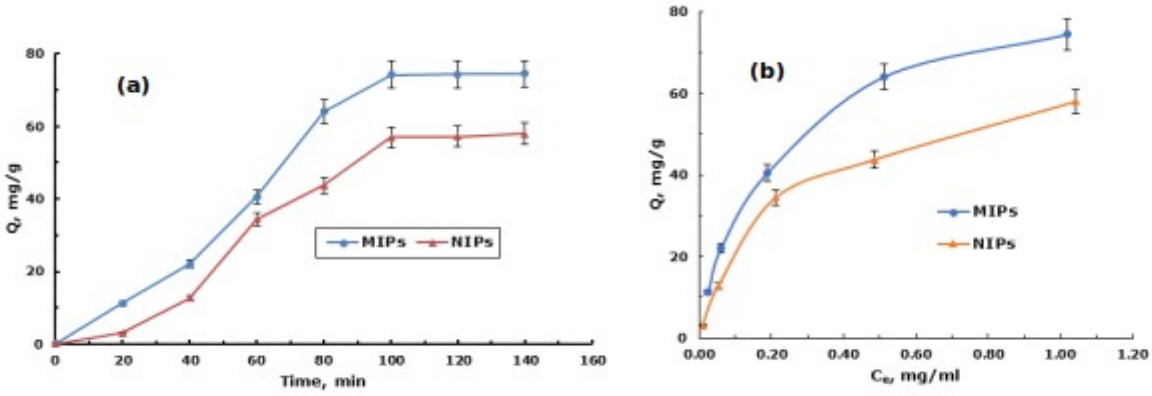

Figure 4: Adsorption kinetics (a) and adsorption isotherms (b) of caffeine on MIPs and NIPs.

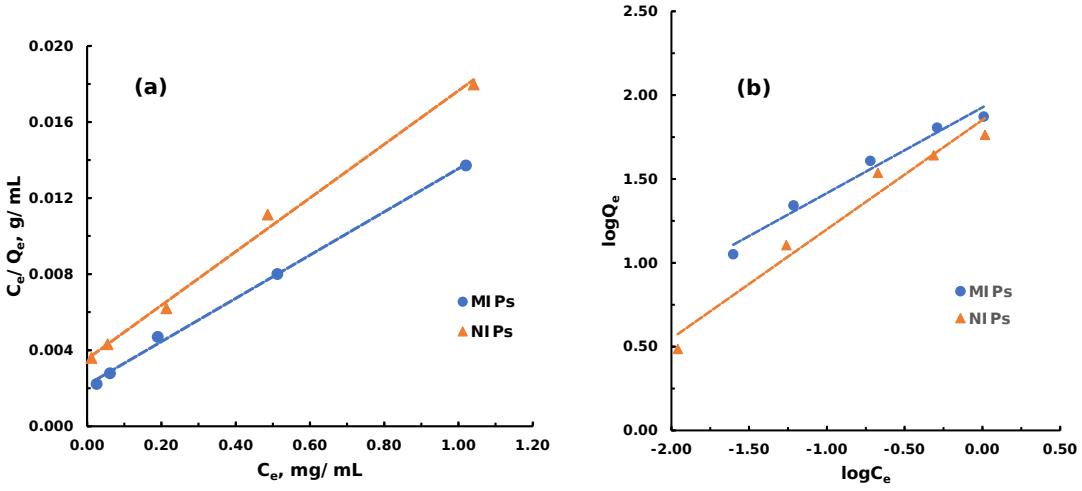

Figure 5: Langmuir isotherms (a) and Freundlich isotherms (b) for caffeine adsorption on MIPs and NIPs.

3.4. The Effect of pH on MIPs and NIPs Adsorption

The effect of pH on the adsorption capacity of MIPs and NIPs with various pH values is shown in Figure 6. Q_e initially increases and subsequently decreases with increasing pH in the pH range of 4–7. The highest value of Q_e is obtained at pH 6, but compared to pH 7, there is a slight difference, which gave the experimental results some similarity to those of Da-Ting et al. (35), and also made pH control easy. Therefore, pH 7 was chosen for further study. The following explanations are possible for this occurrence: The structures of the polymer shrink at low pH because the polymer chains of MIPs and NIPs contain COOH groups, resulting in a low Q_e. However, the structures expand as the pH increases due to reciprocal exclusion of COO– groups, resulting in an increase in Q_e. Furthermore, Q_e is maximized when a suitable hole is produced in the network. However, as the pH rises, the holes in the structure become wider, destroying the gels' selective adsorption capability, and as a result decreasing Q_e. Additionally, MIPs exhibit greater Q_e values than NIPs at all pH values, indicating that unique recognition units for caffeine are formed.

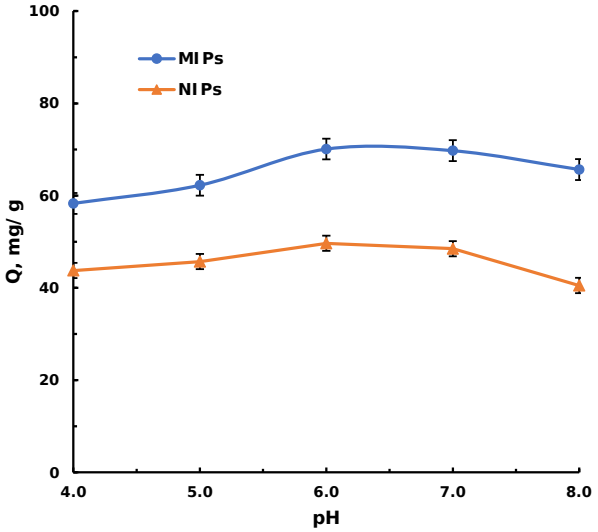

Figure 6: Effect of pH on the adsorption capacity of MIPs and NIPs.

Table 1: Parameters of the equations for the adsorption model of caffeine on MIP and NIP.

Sample	Experimental	Langmuir			Freundlich		
	Q_e (mg/g)	K_L (g/mL)	Q_m (mg/g)	R^2	n	K_F (mg/g)	R^2
MIP	74.40	5.18	87.72	0.9978	1.95	84.43	0.9757
NIP	57.95	4.02	70.92	0.9950	1.53	71.07	0.9646

Table 2: The selectivity of MIPs on caffeine.

Amount of template (mg/L)	K_D (L/g)		α	β
	Caffeine	Theophylline		
0.0	57.95	54.55	1.06	-
0.5	67.84	44.54	1.52	1.43
1.0	74.40	40.21	1.85	1.74

3.5. Selectivity of MIPs

MIPs develop specialized recognition units with certain shapes and sizes when caffeine molecules are cross-linked to the functional monomers of K-g-PAA. These recognition units can be used to selectively adsorb caffeine once the template has been eliminated. Considering the chemical structure of theophylline is similar to that of caffeine, theophylline is used as a competitive molecule to investigate the selectivity of MIPs for caffeine molecules. Table 2 shows the selectivity of MIPs and NIPs in the presence of different templates. K_D, or the static allocation coefficient, is an indicator of the MIPs or NIPs' ability to bind to their target molecules; a high K_D value indicates that MIPs have a high affinity for the target molecules. However, the separation factor and imprinting efficiency measure the selectivity of MIPs or NIPs for target molecules; high values indicate that the MIPs have great selectivity. MIPs have a greater K_D for caffeine than for theophylline. Additionally, as the amount of template increases, the K_D for caffeine increases, whereas the K_D for theophylline slightly decreases, indicating that MIPs have a stronger binding ability for caffeine than theophylline. The variation in adsorption capacity can be attributed to the formation of specific recognition units during the imprinting process. Additionally, as shown in Table 2, both □ and □ exhibit an increasing trend as the amount of template increases, indicating that the amount of template affects the recognition performance of MIPs. Of course, with the increase in the amount of template, the number of specific recognition units in MIPs is increased, and the affinity of MIPs to caffeine becomes stronger.

The adsorption capacities of other adsorbents for caffeine MIPs reported in previous studies were compared in the present study (Table 3). It is evident that the caffein MIPs based on konjac, which were prepared by using a graft copolymer of konjac and acrylic acid as the functional monomers, and N, N′-methylenebisacrylamide as the cross-linker, showed the highest adsorption capacity.

Table 3: Adsorption capacities of different MIPs for caffeine.

Preparation of caffeine MIPs	Q_m	Reference
Functional monomer: methacrylic acid Cross-linker: ethylene glycol dimethacrylate	28.10	44
Functional monomer: methacrylic acid Cross-linker: ethylene glycol dimethacrylate	39.65	45
Functional monomer: konjac glucomannan/acrylic acid Cross-linker: N, N′-methylenebisacrylamide	62.97	35
Functional monomer: konjac/acrylic acid Cross-linker: N, N′-methylenebisacrylamide	87.72	This study

3.6. Caffeine Adsorption Capability of MIPs in Coffee Brewed in an Espresso

In terms of the adsorption capacity of caffeine from coffee brewed in an espresso, MIPs demonstrate a higher percentage removal of caffeine (75.66%). Therefore, MIPs have the potential to be applied in future work.

4. CONCLUSION

In this study, MIPs demonstrated a high capacity for caffeine adsorption. The Langmuir equation is suited to describing the adsorption behaviour of molecularly imprinted polymers for caffeine; the maximum adsorption of caffeine was 87.72 mg/g, which occurred near pH 7 within 120 min. The Langmuir adsorption isotherm model displayed the monolayer adsorption of caffeine molecules on the MIPs. Caffeine extraction from aqueous solution was more efficient using MIPs because they exhibit significantly higher affinity and selectivity for the caffeine used as the template than for similar molecules. Therefore, it can be potentially used for the extraction and separation of caffeine from coffee brewed in an espresso.

5. CONFLICT OF INTEREST

The author declares that there is no conflict of interest.

6. ACKNOWLEDGMENTS

The authors gratefully acknowledge the support of this research by Lampang Rajabhat University and the Center of Excellence for Innovation in Chemistry (PERCH-CIC), Ministry of Higher Education, Science, Research, and Innovation (MHESI).

7. REFERENCES

1. James JE. Caffeine and cognitive performance: persistent methodological challenges in caffeine research. Pharmacol Biochem Behav. 2014;124:117-122. Available from: <DOI>

2. Rodriguez RS, Haugen R, Rueber A, Huang CC. Reversible neuronal and muscular toxicity of caffeine in developing vertebrates. Comp Biochem Physiol C. Pharmacol Toxicol. 2014;163:47-54. Available from: <DOI>

3. Silvarolla MB, Mazzafera P, Fazuoli LC. Plant biochemistry: a naturally decaffeinated arabica coffee. Nature. 2004;429:826-826. Available from: <DOI>

4. Bichsel B. Diffusion phenomena during the decaffeination of coffee beans. Food Chemistry. 1979;4(1):53-62. Available from: <DOI>

5. Zosel K. Separation with supercritical gases: practical applications, Angewandte Chemie International Edition in English. 1978;17(10):702-709. Available from: <DOI>

6. Udaya sankar K, Manohar B, Chokkalingam AA. A note on supercritical carbon dioxide decaffeination of coffee. J Food Sci Technol. 1986;23(6):326-328. Available from: <DOI>

7. Ramalakshmi K, Raghavan B. Caffeine in coffee: its removal Why and how. Crit Rev Food Sci Nutr. 1999;39(5):441-456. Available from: <DOI>

8. Birtigh A, Liu K, Johannsen M. Regeneration methods for caffeine-loaded CO_2. Sep Sci Technol. 1995;30(17):3265-3286. Available from: <DOI>

9. Farah A, Paulis T, Moreira D. P. Chlorogenic acids and lactones in regular and water-decaffeinated arabica coffees. J Agric Food Chem. 2006;54(2):374-381. Available from: <DOI>

10. Machmudah S, Kitada K, Sasaki M. Simultaneous extraction and separation process for coffee beans with supercritical CO_2 and water. Ind Eng Chem Res. 2011;50(4):2227-2235. Available from: <DOI>

11. He CY, Liu F, Li KA, Liu HW. Molecularly imprinted polymer film grafted from porous silica for selective recognition of testosterone. Anal Lett. 2006;39(2):275-286. Available from: <DOI>

12. Yang HH, Zhang SQ, Tan F, Zhuang ZX, Wang XR. Surface molecularly imprinted nanowires for biorecognition. J Am Chem Soc. 2005;127(5):1378-1379. Available from: <DOI>

13. Sun Y. Molecularly imprinted polymer for 2, 4-dichlorophenoxyacetic acid prepared by a sol-gel method. J Chem Sci. 2014;126(4):1005-1011. Available from: <DOI>

14. Tadi KK, Motghare RV. Computational and experimental studies on oxalic acid imprinted polymer. J Chem Sci. 2013;125(2):413-418. Available from: <DOI>

15. Sellergren B. Molecularly Imprinted Polymers, Man made mimics of antibodies and their applications in analytical chemistry, Techniques and Instrumentation in Analytical Chemistry. Elsevier Publishers. 2001;23.

16. Kupai J, Razali M, Büyüktiryaki S, Keçili R, Szekely G. Long-term stability and reusability of molecularly imprinted polymers. Polym Chem. 2017;8:666-673. Available from: <DOI>

17. Suravajhala R, Burri H R, Malik B. Development of highly specific and selectively recognizing caffeine imprinted polymer nanomaterials with EGDMA crosslinker. Current Nanomaterials, 2022;7(1):65-72. Available from: <DOI>

18. Theodoridis G, Manesiotis P. Selective solid-phase extraction sorbent for caffeine made by molecular imprinting. J Chromatogr A. 2002;948(1-2):163-169. Available from: <DOI>

19. Farrington K, Magnerb E, Regan F. Predicting the performance of molecularly imprinted polymers: Selective extraction of caffeine by molecularly imprinted solid phase extraction. Anal Chim Acta. 2006;566:60-68. Available from: <DOI>

20. He C, Long Y, Pan J, Li K, Liu F. Application of molecularly imprinted polymers to solid-phase extraction of analytes from real samples. J Biochem Biophys. Methods. 2007;70(2):133-150. Available from: <DOI>

21. Saloni J, Lipkowski P, Dasary SSR, Anjaneyulu Y, Yu H, Hill GJr. Theoretical study of molecular interactions of TNT, acrylic acid, and ethylene glycol dimethacrylate-elements of molecularly imprinted polymer modelling process. Polymer. 2011;52(4):1206-1216. Available from: <DOI>

22. Ge Y, Butler B, Mirza F, Habib-Ullah S, Fei D. Smart molecularly imprinted polymers: Recent developments and applications. Macromol Rapid Commun. 2013;34(11):903-915. Available from: <DOI>

23. Piletsky SA, Andersson HS, Nicholls A. The rational use of hydrophobic effect-based recognition in molecularly imprinted polymers. J Mol Recog. 1998;11(1-6):94-97. Available from: <DOI>

24. Sreenivasan K. Synthesis and evaluation of a Beta cyclodextrinbased molecularly imprinted copolymer. J Appl Polym Sci. 1998;70(1):15-18. Available from: <DOI>

25. Wang Y, Wang E, Wu Z, Li H, Zhu Z, Zhu X, et al. Synthesis of chitosan molecularly imprinted polymers for solid-phase extraction of methandrostenolone. Carbohydr Polym. 2014;101:517-523. Available from: <DOI>

26. Zhang YL, Zhang J, Dai CM, Zhou XF, Liu SG. Sorption of carbamazepine from water by magnetic molecularly imprinted polymers based on chitosan-Fe_3O_4. Carbohydr Polym. 2013;97(2):809-816. Available from: <DOI>

27. Yıldırım A, Acay H, Baran A. Synthesis and characterization of molecularly imprinted composite as a novel adsorbent and competition with non-imprinting composite for removal of dye. J. Turk. Chem. Soc., Sect. A: Chem. 2021;8(2):609-622. Available from: <DOI>

28. Lin Y, Tang SQ, Mao X, Bao LJ. Protein recognition via molecularly imprinted agarose gel membrane. J Biomed Mater Res A. 2008;85(3):573-581. Available from: <DOI>

29. Zhao KY, Cheng GX, Huang JJ, Ying, XG. Rebinding and recognition properties of protein-macromolecularly imprinted calcium phosphate/alginate hybrid polymer microspheres. React Funct Polym. 2008;68(3):732-741. <DOI>

30. Brenner T, Wang Z, Achayuthakan P, Nakajima T, Nishinari K. Rheology and synergy of κ-carrageenan/locust bean gum/konjac glucomannan gels. Carbohydr Polym. 2013;98(1):754-760. <DOI>

31. Ratcliffe I, Williams PA, English RJ, Meadows J. Small stain deformation measurements of konjac glucomannan solutions and influence of borate cross-linking. Carbohydr Polym. 2013;95(1):272-281. Available from: <DOI>

32. Tian DT, Li SR, Liu XP, Wang JS, Hu S, Liu CM. Synthesis and properties of konjac glucomannangraft-poly(acrylic acid-co-trimethylallyl ammonium chloride) as a novel polyampholytic superabsorbent. Adv Polyml Tech. 2013;32(S1):E131-E140. Available from: <DOI>

33. Wu WT, Yang LC, Chen HL. Effects of konjac glucomannan, inulin and cellulose on acute colonic responses to genotoxic azoxymethane. Food Chem. 2014;155:304-310. Available from: <DOI>

34. Zhang C, Chen JD, Yang FQ. Konjac glucomannan, a promising polysaccharide for OCDDS. Carbohydr Polym. 2014;104:175-181. Available from: <DOI>

35. Da-Ting T, Yu-Ch, Z, Ling X, Fang-Ting L. Synthesis and properties of caffeine molecularly imprinted polymers based on konjac glucomannan. Adv Polym Techno. 2017; 36(1):68-76. Available from: <DOI>

36. Tan CJ, Wangrangsimakul S, Bai R, Tong YW. Defining the Interactions between Proteins and Surfactants for Nanoparticle Surface Imprinting through Miniemulsion Polymerization. Chem Mater. 2008;20(1):118-127. Available from: <DOI>

37. Clarke RJ. In Proceedings of the 9th Coll. ASIC. 1980;467-472.

38. Rofti J. In Proceedings of the 5th Coll. ASIC. 1971;179-200.

39. Kai A, Huiting K, Lilei Z, Lianxiong G, Dating T. Preparation and properties of thermosensitive molecularly imprinted polymer based on konjac glucomannan and its controlled recognition and delivery of 5-fluorouracil. J Drug Deliv Sci Technol. 2020;60:101977. Available from: <DOI>

40. Atia AA, Donia AM, Yousif AM. Removal of some hazardous heavy metals from aqueous solution using magnetic chelating resin with iminodiacetate functionality. Sep Purif Technol. 2008;61(3):348-357. Available from: <DOI>

41. Demirel G, Özçetin G, Turan E, Çaykara T. pH/temperature-sensitive imprinted ionic poly (N-tert-butylacrylamide-co-acrylamide/maleic acid) hydrogels for bovine serum albumin. Macromol Biosci. 2005;5(10):1032-1037. Available from: <DOI>

42. Kimhi O, Bianco-Peled H. Study of the interactions between protein-imprinted hydrogels and their templates. Langmuir. 2007;23(11):6329-6335. Available from: <DOI>

43. Li N, Ng TB, Wong JH, Qiao JX, Zhang YN, Zhou R, et al. Separation and purification of the antioxidant compounds, caffeic acid phenethyl ester and caffeic acid

from mushrooms by molecularly imprinted polymer. Food Chem. 2013;139(1-4):1161-1167. Available from: <DOI>

44. Wei S-L, Guo X-J, Wang H-W, Tian Y-X, Yan Z-J. Preparation of caffeine molecularly imprinted polymers and application on solid phase extraction. Chinese J Anal Chem. 2012;40(07):1071-1075. Available from: <DOI>

45. Yinzhe J, Dae-Ki C, Kyung H R. Adsorption isotherms of caffeine on molecular imprinted polymer. Korean J. Chem. Eng. 2008;25(4):816-818. Available from: <DOI>

JOTCS A
Journal of the Turkish Chemical Society
Section: A
Chemistry
TURKISH CHEMICAL SOCIETY

Trimethylolpropane-based Biolubricant Synthesis from Sweet Almond (*Prunus amygdalus dulcis*) Seed Oil for Use in Automotive Applications

Aliru Olajide Mustapha*, Aishat Babatunde, Omowunmi Akinola, Henry Samuel Olododo, Yemisi Tokunbo Afolabi, and Tijani Abdulfatai

*Department of Chemistry and Industrial Chemistry, Faculty of Pure and Applied Sciences, Kwara State University Malete, PMB 1530, Ilorin, Kwara State, Nigeria.

Abstract: This paper presents the synthesis of a sweet almond oil-based trimethylolpropane biolubricant and the evaluation of its temperature-dependent viscosity properties. The oil was converted into biodiesel by the transesterification process after extraction, refining, and acid-alkaline transesterification. After, biolubricant was produced by further transesterifying biodiesel with trimethylolpropane at 105 °C at a ratio of 3.9:1 for a 60-minute reaction time with a potassium hydroxide catalyst concentration of 1 wt.%. According to the American Standard Test Methods (ASTM), the biolubricant's pour point and index of viscosity were determined to be -4 °C and 267.50, respectively. The measured viscosities were 42.80, 30.18, 21.39, 12.25, and 8.90 cSt. at 30, 40, 60, 80, and 100 °C, demonstrating an inverse relationship between temperature and lubricant viscosity. The difference between the FTIR spectra of the biodiesel and the biolubricant at 1755.74 versus 1743.96 cm^{-1} verifies the ester group. Sweet almond oil has a higher iodine content than unsaturated glycerides (9.52 g of iodine per 100 g of oil sample) and contains 53.478% more unsaturated fatty acids than saturated fatty acids and 71.725% unsaturated fatty acids for biolubricant. Linoleic acid made up the majority of the fatty acids in the oil and synthetic biolubricant, with percentages of 31.44 and 45.93%, respectively. The biolubricant and oil from sweet almonds contained palmitic, linoleic, and oleic acids. The biolubricant has the potential to function as light gear oil for automobiles because its characterization results correlate favorably with the ISO VG-32 criteria.

Keywords: transesterification, biolubricant, biodiesel, sweet almond, trimethylolpropane.

Submitted: October 02, 2022. **Accepted:** February 12, 2023.

Cite this: Mustapha AO, Babatunde A, Akinola O, Olododo HS, Afolabi YT, Abdulfatai T. Trimethylolpropane-based Biolubricant Synthesis from Sweet Almond (Prunus amygdalus dulcis) Seed Oil for Use in Automotive Applications. JOTCSA. 2023;10(2):371–80.

DOI: https://doi.org/10.18596/jotcsa.1178460.

***Corresponding author. E-mail:** aliru.mustapha@kwasu.edu.ng.

1. INTRODUCTION

Energy consumption has increased as the world population has grown, as well as the level of industrialization and modernization. Society has changed significantly over the past century and has become increasingly dependent on fossil fuels, causing a gradual exhaustion of fuel supplies to the point where this nonrenewable energy source is expected to be depleted in the medium term, resulting in increased research and development efforts for alternatives to standard fossil fuels for energy. Biolubricant is the sole renewable energy option capable of replacing petroleum in the transportation sector (1). To enhance the management of natural resources and the environment in order to improve people's quality of life and the preservation and utilization of biodiversity, the automobile and machine industries have begun to focus on improving environmentally friendly and energy-efficient technology. Technology geared toward low-

pollution fuel combustion and exhaust, as well as vehicle economy, is projected to decrease environmental issues. Lubrication is required in the engine parts to decrease friction between them (2).

Vegetable oil has become a substitute for future fuels and oleochemical needs as a result of growing worldwide concern over climate change. Inevitably and gradually, renewable raw materials will need to replace fossil fuels (petrol, gas, and carbon) in the production of fuel and goods for the chemical industry. Currently, green lubricants manufactured from renewable raw resources are gradually replacing petroleum-based lubricants. Vegetable oils are typically used to create biolubricants because they have great application-related qualities like very low toxicity and high biodegradability, as well as good lubricity, a high viscosity index, and good stability. Factors that have fueled global research and development of lubricants derived from renewable resources in order to promote their widespread use in a variety of applications (3,4). Vegetable oils do, however, have some technical shortcomings that need to be addressed, particularly those pertaining to stability and the constrained range of viscosity values that are now available. Their polar properties and long-chain fatty acids produce a highly durable lubricant layer that reduces wear and friction by having a strong interaction with metallic surfaces (5).

In recent years, a wide range of vegetable oils have been researched to learn more about their features and potential for use as lubricants. A valuable raw resource for the production of eco-friendly lubricants is almond oil, which is derived from sweet almond seeds because of its favorable low-temperature performance and high concentration of olefinic double bonds. Almond oil has been found to be more fluid at lower temperatures than many vegetable oils (5–7). This study's aim was to produce and assess sweet almond oil's lubricating potential and test the effects of the lubricant's viscosity at various temperatures.

2. MATERIALS AND METHODS

Sweet almond fruit seeds were bought at a market in Ilorin, while chemicals and reagents like iso-propyl alcohol (IPA), phenolphthalein, hexane, methanol, sodium hydroxide, sulfuric acid, hydrochloric acid, sodium chloride, charcoal, trimethylolpropane (TMP), potassium hydroxide, glacial acetic acid, thiosulfate, chloroform, and Wiji's reagent were obtained from Sigma-Aldrich.

2.1. Extraction and Refinement of Crude Sweet Almond Oil

The dried sweet almond seeds were sized down using a local grinder. After that, they spent 48 hours submerged in n-hexane at a 2:1 n-hexane to seed ratio. The solution was sieved and distilled to remove the hexane and collect the oil at the bottom of the flask. Each soak bottle underwent two of these steps. The crucial step in the manufacturing of biodiesel is crude oil refinement since the crude oil contains contaminants, such as phosphorus compounds, which can be eliminated by using refining methods described by Mustapha *et al.* (8).

2.2. Trans-esterification

A 20% weight-to-weight methanol and 5% weight-to-weight tetraoxosulfate (iv) were heated and stirred for an hour at 60 to 65 ^{o}C and the stirrer's speed was set to 700 rpm, and refined sweet almond oil (RSAO) samples were taken using a pipette to determine the oil's% FFA.

Afterward, a refluxing condenser, a magnetic stirrer, a thermometer and a two-nec, round-bottomed flask was filled with 100 g of the refined sample, which was weighed and placed on a hot plate. A 1.0 g of potassium hydroxide (KOH) was put in 89.54 mL of methanol and then added to the flask as the catalyst. The reaction products were then allowed to settle for several hours to produce two distinct liquid phases before the flask was eventually removed from the hot-plate. The top portion of sweet almond biodiesel (SABD) was separated from the bottom portion (glycerol) by decantation, and the excess catalyst was then washed away three times with warm water heated to 80 °C until the wash water became clear. Finally, the ester section was dried at 100 °C for 30 minutes.

2.3. Synthesis of Biolubricant

In the biolubricant synthesis, the reaction vessel containing 20 mL of sweet almond methyl ester (SAME) was filled, stirred, and heated to 70 °C. KOH, the catalyst, was measured out and dissolved in 5 mL of methanol. The catalyst mixture was heated for 10 minutes before being added drop by drop to the reaction vessel. A 1.0 g of trimethylolpropane (TMP) was put into the mixture and the reaction lasts for four hours at a temperature of 100 °C (6).

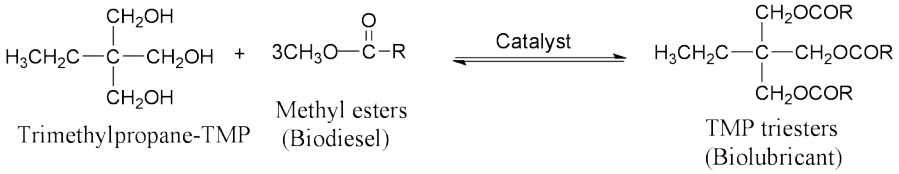

Figure 1: Synthesis of trimethylolpropane-based biolubricant.

2.4. Characterization of Biodiesel and Biolubricant

The American Oil Chemists' Society (9) standard was used to evaluate the oil's qualities, while the ASTM Standard would be used to characterize the biolubricant that was produced (10).

2.5. Determination of temperature on viscosity

The synthetic biolubricant sample's viscosity was determined at 30, 40, 60, 80, and 100 ^{o}C. First, the sample was transferred into a 100-mL beaker. The oil sample was heated to the required temperature while being stirred constantly on a heating mantle. The Brookfield® (Synchrolectric Viscometer: RVT) was turned on to measure the viscosity of the sample, and it was left running until a stable reading was recorded.

2.6. Gas Chromatography-Mass Spectrometry (GCMS) Analyses

Utilizing an Agilent 19091J-413: 3516.15684; GCMS analyses were performed to evaluate the fatty acid composition of oil. The carrier gas used was helium in a capillary column (HP-5: 5 5% Phenyl Methyl Siloxane) linked to a GCMS Agilent 5975 inert XL mass selector detector (MSD: 3000 eV) (1 mL/min). The analyte separation was achieved by configuring at 45 ^{o}C (hold time: 1.1052 min), increase to 325 ^{o}C at 1.5487 mL/min for 0 min, and then finish at 0.57353 mL/min for 2 min. for mass spectrometry (MS Source: maximum temperature of 250 ^{o}C, MS Quad: maximum temperature of 150 ^{o}C). The quantity was calculated using the total ion corresponding area (TIC) in scan mode (scan range 50-600) throughout the course of 35.5 minutes.

2.7. Fourier Transform Infrared (FTIR) Determinations

The University of Ilorin's FTIR 8400 S Shimadzu spectrometer established the functional unit and the vacuum hydraulically pressed a 0.01 g sample with 0.01 g of KBr creates translucent pellets after homogenization of pellets with pestle and mortar. A detector connected to a computer continued to collect waves while it scanned a sample in the infrared, providing descriptions of the material's spectra. Samples were typically scanned between 600 and 4000 cm^{-1} of absorption. The fundamental spectrum type of the tested sample was determined by the study's findings to be its chemical composition, molecular structure, and particular functional groups.

3. RESULTS AND DISCUSSION

3.1. Sweet Almond's Properties

The values of the refined oil's characteristics are displayed in Table 1. The FFA was 2.82% and the acid value was 5.611 (mg/KOH), respectively, while refined oil has an FFA of 0.738% and an acid value of 1.475 (mg/KOH).

Table 1: Physicochemical properties of refined sweet almond oil.

Test	Refined Oil
Color	Gold
Density (g/cm^3, 40 ^{o}C)	0.87± 0.01
Specific gravity (g/mL, 30 ^{o}C)	0.89± 0.04
Viscosity (cp, 40 ^{o}C)	4.0± 0.03
Kinematic viscosity (cSt)	4.59
Acid value (mg/KOH)	5.6 ± 0.019
Free fatty acid (FFA) (%)	2.82%
Iodine value (I_2/100g)	9.52 ± 0.01

To prevent excessive saponification of the oil, the FFA level of the oil must be decreased via esterification to 1% or less. Refined oil has a viscosity of 4.0 cSt and the success of the oil to biodiesel conversion was demonstrated by the viscosity reduction to 3.8 cSt.

3.2. Biodiesel and biolubricant properties

Viscosity is an important aspect of lubricating oil, as seen in Table 2. It measures the fluid's flow resistance at the proper temperature. At 40 and 100 °C, the biolubricant's viscosity was 42.1 and 8.9 cSt, respectively.

This result is significantly higher than the ISO-specified requirements for the light gear oil viscosity grade, 28.8 and 4.1 cSt. The biolubricant that was developed appears to have a higher viscosity index (VI), which suggests that it can be used successfully over a wide temperature range. It may be feasible to connect the temperature-dependent reduction in viscosity with the force of attraction between liquid molecules (18). A dimensionless quantity called the viscosity index is used to indicate the correlation between a product's kinematic viscosity and temperature. Viscosity index of 130 is suitable for use in a wide range of engines because viscosity decreases as the index rises and vice versa.

The discovered value complies with light gear oil ISO VG220 and ISO VG46. Additionally, as shown in Table 2, it has a greater viscosity index than biolubricants derived from other vegetable oils including sesame and jathropa. The usability of a lubricant at low temperatures is determined by its pour point. The biolubricant made from sweet almonds has a -6 ^{o}C pour point. This figure complied with the ISO VG 32 standard standards' -6 ^{o}C gear oil temperature limit. Table 2 further reveals that this study's pour point of 1.3 ^{o}C reported for neem oil-based lubricant by Mohammed *et al* (11) was comparable. This result illustrates that at lower temperatures, sweet almond biolubricant can perform without clogging the filter.

To evaluate a lubricant's flammability, one looks at its flash point to be 210 ^{o}C which is the biolubricant made from sweet almond oil's flash point. Compared to the corresponding biodiesel's 138 ^{o}C value, this flash point value is a significant improvement (19). This elevated flash point is the outcome of basic oil's chemical modification. The result meets the 204–250 ^{o}C temperature range of the ISO VG 68 and ISO VG 32 standard well. As can be seen in Table 2, the outcomes are nearly in line with the stated 262 °C for the biolubricant made from neem oil.

Sweet almond oil-based lubricants were particularly safe to use and store because they were created without methanol.

3.3. Temperature Effects on Sweet Almond Oil's Viscosity

Table 2 provides a list of the various viscosity grades that ISO demands. The main grading standards are the pour point and viscosity index. At temperatures between 30, 40, 60, 80, and 100 °C, respectively, the measured viscosities were 42.80, 30.18, 21.39, 12.25, and 8.90 cSt.

The data in Figure 1 demonstrate the negative relationship between lubricant viscosity and temperature. The calculated viscosity index was based on the obtained viscosities at 40 and 100 ^{o}C, was then used to calculate the viscosity grade.

The lubricant's molecules are attracted to one another by a cohesive force that lessens with increasing temperature, decreasing the lubricant's viscosity (18,19).

The lubricant's extremely high viscosity index may possibly be responsible for this slight drop in viscosity with rising temperature. This variance also shows that the synthetic biolubricant is acceptable for use as motor oil due to its amazing stability across such a wide temperature range (16, 17).

3.4. Fourier Transform Infrared (FTIR) Analyses

The transmittance versus wave number plot of the infrared radiation spectrum results in a horizontal variation in the bond vibration energy. Figure 3 peak plots show low transmittance and considerable absorption. The wave number on the horizontal as we move, axis gets bigger to the left. Peak less regions show that photons are not absorbing at that frequency, demonstrating that the molecule does not contain that specific bond at that frequency. Figure 3 presents the results of the FTIR analysis of the chemical composites of RCO (a), CAME (b), and CABL (c). The key IR peak regions for RCO and CAME were revealed by the FTIR spectroscopy data, indicating that chemical alterations were observing the fingerprints (500-4000 cm^{-1}). In the spectral spectrum of 1487.17 cm^{-1}, mono, di, and triglycerides of the glycerol group O-CH_2 were found (a). O-H stretching vibration (alcohol) was 2855.76 - 2695.76 cm^{-1}. In a comparable FTIR observation, Silva *et al*. (21) also observed that the C-H was an aliphatic stretching vibration. The IR spectrum between 1701.46 and 1750.45 cm^{-1} in RCO and CAME coincides with the presence of an ester carbonyl group. The FTIR spectra of CABL and CAME exhibit absorption bands at 1755.74 and 1743.96 cm^{-1}, respectively. These absorption bands, which were used to demonstrate the presence of oxygen in CABL and CAME, were created by the C-O and C=O stretching vibrations in ester (18). The figure shows that the hydroxide group peak in RCO, which was quite prominent (3a) and may be ignored in CAME (3b), was recorded at 3701.19 cm^{-1}. This shows that the bio-lubricant

esterification reaction was very close to being finished (3c).

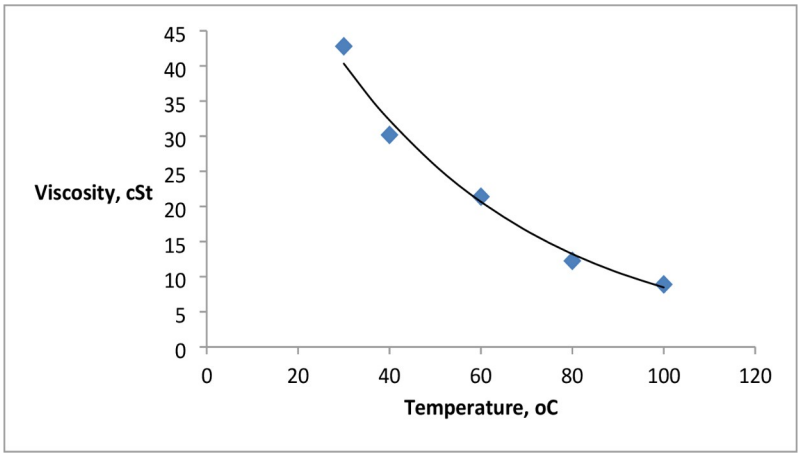

Figure 2: Effect of temperature on SABL viscosity.

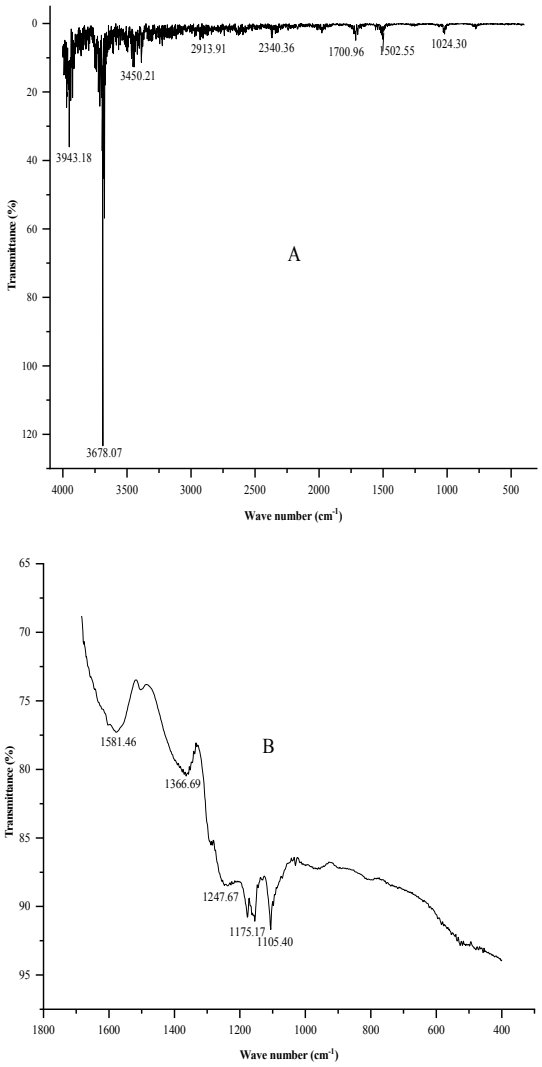

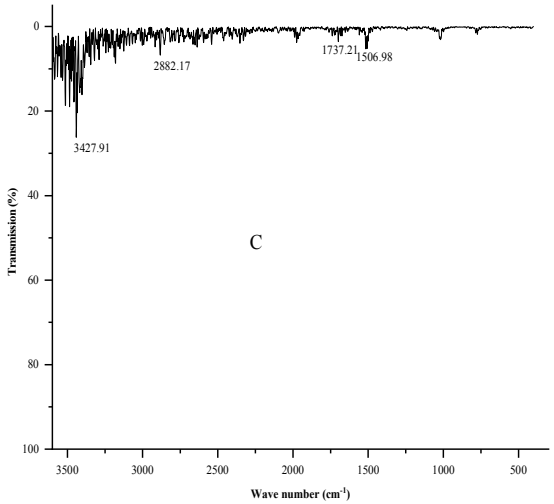

Figure 3: FTIR spectra of (A): RSAO (B): SAME (C): SABL.

Table 2: Properties of Sweet Almond biodiesel and biolubricant.

Properties	**Biodiesel**	**Sweet Almond Lube**	**[a]Jathropa Lube**	**[b]Neem Lube**	**[c] Sesame Lube**	**[d] ISO Viscosity Grade**		
						46	**32**	**68**
Flash point (ºC)	138	210	-	262	-	220	204	250
Pour point(ºC)	-8	-6	-7	1.3	-12	-10	-6	< - 10
Viscosity 40 ºC, (cSt)	37.2	42.1	55.17	190	35.43	≥41.4	≤28.8	>61.4
Viscosity 100 ºC, (cSt)	8.0	8.9	10.96	70	7.93	≥4.1	≥4.1	> 4.10
[e] ASTM D2270 Viscosity index	195.72	198.79	195.22	397	206	≥90	≥90	> 198

[a] (10); [b] (11); [c] (12); [d] (13); [e] (16)

3.5. Assessment of Free Fatty Acid

To quantify free fatty acids, GC-MS analyses were used. Castor oil was chosen for GC-MS analysis for fatty acid profile evaluation based on the high lubricating qualities discovered in synthetic biolubricant evaluation. Table 3 shows the castor oil's fatty acid makeup before it was esterified into a biolubricant using GC-MS analysis.

Table 3: Sweet almond oil and biolubricant FFA content (wt.%).

Refined sweet almond oil (RSAO)			**Sweet almond biolubricant (SABL)**		
Fatty acid	**Satn**	**Area (wt.%)**	**Fatty esters**	**Satn**	**Area (wt.%)**
Palmitic acid	$C_{16}H_{32}O_2$	15.087	Pentadecanoic acid, 14-methyl-, methyl ester	$C_{19}H_{36}O_2$	7.683
Linoleic acid	$C_{18}H_{32}O_2$	31.439	Palmitic acid methyl ester	$C_{16}H_{32}O_2$	28.275
Oleic acid	$C_{18}H_{34}O_2$	16.710	Linoleic acid ethyl ester	$C_{18}H_{32}O_2$	45.926
1,15-Pentadecanedioic acid	$C_{15}H_{28}O$	5.326	Oleic acid ester	$C_{18}H_{34}O_2$	18.116
Others		31.438			
Total FAME		68.562	Total Triester		100
Total unsaturated FFA		53.475	Total unsaturated FFA		71.725

Note: Results were extracted from the GC-MS spectra. Satn: Saturation.

According to the GC-MS results, the RSAO contains 53.48% more unsaturated fatty acids than the saturated ones (15.087%), including palmitic acid, linoleic acid, oleic acid, and 1,15-pentadecanedioic acid and biolubricant has 71.73%. As a result, the oil has a higher iodine content (9.52 of iodine per 100 g of sample), since unsaturated glycerides have a limited ability for iodine absorption. Given that most vegetable oils do not coagulate at room temperature and have a high unsaturation level, this oil is good for the synthesis of biolubricants (20, 22). Figures 4 and 5 display the fatty acid profiles of the RSAO and SABL having 71.725% percentage contents. Comparable variations between the RSAO and SABL showed hardly any compositional alterations.

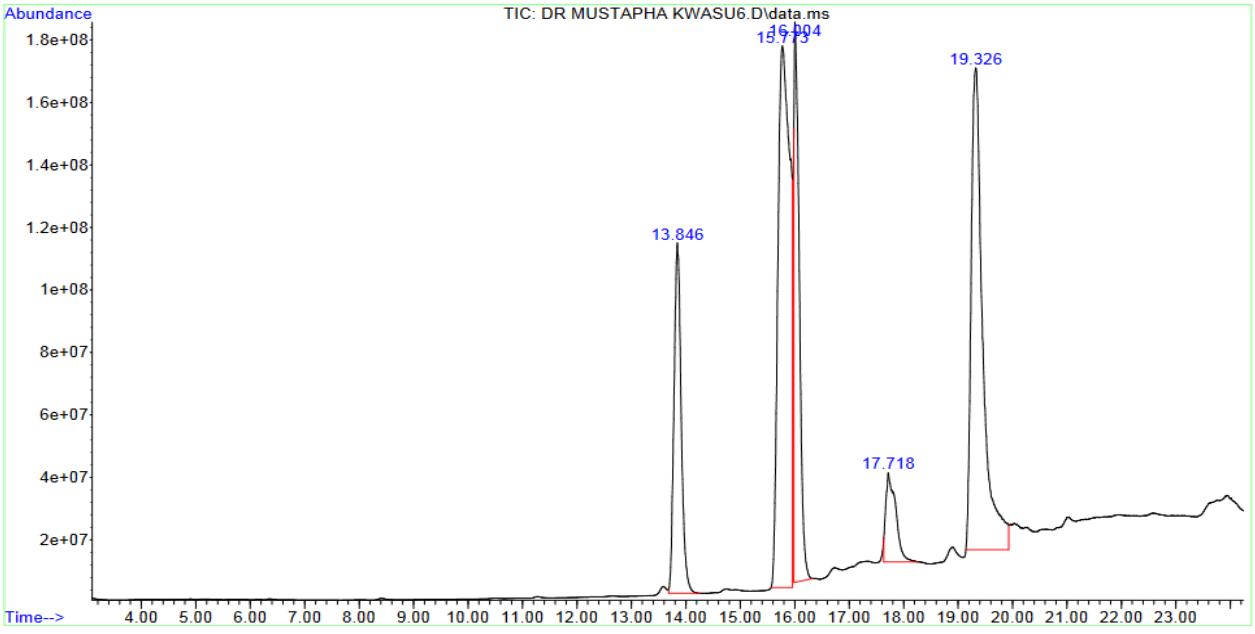

Figure 4: Fatty acids profile in refined SAO .

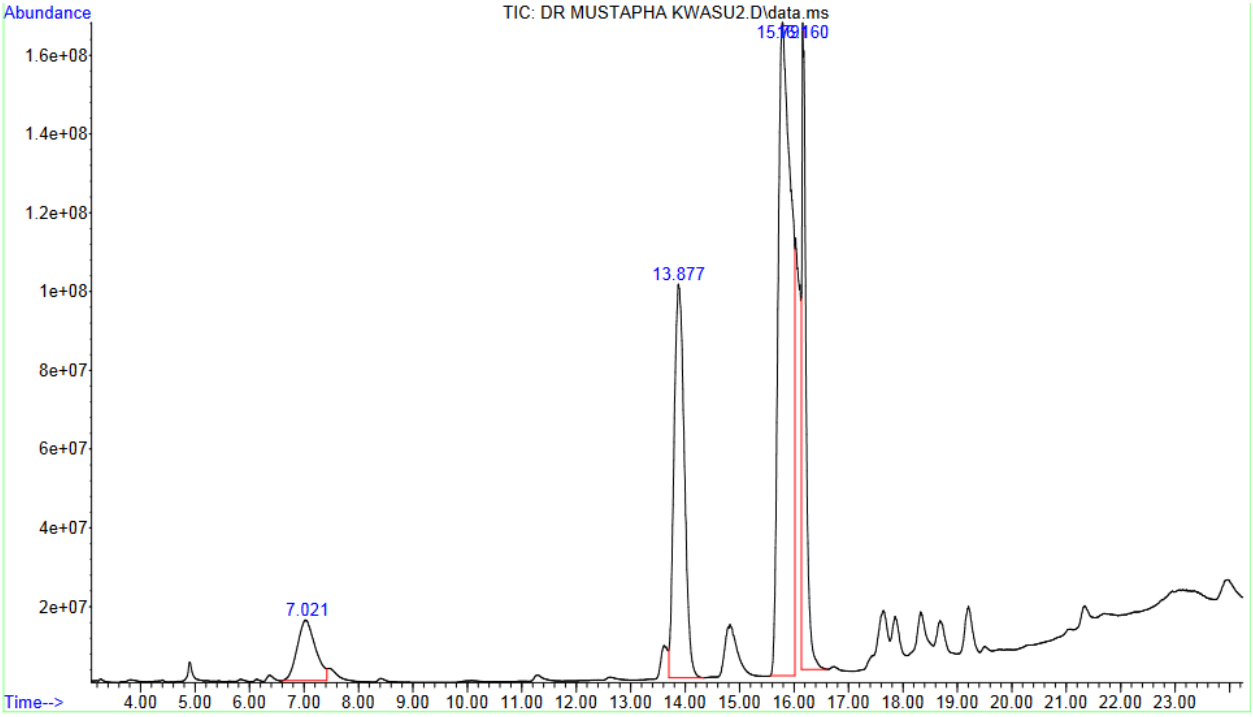

Figure 5: Fatty acids profile in SABL .

4. CONCLUSION

The trans-esterification process created the sweet almond biodiesel, which was then used to synthesize a biolubricant and evaluate its primary lubricating properties. When compared to ISO standards, these characteristics match those of viscosity grade VG-32 exactly. Therefore, synthetic biolubricants can successfully replace petroleum-based lubricants in industrial and agricultural machinery. The number of carbonyl groups in the produced bio-lubricant, which showed the evolution of the lubricant, occurred from 1743.96 cm^{-1} in SAME to 1755.74 cm^{-1} in the biolubricant when it was evaluated by FTIR. This study has shown that castor plant oils have the potential to be used to make ecologically friendly lubricants that are notably consistent with the specifications for automobile light gear oil.

5. REFERENCES

1. Cecilia JA, Ballesteros Plata D, Alves Saboya RM, Tavares de Luna FM, Cavalcante CL, Rodríguez-Castellón E. An Overview of the Biolubricant Production Process: Challenges and Future Perspectives. Processes. 2020 Feb 25;8(3):257. Available from: <URL>.

2. Salimon J, Abdullah BM, Yusop RM, Salih N. Synthesis, reactivity and application studies for different biolubricants. Chemistry Central Journal. 2014 Dec;8(1):16. Available from: <URL>.

3. Alves SM, Barros BS, Trajano MF, Ribeiro KSB, Moura E. Tribological behavior of vegetable oil-based lubricants with nanoparticles of oxides in boundary lubrication conditions. Tribology International. 2013 Sep;65:28–36. Available from: <URL>.

4. Bart JCJ, Gucciardi E, Cavallaro S. Renewable lubricants. In: Biolubricants [Internet]. Elsevier; 2013 [cited 2023 Mar 13]. p. 1–9. Available from: <URL>.

5. Delgado AE, Aperador WA. Estudio Comparativo del Poder Lubricante y Estabilidad Oxidativa entre el Aceite de Ajonjolí y Aceite Mineral 360. Inf tecnol. 2014;25(4):79–90. Available from: <URL>.

6. Alang MB, Ndikontar MK, Sani YM, Ndifon PT. Synthesis and Characterisation of a Biolubricant from Cameroon Palm Kernel Seed Oil Using a Locally Produced Base Catalyst from Plantain Peelings. GSC. 2018;08(03):275–87. Available from: <URL>.

7. Syahrullail S, Kamitani S, Shakirin A. Performance of Vegetable Oil as Lubricant in Extreme Pressure Condition. Procedia Engineering. 2013;68:172–7. Available from: <URL>.

8. Mustapha AO, Adepoju RA, Ajiboye RY, Afolabi YT, Jimoh AA, Abdulsalam ZA. Production, properties and fatty acids profile of some refined vegetable oils based biodiesels. Asian Journal of Advances in Research. 2021;17–26.

9. AOCS. Saponification Value of Fats and Oils Cd 3-25 [Internet]. American Oil Chemists' Society; 2010. Available from: <URL>.

10. S B. Production of biolubricant from Jatropha curcas seed oil. J Chem Eng Mater Sci. 2013 Sep 30;4(6):72–9. Available from: <URL>.

11. Mohammed D. Synthesis of biolubricant from vegetable oils [Master's Thesis]. [Nigeria]: Ahmadu Bello University; 2015. Available from: <URL>.

12. Audu T, Aluyor E, Egualeona S, Momoh S. Extraction and characterization of Chrysophyllum albidum and Luffa cylindrica seed oils. Petroleum Technology Development Journal. 2013;3(1):1–7.

13. Rudnick L. Automotives gear lubricants. Jl of Chemistry and Technology. 2006;425–40.

14. Dodos G, Zannikos F, Lois E. Utilization of sesame oil for the production of bio-based fuels and lubricants. School of Chemical Engineering, Laboratory of Fuel Technology and Lubricants, National Technical University of Athens. 2011;15780.

15. Musa U, Mohammed I, Sadiq M, Aberuagba F, Olurinde A, Obamina R. Synthesis and characterization of trimethylolpropane-based biolubricants from castor oil. In: Proceedings of the 45th Annual Conference of NSChE. 2015. p. 5–7.

16. D02 Committee. Practice for Calculating Viscosity Index from Kinematic Viscosity at 40 and 100C [Internet]. ASTM International; [cited 2023 Mar 13]. Available from: <URL>.

17. John M, Thomas S. Biofibres and biocomposites. Carbohydrate Polymers. 2008 Feb 8;71(3):343–64. Available from: <URL>.

18. Narayana Sarma R, Vinu R. Current Status and Future Prospects of Biolubricants: Properties and Applications. Lubricants. 2022 Apr 16;10(4):70. Available from: <URL>.

19. Ahmad U, Raza Naqvi S, Ali I, Saleem F, Taqi Mehran M, Sikandar U, et al. Biolubricant production from castor oil using iron oxide nanoparticles as an additive: Experimental, modelling and tribological assessment. Fuel. 2022 Sep;324:124565. Available from: <URL>.

20. Appiah G, Tulashie SK, Akpari EEA, Rene ER, Dodoo D. Biolubricant production via esterification and transesterification processes: Current updates and perspectives. Intl J of Energy Research. 2022 Mar 25;46(4):3860–90. Available from: <URL>.

21. da Silva JAC, Habert AC, Freire DMG. A potential biodegradable lubricant from castor biodiesel esters: A potential biodegradable lubricant from castor biodiesel esters. Lubr Sci. 2013 Jan;25(1):53–61. Available from: <URL>.

22. Kleinaitė E, Jaška V, Tvaska B, Matijošytė I. A cleaner approach for biolubricant production using biodiesel as a starting material. Journal of Cleaner Production. 2014 Jul;75:40–4. Available from: <URL>.

JOTCS A
Journal of the Turkish Chemical Society
Section: A
Chemistry

TURKISH CHEMICAL SOCIETY

Amino Acid Content of the Seeds of Some Species from *Trigonella* L. Genus Collected from Turkey

Ş. Selma URAS GÜNGÖR[1*]

[1]Mersin University, Pharmacy Faculty, Pharmacognosy Department, Mersin, 33169, Turkey

Abstract: A study was undertaken to evaluate the amino acid composition of the seeds of *Trigonella cylindracea* Desv., *Trigonella mesopotamica* Hub.-Mor. and *Trigonella smyrnea* Boiss. which are growing wild in Turkey. The seeds of three species contain both essential (histidine, isoleucine, leucine, lysine, methionine, phenylalanine, threonine, valine, arginine, and tryptophan) and non-essential (alanine, aspartic acid, glycine, glutamic acid, proline, serine, and tyrosine) amino acids. The major amino acid was glutamic acid with a value of 4819 mg/100 g (*T. cylindracea*), 5888 mg/100 g (*T. mesopotamica*) and 4146 mg/100 g (*T. smyrnea*). Among the essential amino acids, lysine is found at the highest rate in all three species. The highest amount of lysine was found in the seeds of *T. mesopotamica*, followed by the seeds of *T. cylindracea* and *T. smyrnea* (3352±0.02 mg/100 g, 3059±0.03 mg/100 g and 2947±0.04 mg/100 g, respectively). The literature review showed that the amino acid composition of the studied seeds were evaluated for the first time in this study, therefore; our study provides important preliminary data to the literature in terms of evaluating the chemical compositions of three *Trigonella* species.

Keywords: *Trigonella cylindracea, Trigonella mesopotamica, Trigonella smyrnea,* Amino acid, Chemical composition.

Submitted: September 19, 2022. **Accepted:** March 14, 2023.

Cite this: Uras Güngör ŞS. Amino Acid Content of the Seeds of Some Species from Trigonella L. Genus Collected from Turkey. JOTCSA. 2023;10(2):381–4.

DOI: https://doi.org/10.18596/jotcsa.1177340.

***Corresponding author. E-mail:** urasselma@mersin.edu.tr.

1. INTRODUCTION

Traditional medicines based on medicinal plants which have been used to treat illness or to prevent progression of chronic disease have a long history dates back to approximately 2500 years (1). In recent years, plant foods play an important role in traditional medicine in health care. Some plant foods have rich bioactive and nutritive contents, and these have been used in traditional medicine to prevent or inhibit various human diseases (2).

Amino acids are found in plants and are the basic building blocks of proteins. Amino acids are essential for protein synthesis and have various functions in the body. It is necessary to take them into the diet, since their deficiency will cause severe decreases in protein biosynthesis, therefore, the amount of total protein in the organism may also decrease. For these reasons, it is concluded that amino acids play important roles in the human body (3).

The genus *Trigonella* L. which is widely distributed throughout the Mediterranean region, Europe, South and North Africa, West Asia, and South Australia is a genus of traditional medicinal plants belonging to the Fabaceae family and includes approximately 135 species (4). The most well-known Trigonella species is *Trigonella foenum-graecum*, known as fenugreek. Fenugreek possesses an important position throughout the world to add flavor and taste in various foodstuffs which has been long known as a potent herb in traditional medicine. Its seeds contain proteins with a nutritive amino acid profile, as well as lipids, saponin, flavonoid, polyphenol, alkaloid, mucilage and other functional elements (5, 6) and have many medicinal properties such as antidiabetic, antioxidant, anticancer, gastroprotective and hepatoprotective effects (7).

The genus *Trigonella* comprises about 34 taxa which are represented by 10 sections in Turkey (4). *T. cylindracea* Desv., *T. mesopotamica* Hub.-Mor.

and *T. smyrnea* Boiss. species belongs to the section Cylindricae Boiss. and are known as Boruboyotu, Dicleboyotu and Efeboyotu, respectively, in Turkey. The species *T. foenum-graecum* is widely studied worldwide however there is few studies on other species of this genus.

We have previously conducted studies on the chemical compositions of some *Trigonella* species (*T. kotschyi*, *T. filipes*, *T. cilicica*, *T. strangulata* and *T. rhytidocarpa*) and their amino acid compositions have also been investigated (8-10). In this study, it was aimed to investigate, for the first time, the amino acid profile of three different *Trigonella* species (*T. cylindracea* Desv., *T. mesopotamica* Hub.-Mor. and *T. smyrnea* Boiss.) collected from their natural habitats.

2. MATERIALS AND METHODS

2.1. Chemicals

In this study, most of the analytes were obtained from Sigma-Aldrich (St. Louis, MO, USA) except for acetonitrile, ammonium acetate, sodium hydroxide, ethanol, acetic acid, and hydrochloric acid were purchased from Merck (Darmstadt, Germany). All aqueous solutions were prepared with doubly distilled water obtained from Milli-Q System (Millipore, Bedford, MA, USA). During hydrolysis and sample preparation extra-pure nitrogen was used.

2.2. Plant Materials

T. cylindracea, *T. mesopotamica* and *T. smyrnea* were collected from different regions of Turkey (Table 1). Voucher specimens were identified by Prof. Dr. Ahmet İLÇİM (Department of Biology, Faculty of Sciences and Arts, Mustafa Kemal University, Antakya, Hatay, TURKEY) and Assist. Prof. Dr. Ş. Selma URAS GÜNGÖR (Department of Pharmacognosy, Faculty of Pharmacy, Mersin University, Mersin, TURKEY) and stored in the Herbarium of the Faculty of Sciences and Arts, Mustafa Kemal University.

Table 1: Localities and voucher numbers of the studied *Trigonella* species.

Species	Localities	Voucher number
T. cylindracea Desv.	C4 Içel:Tömük, 0-20 m, Ş.S.Uras Güngör	MKU1755
T. mesopotamica Hub.-Mor.	C6 Kahramanmaraş:Çağlayancerit, 1300-1500 m, Ş.S.Uras Güngör, A. İlçim	MKU1754
T. smyrnea Boiss.	C2 Antalya:Gömbe, 1150 m, Ş.S.Uras Güngör	MKU1782

2.3. Amino Acid Analysis

Acid hydrolysis and derivatization of proteins for the determination of 16 amino acids, including aspartic acid, serine, glutamic acid, glycine, histidine, arginine, alanine, threonine, lysine, leucine, proline, tyrosine, isoleucine, valine, phenylalanine, and methionine from seeds of *Trigonella* species were performed with a minor modification to the method reported by Eroglu et al., (2016) (11). The powdered seeds (0.1-1 g) were dissolved in HCl (6 M, 20 mL) in hydrolysis tubes and hydrolyzed for 24 hours at 110 °C in an oven under nitrogen atmosphere. The mixture was then allowed to cool to room temperature. Immediately after protein hydrolysis, precolumn derivatization with phenylisothiocyanate was used. Dry samples were dissolved in 20 µL of ethanol:water:triethylamine (2:2:1) and then dried under vacuum. Finally, derivatization was performed using 20 µL of derivatization reagent [ethanol: water: triethylamine: phenylisothiocyanate (7:1:1:1)] for 20 minutes at room temperature, then the reagent was separated under vacuum at 45 °C. Derivatized samples were dissolved in 0.1 mL of 0.14 M sodium acetate and adjusted to pH 6.4 with dilute acetic acid.

Alkaline hydrolysis to determine tryptophan was performed according to the method reported by Cevikkalp et al., (2016) (12). A standard stock solution of tryptophan (100 µg/mL) was prepared with water (pH 6.3) and stored in the dark at 4 °C for up to one month. The powdered seeds (0.1-1 g) were dissolved with 20 mL of 5 N NaOH under nitrogen atmosphere. After the mixture was hydrolyzed in an oven at 120 °C for 12 hours, the hydrolysates were cooled to room temperature and adjusted to pH 6.3 using diluted HCl. The Prominence ultra-fast liquid chromatography system (Shimadzu, Tokyo, Japan) equipped with a binary pump and UV/Vis detectors were used for analysis. A reversed phase analytical column [Shim-pact XR-ODS (75 mm x 3.0 mm i.d.)] with a fluorescence detector was used for separation and detection. The analysis conditions were as follows; mobile phase A: 10 mmol/L (potassium phosphate buffer (pH: 7.0), mobile phase B: acetonitrile [5% (0 to 0.3 minutes), 5% to 40% (0.3 to 3.4 minutes) min)], 40 °C column temperature, 1.2 mL/min flow rate, 1 µL injection volume. The amount of amino acids was presented as mg of amino acid/100 g of dry sample.

3. RESULTS AND DISCUSSION

The amino acid compositions of the studied species (*T. cylindracea*, *T. mesopotamica*, *T. smyrnea*) are presented in Table 2. The presence of various essential amino acids (histidine, isoleucine, leucine, lysine, methionine, phenylalanine,

threonine, valine, arginine, and tryptophan) and non-essential amino acids (alanine, aspartic acid, glycine, glutamic acid, proline, serine and tyrosine) has been demonstrated in the studied seeds.

It was determined that the amounts of lysine, isoleucine, arginine, aspartic acid, and glutamic acid in the seeds of all three species were higher than the other amino acids. Among the essential amino acids, lysine was found at the highest rate in all three species. The highest amount of lysine was found in the seeds of *Trigonella mesopotamica*, followed by the seeds of *Trigonella cylindracea* and *Trigonella smyrnea* (3352±0.02 mg/100 g, 3059±0.03 mg/100 g and 2947±0.04 mg/100 g, respectively). Arginine and isoleucine content of *Trigonella cylindracea*, *Trigonella mesopotamica,* and *Trigonella smyrnea* seeds were 2599±0.02 mg/100 g, 3264±0.03 mg/100 g, 2203±0.05 mg/100 g, and 2283±0.02 mg/100 g, 2679±0.05 mg/100 g, and 2401±0.03 mg/100 g, respectively. Among the non-essential amino acids, glutamic acid was determined at the highest rate in all three species. The highest amount of glutamic acid was found in the seeds of *Trigonella mesopotamica*, followed by the seeds of *Trigonella cylindracea* and *Trigonella smyrnea* (5888±0.15 mg/100 g, 4819±0.12 mg/100 g, and 4146±0.11 mg/100 g, respectively). This was followed by the aspartic acid and proline (Table 2).

Table 2: Amino acid composition of *T. cylindracea*, *T. mesopotamica* and *T. smyrnea* seeds.

Amino acid	Symbol	*T. cylindracea* mg/100 g	*T. mesopotamica* mg/100 g	*T. smyrnea* mg/100 g
Essential amino acids				
Histidine	HIS	981±0.04	1384±0.02	1192±0.05
Isoleucine	ILE	2283±0.02	2679±0.05	2401±0.03
Leucine	LEU	966±0.03	1145±0.04	1093±0.02
Lysine	LYS	3059±0.03	3352±0.02	2947±0.04
Methionine	MET	195±0.02	328±0.02	372±0.01
Phenylalanine	PHE	1431±0.04	1640±0.03	1451±0.02
Threonine	THR	789±0.02	960±0.01	968±0.01
Valine	VAL	1136±0.03	1350±0.04	1339±0.03
Arginine	ARG	2599±0.02	3264±0.03	2203±0.05
Tryptophan	TRP	314±0.02	334±0.03	312±0.01
Non-essential amino acids				
Alanine	ALA	1181±0.01	1409±0.02	1316±0.04
Aspartic acid	ASP	2305±0.09	2802±0.08	1343±0.05
Glycine	GLY	1588±0.02	1905±0.06	1679±0.02
Glutamic acid	GLU	4819±0.12	5888±0.15	4146±0.11
Proline	PRO	1778±0.02	2279±0.06	1958±0.05
Serine	SER	1197±0.03	1383±0.04	1271±0.03
Tyrosine	TYR	846±0.01	980±0.01	1018±0.04

Data presented as mean±SD (n=3).

Feyzi et al. (2015) studied fenugreek protein isolate. They found that high quantities of glutamic acid (199.80 g/kg), aspartic acid (116.80 g/kg), leucine (93.70 g/kg), threonine (80.01 g/kg), and arginine (75.70 g/kg) were observed in fenugreek protein isolate (13). Aljuhaimi et al. (2018) investigated amino acid compositions of *T. foenum-graecum* seeds from India, Saudi Arabia, Yemen, and Turkey. Those results showed that major amino acids were determined as glutamic acid (3.79-4.82 % w/w), aspartic acid (2.65-3.31 % w/w), arginine (2.45-3.26 % w/w), leucine (1.67-2.09 % w/w), and lysine (1.63-1.95 % w/w) (14). In another study conducted by our group, the amino acid compositions of *T. kotschyi*, *T. filipes* and *T. cilicica* seeds were studied, and it was determined that the amounts of leucine, lysine, aspartic acid and glutamic acid in the seeds of all three species were higher than the other amino acids (8). As a result of amino acid analysis of *T. strangulata* seeds, it was found that the amounts of lysine (2482 mg/100 g), arginine (2244 mg/100 g), and leucine (2053 mg/100 g) were higher than other amino acids (9). In the amino acid composition study conducted on *T. rhytidocarpa* seeds, we found that the amounts of glutamic acid, lysine and arginine were 5116 mg/100 g, 4278 mg/100 g, and 4001 mg/100 g, respectively (10). Yasothai (2021) studied amino acid composition of fenugreek seeds from Indian samples and found that the major amino acids were

determined as histidine (2.08 g/100 g), leucine (1.53 g/100 g), glycine (1.21 g/100 g) and lysine (1.13 g/100 g) (15). Our results for the studied seeds were quite similar to the report by Gungor et al. (10) with some quantitative differences.

4. CONCLUSION

Glutamic acid was the major amino acid in the seeds of *T. cylindracea*, *T. mesopotamica* and *T. smyrnea*. It is an acidic type of an amino acid that helps in the synthesis of glutathione. Glutamic acid, a multifunctional amino acid, is involved in excitatory neurotransmission and taste perception. It also plays an important role in the gastric phase of digestion by increasing gastric exocrine secretion when consumed with food (3, 16). As a result, the amino acid compositions of the studied species were determined for the first time in this study. It is thought that further research should be done for these species to be considered as nutritional food and for their possible biological activities.

5. ACKNOWLEDGMENTS

The authors gratefully acknowledge to TÜBİTAK Marmara Research Center. The author also thanks Prof. Dr. Ahmet İLÇİM (Department of Biology, Faculty of Sciences and Arts, Mustafa Kemal University, Antakya, Hatay, TURKEY) for the determination of the plant.

6. REFERENCES

1. Salma S, Suraby K, Ramakrishnan L. Antioxidant Analysis and Phytochemical Detection of the Some Selected Spices (Ajwain, Coriander, Cumin, Fennel, Fenugreek). Research journal of pharmaceutical biological and chemical sciences. 2017;8(6):78–84.

2. Özkan G, Göktürk RS, Kıralan M, Ramadan MF. Fatty acids and tocopherols of Turkish Salvia fruticose, Salvia tomentosa, Stachys aleurites and Stachys cretica subsp. anatolica seed oils. La rivista Italiana delle sostanze grasse. 2018;XCV(Ge/Ma).

3. Akram M, Asif H, Uzair M, Akhtar N, Madni A, Shah SA, et al. Amino acids: A review article. Journal of medicinal plants research. 2011;5(17):3997–4000.

4. Akan H, EkïCï M, Aytaç Z. The synopsis of the genus Trigonella L. (Fabaceae) in Turkey. Turk Journal of Botany. 2020 Nov 30;44(6):670–93. Available from: <URL>.

5. Żuk-Gołaszewska K, Wierzbowska J, Żuk-Gołaszewska K. Fenugreek: productivity, nutritional value and uses. Journal of Elementology [Internet]. 2017 Jun 6 [cited 2023 Mar 20];(3/2017). Available from: <URL>.

6. Wani SA, Kumar P. Fenugreek: A review on its nutraceutical properties and utilization in various food products. Journal of the Saudi Society of Agricultural Sciences. 2018 Apr;17(2):97–106. Available from: <URL>.

7. Srinivasan K. Fenugreek (*Trigonella foenum-graecum*): A Review of Health Beneficial Physiological Effects. Food Reviews International. 2006 Jul;22(2):203–24. Available from: <URL>.

8. Uras G, Kokdil G. Phytochemical screening and antioxidant activity of Trigonella cariensis seeds. Botanica Serbica. 2022;46(2):209–16. Available from: <URL>.

9. Selma UGS, Gamze K. Tocopherol, sterol and amino acid compositions of Trigonella strangulata Boiss. seeds. International Research Journal of Pharmacy and Medical Sciences (IRJPMS). 2018;2(1):36–9.

10. Gungor SSU, Guzel S, Ulger M, Kokdil G. Chemical Composition and Antioxidant and Antimicrobialactivities of Turkish Endemic Trigonella rhytidocarpa Seeds. Chemistry of Natural Compounds. 2021 Jan;57(1):136–40. Available from: <URL>.

11. Eroglu N, Akkus S, Yaman M, Asci B, Silici S. Amino Acid and Vitamin Content of Propolis Collected by Native Caucasican Honeybees. Journal of Apicultural Science. 2016 Dec 1;60(2):101–10. Available from: <URL>.

12. Çevikkalp SA, Löker GB, Yaman M, Amoutzopoulos B. A simplified HPLC method for determination of tryptophan in some cereals and legumes. Food Chemistry. 2016 Feb;193:26–9. Available from: <URL>.

13. Feyzi S, Varidi M, Zare F, Varidi MJ. Fenugreek (*Trigonella foenum graecum*) seed protein isolate: extraction optimization, amino acid composition, thermo and functional properties: Extraction optimization of fenugreek seed protein. Journal of the Science of Food and Agriculture. 2015 Dec;95(15):3165–76. Available from: <URL>.

14. Aljuhaimi F, Şimşek Ş, Özcan MM, Ghafoor K, Babiker EE. Effect of location on chemical properties, amino acid and fatty acid compositions of fenugreek (*Trigonella foenum-graecum* L.) seed and oils. Journal of Food Processing and Preservation. 2018 Apr;42(4):e13569. Available from: <URL>.

15. Yasothai R. Fatty acid composition of fenugreek (Trigonella foenum-graecum L.) seed and Galactomannan depleted fenugreek residue. The Pharma Innovation Journal. 2021;10(7):1509–11.

16. Zareian M, Ebrahimpour A, Bakar FA, Mohamed AKS, Forghani B, Ab-Kadir MSB, et al. A Glutamic Acid-Producing Lactic Acid Bacteria Isolated from Malaysian Fermented Foods. International Journal of Molecular Sciences. 2012 May 7;13(5):5482–97. Available from: <URL>.

JOTCS A
Journal of the Turkish Chemical Society
Section: A
Chemistry
TURKISH CHEMICAL SOCIETY

Molecular docking studies and biological activities of benzenesulfonamide-based thiourea and thiazolidinone derivatives targeting cholinesterases, α-glucosidase, and α-amylase enzymes

Mehtap Tugrak Sakarya[1*], Halise Inci Gul[2], Cem Yamali[3], Parham Taslimi[4], and Tugba Taskin Tok[5,6]

[1]Gaziosmanpasa University, Department of Pharmaceutical Chemistry, Tokat, Turkey.
[2]Ataturk University, Department of Pharmaceutical Chemistry, Erzurum, Turkey.
[3]Cukurova University, Department of Basic Pharmaceutical Sciences, Adana, Turkey.
[4]Bartin University, Department of Biotechnology, Faculty of Science, Bartin, Turkey.
[5]Gaziantep University, Department of Chemistry, Gaziantep, Turkey.
[6]Gaziantep University, Department of Bioinformatics and Computational Biology, Gaziantep, Turkey.

Abstract: Alzheimer's disease (AD) and diabetes mellitus (DM) are related to abnormal changes in enzyme activity. While acetylcholinesterase (AChE) and butyrylcholinesterase (BChE) are the primary targets in the treatment of Alzheimer's disease (AD), α-glucosidase (α-Gly) and α-amylase (α-Amy) enzymes are known for diabetes mellitus (DM). Here, benzenesulfonamide-based thiourea and thiazolidinone derivatives such as AChE, BChE, α-Gly, and α-Amy inhibitors were reported. The results revealed that compounds **1d** and **2c** showed promising AChE and BChE inhibition effects. Compound **2a** was the most potent inhibitor against α-glycosidase and α-amylase, respectively. Molecular docking studies indicated that the lead compounds' binding energy values and molecular interactions were better than that of tacrine and acarbose. The most bioactive compounds may be considered potent leads for further studies.

Keywords: Thiazolidinone, Benzamide, 'Alzheimer's disease, Diabetes Mellitus, Molecular Docking, Synthesis

Submitted: May 8, 2022. **Accepted:** October 26, 2022.

Cite this: Tugrak Sakarya M, Gul HI, Yamali C, Taslimi P, Taskin Tok T. Molecular docking studies and biological activities of benzenesulfonamide-based thiourea and thiazolidinone derivatives targeting cholinesterases, α-glucosidase, and α-amylase enzymes. JOTCSA. 2023;10(2):385-424

DOI: https://doi.org/10.18596/jotcsa.1111172

***Corresponding author's E-mail:** mehtaptugrak@hotmail.com

1. INTRODUCTION

Alzheimer's disease (AD) is a neurodegenerative disease in the elderly worldwide characterized by degeneration of cholinergic neurons in the brain. Decreased cholinergic signal transmission leads to some cognitive dysfunctions during the progression of the disease (1). Based on the cholinergic approach, acetylcholinesterase (AChE) and butyrylcholinesterase (BChE) enzymes are considered therapeutic targets of AD (2). Presently, the most used anti-AD drugs in the clinic are AChE inhibitors such as donepezil, rivastigmine, and galantamine (3, 4) (Figure 1). AChE inhibitors interact mainly on the active catalytic site (CAS) below AChE (3). This situation may relieve the symptoms of patients with mild to moderate. However, recent studies have demonstrated that the peripheral active site (PAS) is closely related to the neurotoxic cascade of AD. Therefore, dual interactions with CAS and PAS sites lead to favorable AChE inhibitory activity (3).

Diabetes has become a severe health problem globally since 425 million people have diabetes, and it is expected to reach approximately 700 million by 2045 (5). Type 2 diabetes (T2D, not insulin-dependent) affects 85-90% of the entire diabetic population (6). The most effective way to prevent T2D is to inhibit starch hydrolysis from slowing glucose absorption in starchy foods. Alpha (α)-amylase and alpha (α)-glucosidase is two main

hydrolytic enzymes that have a role in this process (7, 8). Acarbose is the oral glucose-lowering drug used in the treatment that delays glucose absorption. Despite acarbose being a popular glucose-lowering drug, it causes severe side effects such as liver disorders, diarrhea, flatulence, and abdominal cramps (9, 10). In addition, glibenclamide, gliquidone, rosiglitazone, and pioglitazone are widely used for the initial treatment of T2D (Figure 1) (11-14). Using these hypoglycemic agents may lead to gastrointestinal reactions, skin allergies, and hypoglycemia (11, 12). Therefore, discovering novel and effective drug candidates for treating diabetes without causing side effects is needed.

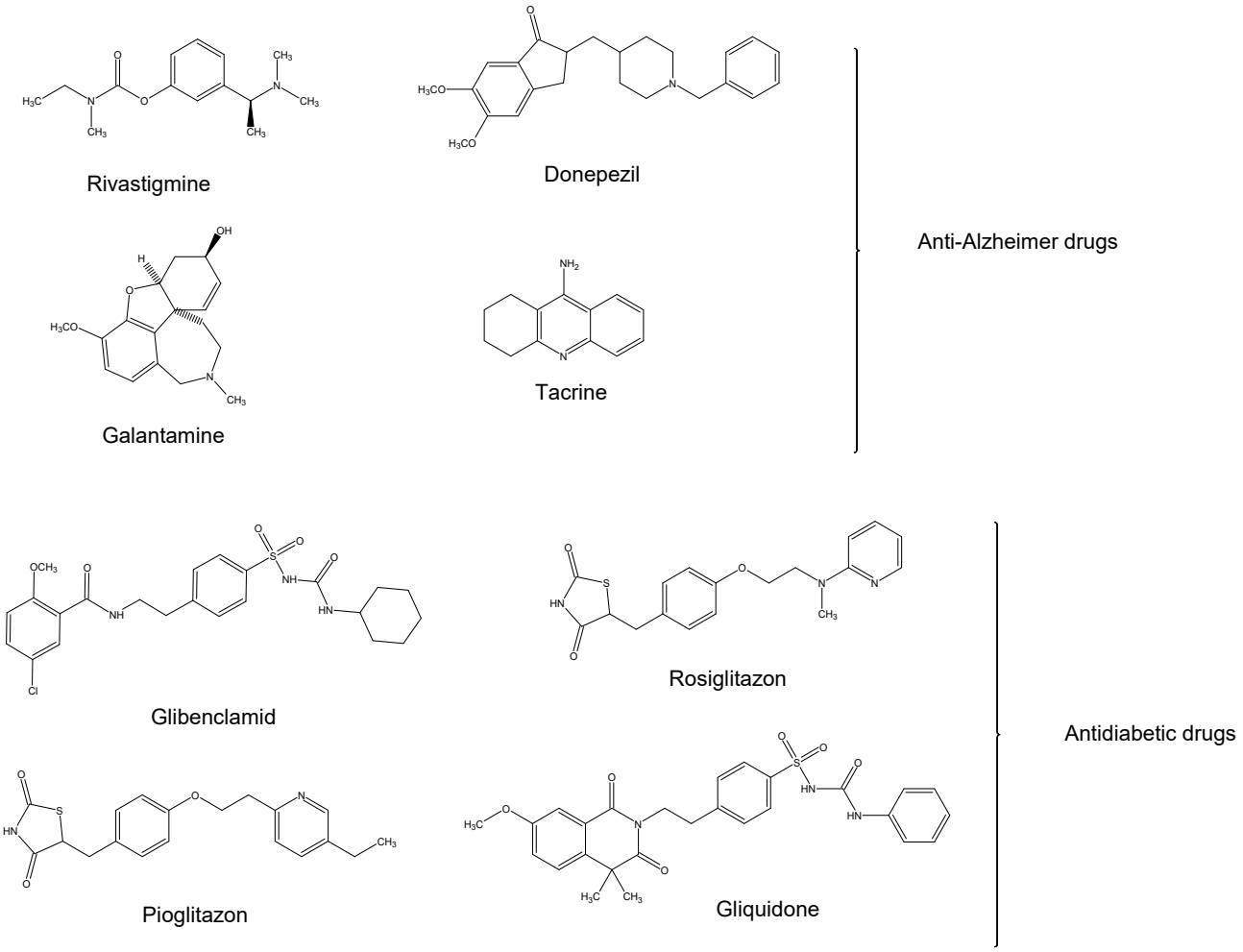

Figure 1: Commonly used drugs in Alzheimer's disease (up) and diabetes mellitus (down)

Clinical studies have shown that diabetes increases the risk of AD. Diabetes patients have 1.5-2 times more risk of having AD than healthy people (15-17). Clinical studies point out that both diseases have common pathological mechanisms to exacerbate neurodegeneration in the brain. Relationships between diabetes and AD have been studied in detail, and studies have reported that hyperglycemia, vascular damage, hypoglycemia, and insulin resistance are among the most likely pathophysiological causes (18-20). In addition, in both diseases, oxidative stress, vascular dysfunctions, amyloidogenesis, and disorders in glucose and fatty acid metabolism occur, and oxidatively modified proteins accumulate (21, 22). In addition, neuropathological markers of AD such as APP, Aβ, and phosphatase increased in using both T1D and T2D model transgenic rats; on the other hand, intracellular components in the insulin receptor pathway such as phospho AKT (protein kinase B), phospho glycogen synthase kinase-3β (GSK3β) have been shown to decrease (20). Hypothetical models are suggested that diabetes mellitus induces AD pathology and cognitive dysfunction (23).

Thiazolidinone derivatives show a wide range of biological activities such as anti-Alzheimer, antidiabetic, antibacterial, anticancer, and antitubercular (24-26). Recently, the effect of thiazolidinone analogs as a muscarinic receptor 1 (M1) agonist in Alzheimer's dementia models were reported. Based on the results obtained, derivative **1** (Figure 2), which has the diphenylamine moiety attached to the nitrogen of the thiazolidinone, showed a significant affinity for M1 receptor binding (1). In another study, thiazole-based compounds were reported as AChE inhibitors at the nanomolar level. According to the study, compounds **2** (Figure 2) and **3** (Figure 2) could be considered potent AChE inhibitors with IC_{50} values of 103.24 nM and 108.94

nM. The thiazole core was also reported as an important moiety having promising interactions with the active site of AChE (27).

Primary and secondary sulfonamide derivatives are valuable compounds with different biological activities in drug discovery. Markowicz-Piaseckaa et al. (28) reported the effects of sulfonamide derivatives of metformin on both AChE, BuChE activity, and β-amyloid aggregation. Compound **4** (Figure 2) inhibited AChE in a mixed-type manner at micromolar concentrations (IC_{50}=212.5 ± 48.3 μmol/L). Compound **4** also inhibited Aβ aggregation at 200 μmol/L (28). Our studies also indicated that sulfonamide-based compounds could be considered potent and selective cholinesterase inhibitors. In our previous study, 4-(3-(difluorophenyl)-5-(dimethoxyphenyl)-4,5-dihydropyrazol-1-yl) benzenesulfonamides (**5-12**) (Figure 2) inhibited AChE enzyme in the range of 3.28 ± 1.47 – 9.77 ± 1.86 nM (29). AChE inhibition and molecular docking studies showed that pyrazole-based benzenesulfonamide derivative **13** (Figure 2) also showed a good inhibitory effect with a Ki value of 22.713 ± 10.33 nM (30).

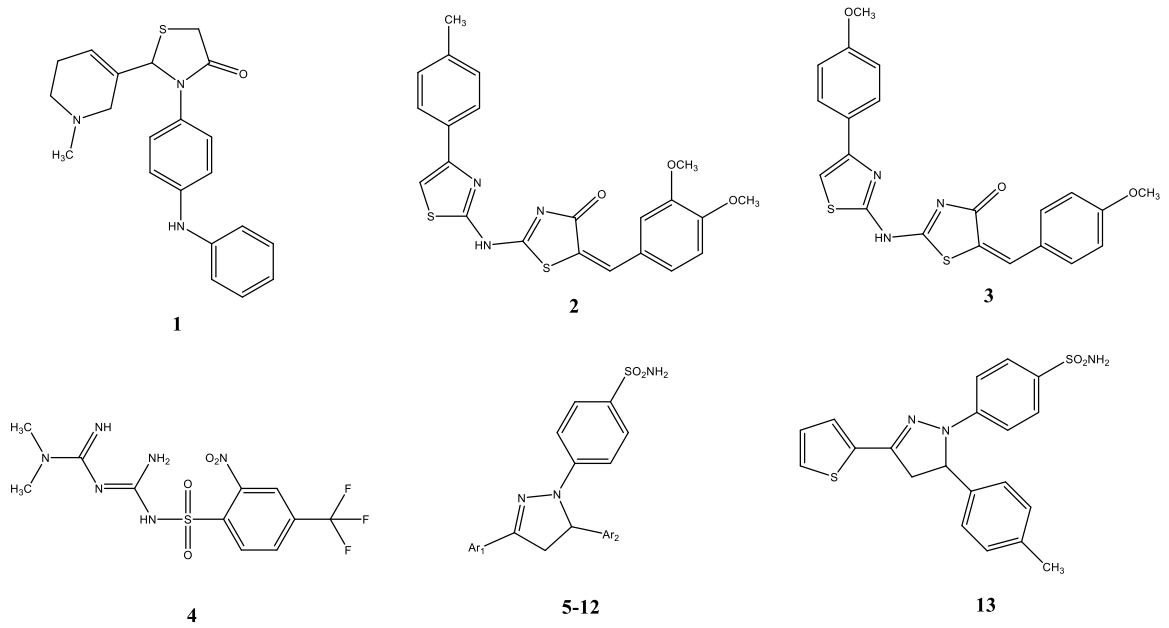

Figure 2: Structures of the compounds **1-13**

Based on the reports, we synthesized thiazolidinone derivatives (Figure 3) to evaluate their *in vitro* biological effects on AChE, BChE, α-Amy, and α-Gly enzymes. Moreover, docking studies were carried out on the most potent compounds to predict the binding poses to the enzymes studied.

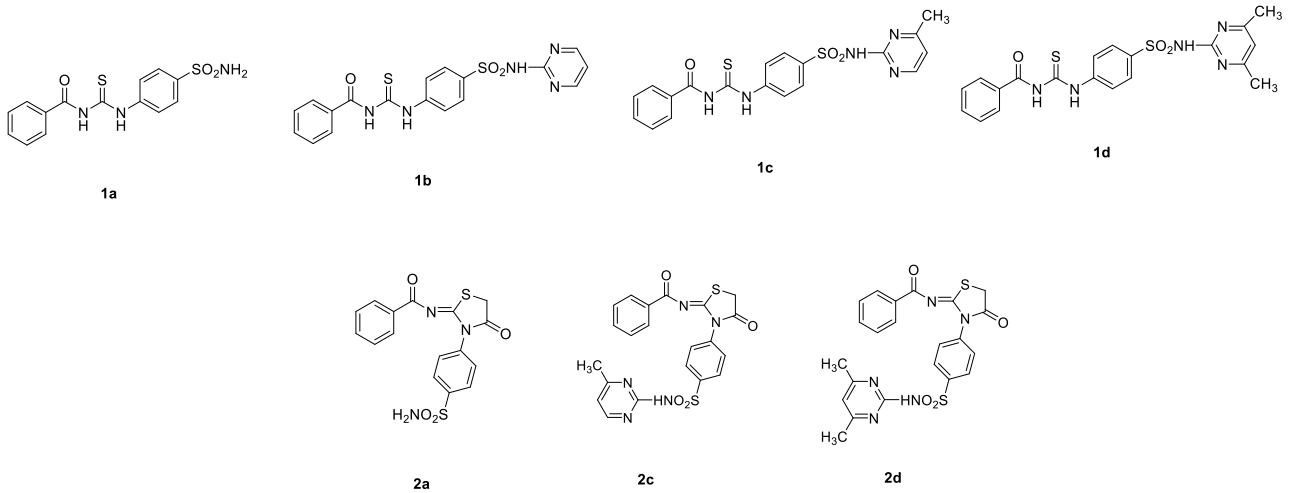

Figure 3: Chemical structures of the thiazolidinone derivatives **1a-d, 2a, 2c, 2d**

2. EXPERIMENTAL SECTION

2.1. Chemistry

^{1}H NMR (400 MHz) and ^{13}C NMR (100 MHz) spectra in DMSO-d_6 (Merck) were taken using a Varian Mercury Plus spectrometer, Varian Inc., Palo Alto, California, US A liquid chromatography ion trap-time of flight tandem mass spectrometer (Shimadzu, Kyoto, Japan) was used to get Mass spectra (HRMS) for the compounds. Data analysis was done by 'Shimadzu's LCMS Solution software. 9100/IA9100 instrument (Bibby Scientific Limited, Staffordshire, UK) was used to determine melting points. Reactions were monitored by Thin Layer Chromatography (TLC) using silica gel HF254 (Merck Art 5715).

2.2. General synthesis procedure of 1a-d, Figure 4

The thiourea substituted derivatives **1a-d** used as a starting compound were synthesized previously, and all chemistry details were given in the literature (31).

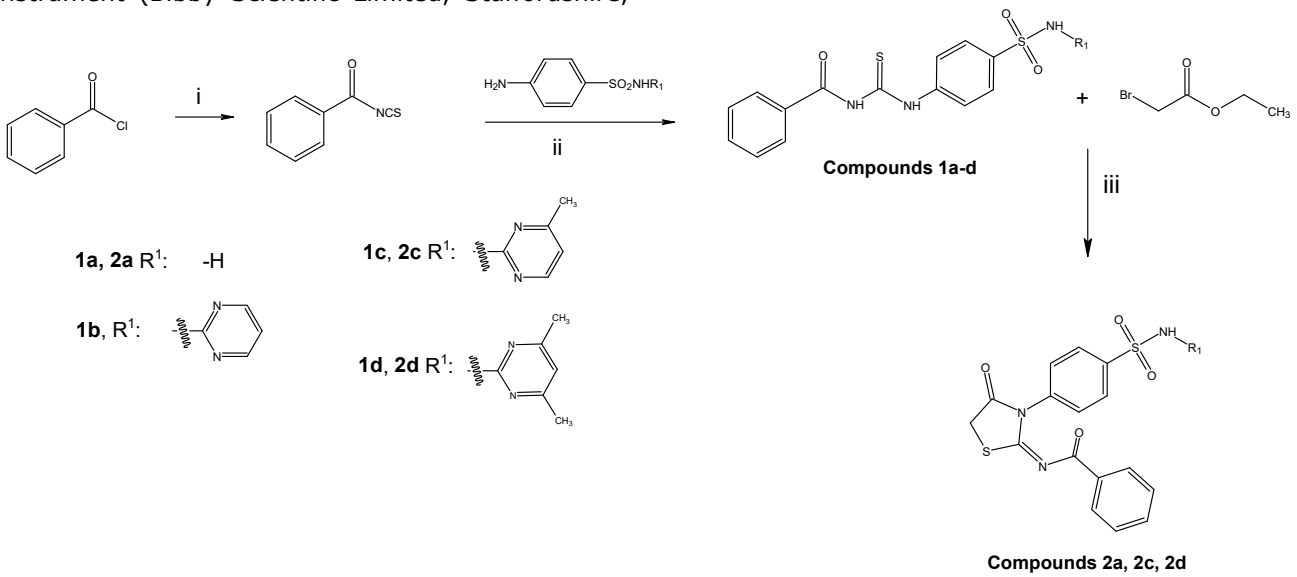

Reaction conditions: (i) KSCN, acetone, reflux, 1.5 hours; (ii) acetone, reflux, 4-8 hours; (iii) ethyl bromoacetate, EtOH, reflux, 15-24 hours

Figure 4: Synthesis of the compounds **1a-d, 2a, 2c, 2d.**

*N-[(4-Sulfamoylphenyl)carbamothioyl]benzamide (**1a**)*

White-colored solid, mp: 234-236°C, yield 86 %. ^{1}H NMR (DMSO-d_6, ppm, 400 MHz), δ 12.72 (s, 1H, NH), 11.70 (s, 1H, NH), 8.00-7.98 (m, 2H, Ar-H), 7.93-7.85 (m, 4H, Ar-H), 7.70-7.66 (m, 1H, Ar-H), 7.57-7.53 (m, 2H, Ar-H), 7.41 (s, 2H, NH_2); ^{13}C NMR (DMSO-d_6, ppm, 100 MHz) δ 179.9 (C=S), 168.7 (C=O), 141.8, 141.4, 133.7, 132.5, 129.2, 128.9, 126.7, 124.8; HRMS (ESI-MS) $C_{14}H_{13}N_3O_3S_2$, Calculated $[M-H]^-$: 334.0326; Found $[M-H]^-$: 334.0330.

*N-{[4-(N'-(Pyrimidin-2-yl)sulfamoyl)phenyl]carbamothioyl}benzamide (**1b**)*

Light cream-colored solid, mp: 250-252°C, yield 88 %. ^{1}H NMR (DMSO-d_6, ppm, 400 MHz), δ 12.75 (s, 1H, NH), 11.70 (s, 1H, NH), 8.54-8.52 (m, 2H, Ar-H), 8.03-7.97 (m, 7H, Ar-H, NH), 7.69-7.65 (m, 1H, Ar-H), 7.56-7.52 (m, 2H, Ar-H), 7.08-7.05 (m, 1H, Ar-H); ^{13}C NMR (DMSO-d_6, ppm, 100 MHz) δ 179.7 (C=S), 168.6 (C=O), 158.9, 157.3, 142.3, 137.8, 133.7, 132.5, 129.2, 128.9, 128.7, 124.3, 116.3; HRMS (ESI-MS) $C_{18}H_{15}N_5O_3S_2$, Calculated $[M+Na]^+$: 436.0509; Found $[M+Na]^+$: 436.0502.

*N-{[4-(N'-(4-Methylpyrimidin-2-yl)sulfamoyl)phenyl]carbamothioyl}benzamide (**1c**)*

Light white-colored solid, mp: 231-232°C, yield 80 %. ^{1}H NMR (DMSO-d_6, ppm, 400 MHz), δ 12.75 (s, 1H, NH), 11.69 (s, 1H, NH), 8.35-8.33 (m, 1H, Ar-H), 8.03-7.94 (m, 7H, Ar-H, NH), 7.68-7.65 (m, 1H, Ar-H), 7.56-7.53 (m, 2H, Ar-H), 6.92-6.91 (m, 1H, Ar-H), 2.33 (s, 3H, CH_3); ^{13}C NMR (DMSO-d_6, ppm, 100 MHz) δ 179.7 (C=S), 168.6 (C=O), 158.7, 157.2, 156.9, 142.1, 138.0, 133.7, 132.5, 129.2, 128.9, 124.1, 23.7; HRMS (ESI-MS) $C_{19}H_{17}N_5O_3S_2$, Calculated $[M+H]^+$: 428.0846; Found $[M+H]^+$: 428.0834.

*N-{[4-(N'-(4,6-Dimethylpyrimidin-2-yl)sulfamoyl)phenyl]carbamothioyl}benzamide (**1d**)*

White-colored solid, mp: 216-218°C, yield 84 %. ^{1}H NMR (DMSO-d_6, ppm, 400 MHz), δ 12.74 (s, 1H, NH), 11.69 (s, 1H, NH), 8.03-7.92 (m, 7H, Ar-H), 7.68-7.64 (m, 1H, Ar-H), 7.56-7.52 (m, 2H, Ar-H), 6.76 (s, 1H, NH), 2.26 (s, 6H, CH_3); ^{13}C NMR (DMSO-d_6, ppm, 100 MHz) δ 179.2 (C=S), 168.1 (C=O), 158.9, 157.2, 156.0, 142.3, 141.4, 133.2, 132.0, 128.69, 128.66, 128.4, 123.4, 22.7; HRMS (ESI-MS) $C_{20}H_{19}N_5O_3S_2$, Calculated $[M+H]^+$: 442.1002; Found $[M+H]^+$: 442.1006.

2.3. General procedure for the synthesis of iminothiazolidinone-sulfonamide hybrids 2a, 2c, 2d, Figure 4

To a stirred solution of thiourea substituted derivatives (**1a-d**) (0.5 mmol) in ethanol (10 mL) were added the ethyl bromoacetate (0.05 mL, 0.5 mmol) and sodium acetate (0.09 g, 1 mmol). The

reaction mixture was refluxed for 15–24 h, and the progress of the reaction was monitored by TLC. On completion, the precipitates formed were filtered and recrystallized from ethanol to afford the products (**2a**, **2c**, **2d**).

*N-(4-oxo-3-(4-sulfamoylphenyl)thiazolidin-2-ylidene)benzamide (**2a**)*

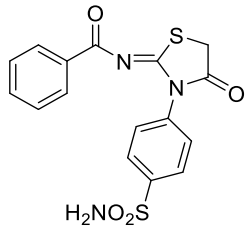

Light white-colored solid, mp: 269-271°C, yield 70 %. ^{1}H NMR (DMSO-d_6, ppm, 400 MHz), δ 8.09 (d, 2H, Ar-H, *J*= 8.5 Hz), 7.84 (d, 2H, Ar-H, *J*= 8.3 Hz), 7.70–7.20 (m, 5H, Ar-H), 6.65 (s, 2H, SO_2NH_2), 4.20 (s, 2H, thiazolidinone); ^{13}C NMR (DMSO-d_6, ppm, 100 MHz) δ175.3 (C=O), 174.0 (C=O), 173.3 (C=N),144.2, 143.3, 138.0, 134.2, 132.3, 129.3, 128.0, 126.2, 33.8; HRMS (ESI-MS) $C_{16}H_{13}N_3O_4S_2$, Calculated $[M+H]^+$: 376.0347; Found $[M+H]^+$: 376.04215.

*N-{3-[4-(N-(4-methylpyrimidin-2-yl)sulfamoyl)phenyl]-4-oxothiazolidin-2-ylidene}benzamide (**2c**)*

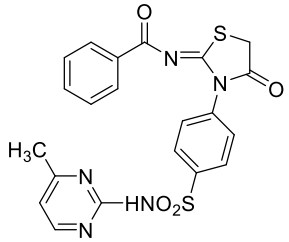

Cream-colored solid, mp: 261-262°C, yield 60 %. ^{1}H NMR (DMSO-d_6, ppm, 400 MHz), δ 8.34 (d, 1H, Ar-H, *J*= 5.1 Hz), 8.15 (d, 2H, Ar-H, *J*= 8.4 Hz), 7.82-7.77 (m, 2H, Ar-H), 7.64 (d, 2H, Ar-H, *J*= 8.4 Hz), 7.57-7.53 (m, 2H, Ar-H), 7.37-7.34 (m, 2H, Ar-H), 6.91 (s, 1H, SO_2NH), 4.14 (s, 2H, thiazolidinone), 2.28 (s, 3H, CH_3); ^{13}C NMR (DMSO-d_6, ppm, 100 MHz) δ 176.7 (C=O), 174.6 (C=O), 173.4 (C=N), 157.9, 157.2, 141.9, 139.1, 135.5, 134.0, 129.9, 129.3, 129.2, 129.1, 114.9, 34.3, 23.8; HRMS (ESI-MS) $C_{21}H_{18}N_5O_4S_2$, Calculated $[M+H]^+$: 468.0722; Found $[M+H]^+$: 468.0777.

*N-{3-[4-(N-(4,6-dimethylpyrimidin-2-yl)sulfamoyl)phenyl]-4-oxothiazolidin-2-ylidene}benzamide (**2d**)*

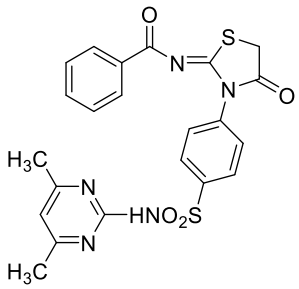

Cream-colored solid, mp: 259-260°C, yield 65 %. ^{1}H NMR (DMSO-d_6, ppm, 400 MHz), δ 8.14 (d, 2H, Ar-H, *J*= 8.4 Hz), 7.79 (d, 2H, Ar-H, *J*= 8.1 Hz), 7.64-7.53 (m, 4H, Ar-H), 7.37-7.34 (m, 2H, Ar-H), 6.75 (s, 1H, SO_2NH), 4.14 (s, 2H, thiazolidinone), 2.23 (s, 6H, CH_3); ^{13}C NMR (DMSO-d_6, ppm, 100 MHz) δ 176.8 (C=O), 174.6 (C=O),173.4 (C=N),156.6, 142.3, 138.8, 135.5, 133.9, 129.8, 129.3, 129.2, 129.1, 34.3, 23.3; HRMS (ESI-MS) $C_{22}H_{19}N_5O_4S_2$, Calculated $[M+H]^+$: 482.0878; Found $[M+H]^+$: 482.09463.

2.4. Pharmacological/biological assays

2.4.1. Acetylcholinesterase and Butyrylcholinesterase inhibition studies

The inhibition effects of the compounds on AChE and BChE enzymes, which were obtained from Electrophorus electricus and equine serum, were performed according to literature (32, 33). Also, acetylthiocholineiodide (AChI) / butyrylthiocholine iodide (BChI) and 5,5′-dithiobis(2-nitrobenzoicacid) (DTNB)were used as substrates for cholinergic reactions (34). Briefly, 0.1 mL of Tris/HCl buffer (pH 8.0, 1.0 M) and different volumes of the compounds solutions. Then, 50 µL of AChE/BChE (5.32×103EU) was transferred to the solutions and incubated for 15 min at room temperature. After this short incubation period, 50 µL of DTNB (0.5 mM) was added, and the reaction started with the addition of 50 µL of AChI/BChI (10 mM). The formation of yellow-colored 5-thio-2-nitrobenzoate anion spectrophotometrically measured the enzymatic hydrolysis as the result of the reaction of DTNB with thiocholine at a wavelength of 412 nm. Also, one AChE unit is the quantity of AChE, which hydrolyses 1.0 mol of AChI to choline(Ch) and acetate per minute at pH 8.0 at 37°C. Similarly, one BChE unit is the quantity of BChE, which hydrolyze s1.0 mol of BChI to Ch and butyrate per min at pH 8.0 at 37°C (35).

2.4.2. α-Glycosidase inhibition studies

α-Glycosidase inhibition effect of the compounds was made according to the method of Tao et al. (36). *p*-Nitrophenyl-D-glucopyranoside (p-NPG) was used as substrate. First, 75 µL of phosphate buffer solution (5 mM, pH 7.4) was added to 20 µL of *α*-glycosidase solution (0.15EU/mL), which was prepared in phosphate buffer (pH 7.4, 5 mM) and 5 µLof different concentrations of the compounds. Then, it was preincubated at 35°C for 10 min before adding *p*-NPG to initiate the reaction. Also, 20 µL of *p*-NPG was transferred in phosphate buffer (pH 7.4, 5 mM) after a short incubation period at 35°C. The absorbances were measured at 405 nm. One *α*-glycosidase unit is the quantity of enzyme that catalyzes the hydrolysis of 1.0 mol *p*-NPG per minute at pH 7.4 (37).

2.4.3. α-Amylase inhibition studies

α-Amylase inhibitory effects of the compounds were realized according to the procedure of Xiao (38) using starch as substrate. For starch preparation, 0.4 M starch mixture was prepared in 80 mL NaOH solution at 80°C for 30 min. Then, 35 µL of starch solution, 35 µL of phosphate buffer (pH 6.9), and 10 µL of different concentrations of the compounds were mixed and incubated at 35°C for 25 min. Lastly, 20

µL of the *α*-amylase solution was added to the final mixture and reincubated for 25 min. The reactions were finished by adding 50 µL of HCl (0.1 M) to each tube. The absorbance was measured at 580 nm. One *α*-amylase unit is defined as the quantity of *α*-amylase required to release 1 µmol of reducing sugar estimated as glucose per min (pH 6.9, 40°C) (37).

2.4.4. Molecular docking study

The compounds (**1a-1d** and **2a, 2c, 2d**) as ligands were sketched and done geometry and frequency optimization at DFT/B3LYP/6-31G* level of Gaussian 09 (39) Figure 5. The X-ray crystal structures of the first three chosen enzymes were uploaded from the Protein Data Bank (PDB as follows: 4EY6 for acetylcholinesterase (AChE), 1P0I for butyrylcholinesterase (BChE) and 1DHK for alpha Amylase (α-Amy) (40). In addition, the potential patterns of the first three enzymes were examined, and the findings in Figures S1-S3 are summarized in the supplementary file. In our study, in vitro studies were conducted against the alpha-glucosidase enzyme from Saccharomyces cerevisiae. Since the 3D structure of the glucosidase enzyme (Saccharomyces cerevisiae a-glucosidase, maltase, EC 3.2.1.20) is not available, within the scope of molecular docking study, Sequence alignment and homology modeling for the relevant species target were performed using Discovery Studio (DS) 3.5 software (41). The homology model for S. cerevisiae α-glucosidase was constructed using the crystal structure of α-D-glucose-linked isomaltase from S. cerevisiae (PDB ID: 3AJ7 and 3A4A), which shares 71.9% identical and 87.2% identical sequence with α-glucosidase. Figure 6 shows the Ramachandran plot with 96.36% of the residue in the most preferred region, 0.17% in the outside area, and 0.58% in the rotamer disallowed regions. Analysis of the Ramachandran plot further strengthens the quality of the S. cerevisiae alpha glucosidase homology model. Therefore, a validated and analyzed homology model was used for the docking study, as given in Figure S4. Furthermore, the molecular docking interactions of the model structure and control compound acarbose created in the study were compared with the existing data in the literature and verified, Figure S5 (42) in supplementary data.

The missing atoms in the respective structures were added, and partial charges were assigned by Discovery Studio (DS) 3.5 (43). Finally, all targets were minimized with CHARMM "55" forcefield. The binding spaces were defined and edited by the binding site tools in DS 3.5 for all the targets in this work. The docking processes were performed by AutoDock Vina (44). The number of modes (poses) was set to 200, and those that displayed the lowest binding energy were chosen for further analysis. All schematic binding interactions were demonstrated with the aid of DS 3.5 (43). Besides these, positive compounds, Tacrine (TAC) for AChE and BChE enzymes, and Acarbose (ACR) for alpha-amylase and alpha-glucosidase were compared and discussed with new compounds.

3. RESULTS AND DISCUSSION

3.1. Chemistry

The compounds **2a, 2c, and 2d** reported were synthesized according to the method outlined in Figure 4. The thiourea-substituted intermediates used were synthesized according to the procedure previously reported by our group (Figure 4) (31). All compounds were characterized and confirmed by ^{1}H NMR, ^{13}C NMR, and HRMS spectral methods (31). Sulfanilamide-based thiourea compounds (1a-d, 1 mmol) were dissolved in ethanol to obtain target compounds. Then, ethyl bromoacetate (1 mmol) and sodium acetate (2 mmol) were added, respectively, and the reaction mixture was refluxed. The reactions were completed in 15-24 h with yields ranging from 60 to 70%. Compounds **2c** and **2d**, which are among the final compounds, were initially reported in the present study (Figure 4). In ^{1}H NMR spectra for the representative compound **2c**, the characteristic methylene protons of the thiazolidinone ring were seen as a singlet at δ 4.14 ppm, and the signals for the -NH- proton were seen at δ 6.91 ppm. In ^{13}C NMR spectra, aromatic and aliphatic peaks of the compounds were at the expected areas. Further HRMS data confirmed the compound **2c** with the values of calculated $[M+H]^+$: 468.0722 and found $[M+H]^+$: 468.0777.

3.2. Bioactivity results

AChE enzyme inactivates the acetylcholine in synaptic spaces by breaking it down into acetate and choline. If acetylcholine in synaptic spaces is inactivated too much, nerve conduction is interrupted, and AD is seen. Anti-cholinesterase drugs, which are utilized in AD therapy, are reversible protein inhibitor compounds (45). They are utilized to postpone the onset of symptoms associated with patient lifestyles like rationale judgment, memory, ability to speak and think, and other thought processes. Selective BChE inhibition is also potentially advantageous for the therapy of AD. It circumvents the classical cholinergic toxicity, a widespread side impact of these inhibitors (46).

ChE inhibition assays of the compounds were investigated according to 'Ellman's method (32). Compounds showed promising inhibitory activities with K_I values ranging between 41.56±6.34 to 88.21±8.32 nM for AChE and 92.18±10.25 to 419.46±58.12 nM for BChE (Table 1). Tacrine, which was the first drug for palliative treatment of AD, had IC_{50} - K_I values of 244.94 nM - 201.85±22.54 nM (AChE) and 216.40 nM - 187.32±34.77 nM (BChE), respectively. Compounds **1d** and **2c** were the most effective ChE inhibitors, with K_I values of 41.56±6.34 and 92.18±10.25 nM against AChE and BChE, respectively. The order of K_I inhibitory activities of the compounds against AChE was **1d** < **2c** < **2d** < **1a** < **2a** < **1c** < **1b**. Moreover, this order was **2c** < **1c** < **1b** < **1a** < **1d** < **2a** < **2d** against BChE. Based on the IC_{50} values, compounds had IC_{50} in the 33.27-93.85 nM range and 105.91-412.52 nM towards AChE and BChE, respectively. The compounds were more favorable AChE inhibitors with lower K_I values

than BChE, so compounds could be considered selective AChE inhibitors.

The American Diabetes Association and the European Diabetes Research Association recommend using α-amylase and α-glycosidase inhibitors as potential first-line agents or in combination with other antihyperglycemic drugs. α-Amylases are the main target in the treatment of diabetes because inhibition of these enzymes delays glucose absorption. Delaying carbohydrate digestion by inhibitors of digestive enzymes in the gut is seen as a novel approach to diabetes treatment as it provides a way to reduce hyperglycemia (47, 48).

In this study, the α-glycosidase inhibitory activity of the derivatives was determined against the yeast form of this enzyme (Table 1). Enzyme inhibitory results indicated that compounds tested (K_I values = 9.69±1.33 - 111.51±10.66 nM) against α-glycosidase showed better potency than reference acarbose (K_I value = 12600±780 nM. The most active α-glycosidase inhibitors were **2a** and **2d,** with K_I values of 9.69±1.33 and 24.65±5.74 nM. All of the compounds were more potent inhibitors than reference acarbose towards α-amylase. Among them, compound **2a** showed remarkable inhibition with an IC_{50} value of 98.13 nM. Based on the IC_{50} values, α-glycosidase enzyme inhibition studies of the compounds released that 'compounds' IC_{50} values varied in the 8.37-99.35 nM range. Compared to the standard used, the most effective antidiabetic activity and their IC_{50} values were **2a** (8.37 nM), **2d** (27.58 nM), **1d** (46.85 nM), **1c** (57.21 nM) and **2c** (60.48 nM). The results also demonstrated that all these compounds (IC_{50} values = 98.13 – 507.32 nM) showed better inhibitory potency than acarbose (IC_{50} value = 10000 nM) against α-amylase. Therefore, **2a** could be considered both α-glycosidase and α-amylase enzyme inhibitors in this study.

Table 1: α-glycosidase (α-Gly) and α-amylase (α-Amy), acetylcholinesterase (AChE), and butyrylcholinesterase (BChE) enzymes inhibition effects of the compounds.

Compounds	IC_{50} (nM)								K_I (nM)		
	AChE	r^2	BChE	r^2	α-Gly	r^2	α-Amy	r^2	AChE	BChE	α-Gly
1a	41.04	0.9416	234.57	0.9534	61.27	0.9885	395.47	0.9302	51.57±13.85	193.26±14.26	75.42±16.52
1b	71.26	0.9369	129.41	0.9378	99.35	0.9656	507.32	0.9376	88.21±8.32	114.31±8.01	111.51±10.66
1c	93.85	0.9631	105.91	0.9147	57.21	0.9221	283.24	0.9728	78.98±17.46	95.88±8.28	55.31±8.54
1d	53.27	0.9725	213.85	0.988	46.85	0.9485	244.51	0.9057	41.56±6.34	222.04±35.43	51.26±8.75
2a	70.4	0.9621	288.21	0.9233	8.37	0.9324	98.13	0.9629	64.47±9.01	266.74±46.91	9.69±1.33
2c	33.27	0.9354	106.52	0.9764	60.48	0.9054	398.3	0.9714	45.98±10.45	92.18±10.25	62.45±9.83
2d	46.21	0.9606	412.52	0.9361	27.58	0.9344	112.54	0.9248	50.25±7.71	419.46±58.12	24.65±5.74
TAC*	244.94	0.9723	216.40	0.9888	-	-	-	-	201.85±22.54	187.32±34.77	-
ACR**	-	-			22800	0.9505	10000	0.9724	-		12600±780

*Tacrine (TAC) was used as a control for ChEs.
**Acarbose (ACR) was used as a control for α-glycosidase and α-amylase enzymes.

3.3. Basic structure-activity relationships (SARs)

Basic SARs discussion based on compounds' K_I values against AChE and BChE enzymes was given as follows. Initially, when inhibitory activities of thiourea substituted derivatives **1a–d** towards AChE were considered, compounds **1d**, bearing 4,6-dimethylpyrimidin-2-yl were found to be more effective inhibitors than other pyrimidine analogs **1b** and **1c**. Moreover, compound **1d** was also approximately five times more potent inhibitor than reference tacrine. Among pyrimidine derivatives, it could be expressed that substituting the additional methyl groups on the ring led to an increasing AChE inhibitory effect. However, it could be seen from K_I values non-substituted primary 4-sulfamoylphenyl bearing compound **1a** (51.57 nM) has similar inhibitory potency on AChE when compared with **1d** (41.56 nM). These interesting results showed that the replacement of hydrogen atoms on the sulfamoyl group with a bigger size 4,6-dimethylpyrimidin-2-yl moiety did not increase inhibitory potency magnificently, while pyrimidin-2-yl and 4-methylpyrimidin-2-yl bearing compounds decreased inhibitory potency compared to **1a.**

For inhibitory effects of **1a–d** against BChE, the most potent compound was **1c** having 4-methylpyrimidin-2-yl, among others, and it was found two times more potent than tacrine. In contrast to AChE results, compound **1c** having a mono methyl group, increased inhibitory potency compared to non-substituted **1a** and **1d**. Furthermore, compounds **1a–d** showed selective AChE inhibition properties compared to BChE.

When AChE inhibition effects of iminothiazolidinone-sulfonamide derivatives **2a, 2c,** and **2d** were examined, compound **2c** having 4-methylpyrimidin-2-yl was the most effective second compound among

all compounds. Converting the compounds from **1a** to **2a** and from **1d** to **2d** decreased AChE inhibitory effects, except for the **1c**-**2c** compound pair**.** It can be also said that converting flexible thiourea moiety into rigid iminothiazolidinone increased the inhibitory ability of compound **2c**. For the effects on BChE, similar to AChE results, converting the compounds from flexible to rigid structure decreased the BChE inhibitory effects of the compounds, except the **1c**-**2c** compound pair since **1c** and **2c** had very similar Ki values. These discrepancies showed that unique amino acid residues of active sides of both ChEs might lead to different molecular interactions. As a result, converting thiourea into iminothiazolidinone is a preferable modification to obtain more potent ChE inhibitors.

Different chemical structures of the compounds also tested remarkably affected α-glycosidase and α-amylase inhibition properties. So, converting flexible compound **1a,** having 4-sulfamoylphenyl, into rigid compound **2a** led to obtaining an eight times more potent α-glycosidase inhibitor. Similarly, compound **2a** was found to be more potent than its flexible analog **1a** towards α-amylase. It may be said that the non-substituted 4-sulfamoylphenyl group was more favorable than pyrimidine analogs towards α-glycosidase in contrast to ChEs inhibitory results. In addition, iminothiazolidinone derivatives were generally more potent towards α-glycosidase and α-amylase enzymes.

According to all bioassay results, some important outputs may be concluded that compound **2a** could be considered the potential antidiabetic agent since it was a dual inhibitor of enzymes targeting diabetes. Compound **2a** was also a promising inhibitor of AChE at 64.47 nM. Also, compound **2a** may be considered for further pharmacological models to investigate if there is any connection or common point between cholinesterase and diabetes pathways. Among the series, while compound **1d** was five times more selective inhibitor of AChE, compound **2c** was a dual inhibitor of AChE and BChE.

3.4. Molecular docking study

A molecular modeling study was conducted to investigate and evaluate the structural how and why relations of these biological activities of the related compounds because the two compounds with the best activity that were synthesized in this study gave good results against the four enzymes. The following studies have been handled within the scope of this primary purpose. Optimizing the compounds primarily in terms of geometry and energy is essential. Because the three-dimensional orientation or placement of each compound evaluated directly affects its biological activity. Energy minimization aims to find a set of coordinates representing the minimum energy conformation for the given structure. In this context, the optimal 3D poses of the optimized compounds (**1a-1d** and **2a, 2c, 2d**) in the study are represented in Figure 5. Figure 5 gives us information about the distance, angle, or torsional angle of each atom in the compound with the surrounding atoms and briefly in the geometric structure. Detailed information on the optimized compounds was also given in Table S1 in the Supplementary file.

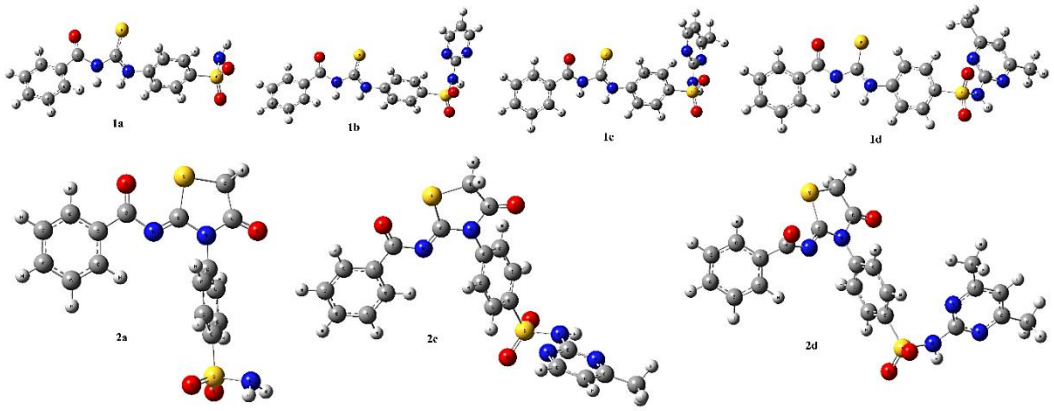

Figure 5: The optimized compounds (**1a-1d** and **2a,2c,2d**) at DFT/B3LYP/6-31G* level using Gaussian09.

In the study, the molecular docking method explains the relationship between the chemical structure of the biological effect of two active compounds showing activity as a result of in vitro analysis for each enzyme.

The two most effective compounds for AChE are compounds **1d** and **2c** (Figure S1). In fact, the binding energy of compound **1d** is -12.43 kcal/mol, while compound **2c** and TAC are -12.32 and -7.37 kcal/mol, respectively. In the meantime, the display of the control compound Tacrine and the orientation in which the two potential compounds interact with the same enzyme is summarized in the overlaid image. The aim is to explain which structural or chemical difference arises from the difference in biological activities of compounds **1c** and **2d** with the target enzyme.

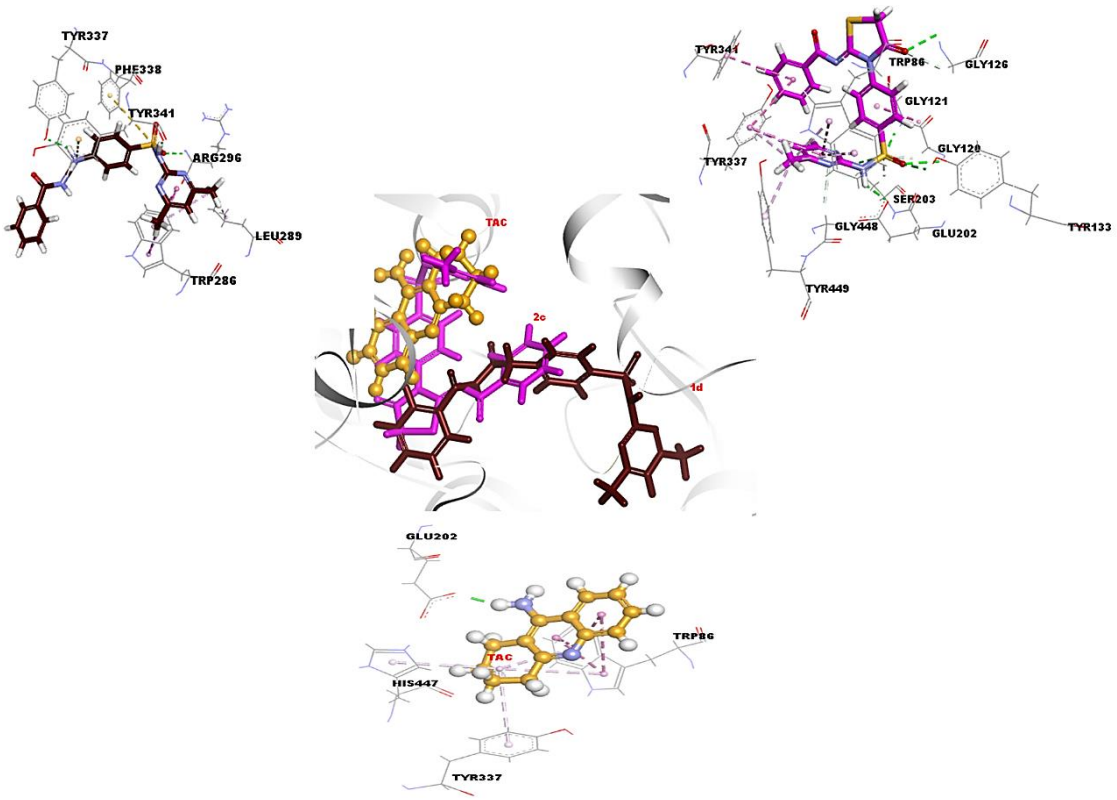

Figure 6: Docking interactions and superimposed form of compound **1d** (brown color, stick form), **2c** (dark pink color, stick form), and TAC (orange, ball, and stick form) with AChE enzyme, respectively.

In this study, the search space of AChE was defined to encompass two distinct binding sites, CAS and PAS. The CAS consisted of amino acids SER203, HIS447, and GLU334, whereas the PAS consisted of amino acids TYR72, ASP74, TYR124, TRP286, and TYR341. Based on Table S2 (Supplementary file), compound **2c** was able to bind to both CAS and PAS simultaneously. The absence of CAS binding was noted in compound **1d**. It exhibited that compound **1d** is bound to TRP286 and TYR341 in the PAS, while compound **2c** is bound to SER203 in the CAS and TYR341 in the PAS.

For BChE, compounds **1c** and **2c** show a more remarkable tendency to bind with the target protein. In particular, compound **2c** has five hydrogen bonds with Gly116, Gly117, Ala199, Ser198, and Ser79 residues in the active site of the related target; two electrostatic interactions with His438 and Asp70; one π-lone pair bond with Trp82, and eight hydrophobic interactions with His438, Trp231, Phe329, Ala328, and Leu286 amino acids. The second-best compound with the target mentioned above model, **1c**, formed eight H-bonds, two electrostatic interactions, and seven hydrophobic interactions. These two compounds interact better than tacrine as a positive compound of BChE. This case is also demonstrated by the binding energy values obtained from the docking calculation (as given in Table 2). As seen in Figure 7, besides the type and number of bonding of the compounds with BChE, the surface areas of the compounds and their volumes in the interaction area have an important place in their effectiveness.

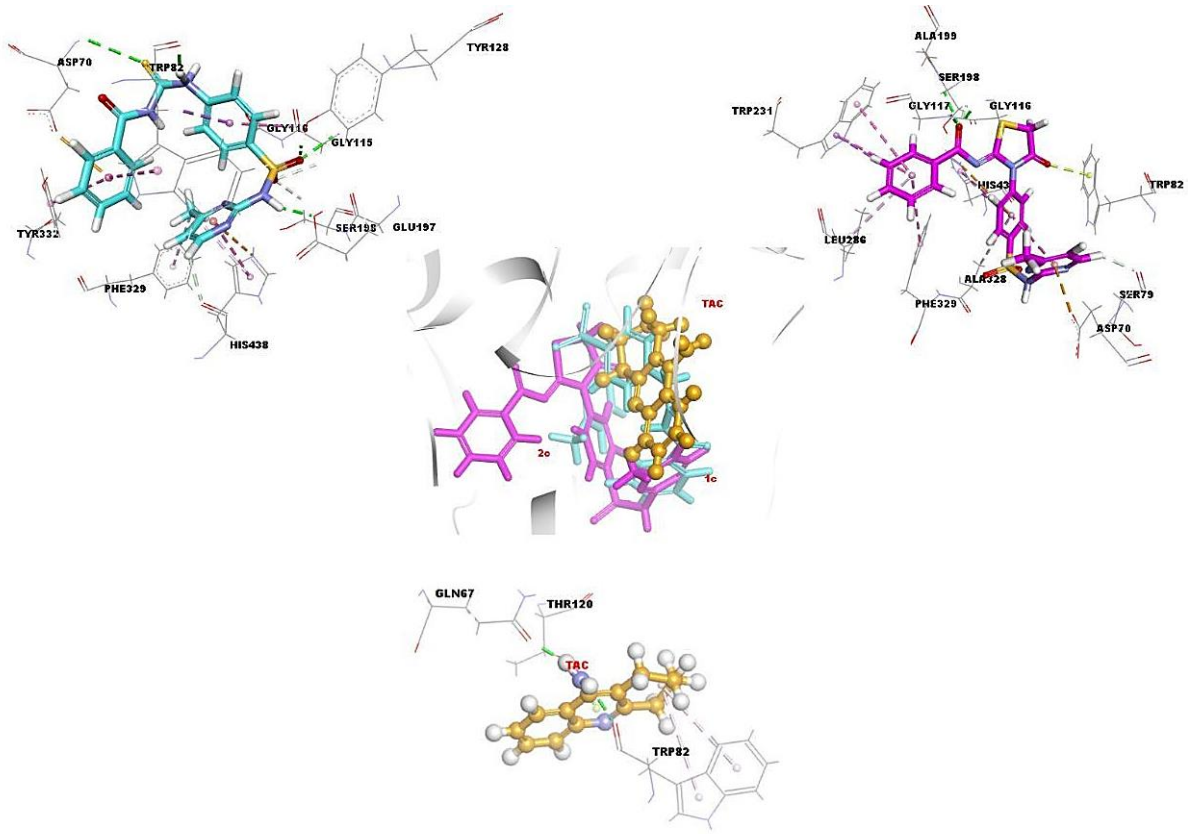

Figure 7: Docking interactions and superimposed form of compound **1c** (turquoise blue color, stick form), **2c** (dark pink color, stick form), and TAC (orange, ball, and stick form) with BChE, respectively.

Table 2: Docking summary of the two potent compounds [**1d** and **1c** for AChE; **1c** and **2c** for BChE; **2a** and **2d** for α-Amy; **2a** and **2d** for α-Gly], TAC and ACR with the target enzymes, respectively.

AChE	**Free Energy of Binding (kcal/mol)**	**RMSD (Å)**
1d	-12.43	0.5946
2c	-12.32	0.8157
TAC	*-7.37*	0.9237
BChE	**Free Energy of Binding (kcal/mol)**	**RMSD (Å)**
1c	-11.02	0.3992
2c	-11.45	1.4512
TAC	*-6.81*	1.5893
α-Amy	**Free Energy of Binding (kcal/mol)**	**RMSD (Å)**
2a	-9.84	0.0923
2d	-8.40	0.4206
ACR	*-5.37*	0.5871
α-Gly	**Free Energy of Binding (kcal/mol)**	**RMSD (Å)**
2a	-11.86	0.1119
2d	-9.57	0.7522
ACR	*-7.53*	1.8320

The acarbose structure, which was chosen as the standard during the molecular docking study, primarily interacted with the model enzyme (Figure S3). Based on the orientation and interactions of the reference compound with the target enzyme, molecular docking studies of two active compounds (**2a** and **2d**) in the in vitro analysis were carried out. The compound **2a** with the Porcine Pancreatic Alpha-Amylase model displayed a binding energy value of -9.84 kcal/mol, and it formed four H-bonds with Arg195, Asp197, Glu233, and His101 residues; three π-sulfur interactions with Trp58, Tyr62, and His299; and three hydrophobic interactions with Trp59, Tyr62, and Trp58. The compound **2d** with α-Amy demonstrated a binding energy value of -8.40 kcal/mol and occurred three H-bonds with His101, His201, and Asp197 amino acids; electrostatic interaction with Asp300; seven hydrophobic interactions with Tyr62, Trp58, His299, Leu162, Ala198, and Ile235 residues (Figure 8). Further, compound **2a** exhibits a better binding affinity than compound **2d** and acarbose (ACR) for α-Amy (BE: -5.37 kcal/mol in Table 2). The findings from the docking are tabulated in detail in Table S2 in the Supplementary file.

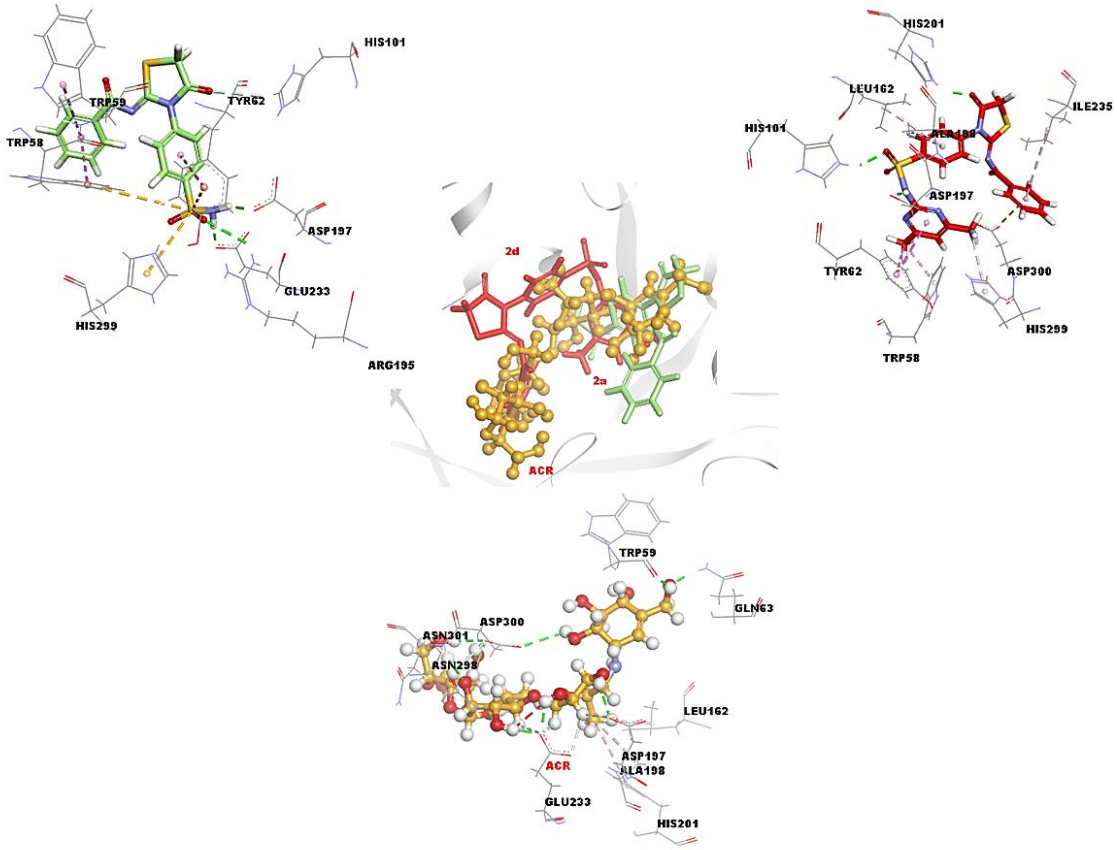

Figure 8: Docking interactions and superimposed form of compound **2a** (light green color, stick form), **2d** (red color, stick form), and ACR (orange, ball, and stick form) with α-Amy, respectively.

Similarly, compounds **2a** and **2d** showing activity for α-Amy also displayed the best activity values with the α-Gly target protein. It was observed that the behaviors of the compounds at α-Gly have a high number of H-bonds and a low number of hydrophobic bonds compared to their behavior in α-Amy, (Figure 9). This is a consequence of the fact that there is more hydrophilic surface than hydrophobic surfaces in the active site of the respective target protein, α-Gly. As a result, the interactions between the compounds mentioned above with α-Gly presented a better binding affinity than their interactions with the α-Amy target, as shown in Table 2.

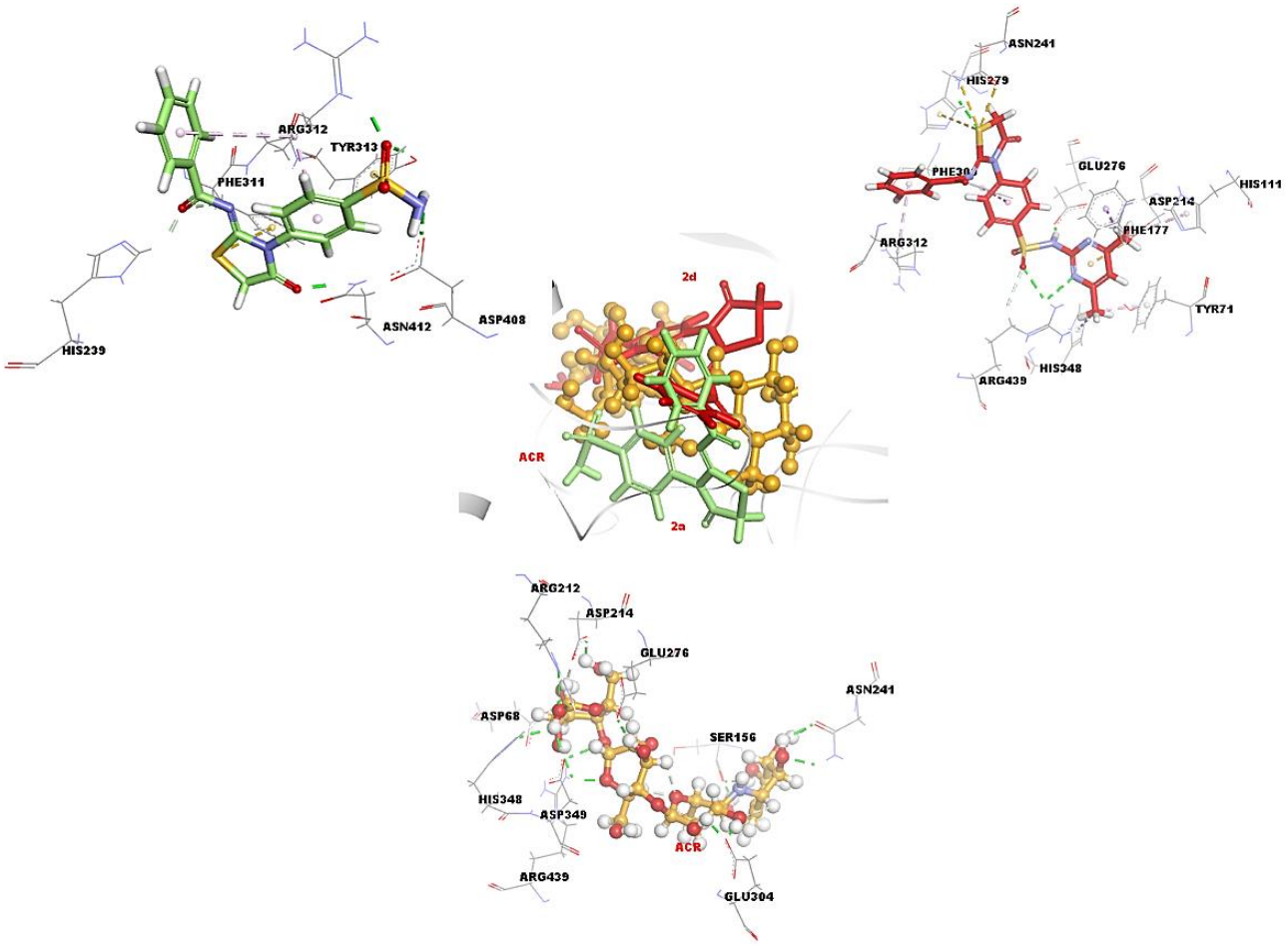

Figure 9: Docking interactions and superimposed form of compound **2a** (light green color, stick form), **2d** (red color, stick form), and **ACR** (orange, ball, and stick form) with α-Gly, respectively.

4. CONCLUSION

In conclusion, thiourea-substituted benzenesulfonamides (**1a–d**) and iminothiazolidinone derivatives (**2a, 2c, 2d**) were evaluated as potent AChE, BChE, α-Gly, and α-Amy inhibitors. Compounds showed inhibitory enzyme effects at the nanomolar level. According to all bioassay results, some important outputs concluded that compound 2a could be considered the potential antidiabetic agent since it was a dual inhibitor of enzymes targeting diabetes. Compound **2a** was also a promising inhibitor of AChE at 64.47 nM. Therefore, compound **2a** may be considered for further pharmacological models. Among the series, while compound **1d** was five times more selective inhibitor of AChE, but compound 2c could be considered a dual inhibitor of AChE and BChE at lower concentrations. The binding energy of the potent compounds was found to be more favorable than references towards all enzymes. Molecular docking studies revealed remarkable interactions between ligands and enzymes. Lead compounds having promising bioactivities could be used to design more potent compounds.

5. CONFLICT OF INTEREST

The authors report no conflict of interest and are responsible for the contents and authoring of the present paper.

6. ACKNOWLEDGMENTS

The authors would like to thank Ataturk University for financial support (Project Number: TAB-8919) and C. Kazaz (Prof. Dr., Ataturk University), B. Anil (Ph.D., Ataturk University), Serkan Levent (M.Sc. Anadolu University) and Mustafa Gul (Prof. Dr. Ataturk University) for their supports.

7. REFERENCES

1. Sadashiva CT, Narendra Sharath Chandra JN, Kavitha CV, Thimmegowda A, Subhash MN, Rangappa KS. Synthesis and pharmacological evaluation of novel N-alkyl/aryl substituted thiazolidinone arecoline analogues as muscarinic receptor 1 agonist in Alzheimer's dementia models. Eur J Med Chem [Internet]. 2009 Dec 1;44(12):4848–54. Available from: <URL>.

2. Genc Bilgicli H, Taslimi P, Akyuz B, Tuzun B, Gulcin İ. Synthesis, characterization, biological evaluation, and molecular docking studies of some piperonyl-

based 4-thiazolidinone derivatives. Arch Pharm (Weinheim) [Internet]. 2020 Jan 28;353(1):1900304. Available from: <URL>.

3. Zhu J, Wang L-N, Cai R, Geng S-Q, Dong Y-F, Liu Y-M. Design, synthesis, evaluation and molecular modeling study of 4-N-phenylaminoquinolines for Alzheimer disease treatment. Bioorg Med Chem Lett [Internet]. 2019 Jun 1;29(11):1325–9. Available from: <URL>.

4. Wilkinson DG, Francis PT, Schwam E, Payne-Parrish J. Cholinesterase Inhibitors Used in the Treatment of Alzheimer's Disease. Drugs Aging [Internet]. 2004 Aug 31;21(7):453–78. Available from: <URL>.

5. Avogaro A, Fadini GP. The Effects of Dipeptidyl Peptidase-4 Inhibition on Microvascular Diabetes Complications. Diabetes Care [Internet]. 2014 Oct 1;37(10):2884–94. Available from: <URL>.

6. Danaei G, Finucane MM, Lu Y, Singh GM, Cowan MJ, Paciorek CJ, et al. National, regional, and global trends in fasting plasma glucose and diabetes prevalence since 1980: systematic analysis of health examination surveys and epidemiological studies with 370 country-years and 2·7 million participants. Lancet [Internet]. 2011 Jul 2;378(9785):31–40. Available from: <URL>.

7. Poovitha S, Parani M. In vitro and in vivo α-amylase and α-glucosidase inhibiting activities of the protein extracts from two varieties of bitter gourd (Momordica charantia L.). BMC Complement Altern Med [Internet]. 2016 Jul 18;16(S1):185. Available from: <URL>.

8. Min SW, Han JS. Polyopes lancifolia Extract, a Potent α-Glucosidase Inhibitor, Alleviates Postprandial Hyperglycemia in Diabetic Mice. Prev Nutr Food Sci [Internet]. 2014 Mar 31;19(1):5–9. Available from: <URL>.

9. Jo S-H, Cho C-Y, Lee J-Y, Ha K-S, Kwon Y-I, Apostolidis E. In vitro and in vivo reduction of post-prandial blood glucose levels by ethyl alcohol and water Zingiber mioga extracts through the inhibition of carbohydrate hydrolyzing enzymes. BMC Complement Altern Med [Internet]. 2016 Dec 31;16(1):111. Available from: <URL>.

10. Zhang B, Xing Y, Wen C, Yu X, Sun W, Xiu Z, et al. Pentacyclic triterpenes as α-glucosidase and α-amylase inhibitors: Structure-activity relationships and the synergism with acarbose. Bioorg Med Chem Lett [Internet]. 2017 Nov 15;27(22):5065–70. Available from: <URL>.

11. Cheng AYY. Oral antihyperglycemic therapy for type 2 diabetes mellitus. Can Med Assoc J [Internet]. 2005 Jan 18;172(2):213–26. Available from: <URL>.

12. Levetan C. Oral antidiabetic agents in type 2 diabetes. Curr Med Res Opin [Internet]. 2007 Apr 1;23(4):945–52. Available from: <URL>.

13. Oz Gul O, Cinkilic N, Gul CB, Cander S, Vatan O, Ersoy C, et al. Comparative genotoxic and cytotoxic effects of the oral antidiabetic drugs sitagliptin, rosiglitazone, and pioglitazone in patients with type-2 diabetes: A cross-sectional, observational pilot study. Mutat Res Toxicol Environ Mutagen [Internet]. 2013 Sep 18;757(1):31–5. Available from: <URL>.

14. Wang S-L, Dong W-B, Dong X-L, Zhu W-M, Wang F-F, Han F, et al. Comparison of twelve single-drug regimens for the treatment of type 2 diabetes mellitus. Oncotarget [Internet]. 2017 Sep 22;8(42):72700–13. Available from: <URL>.

15. Brands AMA, Biessels GJ, de Haan EHF, Kappelle LJ, Kessels RPC. The Effects of Type 1 Diabetes on Cognitive Performance. Diabetes Care [Internet]. 2005 Mar 1;28(3):726–35. Available from: <URL>.

16. Butterfield DA, Di Domenico F, Barone E. Elevated risk of type 2 diabetes for development of Alzheimer disease: A key role for oxidative stress in brain. Biochim Biophys Acta - Mol Basis Dis [Internet]. 2014 Sep;1842(9):1693–706. Available from: <URL>.

17. Zhang J, Chen C, Hua S, Liao H, Wang M, Xiong Y, et al. An updated meta-analysis of cohort studies: Diabetes and risk of Alzheimer's disease. Diabetes Res Clin Pract [Internet]. 2017 Feb 1;124:41–7. Available from: <URL>.

18. Roriz-Filho JS, Sá-Roriz TM, Rosset I, Camozzato AL, Santos AC, Chaves MLF, et al. (Pre)diabetes, brain aging, and cognition. Biochim Biophys Acta - Mol Basis Dis [Internet]. 2009 May 1;1792(5):432–43. Available from: <URL>.

19. Biessels GJ, Staekenborg S, Brunner E, Brayne C, Scheltens P. Risk of dementia in diabetes mellitus: a systematic review. Lancet Neurol [Internet]. 2006 Jan 1;5(1):64–74. Available from: <URL>.

20. Li Z, Zhang W, Sima AAF. Alzheimer-Like Changes in Rat Models of Spontaneous Diabetes. Diabetes [Internet]. 2007 Jul 1;56(7):1817–24. Available from: <URL>.

21. Arab L, Sadeghi R, G. Walker D, Lue L-F, N. Sabbagh M. Consequences of aberrant insulin regulation in the brain: Can treating diabetes be effective for alzheimers disease. Curr Neuropharmacol [Internet]. 2011 Dec 1;9(4):693–705. Available from: <URL>.

22. Maher PA, Schubert DR. Metabolic links between diabetes and Alzheimer's disease. Expert Rev Neurother [Internet]. 2009 May 9;9(5):617–30. Available from: <URL>.

23. Jolivalt CG, Hurford R, Lee CA, Dumaop W, Rockenstein E, Masliah E. Type 1 diabetes exaggerates features of Alzheimer's disease in APP transgenic mice. Exp Neurol [Internet]. 2010 Jun 1;223(2):422–31. Available from: <URL>.

24. Li Y-S, Hu D-K, Zhao D-S, Liu X-Y, Jin H-W, Song G-P, et al. Design, synthesis and biological evaluation

of 2,4-disubstituted oxazole derivatives as potential PDE4 inhibitors. Bioorg Med Chem [Internet]. 2017 Mar 15;25(6):1852–9. Available from: <URL>.

25. Rouf A, Tanyeli C. Bioactive thiazole and benzothiazole derivatives. Eur J Med Chem [Internet]. 2015 Jun 5;97(1):911–27. Available from: <URL>.

26. Jain AK, Vaidya A, Ravichandran V, Kashaw SK, Agrawal RK. Recent developments and biological activities of thiazolidinone derivatives: A review. Bioorg Med Chem [Internet]. 2012 Jun 1;20(11):3378–95. Available from: <URL>.

27. Hemaida AY, Hassan GS, Maarouf AR, Joubert J, El-Emam AA. Synthesis and biological evaluation of thiazole-based derivatives as potential acetylcholinesterase inhibitors. ACS Omega [Internet]. 2021 Jul 27;6(29):19202–11. Available from: <URL>.

28. Markowicz-Piasecka M, Huttunen KM, Sikora J. Metformin and its sulphonamide derivative simultaneously potentiateanti-cholinesterase activity of donepezil and inhibit beta-amyloid aggregation. J Enzyme Inhib Med Chem [Internet]. 2018 Jan 1;33(1):1309–22. Available from: <URL>.

29. Yamali C, Gul HI, Kazaz C, Levent S, Gulcin I. Synthesis, structure elucidation, and in vitro pharmacological evaluation of novel polyfluoro substituted pyrazoline type sulfonamides as multi-target agents for inhibition of acetylcholinesterase and carbonic anhydrase I and II enzymes. Bioorg Chem [Internet]. 2020 Mar 1;96:103627. Available from: <URL>.

30. Yamali C, Gul HI, Ece A, Taslimi P, Gulcin I. Synthesis, molecular modeling, and biological evaluation of 4-[5-aryl-3-(thiophen-2-yl)-4,5-dihydro-1 *H* -pyrazol-1-yl] benzenesulfonamides toward acetylcholinesterase, carbonic anhydrase I and II enzymes. Chem Biol Drug Des [Internet]. 2018 Apr 1;91(4):854–66. Available from: <URL>.

31. Tugrak M, Gul HI, Demir Y, Gulcin I. Synthesis of benzamide derivatives with thiourea-substituted benzenesulfonamides as carbonic anhydrase inhibitors. Arch Pharm (Weinheim) [Internet]. 2021 Feb 12;354(2):e2000230. Available from: <URL>.

32. Ellman GL, Courtney KD, Andres V, Featherstone RM. A new and rapid colorimetric determination of acetylcholinesterase activity. Biochem Pharmacol [Internet]. 1961 Jul 1;7(2):88–95. Available from: <URL>.

33. Cetin Cakmak K, Gülçin İ. Anticholinergic and antioxidant activities of usnic acid-an activity-structure insight. Toxicol Reports [Internet]. 2019 Jan 1;6:1273–80. Available from: <URL>.

34. Buldurun K, Turan N, Bursal E, Aras A, Mantarcı A, Çolak N, et al. Synthesis, characterization, powder X-ray diffraction analysis, thermal stability, antioxidant properties and enzyme inhibitions of M(II)-Schiff base ligand complexes. J Biomol Struct Dyn [Internet]. 2021 Nov 22;39(17):6480–7. Available from: <URL>.

35. Behçet A, Çağlılar T, Barut Celepci D, Aktaş A, Taslimi P, Gök Y, et al. Synthesis, characterization and crystal structure of 2-(4-hydroxyphenyl)ethyl and 2-(4-nitrophenyl)ethyl Substituted Benzimidazole Bromide Salts: Their inhibitory properties against carbonic anhydrase and acetylcholinesterase. J Mol Struct [Internet]. 2018 Oct 15;1170:160–9. Available from: <URL>.

36. Tao Y, Zhang Y, Cheng Y, Wang Y. Rapid screening and identification of *α* -glucosidase inhibitors from mulberry leaves using enzyme-immobilized magnetic beads coupled with HPLC/MS and NMR. Biomed Chromatogr [Internet]. 2013 Feb;27(2):148–55. Available from: <URL>.

37. Bal S, Demirci Ö, Şen B, Taşkın Tok T, Taslimi P, Aktaş A, et al. Silver *N* -heterocyclic carbene complexes bearing fluorinated benzyl group: Synthesis, characterization, crystal structure, computational studies, and inhibitory properties against some metabolic enzymes. Appl Organomet Chem [Internet]. 2021 Sep 20;35(9):e6312. Available from: <URL>.

38. Xiao Z, Storms R, Tsang A. A quantitative starch–iodine method for measuring alpha-amylase and glucoamylase activities. Anal Biochem [Internet]. 2006 Apr 1;351(1):146–8. Available from: <URL>.

39. Gaussian 09, revision E.01, MJ Frisch, WW Trucks, HB Schlegel, GE Scuseria, MA Robb, JR Cheeseman, G Scalmani, V. Barone, B. Mennucci, G.A.e.a. Petersson, Gaussian, Inc,. Wallingford CT; 2009. p. S162-173.

40. Bank RPD RCSB PDB:Homepage. BRRP [Internet]. 2021 [cited 2021 May 24]. Available from: <URL>.

41. Accelrys Software Inc. Discovery studio modeling environment, Release 3.5 Accelrys Software Inc. San Diego; 2013.

42. Mugaranja KP, Kulal A. Alpha glucosidase inhibition activity of phenolic fraction from Simarouba glauca: An in-vitro, in-silico and kinetic study. Heliyon [Internet]. 2020 Jul 1;6(7):e04392. Available from: <URL>.

43. Brooks BR, Bruccoleri RE, Olafson BD, States DJ, Swaminathan S, Karplus M. CHARMM: A program for macromolecular energy, minimization, and dynamics calculations. J Comput Chem [Internet]. 1983 Jun 1;4(2):187–217. Available from: <URL>.

44. Trott O, Olson AJ. AutoDock Vina: Improving the speed and accuracy of docking with a new scoring function, efficient optimization, and multithreading. J Comput Chem [Internet]. 2009 Jan 1;31(2):455–61. Available from: <URL>.

45. Huseynova M, Medjidov A, Taslimi P, Aliyeva M. Synthesis, characterization, crystal structure of the coordination polymer Zn(II) with thiosemicarbazone

of glyoxalic acid and their inhibitory properties against some metabolic enzymes. Bioorg Chem [Internet]. 2019 Mar 1;83:55–62. Available from: <URL>.

46. Biçer A, Taslimi P, Yakalı G, Gülçin I, Serdar Gültekin M, Turgut Cin G. Synthesis, characterization, crystal structure of novel bis-thiomethylcyclohexanone derivatives and their inhibitory properties against some metabolic enzymes. Bioorg Chem [Internet]. 2019 Feb 1;82:393–404. Available from: <URL>.

47. Demir Y, Taslimi P, Ozaslan MS, Oztaskin N, Çetinkaya Y, Gulçin İ, et al. Antidiabetic potential: In vitro inhibition effects of bromophenol and diarylmethanones derivatives on metabolic enzymes. Arch Pharm (Weinheim) [Internet]. 2018 Dec 1;351(12):e1800263. Available from: <URL>.

48. Gulçin İ, Taslimi P, Aygün A, Sadeghian N, Bastem E, Kufrevioglu OI, et al. Antidiabetic and antiparasitic potentials: Inhibition effects of some natural antioxidant compounds on α-glycosidase, α-amylase and human glutathione S-transferase enzymes. Int J Biol Macromol [Internet]. 2018 Nov 1;119:741–6. Available from: <URL>.

SUPPLEMENTARY MATERIAL

Molecular docking studies and biological activities of benzenesulfonamide-based thiourea and thiazolidinone derivatives targeting cholinesterases, α-glucosidase, and α-amylase enzymes

Mehtap Tugrak Sakarya[1*], Halise Inci Gul[2], Cem Yamali[3], Parham Taslimi[4], Tugba Taskin Tok[5,6]

[1]Gaziosmanpasa University, Department of Pharmaceutical Chemistry, Tokat, Turkey.
[2]Ataturk University, Department of Pharmaceutical Chemistry, Erzurum, Turkey.
[3]Cukurova University, Department of Basic Pharmaceutical Sciences, Adana, Turkey.
[4]Bartin University, Department of Biotechnology, Faculty of Science, Bartin, Turkey.
[5]Gaziantep University, Department of Chemistry, Gaziantep, Turkey.
[6]Gaziantep University, Department of Bioinformatics and Computational Biology, Gaziantep, Turkey.

Table S1. Data of the optimized structures (**1a-1d** and **2a,2c,2d**) at DFT/B3LYP/6-31G* basis set using Gaussian 09.

Compound 1a					
			Coordinates (Angstroms)		
Center Number	Atomic Number	Atomic Type	X	Y	Z
1	6	0	-4.905464	-0.088218	-0.089881
2	6	0	-3.702342	0.758615	-0.385636
3	7	0	-2.479523	0.16078	-0.025686
4	6	0	-1.211958	0.760437	0.04181
5	7	0	-0.250668	-0.182371	-0.266702
6	6	0	1.153215	-0.157642	-0.150076
7	8	0	-3.77946	1.840293	-0.929724
8	16	0	-0.956246	2.336451	0.460856
9	6	0	1.866096	-1.051244	-0.969633
10	6	0	3.248831	-1.140544	-0.888835
11	6	0	3.931358	-0.327789	0.017979
12	6	0	3.23618	0.550127	0.849285
13	6	0	1.849034	0.640644	0.769803
14	6	0	-4.939998	-1.055699	0.925382
15	6	0	-6.102387	-1.791948	1.154985
16	6	0	-7.235983	-1.570365	0.371208
17	6	0	-7.211224	-0.599039	-0.633518
18	6	0	-6.055372	0.143629	-0.857913
19	16	0	5.713324	-0.430611	0.124339
20	8	0	6.116765	-1.779315	-0.285737
21	8	0	6.110139	0.146808	1.412768
22	7	0	6.241612	0.602087	-1.117964
23	1	0	-2.51952	-0.82907	0.183877
24	1	0	-0.592581	-0.962989	-0.815748
25	1	0	1.329345	-1.679957	-1.676888

26	1	0	3.79422	-1.839326	-1.513738
27	1	0	3.778237	1.149701	1.572565
28	1	0	1.312277	1.323248	1.412497
29	1	0	-4.079969	-1.209125	1.572523
30	1	0	-6.125117	-2.529618	1.952138
31	1	0	-8.139804	-2.146639	0.548973
32	1	0	-8.095221	-0.419318	-1.238834
33	1	0	-6.019936	0.911845	-1.623379
34	1	0	6.961759	0.119303	-1.652495
35	1	0	6.603674	1.466978	-0.720354

Compound 1b					
			Coordinates (Angstroms)		
Center Number	Atomic Number	Atomic Type	X	Y	Z
1	6	0	6.161601	0.285754	0.16655
2	6	0	4.82776	0.963087	0.285433
3	7	0	3.733811	0.127119	-0.008313
4	6	0	2.393582	0.497718	-0.205923
5	7	0	1.574433	-0.522426	0.235837
6	6	0	0.191443	-0.747221	0.089498
7	8	0	4.706909	2.11419	0.649483
8	16	0	1.924203	1.924142	-0.891645
9	6	0	-0.398044	-1.628333	1.014171
10	6	0	-1.743984	-1.955312	0.924044
11	6	0	-2.511326	-1.394103	-0.098543
12	6	0	-1.938773	-0.530227	-1.032436
13	6	0	-0.588864	-0.203832	-0.942631
14	6	0	6.401232	-0.806735	-0.680106
15	6	0	7.67377	-1.373637	-0.752285
16	6	0	8.713812	-0.856809	0.022097
17	6	0	8.483794	0.239522	0.857969
18	6	0	7.217069	0.813102	0.924013
19	8	0	-4.235465	-1.836872	-0.228527
20	8	0	-4.447338	-3.097488	0.487648
21	7	0	-4.656194	-1.660968	-1.614556
22	1	0	-5.042411	-0.719283	0.783879
23	1	0	3.937999	-0.863642	-0.053603
24	1	0	2.009695	-1.142937	0.909047
25	1	0	0.205465	-2.059631	1.809991
26	1	0	-2.195122	-2.645088	1.628712
27	1	0	-2.55097	-0.115234	-1.823567
28	1	0	-0.145748	0.469826	-1.661348
29	1	0	5.61264	-1.192549	-1.321416
30	1	0	7.854291	-2.210892	-1.420521
31	1	0	9.703789	-1.301275	-0.032558
32	1	0	9.294127	0.648424	1.454905

33	1	0	7.021085	1.673249	1.555762
34	1	0	-5.660158	-1.181466	1.444181
35	6	0	-5.378573	0.592046	0.467583
36	6	0	-6.696922	2.374223	0.926651
37	6	0	-4.994631	2.484067	-0.710251
38	6	0	-6.025279	3.131248	-0.032617
39	1	0	-7.514221	2.796903	1.508612
40	1	0	-4.4122	2.996873	-1.473577
41	1	0	-6.288254	4.16252	-0.237919
42	7	0	-6.391347	1.100948	1.18644
43	7	0	-4.652378	1.215842	-0.466965

Compound 1c					
			Coordinates (Angstroms)		
Center Number	Atomic Number	Atomic Type	X	Y	Z
1	6	0	-6.181604	0.106647	-0.57759
2	6	0	-4.733041	-0.182091	-0.353459
3	7	0	-4.099737	0.603553	0.593471
4	6	0	-2.752579	0.620885	1.011199
5	7	0	-1.980576	-0.29093	0.37879
6	6	0	-0.611572	-0.604912	0.467623
7	8	0	-4.150098	-1.078898	-0.968724
8	16	0	-2.345371	1.739895	2.186499
9	6	0	-0.171694	-1.607126	-0.42018
10	6	0	1.154024	-2.01285	-0.429584
11	6	0	2.054929	-1.411375	0.453278
12	6	0	1.634558	-0.425545	1.344277
13	6	0	0.302457	-0.017116	1.355619
14	6	0	-6.786529	1.332201	-0.258509
15	6	0	-8.144299	1.527975	-0.505203
16	6	0	-8.90836	0.504306	-1.068883
17	6	0	-8.30892	-0.713716	-1.399304
18	6	0	-6.951474	-0.909953	-1.162072
19	16	0	3.752844	-1.962526	0.461465
20	8	0	3.81183	-3.294528	-0.146811
21	8	0	4.323484	-1.694288	1.777534
22	7	0	4.521858	-1.000153	-0.726784
23	1	0	-4.658999	1.259691	1.122358
24	1	0	-2.508464	-0.859002	-0.293889
25	1	0	-0.880841	-2.070706	-1.101391
26	1	0	1.489022	-2.796386	-1.100152
27	1	0	2.349273	0.023292	2.023134
28	1	0	-0.026801	0.744626	2.046993
29	1	0	-6.204417	2.156086	0.145938
30	1	0	-8.602479	2.482597	-0.263862
31	1	0	-9.967305	0.658356	-1.256604

32	1	0	-8.899935	-1.509627	-1.843166
33	1	0	-6.467104	-1.845625	-1.419789
34	1	0	5.043243	-1.56839	-1.387676
35	6	0	5.003262	0.294146	-0.5519
36	6	0	6.45606	1.894156	-1.276755
37	6	0	4.901187	2.296578	0.478808
38	6	0	5.928007	2.777455	-0.328216
39	1	0	4.440469	2.929515	1.235427
40	1	0	6.300028	3.790802	-0.22624
41	7	0	5.993597	0.639711	-1.383988
42	7	0	4.414907	1.056949	0.377108
43	6	0	7.564676	2.285517	-2.216388
44	1	0	8.431915	1.632361	-2.068687
45	1	0	7.241264	2.157927	-3.255385
46	1	0	7.874962	3.323283	-2.067163

Compound 1d					
			Coordinates (Angstroms)		
Center Number	Atomic Number	Atomic Type	X	Y	Z
1	6	0	-6.357565	0.010588	0.529953
2	6	0	-4.888583	0.228924	0.369352
3	7	0	-4.207512	-0.74386	-0.341585
4	6	0	-2.848323	-0.820025	-0.709762
5	7	0	-2.117901	0.240771	-0.299609
6	6	0	-0.761257	0.579743	-0.461191
7	8	0	-4.323669	1.211386	0.857298
8	16	0	-2.377051	-2.178911	-1.565389
9	6	0	-0.345771	1.7305	0.237665
10	6	0	0.964046	2.177445	0.150471
11	6	0	1.87271	1.468972	-0.639998
12	6	0	1.474753	0.336046	-1.34719
13	6	0	0.159076	-0.114391	-1.261436
14	6	0	-6.991884	0.687063	1.582443
15	6	0	-8.359113	0.532605	1.792662
16	6	0	-9.109288	-0.287034	0.945555
17	6	0	-8.488452	-0.948017	-0.116076
18	6	0	-7.117956	-0.802575	-0.324595
19	16	0	3.550965	2.064167	-0.774658
20	8	0	3.568889	3.486262	-0.420301
21	8	0	4.113747	1.581577	-2.032098
22	7	0	4.36126	1.360022	0.554312
23	1	0	-4.71424	-1.572202	-0.624918
24	1	0	-2.666145	0.91031	0.252551
25	1	0	-1.061145	2.276263	0.847751
26	1	0	1.279985	3.072342	0.675074
27	1	0	2.195161	-0.192265	-1.959255

28	1	0	-0.152653	-0.991508	-1.809359
29	1	0	-6.394959	1.326426	2.223864
30	1	0	-8.841031	1.052589	2.615563
31	1	0	-10.177071	-0.404943	1.10769
32	1	0	-9.071456	-1.571159	-0.787851
33	1	0	-6.663253	-1.296256	-1.179466
34	1	0	4.872001	2.053595	1.092336
35	6	0	4.875483	0.065982	0.617842
36	6	0	6.363866	-1.334012	1.610858
37	6	0	4.806707	-2.105917	-0.036762
38	6	0	5.851296	-2.387073	0.847157
39	1	0	6.251732	-3.390941	0.938344
40	7	0	5.877008	-0.090102	1.492763
41	7	0	4.304291	-0.86648	-0.147004
42	7	0	7.484307	-1.526976	2.597306
43	1	0	8.326038	-0.872925	2.344412
44	1	0	7.153132	-1.247187	3.603746
45	1	0	7.83407	-2.562791	2.616199
46	6	0	4.183898	-3.162405	-0.9086
47	1	0	4.607382	-4.151468	-0.71378
48	1	0	3.101794	-3.199295	-0.742117
49	1	0	4.338575	-2.915591	-1.965297

Compound 2a					
			Coordinates (Angstroms)		
Center Number	Atomic Number	Atomic Type	X	Y	Z
1	6	0	-4.708362	-3.637217	-0.078839
2	6	0	-3.577958	-4.454976	-0.176521
3	6	0	-2.302429	-3.886608	-0.20632
4	6	0	-2.152375	-2.502493	-0.13803
5	6	0	-3.283533	-1.678219	-0.039722
6	6	0	-4.56291	-2.25514	-0.011293
7	6	0	-3.171144	-0.196563	0.032779
8	8	0	-4.162494	0.531	0.104144
9	7	0	-1.860159	0.296745	0.014567
10	6	0	-1.68777	1.571186	0.040113
11	7	0	-0.400644	2.110934	0.01772
12	6	0	-0.292924	3.51179	0.006078
13	6	0	-1.664293	4.15729	0.059647
14	16	0	-2.937844	2.836123	0.093961
15	8	0	0.756835	4.112669	-0.039865
16	6	0	0.775489	1.285172	-0.001773
17	6	0	0.995272	0.36193	1.025005
18	6	0	2.142418	-0.424613	1.009175
19	6	0	3.063948	-0.265743	-0.027828
20	6	0	2.850886	0.65271	-1.053827

21	6	0	1.696165	1.433454	-1.039656
22	16	0	4.541581	-1.283722	-0.052434
23	8	0	4.216618	-2.566445	0.577264
24	8	0	5.111916	-1.193445	-1.399975
25	7	0	5.577909	-0.484209	1.028314
26	1	0	-5.700367	-4.079934	-0.056078
27	1	0	-3.692311	-5.534548	-0.229912
28	1	0	-1.424379	-4.521858	-0.283611
29	1	0	-1.167766	-2.049636	-0.162311
30	1	0	-5.425785	-1.601561	0.063893
31	1	0	-1.792832	4.800952	-0.815301
32	1	0	-1.728031	4.783986	0.953897
33	1	0	0.265697	0.251774	1.818581
34	1	0	2.318328	-1.159886	1.786748
35	1	0	3.569987	0.739744	-1.860642
36	1	0	1.512851	2.151822	-1.830113
37	1	0	5.954362	-1.166824	1.683641
38	1	0	6.32483	-0.018748	0.516086

Compound 2c					
			Coordinates (Angstroms)		
Center Number	Atomic Number	Atomic Type	X	Y	Z
1	6	0	-6.0069	-3.639133	0.739185
2	6	0	-4.93079	-4.450642	0.365706
3	6	0	-3.704086	-3.875452	0.026318
4	6	0	-3.548636	-2.490588	0.059555
5	6	0	-4.625253	-1.672663	0.434274
6	6	0	-5.855972	-2.256403	0.773299
7	6	0	-4.505006	-0.190689	0.483508
8	8	0	-5.450216	0.53082	0.805219
9	7	0	-3.242829	0.309647	0.139684
10	6	0	-3.073026	1.58467	0.133062
11	7	0	-1.834984	2.131656	-0.207816
12	6	0	-1.737521	3.532963	-0.229973
13	6	0	-3.053023	4.170722	0.174138
14	16	0	-4.273271	2.842291	0.513136
15	8	0	-0.734797	4.140488	-0.531165
16	6	0	-0.700038	1.312384	-0.536171
17	6	0	-0.221671	0.382236	0.39031
18	6	0	0.884136	-0.40167	0.073515
19	6	0	1.50314	-0.228365	-1.165181
20	6	0	1.033672	0.699779	-2.094592
21	6	0	-0.077809	1.475982	-1.775293
22	16	0	2.904142	-1.255383	-1.605538
23	8	0	2.812075	-2.502263	-0.85348
24	8	0	3.047034	-1.241601	-3.063038

25	7	0	4.263599	-0.352487	-1.103514
26	1	0	-6.961093	-4.087287	1.002478
27	1	0	-5.049606	-5.530729	0.338854
28	1	0	-2.868528	-4.505812	-0.265148
29	1	0	-2.602045	-2.032211	-0.203214
30	1	0	-6.677236	-1.607566	1.059505
31	1	0	-3.39936	4.822068	-0.6334
32	1	0	-2.891346	4.788361	1.062329
33	1	0	-0.720789	0.264469	1.344912
34	1	0	1.275185	-1.128396	0.774465
35	1	0	1.51995	0.797346	-3.058721
36	1	0	-0.4598	2.201654	-2.483718
37	1	0	4.938691	-0.242186	-1.854367
38	6	0	4.796881	-0.307625	0.182949
39	6	0	6.643478	0.092662	1.457593
40	6	0	4.533513	-0.445228	2.417187
41	6	0	5.876405	-0.134571	2.60625
42	1	0	3.877069	-0.630456	3.265748
43	1	0	6.307488	-0.070388	3.59905
44	7	0	3.967546	-0.526869	1.209727
45	7	0	6.098851	-0.002969	0.235556
46	6	0	8.104877	0.44578	1.517963
47	1	0	8.470579	0.483032	2.547639
48	1	0	8.693583	-0.289411	0.958495
49	1	0	8.277049	1.419693	1.046172

Compound 2d					
			Coordinates (Angstroms)		
Center Number	Atomic Number	Atomic Type	X	Y	Z
1	6	0	-7.650499	-1.459049	0.203127
2	6	0	-7.227246	-2.554035	-0.543555
3	6	0	-5.868857	-2.821916	-0.678319
4	6	0	-4.928928	-1.993855	-0.074187
5	6	0	-5.35466	-0.893535	0.671338
6	6	0	-6.718121	-0.629786	0.816125
7	6	0	-4.36931	-0.005798	1.343548
8	8	0	-4.417112	0.359707	2.499719
9	7	0	-3.213692	0.375696	0.573152
10	6	0	-2.955162	1.493852	-0.008666
11	7	0	-1.703108	1.591923	-0.731365
12	6	0	-1.446272	2.896424	-1.283601
13	6	0	-2.623897	3.839135	-1.139993
14	16	0	-3.91549	3.001471	-0.167521
15	8	0	-0.392534	3.155496	-1.827218
16	6	0	-0.634532	0.617918	-0.551924

17	6	0	0.066457	0.534811	0.652835
18	6	0	1.081885	-0.405541	0.788895
19	6	0	1.410848	-1.265906	-0.261501
20	6	0	0.698726	-1.1662	-1.460495
21	6	0	-0.320213	-0.234779	-1.613899
22	16	0	2.686453	-2.485018	-0.074681
23	8	0	2.930428	-2.796178	1.315886
24	8	0	2.476886	-3.585799	-1.00786
25	7	0	4.09796	-1.661489	-0.761111
26	1	0	-8.720021	-1.250984	0.313394
27	1	0	-7.964081	-3.207427	-1.02272
28	1	0	-5.536373	-3.688263	-1.260053
29	1	0	-3.859805	-2.212349	-0.17968
30	1	0	-7.05175	0.224503	1.416719
31	1	0	-3.01177	0.224503	1.416719
32	1	0	-2.315625	4.778854	-0.644403
33	1	0	-0.173829	1.193221	1.496215
34	1	0	1.637743	-0.464353	1.736835
35	1	0	0.937906	-1.840932	-2.294602
36	1	0	-0.862503	-0.175219	-2.565066
37	1	0	4.575184	-2.133797	-1.508776
38	6	0	4.872838	-0.62414	-0.193703
39	6	0	6.858397	0.611975	-0.203009
40	6	0	5.07134	1.141918	1.325649
41	6	0	6.351938	1.410254	0.83022
42	1	0	6.94683	2.231517	1.243435
43	7	0	4.326684	0.126545	0.810707
44	7	0	6.120052	-0.407366	-0.716912
45	6	0	8.21879	0.842032	-0.760956
46	1	0	8.482405	1.907828	-0.730846
47	1	0	8.966992	0.298502	-0.166581
48	1	0	8.314225	0.501631	-1.800858
49	6	0	4.484071	1.949191	2.429271
50	1	0	4.617828	3.022586	2.238608
51	1	0	3.410487	1.763763	2.57146
52	1	0	4.988567	1.715155	3.377273

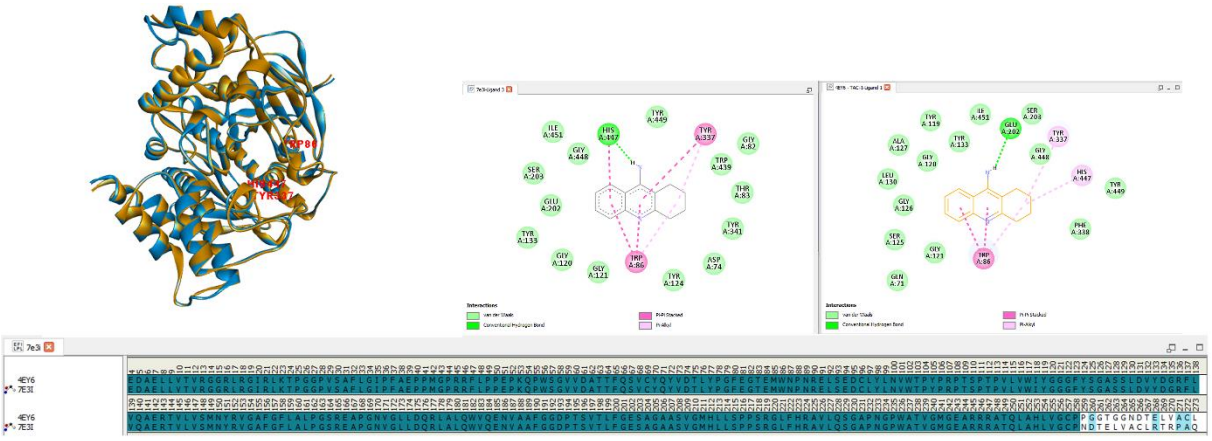

Figure S1. Superimposed structures, sequences of the two Human Acetylcholinesterase models, 7E3I (orange color) and 4EY6 (blue color). 2D docking poses and interactions of Tacrine in the two PDB models.

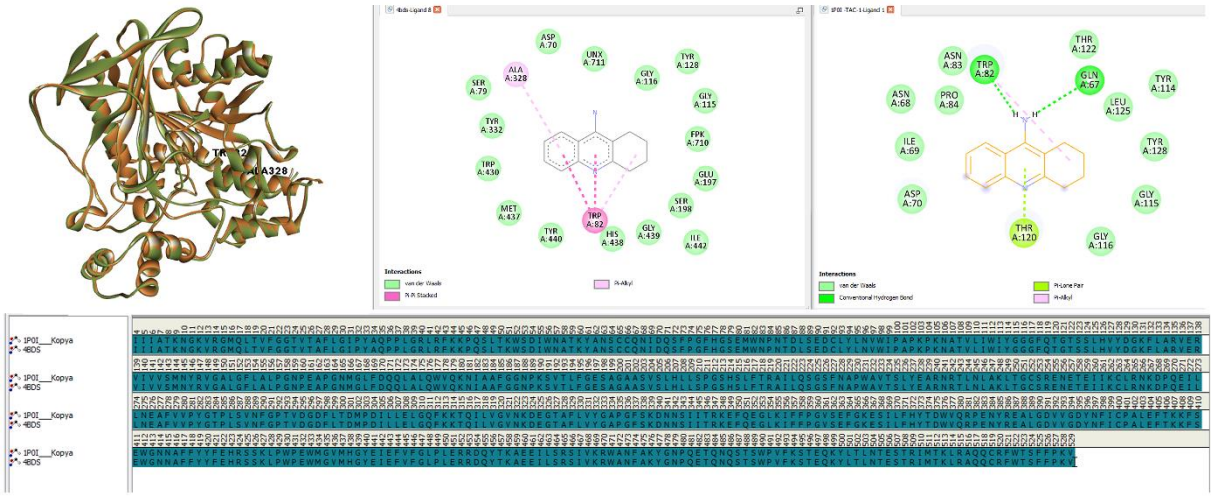

Figure S2. Superimposed structures, sequences of the two Human butyrylcholinesterase models, 4BDS (green color) and 1P0I (orange color). 2D docking poses and interactions of Tacrine in the two PDB models.

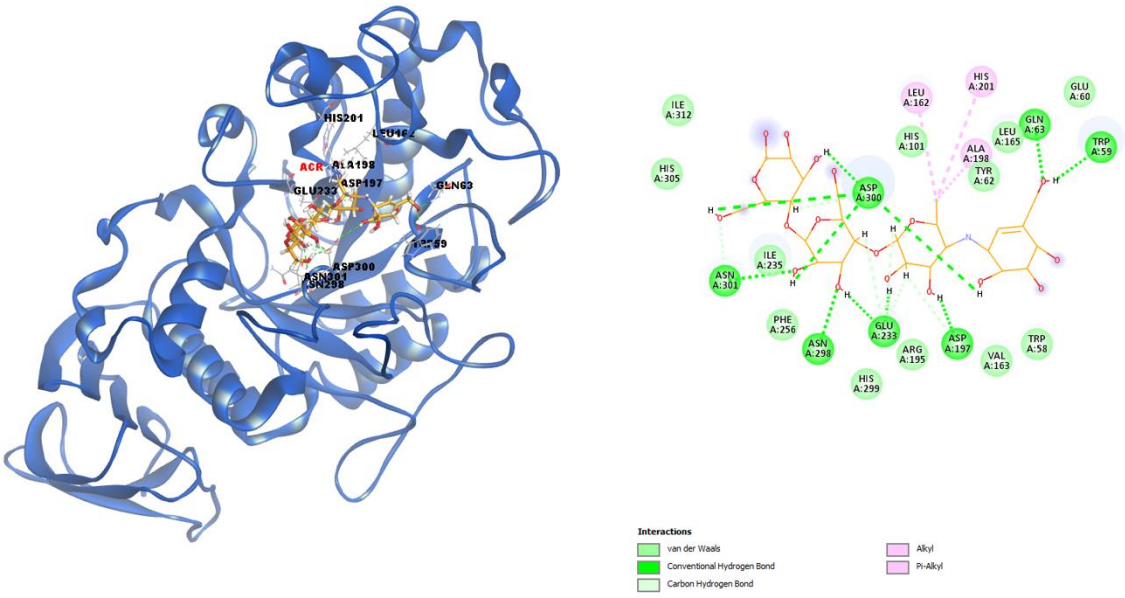

Figure S3. 3D and 2D docking poses and interactions of acarbose in the **Porcine Pancreatic Alpha-Amylase** model (1DHK, blue color).

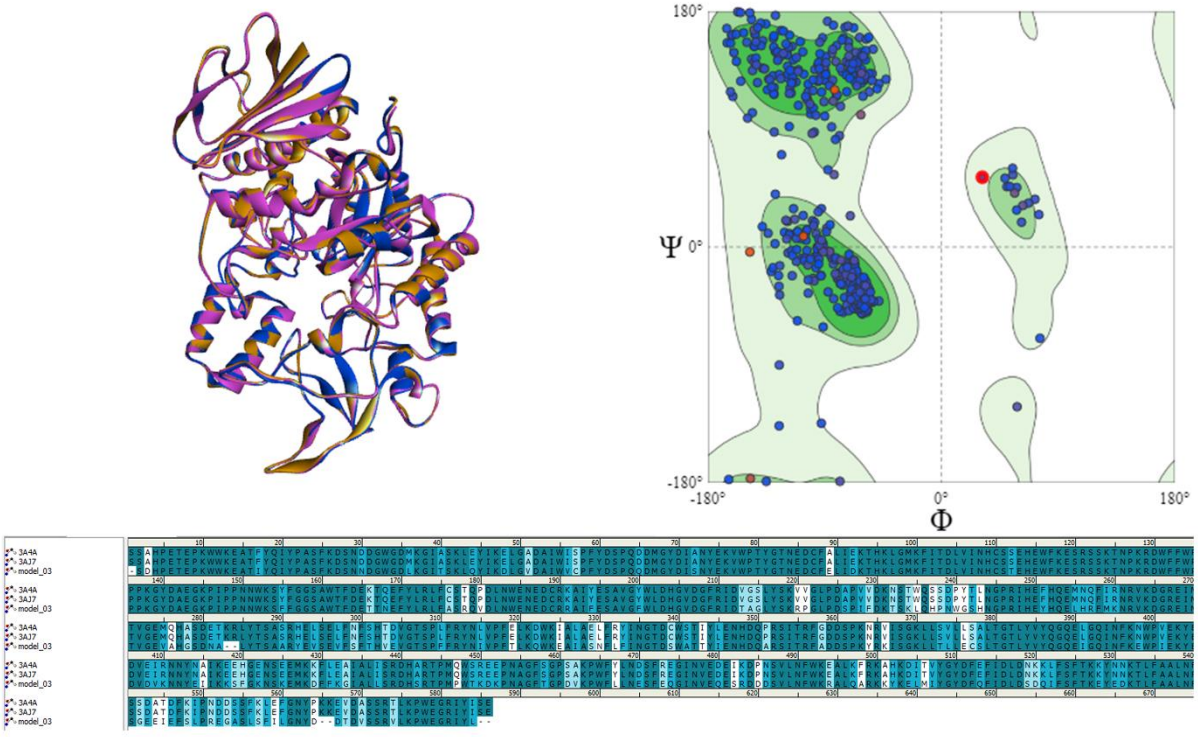

Figure S4. Superimposed structures, sequences of the two isomaltase /α-methylglucosidase from S. cerevisiae models, 3AJ7 (blue color) and 3A4A (orange color) and model3 (pink color). Ramachandran plot for homology model of yeast alpha glucosidase (model 3). The homology model was built and The model was validated and authenticated by Ramachandran plot using DS 3.5 software.

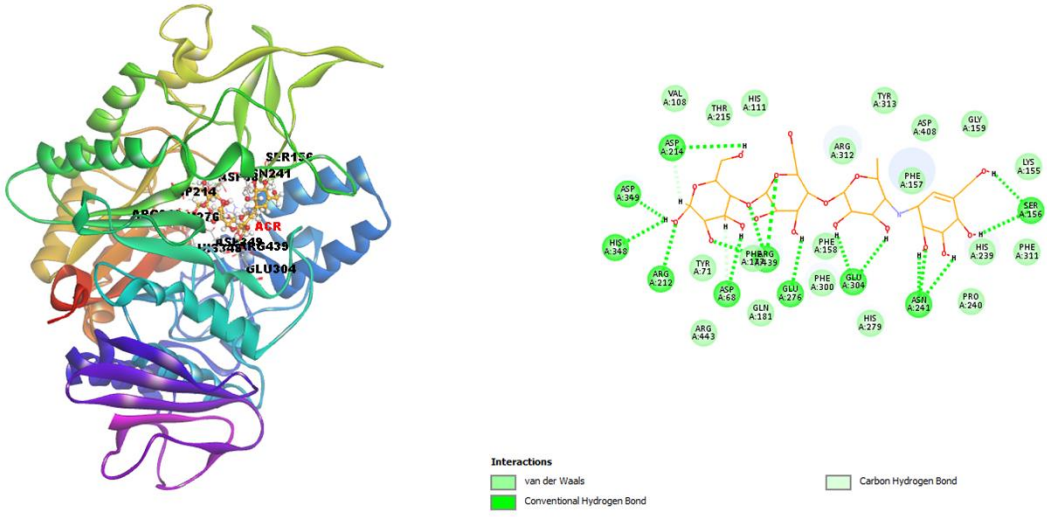

Figure S5. 3D and 2D docking poses and interactions of acarbose in the homology model of yeast alpha glucosidase (model 3).

Table S2. Interaction types and distances of **1d, 2c** and *Tacrine (TAC) compounds against AChE; **1c, 2c** and *Tacrin (TAC) compounds against BChE; **2a, 2d** and *Acarbose (ACR) compounds against α-Amy and **2a, 2d** and *Acarbose (ACR) compounds against α-Gly. The (*) mark indicates positive compounds of respective targets.

Interactions (hAChE)	**Distance Å**	**Bonding**	**Bonding Types**	**Binding site of target (hAChE)**	**Binding site of ligand (1d)**
A:ARG296:HN - :1d:O21	2.6589	Hydrogen Bond	Conventional Hydrogen Bond	A:ARG296:HN	:1d:O21
:1d:H34 - A:TYR341:O	1.8545	Hydrogen Bond	Conventional Hydrogen Bond	A:TYR341:O	:1d:H34
:1d:H8 - A:TYR337:OH	2.2266	Hydrogen Bond	Conventional Hydrogen Bond	A:TYR337:OH	:1d:H8
:1d:N5 - A:TYR341	4.9855	Electrostatic	Pi-Cation	A:TYR341	:1d:N5
:1d:H20 - A:TRP286	2.8476	Hydrophobic	Pi-Sigma	A:TRP286	:1d:H20
:1d:S19 - A:PHE338	5.9157	Other	Pi-Sulfur	A:PHE338	:1d:S19
A:TRP286 - :1d	5.2246	Hydrophobic	Pi-Pi Stacked	A:TRP286	:1d
A:TRP286 - :1d	4.0409	Hydrophobic	Pi-Pi Stacked	A:TRP286	:1d
:1d:C42 - A:LEU289	4.7763	Hydrophobic	Alkyl	A:LEU289	:1d:C42
A:TRP286 - :1d:C42	5.0362	Hydrophobic	Pi-Alkyl	A:TRP286	:1d:C42
A:TRP286 - :1d:C46	4.0117	Hydrophobic	Pi-Alkyl	A:TRP286	:1d:C46
Interactions (hAChE)	**Distance Å**	**Bonding**	**Bonding Types**	**Binding site of target (hAChE)**	**Binding site of ligand (2c)**
A:GLY120:HN - :2c:O24	2.7093	Hydrogen Bond	Conventional Hydrogen Bond	A:GLY120:HN	:2c:O24
A:GLY121:HN - :2c:O23	2.2188	Hydrogen Bond	Conventional Hydrogen Bond	A:GLY121:HN	:2c:O23
A:GLY126:HN - :2c:O15	2.8364	Hydrogen Bond	Conventional Hydrogen Bond	A:GLY126:HN	:2c:O15
A:TYR133:HH - :2c:O24	2.2594	Hydrogen Bond	Conventional Hydrogen Bond	A:TYR133:HH	:2c:O24
A:SER203:HG - :2c:O23	2.9305	Hydrogen Bond	Conventional Hydrogen Bond	A:SER203:HG	:2c:O23
:2c:H37 - A:GLU202:OE1	2.1276	Hydrogen Bond	Conventional Hydrogen Bond	A:GLU202:OE1	:2c:H37
A:GLY120:HA1 - :2c:O23	2.2252	Hydrogen Bond	Carbon Hydrogen Bond	A:GLY120:HA1	:2c:O23
A:GLY126:HA2 - :2c:O15	2.5275	Hydrogen Bond	Carbon Hydrogen Bond	A:GLY126:HA2	:2c:O15
A:SER203:HB1 - :2c:O23	2.1507	Hydrogen Bond	Carbon Hydrogen Bond	A:SER203:HB1	:2c:O23
A:GLY448:HA1 - :2c:N45	2.5325	Hydrogen Bond	Carbon Hydrogen Bond	A:GLY448:HA1	:2c:N45
:2c:H14 - A:TYR337	2.3771	Hydrophobic	Pi-Sigma	A:TYR337	:2c:H14
A:TRP86 - :2c	4.9761	Hydrophobic	Pi-Pi T-shaped	A:TRP86	:2c
A:TRP86 - :2c	4.7236	Hydrophobic	Pi-Pi T-shaped	A:TRP86	:2c
A:TYR337 - :2c	4.7022	Hydrophobic	Pi-Pi T-shaped	A:TYR337	:2c
A:TYR337 - :2c	4.8115	Hydrophobic	Pi-Pi T-shaped	A:TYR337	:2c
A:TYR341 - :2c	4.5476	Hydrophobic	Pi-Pi T-shaped	A:TYR341	:2c

A:GLY120:C,O;GLY121:N - :2c	3.6875	Hydrophobic	Amide-Pi Stacked	A:GLY120:C,O;GLY121:N	:2c
A:TRP86 - :2c:C46	3.8015	Hydrophobic	Pi-Alkyl	A:TRP86	:2c:C46
A:TRP86 - :2c:C46	4.0886	Hydrophobic	Pi-Alkyl	A:TRP86	:2c:C46
A:TYR337 - :2c:C46	4.1056	Hydrophobic	Pi-Alkyl	A:TYR337	:2c:C46
A:TYR449 - :2c:C46	4.2911	Hydrophobic	Pi-Alkyl	A:TYR449	:2c:C46
Interactions (hAChE)	**Distance Å**	**Bonding**	**Bonding Types**	**Binding site of target (hAChE)**	**Binding site of ligand (TAC)**
:TAC:H27 - A:GLU202:OE1	1.9707	Hydrogen Bond	Conventional Hydrogen Bond	A:GLU202:OE1	:TAC:H27
A:TRP86 - :TAC	4.09792	Hydrophobic	Pi-Pi Stacked	A:TRP86	:TAC
A:TRP86 - :TAC	4.9289	Hydrophobic	Pi-Pi Stacked	A:TRP86	:TAC
A:TRP86 - :TAC	3.7454	Hydrophobic	Pi-Pi Stacked	A:TRP86	:TAC
A:TRP86 - :TAC	4.6813	Hydrophobic	Pi-Pi Stacked	A:TRP86	:TAC
A:TRP86 - :TAC	4.9323	Hydrophobic	Pi-Alkyl	A:TRP86	:TAC
A:TRP86 - :TAC	4.6616	Hydrophobic	Pi-Alkyl	A:TRP86	:TAC
A:TYR337 - :TAC	4.8422	Hydrophobic	Pi-Alkyl	A:TYR337	:TAC
A:HIS447 - :TAC	4.5681	Hydrophobic	Pi-Alkyl	A:HIS447	:TAC

Interactions (hBChE)	**Distance Å**	**Bonding**	**Bonding Types**	**Binding site of target (hBChE)**	**Binding site of ligand (1c)**
A:ASP70:HN - :1c:S8	3.0736	Hydrogen Bond	Conventional Hydrogen Bond	A:ASP70:HN	:1c:S8
A:GLY115:HN - :1c:O20	2.2901	Hydrogen Bond	Conventional Hydrogen Bond	A:GLY115:HN	:1c:O20
A:TYR128:HH - :1c:O20	2.5398	Hydrogen Bond	Conventional Hydrogen Bond	A:TYR128:HH	:1c:O20
:1c:H24 - A:TRP82:O	1.6675	Hydrogen Bond	Conventional Hydrogen Bond	A:TRP82:O	:1c:H24
:1c:H34 - A:GLU197:OE2	2.0978	Hydrogen Bond	Conventional Hydrogen Bond	A:GLU197:OE2	:1c:H34
A:GLY115:HA1 - :1c:O21	2.6060	Hydrogen Bond	Carbon Hydrogen Bond	A:GLY115:HA1	:1c:O21
A:SER198:HB1 - :1c:O21	2.4618	Hydrogen Bond	Carbon Hydrogen Bond	A:SER198:HB1	:1c:O21
:1c:H18 - A:HIS438:O	2.4106	Hydrogen Bond	Carbon Hydrogen Bond	A:HIS438:O	:1c:H18
A:HIS438:NE2 - :1c	4.1840	Electrostatic	Pi-Cation	A:HIS438:NE2	:1c
A:ASP70:OD2 - :1c	3.4519	Electrostatic	Pi-Anion	A:ASP70:OD2	:1c
A:TRP82:HB1 - :1c	2.9088	Hydrophobic	Pi-Sigma	A:TRP82:HB1	:1c
A:TRP82 - :1c	4.5388	Hydrophobic	Pi-Pi T-shaped	A:TRP82	:1c
A:TYR332 - :1c	5.2747	Hydrophobic	Pi-Pi T-shaped	A:TYR332	:1c
A:HIS438 - :1c	4.4959	Hydrophobic	Pi-Pi T-shaped	A:HIS438	:1c
A:GLY115:C,O;GLY116:N - :1c	3.9525	Hydrophobic	Amide-Pi Stacked	A:GLY115:C,O;GLY116:N	:1c

A:PHE329 - :1c:C43	4.9780	Hydrophobic	Pi-Alkyl	A:PHE329	:1c:C43
A:HIS438 - :1c:C43	4.6457	Hydrophobic	Pi-Alkyl	A:HIS438	:1c:C43
Interactions (hBChE)	**Distance Å**	**Bonding**	**Bonding Types**	**Binding site of target (hBChE)**	**Binding site of ligand (2c)**
A:GLY116:HN - :2c:O8	1.9683	Hydrogen Bond	Conventional Hydrogen Bond	A:GLY116:HN	:2c:O8
A:GLY117:HN - :2c:O8	2.0866	Hydrogen Bond	Conventional Hydrogen Bond	A:GLY117:HN	:2c:O8
A:ALA199:HN - :2c:O8	2.3976	Hydrogen Bond	Conventional Hydrogen Bond	A:ALA199:HN	:2c:O8
A:SER198:HB1 - :2c:O8	2.1835	Hydrogen Bond	Carbon Hydrogen Bond	A:SER198:HB1	:2c:O8
:2c:H13 - A:SER79:O	2.0776	Hydrogen Bond	Carbon Hydrogen Bond	A:SER79:O	:2c:H13
A:HIS438:NE2 - :2c	4.7794	Electrostatic	Pi-Cation	A:HIS438:NE2	:2c
A:ASP70:OD2 - :2c	2.8678	Electrostatic	Pi-Anion	A:ASP70:OD2	:2c
A:HIS438:HD2 - :2c	2.8974	Hydrophobic	Pi-Sigma	A:HIS438:HD2	:2c
:2c:H11 - A:TRP231	2.8851	Hydrophobic	Pi-Sigma	A:TRP231	:2c:H11
:2c:O15 - A:TRP82	2.7144	Other	Pi-Lone Pair	A:TRP82	:2c:O15
A:TRP231 - :2c	5.3616	Hydrophobic	Pi-Pi T-shaped	A:TRP231	:2c
A:TRP231 - :2c	5.3187	Hydrophobic	Pi-Pi T-shaped	A:TRP231	:2c
A:PHE329 - :2c	5.1296	Hydrophobic	Pi-Pi T-shaped	A:PHE329	:2c
A:HIS438 - :2c	5.1117	Hydrophobic	Pi-Pi T-shaped	A:HIS438	:2c
:2c - A:ALA328	5.0903	Hydrophobic	Pi-Alkyl	A:ALA328	:2c
:2c - A:LEU286	5.0752	Hydrophobic	Pi-Alkyl	A:LEU286	:2c
Interactions (hBChE)	**Distance Å**	**Bonding**	**Bonding Types**	**Binding site of target (hBChE)**	**Binding site of ligand (TAC)**
:TAC:H26 - A:TRP82:O	2.0179	Hydrogen Bond	Conventional Hydrogen Bond	A:TRP82:O	:TAC:H26
:TAC:H27 - A:GLN67:OE1	1.9669	Hydrogen Bond	Conventional Hydrogen Bond	A:GLN67:OE1	:TAC:H27
A:THR120:OG1 - :TAC	2.8443	Other	Pi-Lone Pair	A:THR120:OG1	:TAC
A:TRP82 - :TAC	5.3361	Hydrophobic	Pi-Alkyl	A:TRP82	:TAC
A:TRP82 - :TAC	5.0819	Hydrophobic	Pi-Alkyl	A:TRP82	:TAC

Interactions (α-Amy)	**Distance Å**	**Bonding**	**Bonding Types**	**Binding site of target (α-Amy)**	**Binding site of ligand (2a)**
A:ARG195:HH12 - :2a:O23	2.7789	Hydrogen Bond	Conventional Hydrogen Bond	A:ARG195:HH12	:2a:O23
:2a:H37 - A:ASP197:OD1	1.7643	Hydrogen Bond	Conventional Hydrogen Bond	A:ASP197:OD1	:2a:H37
:2a:H38 - A:GLU233:OE2	1.8153	Hydrogen Bond	Conventional Hydrogen Bond	A:GLU233:OE2	:2a:H38
A:HIS101:HE1 - :2a:O15	3.0949	Hydrogen Bond	Carbon Hydrogen Bond	A:HIS101:HE1	:2a:O15
:2a:S22 - A:TRP58	5.9748	Other	Pi-Sulfur	A:TRP58	:2a:S22

:2a:S22 - A:TYR62	4.0881	Other	Pi-Sulfur	A:TYR62	:2a:S22
:2a:S22 - A:HIS299	4.4537	Other	Pi-Sulfur	A:HIS299	:2a:S22
A:TRP59 - :2a	4.6373	Hydrophobic	Pi-Pi Stacked	A:TRP59	:2a
A:TYR62 - :2a	4.1764	Hydrophobic	Pi-Pi Stacked	A:TYR62	:2a
A:TRP58 - :2a	4.8265	Hydrophobic	Pi-Pi T-shaped	A:TRP58	:2a
Interactions (α-Amy)	**Distance Å**	**Bonding**	**Bonding Types**	**Binding site of target (α-Amy)**	**Binding site of ligand (2d)**
A:HIS101:HE2 - :2d:O23	2.0095	Hydrogen Bond	Conventional Hydrogen Bond	A:HIS101:HE2	:2d:O23
A:HIS201:HE2 - :2d:O15	1.9414	Hydrogen Bond	Conventional Hydrogen Bond	A:HIS201:HE2	:2d:O15
:2d:H37 - A:ASP197:OD2	1.8565	Hydrogen Bond	Conventional Hydrogen Bond	A:ASP197:OD2	:2d:H37
A:ASP300:OD1 - :2d	3.6214	Electrostatic	Pi-Anion	A:ASP300:OD1	:2d
A:TYR62 - :2d	4.0569	Hydrophobic	Pi-Pi Stacked	A:TYR62	:2d
A:TRP58 - :2d:C45	3.9258	Hydrophobic	Pi-Alkyl	A:TRP58	:2d:C45
A:TYR62 - :2d:C45	4.2632	Hydrophobic	Pi-Alkyl	A:TYR62	:2d:C45
A:HIS299 - :2d:C49	3.9176	Hydrophobic	Pi-Alkyl	A:HIS299	:2d:C49
:2d - A:LEU162	4.8026	Hydrophobic	Pi-Alkyl	A:LEU162	:2d
:2d - A:ALA198	4.4036	Hydrophobic	Pi-Alkyl	A:ALA198	:2d
:2d - A:ILE235	5.0145	Hydrophobic	Pi-Alkyl	A:ILE235	:2d
Interactions (α-Amy)	**Distance Å**	**Bonding**	**Bonding Types**	**Binding site of target (α-Amy)**	**Binding site of ligand (ACR)**
A:GLN63:HE22 - :ACR:O18	1.6702	Hydrogen Bond	Conventional Hydrogen Bond	A:GLN63:HE22	:ACR:O18
A:ASN298:HD21 - :ACR:O7	2.0254	Hydrogen Bond	Conventional Hydrogen Bond	A:ASN298:HD21	:ACR:O7
A:ASN301:HN - :ACR:O9	2.6100	Hydrogen Bond	Conventional Hydrogen Bond	A:ASN301:HN	:ACR:O9
:ACR:H77 - A:ASP300:OD2	2.9104	Hydrogen Bond	Conventional Hydrogen Bond	A:ASP300:OD2	:ACR:H77
:ACR:H87 - A:TRP59:O	1.7371	Hydrogen Bond	Conventional Hydrogen Bond	A:TRP59:O	:ACR:H87
:ACR:H70 - A:ASP197:OD1	2.2595	Hydrogen Bond	Conventional Hydrogen Bond	A:ASP197:OD1	:ACR:H70
:ACR:H72 - A:GLU233:OE2	1.9303	Hydrogen Bond	Conventional Hydrogen Bond	A:GLU233:OE2	:ACR:H72
:ACR:H73 - A:GLU233:OE2	1.7352	Hydrogen Bond	Conventional Hydrogen Bond	A:GLU233:OE2	:ACR:H73
:ACR:H74 - A:ASP300:OD1	2.2284	Hydrogen Bond	Conventional Hydrogen Bond	A:ASP300:OD1	:ACR:H74
:ACR:H81 - A:ASP300:OD1	1.6743	Hydrogen Bond	Conventional Hydrogen Bond	A:ASP300:OD1	:ACR:H81
:ACR:H86 - A:ASP300:OD1	2.5189	Hydrogen Bond	Conventional Hydrogen Bond	A:ASP300:OD1	:ACR:H86
A:ASN301:HA - :ACR:O17	1.9122	Hydrogen Bond	Carbon Hydrogen Bond	A:ASN301:HA	:ACR:O17
:ACR:H15 - A:GLU233:OE2	2.8086	Hydrogen Bond	Carbon Hydrogen Bond	A:GLU233:OE2	:ACR:H15
:ACR:H20 - A:GLU233:OE2	2.3565	Hydrogen Bond	Carbon Hydrogen Bond	A:GLU233:OE2	:ACR:H20

:ACR:H27 - A:ASP197:OD1	2.7183	Hydrogen Bond	Carbon Hydrogen Bond	A:ASP197:OD1	:ACR:H27
:ACR:H27 - A:GLU233:OE1	2.5169	Hydrogen Bond	Carbon Hydrogen Bond	A:GLU233:OE1	:ACR:H27
:ACR:H37 - A:ASP300:OD1	2.8195	Hydrogen Bond	Carbon Hydrogen Bond	A:ASP300:OD1	:ACR:H37
A:ALA198 - :ACR:C35	4.4052	Hydrophobic	Alkyl	A:ALA198	:ACR:C35
:ACR:C35 - A:LEU162	4.5427	Hydrophobic	Alkyl	A:LEU162	:ACR:C35
A:HIS201 - :ACR:C35	5.1708	Hydrophobic	Pi-Alkyl	A:HIS201	:ACR:C35

Interactions (α-Gly)	**Distance Å**	**Bonding**	**Bonding Types**	**Binding site of target (α-Gly)**	**Binding site of ligand (2a)**
A:ARG312:HE - :2a:O23	1.7950	Hydrogen Bond	Conventional Hydrogen Bond	A:ARG312:HE	:2a:O23
A:TYR313:HH - :2a:O23	2.0359	Hydrogen Bond	Conventional Hydrogen Bond	A:TYR313:HH	:2a:O23
A:ASN412:HD22 - :2a:O15	1.9822	Hydrogen Bond	Conventional Hydrogen Bond	A:ASN412:HD22	:2a:O15
:2a:H38 - A:ASP408:OD1	2.1588	Hydrogen Bond	Conventional Hydrogen Bond	A:ASP408:OD1	:2a:H38
A:HIS239:HE1 - :2a:O8	1.8895	Hydrogen Bond	Carbon Hydrogen Bond	A:HIS239:HE1	:2a:O8
A:PHE311:HA - :2a:O8	2.3282	Hydrogen Bond	Carbon Hydrogen Bond	A:PHE311:HA	:2a:O8
:2a:S14 - A:PHE311	4.6604	Other	Pi-Sulfur	A:PHE311	:2a:S14
:2a:S22 - A:TYR313	5.4500	Other	Pi-Sulfur	A:TYR313	:2a:S22
:2a - A:ARG312	3.8643	Hydrophobic	Pi-Alkyl	A:ARG312	:2a
:2a - A:ARG312	4.8447	Hydrophobic	Pi-Alkyl	A:ARG312	:2a
Interactions (α-Gly)	**Distance Å**	**Bonding**	**Bonding Types**	**Binding site of target (α-Gly)**	**Binding site of ligand (2d)**
A:ASN241:HD22 - :2d:S14	2.3887	Hydrogen Bond	Conventional Hydrogen Bond	A:ASN241:HD22	:2d:S14
A:ARG439:HH11 - :2d:O23	2.4599	Hydrogen Bond	Conventional Hydrogen Bond	A:ARG439:HH11	:2d:O23
A:ARG439:HH11 - :2d:N44	2.7297	Hydrogen Bond	Conventional Hydrogen Bond	A:ARG439:HH11	:2d:N44
:2d:H37 - A:GLU276:OE2	1.9451	Hydrogen Bond	Conventional Hydrogen Bond	A:GLU276:OE2	:2d:H37
A:ARG439:HD2 - :2d:O23	2.9097	Hydrogen Bond	Carbon Hydrogen Bond	A:ARG439:HD2	:2d:O23
:2d:S14 - A:ASN241:OD1	3.1329	Other	Sulfur-X	A:ASN241:OD1	:2d:S14
:2d:S14 - A:ASN241:ND2	3.2850	Other	Sulfur-X	A:ASN241:ND2	:2d:S14
A:ASP214:OD1 - :2d	3.7694	Electrostatic	Pi-Anion	A:ASP214:OD1	:2d
:2d:H15 - A:PHE177	2.3103	Hydrophobic	Pi-Sigma	A:PHE177	:2d:H15
:2d:S14 - A:HIS279	5.2535	Other	Pi-Sulfur	A:HIS279	:2d:S14
A:PHE300 - :2d	4.7758	Hydrophobic	Pi-Pi T-shaped	A:PHE300	:2d
A:TYR71 - :2d:C45	3.6057	Hydrophobic	Pi-Alkyl	A:TYR71	:2d:C45
A:HIS111 - :2d:C49	4.2511	Hydrophobic	Pi-Alkyl	A:HIS111	:2d:C49

A:HIS348 - :2d:C45	4.4027	Hydrophobic	Pi-Alkyl	A:HIS348	:2d:C45
:2d - A:ARG312	4.0951	Hydrophobic	Pi-Alkyl	A:ARG312	:2d
Interactions (α-Gly)	**Distance Å**	**Bonding**	**Bonding Types**	**Binding site of target (α-Gly)**	**Binding site of ligand (ACR)**
A:ARG212:HH12 - :ACR:O16	2.7103	Hydrogen Bond	Conventional Hydrogen Bond	A:ARG212:HH12	:ACR:O16
A:ARG212:HH22 - :ACR:O16	2.1753	Hydrogen Bond	Conventional Hydrogen Bond	A:ARG212:HH22	:ACR:O16
A:ASN241:HD22 - :ACR:O10	2.1833	Hydrogen Bond	Conventional Hydrogen Bond	A:ASN241:HD22	:ACR:O10
A:ARG439:HH11 - :ACR:O3	1.8509	Hydrogen Bond	Conventional Hydrogen Bond	A:ARG439:HH11	:ACR:O3
A:ARG439:HH11 - :ACR:O15	2.2442	Hydrogen Bond	Conventional Hydrogen Bond	A:ARG439:HH11	:ACR:O15
A:ARG439:HH12 - :ACR:O4	2.3330	Hydrogen Bond	Conventional Hydrogen Bond	A:ARG439:HH12	:ACR:O4
:ACR:H77 - A:ASN241:OD1	2.0611	Hydrogen Bond	Conventional Hydrogen Bond	A:ASN241:OD1	:ACR:H77
:ACR:H80 - A:ASN241:OD1	2.2174	Hydrogen Bond	Conventional Hydrogen Bond	A:ASN241:OD1	:ACR:H80
:ACR:H82 - A:SER156:O	2.2023	Hydrogen Bond	Conventional Hydrogen Bond	A:SER156:O	:ACR:H82
:ACR:H87 - A:SER156:O	1.9009	Hydrogen Bond	Conventional Hydrogen Bond	A:SER156:O	:ACR:H87
:ACR:H70 - A:GLU304:OE2	1.9899	Hydrogen Bond	Conventional Hydrogen Bond	A:GLU304:OE2	:ACR:H70
:ACR:H72 - A:GLU304:OE2	1.7773	Hydrogen Bond	Conventional Hydrogen Bond	A:GLU304:OE2	:ACR:H72
:ACR:H73 - A:GLU276:OE2	2.1563	Hydrogen Bond	Conventional Hydrogen Bond	A:GLU276:OE2	:ACR:H73
:ACR:H81 - A:ASP68:OD2	2.4232	Hydrogen Bond	Conventional Hydrogen Bond	A:ASP68:OD2	:ACR:H81
:ACR:H85 - A:HIS348:NE2	2.3192	Hydrogen Bond	Conventional Hydrogen Bond	A:HIS348:NE2	:ACR:H85
:ACR:H85 - A:ASP349:OD2	1.9445	Hydrogen Bond	Conventional Hydrogen Bond	A:ASP349:OD2	:ACR:H85
:ACR:H86 - A:ASP214:OD2	2.0583	Hydrogen Bond	Conventional Hydrogen Bond	A:ASP214:OD2	:ACR:H86
:ACR:H38 - A:ASP68:OD2	2.3359	Hydrogen Bond	Carbon Hydrogen Bond	A:ASP68:OD2	:ACR:H38
:ACR:H40 - A:ASP214:OD1	1.8479	Hydrogen Bond	Carbon Hydrogen Bond	A:ASP214:OD1	:ACR:H40

1a

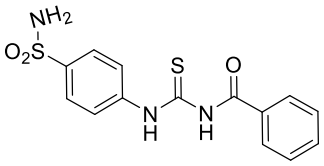

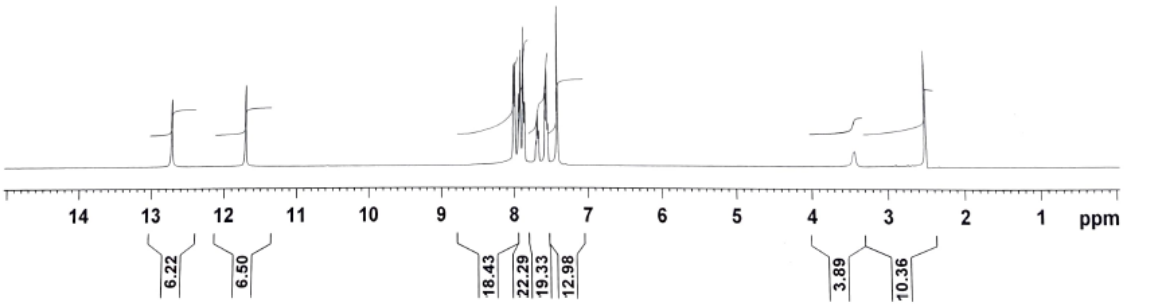

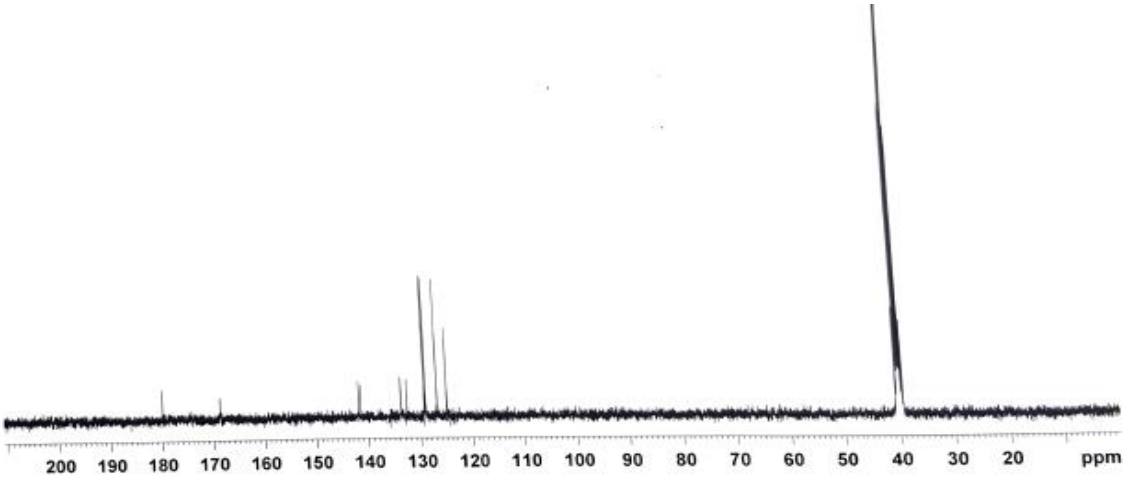

C14 H13 N3 O3 S2 [M-H]- : Predicted region for 334.0326 m/z

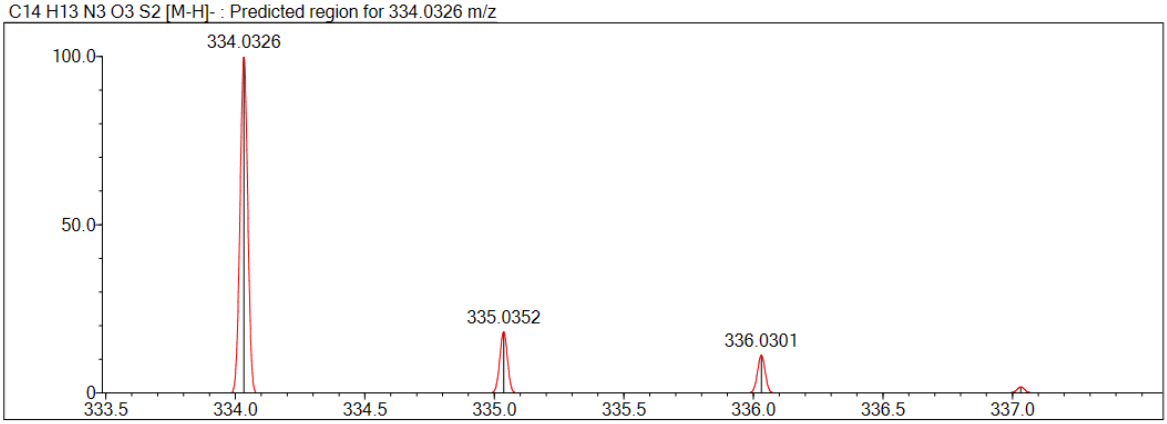

Rank	Score	Formula (M)	Ion	Meas. m/z	Pred. m/z	Df. (mDa)	Df. (ppm)	Iso	DBE
1	29.90	C14 H13 N3 O3 S2	[M-H]-	334.0330	334.0326	0.4	1.20	30.05	10.0

1b

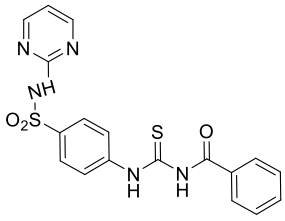

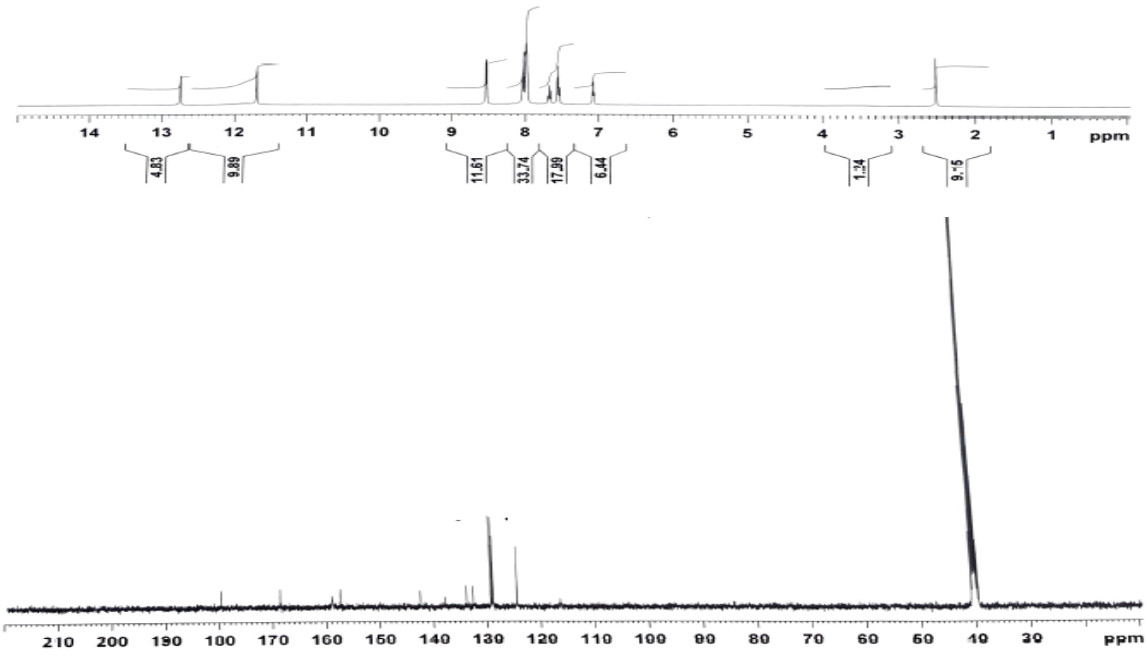

C18 H15 N5 O3 S2 [M+Na]+ : Predicted region for 436.0509 m/z

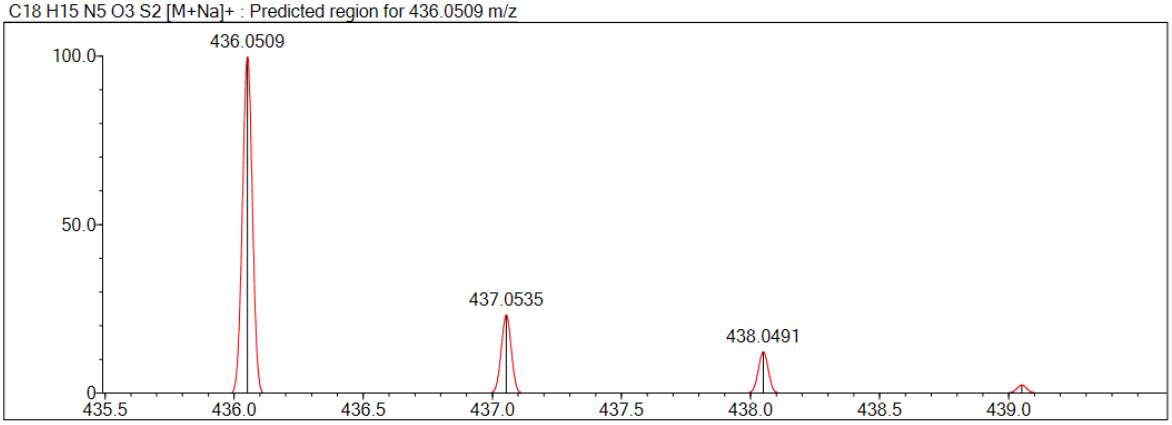

Rank	Score	Formula (M)	Ion	Meas. m/z	Pred. m/z	Df. (mDa)	Df. (ppm)	Iso	DBE
1	68.24	C18 H15 N5 O3 S2	[M+Na]+	436.0502	436.0509	-0.7	-1.61	69.30	14.0

1c

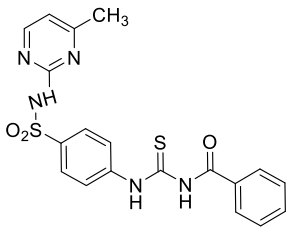

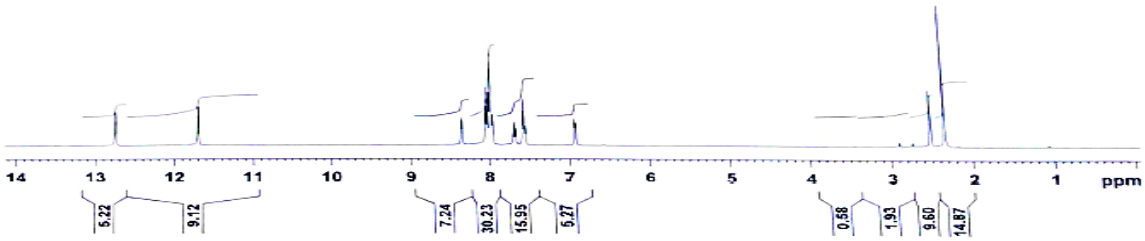

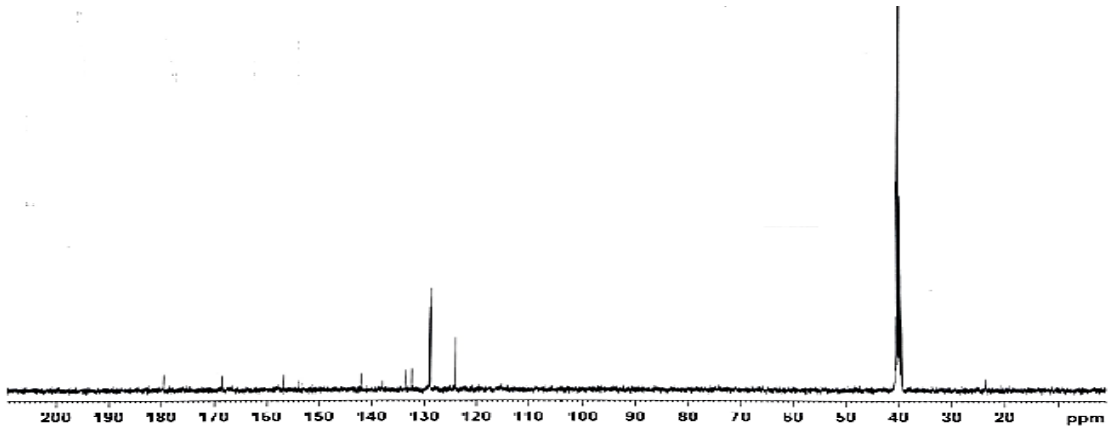

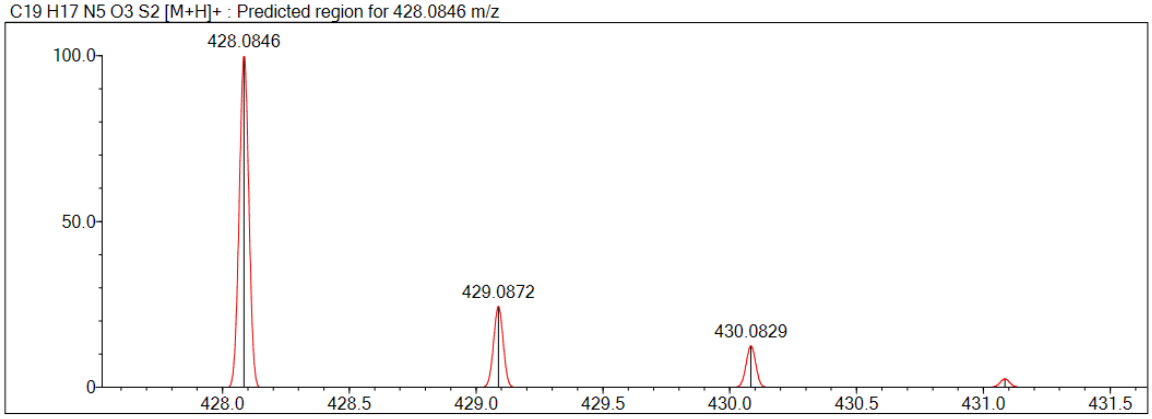

Rank	Score	Formula (M)	Ion	Meas. m/z	Pred. m/z	Df. (mDa)	Df. (ppm)	Iso	DBE
1	37.19	C19 H17 N5 O3 S2	[M+H]+	428.0834	428.0846	-1.2	-2.80	38.94	14.0

1d

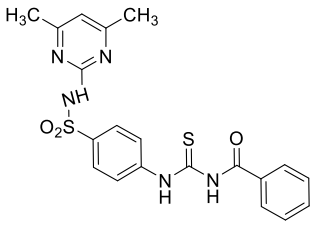

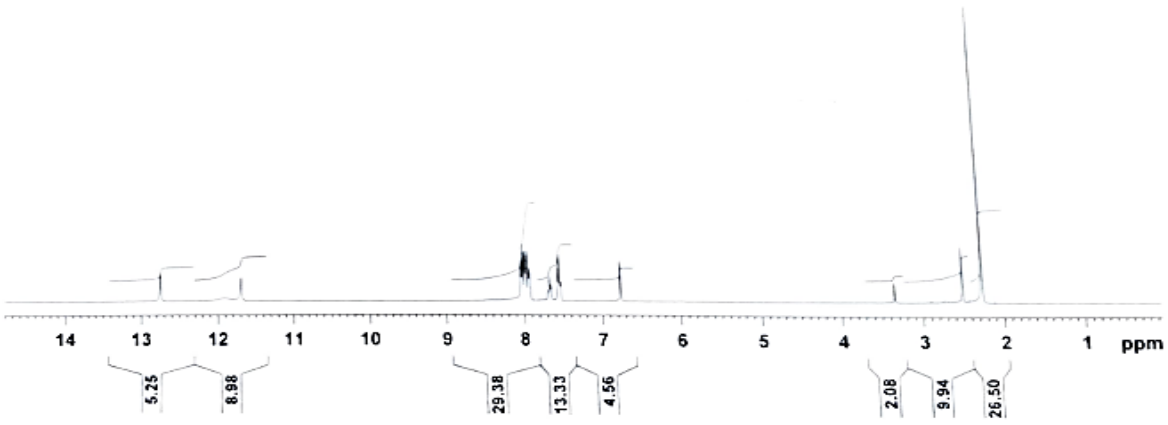

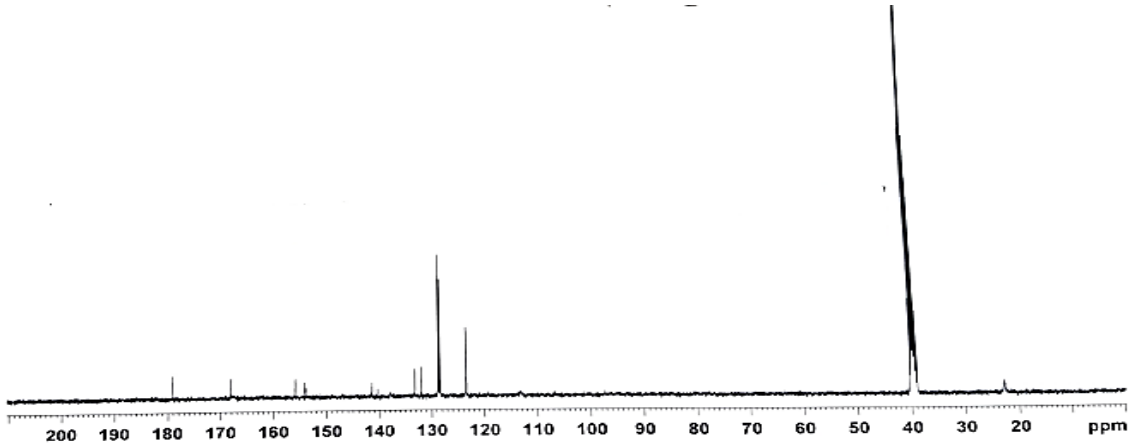

C20 H19 N5 O3 S2 [M+H]+ : Predicted region for 442.1002 m/z

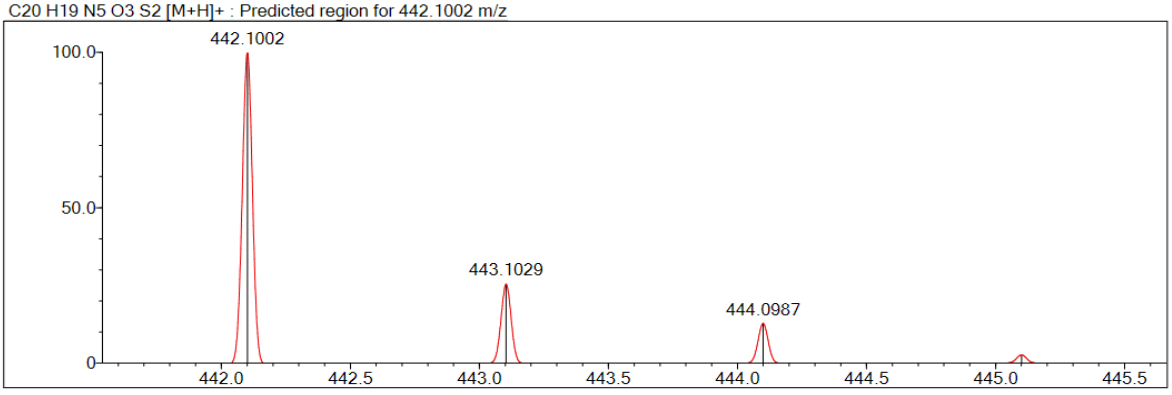

Rank	Score	Formula (M)	Ion	Meas. m/z	Pred. m/z	Df. (mDa)	Df. (ppm)	Iso	DBE
1	63.26	C20 H19 N5 O3 S2	[M+H]+	442.1006	442.1002	0.4	0.90	63.26	14.0

2a

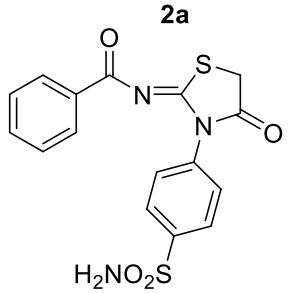
O
S
N
N
O
H_2NO_2S

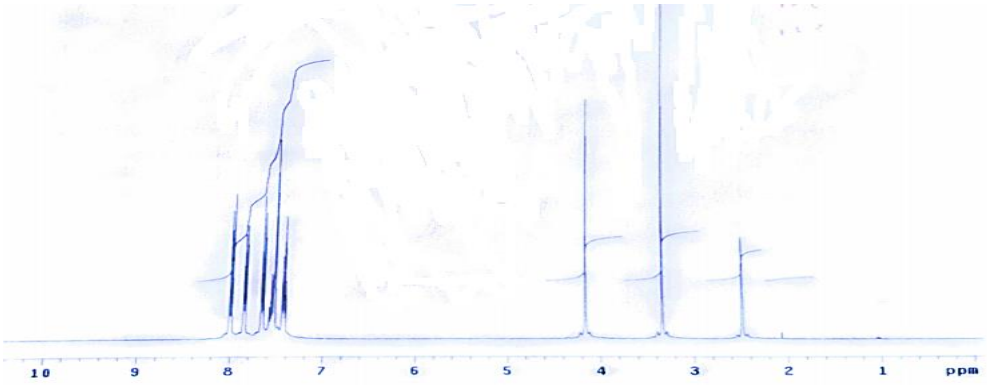
10
9
8
7
6
5
4
3
2
1
ppm

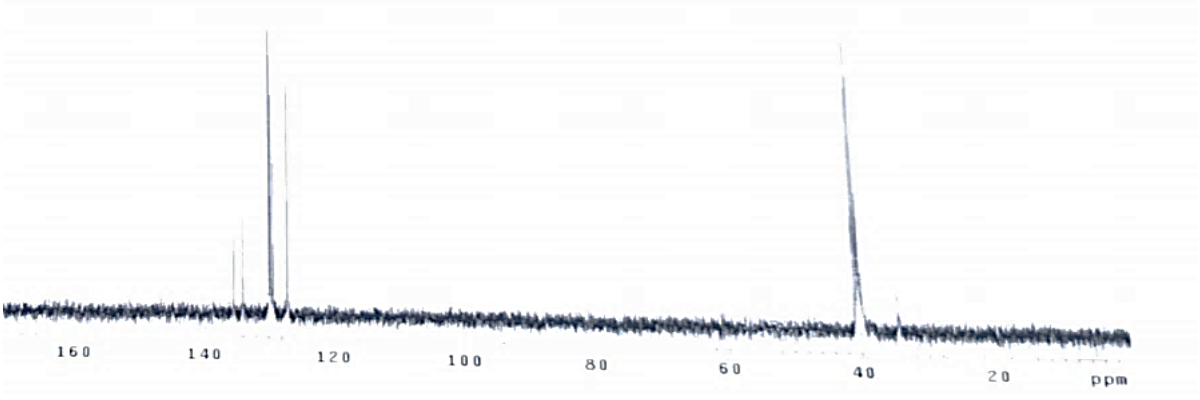
160
140
120
100
80
60
40
20
ppm

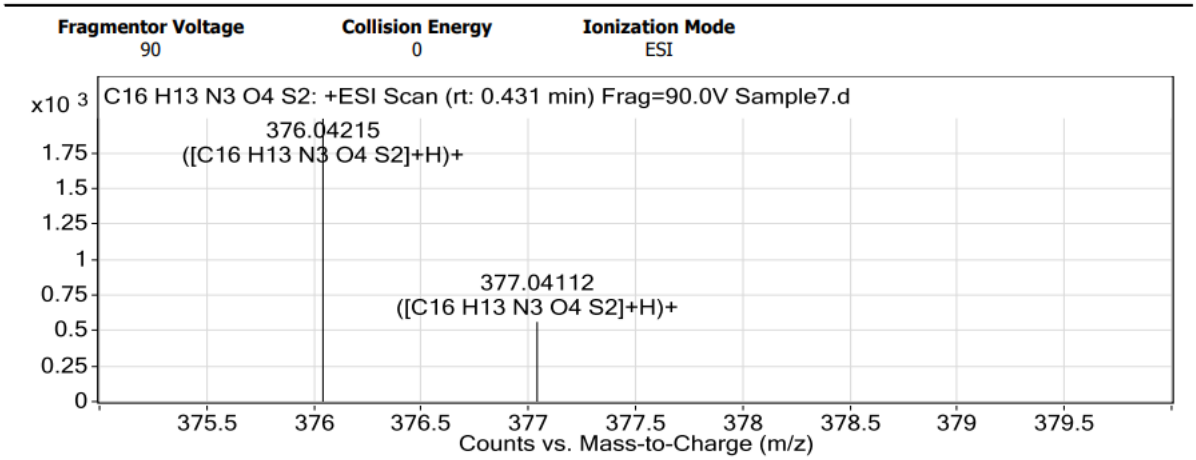
Fragmentor Voltage
90
Collision Energy
0
Ionization Mode
ESI
x10 3
C16 H13 N3 O4 S2: +ESI Scan (rt: 0.431 min) Frag=90.0V Sample7.d
376.04215
([C16 H13 N3 O4 S2]+H)+
377.04112
([C16 H13 N3 O4 S2]+H)+
1.75
1.5
1.25
1
0.75
0.5
0.25
0
375.5
376
376.5
377
377.5
378
378.5
379
379.5
Counts vs. Mass-to-Charge (m/z)

2c

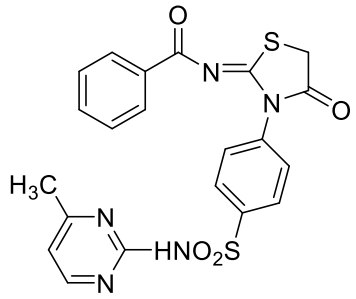
O
N
S
N
O
H3C
N
HNO2S
N

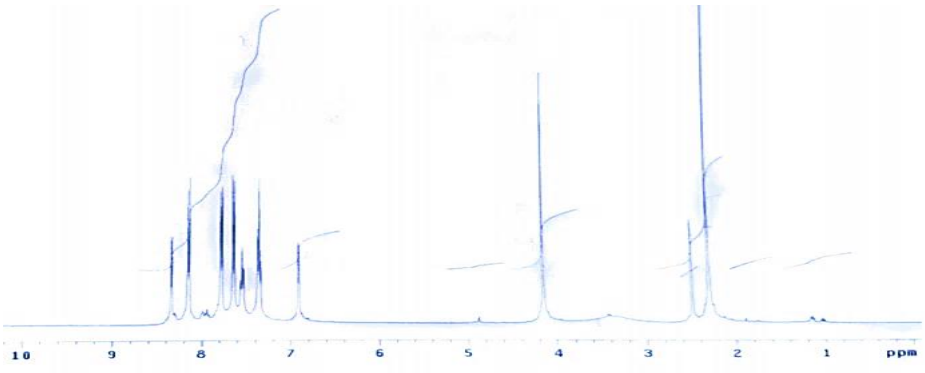
10
9
8
7
6
5
4
3
2
1
ppm

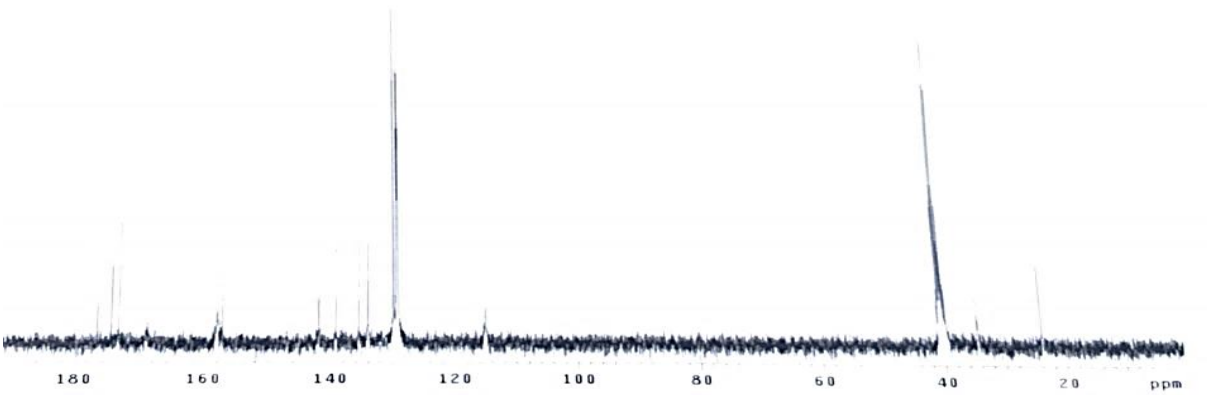
180
160
140
120
100
80
60
40
20
ppm

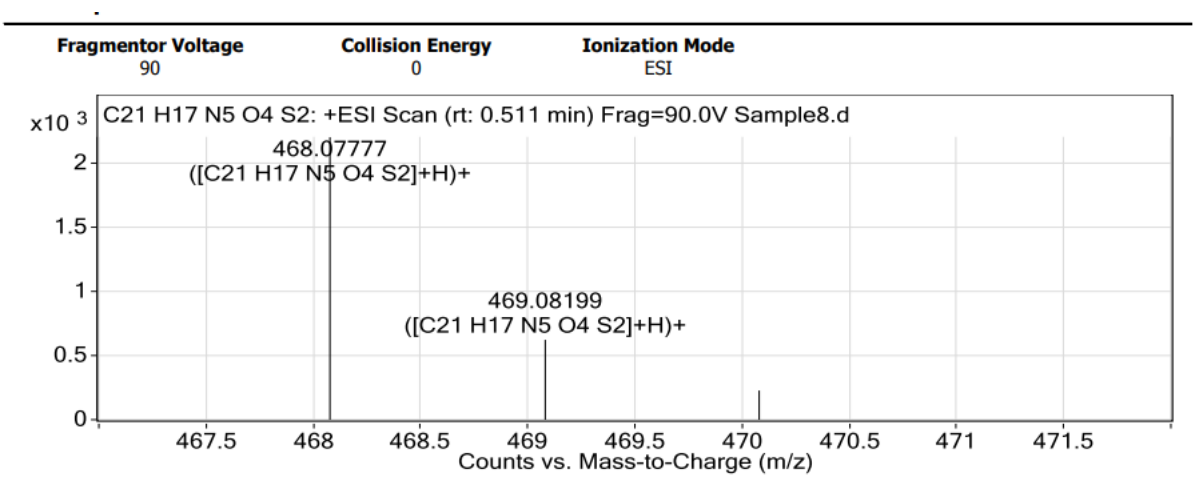
Fragmentor Voltage
90
Collision Energy
0
Ionization Mode
ESI
x10 3
C21 H17 N5 O4 S2: +ESI Scan (rt: 0.511 min) Frag=90.0V Sample8.d
468.07777
([C21 H17 N5 O4 S2]+H)+
469.08199
([C21 H17 N5 O4 S2]+H)+
2
1.5
1
0.5
0
467.5
468
468.5
469
469.5
470
470.5
471
471.5
Counts vs. Mass-to-Charge (m/z)

2d

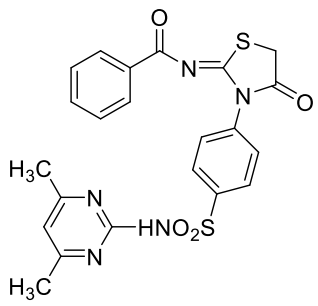

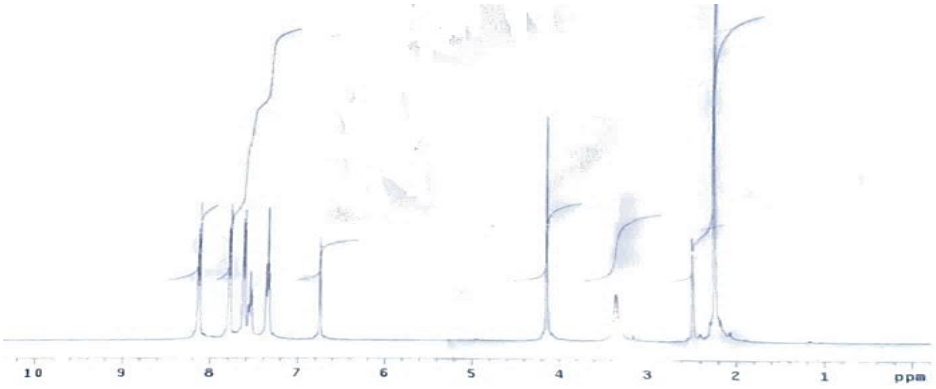

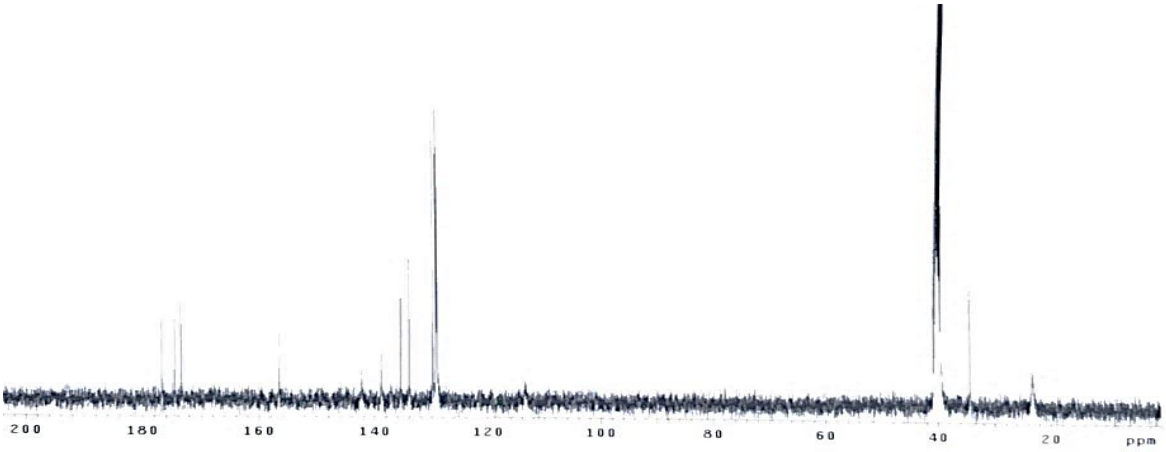

-

Fragmentor Voltage	Collision Energy	Ionization Mode
90	0	ESI

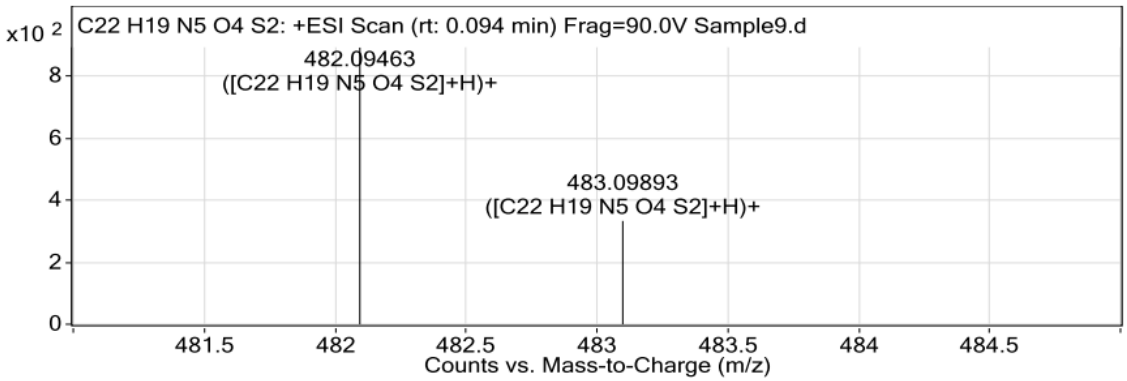

JOTCS A
Journal of the Turkish Chemical Society
Section: A
Chemistry
TURKISH CHEMICAL SOCIETY

Optimization of extraction condition of *Gynura procumbens* extract enriched with flavonoid and antioxidant compounds using Response Surface Methodology

Devi Permatasari[1*], Anisyah Is Purwati[1], Hismiaty Bahua[2], and Agus Supriyono[1]

[1]RC for Pharmaceutical Ingredients and Traditional Medicine, Research Organization for Health, National Research and Innovation Agency, South Tangerang, 15314, Indonesia
[2]RC for Sustainable Production System and Life Cycle Assessment, Research Organization for Energy and Manufacture, National Research and Innovation Agency, South Tangerang, 15314, Indonesia

Abstract: *Gynura procumbens* is known as one of the herbal medicinal plants found in Indonesia and has been used from time to time. It is claimed to have various efficacy such as anti-hyperglycemic, anti-hypertension, anti-microbial, anti-cancer, and antioxidant. Other studies mention that G. *procumbens* possessed high antioxidant compounds and had been used as a natural-based medicinal supplement. However, further studies on optimizing the extraction process of *Gynura procumbens* in Indonesia have yet to be reported. Therefore, this study aimed to optimize the extraction condition of *G. procumbens* leaves by maceration with three variables: solvent concentration, extraction time, and the ratio of solid-liquid used. Each of those variables contained three different levels. Determination of total flavonoid and antioxidant activity was measured using aluminium chloride colourimetric assay and 2, 2-diphenyl-1-picryl-hydrazil (DPPH) assay, respectively. In the optimization process, Response Surface Methodology (RSM) was used to explore the main effects and interaction between parameters and their correlations with dependent variables. The results were analyzed using the Box-Behnken method using Minitab software 17. This study shows that the most significant effect of the variable for both flavonoid and antioxidant activity was solvent concentration, with a $P<0.05$. The results showed that the extraction process to obtain *G. procumbens* extract with optimal flavonoid content and antioxidant activity (IC_{50}) was predicted at 70% solvent concentration, 1 h maceration time, and a solid-liquid ratio of 1:9.8 w/v, with results of 17.599 mg QE/g extract and 0.211 mg/mL, respectively. This study was expected to complement other studies and can be used as an additional reference for the development of the extraction process on a larger scale.

Keywords: *Gynura procumbens,* Optimization, Antioxidant activity, Flavonoid content, Response Surface Methodology.

Submitted: September 15, 2022. **Accepted:** March 14, 2023.

Cite this: Permatasari D, Purwati AI, Bahua H, Supriyono A. Optimization of extraction condition of Gynura procumbens extract enriched with flavonoid and antioxidant compounds using Response Surface Methodology. JOTCSA. 2023;10(2):425–34.

DOI: https://doi.org/10.18596/jotcsa.1172970.

***Corresponding author. E-mail:** devi.permatasari@brin.go.id.

1. INTRODUCTION

Gynura procumbens or "Sambung Nyawa"-as local people said- is one of the herbal medicines widely known for its efficacy as anti-hypertension, anti-hyperglycemia, anti-cancer, anti-microbial, antioxidant, and also anti-inflammation (1). As the American people said, this longevity spinach possesses high antioxidant activity (2), which can be a source of longer-lasting health quality, like the origin of the name. Antioxidant itself is one of the chemical compounds used to prevent oxidative stress in the biological system within the body that has the potential to cause diseases (3). Antioxidant compounds eliminate free radicals through specific mechanisms and can be obtained from endogenous (enzymes within the body) or exogenous sources (food, nutritional supplements, or pharmaceuticals) (4). The previous study mentioned that Sambung Nyawa leaves contains phenolics compounds such as gallic acid, protocatechuic acid, hydroxybenzoic acids (HBA),

vanillic acid, and syringic acid, while other study reported that it has flavonoid compounds like rutin, quercetin, kaempferol, myricetin, and apigenin that can be served as an antioxidant and an anti-photoaging agents (5,6).

This study focused on the optimization process which was conducted by using Response Surface Methodology (RSM), a technique to optimize the response from the experiment as influenced by its variables. This tool is helpful for modelling and analysis using mathematical and statistical approaches (7), selecting and constructing the variables needed to produce reliable results in the response optimizer. RSM has been used in the optimization process to reduce experimental trials. Thus, the study can be less expensive and less time-consuming (8–10). The most common design used in RSM is Box-Behnken Design, which requires three central points in the experiments (James Regun Karmoker). However, the final results generated from one experiment to another might have slight differences because of the variance in setting each variable within a specific range (11). The extraction process is commonly influenced by multiple variables. Therefore, the effects should be evaluated simultaneously to obtain accurate results.

In this study, the extraction process was conducted using a traditional maceration technique and assisted with stirring to increase the effectiveness of the process (12). Maceration was a method to get plant extracts easily and effectively. This process can be easily upgraded on a lab, pilot, or larger scale, like for a manufacturer. Despite the extraction technique, the extract's quality can be affected by many other factors, such as time of extraction, temperature, type and concentration of the solvent, and the solid-liquid ratio between the dry sample and solvent (13).

Based on previous studies, many studies of the antioxidant activity of this plant have been carried out, including the influence of the part of the plant used (14) and the effect of different solvents used in the extraction process (2,15). Another study also showed that this plant could be cultivated and produced in large quantities as a natural and affordable health supplement, especially in tropical countries (16). Hence, this study aims to equip previous studies by finding the maximum operating conditions in the extraction process using Response Surface Methodology to produce an extract with high total flavonoid content (TFC) and antioxidant activity. Besides, this study also aimed to find a contribution between each independent variable with the result within the extraction process.

2. EXPERIMENTAL SECTION

2.1. Chemical and reagents

Quercetin ≥95% (HPLC), 2, 2-diphenyl-1-picryl-hydrazil (DPPH), and Aluminum chloride were purchased from Sigma Chemical Company (St. Louis MO, USA). Potassium acetate was purchased from BDH Chemicals Ltd (Poole, England). HPLC-grade methanol was obtained from Merck, 96% food-grade ethanol was obtained from a local supplier, and all other solvents were analytical or HPLC grade.

2.2. Plant collection

Sambung nyawa or *Gynura procumbens leaves* were harvested from cultivation by BRIN in Sulusuban, Lampung. Fresh leaves of *G. procumbens* were dried using an oven with a temperature of up to 60 °C, then ground into a semi-powder using a milling machine before use.

2.3. Extraction

30 g of powdered leaves *of G. procumbens* were extracted in glassware with a magnetic stirrer using food-grade ethanol with various levels of solvent concentration, time of extraction, and solid-liquid ratio (w/v). Each variable contains 3 levels, as stated in the experiment design in Minitab below. The stirring process was conducted at 500 rpm using an IKA magnetic stirrer, and then the filtrate was filtered using filter paper and concentrated using a Buchi rotary vacuum evaporator.

Table 1: The design of the variable used in the experiment.

Independent Variables	Levels of Variables			Dependent Variables
	-1	0	1	
Ethanol Concentration (X_1, %)	30	50	70	Yield (Y_1, %)
Time for Maceration (X_2, h)	1	2	3	TFC (Y_2, mg QE / g extract)
Solid-Liquid Ratio (X_3, w/v)	1:8	1:10	1:12	IC 50 (Y_3, mg/mL)

The yield extract of *G. procumbens* obtained from the experiment was then calculated using the equation below:

$$Yield(\%) = \frac{Mass\ of\ extract\ (g)}{Mass\ of\ G.\ procumbens\ leaves} x\ 100 \quad (1)$$

2.4. Determination of total flavonoid assay

The total flavonoid content (TFC) of the extracts was determined by the aluminium chloride colourimetric method by Dyah (17) with a slight modification. Quercetin solution in methanol with various concentrations from 15-50 ppm was used as a standard. A standard solution and a viscous extract of *G. procumbens* leaves in methanol with an amount of 0.5 mL were put into the test tube containing 1.5 mL of methanol. Then 0.1 ml of $AlCl_3$ (10%) and 1 M CH_3COOK were added into the test tube, respectively. The solution was then homogenized and incubated for 30 minutes. Then, using a UV–Vis spectrophotometer (Genesys 10 UV, Thermo Electron Corporation, USA), the samples were measured in wavelength 433 nm (Optimum for Quercetin). The absorbance of the standard series of concentrations shows y= 0.0151x – 0.0055 with the value of R^2 = 0.9992. Then, the total flavonoid content from *G. procumbens* extracts was obtained using the formula below:

$$TFC\left(mg\,QE/g\,extract\right)=\frac{C\times V}{M} \quad (2)$$

$$Total\,Flav.\,Cont.\left(\%\right)=\frac{C\times V\times fp\times 10^{(-3)}}{Wu}\,x\,100$$

With :
C : TFC from the standard equation (mg/mL)
V : Volume extract (mL)
M : Mass extract (g)

2.5. Determination of antioxidant activity

Free radical scavenging activity from *G. procumbens* extract was determined by using 0.5 mM DPPH (2, 2-diphenyl-1-picryl-hydrazil) according to Pant (18), with some modifications. A series of concentrations from each sample extract *G. procumbens* were made to determine IC_{50}. Briefly, 240 µL extract of *G. procumbens* and 60 µL were added to 96-well plates, respectively. Then the samples were homogenized and incubated for 30 minutes in a dark place. Using an Elisa Thermo Multiskan Ascent 354 microplate reader, the absorbance of samples was measured at wavelength 520 nm. The free radical scavenging activity (or inhibition percentage**)** and IC_{50} value were obtained using the formula below:

$$Inh\left(\%\right)=\frac{\mathrm{Abs}\,of\,Blank-\mathrm{Abs}\,of\,Sample}{\mathrm{Abs}\,of\,Blank}\,x\,100 \quad (3)$$

$$lC\,50=\frac{50-a}{b} \quad (4)$$

with a = intercept and b = slope from linear regression.

2.6. Statistical Analysis

Data processing and the design of the experiment were conducted using Minitab 17 with response surface methodology (RSM). Box-Behnken was chosen as a design planner, using three variables with three levels in each variable. It was more efficient than the 2^k level factorial (19) because the number of runs can be deducted. The relationship between independent variables and the response will be provided by a second-order polynomial equation. Thus, the total number of runs with two-times replication was 30.

3. RESULTS

3.1. Effect of extraction condition and its correlation in each variable response

The results of experimental data obtained from Box-Behnken are shown in Table 2. The experiment result showed that a more significant yield was obtained at the lowest concentration of ethanol. On the contrary, the higher TFC and IC_{50} values were obtained at the highest concentration of the solvent.

The maximum yield resulting from the experiment was obtained at a configuration of 30% solvent concentration, 3 hours maceration time, and a 1:10 ratio of solid-liquid with a value of 54.78%. Meanwhile, the extract with the highest flavonoid content (TFC), 18.89 mg QE/g extract, can be obtained at a setting of 70% solvent concentration, 2 hours maceration, and a 1:12 sol:liq ratio, whereas the same solvent concentration, 3 hours maceration time, and a 1:10 ratio of sol:liq can produce the lowest IC_{50} values at 0.28 mg/mL. The higher amount of extract and flavonoid content showed a higher value of yield (Y_1) and TFC (Y_2), while the lower value of IC_{50} (Y_3) showed the more prominent free radicals scavenging (antioxidant) activity.

Table 2: Result of each dependent variable; Yield, TFC, and IC_{50} from the experiment and predicted models from RSM.

	Independent Variables			**Dependent Variables**			**Predicted Dependent Variables**		
Run order	**Ethanol Concentration (X_1, %)**	**Time for Maceration (X_2, h)**	**Solid-Liquid ratio (X_3, w/v)**	**Yield (Y_1, %)**	**TFC (Y_2, mg QE / g Extract)**	**IC 50 (Y_3, mg/mL)**	**Yield (Y_1, %)**	**TFC (Y_2, mg QE / g Extract)**	**IC 50 (Y_3, mg/mL)**
1	30	1	10	35.60 ± 6.60	0.32 ± 0.01	1.66 ± 0.38	38.65	0.09	1.79
2	70	1	10	14.43 ± 1.37	17.62 ± 0.23	0.32 ± 0.05	16.57	17.65	0.22
3	30	3	10	54.78 ± 13.60	0.33 ± 0.06	1.89 ± 0.18	52.64	0.29	1.99
4	70	3	10	14.75 ± 1.01	16.16 ± 3.14	0.28 ± 0.07	11.70	16.39	0.14
5	30	2	8	43.44 ± 3.50	0.25 ± 0.01	2.64± 0.32	43.21	0.85	2.40
6	70	2	8	12.86 ± 1.32	15.81 ± 1.57	0.28 ± 0.07	13.54	16.15	0.28
7	30	2	12	49.54 ± 0.95	0.25 ± 0.03	1.82 ± 0.04	48.87	-0.08	1.82
8	70	2	12	15.30 ± 0.75	18.89 ± 2.19	0.29 ± 0.07	15.53	18.28	0.53
9	50	1	8	15.26 ± 0.99	3.29 ± 1.32	0.29 ± 0.08	12.45	2.92	0.39
10	50	3	8	14.11 ± 0.44	2.09 ± 0.14	0.35 ± 0.07	16.49	1.52	0.49
11	50	1	12	18.12 ± 0.64	2.10 ± 0.01	0.40 ± 0.11	15.75	2.66	0.26
12	50	3	12	18.01 ± 1.26	2.61 ± 0.75	0.37 ± 0.12	20.83	2.99	0.28
13	50	2	10	17.77 ± 0.90	2.33 ± 0.30	0.42 ± 0.16	17.19	2.11	0.40
14	50	2	10	16.83 ± 0.75	1.86 ± 0.13	0.42 ± 0.01	17.19	2.11	0.40
15	50	2	10	16.98 ± 1.53	2.13 ± 0.27	0.35 ± 0.03	17.19	2.11	0.40

*(Data expresses as mean ± SD, n = 2)

The interaction between independent and dependent variables was processed with ANOVA. The variable that held a significant effect in the experiment expressed with a P-value <0.05, indicates that the model's prediction was significant at 5% (20). Table 3 below showed that solvent concentration (X_1) had the most significant effect on all dependent variables (Y_1, Y_2, Y_3) with P<0.001. In addition, for the dependent variable yield, extraction time (X_2) and its correlation with solvent concentration (X_1X_2) showed a significant impact in the experiment with P=0.046 and P=0.005 successively. Furthermore, the correlation between solvent concentration and sol:liq ratio (X_1X_3) proved to be significant with P<0.05 for Antioxidant/IC_{50} values (Y_3).

Table 3: Correlation of yield, TFC, and antioxidant activity to each independent variable in the experiment.

Factor	Yield (Y_1, %)		TFC (Y_2, mg QE/g extract)		IC_{50} (Y_3, mg/mL)	
	***F*-value**	***P*-value**	***F*-value**	***P*-value**	***F*-value**	***P*-value**
Regression	34.16	< 0.001	134.98	< 0.001	45.51	< 0.001
X_1	216.67	< 0.001*	952.21	< 0.001*	283.52	< 0.001*
X_2	4.54	0.046*	0.96	0.339	0.29	0.595
X_3	3.19	0.089	1.21	0.283	2.73	0.114
X_1X_2	9.71	0.005*	0.9	0.353	0.93	0.345
X_1X_3	0.37	0.552	3.96	0.06	8.38	0.009*
X_2X_3	0.03	0.865	1.25	0.277	0.08	0.777
X_1^2	71.31	< 0.001*	253.21	< 0.001*	106.75	< 0.001*
X_2^2	0.15	0.704	0.08	0.787	3.08	0.095
X_3^2	0.02	0.895	0.58	0.457	1.42	0.247
Lack of fit	2.49	0.096**	1.13	0.367**	6.77	0.003***

*Significant for P <0.05; **Significant for lack of fit P > 0.05; ***Non-significant lack of fit P > 0.05

3.2. Fitting the RSM model

Several conditions must be fulfilled to prove the suitability of the experiment with the RSM model, which was the P-value of the model <0.05 (significant) and the P-value for the lack of fit being >0.05 (non-significant), and coefficient determination (R^2) (21). The lack of fit from Table 3 showed that it was non-significant (P>0.05) for Yield (Y_1) and TFC (Y_2); therefore, the RSM model fitted well with the prediction from the experiment (20). Although the condition of lack of fit in IC_{50} was significant (P<0.05) and did not meet the requirement, the model can still be used (21). Normality and residual plot were also considered as additional information to ensure the suitability of the predicted RSM model with the experiment (19). The experiment's results were considered good, showing homogeneous data distribution around the linear line in the normality plot and heterogeneous data distribution in the residual plot. Each dependent variable in this experiment shows that the experimental data were normally distributed (data not shown). Thus, mathematical models from the experimental data were expressed as equations 5-7 below:

$$Y_1 = 17.194 - 15.754X_1 + 2.281X_2 + 1.911X_3 - 4.717X_1X_2 - 0.916X_1X_3 + 0.261X_2X_3 + 13.303X_1^2 - 0.608X_2^2 - 0.210X_3^2 \quad (5)$$

$$Y_2 = 2.108 + 8.415X_1 - 0.267X_2 + 0.301X_3 - 0.367X_1X_2 + 0.768X_1X_3 + 0.431X_2X_3 + 6.388X_1^2 + 0.110X_2^2 + 0.305X_3^2 \quad (6)$$

$$Y_3 = 0.396 - 0.854X_1 + 0.027X_2 - 0.084X_3 - 0.069X_1X_2 + 0.208X_1X_3 - 0.021X_2X_3 + 0.772X_1^2 - 0.131X_2^2 + 0.089X_3^2 \quad (7)$$

Table 4: Differences in coefficient of equation between experimental and predictional study.

Factor	Yield (%)		TFC (mg QE/g Extract)		IC_{50} (mg/mL)	
	Exp. Coef	***Pred. Coef***	***Exp. Coef***	***Pred. Coef***	***Exp. Coef***	***Pred. Coef***
Constant	17.194	85.502	2.108	40.151	0.396	11.466
X_1	-15.754	-3.413	8.415	-1.331	-0.854	-0.281
X_2	2.281	15.199	-0.267	-1.946	0.027	0.828
X_3	1.911	2.889	0.301	-2.764	-0.084	-0.726
X_1X_2	-4.717	-0.236	-0.367	-0.018	-0.069	-0.003
X_1X_3	-0.916	-0.023	0.768	0.019	0.208	0.005
X_2X_3	0.261	0.131	0.431	0.216	-0.021	-0.010
X_1^2	13.303	0.033	6.388	0.016	0.772	0.002
X_2^2	-0.608	-0.608	0.110	0.110	-0.131	-0.131
X_3^2	-0.210	-0.053	0.305	0.076	0.089	0.022
	R^2	**Adjusted R^2**	**R^2**	**Adjusted R^2**	**R^2**	**Adjusted R^2**
	93.89%	91.14%	98.38%	97.65%	95.34%	93.25%

The experiments also resulted in model predictions, as shown in Table 4 above. Compared with the experimental data, the coefficients of the predicted models were drastically different. However, the predicted model was still considered valid because of R^2 and Adj. R^2 was still around 0.9 for all dependent variables, meaning 90% of the total variation can be explained by the models. R^2 was used to evaluate the accuracy between predicted and experimental values (22). The closer value of R^2 to 1 indicates the fitness of the models and the experimental data (23). The difference value between R^2 and Adj. R^2 means the percentage of total variation not explained by the models (24). Values of the dependent variable from the predicted RSM models are shown in Table 4.

3.3. Optimization of extraction condition

Contour plot graphs below visualized the correlation between X_1, X_2, X_3, and Y_1, Y_2, and Y_3 more easily. From Figure 1, the maximum TFC value (dark green area) was obtained in the range of higher solvent concentrations (X_1) and sol:liq ratios (X_3). Meanwhile, extraction time (X_2) did not significantly affect the response. Thus, the maximum TFC value can be obtained using a 70% solvent concentration with a 2-hour extraction time and a 1:12 sol:liq ratio.

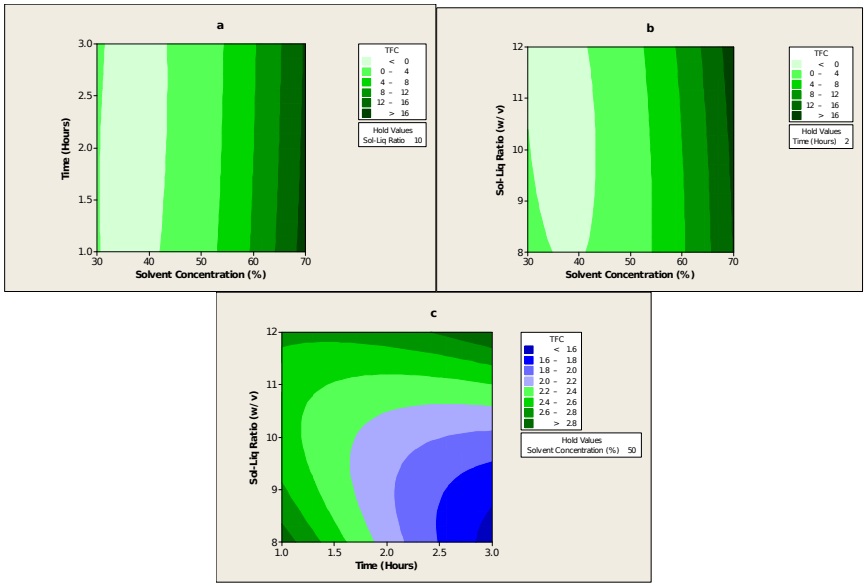

Figure 1: Contour plot on TFC in correlation with; a) time vs solvent concentration, b) sol:liq ratio vs solvent concentration, and c) sol:liq ratio vs time.

In contrast with Figure 2, the highest antioxidant activity/the lowest IC_{50} value obtained was marked with a light green colour. Higher levels of X_1 increase the antioxidant activity proportionally, while X_2 and X_3 have almost no effect. For the sol:liq ratio variable (X_3), the antioxidant activity content did not show any alteration as the ratio increased. The details of the plots can be seen in Figure 2. To sum up, determining exact values in each parameter to produce the lowest IC_{50} values was more challenging in this case than in the TFC, except for the solvent concentration. Therefore, a response optimizer was used to gain more reliable setting parameters by combining calculations from experimental and predicted models.

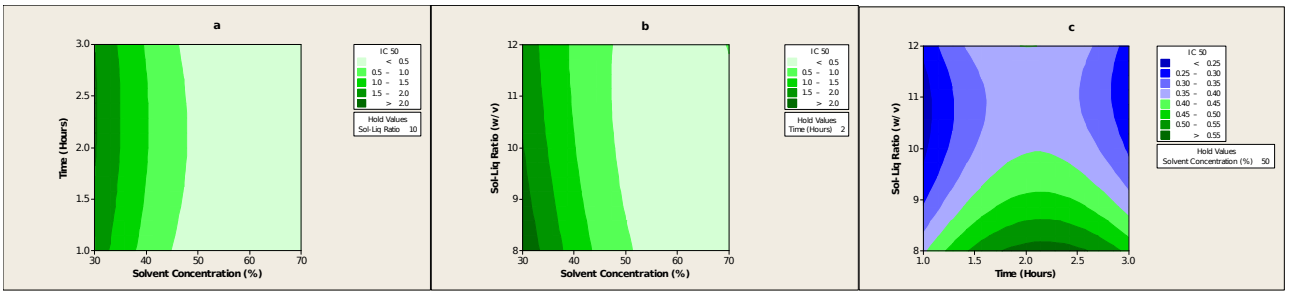

Figure 2: Contour plot on IC_{50} in correlation with; a) time vs solvent concentration, b) sol:liq ratio vs solvent concentration, and c) sol:liq ratio vs time.

Optimization was carried out to produce an extract with maximum TFC and antioxidant activity. Response optimizers were used by adding dependent variables like TFC and IC_{50} at the maximum setting. Response optimizer from Figure 3 showed that to obtain the maximum content of flavonoid and antioxidant activity, the extraction condition should be set at 70% solvent concentration, 1 hour extraction time, and almost a 1:10 ratio in the sol:liq ratio. This condition was likely to have a similar result as predicted since the composite desirability was considered high (>0.9). However, the result will not produce a high-yield extract since it was excluded from the optimizer, and the correlation of yield with the desired parameters was the opposite.

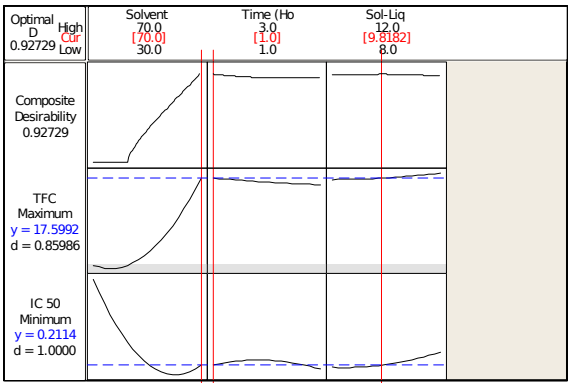

Figure 3: Optimization plot of operation process for extraction of *G. procumbens* for high TFC and IC_{50}.

4. DISCUSSION

The bioactivities of the plant medicines, especially antioxidant activity, were strongly influenced by the solvent concentration, while other variables did not show a significant effect (8). Solvent concentration plays a major role in the amount of flavonoid, antioxidant, and other bioactive compounds (23). The extraction of *G. procumbens* with methanol has more TPC and antioxidant activity than extraction with ethanol or water (25). However, the extract with ethanol still contained the high antioxidant quality of extract (8,15). A solvent with more water composition was likely to draw the polysaccharides inside the sample out, resulting in a higher yield obtained and lower activity. Meanwhile, the extraction time only affected the yield produced and did not affect the antioxidant activity (26). Therefore, this variable did not appear to be significant (24).

Sol:liq variable in this study did not appear to hold any significance in antioxidant and total flavonoid content. Meanwhile, in correlation with solvent concentration, it did contain a significant role in determining antioxidant activity (20,24,27–29) as others because of the maximum amount of solvent that penetrated the sample. A solvent with a higher ethanol composition has a lower dielectric constant that can disrupt the plant matrices easier, as the extraction process involves the mass transfer between solid and liquid. Mass transfer depends on driving forces and resistance within the process. Different concentrations, as a result of the sol:liq ratio, lead to a higher driving force and diffusion rate (27,29).

Long exposures in variables such as sol:liq ratio, extraction temperature, and time resulted in the extract with the highest yield. Nevertheless, as the temperature increased, the antioxidant activity decreased (20). Extraction temperature is likely to have more influence on maximizing the yield produced while affecting the antioxidant activity content within it (22,30). TFC and radical scavenging activity decreased as the temperature rose due to the degradation of bioactive compounds, which are commonly sensitive to heat (23,30).

Many compounds can be classified as having antioxidant activity, including flavonoid compounds. It was known to have potent scavengers of free radicals and was potentially used as medicine for oxidative damage and degenerative diseases such as cancer (31). Previous studies stated that the ethyl acetate fraction of *G. procumbens* extracts exhibits antioxidant activity with IC_{50} values of 0.05 mg/mL (2) and 0.2 mg/mL (5). This ethyl acetate fraction contains some flavonoid compounds such as myricetin, quercetin, rutin, apigenin, and kaempferol that are responsible for antioxidant activity within the fraction. Another experiment showed crude methanol extract contains a TFC value of 10.33 mg QE/g DW and an IC_{50} 0.47 mg/mL, proving that both variables have some correlation (5). However, the result can not be compared with this experiment due to the differences in the solvent used. Medicinal plants were known to have very high antioxidant activity with IC_{50} less than 0.05 mg/mL and high with IC_{50} around 0.05-0.1 mg/mL, while the IC_{50} around 0.1-0.15 mg/mL and 0.15-0.2 mg/mL were mentioned as medium and low antioxidant capacity (32). The value was still higher than IC_{50} obtained in this experiment (0.28 mg/mL). However, judging from previous studies, further purification of this extract allows for an increase in the antioxidant activity of this plant.

5. CONCLUSION

To be concluded, the established RSM models were adequate for determining extraction conditions for certain goals. This experiment shows that for obtaining an extract with both maximum TFC and antioxidant activity, extraction conditions must be held at 70% solvent concentration, 1 hour extraction time, and a 9.8 sol:liq ratio with an estimated value of 17.599 mg QE/g extract and 0.211 mg/ml, respectively. Further, this experiment still needs some validation of the result suggested by the optimizer. Besides, this method can also be used for other traditional medicines. It can be developed as an optimization tool for the purified extract to elevate the effectiveness of the traditional medicines used.

6. CONFLICT OF INTEREST

The authors state no conflict of interest.

7. ACKNOWLEDGMENTS

This study was funded using DIPA and supported by colleagues from Research Center for Pharmaceutical Ingredients and Traditional Medicine and the National Research and Innovation Agency as a supporting institution related to the authors.

8. REFERENCES

1. Tan H, Chan K, Pusparajah P, Lee L, Goh B, Lee L. Gynura procumbens : An Overview of the Biological Activities. Front Pharmacol. 2016;7(52):1–14. Available from: <DOI>

2. Yam MF, Sadikun A, Asmawi MZ, Rosidah. Antioxidant potential of Gynura procumbens. Pharm Biol. 2008 Sep;46(9):616–25. Available from: <DOI>

3. Werdhasari A. Peran Antioksidan Bagi Kesehatan. J Biotek Medisiana Indones. 2014;3(2):59–68. <DOI>

4. Francenia Santos-Sánchez N, Salas-Coronado R, Villanueva-Cañongo C, Hernández-Carlos B. Antioxidant Compounds and Their Antioxidant Mechanism. IntechOpen. 2019;1–28. Available from: <URL>

5. Kaewseejan N, Sutthikhum V, Siriamornpun S. Potential of Gynura procumbens leaves as source of flavonoid-enriched fractions with enhanced antioxidant capacity. J Funct Foods [Internet]. 2015;12:120–8. Available from: <DOI>

6. Kim J, Lee C, Kyung E, Lee S, Park N, Kim H, et al. Inhibition effect of Gynura procumbens extract on UV-B-induced matrix-metalloproteinase expression in human dermal fibroblasts. J Ethnopharmacol. 2011;137(1):427–33. Available from: <DOI>

7. Montgomery DC. Design and Analysis of Experiments Eighth Edition. Arizona State University. Vol. 2009, Copyright. 2013. 2001 p. ISBN: 978-1-118-14692-7. Available from: <URL>

8. Şahin S, Şamli R. Optimization of olive leaf extract obtained by ultrasound-assisted extraction with response surface methodology. Ultrason Sonochem. 2013;20(1):595–602.Available from: <DOI>

9. Khuri AI, Mukhopadhyay S. Response surface methodology. Wiley Interdisciplinary Reviews: Computational Statistics. 2010;2(2):128–49. Available from: <DOI>

10. Vuong Q V., Nguyen VT, Thanh DT, Bhuyan DJ, Goldsmith CD, Sadeqzadeh E, et al. Optimization of ultrasound-assisted extraction conditions for euphol from the medicinal plant, Euphorbia tirucalli, using response surface methodology. Ind Crops Prod. 2015;63:197–202. Available from: <DOI>

11. Khuri AI. Response Surface Methodology and Its Applications In Agricultural and Food Sciences. Biometrics Biostat Int J. 2017;5(5):155–63. Available from: <DOI>

12. Hairon H, Sabtu R, Talib NA, Awang MA, Aziz R, Suan CL, et al. Extraction of Gynura procumbens Leaves (Sambung Nyawa) with Different Parameters Using Maceration Process. In: 6th International Conference on Biotechnology for the Wellness Industry (ICBWI). Malaka, Malaysia: Institute of Bioproduct Development, Faculty of

Chemical and Energy Engineering, Universiti Teknologi Malaysia; 2016. p. 131–3.

13. Rosidah I, Bahua H, Mufidah R, Pongtuluran OB. Pengaruh Kondisi Proses Ekstraksi Batang Brotowali (Tinospora crispa (L) Hook.f & Thomson) Terhadap Aktivitas Hambatan Enzim Alfa Glukosidase. Vol. 25, Media Penelitian dan Pengembangan Kesehatan. 2015;25(4):203-210. Available from: <URL>

14. Krishnan V, Ahmad S, Mahmood M. Antioxidant Potential in Different Parts and Callus of Gynura procumbens and Different Parts of Gynura bicolor. Biomed Res Int. 2015;2015. Available from: <DOI>

15. S.S. Maw, M.M. Mon, Z.K. Oo. Study on Antioxidant and Antitumor Activities of Some Herbal Extracts. World Acad Sci Eng Technol. 2011;51:450–5. Available from: <URL>

16. Tristantini D, Setiawan H, Santoso LL. Feasibility assessment of an encapsulated longevity spinach (Gynura procumbens l.) extract plant in Indonesia. Appl Sci. 2021 May 1;11(9). Available from: <DOI>

17. Dyah NA, Endang K, Fahrauk F. Penetapan Kadar Flavonoid Metode AlCl3 Pada Ektsrak MEtanol Kulit Buah KAKAO (Theobroma cacao L.). Kartika J Ilm Farm. 2014;2(2):45–9. Available from: <DOI>

18. Pant G, Simaria C, Varsi RAH, Bhan P, Sibi G. In vitro Anti-Cholesterol and Antioxidant Activity of Methanolic Extracts from Flax Seeds (Linum usitatissimum L .). Res J Med Plant. 2015;9(6):300–6. Available from: <DOI>

19. Faulina R, Andari S, Anggraeni D. Response surface methodology (RSM) dan aplikasinya. Magister Stat Its. 2011;152–75. Available from: <URL>

20. Chuyen H V., Roach PD, Golding JB, Parks SE, Nguyen MH. Optimisation of extraction conditions for recovering carotenoids and antioxidant capacity from Gac peel using response surface methodology. Int J Food Sci Technol. 2017;52(4):972–80. Available from: <DOI>

21. Karmoker JR, Hasan I, Ahmed N, Saifuddin M, Reza MS. Development and Optimization of Acyclovir Loaded Mucoadhesive Microspheres by Box – Behnken Design. Dhaka Univ J Pharm Sci. 2019;18(1):1–12. Available from: <DOI>

22. Aydar AY, Bagdatlioglu N, Köseoglu O. Effect of ultrasound on olive oil extraction and optimization of ultrasound-assisted extraction of extra virgin olive oil by response surface methodology (RSM). Grasas y Aceites. 2017;68(2). Available from: <DOI>

23. Shirzad H, Niknam V, Taheri M, Ebrahimzadeh H. Ultrasound-assisted extraction process of phenolic antioxidants from Olive leaves: a nutraceutical study using RSM and LC–ESI–DAD–MS. J Food Sci Technol. 2017;54(8):2361–71. Available from: <DOI>

24. Elksibi I, Haddar W, Ben Ticha M, Gharbi R, Mhenni MF. Development and optimisation of a non conventional extraction process of natural dye from olive solid waste using response surface methodology (RSM). Food Chem. 2014;161:345–52. Available from: <DOI>

25. A. Akowuah G, Ahmad M, M. Fei Y. Effects of Gynura procumbens Leaf Extracts on Plasma Lipid Peroxidation and Total Antioxidant Status in CCl4-Treated Rats. Nat Prod Journale. 2013;2(4):247–51. Available from: <DOI>

26. Tian Y, Xu Z, Zheng B, Martin Lo Y. Optimization of ultrasonic-assisted extraction of pomegranate (Punica granatum L.) seed oil. Ultrason Sonochem. 2013;20(1):202–8. Available from: <DOI>

27. Yan F, Fan K, He J, Gao M. Ultrasonic-Assisted Solvent Extraction of Carotenoids From Rapeseed Meal: Optimization Using Response Surface Methodology. J Food Qual. 2015;38(6):377–86. Available from: <DOI>

28. Raza A, Li F, Xu X, Tang J. Optimization of ultrasonic-assisted extraction of antioxidant polysaccharides from the stem of Trapa quadrispinosa using response surface methodology. Int J Biol Macromol. 2017;94:335–44. Available from: <DOI>

29. Samaram S, Mirhosseini H, Tan CP, Ghazali HM, Bordbar S, Serjouie A. Optimisation of ultrasound-assisted extraction of oil from papaya seed by response surface methodology: Oil recovery, radical scavenging antioxidant activity, and oxidation stability. Food Chem. 2015;172:7–17. Available from: <DOI>

30. Akowuah GA, Mariam A, Chin JH. The effect of extraction temperature on total phenols and antioxidant activity of Gynura procumbens leaf. Pharmacogn Mag. 2009;4(17):81–5. Available from: <URL>

31. Zainol MK, Abd-Hamid A, Yusof S, Muse R. Antioxidative activity and total phenolic compounds of leaf, root and petiole of four accessions of Centella asiatica (L.) Urban. Food Chem. 2003;81(4):575–81. Available from: <DOI>

32. Tristantini D, Ismawati A, Tegar Pradana B, Gabriel Jonathan J. Pengujian Aktivitas Antioksidan Menggunakan Metode DPPH pada Daun Tanjung (Mimusops elengi L). Semin Nas Tek Kim Kejuangan. Prosiding Seminar Nasional Teknik Kimia “Kejuangan” 17 Mar 2016;ISSN 1693-4393:1–7. Available from: <URL>

JOTCS A
Journal of the Turkish Chemical Society
Section: A
Chemistry
TURKISH CHEMICAL SOCIETY

Antibacterial and Antioxidant Activity Evaluation of Bis-Substituted İsovanillin Derivatives

Zehra Tekin[1,2*], Yener Tekeli[3], Zehra Küçükbay[2], Nebih Lolak[4], Gönül Yapar[5], and Suleyman Akocak[4*]

[1]Adıyaman University, Faculty of Pharmacy, Department of Basic Pharmaceutical Sciences, 02040, Adıyaman, Turkey.
[2]Inönü University, Faculty of Pharmacy, Department of Basic Pharmaceutical Sciences, Malatya, Turkey.
[3] Adıyaman University, Faculty of Pharmacy, Department of Pharmaceutical Biotechnology, 02040, Adıyaman, Turkey.
[4] Adıyaman University, Faculty of Pharmacy, Department of Pharmaceutical Chemistry, 02040, Adıyaman, Turkey.
[5]Istanbul Technical University, Faculty of Arts and Sciences, Department of Chemistry, 34469, Istanbul, Turkey.

Abstract: Herein, a series of twelve bis-hydrazone substituted isovanilline derivatives **3(a-l)**, were freshly re-synthesized by the reaction of bis-aldehydes with substituted hydrazide derivatives since these compounds previously showed potent aldose reductase inhibition properties. The obtained compounds were tested for their potential antibacterial and antioxidant activities. In the present study, four different bacterial strains were used, including Gram-positive (*Staphylococcus aureus* ATCC 29213, *Enterococcus faecalis* ATCC 29212) and Gram-negative (*Pseudomonas aeruginosa* ATCC 10231, *Escherichia coli* ATCC 25912). On the other hand, the antioxidant capacities of freshly re-synthesized bis-hydrazone substituted isovanilline derivatives were determined by using several antioxidant methods, including DPPH free radical scanvenging, TEAC cupric reducing (CUPRAC) and metal chelating activity methods. Several lead molecules were discovered as a potential bacterial inhibitors against S. *aureus* and *E. coli* bacterial strains. More specifically, compounds **3g** (R=-H) and **3j** (R= -4Cl) showed great inhibition properties against *E. coli* bacterial strains by having MIC values of 1.56 and 6.25 µg/mL, respectively. Moreover, none of the compounds showed potent antioxidant activity against tested methods with respect to compared standards.

Keywords: Hydrazone, Isovanillin, Antioxidant, Antibacterial.

Submitted: October 29, 2022. **Accepted:** . February 16, 2023

Cite this: Tekin Z, Tekeli Y, Küçükbay F, Lolak N, Yapar G, Akocak S. Antibacterial and Antioxidant Activity Evaluation of Bis-Substituted Isovanillin Derivatives. JOTCSA. 2023;10(2):435-442.

DOI: https://doi.org/10.18596/jotcsa.1196335

***Corresponding authors. E-mail:** ztekin@adiyaman.edu.tr, sakocak@adiyaman.edu.tr

1. INTRODUCTION

Bacterial infections are considered one of the most important infectious diseases, although generally only a small percentage of bacteria cause infection and disease, but their impact on public health is significant and serious. In recent years, researchers have been able to make great progress in the development of antibacterial drugs, but the need remains urgent to discover new antibacterial drugs because of the rapid growing of multidrug-resistant bacteria with potentially devastating consequences (1–4).

Historically, natural products (NPs) were a rich source of bioactive molecules and they are one of the most important sources of inspiration for developing many therapeutic drugs (5). Isovanillin (3-hydroxy-4-methoxybenzaldehyde) is a phenolic aldehyde isolated from a number of plants including *Pycnocycla spinose*, *Alpinia oxyphylla* extract which is used in particular in the pharmaceutical cosmetics, the flavors and fragrance industry, and

agrochemical (6-10). In addition to its potency as a selective inhibitor of aldehyde oxidase, it is also shown to be an important intermediate for the synthesis and production of some functional catechol derivatives such as methyldopa (11). On the other hand, it is considered as a cornerstone in the synthesis of many important pharmaceutical compounds such as morphine, and galantamine (12-14). Moreover, isovanillin-containing plants have been traditionally used in folk medicine for treatment of many diseases such as cancer, depression, hypertension, hyperglycemic and diarrhea (15-18).

Hydrazones containing an azometine -NHN=CH- group found an important scaffold for new drug design and development studies. Many compounds containing hydrazone group in their structure attracted medicinal chemists interest due to its biological importance as antimicrobial, antimalarial, antitubercular, antifungal, antiviral, anticonvulsant, antidepressant, anti-inflammatory, analgesic, antiplatelet, anticancer, cardio protective etc. (19-22).

As has been observed in previous studies (23-27), the bis-type compounds may have many advantages including, ditopic interactions in the active site of receptor and more binding affinities with amino acids on the enzyme active sites and that can play an important role in improving the pharmacological activity of this type of compounds. Based on this, in our past work, we have designed and developed a new group of bis-hydrazone compounds bearing isovanillin components and screened these novel derivatives for their activity towards Aldose reductase (ALR2) (28). All the tested compounds demonstrated good activity in nanomolar range as AR inhibitors. In the current study, we decided to re-synthesize and evaluate a series of twelve bis-hydrazone compounds bearing isovanillin derivatives for their biochemical activities towards antibacterial and antioxidant properties with the hope of discovering more effective and safe antibacterial agents.

2. EXPERIMENTAL SECTION

2.1. Materials and Methods

All reagents and solvents that commercially available were purchased from several companies including, Alfa Aesar, Merck, Sigma-Aldrich, and TCI and used without further purification. The FT-IR spectrums of the synthesized compounds were recorded by using Perkin Elmer Spectrum 100 FT-IR spectrometer. Melting points (mp) were determined with SMP20 melting point apparatus and are uncorrected. Nuclear magnetic resonance (^{1}H NMR and ^{13}C NMR) spectra of compounds were obtained using Agilent 500 MHz NNMRS spectrometer in DMSO-d_6 with TMS as an internal standard. Thin layer chromatography (TLC) was applied on Merck silica gel 60 F_{254} plates.

2.2. Chemistry

In order to assess the antibacterial and antioxidant activities of bis-hydrazone substituted isovanilline derivatives **3(a-l)**, the compounds were freshly re-synthesized as previously described by our research group (28). The general synthetic route for the preparation of bis-hydrazone substituted isovanilline derivatives **3(a-l)** were demonstrated in Figure 1. Physicochemical and spectroscopic analysis of re-synthesized compounds **3(a-l)** have been previously performed and the results were described by us (28).

2.3. Antibacterial assay

The antibacterial analyzes were achieved by modified method according to Al-Blewi et al. and our previous studies (29-31). Briefly, the freshly re-synthesized bis-hydrazone substituted isovanilline derivatives **3(a-l)** were dissolved in DMSO and 200 µg/mL stock solution was formed and were determined at ten different concentrations diluted nine times. The four different bacterial strains were added in 100 µL to each microplate well with approximately 10^6 CFU/mL bacteria. The bacterial density was adjusted with a McFarland densitometer. Microplates were incubated for 24 h at 37°C and then optical densities were measured at 600 nm (OD600) using Thermo 3001 ELISA microplate reader. The Minimal inhibitory concentration (MIC) tests were repeated three times for each microorganism that used in the present study and all the bis-hydrazone substituted isovanilline derivatives **3(a-l)**. MICs were obtained after 24 h incubation time. Additionally, control experiments with standard antibacterial agents (Ceftriaxone and ampicillin were used as a positive control) and unvaccinated media (negative control) were performed in parallel and in the same manner as the test compounds.

2.4. DPPH Free radical scavenging assay

In this study, the radical scavenging activity of compounds were determined in 1,1-diphenyl-2-picrylhydrazyl (DPPH) free radical assays applied according to Blois (32). In brief, 1.0 mL sample were added to 0.1 mM DPPH solution. The mixture was kept for 30 min in darkness at room temperature, and the absorbance was then measured at 517 nm. Butylated hydroxyanisole (BHA), butylated hydroxytoluene (BHT), and α-tocopherol were used as positive controls.

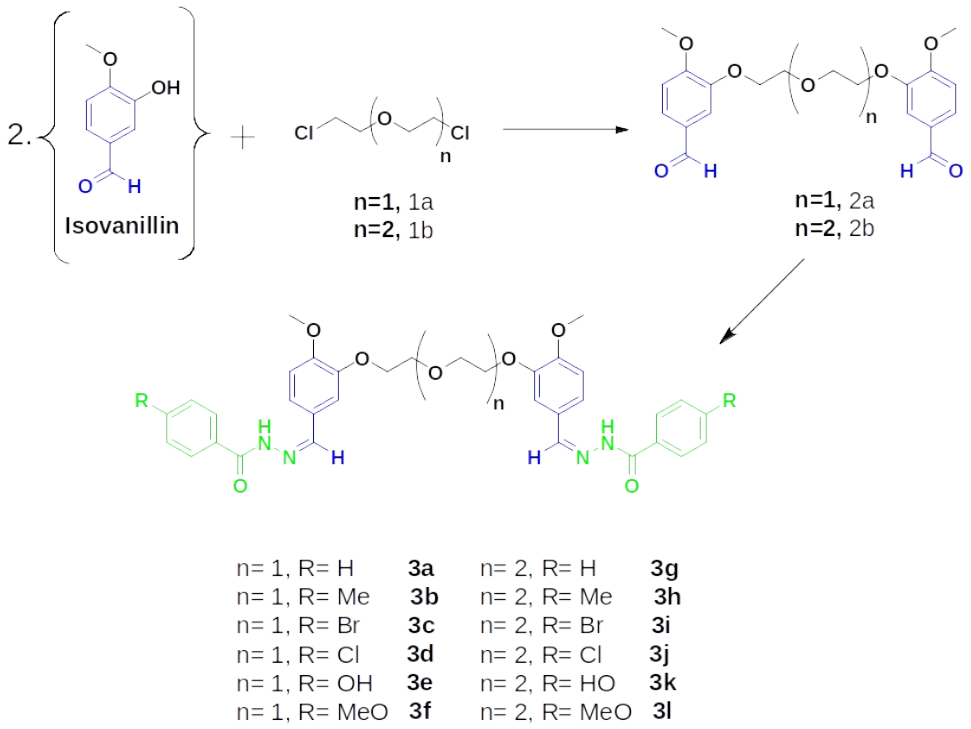

Figure 1: General synthetic route for the synthesis of bis-hydrazone substituted isovanilline derivatives **3(a-l)** (28).

2.5. Metal Chelating Activity

The chelating activity of ferrous iron was determined using the colorimetric method proposed by Carter (33). 50 µL of 2.0 mM $FeCl_2$ were added to compounds of different concentrations. After 10 min incubation at room temperature, 200 µL 5.0 mM ferrozine solution is added. Measure the absorbance of all samples at 562 nm after 25 min incubation. EDTA was used as a positive control.

2.6. Cupric Reducing Antioxidant Capacity (CUPRAC) Assay

Total antioxidant capacity of synthesized compounds were determined using CUPRAC method performed by Apak et al. (34). 1.0 mL of each of the 0.01 M $CuCl_2$, $7.5x10^{-3}$ M neocuproine, NH_4Ac buffer solution (pH 7.00; 0.1 M) were added into the test tube. 50 µL sample or standard solution (BHA, BHT, α-TOC) and 1.05 mL distilled water added to the initial mixture. Measure the absorbance of all samples at 465 nm after 30 min incubation at room temperature.

3. RESULTS AND DISCUSSION

In the current study, we are presenting the synthesis, antibacterial and antioxidant activity of bis-hydrazone substituted isovanilline derivatives **3(a-l)**. These produced compounds were previously synthesized and fully characterized as a potent aldose reductase inhibitors by our research team. By having important biological properties of isovanilline derivatives, in the current work, the antibacterial and several antioxidant assays were focused.

The antibacterial activity assays were applied against four pathogenic bacterial strains, including Gram-negative bacteria and Gram-positive. On the other hand, the antioxidant capacities of freshly re-synthesized bis-hydrazone substituted isovanilline derivatives are determined by using several antioxidant methods, including, TEAC, CUPRAC, metal-chelating, and DPPH free radical scanvenging activity methods.

In general, the re-synthesized compounds showed varying range of antibacterial activity against both Gram-positive as well as Gram-negative tested bacterial strains depending on the chemical nature and substitution on derivatives as the minimum inhibitory concentration values (MIC) were illustrated in Table 1. More specifically, as compared with their linker length, the longer ones have had better activity than their shorter counterparts, in general. The highest antibacterial activity was determined against *E. coli* with the compounds **3g** (R=-H) and **3j** (R= -4Cl) by having MIC values of 1.56 and 6.25 µg/mL, respectively. These compounds were comparable with standard antibiotic drugs ampicillin and ceftriaxon with MIC values of 15.6 and 2.0 µg/mL, respectively. Whereas compound **3a** with no substitution on the phenyl ring and compound **3f** (methoxy group at para position) showed good potency against *E. coli* strains (12.5 µg/mL), which is better than the commercial antibiotic ampicillin (15.6 µg/mL). One of the Gram-positive bacteria strain *S. aureus* was also potently inhibited by some of the compounds, including **3a**, **3f**, **3g** and **3l** with MIC values of 12.5 µg/mL as compared with Standard drug ceftriaxon (31.3 µg/mL). Interestingly, compounds **3a** and **3g**

have same substitution as well as compounds **3f** and **3l** have p-methoxy substitution on the phenyl ring by having only linker length differences. On the other hand, the compounds were less susceptible to Gram-negative bacteria (*P. aeruginosa*) in which some of the compounds showed any activity, including short linker derivatives **3a**, **3c**, **3d** and the one of the longer linker derivative **3g** with no substitution on the phenyl ring. As a result of antibacterial activities of compounds, the best inhibition results were obtained against *E. coli* and *S. aureus* bacterial strains with compound **3g** which can be chosen as a lead molecule since it has an great activity against both bacterial strains.

Table 1: Antibacterial activity of bis-hydrazone substituted isovanilline derivatives **3(a-l)** assayed against Gram-positive and Gram-negative bacterial strains (Minimal Inhibitory Concentration, µg/mL).

Compounds	Antibacterial activity (MIC, µg/mL)			
	Gram-(+) bacteria strains		Gram-(-) bacteria strains	
	S. aureus	***E. faecalis***	***P. aeruginosa***	***E. coli***
3a	12.5	25	ND	12.5
3b	50	12.5	50	50
3c	100	100	ND	100
3d	25	50	ND	100
3e	100	100	25	100
3f	12.5	100	25	12.5
3g	12.5	12.5	ND	1.56
3h	100	50	25	ND
3i	50	25	100	50
3j	50	100	100	6.25
3k	100	25	25	50
3l	12.5	100	100	50
Ampicillin	3.9	3.9	2.0	15.6
Ceftriaxon	31.3	2.0	15.6	2.0

The antioxidant properties of freshly re-synthesized bis-hydrazone substituted isovanilline derivatives **3(a-l)** were assayed using several antioxidant methods, including DPPH free radical scavenging, TEAC CUPRAC, and metal chelating methods. The DPPH results revealed that none of the compounds showed any activity except the compounds **3k** and **3l** which are also having very low DPPH activity at any tested concentrations as demonstrated in Table 2.

4. CONCLUSIONS

In conclusion, the previously synthesized potent aldose reductase inhibitors of bis-hydrazone substituted isovanilline derivatives **3(a-l)** were freshly re-synthesized for their potential antibacterial and antioxidant properties. The produced compounds were tested against two Gram-positive (*S. aureus*, *E. faecalis*) and two Gram-negative (*P. aeruginosa*, *E. coli*) bacterial strains. Also, several antioxidant methods were applied to these compounds, including DPPH free radical scanvenging, TEAC cupric reducing (CUPRAC) and metal chelating activity methods. Unfortunately, these compounds were not susceptible to any tested antioxidant methods. Moreover, several potent compounds were obtained against tested bacterial strains *S. aureus* and *E. coli*. Specifically, compounds **3g** (R=-H) and **3j** (R= -4Cl) showed great inhibition properties against *E. coli* bacterial strains by having MIC values of 1.56 and 6.25 µg/mL, respectively. These compounds were comparable to standard antibiotic drugs ampicillin and ceftriaxon with MIC values of 15.6 and 2.0 µg/mL, respectively. As a result of the antibacterial potency of these compounds, they might be improved and used as a potential leads for the development of antibacterial agents. For this, further research needed to be done, including toxicity studies.

Table 2: DPPH radical scavenging activities of bis-hydrazone substituted isovanilline derivatives **3(a-l)** and controls BHA, BHT, and α-TOC.

Compounds & Standards	DPPH Free Radical Scavenging Activity, %			
	12.5 µg/mL	25.0 µg/mL	37.5 µg/mL	62.5 µg/mL
3a	ND	ND	ND	ND
3b	ND	ND	ND	ND
3c	ND	ND	ND	ND
3d	ND	ND	ND	ND
3e	ND	ND	ND	ND
3f	ND	ND	ND	ND
3g	ND	ND	ND	ND
3h	ND	ND	ND	ND
3i	ND	ND	ND	ND
3j	ND	ND	ND	ND
3k	1.74 ± 0.35	2.36 ± 0.18	2.50 ± 0.19	2.63 ± 0.00
3l	3.60 ± 0.46	4.49 ± 0.30	4.99 ± 0.18	5.37 ± 0.00
BHA	59.85 ± 0.00	63.60 ± 0.00	64.81 ± 0.46	67.16 ± 0.35
BHT	60.22 ± 1.09	65.68 ± 0.63	69.52 ± 0.30	69.64 ± 0.46
α-TOC	63.69 ± 0.46	68.03 ± 1.05	69.64 ± 0.70	70.51 ± 1.15

The TEAC CUPRAC and metal chelating antioxidant properties of compounds were also assayed. The results show that none of the compounds have better activity than the standards and not comparable with them.

Table 3. TEAC CUPRAC and metal chelating antioxidant capasities of bis-hydrazone substituted isovanilline derivatives **3(a-l)** and controls BHA, BHT, α-TOC, and EDTA.

Compounds & Standards	TEAC $_{CUPRAC}$ (mmol TR g^{-1})	Metal Chelating Activity IC_{50} (µg mL^{-1})
3a	0.413 ± 0.006	27.78 ± 0.22
3b	0.455 ± 0.004	30.32 ± 0.16
3c	0.379 ± 0.009	29.19 ± 0.23
3d	0.311 ± 0.002	17.64 ± 0.05
3e	0.215 ± 0.005	ND
3f	0.220 ± 0.005	ND
3g	0.231 ± 0.008	ND
3h	0.249 ± 0.003	ND
3i	0.253 ± 0.004	ND
3j	0.429 ± 0.002	27.21 ± 0.14
3k	0.475 ± 0.006	32.31 ± 0.08

3l	0.470 ± 0.003	42.56 ± 0.06
BHA	2.632 ± 0.007	-----
BHT	3.358 ± 0.003	-----
α-TOC	2.077 ± 0.004	-----
EDTA	-----	1.71 0.19

5. ACKNOWLEDGMENTS

This work was partially funded by the Istanbul Technical University Grants Commission for a research grant (Project Grant No: 33467).

6. REFERENCES

1. Doron S, Gorbach SL. Bacterial Infections: Overview. In: International Encyclopedia of Public Health [Internet]. Elsevier; 2008. p. 273–82. Available from: <URL>

2. Nikaido H. Multidrug Resistance in Bacteria. Annu Rev Biochem [Internet]. 2009 Jun 1;78(1):119–46. Available from: <URL>

3. Holmes AH, Moore LSP, Sundsfjord A, Steinbakk M, Regmi S, Karkey A, et al. Understanding the mechanisms and drivers of antimicrobial resistance. Lancet [Internet]. 2016 Jan 9;387(10014):176–87. Available from: <URL>

4. Brown ED, Wright GD. Antibacterial drug discovery in the resistance era. Nature [Internet]. 2016 Jan 20;529(7586):336–43. Available from: <URL>

5. Atanasov AG, Zotchev SB, Dirsch VM, Supuran CT. Natural products in drug discovery: advances and opportunities. Nat Rev Drug Discov [Internet]. 2021 Mar 28;20(3):200–16. Available from: <URL>

6. Yang L, Feng F, Gao Y. Chemical constituents from herb of Solanum lyratum. China J Chinese Mater medica [Internet]. 2009;34(14):1805–8. Available from: <URL>

7. Xu J, Tan N, Zeng G, Han H, Huang H, Ji C, et al. Studies on chemical constituents in fruit of Alpinia oxyphylla. China J Chinese Mater medica [Internet]. 2009;34(8):990–3. Available from: <URL>

8. Chen W, Tang S, Qin N, Zhai H, Duan H. Antioxidant constituents from Smilax riparia. China J Chinese Mater medica [Internet]. 2012;37(6):806–10. Available from: <URL>

9. Khaliq-uz-Zaman S., Simin K, Ahmad V. Chemical constituents from Asparagus dumosus. Fitoterapia [Internet]. 2000 Jun;71(3):331–3. Available from: <URL>

10. Huang W-B, Du C-Y, Jiang J-A, Ji Y-F. Concurrent synthesis of vanillin and isovanillin. Res Chem Intermed [Internet]. 2013 Jul 26;39(6):2849–56. Available from: <URL>

11. Saari WS, Freedman MB, Hartman RD, King SW, Raab AW, Randall WC, et al. Synthesis and antihypertensive activity of some ester progenitors of methyldopa. J Med Chem [Internet]. 1978 Aug 1;21(8):746–53. Available from: <URL>

12. Uchida K, Yokoshima S, Kan T, Fukuyama T. Total Synthesis of (±)-Morphine. Org Lett [Internet]. 2006 Nov 9;8(23):5311–3. Available from: <URL>

13. Marco-Contelles J, do Carmo Carreiras M, Rodríguez C, Villarroya M, García AG. Synthesis and Pharmacology of Galantamine. Chem Rev [Internet]. 2006 Jan 1;106(1):116–33. Available from: <URL>

14. Adam F, Hamdan MA, Abu Bakar SH, Yusoff MM, Jose R. Molecular recognition of isovanillin crosslinked carrageenan biocomposite for drug delivery application. Chem Eng Commun [Internet]. 2021 May 4;208(5):741–52. Available from: <URL>

15. Cole C, Burgoyne T, Lee A, Stehno-Bittel L, Zaid G. Arum Palaestinum with isovanillin, linolenic acid and β-sitosterol inhibits prostate cancer spheroids and reduces the growth rate of prostate tumors in mice. BMC Complement Altern Med [Internet]. 2015 Dec 5;15(1):264. Available from: <URL>

16. Oketch-Rabah HA. Mondia whitei , a Medicinal Plant from Africa with Aphrodisiac and Antidepressant Properties: A Review. J Diet Suppl [Internet]. 2012 Nov 13;9(4):272–84. Available from: <URL>

17. Dimo T, Rakotonirina S V, Tan P V, Azay J, Dongo E, Cros G. Leaf methanol extract of Bidens pilosa prevents and attenuates the hypertension induced by high-fructose diet in Wistar rats. J Ethnopharmacol [Internet]. 2002 Dec;83(3):183–91. Available from: <URL>

18. Sadraei H, Ghanadian M, Asghari G, Azali N. Antidiarrheal activities of isovanillin, iso-acetovanillon and Pycnocycla spinosa Decne ex.Boiss extract in mice. Res Pharm Sci [Internet]. 2014;9(2):83–9. Available from: <URL>

19. Verma G, Marella A, Shaquiquzzaman M, Akhtar M, Ali M, Alam M. A review exploring biological activities of hydrazones. J Pharm Bioallied Sci [Internet]. 2014;6(2):69–80. Available from: <URL>

20. Rollas S, Küçükgüzel S. Biological Activities of Hydrazone Derivatives. Molecules [Internet]. 2007 Aug 17;12(8):1910–39. Available from: <URL>

21. Narang R, Narasimhan B, Sharma S. A Review on Biological Activities and Chemical Synthesis of Hydrazide Derivatives. Curr Med Chem [Internet]. 2012 Feb 1;19(4):569–612. Available from: <URL>

22. Negi VJ, Sahrma AK, Negi JS, Ram V. Biological Activities of Hydrazone Derivatives in the New Millennium. Int J Pharm Chem [Internet]. 2012 Jan 1;2(4):100–9. Available from: <URL>

23. Akocak S, Alam MR, Shabana AM, Sanku RKK, Vullo D, Thompson H, et al. PEGylated Bis-Sulfonamide Carbonic Anhydrase Inhibitors Can Efficiently Control the Growth of Several Carbonic Anhydrase IX-Expressing Carcinomas. J Med Chem [Internet]. 2016 May 26;59(10):5077–88.

Available from: <URL>

24. Akocak S, Lolak N, Nocentini A, Karakoc G, Tufan A, Supuran CT. Synthesis and biological evaluation of novel aromatic and heterocyclic bis-sulfonamide Schiff bases as carbonic anhydrase I, II, VII and IX inhibitors. Bioorg Med Chem [Internet]. 2017 Jun 15;25(12):3093–7. Available from: <URL>

25. Akocak S, Lolak N, Bua S, Nocentini A, Supuran CT. Activation of human α-carbonic anhydrase isoforms I, II, IV and VII with bis-histamine schiff bases and bis-spinaceamine substituted derivatives. J Enzyme Inhib Med Chem [Internet]. 2019 Jan 1;34(1):1193–8. Available from: <URL>

26. Lolak N, Akocak S, Türkeş C, Taslimi P, Işık M, Beydemir Ş, et al. Synthesis, characterization, inhibition effects, and molecular docking studies as acetylcholinesterase, α-glycosidase, and carbonic anhydrase inhibitors of novel benzenesulfonamides incorporating 1,3,5-triazine structural motifs. Bioorg Chem [Internet]. 2020 Jul 1;100:103897. Available from: <URL>

27. Lolak N, Akocak S, Durgun M, Duran HE, Necip A, Türkeş C, et al. Novel bis-ureido-substituted sulfaguanidines and sulfisoxazoles as carbonic anhydrase and acetylcholinesterase inhibitors. Mol Divers [Internet]. 2022 Sep 22 [cited 2023 Mar 23];Article in:1–15. Available from: <URL>

28. Yapar G, Esra Duran H, Lolak N, Akocak S, Türkeş C, Durgun M, et al. Biological effects of bis-hydrazone compounds bearing isovanillin moiety on the aldose reductase. Bioorg Chem [Internet]. 2021 Dec 1;117:105473. Available from: <URL>

29. Al-blewi FF, Almehmadi MA, Aouad MR, Bardaweel SK, Sahu PK, Messali M, et al. Design, synthesis, ADME prediction and pharmacological evaluation of novel benzimidazole-1,2,3-triazole-sulfonamide hybrids as antimicrobial and antiproliferative agents. Chem Cent J [Internet]. 2018 Dec 1;12(1):110. Available from: <URL>

30. Tekeli Y, Lolak N, Sonmez GD, Tekeli T, Akocak S. Antibacterial, Antioxidant and DNA Cleavage Activity Evaluation of Substituted Phenylureido Sulfaguanidine and Sulfamethazine Derivatives. Pharm Chem J [Internet]. 2022 Jun 26;56(3):345–9. Available from: <URL>

31. Boga M, Tekeli Y, Lolak N, Sonmez GD, Akocak S. Synthesis and Antibacterial, Antioxidant and DNA Cleavage Evaluation of Triazenes Containing Sulfathiazole Moiety. Nov Approaches Drug Des Dev [Internet]. 2022 Jan 11;6(1):555684. Available from: <URL>

32. BLOIS MS. Antioxidant Determinations by the Use of a Stable Free Radical. Nature [Internet]. 1958 Apr;181:1199–200. Available from: <URL>

33. Carter P. Spectrophotometric determination of serum iron at the submicrogram level with a new reagent (ferrozine). Anal Biochem [Internet]. 1971 Apr 1;40(2):450–8. Available from: <URL>

34. Apak R, Güçlü K, Özyürek M, Karademir SE. Novel Total Antioxidant Capacity Index for Dietary Polyphenols and Vitamins C and E, Using Their Cupric Ion Reducing Capability in the Presence of Neocuproine: CUPRAC Method. J Agric Food Chem [Internet]. 2004 Dec 1;52(26):7970–81. Available from: <URL>

JOTCS A
Journal of the Turkish Chemical Society
Section: A
Chemistry
TURKISH CHEMICAL SOCIETY

Photoproduction of High Molecular Weight Poly (*N*-methylpyrrole) under Green Conditions

Kerem Kaya[1]
[1] Istanbul Technical University, Chemistry Department, Istanbul, 34469, Turkey

Abstract: A novel and green photochemical polymerization method of *N*-methylpyrole is reported. Spectral and chromatographic characterizations revealed the formation of high molecular weight polymer (1436 kg/mol) having light absorption in the near-infrared region (~750 nm), high fluorescence emission in the visible region, high conductivity (0.062 S/cm) and good thermal stability. Powder X-ray diffractogram identified a totally amorphous polymer. According to cyclic voltammetry studies the polymer formed (PMPy) possess a relatively low electronic band gap (1.39 eV) which is very important for the (opto)electronic device applications of such materials.

Keywords: Conductive polymers, polypyrrole derivatives, sustainable/green chemistry, photochemical polymerization, step-growth polymerization.

Submitted: January 12, 2023. **Accepted:** April 2, 2023.

Cite this: Kaya K. Photoproduction of High Molecular Weight Poly (N-methylpyrrole) under Green Conditions. JOTCSA. 2023;10(2):443–52.

DOI: https://doi.org/10.18596/jotcsa.1232989.

***Corresponding author. E-mail:** kkaya@itu.edu.tr

1. INTRODUCTION

Following the discovery of the unprecedented conductivity of doped polyacetylene, there have been enormous studies regarding the production of the conductive polymers (CPs) for various applications (1-3). CPs can easily be structurally modified resulting in distinct physicochemical features that have found use in numerous electronic and optoelectronic devices (4-6). Especially, CPs containing heteroatoms such as polythiophene, polyaniline, polypyrrole and their derivatives have been widely used in rechargeable batteries (7), organic photovoltaics (OPVs) (8), light-emitting diodes (LEDs) (9), supercapacitators (10) and biosensors (11).

Among the heteroaromatic CPs, polypyrrole and its derivatives have attracted vast attention due to their straightforward synthesis, high conductivity and insulating properties (12, 13). Poly (*N*-methylpyrrole) (PMPy) compared to polypyrrole, has higher mechanical strength (14), better antimicrobial activity (15), higher adhesion to the metalsurfaces (16) and superior corrosion protection due to its methyl group which possesses hydrophobicity (17). Hence, PMPy and its derivatives have been recently used as anti-corrosion/anti-bacterial material (18). The dopant ions present in PMPy also play a crucial role in the hydrophobicity of the polymer (19). It is a well-known fact that anions such as hexafluorophosphate or tetrafluoroborate possess great hydrophobicity (20).

Most of the synthetic methods regarding the production of PMPy involve chemical (21, 22) and electrochemical oxidation (23-25). In chemical oxidation, excess of a hazardous transition metal salt ($FeCl_3$, $CuCl_2$, $Fe(OTs)_3$) is

usually dissolved in monomer solution of toxic organic solvents such as chloroform, dichloromethane and heated to reflux conditions for 1-2 days under inert atmosphere. Although electrochemical oxidation can be performed in short time (usually in minutes), it has several disadvantages such as the need for sophisticated electrochemical equipment, inefficiency of electrodes during polymerization and the production of very little PMPy which, most of the time, cannot be completely characterized. All these drawbacks faced in both chemical and electrochemical oxidation methods show a great barrier for the sustainable chemistry.

In the context of sustainable chemistry, light-driven chemical methods are the most favorable techniques due to the faster reaction rates, milder reaction conditions and the use of much less or no solvent (bulk photopolymerization) (26, 27). Photopolymerization reactions use only light as the input energy and don't require excess amount of toxic catalysts/solvents (28). Besides these features, photopolymerization methods possess spatiotemporal control which make them versatile for many modern applications including 3D-printing (29).

In spite of the fact that most of the photopolymerization methods concern free-radical polymerization (FRP), cationic photopolymerization reactions exhibit several advantages over their FRP counterpart including the insensitivity to air, low shrinkage and theoretical non-terminating (living) nature (30, 31). It has been previously demonstrated that cationic photopolymerization of technologically important monomers including *N*-ethylcarbazole (32, 33), thiophene (34), and thienothiophene derivatives (35) can be successfully achieved using strong photooxidants such as diphenyliodonium hexafluorophosphate (DPI).

In this work, the green photoproduction of PMPy doped with PF_6^- anions using DPI as one-component photoinitiator in ethanol solvent under near-UV irradiation and ambient conditions is reported. In contrast to insoluble polypyrrole, photoproduced PMPy showed relatively high solubility in most of the polar organic solvents (tetrahydrofuran (THF), dimethyl sulfoxide (DMSO), dimethyl formamide (DMF)). PMPy was structurally characterized using infrared (IR) and nuclear magnetic resonance (NMR) spectroscopies. According to gel-permeation chromatography (GPC), conductivity, UV-vis and fluorescence measurements, the photoproduced PMPy had high molecular weight (1436 kg/mol), high conductivity (0.062 S/cm), broad UV-vis-NIR absorption (reaching near-infrared region) and strong white light photoluminescence, respectively. Thermal stability and crystallinity of the polymer was also investigated using differential scanning calorimeter (DSC), thermogravimetric analysis (TGA) and powder X-ray diffractometry (PXRD), respectively. Cyclic voltammetry studies performed pointed out to relatively low band gap (1.39 eV) which is important for (opto)electronic utilization.

2. MATERIALS AND METHOD

2.1. Materials

N-methylpyrrole (NMPy) (Sigma-Aldrich, 99%) and diphenyliodonium hexafluorophosphate (Sigma-Aldrich, >98%) were kept in the fridge prior to use and used as received. All the other chemical reagents (solvents) including absolute ethanol (96%, Merck), methanol (Merck, 99.8%), tetrahydrofuran (Sigma-Aldrich, 99.9%), dimetylformamide (Merck, 99.8%) and dimethylsulfoxide (Merck, 99.9%) were purified according to conventional techniques prior to use.

2.2. Methods

2.2.1. Photoproduction of PMPy

PMPy was prepared by mixing 900 µL of NMPy (1 mmol) and 852 mg of DPI (2 mmol) in 2 mL of EtOH inside a test tube which was then irradiated using a photoreactor equipped with 12 lamps emitting light nominally at 355 nm (~100 mW/cm^2) for 4 h. Viscous black solution formed were then precipitated into hot n-hexane in order to remove any unreacted NMPy or DPI. After washing with ethanol, PMPy was dried under vacuum for 2 days before any characterization.

2.2.2. Gel permeation chromatography (GPC)

GPC measurements were performed on a TOSOH EcoSEC GPC system equipped with an auto-sampler system, a temperature-controlled pump, a column oven, a refractive index (RI) detector, a purge and degasser unit, and a TSKgel superhZ2000 4.6 mm ID × 15 cm × 2 cm column. Tetrahydrofuran was used as an eluent at flow rate of 1.0 mL/min at 40°C.

2.2.3. UV-vis Spectroscopy

UV-vis spectra were recorded with a Shimadzu UV-1601 double-beam spectrometer equipped with a 50 W halogen lamp and a deuterium lamp which can operate between 200 and 900 nm.

2.2.4.Fluorescence Spectroscopy
Fluorescence meausuerements were performed using Perkin-Elmer LS55 which can operate between 200 and 900 nm. with a slit width of 5 nm and 1 cm path length cuvette.

2.2.5. NMR Spectroscopy
^{1}H NMR and ^{13}C spectra were recorded in deuterated chloroform ($CDCl_3$ with tetramethylsilane as an internal standard) at 500 MHz on an Agilent VNMRS 500 spectrometer at 25° C.

2.2.6. IR Spectroscopy
Fourier-transform infrared (IR) spectra were recorded on a PerkinElmer Spectrum One spectrometer with an ATR accessory (ZnSe, PikeMiracle) and a mercury cadmium telluride (MCT) detector. A total of 32 scans were averaged.

2.2.7. Cyclic Voltammetry
The electrochemical measurements were performed by using a CH Instruments 617D potentiostat− galvanostat system. The electrochemical cell containing a Ag wire as a reference electrode (RE), a Pt wire as counter electrode (CE), and glassy carbon as a working electrode (WE) was immersed in 0.1 M tetrabutylammonium hexafluorophosphate as the supporting electrolyte under argon atmosphere.

2.2.8. Powder X-Ray Diffractography
Crystallographic identification was accomplished by X-ray diffraction (XRD) method on a benchtop Rigaku Miniflex diffractometer with a Cu-Kα radiation source operated at 30 kV and 10 mA. The acquisition angle ranged from 2° to 90°.

2.2.9. Thermal Analysis
Thermogravimetric analysis (TGA) was performed on a Perkin-Elmer Diamond TA/TGA with a heating rate of 10 K/min under constant nitrogen flow of 200 mL/min.

2.2.10. Conductivity Measurements
Conductivity measurements were performed in air at room temperature using a HP3478A digital voltmeter, with a direct 4-wire resistance capability.

3. RESULTS AND DISCUSSION

Following the photopolymerization, precipitation and drying procedures, molecular weight of obtained PMPy was investigated using GPC. The results are tabulated in Table1.

Table 1.GPC results of PMPy obtained by photopolymerization.[a]

Polymer	Conversion (%)[b]	M_n (kg/mol)[c]	$Đ^c$
PMPy	72	1436	1.37

[a]1 mmol of NMPy was mixed with 2 mmol of DPI inside a tube irradiated inside a photoreactor for 4 h. (details can be found in the materials and method section). [b]Determined gravimetrically. [c]Determined using GPC calibrated with polystyrene standards having narrow molecular weight distribution (1.05).

It is interesting to observe GPC traces (Figure 1) belonging to very high molecular weight species since similar CPs are known to have poor solubility in most of the solvents (36). This phenomenon can be attributed to the highly doped nature of PMPy resulting in increased ion-dipole interactions between dopant ions (PF_6^-) and dipole of polar organic solvents such as THF, DMSO and DMF (37). Dispersity index of 1.37 is a clear indication of the step-growth nature of the photopolymerization as similar indices were previously observed in the photoinduced step-growth polymerization of other heteroaromatics monomers (38).

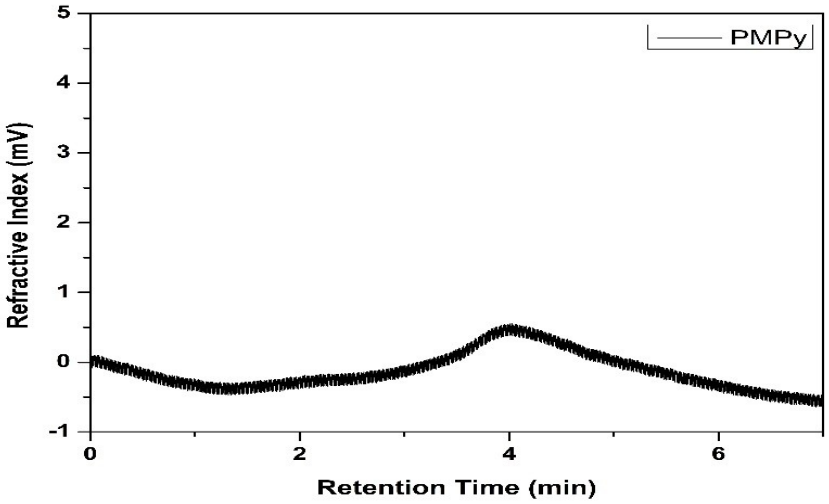

Figure 1. GPC traces of PMPy.

UV-vis absorbance spectrum of the dark colored PMPy in DMSO solvent exhibited strong bathochromic shift (~450 nm) compared to the spectrum of its monomer analogue as can be seen in Figure 2. The absorbance in the near-infrared (NIR) region confirms the presence of high molecular weight species having increased conjugation.

Figure 4a and 4b show ^{1}H and ^{13}C NMR spectra of PMPy, respectively. Clear broadening in the aliphatic region and aromatic region corresponds to *N*-methyl and pyrrole ring protons, respectively, indicating successful polymerization. In the ^{1}H NMR spectrum, the ratio of the integral areas of the aliphatic and aromatic regions are 3:6 instead for 3:2 due the low resolution caused by the insolubility of large molecular weight polymers, the end group aromatic protons of different chain length polymers and due to the presence of NMR solvent $CDCl_3$.

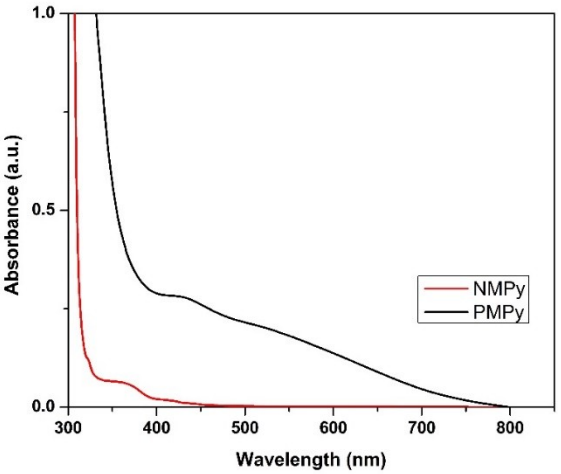

Figure 2. UV-vis spectra of (red) NMPy and black (PMPy) (solvent:DMSO).

Excitation of DMSO solution of PMPy in different wavelengths resulted in fluorescence emissons covering the whole blue-red-green zone (visible to NIR) (Figure 3). causing a strong white light luminescence, especially upon excitation at 355 nm (Figure 3 inset photo).

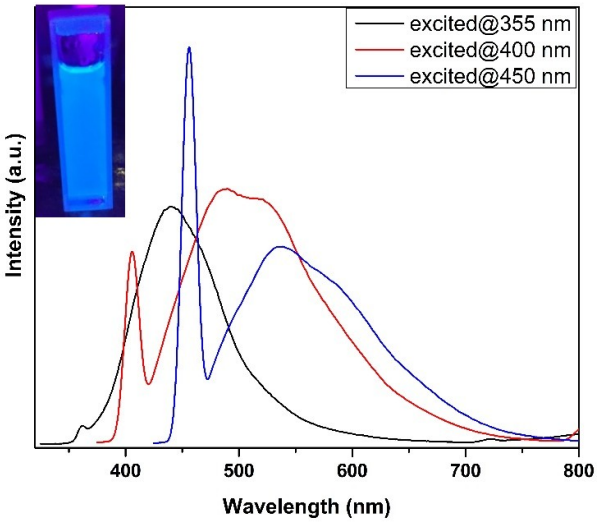

Figure 3. Fluorescence emission of PMPy excited at different wavelength (inset photo shows the white photoluminescence of PMPy excited at 355 nm) (solvent: DMSO).

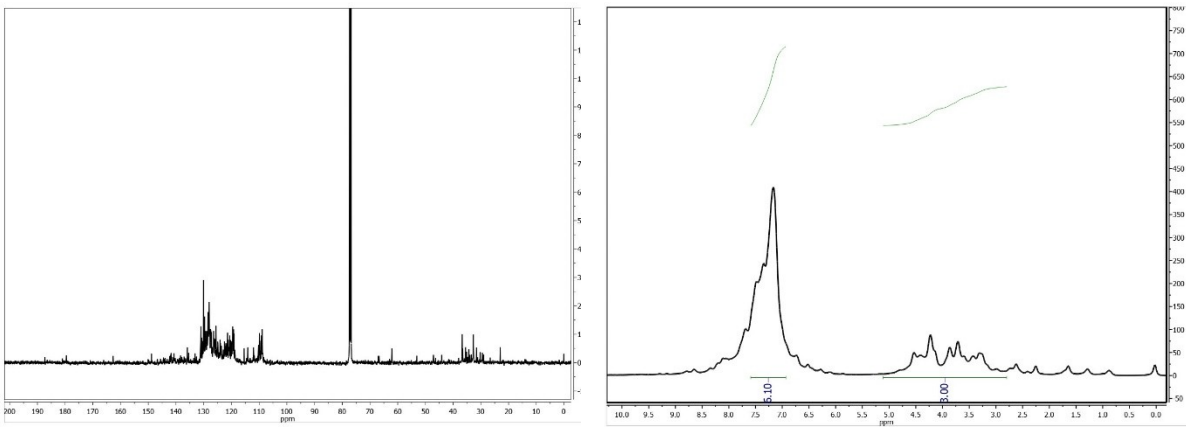

Figure 4. (a) ^{1}H NMR and (b) ^{13}C NMR spectra of PMPy.

Figure 5 shows the IR spectra of NMPy and PMPy. Similar to NMR spectra, clear broadening in the aliphatic and aromatic C-H stretching peaks points out successful polymerization. Minor changes in the fingerprint region might be due to the presence of high conjugation and dopant ions.

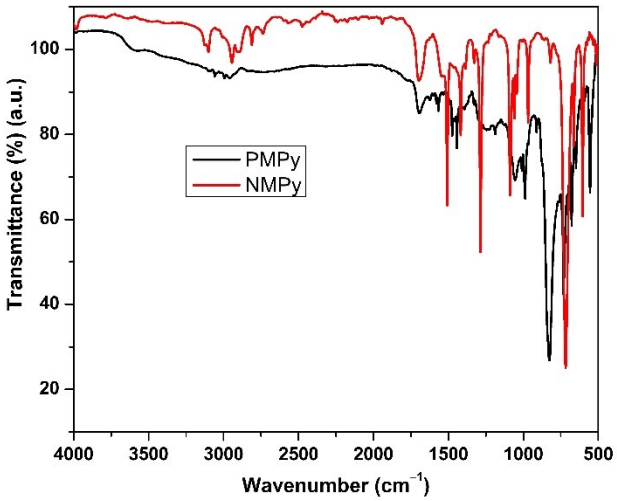

Figure 5. IR spectra of (red)NMPy and (black)PMPy.

In view of the previous laser-flash photolysis results obtained (38), the photopolymerization of NMPy should initiate by the formation of NMPy radical cation through photoinduced electron transfer (PET) within the excited complex (exciplex) formed between DPI and NMPy by irradiation. This is followed by the formation of dimer by coupling of two NMPy radical cations releasing HPF_6 acid. Since the oxidation of dimer is easier than the oxidation of monomer the photopolymerization proceeds through successive PET, coupling and acid release yielding PMPy doped with PF_6^- ion in a step-growth manner (Scheme 1).

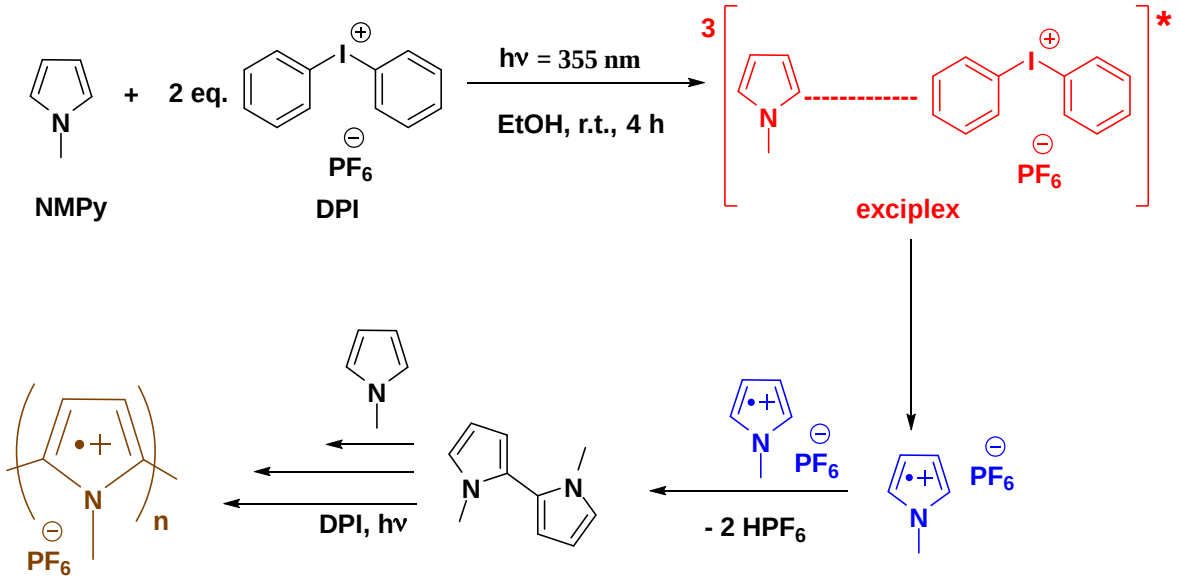

Scheme 1. Plaused mechanism for the photoinduced step-growth polymerization NMPy.

DSC thermogram of PMPy, similar to the literature results, shows no endotherms but two exotherms around 170 °C and 325 °C indicating recrystallization and degradation of the polymer, respectively. (Figure 6a). Thermal stability of the PMPy was also probed using TGA (Figure 6b). PMPy was stable (first 5% loss by weight) until 175 °C where after a sudden loss of weight occurred due to the removal of dopant ions and the gradual

degradation of polymeric chains, as previously observed in another photochemically polymerized *N*-methylpyrrole and *N*-methylindole using phenacyl bromide (38). The attribution of the first weight loss to the removal of dopant ions is due to the fact that the TGA thermogram of dedoped state of similar conjugated polymers (dedoped PEDOT) were previously shown to be thermally stable until the degradation point (39). When DSC and TGA results of PMPy are compared, it is possible to conclude that the two exothermic peaks in the DSC thermogram correspond to two major weight loss temperatures in TGA thermogram of PMPy.

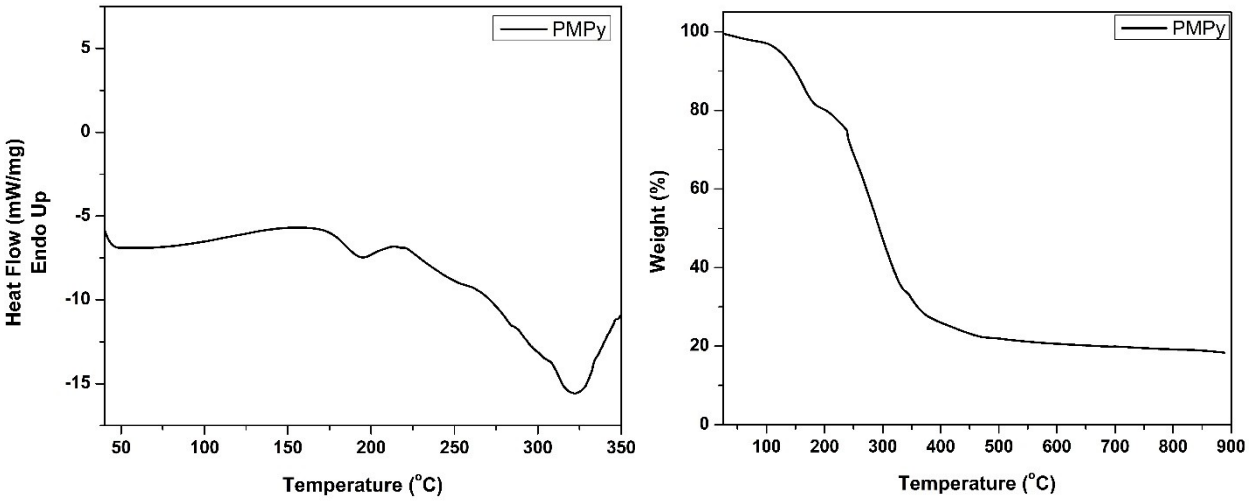

Figure 6. (a) DSC thermogram and (b) TGA thermogram of PMPy.

PXRD diffractogram of PMPy exhibited a totally amorphous nature and was in good agreement with the GPC traces indicating high molecular weight species (Figure 7). The peak around 2θ = 24° corresponds to - stacking between the pyrrole units of PMPy (40). The HOMO and LUMO level of the PMPy was calculated through its electrochemical data of three cycles obtained using cyclic voltammetry (CV) in acetonitrile solution (Figure 8) (HOMO = 1.00 eV (onset) and LUMO = -0.39 eV (onset)). Calculated electronic band gap of 1.39 eV is close to the previously obtained PMPy (1.45 eV) by photopolymerization method (38).

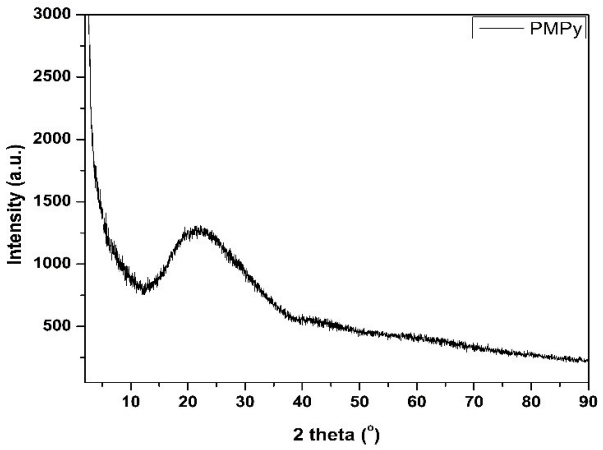

Figure 7. Powder X-Ray diffractogram of PMPy.

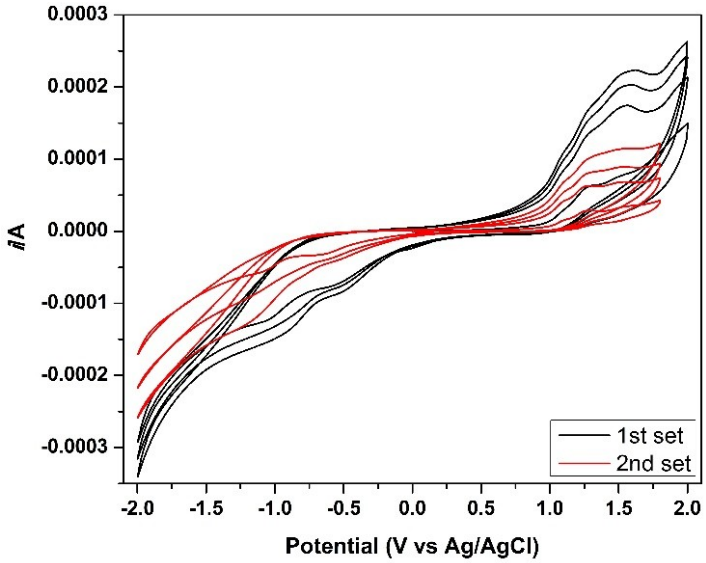

Figure 8. Cyclic voltammogram of PMPy.

4. CONCLUSION

In summary, high molecular weight poly (*N*-methylpyrrole) (PMPy) was photochemically obtained using DPI as one-component photoinitiator under green conditions. According to the previous experimental results obtained through the detection of acid and laser-flash photolysis, the photopolymerization should initiate by the oxidation of the monomer by DPI within the exciplex and should proceed with the coupling of two monomers forming dimer by releasing two protonic species. Propagation of the dimers and oligomers should go on in a step-growth manner finally terminated by hydrogen abstraction possibly from the solvent (EtOH). The method developed has many advantages over the conventional methods ((electro)chemical oxidation) such as the use of ambient conditions, green solvent, straightforward reaction procedure and short reaction time. Considering the strong electron acceptor feature of DPI, this work can be extended for the photopolymerization of other electron donor monomers.

5. CONFLICT OF INTEREST

The author declares no conflict of interest.

6. FUNDING

This work was supported by Istanbul Technical University Scientific Research Projects Coordination Unit.

7. ACKNOWLEDGEMENTS

The author thanks Prof. Yusuf Yagci for his supervision. This paper is dedicated to the memory of Prof. Yusuf Yagci.

8. REFERENCES

1. K N, Rout CS. Conducting polymers: a comprehensive review on recent advances in synthesis, properties and applications. RSC Advances. 2021;11(10):5659-97. <URL>

2. Nezakati T, Seifalian A, Tan A, Seifalian AM. Conductive Polymers: Opportunities and Challenges in Biomedical Applications. Chemical Reviews. 2018;118(14):6766-843. <URL>

3. Prunet G, Pawula F, Fleury G, Cloutet E, Robinson AJ, Hadziioannou G, et al. A review on conductive polymers and their hybrids for flexible and wearable thermoelectric applications. Materials Today Physics. 2021;18:100402. <URL>

4. R. Murad A, Iraqi A, Aziz SB, N. Abdullah S, Brza MA. Conducting Polymers for Optoelectronic Devices and Organic Solar Cells: A Review. Polymers. 2020;12(11):2627. <URL>

5. Heck J, Goding J, Portillo Lara R, Green R. The influence of physicochemical properties on the processibility of conducting polymers: A bioelectronics perspective. Acta Biomaterialia. 2022;139:259-79. <URL>

6. Wu X, Fu W, Chen H. Conductive Polymers for Flexible and Stretchable Organic Optoelectronic Applications. ACS Applied Polymer Materials. 2022;4(7):4609-23. <URL>

7. Aradilla D, Estrany F, Casellas F, Iribarren JI, Alemán C. All-polythiophene rechargeable batteries. Organic Electronics. 2014;15(1):40-6. <URL>

8. Yuan X, Zhao Y, Xie D, Pan L, Liu X, Duan C, et al. Polythiophenes for organic solar cells with efficiency surpassing 17%. Joule. 2022;6(3):647-61. <URL>

9. Langer JJ, Ratajczak K, Frąckowiak E, Golczak S. Water-Induced Tuning of the Emission of Polyaniline LEDs within the NIR to Vis Range. ACS Omega. 2021;6(50):34650-60. <URL>

10. Huang Y, Li H, Wang Z, Zhu M, Pei Z, Xue Q, et al. Nanostructured Polypyrrole as a flexible electrode material of supercapacitor. Nano Energy. 2016;22:422-38. <URL>

11. Sengodu P. 12 - Conjugated polymers-based biosensors. In: Kumar V, Sharma K, Sehgal R, Kalia S, editors. Conjugated Polymers for Next-Generation Applications. 1: Woodhead Publishing; 2022. p. 401-46. <URL>

12. Thadathil A, Pradeep H, Joshy D, Ismail YA, Periyat P. Polyindole and polypyrrole as a sustainable platform for environmental remediation and sensor applications. Materials Advances. 2022;3(7):2990-3022. <URL>

13. Pang AL, Arsad A, Ahmadipour M. Synthesis and factor affecting on the conductivity of polypyrrole: a short review. Polymers for Advanced Technologies. 2021;32(4):1428-54. <URL>

14. Tüken T, Tansuğ G, Yazıcı B, Erbil M. Poly(N-methyl pyrrole) and its copolymer with pyrrole for mild steel protection. Surface and Coatings Technology. 2007;202(1):146-54. <URL>

15. Elibal F, Gumustekin S, Ozkazanc H, Ozkazanc E. Poly(N-methylpyrrole) with high antibacterial activity synthesized via interfacial polymerization method. Journal of Molecular Structure. 2021;1242:130712. <URL>

16. Su W, Iroh JO. Electrodeposition mechanism, adhesion and corrosion performance of polypyrrole and poly(N-methylpyrrole) coatings on steel substrates. Synthetic Metals. 2000;114(3):225-34. <URL>

17. Branzoi F, Mihai MA, Petrescu S. Corrosion Protection Efficacy of the Electrodeposit of Poly (N-Methyl Pyrrole-Tween20/3-Methylthiophene) Coatings on Carbon Steel in Acid Medium. Coatings. 2022;12(8):1062. <URL>

18. Duran B, Bereket G. Cyclic Voltammetric Synthesis of Poly(N-methyl pyrrole) on Copper and Effects of Polymerization Parameters on Corrosion Performance. Industrial & Engineering Chemistry Research. 2012;51(14):5246-55.<URL>

19. Ahmad S. Electropolymerization of poly(methyl pyrrole)/carbon nanotubes composites derived from ionic liquid. Polymer Engineering & Science. 2009;49(5):916-21.<URL>

20. Huddleston JG, Visser AE, Reichert WM, Willauer HD, Broker GA, Rogers RD. Characterization and comparison of hydrophilic and hydrophobic room temperature ionic liquids incorporating the imidazolium cation. Green Chemistry. 2001;3(4):156-64. <URL>

21. Ustamehmetoğlu B, Kelleboz E. Oxidative Copolymerization of Pyrrole and N-Methyl Pyrrole. International Journal of Polymer Analysis and Characterization - Int J Polym Anal Charact. 2003;8:255-68. <URL>

22. Dubitsky YA, Zhubanov BA, Maresch GG. Synthesis of polypyrroles in the presence of ferric tetrafluoroborate. Synthetic Metals. 1991;41(1):373-6. <URL>

23. González-Tejera MJ, Martín G. Electrogeneration of Poly-N-Methylpyrrole Tosylate Doped Films. Electrochemical and Morphological Study. Portugaliae Electrochimica Acta. 2007;25:349-61. <URL>

24. Genies EM, Syed AA. Polypyrrole and poly N-methylpyrrole — An electrochemical study in an aqueous medium. Synthetic Metals. 1984;10(1):21-30. <URL>

25. Mahmoudian MR, Basirun WJ, Alias Y. Synthesis and characterization of poly(N-methylpyrrole)/TiO2 composites on steel. Applied Surface Science. 2011;257(8):3702-8. <URL>

26. Kaya K, Yagci Y. Contemporary Approaches for Conventional and Light-Mediated Synthesis of Conjugated Heteroaromatic Polymers. Macromolecular Chemistry and Physics. 2021;222(24):2100334. <URL>

27. Bagheri A, Jin J. Photopolymerization in 3D Printing. ACS Applied Polymer Materials. 2019;1(4):593-611. <URL>

28. Zou D, Nunes SP, Vankelecom IFJ, Figoli A, Lee YM. Recent advances in polymer membranes employing non-toxic solvents and materials. Green Chemistry. 2021;23(24):9815-43. <URL>

29. Somers P, Liang Z, Johnson JE, Boudouris BW, Pan L, Xu X. Rapid, continuous projection multi-photon 3D printing enabled by spatiotemporal focusing of femtosecond pulses. Light: Science & Applications. 2021;10(1):199. <URL>

30. Malik MS, Schlögl S, Wolfahrt M, Sangermano M. Review on UV-Induced Cationic Frontal Polymerization of Epoxy Monomers. Polymers. 2020;12(9):2146. <URL>

31. Shirai M. Photoinitiated Polymerization. In: Kobayashi S, Müllen K, editors. Encyclopedia of Polymeric Nanomaterials. Berlin, Heidelberg: Springer Berlin Heidelberg; 2015. p. 1579-85. <URL>

32. Sari E, Yilmaz G, Koyuncu S, Yagci Y. Photoinduced Step-Growth Polymerization of N-Ethylcarbazole. Journal of the American Chemical Society. 2018;140(40):12728-31. <URL>

33. Kaya K, Koyuncu S, Yagci Y. Photoinduced synthesis of poly(N-ethylcarbazole) from phenacylium salt without conventional catalyst and/or monomer. Chemical Communications. 2019;55(77):11531-4. <URL>

34. Yagci Y, Jockusch S, Turro NJ. Mechanism of Photoinduced Step Polymerization of Thiophene by Onium Salts: Reactions of Phenyliodinium and Diphenylsulfinium Radical Cations with Thiophene. Macromolecules. 2007;40(13):4481-5. <URL>

35. Celiker T, İsci R, Kaya K, Ozturk T, Yagci Y. Photoinduced step-growth polymerization of thieno[3,4-b] thiophene derivatives. The substitution effect on the reactivity and electrochemical properties. Journal of Polymer Science. 2020;58(17):2327-34. <URL>

36. Hebert DD, Naley MA, Cunningham CC, Sharp DJ, Murphy EE, Stanton V, et al. Enabling Conducting Polymer Applications: Methods for Achieving High Molecular Weight in Chemical Oxidative Polymerization in Alkyl- and Ether-Substituted Thiophenes. Materials (Basel). 2021;14(20):6146. <URL>

37. Abel SB, Frontera E, Acevedo D, Barbero CA. Functionalization of Conductive Polymers through Covalent Postmodification. Polymers. 2022;15(1):205. <URL>

38. Kocaarslan A, Kaya K, Jockusch S, Yagci Y. Phenacyl Bromide as a Single-Component Photoinitiator: Photoinduced Step-Growth Polymerization of N-Methylpyrrole and N-Methylindole. Angewandte Chemie International Edition. 2022;61(36):e202208845. <URL>

39. Kaya K. A green and fast method for PEDOT: Photoinduced step-growth polymerization of EDOT. Reactive and Functional Polymers. 2023;182:105464. <URL>

40. Celiker T, Kaya K, Koyuncu S, Yagci Y. Polypyrenes by Photoinduced Step-Growth Polymerization. Macromolecules. 2020;53(14):5787-94. <URL>

Evaluation of the Structural, Near-Infrared Luminescence, and Radioluminescence Properties of Nd^{3+} Activated TTB-Lead Metatantalate Phosphors

Mustafa İlhan[1*], İlker Çetin Keskin[2]

[1]Department of Environmental Engineering, Faculty of Engineering, Marmara University, Maltepe, 34840, İstanbul, Turkey
[2]Department of Electricity and Energy, Soma Vocational School, Manisa Celal Bayar University, Soma, 45500, Manisa, Turkey

Abstract: The study reports the structural and spectroscopic properties of Nd^{3+} doped lead metatantalate phosphor series fabricated by conventional solid state method. XRD results of the $PbTa_2O_6$ phase confirm the tungsten bronze symmetry and single-phase structure between 0.5 and 10 mol% Nd^{3+} concentrations. The lead decrease in the structure can be associated with maintaining the charge balance and single phase due to evaporation during sintering. In SEM micrographs, the grains exhibited shapeless morphology, and the grain sizes varied from 0.5 to 7 ⁀m. In EDS results, the increase of Ta/Pb ratio in grain surfaces indicated some lead evaporation, as reported in previous studies. The absorption spectrum of $PbTa_2O_6$ host peaked around 275-280 nm, and the band gap was found to be 3.7±0.2 eV. The absorptions of Nd^{3+} doped phophors shifted the high wavelenght or the low band gap, where the band gaps were found between 3.1±0.2 and 3.3±0.2 eV. The PL emissions of the phosphors in near-inrared region were observed with the transitions of $^4F_{3/2}\rightarrow{}^4I_{9/2}$ (at 875 nm) and $^4F_{3/2}\rightarrow{}^4I_{11/2}$ (at 1060 nm) of Nd^{3+}. The RL emissions or X-ray excited luminescence were monitored with the transitions of $^4F_{3/2}\rightarrow{}^4I_{9/2}$ (at 875 nm), $^4F_{3/2}\rightarrow{}^4I_{11/2}$ (at 1065 nm) in the infrared region, and the transitions of $^2F(2)_{5/2}\rightarrow{}^4F_{9/2}$, $^2F(2)_{5/2}\rightarrow{}^2H(2)_{11/2}$, $^2F(2)_{5/2}\rightarrow{}^4G_{5/2}$, $^2F(2)_{5/2}\rightarrow{}^4G_{7/2}$, $^2F(2)_{5/2}\rightarrow{}^4G_{9/2}$ in the visible region corresponding to at around 430, 455, 490, 525, and 570 nm, respectively. PL and RL emissions of the phosphors exhibited the decreasing emission intensity over 5 mol% due to the concentration quenching which may be associated with cross-relaxing mechanism. In the PL and RL spectral profiles, the similarity of splitting levels was attributed to the similarity of the local symmetry of the ligand ions surrounding the Nd^{3+} ion. The CIE coordinates obtained using RL emissions were found close to the blue region due to visible region transitions.

Keywords $PbTa_2O_6$, Near infrared luminescence, Radioluminescence, Nd^{3+}

Submitted: December 09, 2022. **Accepted:** March 22, 2023.

Cite this: İlhan M, Keskin İÇ. Evaluation of the Structural, Near-Infrared Luminescence, and Radioluminescence Properties of Nd3+ Activated TTB-Lead Metatantalate Phosphors. JOTCSA. 2023;10(2):453–66.

DOI: https://doi.org/10.18596/jotcsa.1216564.

*Corresponding author. **E-mail:** mustafa.ilhan@marmara.edu.tr.

1. INTRODUCTION

Rare earth (RE) ions with 4f– 4f inner shell transitions have undoubtedly contributed greatly to the development of luminescence applications and the increase in their usage areas. Therefore, the RE ion activated phosphors lead to numerous innovations in the development of new generation devices in various fields such as screen-display technology, lighting technology, and optical data communication due to some positive features such as long life, energy saving, improved physical durability, small size, fast switching, high efficiency, and environmental friendliness (1-19). The trivalent neodymium ion (Nd^{3+}), one of the oldest trivalent lanthanide ions used in solid-state laser, is well known for its useful laser transitions such as

$^4F_{3/2}\rightarrow{}^4I_{9/2}$, $^4F_{3/2}\rightarrow{}^4I_{11/2}$, and $^4F_{3/2}\rightarrow{}^4I_{13/2}$ (20-29). The $^4F_{3/2}\rightarrow{}^4I_{9/2}$ transition at 880 nm finds application as a powerful diode laser transition while the $^4F_{3/2}\rightarrow{}^4I_{11/2}$ transition stands out due to its easily operated at room temperature and pumped efficiently by flash lamp (29). The scintillator or radioluminescent materials convert the high-energy ionizing radiation of a photon into visible-ultraviolet low energy photon. In radioluminescence process, when the energy absorbed in the host material is induced by high-energy radiation, then the energy passes to the RE emission center and the photons are emitted in a relaxation process. The radioluminescent or scintillator materials are used such as in the high energy or nuclear physics detectors, the advanced techniques for homeland security, the high-tech industrial applications, and the medical imaging techniques (to detect accelerated particles and high-energy photons) (30–36).

There are two polymorphs of $PbTa_2O_6$ formed in the PbO-Ta_2O_5 binary system. The high-temperature polymorph is orthorhombic, and the low-temperature polymorph is rhombohedral. The non-ferroelectric rhombohedral is persistent only below around 1150 °C, while the ferroelectric orthorhombic forms at high temperatures (over 1150 °C), and the Curie point is 265 °C (37,38). The orthorhombic $PbTa_2O_6$ shows close structural similarity with the tungsten bronzes in paraelectric state. Tetragonal tungsten bronze (TTB) based oxide structures, which stand out with their dielectric properties, form a wide family of crystals (39-42). TTB structures exhibit suitable host features for dopant lanthanide ions due to its three different tunnels or multi-location sites that allow cation substitution at different radius and charge (30–32). In the literature, there are some studies on $PbTa_2O_6$ due to its structural, dielectric, ferroelectric (37-39), luminescence (30–32), and photocatalytic properties (43).

In the study, the near infrared photoluminescence and radioluminescence properties of $PbTa_2O_6$:xNd^{3+} (x=0.5, 1.5, 3, 5, 7, 10 mol%) phosphors were studied. Although Eu^{3+} (30,40) and Dy^{3+} (31,32) doped studies of the lead tantalate phophors have been reported previously, the Nd^{3+} doped photoluminescence and X-ray excited luminescence are reported in this study to the best of our knowledge. The spectroscopic and structural characterizations of the ceramic samples were examined by XRD, SEM-EDS, PL, RL and absorption analyses.

2. EXPERIMENTAL SECTION

Undoped and $PbTa_2O_6$:xNd^{3+} (x=0.5, 1.5, 3, 5, 7 and 10 mol%) materials were fabricated by the solid state reaction route, where x represents 2 atomic value due to Nd_2O_3. $Pb(NO_3)_2$, Ta_2O_5 and Nd_2O_3 powders were used as starting and dopant materials with purity of 99% (Sigma–Aldrich), 99.9% (Alfa Aesar), and 99.9% (Alfa Aesar), respectively. Ta_2O_5 and $Pb(NO_3)_2$ powders were weighed and mixed according to $PbTa_2O_6$ stoichiometry. Six different powder mixtures were prepared and Nd_2O_3 dopant was subsequently added at different concentrations into the each powder mixture as $PbTa_2O_6$:0.005Nd^{3+}, $PbTa_2O_6$:0.015Nd^{3+}, $PbTa_2O_6$:0.03Nd^{3+}, $PbTa_2O_6$:0.05Nd^{3+}, $PbTa_2O_6$:0.07Nd^{3+}, $PbTa_2O_6$:0.1Nd^{3+}, and they were homogenized by mixing in agate mortar for 10 min. Final powder mixtures were heat treated at 1250 °C for 6 h in an electric furnace under air atmosphere after pelleting.

The phase structure of the ceramics was investigated by X-ray diffraction (D2 PHASER, Bruker Corp., Germany) using Cu-K$_\alpha$ radiation, Ni filter, scan rate = 2 °/min, 2θ=20-65°. The grain morphology and elemental identification of the samples were carried out by SEM (JSM-5910LV, JEOL Ltd., Japan) equipped with EDS (INCAx-Sight 7274, Oxford Industries, UK) after Au coating. The near emission spectra of Nd^{3+} doped samples were taken using a diode laser of 800 nm at 300 K. The radioluminescence spectra of the Nd^{3+} doped $PbTa_2O_6$ phosphors were taken using a Machlett OEG-50A tube which operates with 30 kV and 15 mA and, the X-ray tube provides white X-rays at a dose rate of 30 Gy/min radioluminescence spectra were taken with a Horiba Jobin Yvon spectrometer connected to a liquid nitrogen-cooled CCD detector. RL analysis was performed under room conditions, the detector integration time was set to 5 seconds and the input-output slit widths were set to 2 mm. The absorption spectra of the undoped sample and Nd^{3+} doped samples were performed by a Perkin-Elmer Lambda spectrophotometer (USA).

3. RESULTS AND DISCUSSION

3.1. XRD and SEM-EDS Results

The XRD results of undoped sample and $PbTa_2O_6$:xNd^{3+} (x=0.5, 1.5, 5, 7 and 10 mol%) samples are shown in Figure 1. As seen in the XRD patterns of all the samples, there are no different minor phases in the range of 20°-65°. XRD analysis showed that the $PbTa_2O_6$ samples crystallized (JCPDS card No. 14–0315) in the tetragonal tungsten bronze symmetry with space group *P4/mbm*. The orthorhombic-tetragonal relationship of $PbTa_2O_6$ along the c-axis in the tungsten bronze structure is shown in Figure 2. The lattice parameters of tetragonal are a=12.49 Å, c=3.875 Å (37), while the cell data for orthorhombic are a_0=17.68 Å, b_0=17.72 Å, c_0=7.754 Å (38). The relation of the orthorhombic–tetragonal cell parameters is $a_0=a\sqrt{2}$, $b_0=a\sqrt{2}$, $c_0=2c$ (38,44), The a, and b constants are nearly equal, where the b/a ratio is about 1.002 (38). So, the XRD patterns of orthorhombic $PbTa_2O_6$ may be indexed quite well as tetragonal due to the extremely small orthorhombic distortion (38,41). The $A_4B_2C_4M_{10}O_{30}$ formula represents the TTB (tetragonal tungsten bronze) structure for the oxide compounds where the pentagonal (A), square (B),

triangle (C) sites have 15, 12, 9 CN, respectively, and the octahedral (M) sites have 6 CN. The A and B sites are occupied by large cations while the C sites occupied by small cations such as Li^{+}. The M octahedral sites are suitable for small radius and high charged cations such as Ta^{5+}, Nb^{5+}. Li et al. (45) studied the distribution of Eu^{3+} atoms in the A (non-centrosymmetric) sites and B (centrosymmetric) sites, which are related to $^{5}D_{0}\rightarrow{}^{7}F_{2}$, and $^{5}D_{0}\rightarrow{}^{7}F_{1}$ transitions, respectively. They suggested that Eu^{3+} atoms could mainly occupy the centrosymmetric sites or then randomly disperse into both centrosymmetric and non-centrosymmetric sites. Accordingly, based on the ionic radius and coordination number (CN), the formation of the single-phase may be attributed to the partial occupation of vacant sites in the lattice by Nd^{3+} ions (1.27 Å for 12 CN, and 1.163 Å for 9 CN), and partial substitution of Nd^{3+} ions by Pb^{2+} ions (1.35 Å for CN 9, and 1.49 Å for CN 12). In addition, although the inclusion of Nd^{3+} ions does not cause any change in the single-phase structure of $PbTa_2O_6$ up to 10 mol %, the charge balance of structure may be somewhat affected. However, during sintering, a lead decrease may occur due to evaporation, which can be helpful in maintaining the charge balance and single-phase structure in the case of RE doping (40,41).

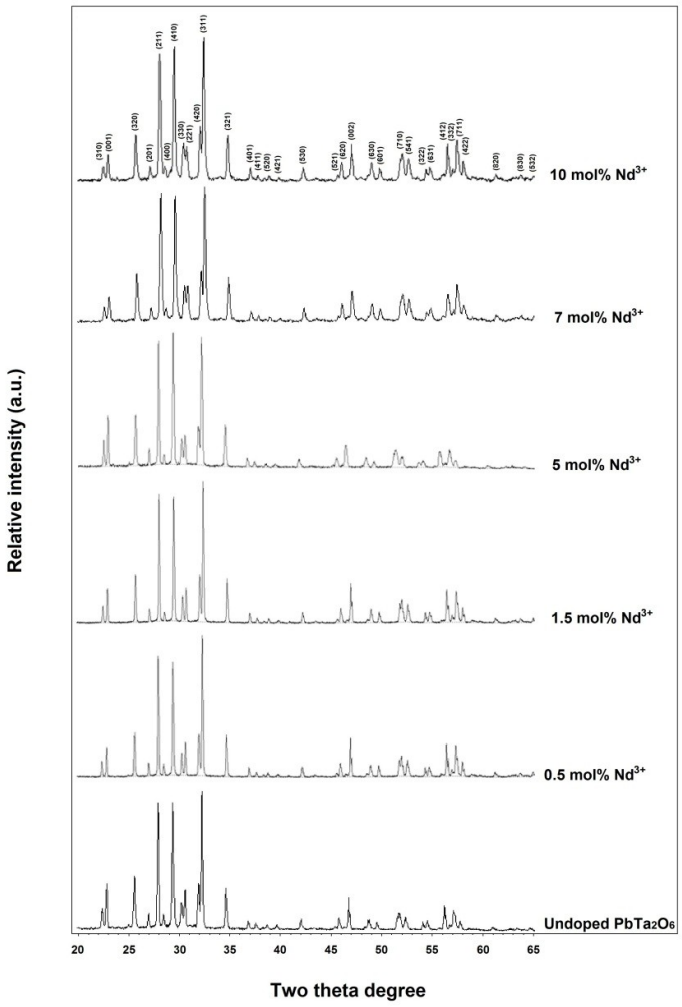

Figure 1: XRD results of undoped, and 0.5, 1.5, 5, 7, 10 mol% Nd^{3+} doped samples.

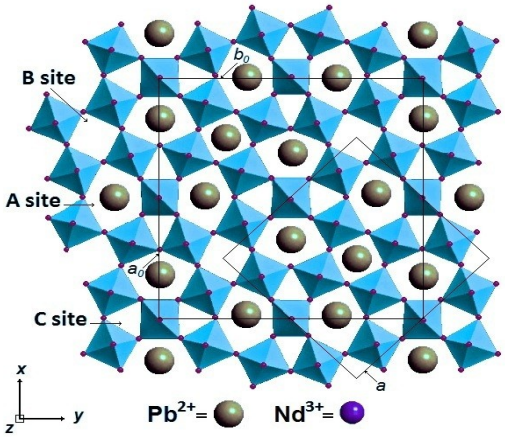

Figure 2: Schematic illustration of the orthorhombic-tetragonal relationship of $PbTa_2O_6$ crystal in the direction of the c axis.

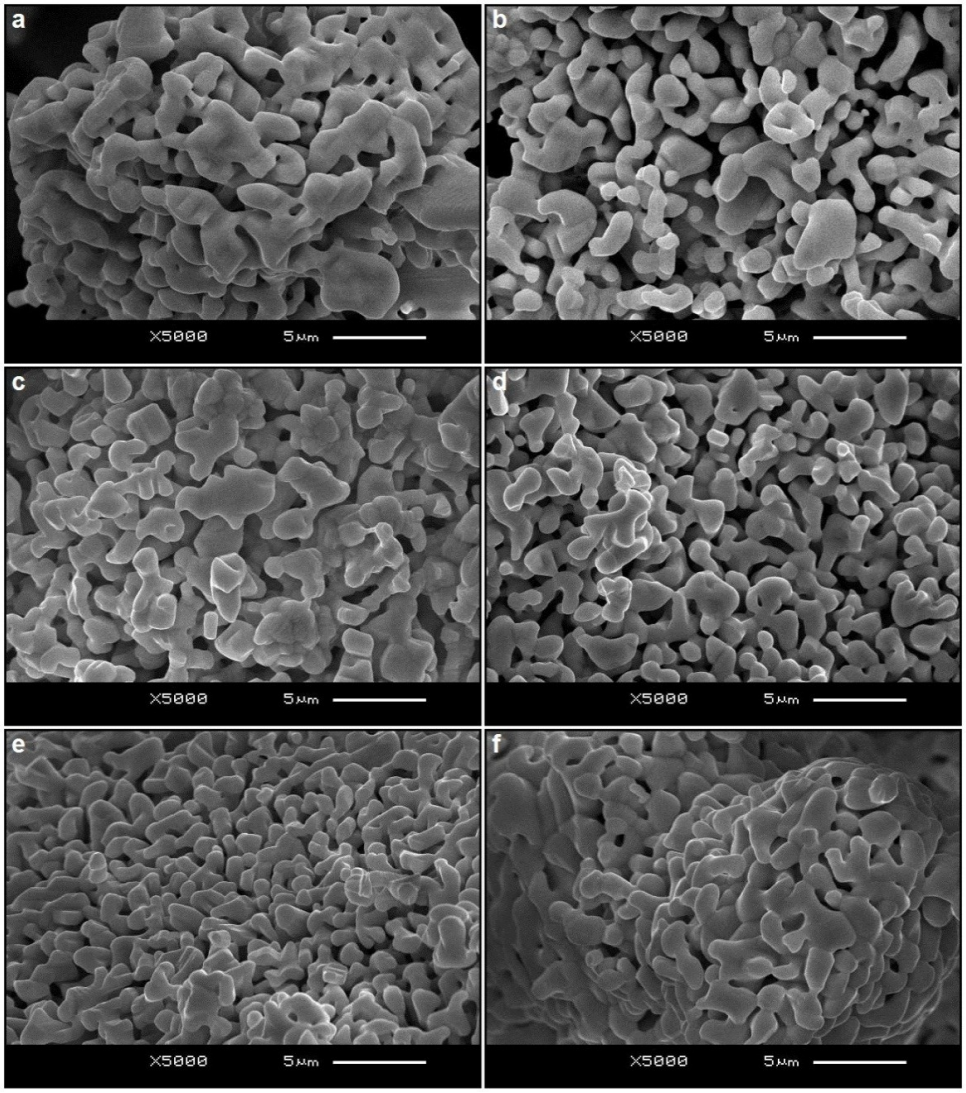

Figure 3: SEM micrographs of (a) undoped and (b) 0.5, (c) 1.5, (d) 5, (e) 7 (f) 10 mol% Nd^{3+} doped samples at 5000× magnifications.

Figure 3(a-f) shows the SEM micrographs at 5.000x magnification for undoped and 0.5, 1.5, 5, 7 and 10 mol% Nd^{3+} doped samples, respectively. The grain shapes of Nd^{3+} doped samples have oval, expanded and a shapeless morphology, while the grain sizes varied from 0.5 to 7 ◡m. Figure 4 shows the EDS spectrum and elemental compositions as "weight (%) and atomic (%)" for 7 mol% Nd^{3+} doped $PbTa_2O_6$ sample were detected by EDS at 20 kV of SEM acceleration voltage. According to the EDS results, the atomic theoretical (%) composition of Ta grains is 21.74, while the atomic (%) composition of lead is 8.17. The high Ta/Pb ratio indicates a decrease in the amount of Pb due to some evaporation, as reported in previous studies (40,41).

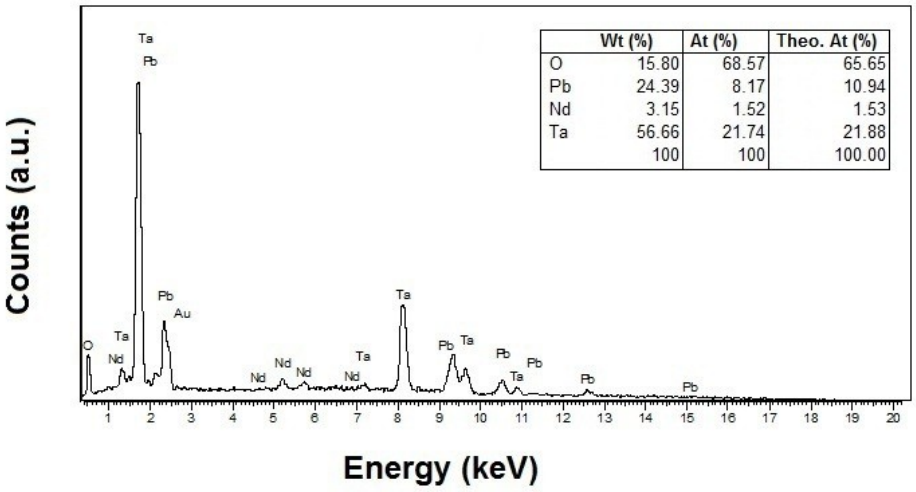

	Wt (%)	At (%)	Theo. At (%)
O	15.80	68.57	65.65
Pb	24.39	8.17	10.94
Nd	3.15	1.52	1.53
Ta	56.66	21.74	21.88
	100	100	100.00

Figure 4: EDS spectrum and wt%, at% elemental compositions, and theoretical at% values for 7 mol% Nd^{3+} doped sample

3.2. Near infrared photoluminescence of Nd^{3+} doped $PbTa_2O_6$ phosphors

Figure 5(a,b) shows the absorption spectra and the band gaps for undoped $PbTa_2O_6$ and 1.5, 5, 10 mol% Nd^{3+} doped phosphors. In Figure 5a, the absorption spectrum of undoped $PbTa_2O_6$ reached the peak value around 275-280 nm, and the band gap was estimated to be 3.7±0.2 eV. Tauc Plot method [46] was used to determine optical band gaps utilizing absorption spectra of undoped $PbTa_2O_6$ and Nd^{3+} doped phosphors. In the literature, the energy gap of $PbTa_2O_6$ is reported by some researchers as 3.7 eV (43) and 3.6-3.9 eV (47), which are consistent with the energy gap found in the study. The optical absorption of phosphors affected by Nd^{3+} concentration and shifted to visible region. In Figure 5b, the optical band gap of $PbTa_2O_6$ host exhibited a decrease with Nd^{3+} concentration. The band gaps of the phosphors were found as 3.3±0.2, 3.2±0.2, and 3.1±0.2 eV for 1.5, 5, and 10 mol% Nd^{3+} concentrations, respectively. The RE^{3+} ion doping can cause increased structural defects in the host lattice and localized states in the band gap, which decreases the energy band gap (48-50). The change in the optical band gap can be explained by the Burstein-Moss phenomenon (51). Accordingly, the dopant ions can cause the formation of subbands in the available band gap, so that the improvement in the conduction property, which becomes continuous depending on the density in the subbands, and eventual merger with the conduction band can occur.

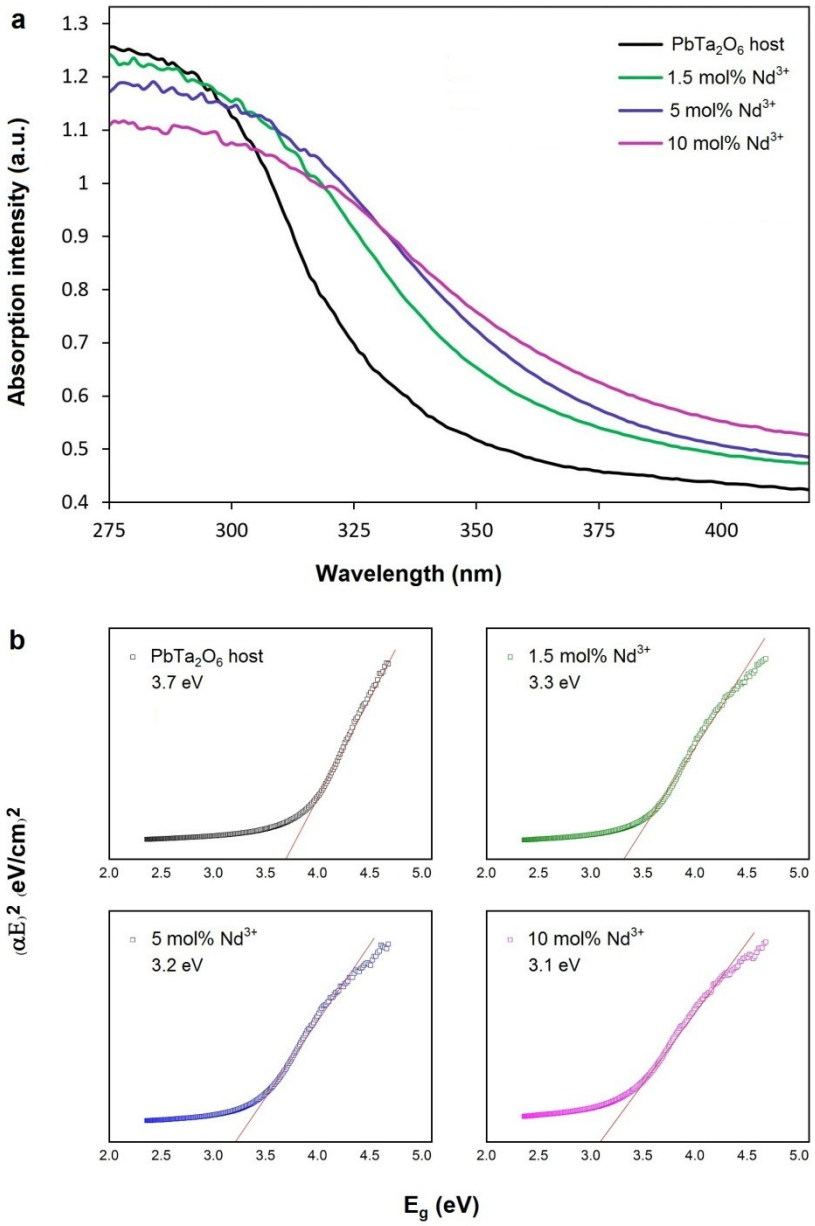

Figure 5: The absorption spectra (a) and the band gaps (b) for the $PbTa_2O_6$ host and $PbTa_2O_6$:xNd^{3+} (x=1.5, 5, 10 mol%) phosphors.

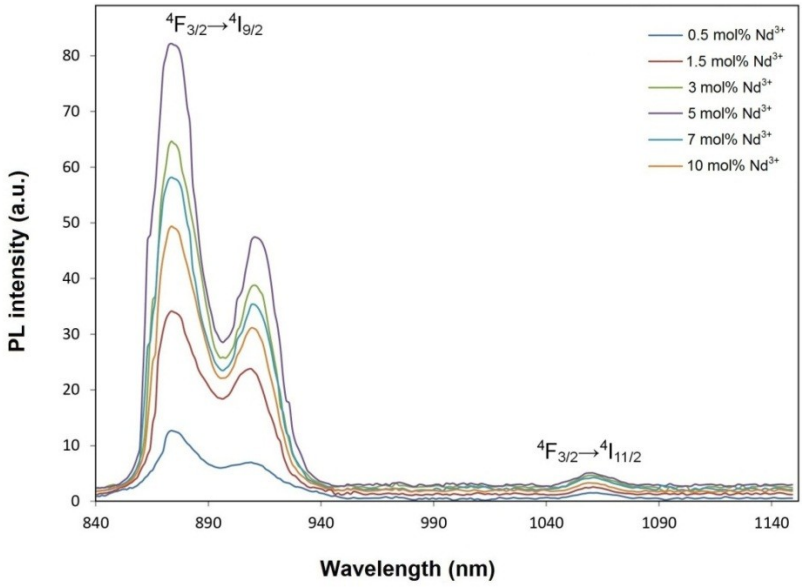

Figure 6: NIR photoluminescence of $PbTa_2O_6$:xNd^{3+} (x=0.5, 1.5, 3, 5, 7, 10 mol%) phosphors by diode laser under 800 nm excitation.

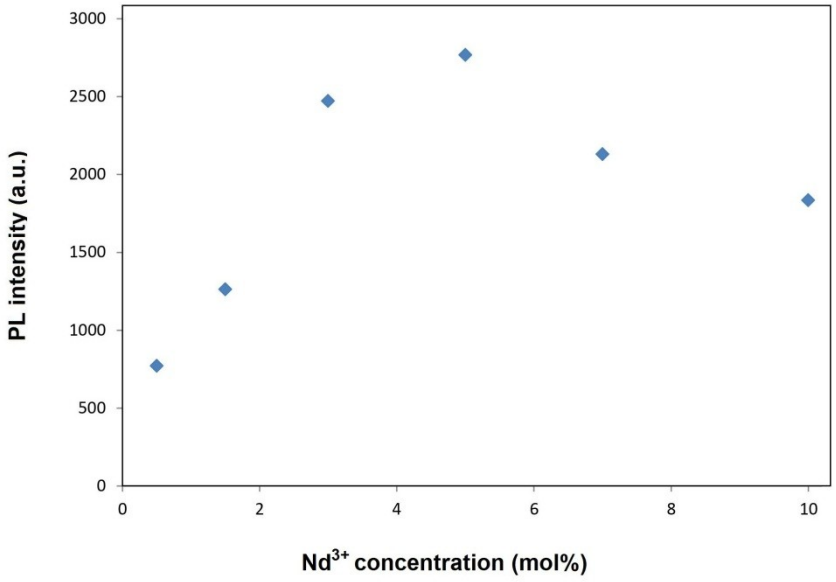

Figure 7: NIR photoluminescence variation of Nd^{3+} doped $PbTa_2O_6$ phosphors depending on doping concentration.

The NIR photoluminescence spectra of $PbTa_2O_6$:xNd^{3+} (x=0.5, 1.5, 3, 5, 7, 10 mol%) phosphors under the excitation of 800 nm using a laser diode are shown in Figure 6. The NIR emissions were recorded corresponding to the $^4F_{3/2}\rightarrow{}^4I_{9/2}$ and $^4F_{3/2}\rightarrow{}^4I_{11/2}$ transitions at 875 and 1060, respectively. The $^4F_{3/2}\rightarrow{}^4I_{9/2}$ transition (at 875 nm) is a potential laser transition that appears to be more intense than the $^4F_{3/2}\rightarrow{}^4I_{11/2}$. Figure 7 shows the change of NIR emissions of $PbTa_2O_6$:Nd^{3+} phosphors depending on doping concentration. As seen in Figure 7, the NIR emission of the phosphor increased up to 5 mol %, and then decreased at 7 and 10 mol% due to the concentration quenching effect. An increase in Nd^{3+} concentration will lead to a shortening of the distance between Nd^{3+}-Nd^{3+}, where the cross-relaxation mechanism is increasingly important (21,32). Thus, the decreasing distance between Nd^{3+} ions will make the cross-relaxation mechanism more effective over 5 mol% Nd^{3+} concentration, and the probability of non-radiative transitions will be higher. The critical distance (R_c) for concentration

quenching will be important, as the decreasing distance of Nd^{3+} ions will promote non-radiative energy transfer. The Blasse's equation (1) estimates the energy transfer between Nd^{3+}-Nd^{3+} ions (52):

$$R_c \approx 2\left(\frac{3V}{4\pi X_c N}\right)^{\frac{1}{3}} \quad \text{(Eq. 1)}$$

Where V is the unit cell volume, N is the number of available sites for dopant ion, X_c is the critical concentration of dopant ion. For $PbTa_2O_6$:Nd^{3+} phosphor, it is X_c =0.10 mol ion in the unit cell (for 0.05 mol), V=604.5 Å^3 (37), and N=5 (6). The critical distance (R_c) between Nd^{3+}–Nd^{3+} ions for energy transfer was calculated as 13.22 Å. Based on Blasse's theory (53), since the Nd^{3+}–Nd^{3+} distance is larger than 5 Å, the effective mechanism will be the multipolar interaction or the mechanism of exchange interaction will ineffective.

3.3. Radioluminescence of Nd^{3+} doped $PbTa_2O_6$ phosphors

Figure 8(a,b) shows the near-infrared and visible region RL emissions under X-ray excitation of $PbTa_2O_6$:xNd^{3+} (x=0.5, 1.5, 3, 5, 7, 10 mol%) phosphors. In Figure 8a, the strong NIR emissions peak about at 875 nm arise from the $^4F_{3/2}\rightarrow{}^4I_{9/2}$ transition, where the splits are observed in the range of 840–950 nm. Also, the weak emission peak is seen around 1065 nm corresponding to the $^4F_{3/2}\rightarrow{}^4I_{11/2}$ transition. The near-infrared emission of the X-ray-excited mechanism exhibited a decrease at 7 and 10 mol% concentrations, similar to PL. As well known for Nd^{3+}, each energy level can be subdivided into 2J+1 sublevels by the local crystal field around the Nd^{3+} ions, but the overall energy level structure of the Nd^{3+} ion does not change greatly in different hosts, because the 4f electrons are shielded by the outer shell $5s^2$ and $5p^6$ electrons (54). On the other hand, impurities such as a secondary phase can cause differences in splitting levels or Stark components where the local symmetry of the ligand ions differs (22-24). As seen from the RL emission spectra in Figure 8a, the $^4F_{3/2}\rightarrow{}^4I_{9/2}$ manifold of Nd^{3+} ions are splitted due to the symmetry of the $PbTa_2O_6$ cation sites, and the splitting levels are similar in the spectral profile. This phenomena may be attributed to the similarity of local symmetry of ligand ions surrounding the Nd^{3+} ion (28). The weak visible RL emissions of the phosphors between 400-600 nm are seen in Figure 8b. The RL emission bands originated from 4f-4f transitions of Nd^{3+} about at 430, 455, 490, 525, and 570 nm correspond to the transitions of the $^2F(2)_{5/2}\rightarrow{}^4F_{9/2}$, $^2F(2)_{5/2}\rightarrow{}^2H(2)_{11/2}$, $^2F(2)_{5/2}\rightarrow{}^4G_{5/2}$, $^2F(2)_{5/2}\rightarrow{}^4G_{7/2}$, and $^2F(2)_{5/2}\rightarrow{}^4G_{9/2}$, respectively.

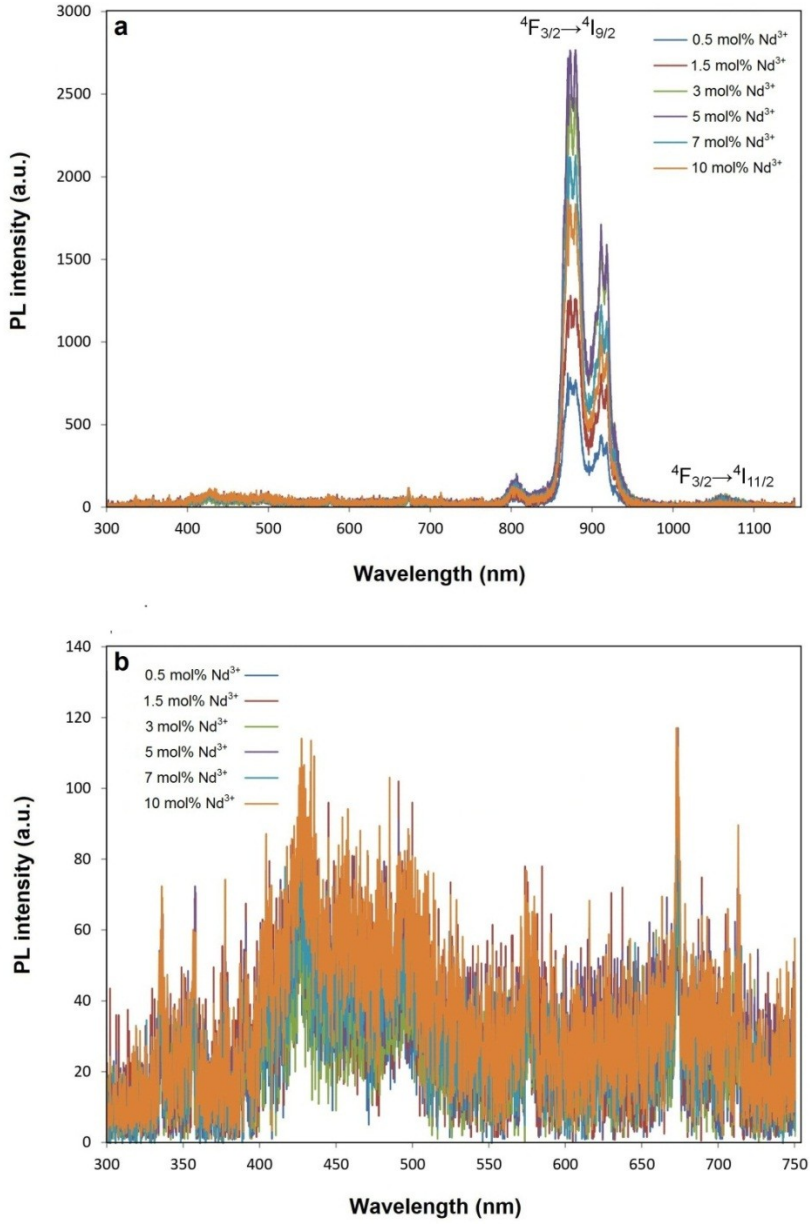

Figure 8: Radioluminescence spectra of the Nd^{3+} doped $PbTa_2O_6$ phosphors, (a) near-infrared emissions, (b) visible emissions.

In Figure 9, the CIE chromaticity diagram of $PbTa_2O_6$:Nd^{3+} under X-ray excitation, and CIE coordinates are given in Table 1. On the basis of the RL spectra, the CIE parameters of all the phosphors were obtained. Usually, the CIE diagram is created using PL emissions, but CIE coordinates can also be presented based on RL spectra as in our previous studies (48, 50). Although there are small coordinate shifts between PL and RL due to the excitation source difference, basically very close values can be obtained. Consequently, the blue region coordinates of Nd^{3+} doped phosphors excited by the strong excitation source or X-ray in the CIE diagram correlate with the visible region transitions corresponding to $^2F(2)_{5/2}\rightarrow{}^4F_{9/2}$, $^2F(2)_{5/2}\rightarrow{}^2H(2)_{11/2}$, $^2F(2)_{5/2}\rightarrow{}^4G_{5/2}$, $^2F(2)_{5/2}\rightarrow{}^4G_{7/2}$ and $^2F(2)_{5/2}\rightarrow{}^4G_{9/2}$.

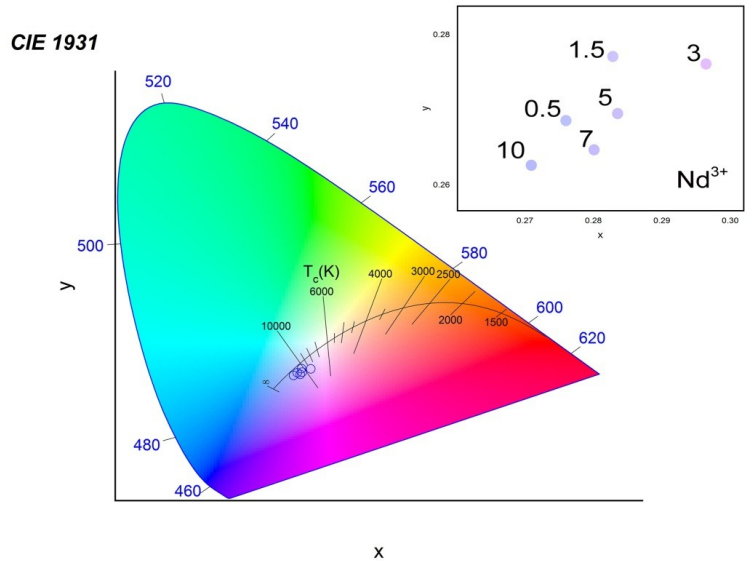

Figure 9: Radioluminescence spectra of the Nd^{3+} doped $PbTa_2O_6$ phosphors, (a) near-infrared emissions, (b) visible emissions.

Table 1: CIE color coordinates of $PbTa_2O_6$:Nd^{3+} phosphors under X-ray excitation source.

Nd^{3+} conc. (%)	CIE coordinates	
	x	***y***
0.5	0.2762	0.2684
1.5	0.2827	0.2769
3	0.2967	0.2763
5	0.2836	0.2696
7	0.2807	0.2649
10	0.2705	0.2627

4. CONCLUSION

The structural and spectral properties of Nd^{3+} doped $PbTa_2O_6$ phosphor fabricated by the conventional solid-state route were investigated in the study. In the XRD results, the single-phase structure Nd^{3+} doped $PbTa_2O_6$ with tetragonal tungsten bronze symmetry were determined between 0.5 and 10 mol % concentrations. SEM micrographs of the grains showed shapeless morphology and the grain sizes varied from 0.5 to 7 ⌣m. EDS results supported some evaporation of Pb during sintering and preservation of the single phase in the structure, similar to the reported studies. The absorption and band gap of $PbTa_2O_6$ host was in agreement with the literature, while the absorptions of Nd^{3+} doped phophors shifted the low band gap energy. The PL emissions in near-infrared region were monitored with the $^4F_{3/2}\rightarrow{}^4I_{9/2}$ and $^4F_{3/2}\rightarrow{}^4I_{11/2}$ transitions at 875 nm, and at 1060 nm of Nd^{3+}, respectively. The RL emissions of $PbTa_2O_6$:Nd^{3+} phosphors were observed by the $^4F_{3/2}\rightarrow{}^4I_{9/2}$, $^4F_{3/2}\rightarrow{}^4I_{11/2}$ transitions in the NIR region, and the weak transitions of the $^2F(2)_{5/2}\rightarrow{}^4F_{9/2}$, $^2F(2)_{5/2}\rightarrow{}^2H(2)_{11/2}$, $^2F(2)_{5/2}\rightarrow{}^4G_{5/2}$, $^2F(2)_{5/2}\rightarrow{}^4G_{7/2}$, $^2F(2)_{5/2}\rightarrow{}^4G_{9/2}$ in the visible region. The strong NIR emissions occurred for the $^4F_{3/2}\rightarrow{}^4I_{9/2}$ transition in both PL and RL, while the the PL and RL emissions decreased over 5 mol% Nd^{3+} due to the concentration quenching. CIE coordinates obtained based on RL emissions were found close to the blue region. The similarity of splitting levels are evident in the PL and RL spectral profiles may be associated with the similarity of the local symmetry of the ligand ions surrounding the Nd^{3+} ion. The Nd^{3+} doped $PbTa_2O_6$ ceramic phosphors with near-infrared luminescence of $^4F_{3/2}\rightarrow{}^4I_{9/2}$ transition may be helpful in future research and photonic applications.

5. CONFLICT OF INTEREST

There is no conflict of interest.

6. REFERENCES

1. Yerpude MM, Nair GB, Dhoble SJ. Green-light emission through energy transfer from Ce^{3+} to Tb^{3+} ions in the $Li2SO_4–Al_2(SO_4)_3$ system. Luminescence 2019;34:382-386. Available from: <DOI>.

2. Yao S, Lv S, Feng Z. Synthesis and photoluminescent properties of Dy^{3+}: $CaYAlO_4$ phosphors. Appl. Phys. A: Mater. Sci. Process. 2021;127:773. Available from: <DOI>.

3. Xue F, Hu Y, Ju G, Chen L, He M, Wang T, Jin Y, Zhang S, Lin J. Photoluminescence and long persistent luminescence properties of a novel green emitting phosphor $Sr_3TaAl_3Si_2O_{14}:Tb^{3+}$. Appl. Phys. A: Mater. Sci. Process. 2016;22:612. Available from: <DOI>.

4. Ekmekçi MK. Influence of europium doping on the crystallization, morphology, and cathodoluminescent properties of $PbNb_2O_6:Eu^{3+}$ phosphors. J. Turk. Chem. Soc. A: Chem. 2022;1129–1140. Available from: <DOI>.

5. Song R, Li H, Zhang H, Tang H, Tang X, Yang J, Zhao H, Zhu J. Tunable luminescence and improved thermostability via Tm–Dy energy transfer in a tellurooxyphosphate phosphor. Appl. Mater. Today 2023;30:101712. Available from: <DOI>.

6. İlhan M, Güleryüz LF. Cathodoluminescence and photoluminescence of $BaTa_2O_6:Sm^{3+}$ phosphor depending on the sintering temperature. Chem. Pap. 2022;76:6963-6974. Available from: <DOI>.

7. Shrivastava R, Khaparde S. Luminescence studies of diopside doped with various concentrations of Dysprosium (III). Res. Chem. Intermed. 2022;48:969-982. Available from: <DOI>.

8. Parganiha M, Dubey V, Shrivastava R, Kaur J. Green light emission in terbium Doped lanthanum zirconate powders. Anal. Chem. Lett. 2022;12:233–243. Available from: <DOI>.

9. Meejitpaisan P, Kaewjaeng S, Ruangthaweep Y, Sangwarantee N, Kaewkhao J. White light emission of gadolinium calcium phosphate oxide and oxyfluoride glasses doped with Dy^{3+}. Mater. Today: Proc. 2021;43:2574–2587. Available from: <DOI>.

10. Luewarasirikul N, Sarachai S, Kim HJ, Kaewkhao J. Enhanced photoluminescence and radioluminescence of Dy^{3+}-doped Ba-Na-B glasses. Radiat. Phys. Chem. 2023;202:110559. Available from: <DOI>.

11. Liu N, Si JY, Cai GM, Tao Y. Crystal structure, luminescence properties and energy transfer of Eu^{3+}/Dy^{3+} doped $GdNbTiO_6$ broad band excited phosphors. RSC Adv. 2016;6:50797. Available from: <DOI>.

12. Li HY, Shen LF, Pun EYB, Lin H. Dy^{3+}-doped germanate glasses for waveguide-typed irradiation light sources. J. Alloys Compd. 2015;646:586-591. Available from: <DOI>.

13. Kavitha V, Rani MP. The influence of Tm^{3+} on the structural, morphological, lifetime, haemocompatibility, and optical properties of sol–gel-synthesized CaS phosphors. Appl. Phys. A: Mater. Sci. Process. 2022;128:1053. Available from: <DOI>.

14. Ding Z, Ding G, Fang L, Peng Z. Luminescent property of $CaWO4:Eu^{3+}$ nanophosphors prepared by molten salt synthesis. Inorg. Nano-Met. Chem. 2022;52:647–652. Available from: <DOI>.

15. İlhan M, Ekmekçi MK, Keskin İÇ. Judd–Ofelt parameters and X-ray irradiation results of $MNb_2O_6:Eu^{3+}$ (M = Sr, Cd, Ni) phosphors synthesized via a molten salt method. RSC Adv. 2021;11:10451. Available from: <DOI>.

16. Gupta SK, Modak B, Tyagi M, Rawat NS, Modak P, Sudarshan K. Harvesting Light from $BaHfO_3/Eu^{3+}$ through ultraviolet, X-ray, and heat stimulation: an optically multifunctional perovskite. ACS Omega 2022:7;5311-5323. Available from: <DOI>.

17. İlhan M, Ekmekçi MK, Demir A, Demirer H. Synthesis and optical properties of novel red–emitting $PbNb_2O_6:Eu^{3+}$ phosphors. J. Fluoresc. 2016;26:1637–1643. Available from: <DOI>.

18. Bruncková H, Medvecký Ľ, Múdra E, Kovalčiková A, Ďurišin J, Šebek M, Girman V. Phase composition of samarium niobate and tantalate thin fims prepared by sol-gel method. Powder Metall. Prog. 2017;17:10–20. Available from: <DOI>.

19. Ekmekçi MK, İlhan M, Güleryüz LF, Mergen A. Study on molten salt synthesis, microstructural determination and white light emitting properties of $CoNb_2O_6:Dy^{3+}$ phosphor. Optik 2017;128:26-33. Available from: <DOI>.

20. He X, Fang B, Zhang S, Lu X, Ding J. Preparation of nanoscale $[(Ba_{0.85}Ca_{0.15})_{0.995}Nd_{0.005}](Ti_{0.9}Hf_{0.1})O_3$ ceramics via hydrothermal method and effect of grain size on multifunctional performance. J. Alloys Compd. 2022;925:166249. Available from: <DOI>.

21. Wang X, Zhao H, Li A, Tian K, Brambilla G, Wang P. Near-infrared luminescence and single-mode laser emission from Nd^{3+} doped compound glass and glass microsphere. Front. Mater. Sci. 2019;6:237. Available from: <DOI>.

22. İlhan M, Keskin İÇ, Çatalgöl Z, Samur R. NIR photoluminescence and radioluminescence characteristics of Nd^{3+} doped $BaTa_2O_6$ phosphor. Int. J. Appl. Ceram. Technol. 2018;15:1594–1601. Available from: <DOI>.

23. Ekmekçi MK, İlhan M, Ege A, Ayvacıklı M. Microstructural and radioluminescence characteristics of Nd^{3+} doped columbite-type $SrNb_2O_6$ phosphor. J. Fluoresc. 2017;27:973–979. Available from: <DOI>.

24. İlhan M, Ekmekçi MK, Oraltay RG, Başak AS. Structural and near-infrared properties of Nd^{3+} activated Lu_3NbO_7 Phosphor. J. Fluoresc. 2017;27:199–203. Available from: <DOI>.

25. Prasad RNA, Vijaya N, Babu P, Mohan NK, Praveena R. Optical absorption and NIR photoluminescence of Nd^{3+}-activated strontium phosphate glasses. J. Electron. Mater. 2020;49:6358-6368. Available from: <DOI>.

26. He X, Fang B, Zhang S, Lu X, Ding J. Preparation and properties of Nd-doped BCTH lead-free ceramics by solid-phase twin crystal method. Curr. Appl. Phys. 2022;38:30-39. Available from: <DOI>.

27. Golyeva EV, Vaishlia EI, Kurochkin MA, Kolesnikov EY, Lähderanta E, Semencha AV, Kolesnikov IE. Nd^{3+} concentration effect on luminescent properties of $MgAl2O_4$ nanopowders synthesized by modified Pechini method. J. Solid State Chem. 2020:289;121486. Available from: <DOI>.

28. Ekmekçi MK, Erdem M, Başak AS, İlhan M, Mergen A. Molten salt synthesis and optical properties of Eu^{3+}, Dy^{3+} or Nd^{3+} doped $NiNb_2O_6$ columbite-type phosphors. Ceram. Int. 2015;41:9680–9685. Available from: <DOI>.

29. Mahamuda Sk, Swapna K, Rao AS, Jayasimhadri M, Sasikala T, Pavani K, Moorthy LR. Spectroscopic properties and luminescence behavior of Nd^{3+} doped zinc alumino bismuth borate glasses. J. Phys. Chem. 2013;74;1308–1315. Available from: <DOI>.

30. İlhan M, Katı Mİ, Keskin İÇ, Güleryüz LF. Evaluation of structural and spectroscopic results of tetragonal tungsten bronze $MTa_2O_6:Eu^{3+}$ (M = Sr, Ba, Pb) phosphors and comparison on the basis of Judd-Ofelt parameters. J. Alloy. Comp. 2022;901:163626. Available from: <DOI>.

31. İlhan M, Güleryüz LF, Keskin İÇ, Katı Mİ. A comparison of spectroscopic properties of Dy^{3+}-doped tetragonal tungsten bronze MTa_2O_6 (M = Sr, Ba, Pb) phosphors based on Judd–Ofelt parameters. Mater. Sci: Mater. Electron 2022;33:16606–16620. Available from: <DOI>.

32. İlhan M, Keskin İÇ, Gültekin S. Assessing of photoluminescence and thermoluminescence properties of Dy^{3+} doped white light emitter TTB-lead metatantalate phosphor. J. Electron. Mater. 2020;49:2436-2449. Available from: <DOI>.

33. Nakauchi D, Okada G, Koshimizu M, Yanagida T. Optical and scintillation properties of Nd-doped $SrAl_2O_4$ crystals. J. Rare Earths 2016;34:757–762. Available from: <DOI>.

34. Kamada K, Kurosawa S, Yamaji A, Shoji Y, Pejchal J, Ohashi Y, Yokota Y, Yoshikawa A. Growth of Nd doped $(Lu, Gd)_3(Ga, Al)_5O_{12}$ single crystal by the micro pulling down method and their scintillation properties. Opt. Mater. 2015;41:32-35. Available from: <DOI>.

35. Sugiyama M, Fujimoto Y, Yanagida T, Yamaji A, Yokota Y, Yoshikawa A. Growth and scintillation properties of Nd-doped $Lu_3Al_5O_{12}$ single crystals by Czochralski and micro-pulling-down methods. J. Cryst. Growth 2013;362:178–181. Available from: <DOI>.

36. Yanagida T, Fujimoto Y, Ishizu S, Fukuda K. Spectrochim. Optical and scintillation properties of Nd differently doped $YLiF_4$ from VUV to NIR wavelengths. Opt. Mater. 2015;41:36–40. Available from: <DOI>.

37. Francombe MH, Lewis B. Structural, dielectric and optical properties of ferroelectric lead metaniobate. Acta Cryst. 1958;11:696. Available from: <DOI>.

38. Subbarao EC, Shirane G, Jona F. X-ray, dielectric, and optical study of ferroelectric lead metatantalate and related compounds. Acta Cryst. 1960;13:226. Available from: <DOI>.

39. Simon A, Jean R. Solid-state chemistry and non-linear properties of tetragonal tungsten bronzes materials. C. R. Chim. 2006;9:1268–1276. Available from: <DOI>.

40. İlhan M. Synthesis, structural characterization, and photoluminescence properties of TTB-type $PbTa_2O_6:Eu^{3+}$ phosphor. Int. J. Appl. Ceram. Technol. 2017;14:1144–1150. Available from: <DOI>.

41. İlhan M, Keskin İÇ. Evaluation of structural behaviour, radioluminescence, Judd-Ofelt analysis and thermoluminescence kinetic parameters of Eu^{3+} doped TTB–type lead metaniobate phosphor. Phys. B: Condens. Matter 2020;585:412106. Available from: <DOI>.

42. Wang BX, Krogstad MJ, Zheng H, Osborn R, Rosenkranz S, Phelan D. Active and passive defects in tetragonal tungsten bronze relaxor ferroelectrics. J. Phys. Condens. Matter 2022;34:405401. Available from: <DOI>.

43. Kato H, Kudo A. New tantalate photocatalysts for water decomposition into H_2 and O_2. Chem. Phys. Lett. 1998;487:492. Available from: <DOI>.

44. Zhang W, Kumada N, Takei T, Yamanaka J, Kinomura N. Preparation and crystal structure of H-$BaTa_2O_6$-type $K_{1.83}Ba_{4.17}Nb_{12.18}O_{36}$ and dielectric properties of the related compounds. Mater. Res. Bull. 2005;40:1177−1186. Available from: <DOI>.

45. Li G, Cheng L, Liao F, Tian S, Jing X, Lin J. Luminescent and structural properties of the series $Ba_{6-x}Eu_xTi_{2+x}Ta_{8-x}O_{30}$ and $Ba_{4-y}K_yEu_2Ti_{4-y}Ta_{6+y}O_{30}$. J. Solid State Chem. 2004;177:875–882. Available from: <DOI>.

46. Tauc J. Optical properties and electronic structure of amorphous Ge and Si. Mater. Res. Bull. 1968;3(1):37-46. Available from: <DOI>.

47. Boltersdorf J, Wong T, Maggard PA. Synthesis and optical properties of Ag(I), Pb(II), and Bi(III) tantalate-based photocatalysts. ACS Catal. 2013;3:2943–2953. Available from: <DOI>.

48. Keskin İÇ, Türemiş M, Katı Mİ, Gültekin S, Arslanlar YT, Çetin A, Kibar R. Detailed luminescence (RL, PL, CL, TL) behaviors of Tb^{3+} and Dy^{3+} doped $LiMgPO_4$ synthesized by sol-gel method. J. Lumin. 2020;225:117276. <DOI>.

49. Ahmed AS, Muhamed SM, Singla ML, Tabassum S, Naqvi AH, Azam A. Band gap narrowing and fluorescence properties of nickel doped SnO_2 nanoparticles. J. Lumin. 2011;131:1–6. Available from: <DOI>.

50. Keskin İÇ. Radioluminescence results, thermoluminescence analysis and kinetic parameters of $Y_2O_3:Ln^{3+}$ (Ln: Dy, Nd, Sm) nanophosphors obtained by sol-gel method. Ceram. Int. 2022;48(14):20579–20590. Available from: <DOI>.

51. Burstein E. Anomalous Optical Absorption Limit in InSb. Phys. Rev. 1954;93:632. <DOI>.

52. Blasse G. Energy transfer between inequivalent Eu^{2+} ions. J. Solid State Chem. 1986;62:207–211. Available from: <DOI>.

53. Blasse G. Energy transfer in oxidic phosphors. Philips Res. Rep. 1969;24:131. Available from: <DOI>.

54. Ayvacıkli M, Kotan Z, Ekdal E, Karabulut Y, Canimoglu A, Guinea JG, Khatab A, Henini M, Can N. Solid state synthesis of $SrAl_2O_4:Mn^{2+}$ co-doped with Nd^{3+} phosphor and its optical properties. J. Lumin. 2013;144:128–132. Available from: <DOI>.

JOTCS A
Journal of the Turkish Chemical Society
Section: A
Chemistry
TURKISH CHEMICAL SOCIETY

Correlation between chemical characteristics and optical spectra of *Spirulina* commercially available on the Bulgarian market

Krastena NIKOLOVA[1*], Tinko EFTIMOV[2,3], Aleksandar PASHEV[4], Metody KARADJOV[5], Christina TZVETKOVA[6], Galia GENTSCHEVA[4,6], Daniel BRABANT[7], Samia FOUZAR[8]

[1]Medical University-Varna, Department of Physics and Biophysics, Varna, 9002, Bulgaria
[2]University of Quebec in Outaouais, Photonics Research Center, Quebec, J8X 3X7, Canada
[3]Bulgarian Academy of Sciences, Central Laboratory of Applied Physics, Plovdiv, 4000, Bulgaria
[4]Medical University—Pleven, Department of Chemistry and Biochemistry, Pleven, 5800, Bulgaria
[5]Bulgarian Academy of Sciences, Geological Institute, Sofia, 1040, Bulgaria
[6]Bulgarian Academy of Sciences, Institute of General and Inorganic Chemistry, Sofia, 1040, Bulgaria
[7]Cégep de l'Outaouais, Campus Louis-Reboul, Gatineau, Québec, QC J8X 1C5, Canada
[8]M'Hamed Bougara University of Boumerdès, Faculty of Technology, UMBB, 35000, Algeria

Abstract: The aggregate of various chemical substances useful for the functioning of the human body are known as nutrients. *Spirulina* has been present in human nutrition since ancient times, but in recent years the interest in it has been particularly increased due to the emergence of numerous alternative methods of nutrition. This study aimed to compare the functional and elemental composition as well as the optical properties of commercial *Spirulina* products available on the Bulgarian market. For this purpose, fluorescence spectroscopy in the ultraviolet and visible range, fourier transform infrared spectroscopy and inductively coupled plasma optical emission spectroscopy were used. The basic components of the analyzed *Spirulina* samples are proteins (1657 and 1537 cm^{-1}) and carbohydrates (1069 and 1054 cm^{-1}) and no meaningful differences between the IR spectra of the samples. Concentrations of important microelements Mg, Fe, Cu, Zn, and Mn varies with the manufacturer. The highest levels for Mg (6.69 g kg^{-1}) were measured in samples from USA, while the *Spirulina* fabricated in Bulgaria exhibits the highest contents of Zn (242 mg kg^{-1}) and Cu (25.4 mg kg^{-1}). All samples followed the tendency Mg>Fe>Mn>Zn>Cu. Making use of a fiber optic spectrometer the fluorescence spectra of the studied samples of *Spirulina* platensis for an excitation wavelength of 380 nm were measured. In these spectra we observe three fluorescence maxima: at 465 nm – nicotinamide dinucleotide phosphate, 640 nm chlorophyll a, and 736 nm due to similar to chlorophyll pigments. A strong positive correlation between the contents of Zn and Cu on the one side and the second fluorescence peak (λ=640 nm) for excitation wavelength at 380 nm. In contrast, a high negative correlation for Fe and the third fluorescence maximum (λ= 736nm) is observed for all excitation wavelengths. The correlation dependencies were obtained with the least squares method with a significance level of $p \leq 0.05$.

Keywords: *Spirulina*, fluorescence spectra, infrared spectra, elements.

Submitted: November 21, 2022. **Accepted:** March 12, 2023.

Cite this: Nikolova K, Eftimov T, Pashev A, Karadjov M, Tzvetkova C, Gentscheva G, et al. Correlation between chemical characteristics and optical spectra of Spirulina commercially available on the Bulgarian market. JOTCSA. 2023;10(2):465–74.

DOI: https://doi.org/10.18596/jotcsa.1207682.

***Corresponding author. E-mail:** kr.nikolova@abv.bg

1. INTRODUCTION

In 1827 P.J.Turpin isolated *Spirulina* from a freshwater sample, and in 1852 Stizenberger wrote the first taxonomic report. These photosynthetic organisms were first considered algae, but in 1962 Stanier and Van Neil included blue-green algae in the prokaryotic kingdom and proposed that these microorganisms be called cyanobacteria (1).

Based on the cylindrical arrangement of the multicellular trichomes, there are two types of filamentous cyanobacteria: *Arthrospira* (*Spirulina*) *maxima* and (*Spirulina*) *platensis* (2). Their main photosynthetic pigment is phycocyanin, which is blue in color (3), they also contain chlorophyll a, carotenoids and various pigments that can give them a red or pink color (4). *Arthrospira* (*Spirulina*) platensis is a natural inhabitant of tropical lakes with alkaline waters (pH>11), these conditions restrict the growth of other microorganisms but allow its cultivation (5). The distribution of *Arthrospira platensis* in nature is not limited only from lakes in Africa to Lake Texcoco in Mexico, it can be found in soil, marine and fresh water, swamps and thermal springs (6). *Arthrospira platensis* is the most widely cultivated alga because it is rich in protein (between 50 % and 70%) with a high biological value due to the content of all essential fatty acids (7, 8). Long-chain fatty acids are dominant, especially palmitic and gamma linoleic acids (9). The latter is of particular importance in the treatment of chronic diseases. *Spirulina* contains polyunsaturated fatty acids such as eicosapentaenoic acid (EPA) and docosahexaenoic acid (10). The consumption of microalgae by vegetarians is extremely valuable due to the high content of vitamins of group B as well as of type A, E, D, K (11). It is a source of the minerals calcium, iron, selenium, and fluorine (11, 12) as well as large amounts of carotenoids such as astaxanthin and zeaxanthin, beta carotene, polyphenols, and chlorophyll (4).

The huge number of bioactive compounds in *Arthrospira platensis* makes it suitable for its inclusion in foods and nutritional supplements (13). There are data that microalgae lower LDL cholesterol and blood pressure (14). It can be prescribed to patients with diabetes because it reduces blood sugar levels (15), relieves mental and physical fatigue of the body (16), increases immunity, and can be used as a probiotic (17). There are already many commercially available brands of health foods made from cultured algae and *spirulina*. Phycocyanins, which are now extracted from *Spirulina*, are used as industrial and food colorings (17).

As fluorescence measurements are far simpler and less costly than chemical analysis of substances it is of practical importance to establish the correlations between fluorescence spectra and the chemical contents of commercially available *Spirulina* samples from different parts in the world. The objective of this study is to investigate and compare the functional and elemental composition and optical characteristics of commercial *Spirulina* products available on the Bulgarian market.

2. MATERIALS AND METHODS

2.1. Samples Under Study

Three commercially available *Spirulina* samples were purchased, cultivated in bioreactors in USA, China (CHN) and Belgium (BEL) as well as *Spirulina/Arthrospira platensis* cultivated in a bioreactor close to Varvara, Bulgaria (BGR).

Three packages from each tested product were purchased. Measurements have been performed on each of them. Average results from three replicates of the experiment were presented.
The data for dietary and energy value expressed in g/100g for *Spirulina* products purchased from the Bulgarian dietary store and taken from the producer's label are given in Table 1.

Table 1: A main dietary and energy value of *Spirulina*[*].

	CHN	BEL	USA
Energy value, kcal	336	358	333
Fats , g/100g	1	6	5
Proteins, g/100g	65	65	56
Carbohydrates, g/100g	13.1	9.5	15

[*]The indicated table does not present data on *Spirulina* from a bioreactor in Bulgaria, since the latter is not available in organic stores and it is in the process of certification and research of the indicated parameters.

2.2. Methods

2.2.1. Fluorescence measurements

The fluorescence characteristics of organic matter from seaweeds were measured using an Ocean Optics QE65000 fiber optic spectrometer, an Ocean optics MonoScan 2000 fiber optic monochromator and broadband Energetiq Laser driven light source (190 nm to 2500 nm). The samples were excited at wavelengths from 220 nm to 720 nm at a 10 nm increment and a spectral bandwidth of around 15 nm. The sample is illuminated by a 1 mm core fiber and fluorescence is captured by a receiving 1mm core fiber oriented at 45° with respect to the excitation fiber to minimize reflected and diffused light. Integration time was 5 s. The experimental set-up is shown in Figure 1.

2.2.2. Excitation emission matrices (EEM)

At each excitation wavelength in the 220 nm to 720 nm the emission spectrum from 200 nm to 1000 nm of each *Spirulina/Arthrospira* sample was captured which permits 3D excitation emission plots to be presented. These color coded 3D spectra for each sample are presented in side and in topographic view in Figure 2. In these figures the emission spectrum is presented in the range of 400 - 800 nm.

2.2.3. Determination of the elements' content

A sample of about 0.3 g is weighed on an analytical balance in Teflon vessels for a microwave digestion system and 10 mL of 67% HNO3 (Suprapur®) was added. Microwave digestion was carried out according to the following procedure: 10 minutes to reach 180 ºC and maintain this temperature for 10 minutes. After cooling solution was transferred into a 25 mL volumetric flask and dilute to the mark with deionized water. The blank sample was run through the entire analytical procedure. The samples were finally filtered through 0.45 µm cellulose membrane filters (Millipore) and kept at 4 ºC.

The content of Mg, Fe, Mn, Cu, and Zn was measured by ICP-OES system ULTIMA 2, Jobin Yvon, (Longjumeau, France). Multi-element standard solution IV for ICP (TraceCERT®, Merck) was used to prepare diluted working standard solutions for instrument calibration.

2.2.4. FT-IR spectra

The FT-IR spectra were recorded on a Thermo Fisher Nicolet iS50 spectrometer equipped with a diamond ATR Accessory and are presented after standard ATR correction performed on the OMNIC software. The IR spectra were recorded from 4000 cm^{-1} to 400 cm^{-1} with an average of 64 scans at a resolution of 4 cm^{-1}. The measurements were carried out directly on the *Spirulina* powder samples.

2.2.5. Statistical analysis

Analysis of variance was used to compare means with a significance level of $p \leq 0.05$ by using SPSS Statistic 22. One-way analysis of variance and Duncan's post hoc test for multiple comparisons based on the parameters studied were performed for all samples studied. The correlation dependences were obtained with the least squares method with a significance level of $p \leq 0.05$.

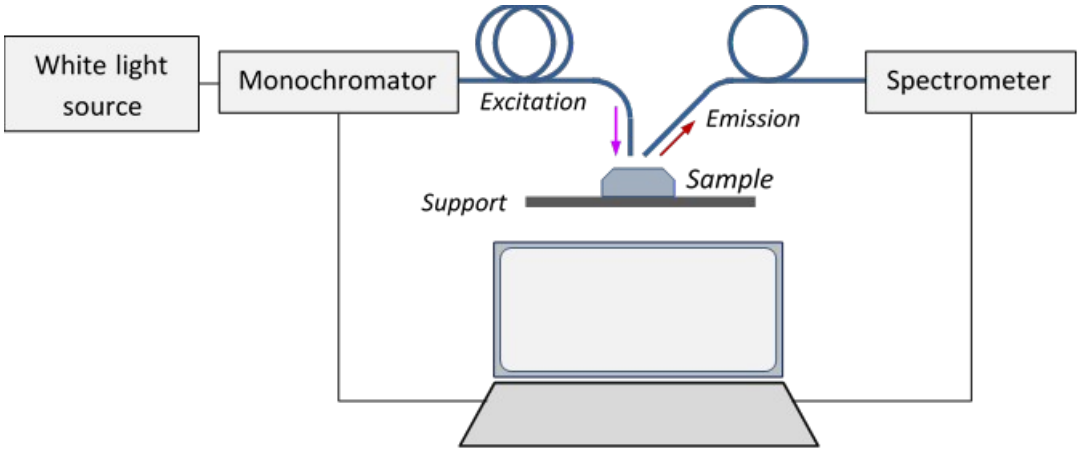

Figure 1: Experimental set-up for measurement of 3D emission excitation matrices.

3. RESULTS AND DISCUSSION

The concentration of Mg, Fe, Mn, Zn, and Cu was determined as elements performing specific functions in the human body. Since the human body cannot produce them on its own, it is necessary to take them through food.

The concentrations of the elements in the samples vary depending on the producers. The obtained values for all five analyzed elements are in the concentration range of other *Spirulina* products described in the literature (3, 18-21). The following trend is observed: Mg > Fe > Mn > Zn > Cu. As expected, the content of Mg in the four products is

the highest compared to the other elements, as it is a macronutrient. It is noteworthy that the concentration of Fe significantly exceeds the concentrations of the other micronutrients. Table 2 lists the quantity of the elements as measured in the samples. The sample from the Bulgarian reactor is the richest in Zn and Cu while in the other samples these elements are found in significantly lower concentrations. The highest concentration of Mg was observed in the USA sample.

The optical properties of *Spirulina* were investigated by fluorescence spectroscopy in the range of 220-720 nm at 10 nm increments. The excitation-emission matrices (EEM) of the studied samples in side and topographic view are presented in Figure 2. It follows from the analysis of the *Spirulina* samples that their optical properties strongly depend on the excitation wavelength. A change was observed if the individual fluorescence spectra around 410, 530, and 660 nm excitation wavelengths. At lower excitation wavelengths, the typical emission peaks around 650 nm and 672 nm associated in the literature with Phycobilisomes were not observed. However, a peak around 700 nm associated with the same substances was seen. This means that their molecules were not directly excited but had instead obtained energy from the excited molecules of carotenoids via resonance transfer or re-absorption.

For excitation in the red part of the visible spectrum from 640 nm to 660 nm range an emission peak in the 710 nm and 715 nm due to Chlorophyll a was observed. Similar excitation wavelengths for substances as Chlorophyll a, Chlorophyll b, Phycocyanin, Phycoerythrin have been reported by Cadondon et al. (22), Li et al. (23), Gobets et al. (24), Karapetyan et al. (25), Akimoto et al. (26), Uebel et al. (27).

Some relations were established between the observed spectra and the content of the metals. A closer inspection of the 3D EEM plots reveals that the fluorescence maxima were observed at an emission wavelength around 735 nm – 736 nm for excitation from 250 nm to 720nm.

However, the maxima and their relative height were different. Fig. 3a shows how the fluorescence intensity at 736 nm changes for each sample as excitation wavelength varied from 220 nm to 720 nm.

There were some peaks for excitation wavelengths of 380, 430, and 560 nm. The emission spectra of the samples for each of these three excitation wavelengths were shown in Fig. 3b) to 3d). The emission spectra exhibited maxima at three wavelengths: 465, 640, and 736 nm were labeled as I, II, and III. Due to the Stokes' shift, fluorescence emission is observed at wavelengths higher than the excitation wavelength. Therefore, for 560 nm fluorescence is observed above 588 nm (Fig. 3d).

Table 2: Content of Mg, Mn, Fe, Zn and Cu in the four *Spirulina* samples (n=3, RSD=3-7%) and reference values described in the literature*.

Elements	BGR	CHN	BEL	USA	Refs. (3, 18-21)
Mg, g/kg	2.57^{d}	2.76^{c}	3.80^{b}	6.69^{a}	0.67 - 9.49
Mn, mg/kg	55.0^{b}	55.4^{b}	49.7^{c}	141^{a}	5 - 554
Fe, mg/kg	317^{d}	868^{b}	447^{c}	1177^{a}	195 - 6500
Zn, mg/kg	242^{a}	18.0^{d}	25.8^{c}	35.4^{b}	3.8 - 375
Cu, mg/kg	25.4^{a}	3.97^{d}	5.23^{c}	11.9^{b}	2.63 - 69.6

*Means in a row with a common superscript letter (a–d) differ ($p < 0.05$) as analyzed by one-way ANOVA.

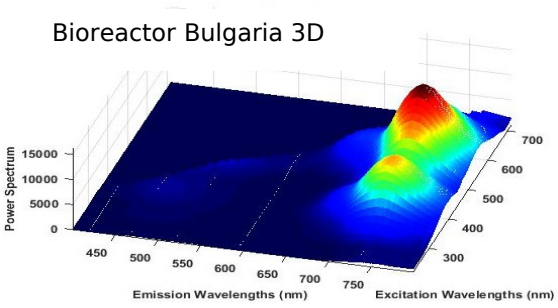

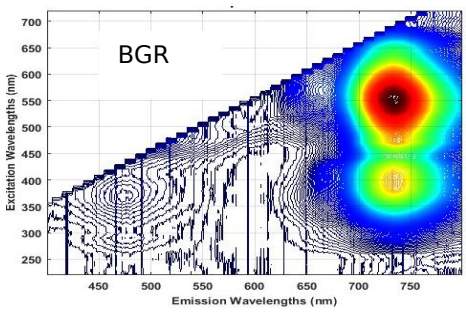

BEL

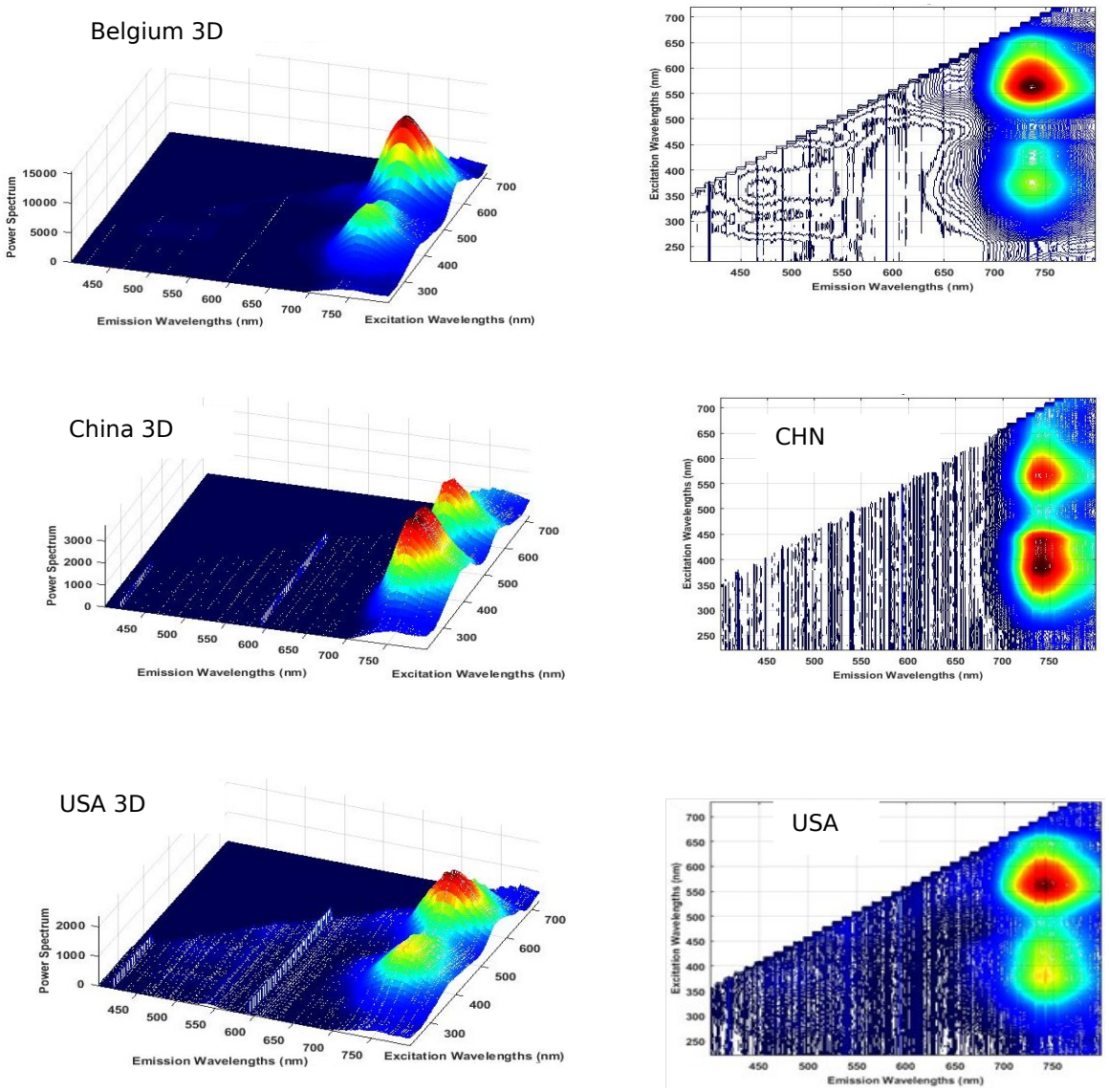

Figure 2: Excitation emission 3D and topographic presentations.

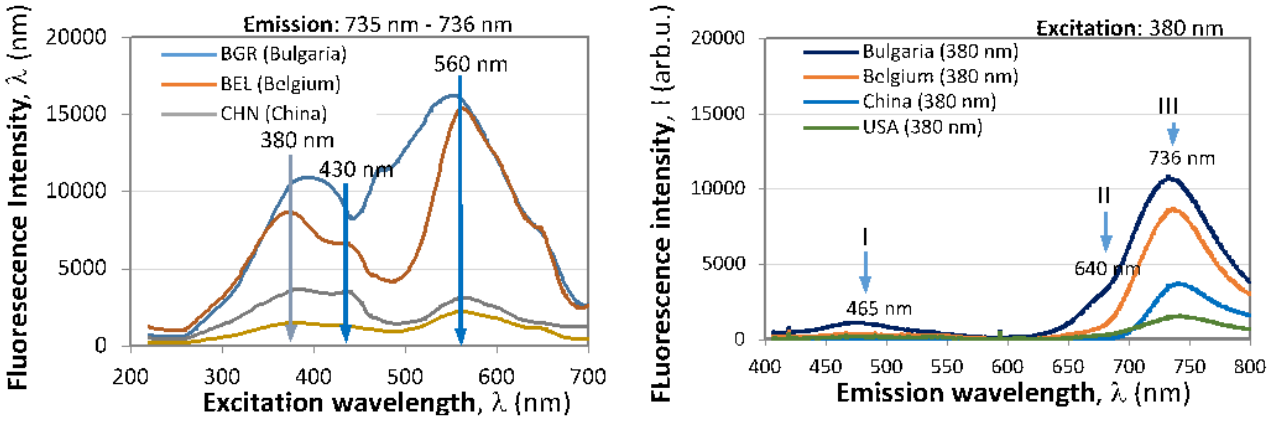

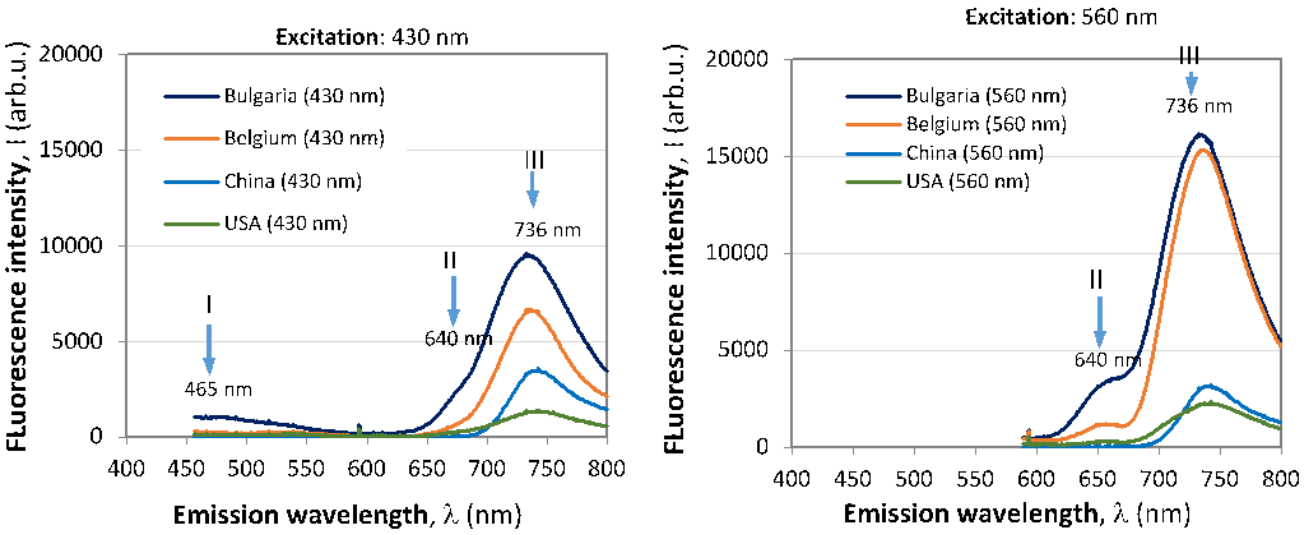

Figure 3: Sections of the 3D EEM plots: a) Dependence on the excitation wavelength for emission at 736 nm; Emission spectra for excitation at b) 380 nm; c) 430 nm; d) 560 nm.

The dependencies of the average intensity around each of these maxima on the contents were plotted for each element for each of the maxima. As examples, the plot for Zn when excited at 430 nm for maxima I (465 nm) and II (640) were shown in fig 4a) and in Fig. 4b) – for Fe at 560 nm for maxima II and III. Two basic observations for all samples must be noted for the two plots in Fig. 4. First, for Zn from Fig. 4a), the intensities of both peaks increased with the content, while for Fe, the intensities decreased with the Fe content. Second, the intensity of the first maximum is higher than the second. These observations are reversed for Fe from Fig.4b). This implies positive and negative correlation between fluorescence intensity and content for the *Spirulina* samples of different origin. There were some peaks for excitation wavelengths of 380, 430, and 560 nm. The emission spectra of the samples for each of these three excitation wavelengths were shown in Fig. 3b) to 3d). The emission spectra exhibited maxima at three wavelengths: 465, 640, and 736 nm were labeled as I, II, and III.

The correlation between the content of each metal and the intensity of each maximum I, II, and III for each excitation wavelength were obtained, and the coefficient r was calculated. The results were summarized in Table 3.

Zn and Cu exhibit a very high positive correlation between their content and the intensity of the maxima I and II for 380 nm excitation and for maximum II at 560 nm. In contrast Fe exhibits very high negative correlation for maximum III and a high correlation for maxima I and II for all excitation wavelengths. Mn exhibits at best a moderate negative correlation for maximum III and low or weak for the other maxima at any excitation.

Figure 5 presents the FT-IR spectra of the *Spirulina* samples. The peak around 3290 cm−1 could be attributed to –OH and –NH groups (28-29). The C-H stretching vibrations could be found around 2920 cm-1 (28). These signals could be assigned to lipid and protein methylene vibrations (30). The adsorption peaks in the region 1700–1400 cm−1 could be assigned to –CO stretches aldehydes, ketones, and carboxylate groups. (31-32, 28). These vibrations could be attributed to functional groups present in proteins in the *Spirulina* sample (31). More specifically, these signals represent the vibrations of amides I and II, from the protein in Spirulina powder (30). The signals in the region 1100-1000 cm-1 belong to functional groups in the carbohydrate components in the samples (31-32).

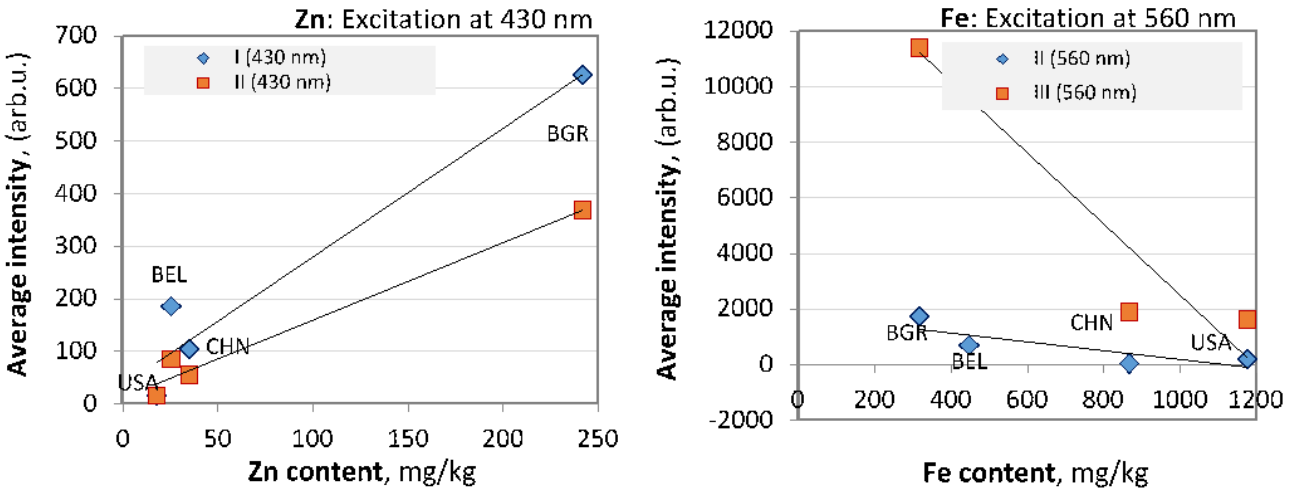

Figure 4: Plots of the average power at particular maxima vs. the content of a definite metal: a) Zn at 430 nm excitation for maxima I and II; Fe at 560 nm excitation for maxima II and III.

Table 3: Correlation coefficient between metal contents and maximum intensity.

	380 nm excitation			430 nm excitation			560 nm excitation		
Max	I	II	III	I	II	III	I	II	III
Mg	-0.38	-0.45	-0.65	-0.41	-0.43	-0.68		-0.45	-0.50
Mn	-0.32	-0.35	-0.69	-0.31	-0.3	-0.66		-0.40	-0.61
Fe	-0.78	-0.77	-0.98	-0.74	-0.71	-0.95		-0.82	-0.95
Zn	0.93	0.97	0.75	0.97	0.99	0.84		0.93	0.63
Cu	0.88	0.90	0.58	0.92	0.93	0.67		0.85	0.40

Positive: Very High: 0.9-1 High: 0.7-0.9 Moderate: 0.5-0.7 Low: 0.3-0.5 Very low: 0-0.3

Negative: Very High: 0.9-1 High: 0.7-0.9 Moderate: 0.5-0.7 Low: 0.3-0.5 Very low: 0-0.3

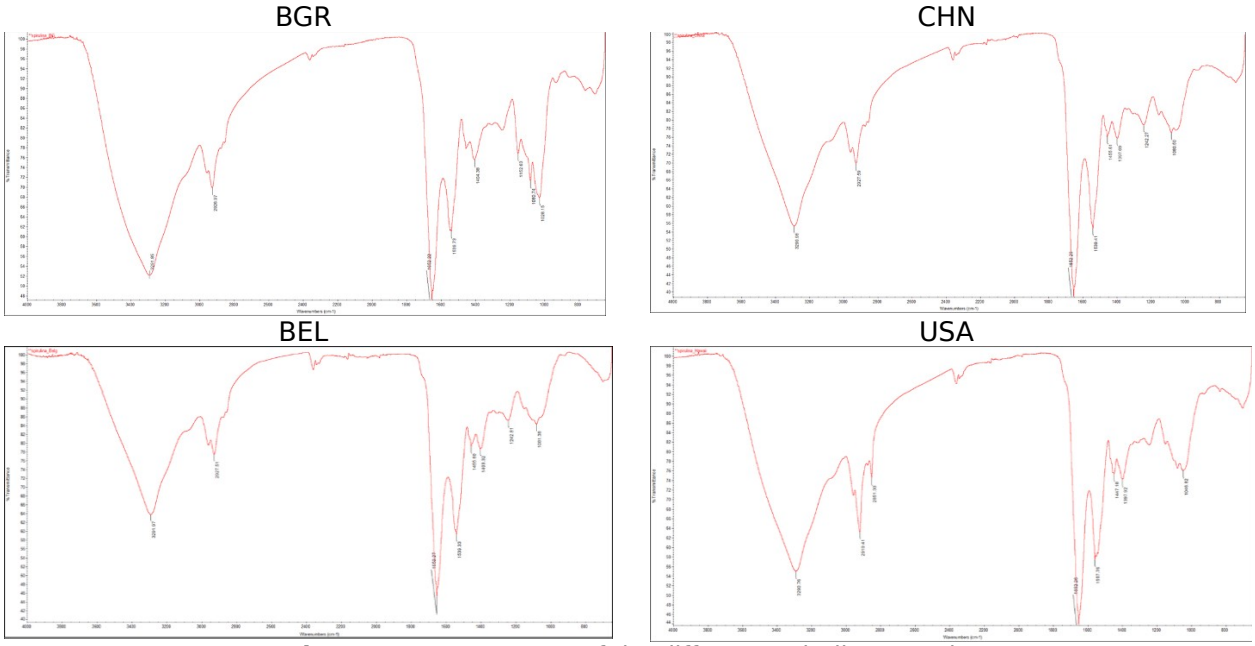

Figure 5: FT-IR spectra of the different *Spirulina* samples.

4. CONCLUSION

All investigated samples have a similar functional composition. The resulting signals in the different regions of the IR spectrum can be assigned to proteins, and carbohydrates. *Spirulina* is a good source of essential elements such as magnesium and iron, a trend was observed: Mg > Fe > Mn > Zn > Cu. Comparing the content of each element with the intensity of the maxima for the most effective excitations at 380, 430, and 560 nm show that the presence of Zn and Cu can be linked to the very high positive correlation, while that of Fe to the very high negative correlation with the intensity of fluorescence maxima.

5. REFERENCES

1. Ahsan M, Habib B, Parvin M, Huntington TC, Hasan MR, A review on culture, production and use of spirulina as food for humans and feeds for domestic animals and fish. FAO Fisheries and Aquaculture Circular [Internet]. Rome: Food And Agriculture Organization Of The United Nations; 2008, Available from: <URL>. ISBN 978-92-5-106106-0

2. Sankarapandian V, Nitharsan K, Parangusadoss K, Gangadaran P, Ramani P, Venmathi Maran BA, Jogalekar MP. Prebiotic Potential and Value-Added Products Derived from Spirulina laxissima SV001—A Step towards Healthy Living. BioTech 2022; 11: 13. Available from: <DOI>

3. Masten Rutar J, Jagodic Hudobivnik M, Necemer M, Vogel Mikuš K, Arcon I Ogrinc N. ˇ Nutritional Quality and Safety of the Spirulina Dietary Supplements Sold on the Slovenian Market. Foods 2022; 11: 849. Available from: <DOI>

4. Gentscheva G, Milkova-Tomova I, Pehlivanov I, Gugleva V, Nikolova K, Petkova N, Andonova V, Buhalova D, Pisanova E. Chemical Characterization of Selected Algae and Cyanobacteria from Bulgaria as Sources of Compounds with Antioxidant Activity. Appl. Sci. 2022; 12: 9935. Available from: <DOI> .

5. Araújo R, Vázquez Calderón F, Sánchez López J, Azevedo IC, Bruhn A, Fluch S, Garcia Tasende M, Ghaderiardakani F., Ilmjärv T, Laurans M et al. Current Status of the Algae Production Industry in Europe: An Emerging Sector of the Blue Bioeconomy. Front. Mar. Sci. 2022; 7: 626389. Available from: <DOI>

6. Cifferi O. Spirulina, the edible microorganism. Microbiol Rev. 1983; 47(4): 551-578. Available from: <DOI>

7. Ramírez-Rodrigues MM, Estrada-Beristain C, Metri-Ojeda J, Pérez-Alva A, Baigts-Allende DK. Spirulina platensis Protein as Sustainable Ingredient for Nutritional Food Products Development. Sustainability 2020; 13: 6849. Available from: <DOI>

8. Aouir A, Amiali M, Bitam A, Benchabane A. Raghavan VG. Comparison of the biochemical composition of different Arthrospira platensis strains from Algeria, Chad and the USA. J. Food Meas. Charact. 2017; 11: 913–923. Available from: <DOI>

9. Choopani A, Poorsoltan M. Fazilati M, Latifi AM, Salavati H. Spirulina: A Source of Gamma-linoleic Acid and Its Applications. J. Appl Biotechnol. Rep. 2016; 3: 483–488. Available from: <URL>

10. Grosshagauer S, Kraemer K, Somoza V. The True Value of Spirulina. J. Agric. Food Chem. 2020; 68: 4109–4115. Available from: <DOI>

11. Rzymski P, Budzulak J, Niedzielski P, Klimaszyk P, Proch J, Kozak L, Poniedziałek B, Essential and toxic elements in commercial microalgal food supplements. J. Appl. Phycol. 2019; 31: 3567–3579. Available from: <DOI>

12. Lafarga T, Fernández-Sevilla JM, González-López C, Acién-Fernández FG, Spirulina for the food and functional food industries. Food Res. Int. 2020; 137: 109356. Available from: <DOI>

13. Koli DK, Rudra SG, Bhowmik A, Pabbi S. Nutritional, Functional, Textural and Sensory Evaluation of Spirulina Enriched Green Pasta: A Potential Dietary and Health Supplement. Foods 2022; 11: 979. Available from: <DOI>

14. DiNicolantonio JJ, Bhat AG, OKeefe J. Effects of spirulina on weight loss and blood lipids: A review. Open Heart 2020; 7: e001003. Available from: <DOI>

15. Sorrenti V, Castagna DA, Fortinguerra S, Buriani A, Scapagnini G, Willcox DC. Spirulina Microalgae and Brain Health: A Scoping Review of Experimental and Clinical Evidence. Mar. Drugs 2021; 19: 293. Available from: <DOI>

16. Parada JL, de Caire GZ, de Mulé MCZ, de Cano MMS. Lactic acid bacteria growth promoters from Spirulina platensis. Int. J. Food Microbiol. 1998; 45: 225–228. Available from: <DOI>

17. Pez Jaeschke D, Rocha Teixeira I, Damasceno Ferreira Marczak L, Domeneghini Mercali G. Phycocyanin from *Spirulina*: A review of extraction methods and stability. Food Research International. 2021; 143: 110314. Available from: <DOI>

18. Vicat JP, Jean-Claude Doumnang Mbaigane, Yves Bellion. Contents of macromineral and trace elements in Spirulina (Arthrospira platensis) from France, Chad, Togo, Niger, Mali, Burkina-Faso and Central African Republic. Comptes Rendus Biologies. 2014; 337 (1): 44-52. Available from: <DOI>

19. Janda-Milczarek K, Szymczykowska K, Jakubczyk K, Kupnicka P, Skonieczna-Zydecka K.; Pilarczyk B, Tomza-Marciniak A, Ligenza A, Stachowska E, Dalewski B. Spirulina Supplementsmas a Source of Mineral Nutrients in the Daily Diet. Appl. Sci. 2023; 13: 1011. Available from: <DOI>

20. Yin-Mao Hsu, Jon-Mau Hwang and Taun-Ran Yeh. Inorganic Elements Determination for Algae/Spirulina Food Marketed in Taiwan. Journal of Food and Drug Analysis. 2001; 9(3): 178-182. Available from: <DOI>

21. Fais G, Manca A, Bolognesi F, Borselli M, Concas A, Busutti M, Broggi G, Sanna P, Castillo-Aleman YM, Rivero-Jiménez RA et al. Wide Range Applications of Spirulina:From Earth to Space Missions. Mar.Drugs 2022; 20: 299. Available from: <DOI>

22. Cadondon JG, Ong PMB, Vallar EA, Shiina T, Galvez MCD, Chlorophyll-a Pigment Measurement of Spirulina in Algal Growth Monitoring Using Portable Pulsed LED Fluorescence Lidar System. Sensors 2022; 22: 2940. Available from: <DOI>

23. Li D, Xie J, Zhao Y, Zhao J. Probing connection of PBS with the photosystems in intact cells of Spirulina platensis by temperature-induced fluorescence fluctuation. Biochim Biophys Acta Bioenerg BBA-Bioenergetics. 2003; 1557: 35–40. Available from: <DOI>

24. Gobets B, van Stokkum IH, Rögner M, Kruip J, Schlodder E, Karapetyan NV, Dekker JP, van Grondelle R. Time-Resolved Fluorescence Emission Measurements of Photosystem I Particles of Various Cyanobacteria: A Unified Compartmental Model. Biophysical Journal. 2001; 81(1), 407-424. Available from: <DOI>

25. Karapetyan NV, Dorra D, Schweitzer G, Bezsmertnaya IN, Holzwarth AR, Fluorescence Spectroscopy of the Longwave Chlorophylls in Trimeric and Monomeric Photosystem I Core Complexes from the Cyanobacterium Spirulina platensis, Biochemistry 1997; 36 (45): 13830–13837. Available from: <DOI>

26. Akimoto S, Yokono M, Hamada F, Teshigahara A, Aikawa SH, Kondo A. Adaptation of light-harvesting systems of Arthrospira platensis to light conditions, probed by time-resolved fluorescence spectroscopy. Biochim Biophys Acta Bioenerg BBA-BIOENERGETICS. 2012; 1817 (8): 1483–1489. Available from: <DOI>

27. Uebel U, Kubitz J, Anders A. Laser induced fluorescence spectroscopy of phytoplankton and chemicals with regard to an in situ detection in waters. J. Plant Physiol. 1996; 148 (5): 586–592. Available from: <DOI>

28. Arief VO, Trilestari K, Sunarso J,Indraswati N, Ismadji S. Recent progress on biosorption of heavy metals from liquids using low cost biosorbents: characterization, biosorption parameters and mechanism studies: a review. Clean. 2008; 36: 937–962. Available from: <DOI>

29. Vilar VJP, Botelho CMS, Pinheiro JPS, Domingos RF, Boaventura RAR. Copper removal by algal biomass: biosorbents characterization and equilibrium modelling. J. Hazard. Mater. 2009; 163: 1113–1122. Available from: <DOI>

30. Hai Jing Liu, Chang Hua Xu, Qun Zhou, Feng Wang, Wei Ming Li, Yi Ming Ha, Su Qin Sun. Analysis and identification of irradiated Spirulina powder by a three-step infrared macro-fingerprint spectroscopy. Radiation Physics and Chemistry. 2013; 85:210-217. Available from: <DOI>

31. Liu HJ, Xu CH, Li WM, Wang F, Zhou Q, Li A, Zhao YL, Ha YM, Sun SQ. Analysis of Spirulina powder by Fourier transform infrared spectroscopy and calculation of protein content. Spectroscopy and spectral analysis, 2013; 33(04):977-981. Available from: <DOI>

32. Sukhikh S, Prosekov A, Ivanova S, Maslennikov P, Andreeva A, Budenkova E, Kashirskikh E, Tcibulnikova A, Zemliakova E, Samusev I et al. Identification of Metabolites with Antibacterial Activities by Analyzing the FTIR Spectra of Microalgae. Life, 2022: 12: 1395. Available from: <DOI>

JOTCS A
Journal of the Turkish Chemical Society
Section: A
Chemistry
TURKISH CHEMICAL SOCIETY

Optimizing Bioethanol Production for High Octane Bioethanol-Gasoline Blended Fuel through Fermentation

Sabreen M. Saleh[1], Ahmed G. S. Al-Azzawi[1*]

[1] University of Mosul, Department of Chemistry, Education College For Pure Science, Mosul, 41002, Iraq

Abstract: The present study is to investigate the potential bioethanol production from seasonal fruit wastes as a possible substrate via biochemical fermentation. It is worth mentioning that the waste feedstock was subjected to a pretreatment process before the fermentation process. The fermentation was carried out using cost-effective dry yeast such as Saccharomyces cerevisiae for 5 to 8 days. The main target of this research is to determine bioethanol percentage from fruit wastes that produced through optimization of the bioconversion process. Besides, the selected fruit wastes were evaluated and analyzed for variations in key parameters, which include sugar content, pH value, temperature, alcohol concentrations, and yield during yeast fermentation reaction at 32 °C for the production of alcohol. The present work exhibits a promising approach for bioethanol production on a large scale from inexpensive organic wastes and yeast. Moreover, the bioethanol obtained was blended with pure gasoline to produce ethanol-gasoline blended fuel in various proportions of 0%, 5%, 10%, and 15%. The resulting alternative fuel characteristics were assessed experimentally using American Society for Testing and Materials (ASTM) standards. The bioethanol-gasoline blends including Ried vapor pressure (RVP), density, and Research Octane Number (RON) was determined according to ASTM standard methods. Overall, the results showed that the RON of gasoline was enhanced remarkably with the increase in ethanol ratio.

Keywords: Bioethanol; fermentation; Saccharomyces cerevisiae; Research octane number (RON).

Submitted: February 15, 2023 **Accepted:** April 17, 2023

Cite this: Saleh SM, Al-Azzawi AGS. JOTCSA. 2023; 10(2): 475-86.

DOI: https://doi.org/10.18596/jotcsa.1250955.

***Corresponding author. E-mail:** amsss82@uomosul.edu.iq

1. INTRODUCTION

Nowadays, the growth of the power crisis increases the universal concern as a result of the dependence on traditional fossil fuel, which is being depleted gradually to meet the continuously growing demands in the energy market (1-5). Globally, biofuel is considered an alternative energy source because of its economic and environmental considerations. This type of fuel poses no threat to environmental life, thus helping to effectively decrease greenhouse gas emissions and security of energy supply, which leads to their increasing use (6). It is well known that bioethanol is type of biofuel, which produced through fermentation of saccharide and starchy sources that obtained from plants or algae such as corn grains, sugar-cane, and lignocellulosic biomass, etc. (7). It is an appropriate alternative fuel relative to fossil fuels. Furthermore, it is not a petroleum distillate that can be easily produced via agricultural feedstock or fruit waste (8,9). From another perspective, transforming waste biomass to biofuel and in turn, decreasing the enormous usage of conventional fuels is considered a great achievement in the global energy market. Moreover, the consumer's food chain will not be affected by using various sources of agricultural waste products as the feedstock of bioethanol production. On the other hand, the key fermenting agent such as yeast has contributed to reduce the cost of conversion biomass to bioethanol, it is preferable to use a cheap yeast that is available in local markets, and it is more economical in comparison with other fermentation agents (10). High volume and variety of organic wastes in main central marketplaces are being generated daily, especially with growing up the consumption of local fruits and producing more waste fruits (11). Approximately 50% of fruits

and vegetables produced worldwide become by-products (as solid organic waste) during production processing as estimated in recent available data (12), hence fruit and vegetable biomass is a challenge to the environment all over the world and therefore there is a need to be recycled. This organic waste is a resource of potential energy and significant renewable fuel (13), thus biomass waste will help to produce the cheapest fuel as a result of the conversion of biomass to bioethanol (12). Bioethanol has been employed as an alternative fuel for internal combustion engines due to its renewable nature (14), which is considered the most promising and environmentally friendly renewable liquid fuel over conventional fossil fuel (15). It was clear that bioethanol leads to reducing the net emissions of CO_2. Furthermore, it can boost the octane rating of gasoline (when blended with it by a certain percentage) compared to standard gasoline (14, 16). The gasoline/ethanol mixture can be one of the alternative fuels since ethanol has high octane number compared to pure gasoline. This blended fuel can be utilized in an internal combustion engine without any additives. However, ethanol-gasoline blend fuel will minimize the heating value of the blended fuel as a result of low heating value of ethanol (17).

This study aimed to convert the organic fruit wastes as cheap sources to bioethanol via a fermentation process, followed by the bioethanol being purified using a distillation process to obtain high-purity ethanol for fuel purposes. Bioethanol obtained was blended with gasoline by different ratios to enhance the quality of standard gasoline for a spark-ignition engine. Bio ethanol-gasoline blend was analyzed and tested by various techniques to determine the influence of ethanol on the performance of the fuel.

2. EXPERIMENTAL SECTION

2.1. Materials

All the chemicals and reagents were purchased from Sigma-Aldrich, and Fisher Ltd and used as received without further purification such as 3, 5-dinitro salicylic acid (DNSA), potassium permanganate sodium potassium tartrate, urea reagent and D(+) glucose. White sugar (source of sucrose) and Saccharomyces cerevisiae yeast were commercially available in the main markets.

2.2. Bioethanol Fermentation Procedure and Parameters

2.2.1. Collection and preparation of decaying fruits

The raw samples of overripe fruits like black grape, banana, and red apple were collected from the main local fruit markets, located in Mosul city in Iraq, and then waste fruit samples were packed in a sterilized plastic bag and stored at low temperature in a research laboratory of Chemistry department of Mosul University in a refrigerator until further usage. About 1 Kg of each selected waste fruit was surface sterilized by sodium chloride (NaCl) solution and then rinsed well with distilled water (D.W). The selected waste sample was crushed individually in an electric grinder until it became liquid juice. The extracted fruit juice was collected and transferred to a 1 L flask and then diluted using D.W to 1 L (mix 1). Upon completion, the mixture was heated up to 95°C for 2 hours. The fruit juice was cooled down at ambient temperature and then stored in the refrigerator for further usage.

2.2.2. Fermentation process:

The fermentation method, according to the procedure described in Rishabh and Raj (18), was adopted for bioethanol production with a slight modification. Dried yeast (S. cerevisiae (E 491)) (50 gm) was inoculated into 300 mL of D.W and placed in a 500 mL conical flask under stirring conditions. Followed by 7.5 gm of urea reagent and 235 gm of sucrose or normal white sugar were added to the yeast mixture (mix 2) and then left to stir for 15 minutes at 35–40 °C for activation. Upon completion, the activated yeast inoculum (mix 2) and extracted juice (mix 1) were immediately poured into a 5 L conical flask, followed by D.W was added to a final volume of 3 L. Lab-scale batch of anaerobic fermentation was carried out in a sealed glass vessel of incubator that designed to conduct fermentation reactions. During the fermentation process, the yeast converted the waste sugar source into bioethanol and carbon dioxide as released gas. In the dark, the fermentation of rotten fruit samples was allowed to take place for 5 to 7 days at 32± °C with an agitation speed of 180 rpm. When carbon dioxide stopped to flow into the gas trap, it is considered a good indication of the end of the fermentation reaction. It is worth mentioning that test samples were taken from fermented solution before and after the fermentation process to evaluate bioethanol production and sugar content in the substrate respectively. In addition, the pH value of each fruit waste was measured and recorded before and after fermentation. Upon completion of the fermentation, the next step run was taken out from the incubator. The raw bioethanol, which is obtained by fermentation of waste fruit, was purified and concentrated by using a distillation unit to maximize the alcohol percentage in the final product. At the beginning of the distillation process, simple distillation was performed to produce the distilled liquid (bioethanol) in the range of 45-55 % at 78 °C, but the bioethanol required further purification for fuel purposes. Consequently, the resulting bioethanol was subjected to further purification through fractional distillation at 78 °C, which concentrated to 95% in the second distillation. Furthermore, hydrated bioethanol (95%) was dried using a 3A° molecular sieve to afford anhydrous ethanol (99%) that measured by hydrometer (alcoholmeter). Bioethanol produced was analyzed and confirmed by using FTIR technique.

2.2.3. Estimation of reducing sugars in fermented solution by (DNSA) method:

The reduced sugar content in the fermented solution was measured using DNSA method, which described by Garriga et al (19) with some modifications. (DNSA) the reagent was prepared by dissolving 0.5 gm of (DNSA) in 100 mL of D.W and the solution was stirred at room temperature. Then an aqueous solution (2N) of NaOH (7.5 mL) was slowly added to the DNS solution and stirred at ambient temperature until obtaining a clear solution. A solution containing (15 gm of sodium potassium tartrate in 20 mL of D.W) was added to (DNSA) solution followed by the mixture was filtered by filter paper and diluted with (D.W) to 50 mL using a volume flask. The DNSA reagent solution was kept at a low temperature (below 5°C) in a dark glass bottle. Stock standard solution of glucose, at a concentration ranging from 100 µg/mL (0.1 mg/ mL) to 1000 µg/mL (1 mg/ mL), was prepared using dried test tubes, then standard solutions were diluted to 2 mL with D.W to each test tubes, then 1 mL of DNSA solution was added to each tube and mixed well then covered all tubes with peace of cotton to avoid the loss of liquid due to evaporation. The tubes were kept at 95 °C for 15 minutes in the water bath to develop the red-brown color. After cooling, 5 mL of D.W was added to each test tube to stabilize the color. Thereafter, absorbance was measured by a spectrophotometer (UV-Vis spectrometer-PG instrument limited- Model T92+) at 540 nm.

2.2.4. Determination Of pH:

pH value of the fermented solution was determined and recorded during the fermentation process using a digital pH meter (Eutech instruments- PC 700).

2.2.5. Determination Of Ethanol Concentration:

The collected distillates for each purification step were measured using a hydrometer tool; it was widely used to determine the concentration of alcohol. At 20 °C, a distillate being tested should be placed in a graduated cylinder then the hydrometer would be allowed to float on the distillate to measure and record the concentration of alcohol (%) as shown in Figure 1.

Figure 1: Determination of bioethanol Concentration using a gradual cylinder and hydrometer.

2.2.6. FTIR Spectroscopy:

Fourier Transform Infrared Spectrophotometer (FTIR) is a powerful technique that can be employed to identify some of the functional groups present in a solid, liquid, or gaseous sample. In our study, the functional groups of the bioethanol are analyzed by using FTIR (Bruker Alpha II-ATR, Germany). The absorption frequency spectra are recorded and plotted as transmittance vs wave number. The functional groups in bioethanol from different fruit wastes were confirmed and determined using FT-IR spectroscopy. In brief, bioethanol (1.0 µL) was placed on a fused KBr disc, which is mounted on the cell holder and fixed on the sample beam of IR spectrometer. The running was performed over a spectrum range of 400 to 4000 cm-1 and averaged 16 scans.

2.2.7 Bioethanol-Gasoline Blend Characteristic Tests

2.2.7.1. Sample preparation:

Bioethanol-gasoline blended samples were made by mixing normal gasoline with high-purity bioethanol (99%) in various blended rates (0%, 9%, 11%, 13%, and 15% vol/vol) as shown in Figure 2. The blending process was conducted in a glass bottle which tightly closed under the stirring condition at room temperature for 5 minutes. All tests of bioethanol-gasoline binary blends were carried out in the department of

laboratory and quality control: at Baiji refinery in Iraq.

Figure 2: Collected bottles of bioethanol-gasoline blended samples.

2.2.7.2. Density Test:
The density of each tested sample was determined according to ASTM D4052 (20), using a digital density meter (Rudolph Research Analytical density meter-DDM 2911) as depicted in Figure 3. The fuel sample was injected in digital density meters to determine the density value at 15.5 °C.

Figure 3: Digital density meter apparatus.

2.2.7.3. Reid Vapour Pressure (RVP) Test:
The vapor pressure of pure gasoline and gasoline blends was measured according to the ASTM-D6378 standard (21), using a commercial RVP apparatus (Eralytics Eravap, Vapour Pressure Tester) as depicted in Figure 4. The method covers the use of automated RVP instruments to measure the vapor pressure exerted in a vacuum by hydrocarbon-oxygenate mixtures such as bioethanol-gasoline blended fuels.

Figure 4: Reid vapor pressure apparatus.

2.2.7.4. Research Octane Number (RON):
An octane number is considered one of the major characteristics of gasoline that must be measured accurately for motor fuels like gasoline. RON value of each bioethanol-gasoline blend was determined by a cooperative fuels research engine (Single-cylinder, four-stroke, and spark ignition engine) as shown in Figure 5, for determination of research octane number for base fuel and blended fuels. This method was carried out according to the standard method (ASTM-D2699) (22).

Figure 5: Single cylinder –test engine assembly for RON measurements.

3. RESULTS AND DISCUSSION

The anaerobic fermentation process of overripe fruits was carried out for 5-7 days at 32±2 °C, which produced bioethanol. Bioethanol yield was investigated at different types of fruit waste, black grape waste produced the highest amount of bioethanol (10.9%) with high purity (99%) as shown in Figure 6, whereas red apple ranked second, followed by banana produced the least amount of bioethanol at the same fermentation conditions. Hence, S. cerevisiae has achieved better in grape waste than the other fruits' wastes. A previous study showed that bioethanol yield from grapes, apples, and bananas was around 6.2%, 4.7%, and 5.4% respectively (23). In another study, bioethanol yields from grapes

and apples were 5.2% and 4.5% respectively (18). Many studies have indicated that temperature also plays a crucial role in the fermentation process. Previous studies showed that bioethanol production enhanced with the increase in fermentation temperature that reached a maximum value at 35°C. However, further increasing or decreasing temperature leads to reducing the percentage of bioethanol production, this is probably due to the denaturing of the yeast cells used (24).

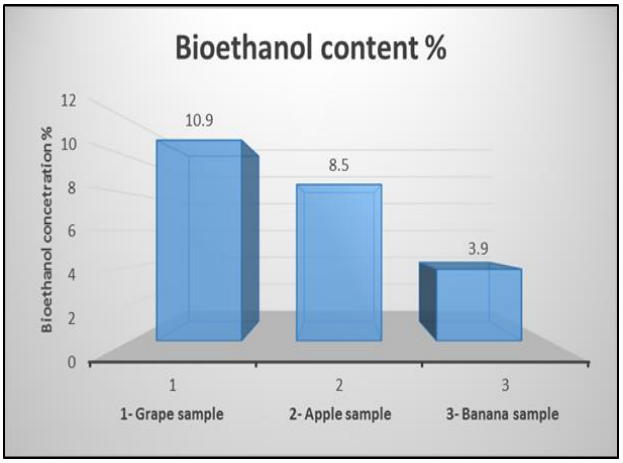

Figure 6: Graph showing a concentration obtained of bioethanol for each fruit waste during fermentation process.

The maximum bioethanol productivity can be obtained depending on the amount of raw material, which means that the bioethanol concentration rises with the increase in sugar content in raw materials. In this study, concentration is the measure of alcoholic content that presented in the distilled liquid. Bioethanol concentration can be expressed in terms of percentage (%). The yield percentage of ethanol was determined in the black grape at 10.9%, and the apple at 8.5%, whereas it was 3.9% for the banana as listed in Table 1 and depicted in Figure 6. With the increase in sugar content in a substrate, ethanol production increased significantly. Comparative studies of bioethanol productivity from varied decaying fruits exhibited that grape waste has higher efficiency compared to other fruit wastes such as apples and bananas. The fermentation process of grape waste is cost-effective and does not produce any toxic by-products. Hence, it can be applied on large scale for industry.

Table 1: Various parameters obtained during fruit waste fermentation.

Sample	pH value before fermentation	pH value after fermentation	Bioethanol %	Fermentation period (days)
Black grape	4.5	4.9	10.9	7
Red apple	4.5	4.8	8.5	7
Banana	4.5	4.7	3.9	5

FTIR spectroscopy analysis identified the presence of methyl (-CH_3) stretch, hydroxyl (-OH) stretch, and –alkane (-CH_2) stretch in pure bioethanol. In the FTIR spectrum (Figure 7 A, B, and C) of each sample, a broad absorption band was found in a wave number range of 3317 cm^{-1} to 3331 cm^{-1} (slightly different in grape, apple, and banana), which corresponds to the OH stretching vibrations. Another peak is assigned at 2973 cm^{-1} as a sharp peak of stretching vibration due to the presence of the methyl group. Previous studies confirmed that wave numbers 2,900 and 3,300 cm^{-1} in FTIR graph of ethanol have been linked to CH and OH molecule groups, respectively (25). Notably, absorbance bands between 1045 cm^{-1} and 1380 cm^{-1} were observed due to stretching bands of the -CH_2 functional group (26).

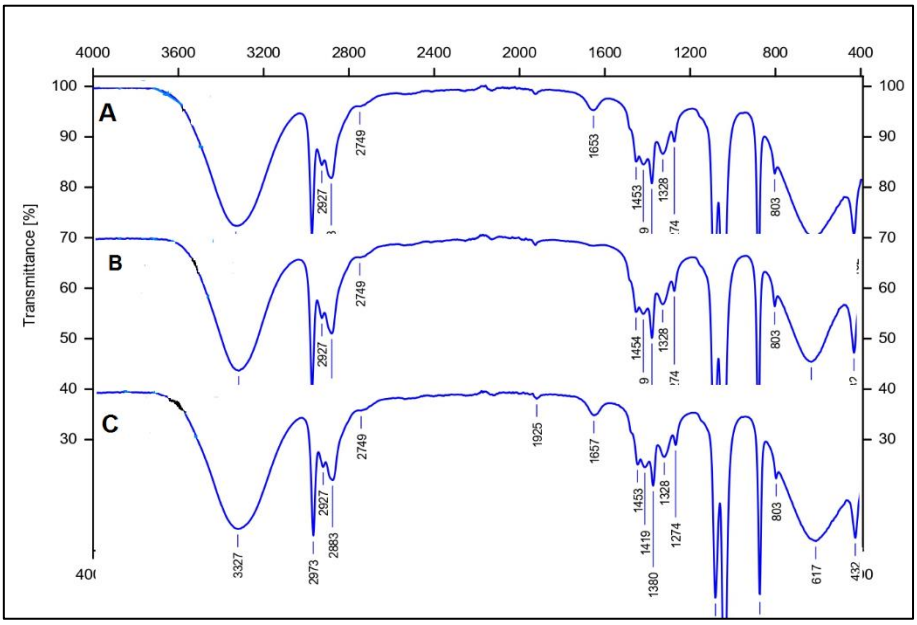

Figure 7: FTIR spectrum of distilled bioethanol, which produced from (A) black grape waste, (B) red apple waste, and (C) banana waste.

The pH parameter has a considerable influence on the alcoholic fermentation process. Based on this work, the initial pH of bioethanol obtained from the selected waste fruits was determined to be 4.5 as shown in Figure 8, while the final PH value of bioethanol obtained was determined in the grape at (4.9), apple (4.8), and banana (4.7). It was noted that the pH value was slightly increased after yeast fermentation; this can be due to the conversion of glucose to bioethanol. In terms of yeast activity, yeast can survive in acidic conditions that ranged from 4 to 6 (23). Another study indicated that the optimum pH value for yeast fermentation to generate bioethanol is 4.5 (27). Janani et al. revealed that a similar range of pH values in waste fruits was observed, the pH value of bioethanol produced from decaying fruits was estimated in the grape at 5.4, apple at 4.5, and banana at 5.1, these results agree with our results (23).

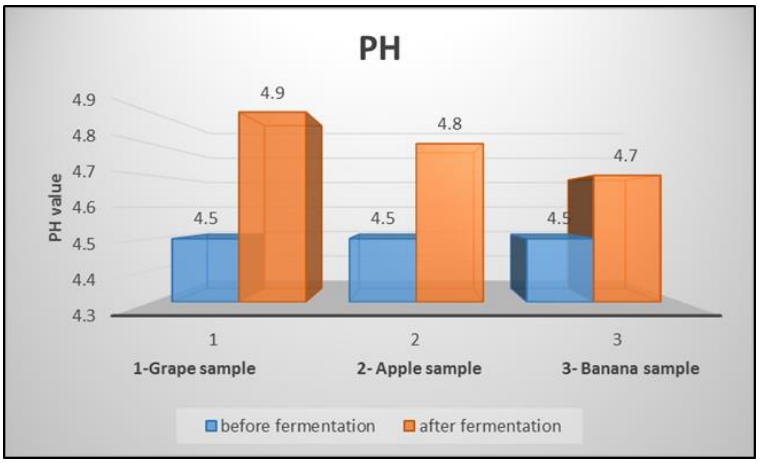

Figure 8: Graph showing a pH obtained of fermented solution for each fruit waste during fermentation process.

The standard curve of stock solution glucose was plotted to determine the reducing sugar and compared to each sample as depicted in Figure 9 a,b,c, and Table 2. The amount of sugar content was assessed using DNS reagent and it was found to drop down remarkably during the fermentation process. The sugar content of overripe fruit extracts was determined by comparing their absorbance taken from each sample to the standard curve of reducing sugar to calculate the sugar content at A 540. Among the three decaying fruit extracts used for the analysis of reducing sugar content, glucose content in grape solution extract dropped from 43 to 23 (mg/mL) after 7 days of

fermentation, whereas glucose level in apple started from 43 (mg/mL) at the beginning of fermentation to 14 (mg/mL) at 7 days. A similar trend was observed in bananas, glucose level in banana waste declined from 18 (mg/mL) to 0.59 (mg/mL) after 5 days of fermentation.

Table 2: Estimation of reducing sugar via DNS standard method.

The volume of standard .glucose solution (mL)	The volume of D.W in mL	Amount of glucose in µg/mL	The volume of DNSA reagent in mL		dilution with D.W in mL	Absorbance at 540 nm
0.0	2	0	1.0 mL	Keep the test tubes in boiling water bath for 10 min	5.0 mL	0.000
0.1	1.9	100				0.010
0.2	1.8	200				0.049
0.4	1.6	400				0.139
0.6	1.4	600				0.267
0.8	1.2	800				0.348
1.0	1.0	1000				0.458

The reducing sugar concentration declined as the fermentation proceeds owing to the consumption of the sugar by Saccharomyces cerevisiae cells to produce bioethanol and carbon dioxide. It is worth mentioning that the initial glucose amount in extracted juice of the grape was diluted to 1:45 with D.W to obtain the absorbance into the standard curve, while the final sugar content of the grape waste extract was diluted to 1:25 with D.W. Other waste fruit extracts (apple and banana) were also diluted with D.W before and after the bioconversion process to measure the reducing sugar values as shown in Table 3.

Table 3: Estimation of sugar content in rotten fruit extracts before and after the fermentation process.

The volume of rotten fruit sample (mL)	The volume of D.W (mL)	The volume of DNSA reagent in mL		Dilution with D.W (mL)	Absorbance at 540 nm	Dilution (D) (mL)	Sugar content (mg/mL)
Grape-(b) (1.0 mL)	1.0	1.0 mL	Keep the test tubes in boiling water bath for 10 min	5.0 mL	0.439	45	43
Grape-(a) (1.0 mL)	1.0				0.417	25	23
Apple- (b) (1.0 mL)	1.0				0.436	45	43
Apple- (a) (1.0 mL)	1.0				0.450	15	14
Banana- (b) (1.0 mL)	1.0				0.420	20	18
Banana-(a) (1.0 mL)	1.0				0.249		0.59

(b): before fermentation process, (a): after fermentation processs, and (D): dilution factor.

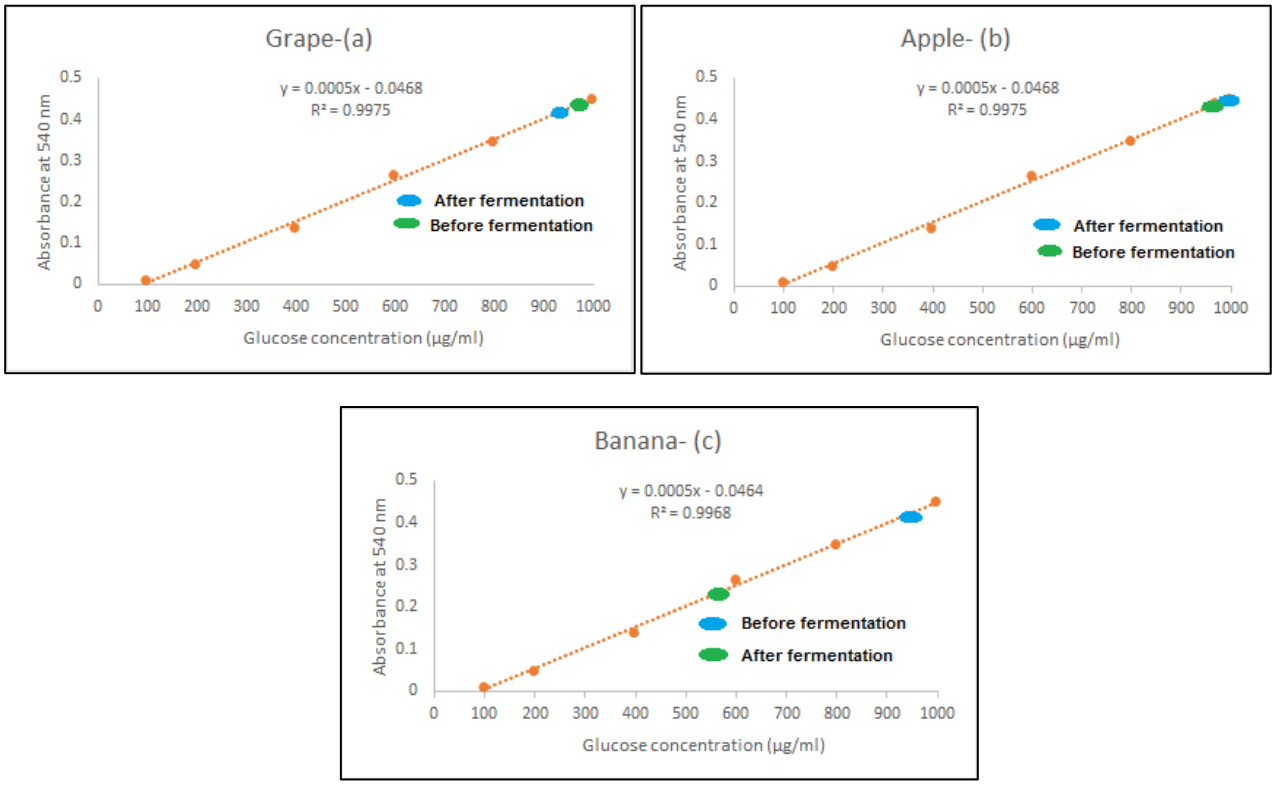

Figure 9: Estimation of sugar content in decaying fruit extracts before and after fermentation: (a) Grape waste. (b) Apple waste, (c) Banana waste.

The present work also focused on conducting tests toward bioethanol-gasoline blend characteristics and performance in different bioethanol ratios to analyze the probability of these blends as an alternative fuel. Therefore, different blend rates of bioethanol–gasoline blended fuels (9%, 11%, 13%, and 15%) were prepared and then sent to the petroleum quality control laboratory at Baiji refinery for ASTM standard analysis. The main results obtained from the ASTM analysis including RVP, density, and RON have been summarized in Table 4, to show the effects of bioethanol addition (9%, 11%, 13%, and 15% by volume) to gasoline on its performance. The results showed the variations of density (g/cm^3), RVP (psia), and RON, which considered as a function of different blend rates of bioethanol–gasoline mixtures.

Table 4: Specifications of regular gasoline and bioethanol-gasoline blends.

Characteristics	Test Method (ASTM)	Base gasoline	Bioethanol ratio in the fuel 9%	11%	13%	15%
Density (g/cm^3 at 15.5 °C)	*ASTM-D4052*	0.7305	0.7353	0.7369	0.7377	0.7395
RVP (psia at 37 °C)	*ASTM-D6378*	10.40	10.33	10.20	10.18	10.00
RON	*ASTM-D2699*	82.5	87.5	87.9	89.0	89.0
Color	Yellow	yellow	yellow	yellow	yellow	Yellow

Figure 10 represents the density values (g/cm^3) of the base gasoline and gasoline blends with bioethanol at various rates. The graph indicated that density increased with increasing the bioethanol content in the gasoline blend. The result is quite common due to the density of bioethanol that higher than the base gasoline.

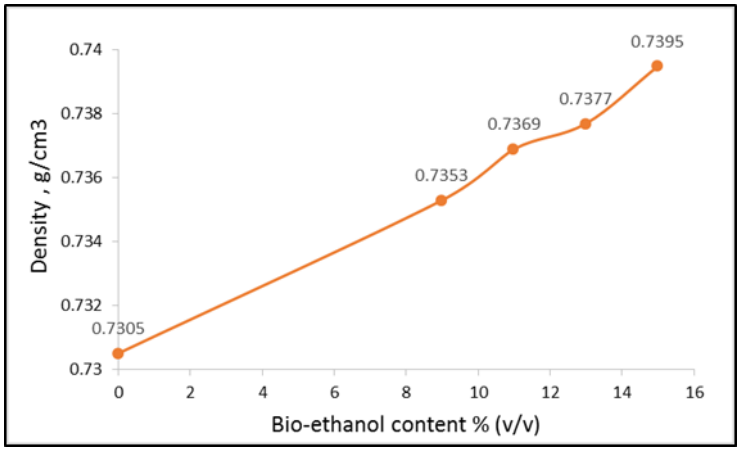

Figure 10: Graph showing density vs bioethanol content ratio to gasoline.

The behavior of bioethanol-gasoline mixtures was significantly different from conventional gasoline despite the fact that the RVP value of ethanol is much lower than that of base gasoline. The RVP value declined slightly when bioethanol was added to regular gasoline in various ratios as depicted in Figure 11. The decrease of RVP from fuel blends is caused by the little amount of water in the bioethanol-gasoline mixture by the increase of the volume of the alcohol mixture, and it may cause gasoline blend volatility change (water is more difficult to evaporate compared to gasoline and alcohol) (28).

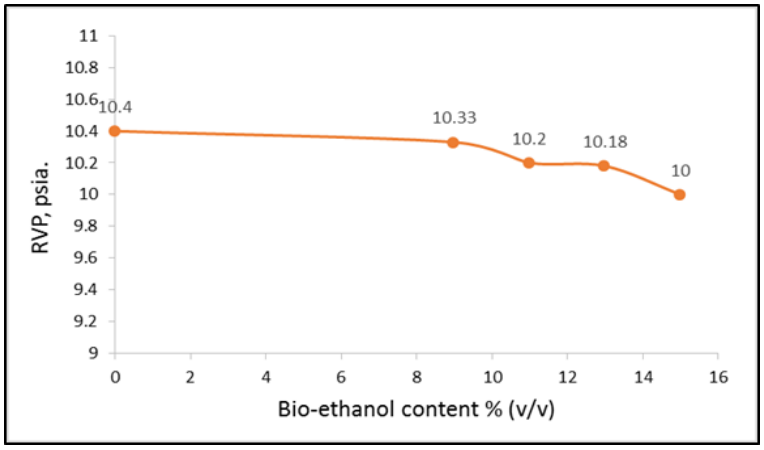

Figure 11: Graph showing RVP vs bioethanol content ratio to gasoline.

From the results of ASTM-D2699, RON of samples varies from 82.5 to 89 depending on the volume (%) of bioethanol added to the sample. The RON increases progressively with the increase of ethanol content as depicted in Figure 12, because of having a high RON value of pure ethanol at 105. It can be observed that the RON value jumped around 7 points when the bioethanol content exceeded 13% by volume, RON of blended fuel did not increase with increasing the bioethanol content to 15% by volume. Therefore, there is no need to increase ethanol content above 13% as it has a negative impact on RON parameter. The result obtained coincided with another study that investigated the impact of a gasoline-bioethanol mixture on the value of gasoline's octane number (16).

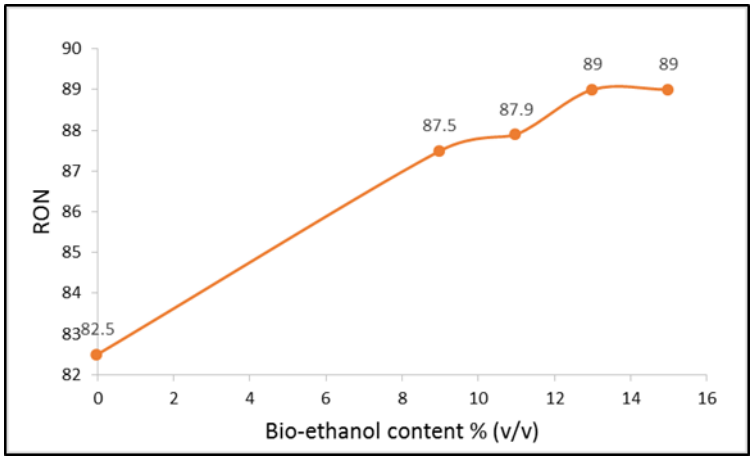

Figure 12: Graph showing RON vs bioethanol content ratio to gasoline.

4. CONCLUSION

In the present study, the results obtained revealed that different decaying fruits could serve as raw materials for bioethanol production via the bioconversion process. Moreover, bioethanol produced can be blended with pure gasoline in various proportions to be used as an alternative fuel to mitigate the demand for conventional fossil fuel resources. From this comparative study, the maximum bioethanol yield was obtained from grape waste (10.9%) followed by apple waste (8.5%) then banana waste (3.9) at 32 °C in acidic conditions (pH 4-5). The S. cerevisiae (yeast) was employed to convert saccharide wastes into bioethanol and carbon dioxide, and then a high concentration of bioethanol was obtained via simple distillation, fractional distillation, and dehydration respectively.

Bioethanol was mixed with conventional gasoline to produce blends that can be used as an alternative fuel for variable speed spark ignition up to 10 vol. % blends without engine modification. Analytical and experimental work on a single-cylinder engine was conducted to evaluate the effect of using bioethanol-gasoline blends instead of the base gasoline on the RON value, which considered a critical fuel property that plays a primary role in the design of the engine. It was clear that gasoline with ethanol content until 13% (v/v) can boost the RON value by 7 more points compared to base gasoline. These blends can be used by the vehicle engine smoothly without any engine modification. The comparative study showed that adding bioethanol to gasoline in different proportions has affected slightly on PVP and density values of blended fuels compared to regular gasoline. It can be concluded that gasoline with 13 %(v/v) bioethanol content can work well as a premium gasoline substitution.

5. CONFLICT OF INTEREST

The authors declared that there is no conflict of interest.

6. ACKNOWLEDGMENTS

We gratefully acknowledge Mosul Uniersity-Iraq for its support of this work. The present study was performed in the research center of the chemistry department at Education College for Pure Science. Furthermore, Gasoline blended samples were sent to the petroleum quality control laboratory: Baiji refinery in Iraq, to characterize and analyze their properties.

7. REFERENCES

1. Zabed H, Faruq G, Sahu JN, Azirun MS, Hashim R, Nasrulhaq Boyce A. Bioethanol production from fermentable sugar juice. The scientific world journal. 2014; 957102. <URL>

2. Gebrehiwot H, Zelelew D. Ricinus communis Seed Oils as a Source of Biodiesel; A Renewable Form of Future Energy. Journal of the Turkish Chemical Society Section A: Chemistry. 2022;9(2):339-54. <URL>

3. Akman E. Enhanced photovoltaic performance and stability of dye-sensitized solar cells by utilizing manganese-doped ZnO photoanode with europium compact layer. Journal of Molecular Liquids. 2020 Nov 1;317:114223. <URL>

4. Akman E, Karapinar HS. Electrochemically stable, cost-effective and facile produced selenium@ activated carbon composite counter electrodes for dye-sensitized solar cells. Solar Energy. 2022 Mar 1;234:368-76. <URL>

5. K Al-Mousoi A, Mohammed MK, Salih SQ, Pandey R, Madan J, Dastan D, Akman E, Alsewari AA, Yaseen ZM. Comparative Study of the Correlation between Diffusion Length of Charge Carriers and the Performance of CsSnGeI3 Perovskite Solar Cells. Energy & Fuels. 2022 Nov 11;36(23):14403-10. <URL>

6. Chew ZL, Tan EH, Sathiamurthy A, Palaniandy L, Woon KS, Phuang ZX. An integrated life-cycle greenhouse gas protocol accounting on oil palm trunk and empty fruit bunch biofuel production. Science of

The Total Environment. 2023 Jan 15;856:159007. <URL>

7. Tse TJ, Wiens DJ, Reaney MJ. Production of bioethanol—A review of factors affecting ethanol yield. Fermentation. 2021;7(4):268. <URL>

8. Jahid M, Gupta A, Sharma D. Production of bioethanol from fruit wastes (banana, papaya, pineapple and mango peels) under milder conditions. Journal of Bioprocessing & Biotechniques. 2018;8(3):1-11. <URL>

9. Hussain SU, Noureen S, Razzaq I, Akhter S, Mehmood F, Razzaq Z, et al. Optimization and Characterization of Acid-Catalyzed Castor Biodiesel and its Blends. Journal of the Turkish Chemical Society Section A: Chemistry. 2022;7(4):1007–22. <URL>

10. Hossain N, Zaini JH, Mahlia T. A review of bioethanol production from plant-based waste biomass by yeast fermentation. International Journal of Technology. 2017; 8(1):5-18. <URL>

11. Wu WH, Hung WC, Lo KY, Chen YH, Wan HP, Cheng KC. Bioethanol production from taro waste using thermo-tolerant yeast Kluyveromyces marxianus K21. Bioresource technology. 2016 Feb 1;201:27-32. <URL>

12. Sagar NA, Pareek S, Sharma S, Yahia EM, Lobo MG. Fruit and vegetable waste: Bioactive compounds, their extraction, and possible utilization. Comprehensive reviews in food science and food safety. 2018;17(3):512-31. <URL>

13. Moneruzzaman Khandaker M, Aliyu Abdullahi U, Dogara Abdulrahman M, Afiza Badaluddin N, Suryati Mohd K. Bio-Ethanol Production from Fruit and Vegetable Waste by Using Saccharomyces cerevisiae. Bioethanol Technologies. IntechOpen; 2021. <URL>

14. Liu S, Lin Z, Zhang H, Fan Q, Lei N, Wang Z. Experimental study on combustion and emission characteristics of ethanol-gasoline blends in a high compression ratio SI engine. Energy. 2023 Apr 3:127398. <URL>

15. Karimi Douna B, Yousefi H. Comparison of energy production and renewable fuels method from algae with other ways of biodiesel production resources. Journal of Renewable and New Energy. 2023 Mar 21;10(1):188-97. <URL>

16. Wibowo CS, Sugiarto B, Zikra A, Budi A, Mulya T, editors. The Effect of Gasoline-Bioethanol Blends to The Value of Fuel's Octane Number. E3S Web of Conferences; 2018: EDP Sciences. <URL>

17. Adian F, Sugiarto B, Wibowo CS, Zikra A, Mulya T, editors. The effect of 5% ethanol in 88, 92, and 98 RON gasoline on motorcycle engine performance. AIP Conference Proceedings; 2019: AIP Publishing LLC. <URL>

18. Chitranshi R, Kapoor R. Utilization of over-ripened fruit (waste fruit) for the eco-friendly production of ethanol. Vegetos. 2021;34(1):270-6. <URL>

19. Garriga M, Almaraz M, Marchiaro A. Actas de Ingeniería. Actas de ingenieria. 2017;3:173-9. <URL>

20. Standard A. D4052. Standard test method for density, relative density, and API gravity of liquids by digital density meter. 2011 ASTM Annual Book of Standards. 2018.

21. Mozaffari P, Baird ZS, Listak M, Oja V. Vapor pressures of narrow gasoline fractions of oil from industrial retorting of Kukersite oil shale. Oil Shale. 2020;37(4):288-303. <URL>

22. Materials ASfTa. Standard Test Method for Research Octane Number of Spark-ignition Engine Fuel: ASTM; 2018. <URL>

23. Janani K, Ketzi M, Megavathi S, Vinothkumar D, Ramesh Babu N. Comparative studies of ethanol production from different fruit wastes using saccharomyces cerevisiae. International Journal of Innovative Research in Science, Journal Engineering and Technology. 2013;2(12):7161-7. <DOI>

24. Du Q, Ye D, Zang X, Nan H, Liu Y. Effect of low temperature on the shaping of yeast-derived metabolite compositions during wine fermentation. Food Research International. 2022;162:112016. <URL>

25. Manzoor MF, Ahmed Z, Ahmad N, Aadil RM, Rahaman A, Roobab U, et al. Novel processing techniques and spinach juice: Quality and safety improvements. Journal of Food Science. 2020;85(4):1018-26. <URL>

26. Kumar R, Ghosh AK, Pal P. Synergy of biofuel production with waste remediation along with value-added co-products recovery through microalgae cultivation: A review of membrane-integrated green approach. Science of the Total Environment. 2020 Jan 1;698:134169. <URL>

27. Wong Y, Sanggari V. Bioethanol production from sugarcane bagasse using fermentation process. Oriental journal of chemistry. 2014;30(2):507-13. <URL>

28. Murachman B, Pranantyo D, Putra ES. Study of gasohol as alternative fuel for gasoline substitution: characteristics and performances. International Journal of Renewable Energy Development. 2014;3(3):175. <URL>

JOTCS A
Journal of the Turkish Chemical Society
Section: A
Chemistry
TURKISH CHEMICAL SOCIETY

Investigation of Radiation-Heterogeneous and Catalytic Processes In The Surface Of $(RaO)_x(SiO_2)_y$ +H_2O System

Zaur Mansimov, Gunel Imanova*, Adil Garibov and Teymur Agayev

Institute of Radiation Problems, ANAS, Baku, AZ-1143, Azerbaijan.

Abstract: In the study, heterogeneous radiolysis of water in adsorption and liquid form was studied in the $(RaO)_x(SiO_2)_y$+H_2O system. The effect of radioactivity of radium cations and process temperature on the release of molecular hydrogen was determined (T=300–673K). The mechanism of heterogeneous radiolysis of water with the participation of the studied system $(RaO)_x(SiO_2)y$+H_2O has been proposed.

Keywords: $(RaO)_x(SiO_2)_y$+H_2O system, heterogeneous radiolysis, the yield of molecular hydrogen, gamma-radiation.

Submitted: May 19, 2022. **Accepted:** April 25, 2023.

Cite this: Imanova G. Investigation of Radiation-Heterogeneous and Catalytic Processes In The Surface Of $(RaO)_x(SiO_2)_y$ +H_2O System. JOTCSA. 2023;10(2):487-492.

DOI: https://doi.org/10.18596/jotcsa.1118855

***Corresponding author's E-mail:** gunel_imanova55@mail.ru.

1. INTRODUCTION

Due to their radiation and thermal stability and unique physicochemical properties, radium silicates are of great interest in various fields of nuclear and radiation technology. Interesting results on the effect of different types of radiation on the physicochemical properties of radium silicates were obtained (1–3). Radium silicates are also of great interest as nuclear materials for high-temperature nuclear and radiation technologies. Therefore, recently there has been growth of interest in radium silicates, and large-scale research of their properties under the action of ionizing radiation is being pursued (4–6).

The regularities of the effect of the composition on the radiation-heterogeneous processes of water decomposition in contact with silicate systems are unknown, and from this point of view, its study is of great interest in radiation catalysis. For this purpose, the kinetics of radiolytic decomposition of water in contact with radium silicate of different activity was studied. In the process of thermovacuum processing in silicate systems, the electron acceptor centers cause deformation in the electronic structure of water molecules adsorbed. Therefore, most of these centers on the surface affect the decomposition of water in contact with radium-silicate systems. Some of these centers may be catalytically active in the thermal decomposition of water.

In these studies (7-13) it is noted that the process of water decomposition in contact with zeolite systems occurs in the temperature range T=723–773K. In this case, the change in thermodynamic functions is due to the presence of strong chemisorption bonds of water molecules in the crystal lattice of zeolite.

Thermocatalytic decomposition of water occurs on the surface of radium silicate systems in the temperature range T=723–773K. These processes play a role in the radiation-thermocatalytic decomposition of water. In order to reveal the share of thermocatalytic processes in the process of radiation-thermocatalytic decomposition of water, the kinetics of hydrogen formation during thermocatalytic and radiation-thermocatalytic decomposition of water in contact with radium-silicate in the temperature range T=573–773K was studied. It was found that radium-silicate systems have thermocatalytic activity in the process of water decomposition at temperatures T≥573K. Therefore, the amount of water in the reaction environment of radiation-heterogeneous processes is usually

expressed by the density of water vapor (ρH_2O) mQ/cm^3 (14-18).

The purpose of this article is to identify the impact of the activity of radium in the water radiolysis and obtaining molecular hydrogen at the radiolytic decomposition of water in the system $(RaO)_x(SiO_2)_y + H_2O$ at different temperatures (T=300–673K).

2. EXPERIMENTAL

Radium-silicate compounds with unique physical and chemical properties with resistance to radiation and temperature are of great interest in the field of nuclear and radiation technologies. Heterogeneous radiolysis of water was carried out in special quartz ampoules under static conditions. The mass $(RaO)_x(SiO_2)_y + H_2O$ system studied in the ampoules is approximately $m=4\cdot10^{-2}g$. Distilled water was taken for research. Water was injected into the ampoules at room temperature in two ways.

In the first case, at high temperatures of T≥373 K, in experiments, the required amount of water is adsorbed in the vapor phase in a pre-calibrated known volume. In the second case, water is added until it completely covers the surface of radium silicate with mass $m_{cat}=4\bullet10^{-2}g$ ($m_{liq}=0.2g$).

Radiation and radiation-thermal processes carried out on an isotope source of γ-quanta ^{60}Co. Power of the absorbed dose of gamma radiation is determined by ferrosulfate, cyclohexane, and methane dosimeters.

The absorbed radiation dose in the studied systems is determined by the relation of their electronic density and dosimetric systems. Ampoules opened in special cell, from where products of a radiolysis came to a chromatographic column. The analysis of products of radiation and heterogeneous processes was carried out on the gas- chromatograph "Svet-102" and gas analyzer "Gazokhrom-3101".

3. RESULTS AND DISCUSSION

The kinetics of the formation of molecular hydrogen at T=300 K during the heterogeneous radiolysis of water in the $(RaO)_x(SiO_2)_y+H_2O_{ads}$ and $(RaO)_x(SiO_2)_y+H_2O_{liq}$ systems was studied.

Figure 1 shows the kinetic curves of molecular hydrogen formation during heterogeneous radiolysis of $(RaO)_x(SiO_2)_y + H_2O$ system in two methods at T=300K.

In the studied systems, based on the starting line part of the kinetic curves, $(RaO)_x(SiO_2)_y+H_2O_{ads}$ (a) (T = 300K, $\rho_{H2O}=5$ mg/cm^3, D = 0.28 Gy/s) and $(RaO)_x(SiO_2)_y+H_2O_{liq}$ systems (b) (T=300 K, $m_{H2O}=0,02$ g, D=0,28 Gy/s), the values of kinetics and velocity of molecular hydrogen formation during radiation heterogeneous decomposition of water were determined. It can be seen from the kinetic curves that the stationary region is observed in both systems after a certain time. Therefore, two sections can be distinguished on the curves:

I. relatively high hydrogen accumulation rate;
II. relatively slow stage of molecular hydrogen accumulation.

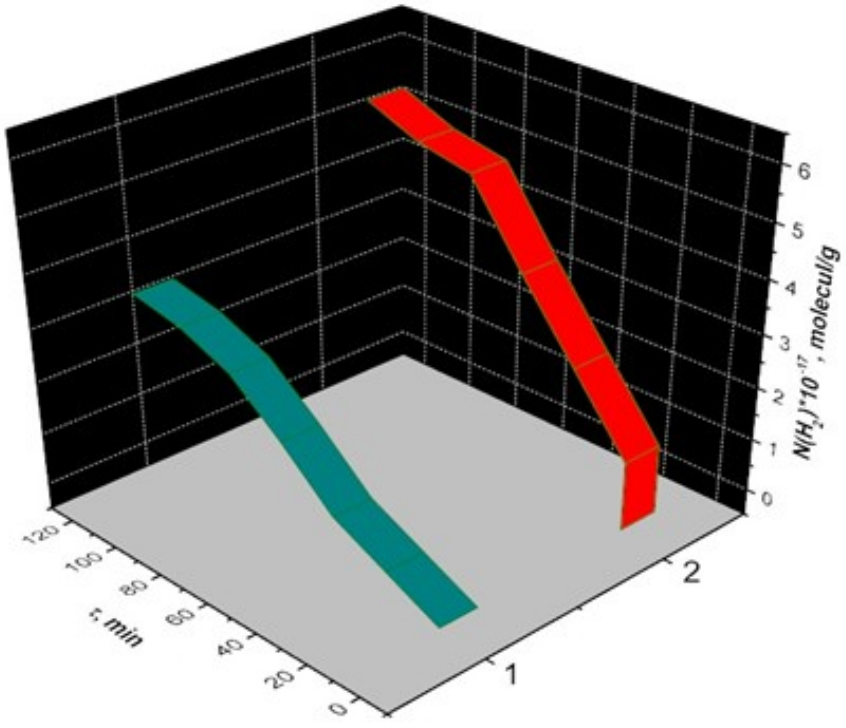

Figure 1: Kinetics of the formation of molecular hydrogen during the radiation-heterogeneous decomposition of water in the systems $(RaO)_x(SiO_2)_y+H_2O$ liquid (1) and adsorbed (2), T=300 K.

The value of the rate of accumulation of molecular hydrogen and the radiation-chemical yield of molecular hydrogen [G(H2)] is determined by the initial linear regions of the kinetic curves, which are given in Table 1.

Table 1: Estimation of molecular hydrogen formation rate and radiation-chemical yield at T =300K.

№	Irradiated systems and process temperature, K	$W(H_2)$, molecule.g^{-1}.s^{-1}	$G(H_2)$, molecule/100 eV
1	$(RaO)_x(SiO_2)_y + H_2O_{ads}$, T=300K	$2.22 \cdot 10^{12}$	0.13
2	$(RaO)_x(SiO_2)_y + H_2O_{liq}$, T=300K	$8.30 \cdot 10^{12}$	0.47

As can be seen, when the surface of radium silicate is completely covered by water, the solid-phase sensors carry more efficient energy transfer processes to the water molecules. As a result, we observe that the value of radiation-chemical emission observed in $(RaO)_x(SiO_2)_y+H_2O_{liq}$ is ca. 3.6 times higher than that of the liquid-adsorbed $(RaO)_x(SiO_2)_y+H_2O_{ads}$ system. This, in turn, clearly shows that energy carriers migrating to the surface have the opportunity to be more actively involved in the breakdown of water molecules.

It was revealed that zirconium dioxide has thermocatalytic activity in the water decomposition process at T > 373 K temperature.

$$H_2O_{\text{abs.}} \rightarrow H_2 + \frac{1}{2}O_2$$

Experimentally it is possible to obtain information about the radiation-thermal processes of hydrogen accumulation during radiation-heterogeneous processes of water decomposition. Kinetic curves of radiation-thermal and thermal processes of water decomposition at temperatures T=373-673 K are shown in Figures 2 and 3. The second slow stage of hydrogen accumulation is not observed in some curves with increasing temperature. The radiation component of radiation-thermal processes in the first approximation is defined as:

$$W_R(H_2) = W_{RT}(H_2) - W_T(H_2)$$

where $W_R(H_2)$ - the rate of formation of molecular hydrogen at the radiation component of processes, $W_{RT}(H_2)$ and $W_T(H_2)$ – the rate of formation of molecular hydrogen during radiation-thermal and thermal processes of water decomposition.

Comparison of the results of experiments carried out under the same conditions shows that when radium-silicate is surrounded by water, the energy carriers formed under the influence of gamma quanta on its surface undergo radiolytic decomposition of water molecules both at surface levels and in contact. The results of radiation-heterogeneous radiolysis of water at different temperatures with the participation of the system $(RaO)_x(SiO_2)_y$ can be explained within the electrophysical model of radiation-heterogeneous processes.

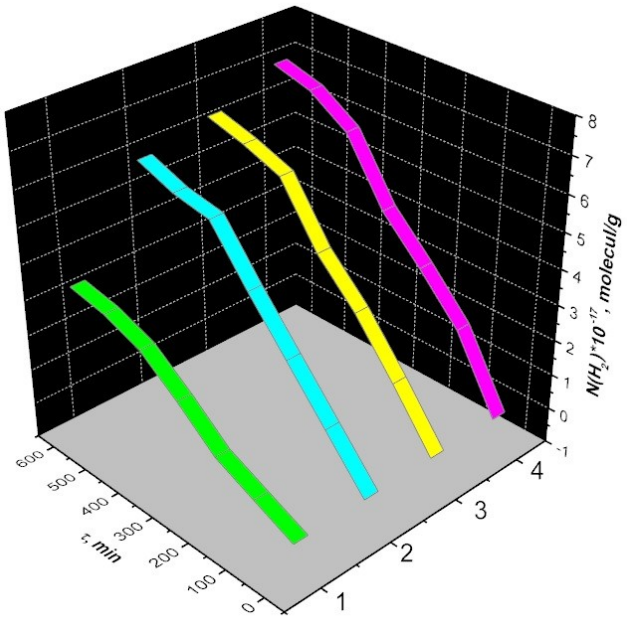

Figure 2: Kinetics of molecular hydrogen accumulation during thermal decomposition of water on the $(RaO)_x(SiO_2)_y+H_2O_{ads}$ system at different temperatures: 1-T=373,2-T=473, 3-T=573, 4-T=673 K, ρ_{H2O}=5mQ/cm^3, D=0,28 Gy/s.

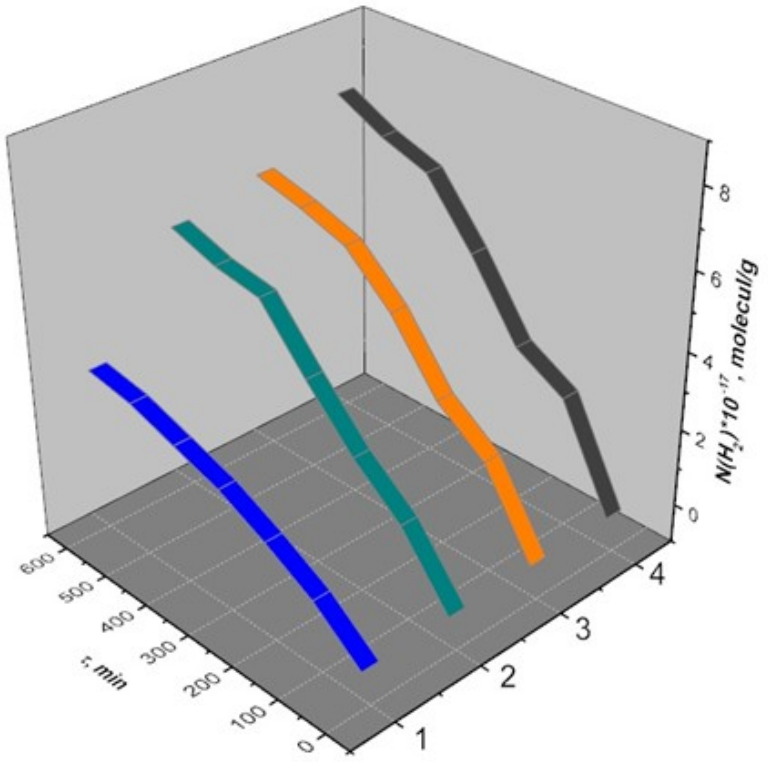

Figure 3: Kinetics of molecular hydrogen accumulation during radiation-thermal decomposition of water on the $(RaO)_x(SiO_2)_y+H_2O_{ads}$ system at different temperatures: 1-T=373,2-T=473, 3-T=573, 4-T=673 K, ρ_{H2O}=5 mQ/cm^3, D=0,28 Gy/s.

The values of radiation-chemical yields were determined from the rate of formation of molecular hydrogen with the radiation component of radiation-thermal processes of water decomposition (Table 2).

Table 2: Velocities of formation of molecular hydrogen and radiation-chemical yields as a result of radiation-thermal and thermal processes with the decomposition of water at different temperatures in the system $(RaO)_x(SiO_2)_y$

№	T, K	$W_{RT}(H_2)$, molecule.g^{-1}.s^{-1}	$W_T(H_2)$, molecule.g^{-1}.s^{-1}	$W_R(H_2)$, molecule.q^{-1}.s^{-1}	$G(H_2)$, molecule/10 eV
1	373	-	-	$0.42\cdot10^{13}$	0.18
2	473	$1.75\cdot10^{13}$	$0.06\cdot10^{13}$	$1.69\cdot10^{13}$	0.85
3	573	$3.05\cdot10^{13}$	$0.11\cdot10^{13}$	$2.94\cdot10^{13}$	1.12
4	673	$8.61\cdot10^{13}$	$4.44\cdot10^{13}$	$4.17\cdot10^{13}$	1.63

Figure 4 shows the molecular hydrogen yield values in the temperature range T=300–673K in radiation-heterogeneous processes in the system $(RaO)_x(SiO_2)_y+H_2O$.

The results from Figure 4 show that an increase in temperature from 300 to 673 K increases the radiation-chemical yield of hydrogen from 0.78 to 1.63 molecules/100 eV. The observed increase in the chemical yield of radiation is explained by the effect of temperature on the process of energy transfer in the system $(RaO)_x(SiO_2)_y+H_2O$. Based on the obtained results, it can be concluded that the surface of radium silicate has thermocatalytic active centers that are activated at different temperatures. Relatively low active centers are involved in the process of thermocatalytic decomposition with increasing temperature. Thus, thermocatalytic and radiation-thermocatalytic cleavage of water occurs during heterogeneous radiolysis of water in contact with radium silicate at T>573K.

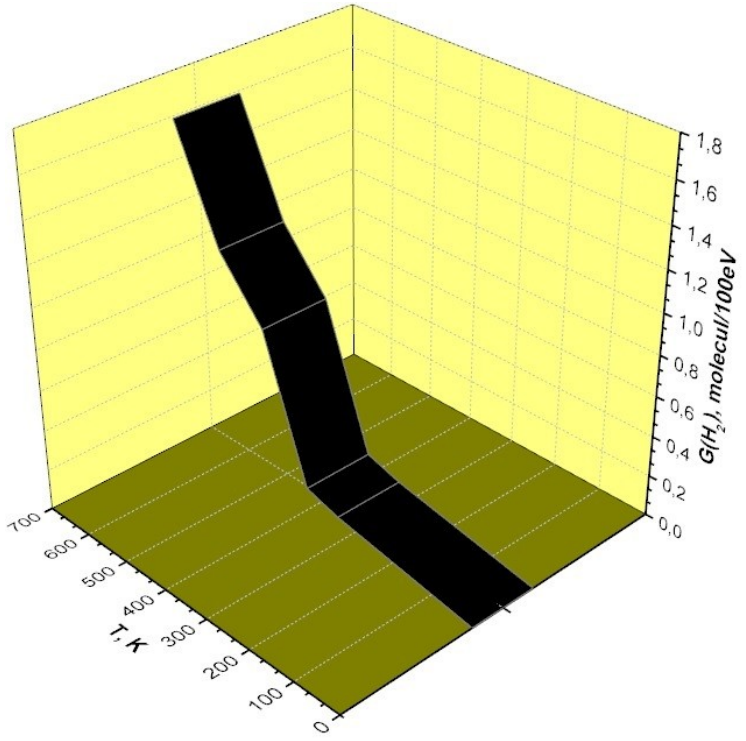

Figure 4: Temperature dependence of the radiation-chemical yields of molecular hydrogen in the $(RaO)_x(SiO_2)_y+H_2O$ system, D=0,3–0,26 Gy/s.

4. CONCLUSION

The kinetics of molecular hydrogen production as a result of radiation-catalytic decomposition of water in the system $(RaO)_x(SiO_2)_y+H_2O$ was studied in the temperature range T=300–673K. It was found that while the liquid water completely covers the surface of the catalyst layer, the radiation chemical yield of molecular hydrogen $G(H_2)$ is higher due to more efficient energy transfer to the water molecule by the particles formed in the solid phase.

5. REFERENCES

1. Vdovenko VM, Dubasov Y V. Analytical chemistry of radium. Wiley. New York; 1973. 187 p.

2. Kuznetsov RA, Butkalyuk PS, Tarasov VA, Baranov AY, Butkalyuk IL, Romanov EG, et al. Yields of activation products in 226Ra irradiation in the high-flux SM reactor. Radiochemistry [Internet]. 2012 Jul 24;54(4):383–7. Available from: <URL>.

3. IAEA1384 Nuclide Explorer tool for retrieving interactively detailed data on radionuclides properties [Internet]. Available from: <URL>.

4. Butkalyuk IL, Butkalyuk PS, Tomilin S V. Investigation of the interaction of radium compounds with structural materials. Phys Electron. 2013;15(4):1053–7.

5. Garibov AA, Agayev TN, Mansimow ZA, Melikova SZ, Eyubov KT. Investigation of radium orthosilicates by methods of FT-IR spectroscopy and derivatography. J Austrian Tech Nat Sci. 2014;7–8:72–5.

6. Butkalyuk IL, Butkalyuk PS, Tomilin S V. Examination of radium compounds interaction with structural materials. Ulyanovsk State University; 2013.

7. Ebaid YY. On the use of reference materials in gamma-ray spectrometric efficiency calibration for environmental samples. J Radioanal Nucl Chem [Internet]. 2009 Apr 18;280(1):21–5. Available from: <URL>.

8. Pikaev AK. Modern radiation chemistry. Radiolysis of gases and liquids. M.: Science. 1986. 440 p.

9. Jafarov YD, Garibov AA, Aliev SA, Iskenderov SM, Krasnoshtanov VR. Calculation of the absorbed dose of gamma irradiation in oxide dielectrics. At Energy. 1987;63(4):269–70.

10. Garibov AA. Radiation-catalytic action of oxide catalysts in the process of water decomposition, Radiation-catalytic processes in dispersed media: Collection of scientific papers, Ed. ed. V.N. Parmon. Novosibirsk: "Nauka", Siberian Branch,. 1992. 121–161 p.

11. Garibov AA, Bakirov MY, Jafarov YD, Velibekov GZ. Regularities of the radiation-catalytic action of Me2+-SiO3 systems in the process of water radiolysis. High Energy Chem. 1984;18(6):502–5.

12. Garibov AA, Melikzade MM, Bakirov MY, Velibekova GZ, Ramazanov MK. Influence of cations on the catalytic properties of silica gel during the radiolysis of adsorbed water molecules. High Energy

Chem. 1982;16(2):130–4.

13. Ovchinnikov AP. Calculation of the distribution of absorbed energy near a flat interface between media during gamma irradiation // Physical chemistry in microelectronics. Krasnoyarsk: KSU; 1976. 23–24 p.

14. Ackerman AF, Grudsky MY, Smirnov VB. Secondary electron radiation from solids under the action of gamma quanta. M.: Energoizdat; 1986. 168 p.

15. Kovalev VP. secondary electrons. Moscow: Energoizdat; 1987. 9 p.

16. Elango MA. Elementary inelastic radiation processes. M.: "Nauka"; 1988. 15 p.

17. Kaplan IP. Investigation of the primary processes of water radiolysis by the method of mathematical modeling. High Energy Chem. 1991;24(4):29.

18. Silin AR, Trukhin AN. Point defects and elementary excitations in crystals and glassy SiO2. Zinatne. 1985;206–14.

JOTCS A
Journal of the Turkish Chemical Society
Section: A
Chemistry
TURKISH CHEMICAL SOCIETY

Probing the Electro-Chemical and Thermal Properties of Polyaniline/MWCNT Nanocomposites

Sharon J. Paul[1], Sarvesh Kumar Singh[1], Jaya Tuteja[2], Arpit Sand[2], and Prakash Chandra[1*]

[1]Bundelkhand University, Department of Chemistry, Jhansi, Uttar Pradesh, 284128, India
[2]Manav Rachna University Department of Chemistry, Faridabad, 121004, India

Abstract: The tremendous interest for robust, clean energy storage devices to comprehend the growing needs of modern gadgets has led to exploration of materials having unprecedented electrochemical and interfacial properties. Here, the present study deals with the synergistic effects of multi walled carbon nanotubes and polyaniline nanocomposites on the electro-chemical and thermal properties for wide-range of applications. The microstructural, structural, and optical characterizations have been evaluated through scanning electron microscopy (SEM), transmission electron microscopy (TEM), X-ray diffraction (XRD), Fourier transform infrared spectroscopy (FTIR), and UV-Vis spectrophotometry. The thermal stability of the product was also studied through thermal gravimetric analysis (TGA) and the room temperature electrical conductivity was also measured. An exceptional enhancement in thermal stability and conductivity has been observed apparently due to interfacial properties of polyaniline (PANI) and multiwalled carbon nanotubes (MWCNTs). Further, in present study we are going to report a comparative analysis of thermal and electrical properties of PANI/MWCNT nanocomposites with different loadings of MWCNTs. The room temperature conductivity as calculated for 1%, 2%, 4% and 8% MWCNT loading is around 2.019, 3.075, 4.48, 8.73 S/cm respectively. The mechanism for thermal and electrical enhancements in PANI-coated MWCNT nanocomposites is also expounded.

Keywords: Nanocomposites, MWCNTs, polyaniline, nanotechnology, polymer nanocomposites

Submitted: September 19, 2022. **Accepted:** April 24, 2023.

Cite this: Paul SJ, Singh SK, Tuteja J, Sand A, Chandra P. Probing the Electro-Chemical and Thermal Properties of Polyaniline/MWCNT Nanocomposites. JOTCSA. 2023;(2):493–504.

DOI: https://doi.org/10.18596/jotcsa.1177040.

***Corresponding author. E-mail:** drprakashcy@gmail.com

1. INTRODUCTION

The advent of nanoscience and nanotechnology has prompted the use of polymer matrix nanocomposites since past few decades. The polymer nanocomposite consists of a polymer guest matrix reinforced with fillers with dimensions in nano-regime. Polymer nanocomposites are an innovative class of uniquely modified materials that come into existence due to the extraordinary collaborations of properties like electrical, magnetic, catalytic, mechanical, biodegradability, etc. between the polymer and nanofiller. Polymer nanocomposites are preferred over metal matrix composites and ceramic matrix composites as they require relatively low processing temperatures for fabrication. Moreover, the polymer matrix also assists to transfer stress through the medium by equally distributing the applied load within the composite (1). Polymer matrix nanocomposites have extensively been investigated the class of intrinsically conducting polymers (ICPs) owing to their intriguing redox and electronic properties (2,3). Carbon nanotubes (CNTs) are viewed as effective reinforcements to produce unique composite materials with novel properties for nano-scale engineering applications.

The dedicated literature studies has revealed that the combination of conducting polymers and

nanomaterials offers an opportunity to improve the mechanical, electrical, and thermal properties, along with introduction of new electronic properties based on interactions between the two compounds. Low density polyethylene nanocomposites incorporated with silicon dioxide nanoparticles (LDPE/SiO_2) have demonstrated high tolerance to the worst conditions when used as high-voltage insulation systems with enhanced thermal and mechanical properties (4). Nanocomposites of polyvinyl chloride (PVC) with titanium oxide (TiO_2) nanoparticles, and LPDE/PVC nanocomposites have been used in power cable insulation with improved electric and dielectric properties (5,6).

Polyaniline (PANI) is considered as the best ICP in terms of technological and commercial aspects. It surpasses other conducting polymers owing to high conductivity (7), better environmental stability (8), unique electro chemical properties (9), availability of cheap monomer (10) and facile synthesis technique (11). Since ever the discovery of CNTs (12) their exceptional, electrical, thermal and mechanical properties (13,14) have made them a vital contributor in vast applications. The inclusion of CNTs as conductive fillers in reinforced PANI matrix gives rise to polymer nanocomposites with new synergies possessing enhanced conductivity, improved thermal and electrical properties, and such a nanocomposite could be deployed for fuel cell (15), solar cell (16), supercapacitor (17), EMI shielding (18), gas sensor (19), and battery materials (20). There have been studies on the potential applications of polyaniline-multi walled carbon nanotubes (PANI/MWCNT) nanocomposites for EMI shielding, supercapacitor, sensors and solar cells. Manganese dioxide, multi walled carbon nanotubes incorporated polyaniline (MnO_2/PANI/MWCNT) nanocomposite showed a specific capacitance of 395.0 $F \cdot g^{-1}$ with 72% consistency over 1000 charge-discharge cycles and capability to be used as an electrode material for supercapacitors (21). PANI/MWCNT composites have also been successfully used in real sample detection and analysis of liquid ammonia (22). PANI/MWCNT/thermally annealed graphene/aerogel/epoxy nanocomposites have shown high efficiency for electromagnetic interference shielding applications with 52.1 S/cm electrical conductivity and 171.3 °C heat resistance index (T_{HRI}) (23). PANI/MWCNT have also shown high microwave absorbing performance when MWCNTs were modified with magnetic nanoparticles of ferric oxide and ferrous oxide (24). The day-by-day progression of CNT-assisted polymeric devices in nano-electronics requires a comprehensive concept and better understanding of the electrical attributes of nanocomposites of PANI and MWCNTs. The present study focuses on a comparative analysis of thermal and electrical properties with different MWCNT loadings that could be helpful to synthesize desired composite for different applications and encourage future studies. Although several efforts have been made in this area yet there is a scope of finding a suitable material whose distinctive properties are not compromised and are stable under ambient conditions. PANI/MWCNT nanocomposites could prove to be the ultimate materials with lightweight and high stability as MWCNTs have high surface area and porosity, and are extremely light-weighted.

Herein, we report the in-situ oxidative polymerization of aniline monomer with surfactant assisted dispersion of MWCNTs to obtain PANI/MWCNT nanocomposites with better performance and profound enhancements in thermal, electrical properties as compared to the original materials. A number of parameters, surface morphology, tunable properties of PANI/MWCNT nanocomposites with different MWCNT loadings, and their correlation with the thermal and electrical properties are investigated. We give an account on the potential of PANI/MWCNT nanocomposite with different MWCNT loadings to expand the known literature and provide better understanding for futuristic studies.

2. MATERIALS AND METHODS

2.1. Materials

MWCNTs were produced in laboratory *via* chemical vapor deposition (CVD) method. The precursors essential for synthesis of nanocomposites *i.e* the monomer aniline was procured from E-Merck India Ltd., potassium persulfate (PPS) was used as an oxidant, cetyl-trimethyl ammonium bromide (CTAB) as a surfactant, HCl to prepare the molar solution and ethanol used for washing the nanocomposites were procured from CDH India Ltd. The water used in the experiments is de-ionized water (DI). All chemicals used are of analytical reagent (AR) grade.

2.2. Synthesis of MWCNTs

MWCNTs were synthesized by CVD process and its average length was ~250 µm and diameter was ~28 nm as reported in our previous work (25). Briefly, ferrocene was dissolved in xylene in a particular ratio. Here, ferrocene was required to obtain Fe catalyst particles and xylene was used for carbon source. This liquid feed was kept in a quartz tube that was placed in the tube furnace. One end of the quartz tube was connected to a bladder in order to collect the exhaust gases while the other end was closed. The tube furnace was kept under argon flow and heated at around 650-800 °C. After achieving the final reaction temperature, the furnace was maintained at that temperature for 30 min and then the reactor was allowed to cool to room temperature. The growth of MWCNTs occurred on surfaces inside the quartz tube.

2.3. Synthesis of PANI/MWCNT Nanocomposites

PANI/MWCNTs nanocomposites were synthesized *via* in situ oxidative polymerization of aniline monomer in the presence of an oxidizing agent and a surfactant. PPS was used as the oxidizing agent and

CTAB was used as a surfactant. Primarily, 1 M HCl stock solution of aniline and PPS were prepared, labeled as solution A (aniline in 1 M HCl) and solution B (PPS in 1 M HCl). The molar ratio of aniline: PPS: CTAB was kept as 1: 0.5: 1. Due to low dispersity of MWCNTs, ultrasonication technique and surfactant was used. Well-dispersed suspension of MWCNTs with different amounts of MWCNTS *i.e*, 1%, 2%, 4%, and 8% in 1 M HCl solution using CTAB and ultrasonication were obtained. This MWCNT solution was added to solution A on constant stirring. Later, solution B was added slowly, dropwise to the dispersion of MWCNTs and solution A to polymerize aniline monomer. The MWCNTs are mixed in the course of the polymerization process, to ensure uniform distribution and homogeneous coating of PANI over MWCNTs. The reaction mixture was kept on constant agitation on magnetic stirrer for 24 hrs and it gradually turned into greenish black slurry. It was then filtered through vacuum filtration and the residue was repeatedly washed with DI water and ethanol via centrifugation in order to remove the unreacted oligomers or the residual impurities. The as-synthesized PANI/MWCNTs nanocomposites with different MWCNT content were dried at 60 °C in air oven, then ground into fine powder with the help of a motor-powered pestle. Pure polyaniline was also synthesized in the same manner without the use of surfactant and MWCNTs. The reason for selecting HCl as the stock solution medium rather than any other protic acid is clearly indicated in our previous work (25). The optical images of as-synthesized powdered PANI/MWCNT nanocomposite and dispersion of PANI/MWCNT nanocomposite is shown in Figure S1.

2.4. Measurements

X-ray diffraction (XRD) patterns were recorded in the 2θ range from 10 to 60 degrees through Rigaku: MiniFlex, CuKα1; λ = 1.5406 Å. The structural examination was performed with the help of SEM-EVO SEM MA15/18 and TEM - Tecnai G20-twin, 200 kV with super twin lenses having 0.144 nm point and 0.232 nm line resolution, respectively. FTIR studies were performed using a Perkin Elmer 3725 instrument from 400 cm^{-1} to 4000 cm^{-1} and UV–Vis absorption studies were performed using a Shimadzu UV−1601 spectrophotometer which is calibrated and traceable with the standard sample of Rhodamine B. The TGA studies were carried out under N_2 atmosphere (flow of 100 mL/min) from 24 °C to 700 °C at 10 °C/min, by Thermal Analysis Modulus, SDT Q600 (TA Instruments) controlled through Q Series software.

3. RESULTS AND DISCUSSION

Intrinsically conducting polymer-based nanocomposites with PANI matrix and MWCNTs as efficient reinforced conductive fillers have been synthesized with 1%, 2%, 4%, and 8% MWCNT loadings. The characterization and property determination parameters reveal that PANI/MWCNT nanocomposites have improved thermal and electrical properties when compared to the pristine polymer.

3.1. Structural and Microstructural Studies

The structural studies and microstructural studies were achieved through XRD, SEM, and TEM. The characteristic peaks of PANI appears at around 2θ values of 15°, 20°, and 25°, corresponding to (011), (020) and (200) crystal planes of PANI (26) as shown in supplementary information Figure S2. These peaks arise due to chain propagation by sequential addition of aniline monomers. The pure MWCNT in Figure S3 exhibits a sharp peak at around 2θ value of 26° that correlates to the (002) planes of MWCNT whereas the peaks at around 43° correspond to the (110) and (100) graphitic planes and small amount of catalytic Fe particles incorporated in the walls of MWCNTs during synthesis (27). PANI/MWCNT nanocomposites in Figure 1 show similar crystalline behavior as that of polyaniline. The intense peak at around 25° is the superimposed peak of MWCNTs and PANI. The peaks in the nanocomposites are more prominent with increased peak intensity as compared to pure polyaniline. This is due to the encapsulation of MWCNTs and ordering of PANI along the MWCNT axis (28). However, the peaks of MWCNTs at around 43° fade away in the diffractograms of PANI/MWCNT nanocomposites implying that the MWCNTS are coated effectively by PANI and covalent interactions between the phases is absent (29). It can be inferred that better dispersion of MWCNTs in the PANI polymer matrix improves the crystallinity of the nanocomposites.

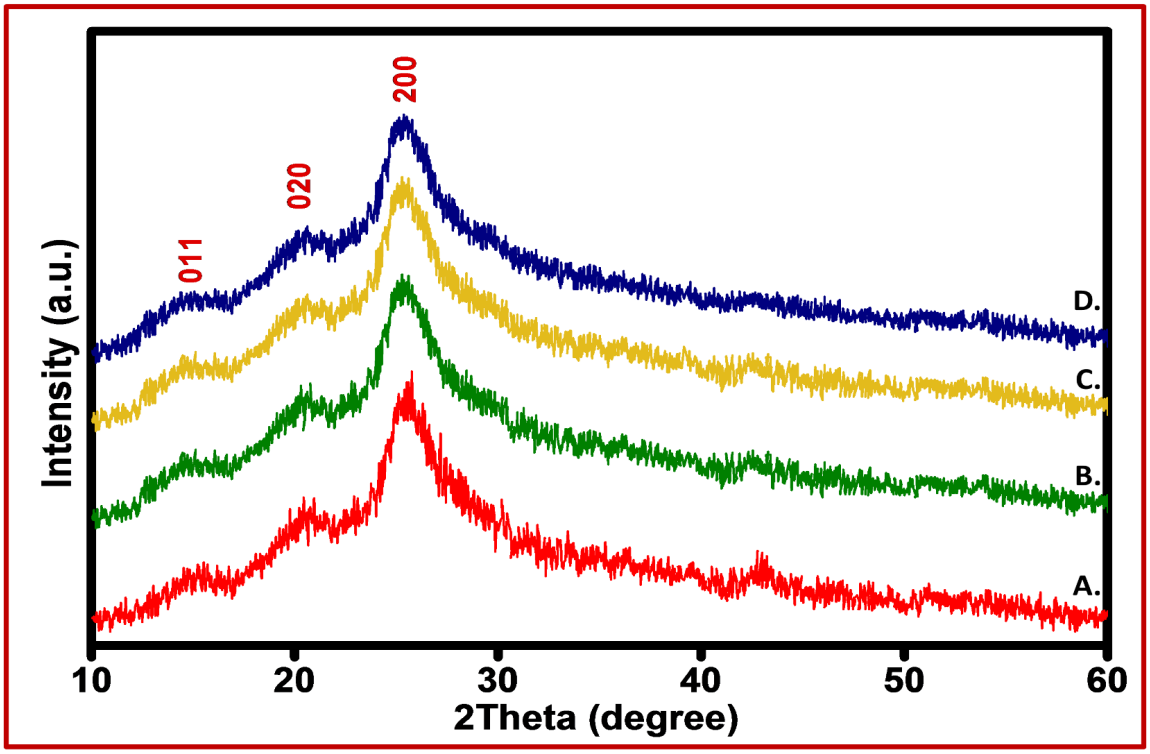

Figure 1: XRD patterns of (A) PANI@1%MWCNT nanocomposite, (B) PANI@2%MWCNT nanocomposite, (C) PANI@4%MWCNT nanocomposite and (D) PANI@8%MWCNT nanocomposite.

The morphology of the as-synthesized PANI/MWCNT nanocomposites was examined by SEM. The homogeneous dispersion of MWCNTs in PANI is clearly discernible from Figure 2, indicating that MWCNTs are well coated by the polymer. Some interwoven fibrous structures are visible that act as a conductive network to facilitate high conductivity as compared to pure PANI. These compatible interactions between MWCNTs and PANI improve the charge transfer process thereby influencing the charge transport properties of the nanocomposites. The highly agglomerated smooth globular morphology of pure PANI is visible in Figure S4. Thereby the increased diameter and rough surface of the tubular structures in the nanocomposites indicate effective polymer coating over the MWCNTs. The micrographs also show a systematic change in morphology of the nanocomposites that with the increase of MWCNTs content the globular structures change to more uniformly coated tubular structures.

To visualize the microstructure more clearly and to support the tubular morphology withdrawn from SEM, HRTEM was also performed. The HRTEM micrographs of PANI/MWCNT nanocomposites are revealed in Figure 3. The surface morphology is tubular and suggests that aniline has undergone polymerization over the MWCNTs core. The interconnected fibrous structures are also clearly visible.

Raman spectra were also used to examine the effect of interaction of PANI and MWCNTs on the structure of the nanocomposites. The Raman studies of PANI and PANI/MWCNT nanocomposite both show characteristic D-band at around 1365 cm^{-1} and G-band at around 1570 cm^{-1}. The D-band corresponds to the disordered graphite structure and structural intensity of sp^3 hybridized carbon atoms. The G-band is attributed to the structural intensity of the sp^2 hybridized carbon atoms and the D/G ratio is used to determine the degree of defects on MWCNTs. The Raman spectra of PANI and PANI/MWCNT nanocomposite in Figure S5 show no significant difference in D/G ratio, therefore indicating that no defects are created on the surface of MWCNTs during the process of polymerization. This also reveals that the interactions are purely physical in nature.

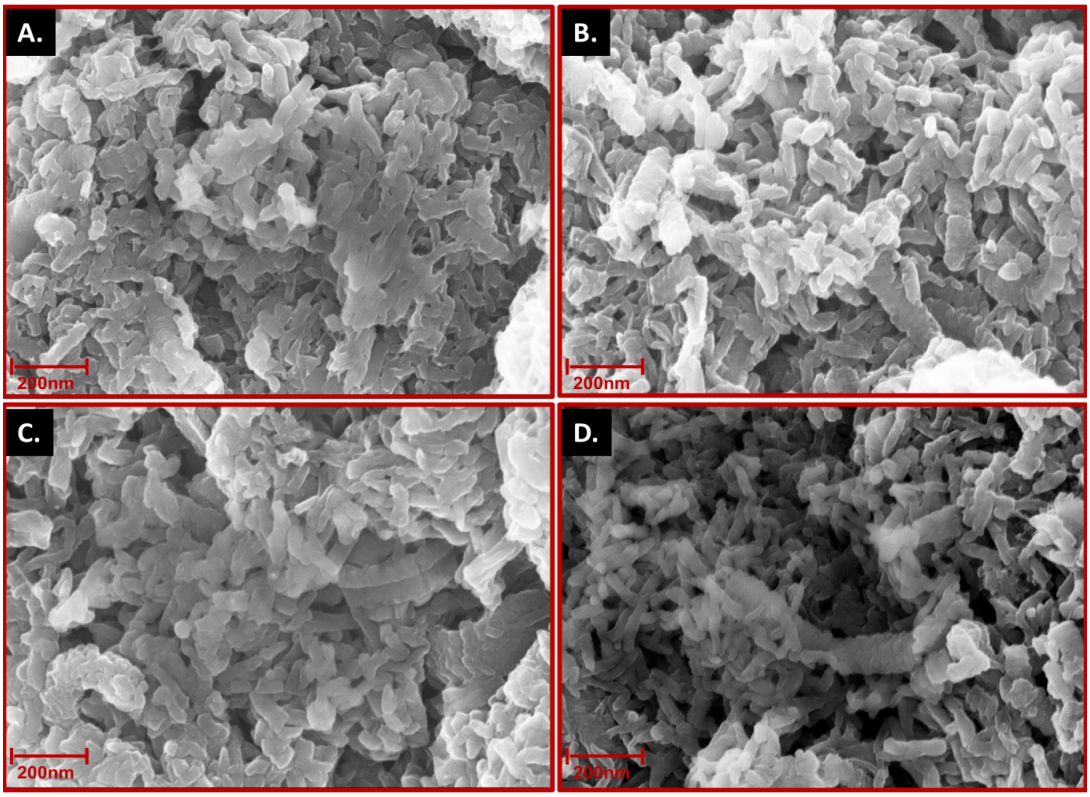

Figure 2: SEM images of (A) PANI@1%MWCNT nanocomposite, (B) PANI@2%MWCNT nanocomposite, (C) PANI@4%MWCNT nanocomposite, and (D) PANI@8%MWCNT nanocomposite.

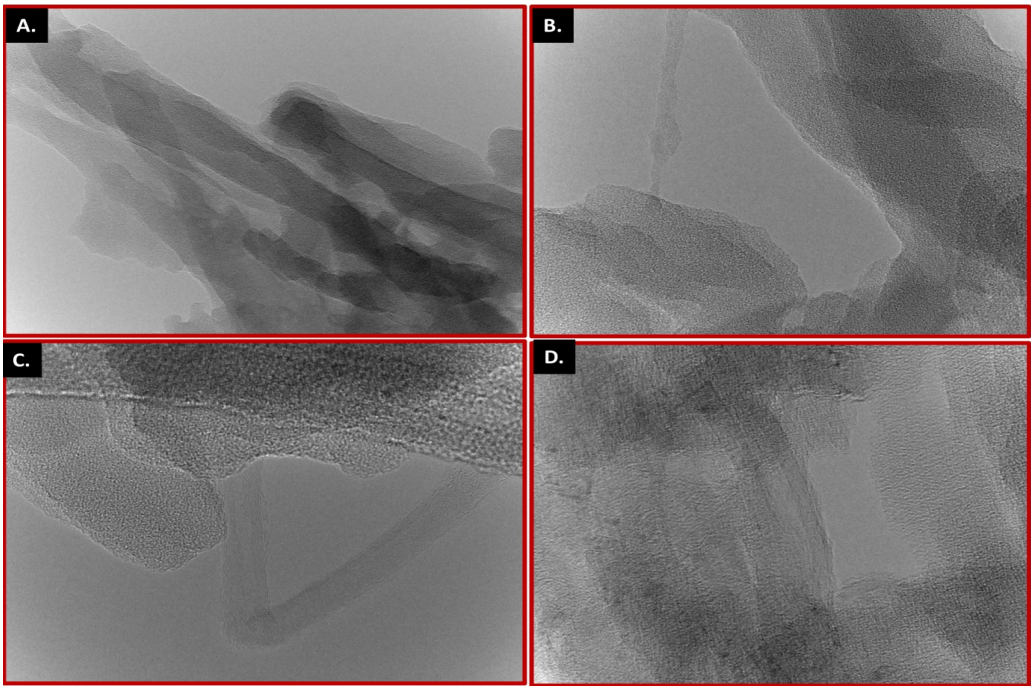

Figure 3: HRTEM images of (A) PANI@1%MWCNT nanocomposite, (B) PANI@2%MWCNT nanocomposite, (C) PANI@4%MWCNT nanocomposite and (D) PANI@8%MWCNT nanocomposite.

3.2. FT-IR Studies

Optical studies were performed to understand the polymer backbone of the polymer nanocomposites and it includes FT-IR and UV-vis spectroscopy. FT-IR spectroscopy helps to elucidate the nature of the interaction amongst PANI and MWCNT and identify the functionalities. Figure 4 depicts the FTIR spectra of PANI/MWCNT nanocomposites. The main characteristic peak of PANI at around 3404 cm^{-1} is associated to the N-H stretching vibration (27). The peak at around 2942 cm^{-1}, 2837 cm^{-1} is due to the asymmetric stretching of CH and symmetric stretching of C-H. The peak at around 1575 cm^{-1} is assigned to C=C stretching mode of the quinoid rings, 1452 cm^{-1} is due to C=C stretching mode of benzenoid rings and the peak at around 1380 cm^{-1} can be related to C-N stretching mode. The peak at around 1050 cm^{-1} and 880 cm^{-1} is attributed to the in-plane and out-of-plane bending vibration of C-H of 1, 4-disubstituted benzenoid ring. Thus it can be inferred that the incorporation of MWCNTs did not affect the polymer backbone. All the obtained peaks were similar as those studied in the literature (30,31) and confirmed the formation of the PANI and its nanocomposites.

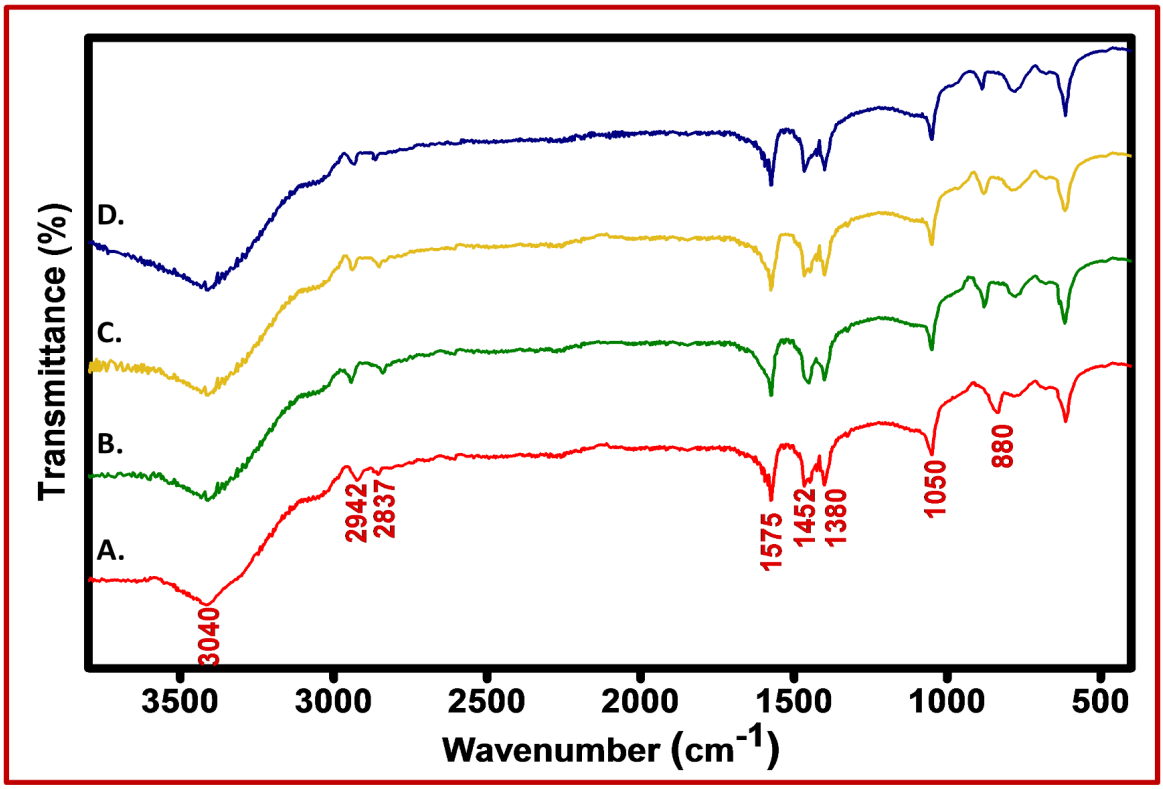

Figure 4: FT-IR spectra of (A) PANI@1%MWCNT nanocomposite, (B) PANI@2%MWCNT nanocomposite, (C) PANI@4%MWCNT nanocomposite and (D) PANI@8%MWCNT nanocomposite.

3.3. UV-Vis Studies

To comprehend the effect of MWCNTs filler on PANI backbone more efficaciously, UV–Vis spectroscopy was performed on all samples. Figure 5 shows the UV-Vis spectra of PANI/MWCNT nanocomposites. The UV-Vis spectrum of PANI in Figure S6 shows absorption peaks at around 342 nm, 435 nm and 860 nm (32). The small absorption peak at around ~342 nm is ascribed to π→π* transition of the benzenoid rings and the shoulder at around ~435 nm signifies polaronic peak indicating the protonation of the polymer and the broad shoulder at ~860 nm shows free carrier tail, which confirms that the presence of MWCNT kept the polymer backbone intact. The PANI/MWCNT nanocomposites demonstrated these characteristic absorption bands but there is a hypsochromic shift of π→π* band. The band which appears at nearly 342 nm in PANI appears at 335 nm, 332, 329 nm, 326 nm in PANI/MWCNT nanocomposites with 1%, 2%, 4% and 8% MWCNTs content. This shift in the *π–π** electronic transition towards shorter wavelength with the addition of the MWCNTs is due to site-selective interactions amongst the quinoid units of PANI and MWCNTs (33, 34). Along with it, the polaronic peaks undergo bathochromic shift as compared to pristine PANI, indicating higher conductivity as the bipolaron/polaron assists in charge transfer processes.

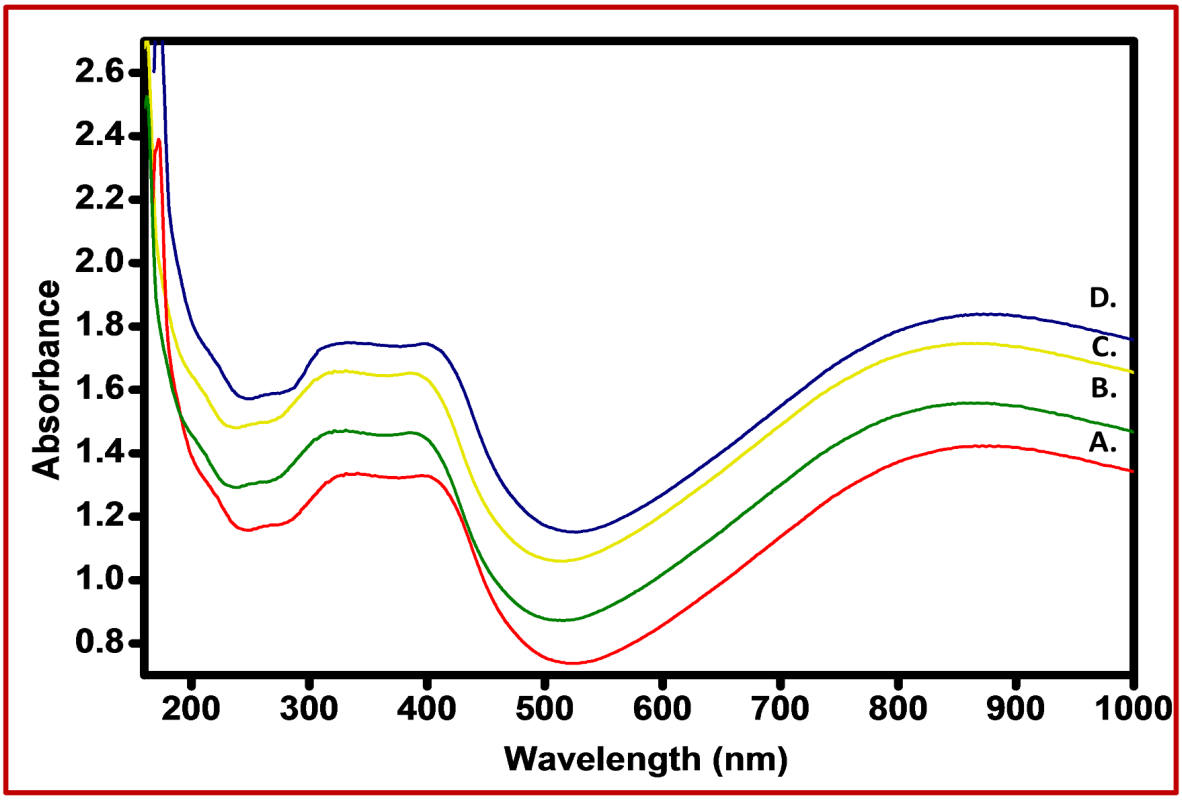

Figure 5: UV-Vis of (A) PANI@1%MWCNT nanocomposite, (B) PANI@2%MWCNT nanocomposite, (C) PANI@4%MWCNT nanocomposite and (D) PANI@8%MWCNT nanocomposite.

3.4. Thermal Analysis

TGA measurement was carried on the nanocomposites to determine the thermal stability enhancements in the nanocomposites after the addition of MWCNTs. This measurement also proved useful to evaluate the maximum possible temperature to endorse the suitable thermal range of the nanocomposites. The thermograms of PANI/MWCNT nanocomposites are shown in Figure 6 and pure PANI is shown in Figure S7. The samples are heated from room temperature up to 700˚C. In pure PANI approximately 15–18 % of weight loss occurs as a consequence of loss of water molecules at around 25˚C until 100˚ C. A slight weight loss is attained up to 400 °C and thereafter a rapid weight loss occurs due to the degradation of the polymer chain. In the case of PANI/MWCNT nanocomposites, the first step weight loss occurs till 100 °C due to loss of water molecules and the second step weight loss occurs till 200 °C due to elimination of dopant. The third step weight loss occurs from 300 °C to 500 °C which involves slow and steady degradation of polymer backbone. The final rapid weight loss occurs due to the complete breakdown of polymer chain till 700 °C. The remaining 30-40% weight left is the char residues of inert materials like the MWCNTs, Fe-catalyst, and some carbonized specks of polymer chain. The thermograms reveal that the thermal stability enhances with the increase in the MWCNTs content. The surface interactions between MWCNTs and PANI increases the thermal stability of the polymer blend, in other words, MWCNTs reduce the mass loss (35, 36). The thermal degradation of PANI is a complex chain process consisting of chain reactions that produce additional active intermediates. MWCNT break these chains at higher temperatures and increase thermal stability and reducing the initial fragmentation of polymer chain. They also indicate significantly enhanced thermal stability of the nanocomposite than that of pure PANI.

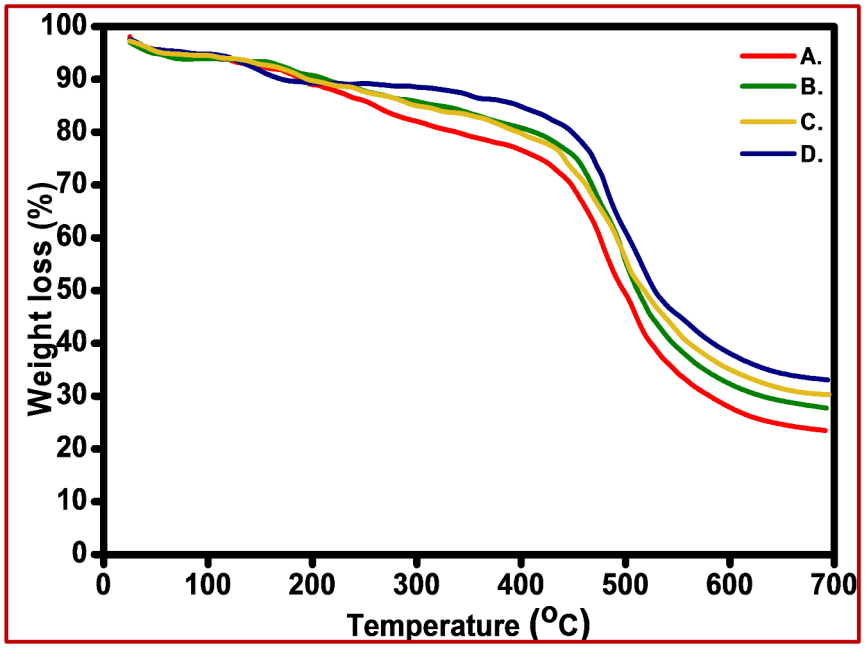

Figure 6: TGA curves of (A) PANI@1%MWCNT nanocomposite, (B) PANI@2%MWCNT nanocomposite, (C) PANI@4%MWCNT nanocomposite and (D) PANI@8%MWCNT nanocomposite.

3.5. Conductivity

The conductivity of the nanocomposites was determined at room temperature. To perform the measurements pellets of approximately the same thickness were made with the help of hydraulic press under identical conditions. Then silver paste was applied on both sides of the pellet to establish contacts for the measurement of bulk resistance. The conductivity was then calculated using the resistance and thickness of pellet through the following equation:

$$\sigma = L/RA$$

where “σ” denotes the conductivity ,“L” denotes the length of the pellet, “R” represents resistance and “A” denotes the cross sectional area of the pellets.

There is continuous increase in conductivity with the increase in the MWCNT content. Such high conductivities of the nanocomposites is attributed to core shell structure, where the micrometer long MWCNTs as core are effectively coated with PANI as shell which is clearly evident from the SEM images. The effectively interacting interface helps to facilitate charge transfer process between the MWCNTs and the conducting emeraldine salt of PANI. MWCNTs prove to be the conducting bridge owing to their extremely conducting behavior and high aspect ratio, joining the PANI individual structures coated over MWCNTs. This further upsurges the coupling amongst the polymer chains and induces enhancements in inter-chain charge transport. This synergistic effect of the two compatible components, PANI and MWCNT leads to raised conductivity of the nanocomposite which is much more than the pure polymer itself thereby profusely improving the electrical properties.

In order to understand the conduction mechanism it is important to understand the structure of both components. In PANI each carbon atom contains an unpaired (π) electron, these electrons overlap and generate charge delocalization over the polymer backbone, creating a pathway for charge mobility throughout the polymer chain (37). This conduction pathway plays a vital role. PANI is conductive in its emeraldine salt state, which is formed by the protonation of the imine group by doping them with acids. This initially form an intermediate bipolar on state by successive rearrangements and then forms a polaron (38, 39). Moreover, MWCNTs being excellent electron acceptors and PANI being a relatively good electron donor, form π- π * between the MWCNTs surface and quinoid unit of PANI (40). It is important to note that undoped form of PANI, *i.e* emeraldine base, which acts as an insulator, has no charge transfer systems in the polymer backbone, thus prohibiting its interaction with MWCNTs (41).

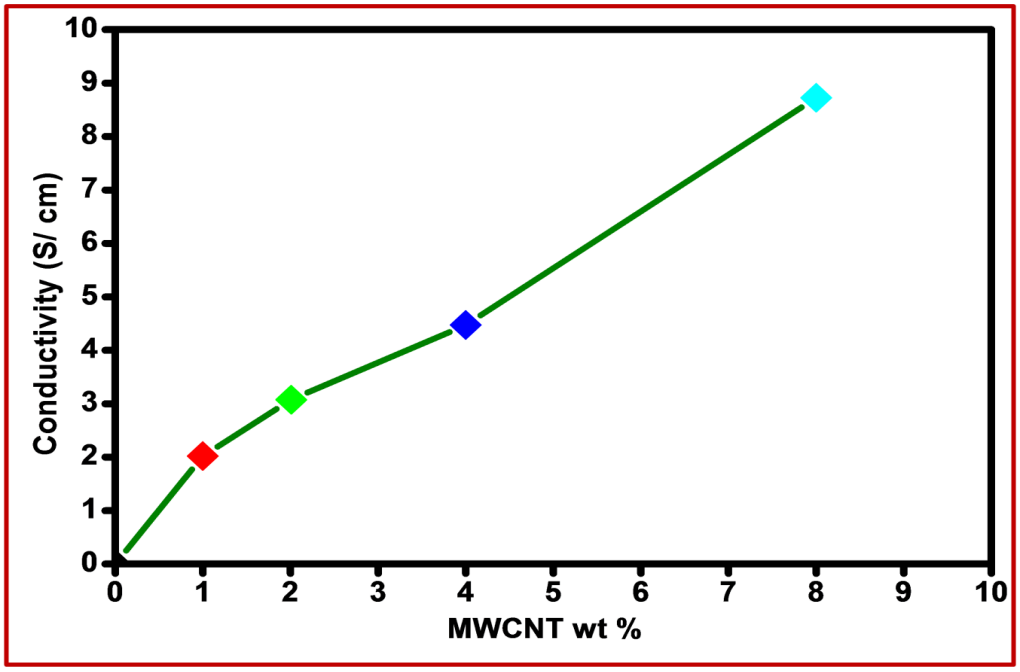

Figure 7: Variation of room temperature conductivity of PANIMWCNT nanocomposites with different MWCNT loadings.

4. CONCLUSION

In the present investigation, PANI/MWCNT nanocomposites with different MWCNTs loading were synthesized by *in-situ* oxidative polymerization. The tubular morphologies of the nanocomposites revealed the core shell structure of homogeneous coating of PANI over MWCNTs. Several parameters were analyzed before deploying the nanocomposites for application perspective. The synergistic effects of PANI and MWCNTs greatly related to the profound enhancements in thermal stability and conductivity of the nanocomposites, thereby keeping the polymer backbone undamaged. The FTIR spectrum that showed the decreased benzoid to quinoid intensity ratio and the blue shift in the π–π *electronic transition in the case of the UV spectrum also confirmed the interaction between the PANI and the MWCNTs. This study suggests that PANI/MWCNT nanocomposites are better electronic materials than pristine PANI, and on increasing the concentration of MWCNTs in PANI changes the behavior of PANI from that of a semiconductor to a metal. Further, as MWCNT doping is increased the thermal stability and conductivity of the PANI/MWCNT nanocomposites is enhanced manifolds.

5. CONFLICT OF INTEREST

The authors declare that the research was conducted in the absence of any commercial or financial relationships that could be construed as a potential conflict of interest.

6. ACKNOWLEDGMENTS

S.J.P would also like to acknowledge DST for providing the funding under INSPIRE-Fellowship Scheme (IF 160064).

7. SUPPLEMENTARY MATERIAL

Supplementary data related to this article consist of XRD patterns of PANI and MWCNT, SEM image of PANI, Raman spectra of PANI and PANI/MWCNT nanocomposite, UV-Vis of PANI, and TGA curve of PANI.

8. REFERENCES

1. Khalil HA, Fizree H, Bhat A, Jawaid M, Abdullah C. Development and characterization of epoxy nanocomposites based on nano-structured oil palm ash. Composites Part B: Engineering. 2013;53:324-33. <URL>

2. Jaymand M. Recent progress in chemical modification of polyaniline. Progress in Polymer Science. 2013;38(9):1287-306. <URL>

3. Bhadra S, Khastgir D, Singha NK, Lee JH. Progress in preparation, processing and applications of polyaniline. Progress in Polymer Science. 2009;34(8):783-810. <URL>

4. Darwish M, Ahmed HM, Mansour D-EA, editors. Thermo-mechanical properties of LDPE/SiO 2 nanocomposites based on chemically functionalized SiO 2 nanoparticles. International Symposium on Electrical Insulating Materials (ISEIM); 2020: IEEE. 241-244. <URL>

5. Abdel-Gawad NM, El Dein AZ, Mansour DEA, Ahmed HM, Darwish MM, Lehtonen M. PVC nanocomposites for cable

insulation with enhanced dielectric properties, partial discharge resistance and mechanical performance. High Voltage. 2020;5(4):463-71. <URL>

6. Mansour D-EA, Abdel-Gawad NM, El Dein AZ, Ahmed HM, Darwish MM, Lehtonen M. Recent advances in polymer nanocomposites based on polyethylene and polyvinylchloride for power cables. Materials. 2020;14(1):66. <URL>

7. Stejskal J, Gilbert R. Polyaniline. Preparation of a conducting polymer (IUPAC technical report). Pure and applied chemistry. 2002;74(5):857-67. <URL>

8. Chiang JC, Macdiarmid AG. Polyaniline - protonic acid doping of the emeraldine form to the metallic regime. Synthetic Metals. 1986;13(1-3):193-205. <URL>

9. Kobayashi T, Yoneyama H, Tamura H. Polyaniline film-coated electrodes as electrochromic display devices. Journal of Electroanalytical Chemistry. 1984;161(2):419-23. <URL>

10. Genies EM, Boyle A, Lapkowski M, Tsintavis C. Polyaniline - a historical survey. Synthetic Metals. 1990;36(2):139-82. <URL>

11. Macdiarmid AG, Chiang JC, Halpern M, Huang WS, Mu SL, Somasiri NLD, et al. Polyaniline - Interconversion of Metallic and Insulating Forms. Molecular Crystals and Liquid Crystals. 1985;121(1-4):173-80. <URL>

12. Iijima S, Ichihashi T. Single-shell carbon nanotubes of 1-nm diameter. Nature. 1993;363(6430):603-5. <URL>

13. Baughman RH, Zakhidov AA, de Heer WA. Carbon nanotubes - the route toward applications. Science. 2002;297(5582):787-92. <URL>

14. Fischer JE, Dai H, Thess A, Lee R, Hanjani NM, Dehaas DL, et al. Metallic resistivity in crystalline ropes of single-wall carbon nanotubes. Physical Review B. 1997;55(8):R4921-R4. <URL>

15. Wang Y, Chen Y, Wen Q, Zheng H, Xu H, Qi L. Electricity generation, energy storage, and microbial-community analysis in microbial fuel cells with multilayer capacitive anodes. Energy. 2019;189:116342. <URL>

16. Zhang H, He B, Tang Q, Yu L. Bifacial dye-sensitized solar cells from covalent-bonded polyaniline–multiwalled carbon nanotube complex counter electrodes. Journal of Power Sources. 2015;275:489-97. <URL>

17. Al-badri M, Albdiry M. Electrochemical performance of ternary s-GN/PANI/CNTs nanocomposite as supercapacitor power electrodes. Periodicals of Engineering and Natural Sciences. 2020;8(4):2484-9. <URL>

18. Zou L, Lan C, Yang L, Xu Z, Chu C, Liu Y, et al. The optimization of nanocomposite coating with polyaniline coated carbon nanotubes on fabrics for exceptional electromagnetic interference shielding. Diamond and Related Materials. 2020;104:107757. <URL>

19. Roy A, Ray A, Sadhukhan P, Naskar K, Lal G, Bhar R, et al. Polyaniline-multiwalled carbon nanotube (PANI-MWCNT): Room temperature resistive carbon monoxide (CO) sensor. Synthetic Metals. 2018;245:182-9. <URL>

20. Wang CY, Mottaghitalab V, Too CO, Spinks GM, Wallace GG. Polyaniline and polyaniline–carbon nanotube composite fibres as battery materials in ionic liquid electrolyte. Journal of Power Sources. 2007;163(2):1105-9. <URL>

21. Huang Y, Lu J, Kang S, Weng D, Han L, Wang Y. Synthesis and application of MnO2/PANI/MWCNT ternary nanocomposite as an electrode material for supercapacitors. Int J Electrochem Sci. 2019;14:9298-310. <URL>

22. Maity D, Manoharan M, Kumar RTR. Development of the PANI/MWCNT Nanocomposite-Based Fluorescent Sensor for Selective Detection of Aqueous Ammonia. Acs Omega. 2020;5(15):8414-22. <URL>

23. Huangfu Y, Ruan K, Qiu H, Lu Y, Liang C, Kong J, et al. Fabrication and investigation on the PANI/MWCNT/thermally annealed graphene aerogel/epoxy electromagnetic interference shielding nanocomposites. Composites Part A: Applied Science and Manufacturing. 2019;121:265-72. <URL>

24. Saeed MS, Seyed-Yazdi J, Hekmatara H. Fe2O3/Fe3O4/PANI/MWCNT nanocomposite with the optimum amount and uniform orientation of Fe2O3/Fe3O4 NPs in polyaniline for high microwave absorbing performance. Journal of Alloys and Compounds. 2020;843. <URL>

25. Paul SJ, Gupta BK, Chandra P. Probing the electrical and dielectric properties of polyaniline multi-walled carbon nanotubes nanocomposites doped in different protonic acids. Polymer Bulletin. 2021;78:5667-83. <URL>

26. Wu T-M, Lin Y-W. Doped polyaniline/multi-walled carbon nanotube composites: Preparation, characterization and properties. Polymer. 2006;47(10):3576-82. <URL>

27. Phang SW, Tadokoro M, Watanabe J, Kuramoto N. Synthesis, characterization and microwave absorption property of doped polyaniline nanocomposites containing TiO2 nanoparticles and carbon nanotubes. Synthetic Metals. 2008;158(6):251-8. <URL>

28. Endo M, Takeuchi K, Hiraoka T, Furuta T, Kasai T, Sun X, et al. Stacking nature of graphene layers in carbon nanotubes and nanofibres. Journal of Physics and Chemistry of Solids. 1997;58(11):1707-12. <URL>

29. Zhang X, Zhang J, Liu Z. Tubular composite of doped polyaniline with multi-walled carbon nanotubes. Applied Physics A. 2005;80:1813-7. <URL>

30. Konyushenko EN, Stejskal J, Trchova M, Hradil J, Kovarova J, Prokes J, et al. Multi-wall carbon nanotubes coated with polyaniline. Polymer. 2006;47(16):5715-23. <URL>

31. Lefrant S, Baltog I, de la Chapelle ML, Baibarac M, Louarn G, Journet C, et al. Structural properties of some conducting polymers and carbon nanotubes investigated by SERS spectroscopy. Synthetic metals. 1999;100(1):13-27. <URL>

32. Li Y, Peng H, Li G, Chen K. Synthesis and electrochemical performance of sandwich-like polyaniline/graphene composite nanosheets. European Polymer Journal. 2012;48(8):1406-12. <URL>

33. Cochet M, Maser WK, Benito AM, Callejas MA, Martinez MT, Benoit JM, et al. Synthesis of a new polyaniline/nanotube composite: "in-situ" polymerisation

and charge transfer through site-selective interaction. Chemical Communications. 2001(16):1450-1. <URL>

34. Ghatak S, Chakraborty G, Meikap A, Woods T, Babu R, Blau W. Synthesis and characterization of polyaniline/carbon nanotube composites. Journal of Applied Polymer Science. 2011;119(2):1016-25. <URL>

35. Pekdemir ME, Kök M, Qader IN, AYDOĞDU Y. Preparation and physicochemical properties of mwcnt doped polyvinyl chloride/poly (ε-caprolactone) blend. Journal of Polymer Research. 2022;29(4):109. <URL>

36. Haruna H, Pekdemir ME, Tukur A, Coşkun M. Characterization, thermal and electrical properties of aminated PVC/oxidized MWCNT composites doped with nanographite. Journal of Thermal Analysis and Calorimetry. 2020;139:3887-95. <URL>

37. Heeger AJ. Nobel Lecture: Semiconducting and metallic polymers: The fourth generation of polymeric materials. Reviews of Modern Physics. 2001;73(3):681-700. <URL>

38. Bhadra S, Khastgir D, Singha NK, Lee JH. Progress in preparation, processing and applications of polyaniline. Progress in Polymer Science. 2009;34(8):783-810. <URL>

39. Wallace G, Spinks G, Teasdale P. Conductive electroactive polymers, Technomic Pub. Co. Inc, USA. 1997:107-25.

40. Zengin H, Zhou W, Jin J, Czerw R, Smith Jr DW, Echegoyen L, et al. Carbon nanotube doped polyaniline. Advanced materials. 2002;14(20):1480-3. <URL>

41. Virji S, Kaner RB, Weiller BH. Hydrogen sensors based on conductivity changes in polyaniline nanofibers. The Journal of Physical Chemistry B. 2006;110(44):22266-70. <URL>

JOTCS A
Journal of the Turkish Chemical Society
Section: A
Chemistry

TURKISH CHEMICAL SOCIETY

Comparison of Major Bioactive Components of Various Solvent Extracts from Algerian *Bunium incrassatum* Umbellules and Antioxidant Activity

Fethi TOUL[1]*, Amina DJENDAR[2]

[1] Mohammed Tahri University, Laboratory of Valorization of Plant Resources and Food Security in Semi-Arid Areas, Department of Biology, Bechar, 08000, Algeria

[2]Abu Bakr Belkaïd University, Department of Biology, Tlemcen, 13000, Algeria

Abstract: The present study was designed to examine the chemical composition and the antioxidant activity of *Bunium incrassatum* extracts prepared in five different solvents with increasing polarities. RP-HPLC analysis resulted in the identification of 12 phenolic compounds, including 8 phenolic acids (caffeic acid, ellagic acid, ferulic acid, gallic acid, rosmarinic acid, sinapic acid, syringic acid, and vanillic acid) and 4 flavonoids (catechin, hesperetin, luteolin, and quercetin). Two different test systems were used to assess the antioxidant activity: DPPH and β-carotene/linoleic acid assays. Methanol extract exhibited the highest DPPH scavenging potential and even low inhibitory effect against β-carotene bleaching, whereas chloroform extract showed the highest effect against β-carotene bleaching and a weak scavenging potential. As expected, methanol extract recorded the highest content of total phenolics (26.57±0.15 mg GAE/g E), while chloroform extract has been found to be the richest in flavonoids.

Keywords: *Bunium incrassatum*, umbellules, antioxidant activity, phenolic compounds, RP-HPLC.

Submitted: October 4, 2022. **Accepted:** March 14, 2023.

Cite this: Toul F, Djendar A. Comparison of Major Bioactive Components of Various Solvent Extracts from Algerian *Bunium incrassatum* Umbellules and Antioxidant Activity. JOTCSA. 2023;10(2):505–512.

DOI: https://doi.org/10.18596/jotcsa.1184342.

***Corresponding author. E-mail:** toul.fethi@univ-bechar.dz

1. INTRODUCTION

For several years, numerous products in the pharmaceutical, cosmetic, and food industries have been the subject of growing concern, criticism, and even health scandals because of the harmful effects of synthetic and chemical compounds they contain (1). In addition, consumers are paying more attention to their lifestyle and environment by changing the way they consume (2). For these reasons, the quest for natural products in the plant kingdom, especially for phenolic compounds, for their physiological properties affecting human health, including antioxidant activity, is at its height (3).

Phenolics' family includes phenolic acids, flavonoids, anthocyanins, highly polymerized substances such as tannins, and other compounds. Flavonoids and phenolic acids are highly valued and used in the pharmaceutical and food industries due to their potent antimicrobial and antioxidant properties that benefit human health (4,5).

The genus Bunium includes seven species, four of which are endemic to the Algerian flora (6). *Bunium incrassatum* (Boiss.) Batt. & Trab., vernacularly called 'Talghouda', is widely spread and its tubers are used for the treatment of thyroid in Algeria, taken alone or in mixtures of two or more ingredients such as honey, olive oil, and goat milk (7). In addition, dried and powdered tubers are regarded as astringent, anti-diarrheic, anti-hemerroidal, and for bronchitis and cough treatment (8). In the collective memory of Algerian society, it is considered as a symbol of misery which recalls the famine of the years of poverty, especially during the Second World War and the period of national revolution between 1954-1962. It was consumed as bread after being powdered and mixed with wheat flour (9).

Despite the socio-economic importance and historical position of *B. incrassatum* within Algerian society, only a few studies have been conducted to investigate its biological activities: the effect of tubers, aerial parts, and seeds' extracts on biochemical, hematological, ovarian and uterine parameters (10,11), antimicrobial activity (8), antioxidant activity (12–14), and chemical composition of extracts (8,12,14) and essential oil (13,15) of tubers.

The present study was conducted to investigate, for the first time, the phenolic profile of the flowering heads of *B. incrassatum* by RP-HPLC, as well as the antioxidant activity of their extracts.

2. EXPERIMENTAL

2.1. Plant Material

The umbrella-shaped clusters (flowering heads) were collected in April 2016, from Djebala, Tlemcen, Algeria. Umbellules were separated from clusters after being identified at the laboratory of botany, Department of Biology, Faculty of Nature, Life, Earth, and Universe Sciences, Abu Bakr Belkaid, University of Tlemcen, Algeria.

Figure 1: A flowering head of *B. incrassatum*.

2.2. Extraction

Twenty grams of freshly ground shade air-dried umbellules were sequentially extracted under reflux for 1 hour with increasing polarity solvents (chloroform, ethyl acetate, acetone, methanol, then water). The extracts were then concentrated to dryness, resolubilized in a few milliliters of their extraction solvents and stored at 4 °C for later use. The following solid residues were obtained, respectively: acetone extract (AcE): 330 mg, chloroform extract (CE): 390 mg, ethyl acetate extract (EAE): 531 mg, methanol extract (ME): 840 mg, and aqueous extract (AqE): 2.56 g.

2.3. Total Phenolic Content (TPC)

The estimation of total phenolics was carried out in triplicate according to the traditional method (16). Briefly, a 200 µL aliquot of extract was mixed with 1 mL of 10 times aqueous diluted Folin-Ciocalteu reagent and 0.8 mL of a 7.5% sodium carbonate solution. The absorbance was measured at 765 nm after 30 minutes of incubation. Gallic acid was used as a standard for the calibration curve. The total phenolic content was expressed as milligrams of gallic acid equivalents per gram of extract (mg GAE/g E).

2.4. Total Flavonoid Content (TFC)

As described by Zhishen et al. (1999) (17), at room temperature, a volume of 500 µL of extract was mixed with 1500 µL of distilled water and 150 µL of 5% $NaNO_2$. After 5 min, 150 µL of $AlCl_3$ 10% were added. Six minutes later, 500 µL of NaOH (1 M) were added. After being thoroughly shaken, the absorbance of the mixture was immediately measured at 510 nm. The total flavonoid content of extracts was expressed as milligrams of catechin equivalents per gram of extract (mg CE/ g E).

2.5. Condensed Tannin Content (CTC)

Condensed tannins were analyzed by the conventional method of Julkunen-Titto. (1985) (18). An aliquot of 50 µL extract was added to 1500 µL of

a 4% (m/v) vanillin/methanol solution. After being stirred, 750 µL of concentrated hydrochloric acid was added. The absorbance was measured at 550 nm after 20 minutes of incubation. Tannin content was expressed as milligrams of tannic acid equivalents per gram of extract (mg TAE/g E).

2.6. DPPH Radical Scavenging Assay

Fifty microliters of various concentrations of extracts were mixed with 1950 µL of a 0.025 g/L DPPH methanolic solution. A negative control, in which the extract was replaced by methanol, was also prepared. After 30 minutes of dark incubation, the absorbance was measured at 515 nm against a methanol blank (19). The radical scavenging activity (RSA) was calculated as the percentage of DPPH discoloration using the following equation:

$$RSA(\%) = (A_C - A_S/A_C) \times 100$$

Where A_C is the control's absorbance and A_S is the absorbance of the tested extract. The 50% inhibitory concentrations (IC_{50}) were then computed using the regression equation of the RSA(%)=f(C) graph. BHA was used as the reference compound.

2.7. β-carotene Bleaching Assay

The antioxidant potential of extracts in apolar conditions was assessed using β-carotene-linoleate model system as described by Moure et al. (2000) (20). β-carotene (0.2 mg) was dissolved in 1 mL of chloroform and mixed with 20 µL of purified linoleic acid and 200 mg of Tween 40 emulsifier. Chloroform was then evaporated, and the resulting mixture was immediately diluted in 100 mL of distilled water. Four milliliters of this reaction mixture were mixed with 200 µL of various extract concentrations. After being stirred, the absorbance was immediately measured (t=0 min) at 470 nm, against a blank consisting of the emulsion without β-carotene. The capped tubes were placed in a water bath at 50 °C for 120 min. A negative control consisting of 200 µL of the extract's solvent instead of extract was also prepared. The antioxidant activity (AA) was calculated using the following equation:

$$AA = \left[\frac{\left(A_{S120} - A_{C120)}\right)}{(A_{C0} - A_{C120})}\right] \times 100$$

Where A_{S120} is the sample absorbance at 120 min; A_{C120} is the negative control absorbance at 120 min; A_{C0} is the negative control absorbance at 0 min.

2.8. Hydrolysis of Extracts for HPLC Analysis

The selected extracts for HPLC analysis (the most potent ones) were hydrolyzed under reflux in a 1.2 M HCl water bath for 1 h (21). Hydrolyzed samples were then filtered through a 0.45 µm syringe-driven filter prior to injection.

2.9. Chromatographic Identification of Phenolic Compounds by HPLC

A 20-µL sample aliquot was analyzed using high performance liquid chromatography system (YL 9100 HPLC system, Korea). Reversed-phase chromatography was performed on a C18 column (250 × 4.6 mm; 5 µm). Data were monitored and analyzed using Clarity data–processing system. The mobile phase consisted of solvent A (water/formic acid 0.4%) and solvent B (acetonitrile). Solvents gradient was used as followed: 0–2 min, 1% B; 2–15 min, 7% B; 15–25 min, 20% B; 25-35 min, 40% B; 35-46 min, 100% B; 46-47 min, 100% B; 47-48 min, 1% B; 48-55 min, 1% B. The flow rate was 1.2 mL/min. UV-detection was performed at 280 nm. Phenolic compounds were identified according to their retention times as well as to their spectral matching with 18 reference standards (14).

2.10. Statistical Analysis

Except for the extraction and chromatographic analyses, all data were expressed as mean ± standard derivation (SD) of three replicates and were statistically analyzed using Excel software.

3. RESULTS AND DISCUSSION

3.1. Results

3.1.1. Total phenolic, flavonoid, and tannin contents

The results of total phenolics, as shown in Table 1, of *Bunium incrassatum* umbellues extracts estimated following the Folin-Ciocalteu method were, decreasingly, methanol (26.57±0.15 mg GAE/g E), ethyl acetate (18.08±0.21 mg GAE/g E), aqueous (17.46±0.43 mg GAE/g E), acetone (11.78±0.01 mg GAE/g E), and chloroform at the end with 11.77±0.09 mg GAE/g E. Differently, the flavonoids dosing results showed the highest content in chloroform extract (19.74±0.37 mg CE/g E), followed by ethyl acetate and methanol extracts. However, aqueous extract recorded the highest tannin content (12.18±0.02 mg TAE/g E), closely followed by methanol extract (12.03±0.02 mg TAE/g E).

3.1.2. Antioxidant activity

For the antioxidant activity assessment, two different model systems were used: the DPPH and β-carotene bleaching assays. The antioxidant potential of the different solvent extracts is inversely proportional to IC50 values. According to the results shown in Table 1, in the DPPH assay, methanol extract showed the highest scavenging potential (1.65±0.18 mg/mL), followed by ethyl acetate extract (1.75±0.13 mg/mL), and the remaining extracts' potentials decreased according to the following order: AqE>CE>AcE. However, the β-carotene bleaching assay indicated a totally different order as follows: CE>EAE>ME>AcE>AqE.

Table 1: Phenolic contents and antioxidant potentials of *B. incrassatum* extracts.

Extracts	Yields (%)	TPC[B] (mg GAE/g E)	TFC[B] (mg CE/g E)	CTC[B] (mg TAE/g E)	IC50[B,C] DPPH (mg/mL)	IC50[B,C] β-Carotene (mg/mL)
Aqueous	12.8	17.46±0.43	9.93±0.12	12.18±0.06	2.05±0.09	4.62±0.16
Methanol	4.2	26.57±0.15	13.79±0.24	12.03±0.02	1.65±0.18	3.09±0.03
Acetone	1.65	11.78±0.01	5.35±0.16	4.77±0.01	2.48±0.11	3.34±0.20
Chloroform	1.95	11.77±0.09	19.74±0.37	7.36±0.01	2.34±0.21	2.05±0.02
Ethyl acetate	2.65	18.08±0.21	16.65±0.15	3.12±0.02	1.75±0.13	2.13±0.10
BHA[A]	/	/	/	/	0.09±0.00	0.24±0.02

[A]Reference compound; [B]mean±SD (n=3); [C]Concentration that showed 50% of activity.

3.2. Discussion

Plant phenolics, as bioactive compounds with potent antioxidant properties and marked effects in the prevention of diseases associated with oxidative stress such as cancer, are the subject of growing interest. Due to their physicochemical properties, there is no universal extraction procedure suitable for the extraction of all plant polyphenols. It is generally known that the solubility of polyphenols depends on the chemical nature of the plant sample as well as the polarity of used solvents (22). No results treating the chemical composition or biological activities of the umbellules' extracts of *B. incrassatum* were found. All the existing ones were about tubers and aerial parts' extracts and essential oils.

The yield of chemical extraction is widely known to be dependent on the solvent's polarity, pH, extraction time, and temperature, as well as the chemical composition of the sample. The solvent and the chemical characteristics of the sample are the two most relevant parameters under the same extraction time and temperature. Previously, solvents such as methanol, ethanol, butanol, acetone, chloroform, and water were extensively utilized for polyphenols' extraction (14,23). The yield results of different solvent extracts of *B. incrassatum* showed the highest yield in aqueous extract, three and four times more than methanol and ethyl acetate extracts, respectively. These results are in accordance with those of Dehimi et al. (2020) (12), where aqueous extract of *B. incrassatum* tubers showed the highest yield (24.48%), much more than methanol and acetone extracts, and are in discordance with those of our previous study (14), in which methanol extract of *B. incrassatum* seeds showed two times more yield than aqueous and chloroform extracts. As can be seen, no relationship between yields and phenolic content was observed. An increase in extraction yield didn't lead to an increase in TPC, TFC, and/or CTC. Even with three and four times less yields, methanol and ethyl acetate extracts showed higher contents of TPC than aqueous extract, which showed the highest CTC. In the same way, chloroform and ethyl acetate showed, respectively, the highest TFC. These results are in discordance with the previous study (14) where methanol extract of *B. incrassatum* seeds showed the highest extraction yield (7.1%), TPC (185.04±4.00 mg GAE/g E), and CTC (33.42±3.56 mg TAE/g E), and also with those reported by Dehimi et al. (2020) (12) on *B. incrassatum* tubes' extracts prepared in different polarity solvents where acetone was shown as the best solvent of total phenolics, flavonoids, and even tannins followed by methanol and water as the second and third best ones. Water frequently records the highest yields because when it is used as the extraction solvent, a large number of inorganic salts and polysaccharide impurities dissolve over and above amides, alcohols, and carboxylic acids (24). However, the variation in solvent ranking towards phenolic content (TPC, TFC, and CTC) might be attributed to the polarity of phenolic compounds in the different organs (umbellules, seeds, and tubers), as well as the environmental circumstances under which the plants grew.

The assessment of antioxidant activity through the DPPH assay showed that methanol extract was the most potent (IC50=1.65±0.18 mg/mL), followed by ethyl acetate extract (1.75±0.13 mg/mL). These IC50 are ten times weaker as compared to the reported results of Algerian *B. incrassatum* seeds' extracts (14) and even weaker than that of the used reference compound (BHA, 0.09±0.00 mg/mL), known as a strong antioxidant. The scavenging potential increased with the increasing concentrations in a dose-dependent manner and was much higher than those reported by Dehimi et al. (2020) (12) and even higher than four different species of Bunium from Turkey (22). It has been proven that the antioxidant activity of plant extracts is related to their phenolic content, suggesting a correlation between TPC and antioxidant activity (25). The chromatographic

analysis of methanol extract (Figure 2) revealed the presence of 06 phenolic compounds: four phenolic acids (gallic acid, syringic acid, ellagic acid, and sinapic acid), a flavone (luteolin), and a flavonol (quercetin). For ethyl acetate extract (Figure 4), seven compounds were identified: 06 phenolic acids (gallic acid, caffeic acid, rosmarinic acid, vanillic acid, syringic acid, and ferulic acid) and a flavanone (hesperetin). Gallic acid was identified in the two extracts but as the major absorbing peak, by far, in methanol chromatogram. Nickavar & Esbati (2012) reported that gallic acid is a strong DPPH scavenger (5.18 µg/mL) and a weak inhibitor of β-carotene bleaching (570 µg/mL) (26). It was also reported that the mass fraction solubility of gallic acid in methanol is 18 times higher than in water and 21 times higher than in ethyl acetate at 25°C, and increases smoothly with temperature (27). However, gallic acid is practically insoluble in chloroform. Ellagic acid and quercetin have been shown to be more effective DPPH scavengers than gallic acid (28). Koleva et al. (2003) have found that if rosmarinic acid and caffeic acid, which are strong antioxidants in polar conditions, were tested only by the β-carotene bleaching assay, they would be considered as weak antioxidants (29). In Figure 4, syringic acid, represented as the strongest absorbing compound's peak, showed in a previous study a strong radical scavenging activity, 1.53 times higher than that of ascorbic acid, in polar environments and a weak activity in lipidic medium (30). Otherwise, chloroform extract, after being the second weaker extract in the methanolic medium of DPPH, exhibited the highest inhibitory potential against β-carotene bleaching, followed by ethyl acetate extract, which can be due to the low polarity of lipophilic compounds soluble in chloroform and highly effective in β-carotene-linoleic acid emulsion system than in methanolic DPPH medium. The chromatogram of chloroform extract (Figure 3) shows the presence of 06 phenolic compounds: three phenolic acids (gallic acid, caffeic acid, and sinapic acid), a flavone (luteolin), a flavanol (catechin), and a flavanone (hesperetin). Two studies reported that chloroform was useful for the extraction of flavonoids, flavonols and phenolic acids (31,32). As for other species, luteolin, quercetin, and syringic acid had been identified in the aerial parts (including flowers) of *Bunium brachyactis*, *B. microcarpum*, and *B. pinnatifolium*, respectively (33). Luteolin, as the main absorbing compound's peak in chloroform extract, is known to be soluble in organic solvents and sparingly soluble in polar ones (34). Von Gadow et al. (1997) reported that in equimolar concentrations, luteolin was slightly more potent than BHA, 33% more potent than vanillic acid, 37% more potent than ferulic acid, and 61% more potent than syringic acid in the β-carotene-linoleic acid emulsion system (35). Sinapic acid has also been shown to have a strong inhibitory effect against β-carotene bleaching and a low DPPH scavenging potential (28).

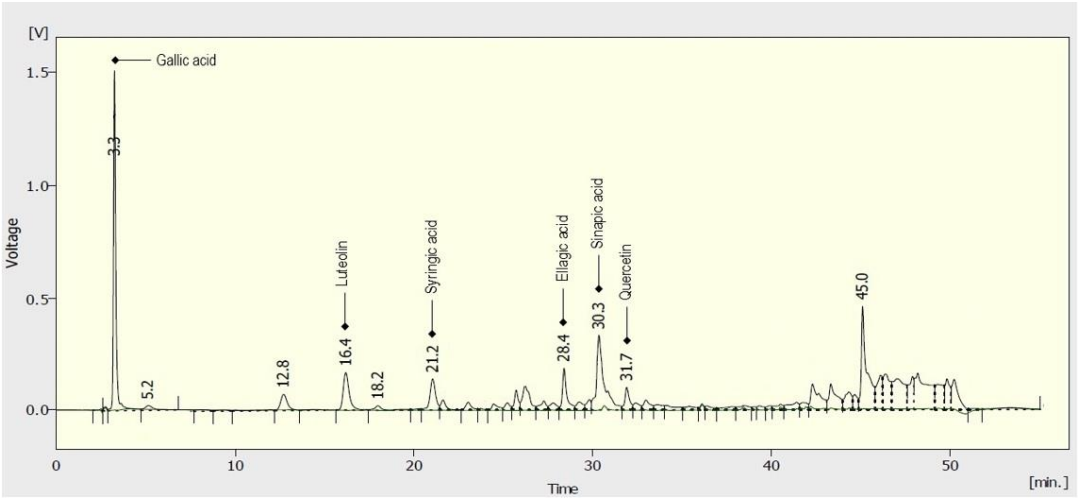

Figure 2: HPLC chromatogram of methanol extract.

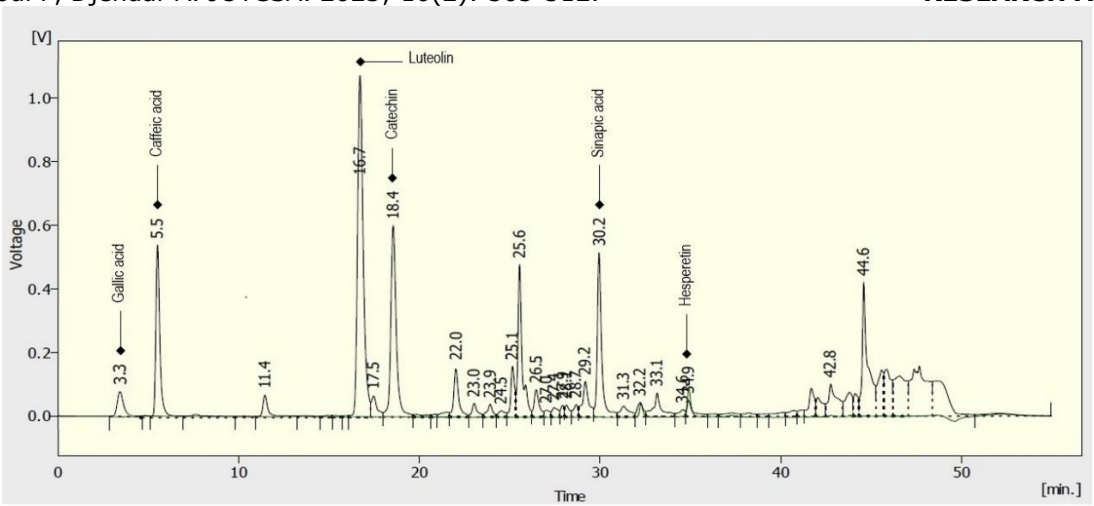

Figure 3: HPLC chromatogram of chloroform extract.

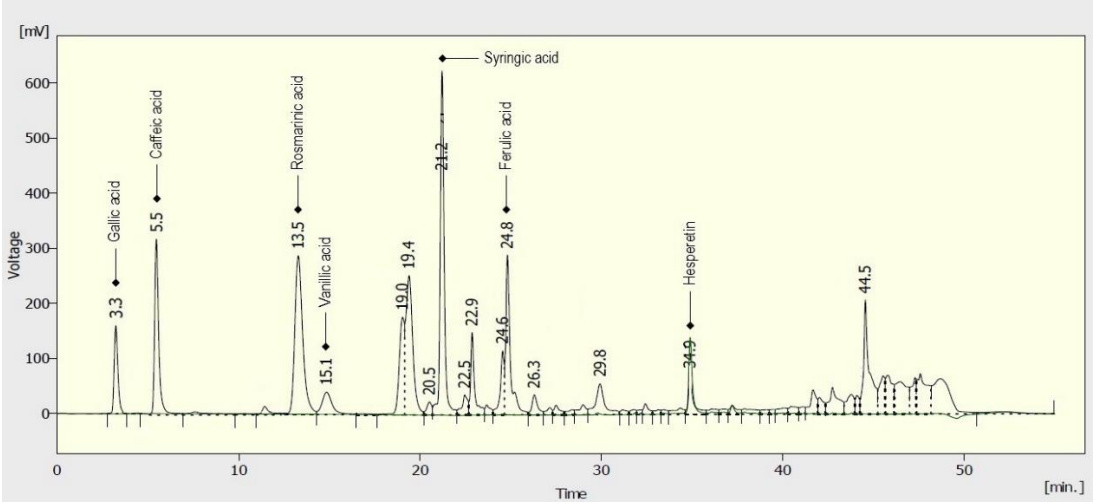

Figure 4: HPLC chromatogram of ethyl acetate extract.

4. CONCLUSION

The present study reports for the first time the quantitative profiles of different solvent extracts of *B. incrassatum* umbellules: TPC, TFC, CTC and the qualitative profiles of phenolics contained in methanol, chloroform, and ethyl acetate extracts due to their high antioxidant potentials. These results support the previous studies showing that the genus *Bunium* is considered as a good source of bioactive compounds that requires further investigation.

5. REFERENCES

1. Jansen T, Claassen L, van Kamp I, Timmermans DRM. 'All chemical substances are harmful.' public appraisal of uncertain risks of food additives and contaminants. Food Chem Toxicol. 2020;136:110959. Available from: <DOI>

2. Carocho M, Morales P, Ferreira ICFR. Natural food additives: Quo vadis? Trends Food Sci Technol. 2015;45(2):284–95. Available from: <DOI>

3. Khatua S, Mitra P, Chandra S, Acharya K. In Vitro Protective Ability of Ramaria aurea Against Free Radical and Identification of Main Phenolic Acids by HPLC. J Herbs Spices Med Plants. 2015;21(4):380–91. Available from: <DOI>

4. Siddiqui MS, Memon AA, Memon S, Baloch SG. Cuscuta reflexa as a Rich Source of Bioactive Phenolic Compounds. J Herbs Spices Med Plants. 2017;23(2):157–68. Available from: <DOI>

5. Pandey MM, Vijayakumar M, Rastogi S, Rawat AKS. Phenolic Content and Antioxidant Properties of Selected Indian Spices of Apiaceae. J Herbs Spices Med Plants. 2012;18(3):246–56. Available from: <DOI>

6. Quezel P, Santa S. Nouvelle flore de l'Algérie et des régions désertiques et Méridionales, Tome II. Edition CNRS, Paris. Paris; 1963.

7. Taïbi K, Ait Abderrahim L, Helal F, Hadji K. Ethnopharmacological study of herbal remedies used for the management of thyroid disorders in Algeria. Saudi Pharm J. 2021;29(1):43–52. Available from: <DOI>

8. Bousetla A, Zellagui A, Derouiche K, Rhouati S. Chemical constituents of the roots of Algerian Bunium incrassatum and evaluation of its antimicrobial activity. Arab J Chem. 2015;8(3):313–6. Available from: <DOI>

9. Robin M. Enquête sur le niveau de vie des populations rurales constantinoises de la conquête jusqu'en 1919. Essai d'histoire économique et sociale. University Press of France; 1962.

10. Attoui N, Berroukeche F, Guedri K, Toul F. Effect of the Roots of Algerian Bunium Incrassatum on Biological, Biochemical and Histological Parameters of Mature Female Rats. Plant Arch. 2021;21(1):201–9. Available from: <DOI>

11. Chentouh S, Boulahbel S, Ouldjaoui A, Hammoudi N, Djebaili H, Adjal F. Effect of organic extracts of Bunium incrassatum on the hematological, ovarian and uterine parameters of mature female rabbit. J Fundam Appl Sci. 2017;9(3):1618–33. Available from: <DOI>

12. Dehimi K, Djoudi Z, Boulaouad A, Maadadi AR, Dahamna S, Khennouf S. A contribution to the valorization of two medicinal plants: Atriplex halimus Sub. Sp. Schweinfurthii and Bunium incrassatum, growing in the region of M'sila (North-East Algeria). Indian J Nov Drug Deliv. 2020;12(4):208–16. Available from: <DOI>

13. Hayet EK, Hocine L, Meriem EK. Chemical composition and biological activities of the essential oils and the Methanolic extracts of Bunium Incrassatum and Bunium Alpinum from Algeria. J Chil Chem Soc. 2017;62(1):3335–41. Available from: <DOI>

14. Toul F, Djendar A, Seladji M, Berroukeche F. Algerian Bunium incrassatum Seeds: Effects of Extraction Solvent Polarity on Phenolic Profile and Antioxidant Activity. J Turkish Chem Soc Sect A Chem. 2022;9(2):475–82. Available from: <DOI>

15. Bousetla A, Kurkcuoglu M, Konuklugil B, Baser KHC, Rhouati S. Composition of essential oil from Bunium incrassatum from Algeria. Chem Nat Compd. 2014;50(4):753–5. Available from: <DOI>

16. Singleton VL, Rossi JA. Colorimetry of total phenolics with phosphomolybdic-phosphotungstic acid reagents. Am J Enol Vitic [Internet]. 1965;16(3):144–58. Available from: <DOI>

17. Zhishen J, Mengcheng T, Jianming W. The determination of flavonoid contents in mulberry and their scavenging effects on superoxide radicals. Food Chem. 1999;64(4):555–9. Available from: <DOI>

18. Julkunen-Tiitto R. Phenolic constituents in the leaves of northern willows: methods for the analysis of certain phenolics. J Agric Food Chem. 1985;33(2):213–7. Available from: <DOI>

19. Sánchez-Moreno C, Larrauri JA, Saura-Calixto F. A procedure to measure the antiradical efficiency of polyphenols. J Sci Food Agric. 1998;76(2):270–6. Available from: <DOI>

20. Moure A, Franco D, Sineiro J, Domínguez H, Núñez MJ, Lema JM. Evaluation of extracts from Gevuina avellana hulls as antioxidants. J Agric Food Chem. 2000;48(9):3890–7. Available from: <DOI>

21. Hertog MGL, Hollman PCH, Venema DP. Optimization of a quantitative HPLC determination of potentially anticarcinogenic flavonoids in vegetables and fruits. J Agric Food Chem. 1992;40(9):1591–8. Available from: <DOI>

22. Rezaie M, Farhoosh R, Iranshahi M, Sharif A, Golmohamadzadeh S. Ultrasonic-assisted extraction of antioxidative compounds from Bene (Pistacia atlantica subsp. mutica) hull using various solvents of different physicochemical properties. Food Chem. 2015;173:577–83. Available from: <DOI>

23. López A, Rico M, Rivero A, de Tangil MS. The effects of solvents on the phenolic contents and antioxidant activity of Stypocaulon scoparium algae extracts. Food Chem. 2011;125(3):1104–9. Available from: <DOI>

24. Liu X, Liu Y, Shan C, Yang X, Zhang Q, Xu N, et al. Effects of five extraction methods on total content, composition, and stability of flavonoids in jujube. Food Chem X. 2022;14:100287. Available from: <DOI>

25. Pereira V V, Borel CR, Silva RR. Phytochemical screening, total phenolic content and antioxidant activity of Byrsonima species. Nat Prod Res. 2015;29(15):1461–5. Available from: <DOI>

26. Nickavar B, Esbati N. Evaluation of the antioxidant capacity and phenolic content of three Thymus species. J Acupunct Meridian Stud. 2012;5(3):119–25. Available from: <DOI>

27. Daneshfar A, Ghaziaskar HS, Homayoun N. Solubility of gallic acid in methanol, ethanol, water, and ethyl acetate. J Chem Eng Data. 2008;53(3):776–8. Available from: <DOI>

28. Chaillou LL, Nazareno MA. New method to determine antioxidant activity of polyphenols. J Agric Food Chem. 2006;54(22):8397–402. Available from: <DOI>

29. Koleva II, Van Beek TA, Linssen JPH, De Groot A, Evstatieva LN. Screening of plant extracts for antioxidant activity: A comparative study on three testing methods. Phytochem Anal. 2002;13(1):8–17. Available from: <DOI>

30. Vo Q V, Bay M Van, Nam PC, Quang DT, Flavel M, Hoa NT, et al. Theoretical and experimental studies of the antioxidant and antinitrosant activity of syringic acid. J Org Chem. 2020;85(23):15514–20. Available from: <DOI>

31. Ignat I, Volf I, Popa VI. A critical review of methods for characterisation of polyphenolic compounds in fruits and vegetables. Food Chem. 2011;126(4):1821–35. Available from: <DOI>

32. Barek S, Rahmoun NM, Aissaoui M, El Haci IA, Bensouici C, Choukchou-Braham EN. Phenolic Contents, Antioxidant, and Antibacterial Activities of the Algerian Genista saharae Solvent Extracts. J Herbs Spices Med Plants. 2020;26(1):1–13. Available from:

[<DOI>]

33. Zengin G, Paksoy MY, Aumeeruddy MZ, Glamocilja J, Sokovic M, Diuzheva A, et al. New insights into the chemical profiling, cytotoxicity and bioactivity of four Bunium species. Food Res Int. 2019;123(January):414–24. Available from: [<DOI>]

34. Cayman Chemical [Internet]. Available from: https://www.caymanchem.com/

35. Gadow AV, Joubert E, Hansmann CF. Comparison of the antioxidant activity of rooibos tea (Aspalathus linearis) with green, oolong and black tea. Food Chem [Internet]. 1997;60(1):73–7. Available from: [<DOI>]

JOTCS A
Journal of the Turkish Chemical Society
Section: A
Chemistry
TURKISH CHEMICAL SOCIETY

Cytarabine determination from urine for Toxicokinetic and Excretion studies by High- Performance Liquid Chromatography-Tandem Mass Spectrometry

İbrahim DANİŞ[1,2,4], Ayşegül GÖLCÜ[3*], Durişehvar ÖZER ÜNAL[1,2*]

[1]Istanbul University, Faculty of Pharmacy, Department of Analytical Chemistry, Istanbul, 34116, Turkey
[2]Istanbul University, Drug Research and Application Center, Istanbul, 34116, Turkey
[3]Istanbul Technical University, Faculty of Science and Letters, Department of Chemistry, Istanbul, 34469, Turkey
[4] Istanbul University, Institute of Graduate Studies in Health Sciences, Istanbul, 34126, Turkey

Abstract: Cytarabine (Cyt) (also known as cytosine arabinoside (ara-C)) used in the treatment of acute myeloid leukemia (AML), acute lymphocytic leukemia (ALL). CYT applied in high doses for treatment can cause renal failure. Monitoring excreted urine drug levels can help kidney failure. For this reason, a method was developed and validated by HPLC-MSMS for urine CYT analysis, which is not included in the literature. In this study, a liquid chromatography (HPLC) with triple quadrupole Mass Spectrometric (MS/MS) method developed for the determination of Cyt from urine for toxicokinetic evaluation. Positive MRM mode selected for the quantification of Cyt. The product and major fragment ion for Cyt 244.0 > 112.0 m/z, for IS 198.0 > 152.0 m/z. The optimal MS parameters for Cyt and IS are as follows Fragmentor 80 V, 70 V, Collision energy, 6, 9 respectively. A novel simple, high-throughput and highly sensitive HPLC-MS/MS method was successfully developed and validated for the determination of Cyt from urine. The developed method has a simple one-step extraction method and a short run time (2.0 minutes) for analysis. The proposed method could be practical and reliable for excretion and toxicokinetic studies and as well as the Therapeutic Drug Monitoring study in humans without an invasive route for Cyt.

Keywords: Cytarabine, therapeutic drug monitoring, toxicokinetics, mass spectrometry.

Submitted: October 17, 2022. **Accepted:** April 6, 2023.

Cite this: Daniş İ, Gölcü A, Özer Ünal D. Cytarabine determination from urine for Toxicokinetic and Excretion studies by High- Performance Liquid Chromatography-Tandem Mass Spectrometry. JOTCSA. 2023;10(2):513-520.

DOI: https://doi.org/10.18596/jotcsa.1190202.

***Corresponding author. E-mail:** durisehvar@gmail.com

1. INTRODUCTION

An average of one million new cancer patients are diagnosed on the world. According to the information obtained, a quarter of these patients treated with surgery and radiotherapy. Most remaining patients receive chemotherapy at any stage of this disease. It is pleasing that a certain number of cancer patients can be fully cured or a long recovery period with chemotherapy, depending on the type of cancer (1,2).

Cyt (3), used in the treatment of acute myeloid leukemia (AML), acute lymphocytic leukemia (ALL), chronic myeloid leukemia (CML) and non-hodgkin lymphoma. Cyt is a nucleotide analog and

its chemical name is 4-Amino-1-beta-D-arabinofuranosyl-2(1H)-pyrimidinone (Figure 1). Cyt metabolized intracellularly to the active triphosphate form (cytosine arabinoside triphosphate). Cyt maximum plasma level is 26.3 µg L-1. Less than 10% of the dose excreted in the urine as unchanged drug. Cyt is an important drug in the treatment of acute myeloid leukemia (AML) (4). High-dose cytarabine (2000 to 3000 mg per square meter of body surface area) is toxic but provides higher relapse-free survival rates than the conventional dose of 100 to 400 mg per square meter (5,6). Cyt has been one of the cornerstone drugs in the treatment of acute myeloid leukemia (AML) for over three decades. It initially used in remission induction therapy at a dose of 100 to 200 mg per square meter of body surface (6). The incidence of adverse reactions appears to be higher in patients with severe renal impairment, associated with an increase in adverse effects in patients (7). Absorption distribution metabolism excretory toxicity (ADMET) studies provide important information about the metabolism and urinary and fecal excretion of compounds.

In addition, ADMET studies are critical in modern drug discovery. The purpose of ADMET studies is not only to understand the metabolism but also how both parent and metabolites are eliminated. Drugs removed from the body by various elimination processes. Drug elimination refers to the irreversible removal of drugs from the body by all routes of elimination. Drug excretion is the removal of the intact drug. Toxicokinetics is essentially the study of how a substance gets into the body and what happens to it in the body. Toxicokinetics deals with what the body does with a drug when given a relatively high dose relative to the therapeutic dose. Monitoring excreted urine drug levels may help renal insufficiency (8). In addition, the information generated from these studies is extremely useful in determining whether the kidney or liver is an important organ in elimination and whether there is any safety concern in hepatic or renal impaired populations.

In this study, it is important to determine the excretion of high-dose CYT from the body at the first stage. For this reason, urine CYT analysis has gained importance in determining whether the drug administered in high doses is excreted from the body and its damage to vital organs such as kidneys and liver. In this study, a reliable and sensitive method was developed for urine analysis of CYT, which is not reported in the literature.

Different liquid chromatographic techniques have been reported in the literature dealing with the determination of Cyt in various samples except urine. For example, cytarabine and uracil-arabinoside from human plasma were determined by Burk et al. by using the ion couple liquid chromatography method (9). Hsieh and his team performed Cyt determinations in mouse plasma using different liquid chromatography-tandem mass spectrometric techniques such as ion-pairing, mixed-mode, and porous graphitic carbon (10-12). The high-performance liquid chromatography-tandem mass spectrometry method for the simultaneous determination of cytarabine and its valyl prodrug cytarabine in rat plasma by Sun et al. (13). There are also other HPLC studies conducted by different groups (14-16) and Cyt has excretion studies in Saliva (8). In toxicokinetic evaluations, it is important to analyze non-invasive urine samples instead of taking blood, and urine analysis of cytarabine, which causes renal failure in high doses. Cytarabine syndrome and acute toxicity may occur within 12 h after the start of drug infusion (17). So it's important to analyze Cytarabin level instead of metabolite. In this study, a liquid chromatography (HPLC) with triple quadrupole Mass Spectrometric method was developed for the determination of Cyt from urine. CYT urine analysis studies have not been found in the literature. Liquid chromatography (HPLC) types of equipment can provide more sensitive and reproducible results. Cyt excretion studies with urine will contribute and guide toxicokinetic studies. The urine analysis method of Cyt, which was developed and validated in this study, can be used in excretion studies. Cyt analysis method from urine has not been found in the literature search.

2. MATERIALS AND METHODS

2.1. Chemicals and Reagents

Cyt working standard was certified to contain 100.25% purity for Cyt. Levodopa was chosen as an Internal standard (IS) and certified to contain 99.82% purity for Levodopa. The water that obtained from a Milli-Q ultrapure water system (Millipore, Barnstead) used as the solvent. Ethanol obtained from Merck (Darmstadt, Germany) used for dilution. Formic acid and Acetonitrile obtained from Merck (Darmstadt, Germany) used for the mobile phase.

2.2. Chromatographic Conditions

Agilent 1260 Infinity Liquid Chromatography system and QQQ-6420 detector were used in this study. Separation was carried out on a Poroshell 120 EC-C18, (4.6 - 50 mm, 2.7 µm) column maintained at 30 °C. The LC mobile phase consisted of Acetonitrile: 0.5% Formic Acid (30:70% v/v). The flow rate was 0.600 mL min-1. The injection volume was 5.0 µL and the runtime was 2.0 minutes.

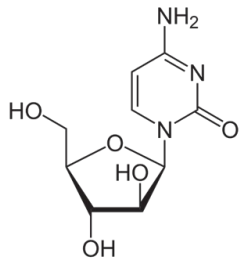

Figure 1: Chemical structure of 4-Amino-1-beta-D-arabinofuranosyl-2(1H)-pyrimidinone.

2.3. Mass Spectrometry Conditions

Detection was carried out by an Agilent 6420 triple quadrupole MS/MS fitted with Agilent Electrospray ionization (ESI) operated in the positive ion mode. Quantification was performed using multiple reaction monitoring (MRM) of the transition ions of m/z 244.0 > 112.0 for Cytarabine and m/z 198.0 > 152.0 for Levodopa, with the dwell time of 100 ms. Nitrogen (99.999% purity) was used as the collision gas. The optimized conditions were as follows: Nebulizer Pressure, 25 psi; Gas Temperature, 300 °C; Gas Flow, 10 (L min-1); Capillary, 5500 V. The MRM transitions and the related optimized Fragmentor Voltage were 80 V for Cyt and 70 V for Levodopa. Collision energy was 6 V for Cyt and 9 V for Levodopa.

2.4. Preparation of Stock and Working Solutions

Standard stock solutions of Cyt 1 mg mL-1 (w/v) and Levodopa (IS) 1 mg mL-1 (w/v) were separately prepared in 5 mL volumetric flasks with distilled water. Working solutions for calibration and quality control samples were prepared from the stock solution by adequate dilution using diluents ethanol. The Internal Standard (IS) working solution (100.0 µg mL-1) was prepared by diluting the stock solution with ethanol.

2.5. Sample Preparation

Working solutions were used to prepare increased volumes tubes that contain 100 µl urine to obtain calibration standards (0.1, 0.5, 5.0, 10.0, 20.0, 30.0, 40.0 µg mL-1) and quality control (15.0, 25.0, 35.0 µg mL-1) samples concentration. 50 µL Internal Standard (IS) working solution (100.0 µg mL-1) spiked tubes. The samples were vortexed for 30 seconds. Samples were extracted for a liquid-liquid extraction with Ethanol. To this, increased volumes ethanol were added to each tube to final volumes are 500 µL. The samples were vortexed for 30 seconds. 0.20 mL of supernatant layer was transferred and analyzed. The developed methods were used to determine urine levels of Cyt for excretion studies.

2.6. Method Validation

The developed method was validated according to the requirements for European Medicine Agency (EMEA) Gıidline on Bioanalytical Method Validation, which includes specificity, linearity, precision, accuracy, limit of detection and limit of quantitation and Matrix effect (18).

2.7. Matrix Effect

Liquid chromatography coupled to mass spectrometry (LC–MS) is a powerful tool for bioanalysis. Reliable bioanalysis requires the characterization of the matrix effect, i.e. influence of the endogenous or exogenous compounds on the analyte signal intensity.

Matrix effects are major concerns in quantitative LC - MS analysis because they detrimentally affect the accuracy, precision, and sensitivity of a method. Therefore, the presence of matrix effects needs to be evaluated during the method development to achieve reliable analytical results.

The matrix effect is evaluated using pool urine from different sources to prepare samples. The matrix factor (MF) is calculated, by calculating the ratio of the peak area in the presence of matrix (measured by analyzing blank matrix spiked with analyte at a concentration of quality control samples after extraction), to the peak area in absence of matrix (pure solution of the analyte). The IS normalized MF is calculated by dividing the MF of the analyte by the MF of the IS. The CV of the IS-normalised MF calculated from the six lots of matrix should not be greater than 15%. Extracted and aqueous samples were compared to determine the MF for the analyte and IS. IS normalized MF for individual series are also determined. The calculated MF of all LQC (low quantity concentration) and HQC (high quantity concentration) samples must be within 0.85 - 1.15 of their nominals concentrations.

Table 1: Accuracy and Precision results of Calibration standards.

	C (µg mL^{-1})	Mean	Error %	Standard Deviation (SD)	Coefficient of variation %CV
ST1	0.1000	0.1028	102.8333	0.0054	5.2027
ST2	0.5000	0.4840	96.8067	0.0326	6.7371
ST3	5.000	5.0408	100.8160	0.0559	1.1090
ST4	10.000	9.9319	99.3187	0.1406	1.4154
ST5	20.000	20.0612	100.3058	0.1681	0.8377
ST6	30.000	29.9903	99.9676	0.3387	1.1295
ST7	40.000	39.9893	99.9733	0.2355	0.5890

2.8. System Suitability

System suitability tests are an integral part of GC and LC methods. These tests are used to verify that the chromatographic system is adequate for the intended analysis. The tests are based on the concept that the equipment, electronics, analytical operations, and samples analyzed constitute an integral system that can be evaluated as such. Resolution is a function of the number of theoretical plates, N (also referred to as efficiency), a, and k.

3. RESULTS AND DISCUSSION

3.1. Results

The analysis was performed in the mass spectrometer using an electrospray (ESI) in the positive ionization mode. The reliability of the method was assessed on the basis of linearity, sensitivity, selectivity, precision, and accuracy. The results obtained for the above parameters, the combination of mobile phase, flow rate, and detector parameters were selected for validation. Out of several tried combinations, a liquid chromatography (HPLC) method with MSMS detection was developed for the determination of Cyt from urine. The analysis was carried out using a Poroshell 120 EC-C18, (4.6 - 50 mm, 2.7 µm) column with a mobile phase consisting of ACN and 0.5% formic acid at a flow rate of 0.5 mL min^{-1}. Levodopa was used as an Internal standard (IS). The mass spectrometer was tuned initially in both positive and negative ionization modes for Cyt. It was observed that the signal intensity of positive ion was much higher than that of a negative ion. Parameters, such as capillary and nozzle voltage, desolvation temperature, ESI source temperature, and flow rate of desolvation gas and cone gas, were optimized to obtain the optimum intensity of molecules of Cyt and IS for quantification. Multiple reaction monitoring (MRM) is a highly specific and sensitive mass spectrometry technique that can selectively quantify compounds within complex mixtures. This technique uses a triple quadrupole MS that firstly targets the ion corresponding to the compound of interest with subsequent fragmentation of that target ion to produce a range of productions. One or more of these fragment product ions can be selected for quantification purposes. Only compounds that meet both these criteria, i.e. specific precursor ion and specific productions corresponding to the mass of the molecule of interest are isolated within the mass spectrometer. Mass spectrometry MRM mode also provides us to analyze compounds with the same retention time. Positive MRM mode was selected for the quantification of Cyt. The product and major fragment ion for from Cyt 244.0 to 112.0 m/z, for IS from 198.0 to 152.0 m/z. The optimal MS parameters for Cyt and IS as follows Fragmentor 80 V, 70 V, Collision energy, 6, 9 respectively.

3.1.1. Selectivity

The selectivity of the method against urinary matrix components was evaluated against human blank urine. Among the analyzed batch, the urine batch showing any interferences at the retention times of analyte and IS. All samples were processed and analyzed using the proposed extraction method (Figure 2).

3.1.2. Linearity

Calibration curves were constructed using matrix-matched calibration standard solutions by plotting the peak area of the quantitative ion of each analyte versus concentrations. For the quantification of the samples, a calibration curve was constructed by spiking blank plasma at seven concentration levels (100 - 40000 ng mL^{-1}). For this purpose, urine samples spiked at seven concentration levels (100 - 40000 ng mL^{-1}) were extracted. The calibration curve regression for Cyt was linear regression. This gave the best fit and coefficient of determination (r^2) for validation and was greater than 0.99 which was in the acceptable range. The average value for r^2 was found to be 0.9926. Calibration curve's equation is $y = 6.8755x - 0.2479$. The concentration range of Cyt was found to be accurate and precise from 100 to 40000 ng mL^{-1} (Table 1). The LOQ of the method 100 ng mL^{-1}, Signal to noise ration of LOQ was found that S/N: 14.1, LOD of the method 50 ng mL^{-1} (S/N: 6).

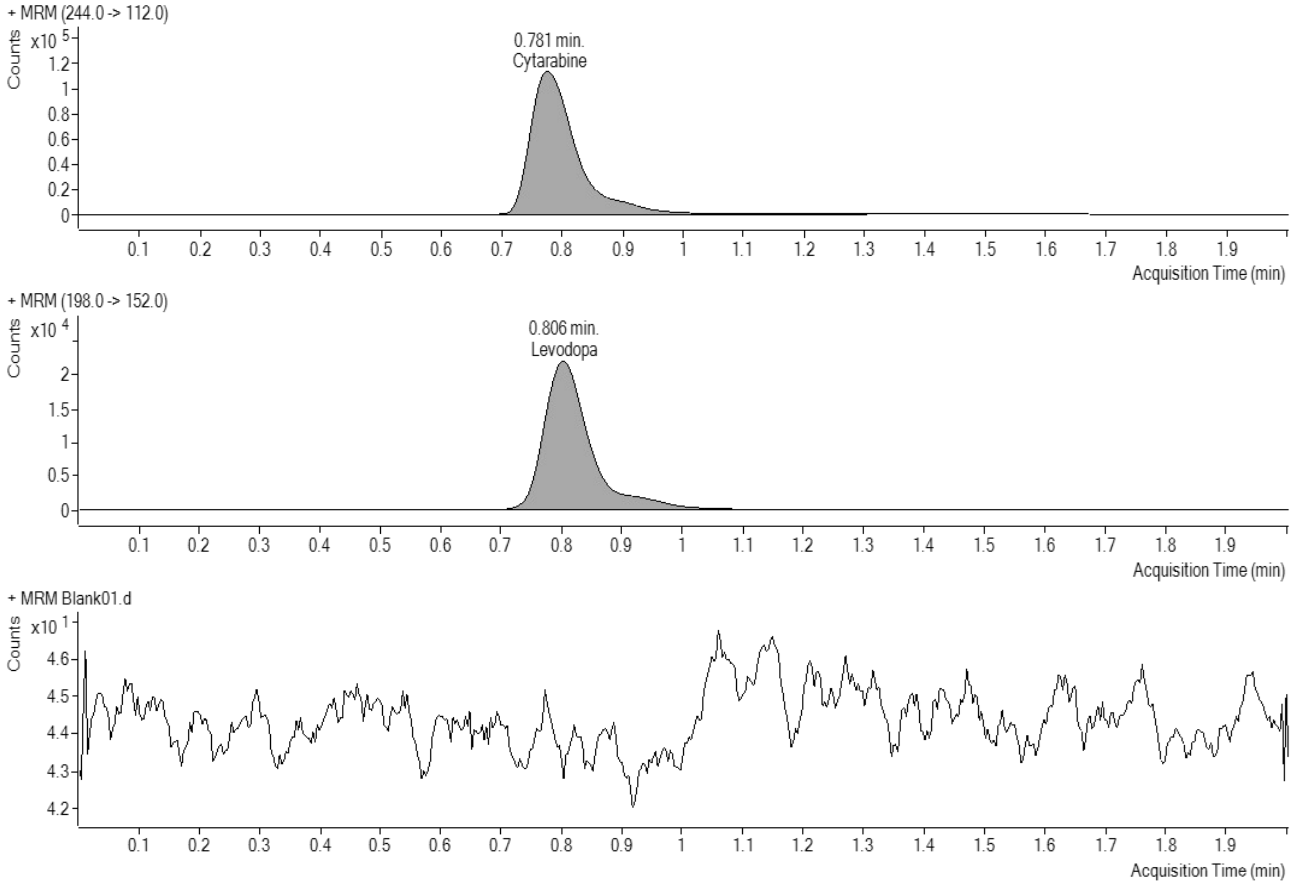

Figure 2: The MRM chromatograms of Cyt (15 µg mL^{-1}, QC1) **(a)**, IS (Levodopa) **(b)** and blank **(c)**

3.1.3. Accuracy and precision

Accuracy and precision of Cyt were calculated at 15000 ng mL^{-1}, 25000 ng mL^{-1} and 350000 ng mL^{-1} levels for the six replicates results are shown in Table 2. The coefficients of variation results were 3.23%, 2.86%, and 2.70% respectively whereas intra-day accuracies were 103.0247 ± 3.0246, 99.06268 ± 0.9373, and 101.0055 ± 1.0055 respectively in urine samples. These results indicate that the method has good precision and accuracy are within the acceptance limit of < 15% and ± < 15% for precision and accuracy respectively.

3.1.4. Matrix effect

The Matrix effect calculated was 2.16 for low concentration and 0.79 for high concentration. The overall CV calculated for the concentration should not be greater than 15%. Therefore ion suppression or enhancement from urine was negligible under current conditions. The formula about matrix effect was given below.

$$\text{Normalized Matrix Factor} = \frac{(\text{Peak area of analyte in the matrix})/(\text{peak area of analyte})}{(\text{Peak area of IS in the matrix})/(\text{Peak area of IS})}$$

3.1.5. System suitability

System suitability parameters found as specified in the guideline. Theorical plate number (N) was calculated as 15700, capacity factor (k') 9.8, resolution (Rs) 14, tailing factor (T) T ≤ 2 for Cyt. Detailed parameters are given in Table 3

Table 2: Accuracy and precision of Cyt in urine (in three validation days, six replicates at different concentration levels per day).

	Intra-day				Inter-day			
QC samples µg mL^{-1}	**Measu-red Concen-tration (µg mL^{-1})**	**Error %**	**SD**	**% CV**	**Measu-red Concent-ration (µg mL^{-1})**	**Error %**	**SD**	**% CV**
15	14.8107	98.7379	0.4796	3.2385	15.2713	101.8087	0.5567	3.6455
25	25.3978	101.5912	0.7275	2.8644	24.7053	98.8213	0.4148	1.6790
35	34.7578	99.3079	0.9386	2.7005	35.1486	100.4245	1.7106	4.8667

Table 3: System suitability results and acceptability limits*.

Parameter	Value (Cyt)	Limit (FDA guidline)
Retention time (min)	0.78	-
Peak Width (W)	0.28	-
Tailing (T)	2	T ≤ 2
Theoretical Plates (N)	15700	N > 2000
Resolution (R)	14	Rs > 2
Capacity Factor (k)	9.8	k’ > 2

*FDA: Center for Drug Evaluation and Research

3.2. Discussion

A novel simple, high-throughput, and highly sensitive LC-MS/MS method was successfully developed and validated for the determination of Cyt from urine. The developed method has a simple one-step extraction method and a short run time (2.0 minutes) for analysis. With the developed method, the toxic effect of CYT applied at high doses can be determined by obtaining information about its excretion by urine analysis. The proposed method could be practical and reliable for excretion studies as well as the Therapeutic Drug Monitoring study in humans without an invasive route for Cyt. The normal dose of Cyt is set at 100 - 400 mg / body surface area, however, high doses of 2000 - 3000 mg / body surface area are given for the treatment of the disease. In this case, determining how much Cyt is excreted from the urine per hour will be effective in determining its toxic level in the body. With the developed method, toxicokinetic studies can be carried out easily and in a short time.

4. CONCLUSION

It is important to determine whether the drug given in high doses is excreted from the body and the damage it causes to vital organs such as kidney and liver. Cyt is metabolized in the body, but less than 10% is excreted without being metabolized. With the developed method, CYT urine analysis will help to determine the harmful effects of the treatment and selection of the therapeutic dose.

5. REFERENCES

1. Burstein HJ, Krilov L, Aragon-Ching JB, Baxter NN, Gabriela Chiorean E, Allen Chow W, et al. JOURNAL OF CLINICAL ONCOLOGY A MESSAGE FROM ASCO’S PRESIDENT. 2017 [cited 2023 May 10]; Available from:<URL>

2. Cronin KA, Lake AJ, Scott S, Sherman RL, Noone AM, Howlader N, et al. Annual Report to the Nation on the Status of Cancer, part I: National cancer statistics. Cancer [Internet]. 2018 Jul 1 [cited 2023 May 10];124(13):2785–800. Available from: <URL>

3. Lamba JK. Genetic factors influencing cytarabine therapy. [Internet]. 2009 Oct 20 [cited 2023 May 10];10(10):1657–74. Available from: <URL>

4. Hamada A, Kawaguchi T, Nakano M. Clinical pharmacokinetics of cytarabine formulations. Clin Pharmacokinet [Internet]. 2002 Sep 13 [cited 2023 May 10];41(10):705–18. Available from: <URL>

5. Lowenberg B, Downing JR, Burnett A. Acute Myeloid Leukemia. [Internet]. 1999 Sep 30 [cited 2023 May 10];341(14):1051–62. Available from: <URL>

6. Löwenberg B, Pabst T, Vellenga E, van Putten W, Schouten HC, Graux C, et al. Cytarabine Dose for Acute Myeloid Leukemia. New England Journal of Medicine [Internet]. 2011 Mar 17 [cited 2023 May 10];364(11):1027–36. Available from: <DOI>

7. Dotson JL, Jamil MO. Successful treatment of cytarabine-related neurotoxicity with corticosteroids, a case series. Int J Hematol [Internet]. 2018 Nov 1 [cited 2023 May 10];108(5):554–7. Available from: <URL>

8. 1. Mori T, Yamazaki R, Nakazato T, Aisa Y, Enoki S, Arai M, et al. Excretion of cytosine arabinoside in saliva

after its administration at high doses. Anti-Cancer Drugs [Internet]. 2006;17(5). Available from: <URL>

9. Burk M, Volmer M, Fartash K, Schneider W. Ion-pair liquid chromatography of cytarabine and uracil-arabinoside in human plasma. Arzneimittelforschung [Internet]. 1995 May 1 [cited 2023 May 10];45(5):616–9. Available from: <URL>

10. Hsieh Y, Duncan CJG. An ion-pairing liquid chromatography/tandem mass spectrometric method for the determination of cytarabine in mouse plasma. Rapid Communications in Mass Spectrometry [Internet]. 2007 Feb 28 [cited 2023 May 10];21(4):573–8. Available from: <URL>

11. Hsieh Y, Duncan CJG, Liu M. A mixed-mode liquid chromatography-tandem mass spectrometric method for the determination of cytarabine in mouse plasma. Journal of Chromatography B. 2007 Jul 1;854(1–2):8–12. <DOI>.

12. HHsieh Y, Duncan CJG, Brisson JM. Porous graphitic carbon chromatography/tandem mass spectrometric determination of cytarabine in mouse plasma. Rapid Communications in Mass Spectrometry [Internet]. 2007 Mar 15 [cited 2023 May 10];21(5):629–34. <DOI>.

13. Sun Y, Sun J, Wen B, Shi S, Xu Y, Chen Y, et al. High-performance liquid chromatography/tandem mass spectrometry method for the simultaneous determination of cytarabine and its valyl prodrug valcytarabine in rat plasma. Journal of Chromatography B. 2008 Jul 1;870(1):121–5. <DOI>.

14. Mistiran AF, Dzarr AA, Gan SH. HPLC method development and validation for simultaneous detection of Arabinoside-C and doxorubicin. [Internet]. 2010 Oct 14 [cited 2023 May 10];20(8):472–81. Available from: <URL>

15. Hilhorst MJ, Hendriks G, Van Hout MWJ, Sillén H, Van De Merbel NC. HPLC–MS/MS method for the determination of cytarabine in human plasma. [Internet]. 2011 Jul 14 [cited 2023 May 10];3(14):1603–11. Available from: <URL>

16. Feldman EJ, Kolitz JE, Trang JM, Liboiron BD, Swenson CE, Chiarella MT, et al. Pharmacokinetics of CPX-351; a nano-scale liposomal fixed molar ratio formulation of cytarabine:daunorubicin, in patients with advanced leukemia. Leuk Res. 2012 Oct 1;36(10):1283–9. <DOI>.

17. Phillips CL, Lane A, Gerbing RB, Alonzo TA, Wilkey A, Radloff G, et al. Genomic variants of cytarabine sensitivity associated with treatment-related mortality in pediatric AML: A report from the children's oncology group. Clinical Cancer Research [Internet]. 2020 Jun 15 [cited 2023 May 10];26(12):2891–7. Available from: <URL>

18. 2** Committee for Medicinal Products for Human Use (CHMP) Guideline on bioanalytical method validation. 1922 [cited 2023 May 10]; Available from: <URL>

JOTCS A
Journal of the Turkish Chemical Society
Section: A
Chemistry
TURKISH CHEMICAL SOCIETY

Use of Pitzer's model to calculate thermodynamic properties of aqueous electrolyte solutions of sulfuric acid

Abdelhakim BEGAR [1]*, Cherif SAIB [2], Mohamed Said CHEBBAH [1]

[1] University of Biskra, Department of Mechanical Engineering, Biskra, 07000, Algeria
[2] University of M'sila, Department of Mechanical Engineering, M'sila, 28000, Algeria

Abstract: Over this study we calculated the coefficients of activity of different species and the concentration in the presence of H^+ ion when H_2SO_4 is alone in solution. The coefficient of average activity was calculated using the model of Pitzer. The constants of dissociation of these reactions were calculated from the values of the free standard energies. The reaction reaches a balance while producing H^+, HSO_4^- and SO_4^{2-}. The research reported here concentrated on the effect of some important operational parameters on dissolution process. The parameters were investigated and their ranges are as follows: initial molality ranging from 0.001 to 5 $mol.kg^{-1}$ and temperatures between 25 and 200°C. Fortran 90 (Mathematical formula translating system) was used to perform all mathematical calculations. The numerical code can be used to calculate the molarity of ion H^+ of an aqueous solution of sulfuric acid. The objective of the present work is to optimize the parameters of leaching such as activity of sulfuric acid on the dissociation phenomena.

Keywords: Leaching, Pitzer, activity, dissociation, molality.

Submitted: May 26, 2022. **Accepted:** April 25, 2023.

Cite this: Begar A, Saib C, Chebbah MS. Use of Pitzer's model to calculate thermodynamic properties of aqueous electrolyte solutions of sulfuric acid. JOTCSA. 2023;10(2):521–8.

DOI: https://doi.org/10.18596/jotcsa.1118833.

***Corresponding author. E-mail:** a.begar@univ-biskra.dz

1. INTRODUCTION

Several test were conducted to develop models to represent the thermodynamic properties of the solutions of electrolyte. The coefficient of average activity was calculated using the model of Pitzer (1-3). The pitzer ion interaction model, similar to the virial equation used for non-ideal gases, has proved to be the most accurate thermodynamic model up to moderate concentrations in aqueous solutions (4,5).

Pitzer et al. (6-8) developed a model for calculation of the properties of the electrolytes starting from a semi numerical models and an improved analysis of the model of DEBYE HUCKEL.

This model links the intermolecular forces and the distribution of the ions to the osmotic pressure and takes into account the influence of forces with short distance in the binary interactions. The expressions of the coefficient of activity and the osmotic coefficient are deduced from the equation of the excess free energy of GIBBS. The obtained equations are analogous to those of GUGGENHEIM.

Pitzer's model is capable of precisely forecasting activity and enthalpy provided that the variation of the parameters with temperature are recognized. This variation has been calculated for some electrolytes (9-11).

Zomaitis et al. suggested to admit the parameters to be constant and to consider the influence of temperature only on the DEBYE-HUCKEL (12).

The mixing terms for ions with same sign but with unequal magnitude are not included in the Pitzer ion interaction, Harvie et al. have found these terms (13).

Archer discovered that an ion strength reliant third virial parameter describing the combined interactions between two similar cations and anion or vice versa (14).

Pitzer et al. introduced a Margules type equation to model aqueous solutions up to a pure salt (15).

Sippola found out that only four parameters with a simple temperature dependency in enough to present the osmotic and activity coefficients (16).

Knopf et al. were found to be extrapolate the measured osmotic coefficient within a maximum deviation of 0.01 (17).

The aim of our work was to optimize leaching parameters such as the activity of sulfuric acid. We developed from fortran 90 a program, for simulating this process and predicting its performance.This numerical code is based on the mathematical description of the detailed physical and chemical phenomena occurring.

2. METHODS

2.1. Thermodynamic Model

The Pitzer thermodynamics model is used extensively to describe the interactions between dissolved ions and solvents (18).

In water, Sulfuric acid is separated according balances (19-22).

$$H_2SO_4 \Leftrightarrow H^+ + HSO_4^- \qquad K_1$$
$$HSO_4^- \Leftrightarrow H^+ + SO_4^{-2} \qquad K_2$$

The dissociation constants of these reactions are calculated from the values of the standard free energy of species considered.

The equilibrium constant is linked to the standard free energy of the reaction by the relation VAN'T HOFF:

$$\frac{\Delta G^0}{T} = -RTLnK$$

he just:

$$K_1 = e^{\left(-\frac{\Delta G^0_{HSO_4^-} - \Delta G^0_{H_2SO_4}}{RT}\right)} = 80.72$$

$$K_2 = e^{\left(-\frac{\Delta G^0_{SO_4^{-2}} - \Delta G^0_{HSO_4^-}}{RT}\right)} = 0.0125$$

K: equilibrium constant
ΔG^0 : standard free energy
T: Temperature (K)
R: Gas constant $Jmol^{-1}K^{-1}$

The high values of the equilibrium constant K_1, translated into strong shift in the balance towards the formation of HSO_4^- and H^+. We admit that in the future the first dissociation H_2SO_4 is total. Only the second equilibrium dissociation will be taken into account ($HSO_4^- \Leftrightarrow H^+ + SO_4^{2-}$).

Pitzer et al. gives value perceptibly different k_2. It adopts the value 0.0105, which corresponds to a compromise (6).

An application of Pitzer 's expression for estimating the coefficient of activity for a mixture of electrolytes to the couple of ions H^+ and SO_4^{-2} in the presence of ions HSO_4^- gives:

$$ln(\gamma_{H_2SO_4}) = 2f^{\gamma} + \frac{4}{3}m_1B_{H_1} + \frac{1}{3}(4m_2 + 2m_H)B_{H_2}^{(0)} + \frac{1}{3}(8m_2 + 2m_H)m_HC_{H_2} + 2m_1m_HB'_{H_1}$$

γ_i: Activity coefficient of a component i
f^{γ}:the derivative of the Debye-Huckel term
m_i: Molale concentration of component i
B_{ij}: Pitzer binary interaction parameters
C_{ij}: Pitzer ternary interaction parameter
HSO_4^- is indexed by 1
SO_4^{-2} is indexed by 2

Because the molecule H_2SO_4 was supposed to be made of two ions H^+ and SO_4^{-2}, then we have:

$$ln\,\gamma_{H_2SO_4} = \frac{1}{3}(2\,ln\,\gamma_H + ln\,\gamma_{SO_4}),$$

Hence; $$3\,ln\,\gamma_{H_2SO_4} = ln(\gamma_{H^+}^2\gamma_{SO_4})$$

The computed exploratory Pitzer showed that $B_{H_2}^{(1)}$ had a negligible effect on the determination of the activity coefficient, expressing β_{H_2} in those circumstances is tantamount to match. β_{H_2} and $B_{H_2}^{(0)}$. On the other hand, good results are obtained either with the combination $B_{H_2}^{(0)}$ and C_{H_2}, or combination C_{H_1} and C_{H_2}, but the first was raised slightly better and has been adopted. It follows $C_{H_1} = 0$.

The term B'_{H_2} is void because it represents the derivative compared to the ionic strength of a term $B_{H_2}^{(0)}$ independent I.

This method ensures the relation:

$$ln(\gamma_H^2\gamma_{SO_4}) = 6f^{\gamma} + 4m_1B_{H_1} + (4m_2 + 2m_H)B_{H_2}^{(0)} + (8m_2 + 2m_H)m_HC_{H_2} + 6m_1m_HB'_{H_1}$$

Now let us apply the expression of the coefficient of activity for a mixture of electrolytes to the couple of ions H^+, HSO_4^- in the presence of ions SO_4^{-2}.

The species H_2SO_4 being supposed constitute of the ions H^+ and HSO_4^-, one thus has:

$$ln\,\gamma_{H_2SO_4} = \frac{1}{2}ln\,\gamma_H\,ln\,\gamma_{HSO_4^-}$$

with; $$ln\,\gamma_H\,ln\,\gamma_{HSO_4} = 2f^{\gamma} + 2(m_1 + m_H)B_{H_1} + 2m_2B_{H_2}^{(0)} + 4m_2m_HC_{h_2} + 2m_1m_HB'_{H_1}$$

The former relationships must be compatible with the balance of dissolution. Hence the expression of the product of the coefficients of activity is as follows:

$$ln(\gamma_{H^+}^2\gamma_{SO_4^-} - ln\,\gamma_{H^+}\gamma_{HSO_4^-} = ln(\frac{\gamma_{H^+}\gamma_{SO_4^-}}{\gamma_{HSO_4^-}}) = 4f^{\gamma} + 2(m_1 - m_H)B_{H_1} + 2(m_2 + m_H)B_{H_2}^{(0)} + 2(2m_2 + m_H)B_{H_2}^{(0)} + 2(2m_2 + m_H)m_HC_{H_2} + 4m_1m_HB'_H$$

where:

$$\frac{\gamma_{H^+}\gamma_{SO_4^-}}{\gamma_{HSO_4^-}} = exp(4f^{\gamma} + 2(m_1 - m_H)B_{H_1} + 2(m_2 + m_H)B_{H_2}^{(0)} + 2(2m_2 + m_H)B_{H_2}^{(0)} + 2(2m_2 + m_H)m_HC_{H_2} + 4m_1m_HB'_H)$$

At weak concentrations, the molality is close to the concentration on the basis of the second balance of the dissolution of the H_2SO_4.

The concentration of the sulfate ions in the solution makes it possible to write the following relationship:

$m = m_1 + m_2$ therefore $m_2 = m - m_1$

According to Pitzer we have:

$$m = \frac{1000C}{1000\rho - MC}$$

m: Molality
C: concentration
M: Molar mass
ρ: Density

On the other hand, because of the electric neutrality of the solution $m_H = m_1 + 2m_2$

From where $m_1 = 2m - m_H$

The constant of equilibrium of dissociation of the H_2SO_4 is then:

$$k_2 = \frac{[H^+][SO_4^{2-}]}{[HSO_4^-]} \bullet \frac{\gamma_H\gamma_{SO_4}}{\gamma_{HSO_4}} = \frac{m_Hm_2}{m_1} \bullet \frac{\gamma_H\gamma_2}{\gamma_1}$$

with; $$m_H = \frac{\frac{K_2m_1}{m_2}}{(\frac{\gamma_H\gamma_2}{\gamma_1})}$$

An average coefficient of activity $\gamma^{\pm}$ can be defined by assuming that the H_2SO_4 is completely dissociated. The following relationship: $4\gamma_{\pm}^3m^3 = \gamma_H^2\gamma_{SO_4}m_H^2m_2$ allows to calculate the average coefficient of activity $\gamma_{\pm}$.

Indeed, the molality of ions H^+ was determined and one calculates $(\gamma_H^2\gamma_{SO_4})$ as follows:

$$ln(\gamma_H^2\gamma_{SO_4}) = 6F^{\gamma} + 4m_1B_{H_1} + (4m_2 + 2m_H)B_{H_2}^{(0)} + (8m_2 + 2m_H)m_HC_{H_2} + 6m_1m_HB'_{H_1}$$

with; $$C_{H_2} = \frac{C_{H_2}^{\gamma}}{2^{\frac{3}{2}}}$$

$$f^{\gamma} = A^{\gamma}\left(\frac{I^{\frac{1}{2}}}{1+1.2I^{\frac{1}{2}}} + \frac{2}{1.2}ln(1+1.2I^{\frac{1}{2}})\right)$$
$$A^{\gamma} = 0.0000043T^2 + 0.002709T + 0.583022$$

I: ionic strength
A^{γ}: DEBYE-HÜCKEL parameter
T: Temperature (K)
The temperature T is given in Kelvin

$$B_{H1} = B_{H1}^{(0)} + \frac{B_{H1}^{(1)}}{2I}(1-(1+2I^{\frac{1}{2}})e^{(-2I^{\frac{1}{2}})})$$
$$B'_{H1} = \frac{B_{H1}^{(1)}}{2I^2}(1-(1+2I^{\frac{1}{2}}+2I)e^{(-2I^{\frac{1}{2}})})$$

$$C_{H_2} = \frac{C_{H_2}^{\gamma}}{2^{\frac{3}{2}}}$$

For an aqueous sulfuric solution, the ionic species involved are: H^+, HSO_4^- and SO_4^{2-}.

Therefore; $$I = \frac{1}{2}m_H + \frac{1}{2}m_1 + \frac{1}{2}m_2 2^2$$

Pitzer provides the following equations, depending on the temperature (8):

$$k_2 = e^{-14.0321+\frac{2825.2}{T}}$$
$$B_{H1}^{(0)} = 0.05584 + \frac{46.040}{T}$$
$$B_{H_1}^{(1)} = -0.65758 + \frac{336.514}{T}$$

$$B_{H_2}^{(0)} = -0.32806 + \frac{98.607}{T}$$

$$C_{H_2} = 0.25333 - \frac{63.124}{T}$$

2.2. Optimization of Model Parameters

The model of Pitzer was applied to calculate the average coefficients of activity and the molality in ion H+ of an aqueous solution of sulfuric acid. To this purpose, the numerical code for solving equations is written (in FORTRAN 90). The program can be used to calculate the molality of ion H^+ of an aqueous solution of H_2SO_4 of an initial molality ranging from 0.001 to 5 mol.kg^{-1} at temperatures between 25 and 200°C.

3. RESULTS

The term $ln\frac{\gamma_H\gamma_2}{\gamma_1}$ involved in the expression of the constant of dissolution depends on the molality mH of ion H^+. An iterative calculation is done by fixing an initial molality mH superior than the initial molality in sulfuric acid. The following equations allow the calculation of a new value of the molality.

A comparison test between the previous and newly calculated value refining the result with an accuracy of 10^{-5} mol.kg^{-1}.

m_1=2m-m_H,
m_2=m-m_1

and;
$$m_H = \frac{\frac{K_2 m_1}{m_2}}{(\frac{\gamma_H\gamma_2}{\gamma_1})}$$

Figure 1 gives the molality in ions H^+ for different temperatures with molalities in H_2SO_4 lying between 0.01 and 0.25 mol kg^{-1}.

Figure 2 provides the molality in ions H^+ for different temperature with molalities in H_2SO_4 from 0.5 to 5 mol.kg^{-1}.

For molality higher than 1 mol.kg^{-1} and temperatures within 170-200°C, the molality in ion H^+ passes by a minimum.

Figure 3 shows the molality of H^+ as a function of the molarity of H_2SO_4 dependence shows between the two molalities whatever the temperature.

It can be noted that the temperature does not any influence on the calculated molality in ion H^+ as a function of the molality in H_2SO_4 at 25°C.

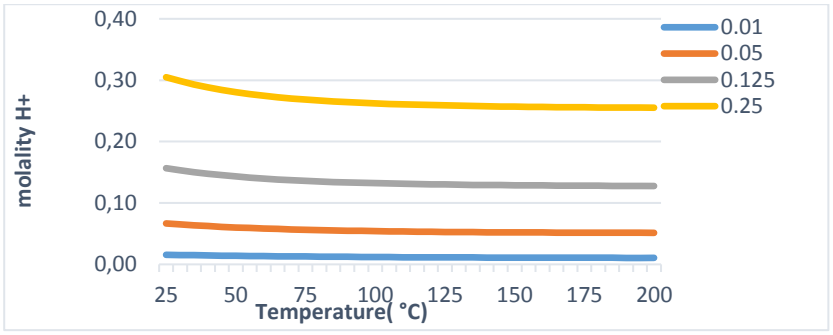

Figure 1: Molality in H^+ versus the temperature for sulfuric aqueous solutions from 0.01 to 0.25 mol kg^{-1}.

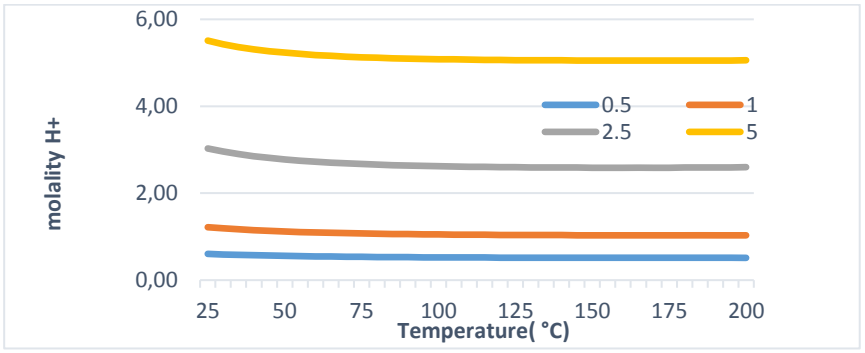

Figure 2: Variation in molality of H^+ as a function of the temperature for sulfuric aqueous solutions in the range of 0.5 to 5 $mol.kg^{-1}$.

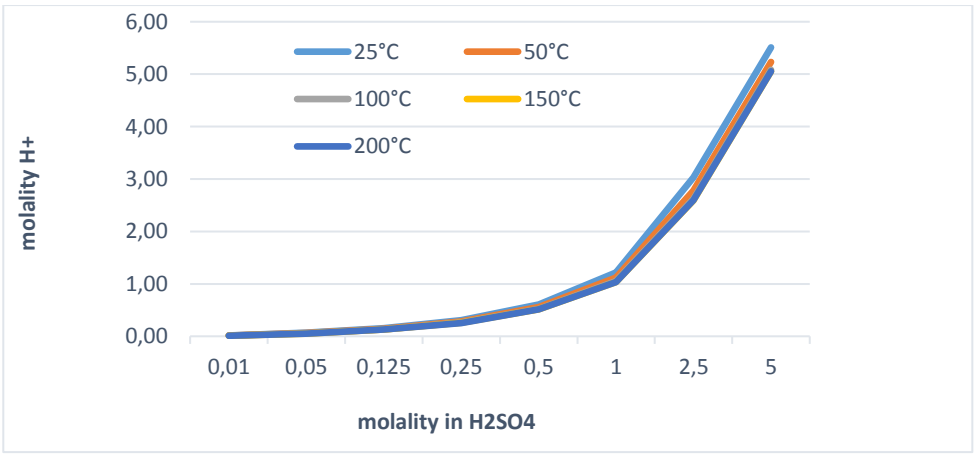

Figure 3: Variation in molality of H^+ versus of that of sulfuric acid at various temperatures.

Let m be the stochiometric concentration in sulfuric acid, and m_H the concentration in ion H^+ in equilibrium.

The expression giving the balance of the sulfate ions can be written as:

$$m_H{}^3 + k_1 m_H{}^2 + (k_1 k_2 - m k_1) m_H - 2 k_1 k_2 = 0$$

The solving of this cubic equation in m_H gives a concentration in ion H^+ at equilibrium for 25 °C approximately with a concentration of ions H^+ equals to 0.135M. The stochiometric concentration m being equal to 0.125M.

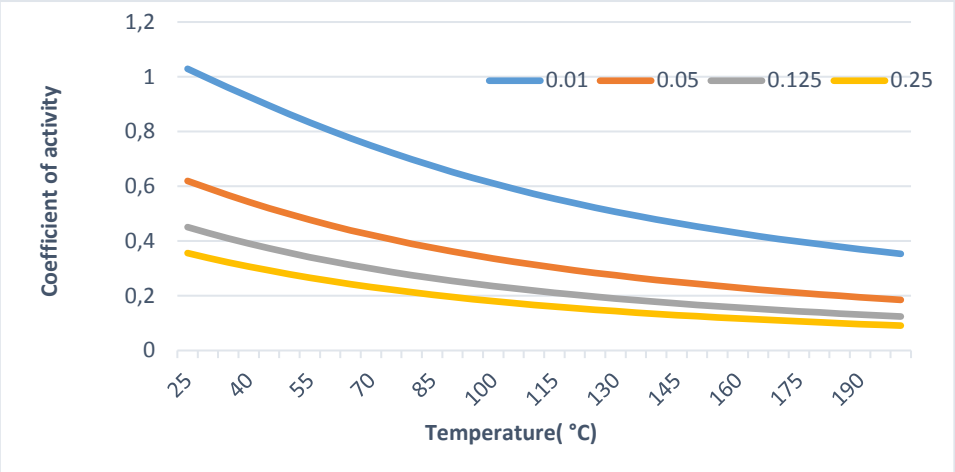

Figure 4: Evolution of the activity coefficient of the H_2SO_4 as a function of the temperature between 0.01 and 0.25.

The comparison with the value extracted from Figure.1 for the same stochiometric concentration gives a value of the concentration in ion H^+ equal to 0.1566519M i.e. a difference of 16.038% compared to the value of this same concentration obtained without taking into account the activities.

Figure 4 gives the values of the activity coefficient of the H_2SO_4 in dependence of the temperature for the molalities ranging from 0.01 to 0.25 $mol.kg^{-1}$. Whatever the molality, the coefficient of activity $\gamma_{\pm}$ for the H_2SO_4 decreases when the temperature increases.

4. CONCLUSION

In the temperature range considered: 25 to 200°C, this study allows the determination of concentration in ion H^+ and the coefficients of activity of different kinds of the H_2SO_4 alone in solution. In an aqueous solution of H_2SO_4, the species reacting are H^+, HSO_4^- and SO_4^{2-}. We can consider that the H_2SO_4 with the two kinds of anions HSO_4^- and SO_4^{2-} and the cations H^+, constitute a mixed electrolyte for the equation of Pitzer.

The solving of the expression giving the balance of the sulfate ions gives a concentration in ion H^+ at equilibrium for 25 °C approximately with a concentration of ions H^+ equals to 0.135M. The stochiometric concentration m being equal to 0.125M. The comparison with the value extracted from figure for the same stochiometric concentration gives a value of the concentration in ion H^+ equal to 0.1566519M i.e., a difference of 16.038% compared to the value of this same concentration obtained without taking into account the activities.

It can be noted that the temperature does not any influence on the calculated molality in ion H^+ as a function of the molality in H_2SO_4 at 25°C.

For molality higher than 1 $mol.kg^{-1}$ and temperatures within 170-200°C, the molality in ion H^+ passes by a minimum.

The coefficient of activity $\gamma_{\pm}$ for the H_2SO_4 decreases when the temperature increases.

The calculation results are in good agreement with those found in literature.

5. REFERENCES

1. Campbell DM, Millero FJ, Roy R, Roy L, Lawson M, Vogel KM, et al. The standard potential for the hydrogen-silver, silver chloride electrode in synthetic seawater. Mar Chem. 1993 Dec 1;44(2–4):221–33. Available from: <DOI>

2. Waters JF, Millero FJ. The free proton concentration scale for seawater pH. Mar Chem. 2013 Feb 20;149:8–22. Available from: <DOI>

3. Clegg SL, Whitfield M. A chemical model of seawater including dissolved ammonia and the stoichiometric dissociation constant of ammonia in estuarine water and seawater from −2 to 40°C. Geochim Cosmochim Acta. 1995 Jun 1;59(12):2403–21. Available from: <DOI>

4. Chihara K, Suzuki ; Finlayson M, Knaehel BA, Hill ; Knoblauch FB, Mitchell K, Shendalman ; Shendalman LH, et al. An NRTL model for representation and prediction of deviation from ideality in electrolyte solutions compared to the models of Chen (1982) and Pitzer (1973). AIChE Journal [Internet]. 1985 Mar 1 [cited 2023 May 23];31(3):392–9. Available from: <URL>

5. Ball F -X, Planche H, Fürst W, Renon H. Representation of deviation from ideality in

concentrated aqueous solutions of electrolytes using a mean spherical approximation molecular model. AIChE Journal [Internet]. 1985 Aug 1 [cited 2023 May 23];31(8):1233–40. Available from: <URL>

6. Pitzer KS, Roy RN, Silvester LF. Thermodynamics of Electrolytes. 7. Sulfuric Acid. J Am Chem Soc [Internet]. 1977 [cited 2023 May 23];99(15):4930–6. Available from: <URL>

7. Pitzer KS, Mayorga G. Thermodynamics of electrolytes. III. Activity and osmotic coefficients for 2-2 electrolytes. J Solution Chem [Internet]. 1974 Jul [cited 2023 May 23];3(7):539–46. Available from: <URL>

8. Bradley DJ, Pitzer KS. Thermodynamics of electrolytes. 12. Dielectric properties of water and Debye-Hückel parameters to 350 °C and 1 kbar. Journal of Physical Chemistry [Internet]. 1979 [cited 2023 May 23];83(12):1599–603. Available from: <URL>

9. Rogers PSZ, Pitzer KS. High-temperature thermodynamic properties of aqueous sodium sulfate solutions. Journal of Physical Chemistry [Internet]. 1981 [cited 2023 May 23];85(20):2886–95. Available from: <URL>

10. Pitzer KS, Raton B, Arbor A, London B. Activity Coefficients in Electrolyte Solutions 2nd Edition. Available from: <URL>

11. Greenberg JP, Møller N. The prediction of mineral solubilities in natural waters: A chemical equilibrium model for the Na-K-Ca-Cl-SO4-H2O system to high concentration from 0 to 250°C. Geochim Cosmochim Acta. 1989 Oct 1;53(10):2503–18. Available from: <DOI>

12. Zemaitis Jr JF, Clark DM, Rafal M, Scrivner NC. Handbook of Aqueous Electrolyte Thermodynamics: Theory & Application. Available from: <URL>

13. Harvie CE, Weare JH. The prediction of mineral solubilities in natural waters: the Na□K□Mg□Ca□Cl□SO4□H2O system from zero to high concentration at 25° C. Geochim Cosmochim Acta. 1980 Jul 1;44(7):981–97. Available from: <DOI>

14. Archer DG. Thermodynamic Properties of the NaCl+H 2 O System I. Thermodynamic Properties of NaCl(cr). Aqueous Sodium Chloride Solutions Journal of Physical and Chemical Reference Data [Internet]. 1992 [cited 2023 May 23];21:15. Available from: <DOI>

15. Pitzer KS, Simonson JM. Thermodynamics of multicomponent, miscible, ionic systems: Theory and equations. Journal of Physical Chemistry [Internet]. 1986 [cited 2023 May 23];90(13):3005–9. Available from: <URL>

16. Sippola H. Critical evaluation of the 2nd dissociation constants for aqueous sulfuric acid. Thermochim Acta. 2012 Mar 20;532:65–77. Available from: <DOI>

17. Thermodynamic Dissociation Constant of the Bisulfate Ion from Raman and Ion Interaction Modeling Studies of Aqueous Sulfuric Acid at Low Temperatures | The Journal of Physical Chemistry A [Internet]. [cited 2023 May 23]. Available from: <URL>

18. Pitzer KS. Activity Coefficients in Electrolyte Solutions. Activity Coefficients in Electrolyte Solutions. 2018 May 4;

19. Que H, Song Y, Chen CC. Thermodynamic Modeling of the Sulfuric Acid−Water−Sulfur Trioxide System with the Symmetric Electrolyte NRTL Model. J Chem Eng Data [Internet]. 2011 Apr 14 [cited 2023 May 23];56(4):963–77. Available from: <DOI>

20. Sippola H. Thermodynamic modelling of concentrated sulfuric acid solutions. Calphad. 2012 Sep 1;38:168–76. Available from: <DOI>

21. Sippola H, Taskinen P. Thermodynamic properties of aqueous sulfuric acid. J Chem Eng Data [Internet]. 2014 Aug 14 [cited 2023 May 23];59(8):2389–407. Available from: <URL>

22. Bouchkira I, Latifi AM, Khamar L, Benjelloun S. Global sensitivity based estimability analysis for the parameter identification of Pitzer's thermodynamic model. Reliab Eng Syst Saf. 2021 Mar 1;207:107263. Available from: <DOI>

JOTCS A
Journal of the Turkish Chemical Society
Section: A
Chemistry
TURKISH CHEMICAL SOCIETY

A Novel Method Development and Validation by Ultra-Performance Liquid Chromatography for Assay of Asciminib in Dosage Form

Pridhvi Krishna Gaddey[1], Raja Sundararajan[1*]

[1]Department of Pharmaceutical Analysis, GITAM School of Pharmacy, GITAM (Deemed to be University), Visakhapatnam, Pincode: 530 045, Andhra Pradesh (State), India.

Abstract: The main objective of the present study was to develop and validate simple, precise, sensitive and accurate UPLC method for the estimation of asciminib in pure and dosage form. The UPLC method was developed by using Waters Acquity liquid chromatographic system and Zorbax Phenyl (100x1.0mm,1.7µm) column. The developed method was validated according to the international conference on harmonization (ICH) guidelines. The chromatographic separation of asciminib with good resolutions has been achieved by using the mobile phase acetonitrile: ammonium dihydrogen phosphate buffer (20:80 v/v) at a flow rate of 0.5 mL/min, injection volume of 5 µL, and at 242 nm wavelength. The validated method was found to be linear in the range of 4 - 60 µg/mL. The limit of detection (LOD) and limit of quantification (LOQ) for asciminib were found to be 0.4 and 0.12 µg/mL respectively. The % RSD was found to be less than 2 % revealing the precision of the developed method. Besides, the recovery rate was observed close to 100 % confirming the accuracy of the method. Minor alterations in the chromatographic conditions have revealed robustness and ruggedness of the developed method. The developed analytical method is simple, precise, sensitive, and reproducible which can be used for the estimation of asciminib.

Keywords: UPLC, Asciminib, Buffer, Method development, Forced degradation studies

Submitted: January 2, 2023. **Accepted:** April 26, 2023

Cite this: Gaddey PK, Sundararajan R. A Novel Method Development and Validation by Ultra-Performance Liquid Chromatography for Assay of Asciminib in Dosage Form. JOTCSA. 2023;10(2):529-40.

DOI: https://doi.org/10.18596/jotcsa.1228364

***Corresponding authors. E-mail:** sraja61@gmail.com

1. INTRODUCTION

Many modifications were made to the techniques of chromatography to overcome the shortcomings like analysis time and the range of compounds that could be detected. Application of pressure was practised by use of pumps to reduce the time of run (1). Technologies like electrochemical methods and spectroscopy were added to enhance detection. The functional efficiency of chromatographic techniques enhanced to a great extent with these developments and modifications and also the range and type of substances that could be analysed (2).

A liquid handling system that can run such columns at significantly higher pressures is now available, as well as chromatographic media with 1.7 µm particle size due to recent developments in pharmaceutical analysis. This technology, known as Ultra performance liquid chromatography (UPLC), has shown improvements in method sensitivity, resolution, and speed when compared to standard HPLC. It uses sub-2-micron particles and extremely high pressure (up to 100 MPa is achievable in UPLC system) (3). When compared to chromatographic systems using analytical columns filled with particles of 5 µm size, the UPLC system can reduce analysis time by up to nine times. Analysis time was reduced by roughly three times when compared to analytical columns packed with particles of 3 µm size (4).

There are numerous potential uses for the UPLC technique in the investigation of pharmaceutical and biological chemicals, and it is a field that is both well-established and rapidly expanding (5). UPLC technique can be used for the determination of particular biological and pharmaceutical compounds that can be determined using UPLC, together with ranges of their respective determination or detection limits and with other associated parameters (6).

Faster and greater UPLC separation can shorten the time needed for method development in research and development laboratories because most

pharmaceutical corporations want to cut expenses and time associated with research and development (7). With the introduction of UPLC, a novel liquid chromatography instrument system was created that increases throughput and analytical speed without sacrificing chromatographic performance (8).

UPLC systems reduce column re-equilibration time, which results in a significant reduction in solvent usage. Injection volume in UPLC is over 10 times less than in HPLC, leading to acceptable peak forms and little impacts linked to column diameter. With higher resolution and speed of LC analyses, UPLC boosts data quality and productivity by providing more data per unit of work (9).

The IUPAC name of asciminib was N-[4-[chloro(difluoro)methoxy] phenyl]-6-[(3R)- 3-hydroxypyrrolidin-1-yl]-5-(1H-pyrazol-5-yl) pyridine-3-carboxamide. The molecular formula of asciminib was $C_{20}H_{18}ClF_2N_5O_3$. Asciminib was a selective allosteric inhibitor of BCR/ABL1, strongly binding to the myristoyl pocket of ABL1 kinase. The GNF2 chemical asciminib had been found as having the unique ability to cause a significant bend in the domain's C-terminal helix. Asciminib inhibits downstream signalling by regaining the initial autoregulatory mechanism that caused the inactive conformation; however, it is 100 times more potent than other GNF2 drugs (10). More than 60 distinct kinases, including SRC kinases, G-protein receptors, ion channels, nuclear receptors, and transporters, were shown to be inactive against the medication in several tests (11). The National Comprehensive Cancer Network introduced asciminib as a new therapy option in 2021 after the US FDA granted it approval. The recommended dosage was 40 mg BID or 80 mg QD (12).

A comprehensive review of the literature on asciminib revealed no methods like HPLC, UPLC or LC-MS for determining asciminib in pharmaceutical formulations and bulk drugs. The goal of this study was to create and evaluate a stability-indicating RP-UPLC technique for determining asciminib in bulk and pharmaceutical dosage forms.

2. EXPERIMENTAL

2.1. Reagents and Chemicals

Asciminib (Figure 1) pure bulk drug (API), Asciminib dosage form tablets (Scemblix), acetonitrile, ortho-phosphoric acid, and ammonium dihydrogen phosphate were used. Merck provided all of the HPLC grade solvents. Whatman filter (0.22 µ) were employed to filter all of the solvents and solutions used. The asciminib drug sample was obtained from Shree Icon labs, Vijayawada, India as gift sample.

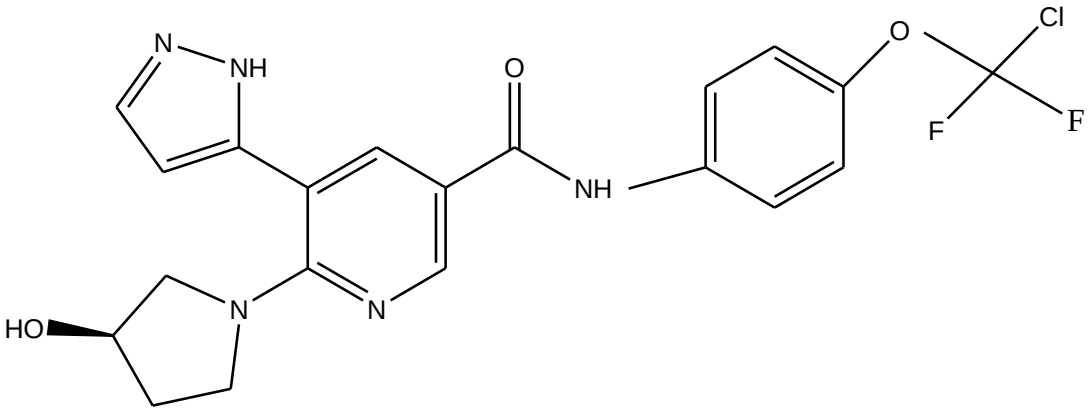

Figure 1: Structure of Asciminib.

2.2. Instrumentation and Conditions for Chromatography

The chemicals were weighed on an electronic balance-Denver. The pHs of the buffers were measured by means of pH meter -BVK enterprises. The solutions were sonicated or degassed using ultrasonicator-BVK enterprises. The chromatography analysis was performed using Waters Acquity liquid chromatographic system and the signal was detected using PDA detector with empower 2 software. UPLC method development and validation was carried out on a Phenyl (100x1.0mm,1.7µm) column, using a mobile phase of acetonitrile: ammonium dihydrogen phosphate buffer (20:80 v/v) with a flow rate of 0.5 mL/min. The sample injection volume was 5 µL. The column temperature was ambient. From the UV spectrum of asciminib, 242 nm wavelength was chosen which displays the maximum absorbance. The eluted compounds were monitored at 242 nm.

2.3. Preparation of Solutions

2.3.1. Buffer- Ammonium dihydrogen phosphate

Precisely weighed 1.15 grams of ammonium dihydrogen phosphate was transferred into thousand millilitres volumetric flask. Nine hundred millilitres HPLC grade water was added and sonicated. Lastly, orthophosphoric acid solution was used to correct the pH to 3.0 and the volume was made up with water.

2.3.2. Mobile phase

Mobile phase used for elution was acetonitrile: ammonium dihydrogen phosphate buffer in the ratio of 20:80 v/v. A 0.22 µ filter was used to filter the mobile phase. The diluent was chosen based on the drugs' solubility. Ethanol was used as diluent.

2.3.3. Preparation of standard stock solution

Precisely weighed 40 mg of asciminib was taken into a 100mL volumetric flask. 75% of the dilutants were put in the flask. Then, the flask was sonicated for ten minutes. The flask was then filled with diluent.

2.3.4. Preparation of standard working solution
Standard stock solution of 5 mL was transferred to a volumetric flask of 50 mL. 75% of the dilutants were put in the flask. Then, the diluent was used to make up to the volume.

2.3.5. Preparation of sample stock solution
The average weight of ten pills was determined. The weight comparable to 1 pill was weighed after the tablets were crushed into powder. The powder was then placed to a hundred millilitres volumetric flask. Diluents were used to make up to 100 mL of volume, which was then filtered using a 0.22 µ syringe filter.

2.3.6. Preparation of sample working solution
Filtrated sample stock solution of five millilitres was moved into a volumetric flask with a capacity of 50 mL. Then, the solution was prepared with made up with diluent.

2.4. Method Development and Validation Parameters
Mobile phase was pumped for around thirty minutes to saturate the column and the base line was adjusted. Various mobile phase ratios, buffers, and other parameters were changed to develop the method.

2.4.1. Linearity
Appropriate volumes of asciminib standard working solution were utilized to prepare seven standard drug concentrations covering the calibration range of 4 - 60 µg/mL. Each solution was injected into the instrument and peaks were recorded. The calibration curves were obtained by plotting peak area versus concentration. To statistically assess the linearity of the results, the correlation coefficient (R) and the linear regression equation were used.

2.4.2. Accuracy
Recovery studies have been used to verify the method's accuracy at 50%, 100%, and 150% level. A known amount of asciminib drug was spiked discretely to pre-analysed samples of the stated levels. The percent recovery of each level was calculated after each spiked level was administered into the UPLC system.

2.4.3. Precision
Method precision was executed by spiking the sample with asciminib at hundred percent of the quantified limit concerning the sample concentration in 6 preparations. Six homogenous replicates were injected. Then, the amount of asciminib was calculated to determine the percent relative standard deviation.

In six preparations, the intermediate precision was achieved by spiking the sample with asciminib at hundred percent of the prescribed limit in terms of sample concentration. The intermediate precision investigation was conducted on various days with various analysts.

2.4.4. LOD and LOQ
The limit of detection (LOD) and the limit of quantification (LOQ) were derived by means of the subsequent equations based on the slope of the calibration curve and the SD of linearity responses.

LOD = 3.3 × Standard deviation (SD) / slope
LOQ = 10 × Standard deviation (SD) / slope

2.4.5. System suitability parameters
Six replicates of asciminib working standard samples were injected to assess system suitability, and metrics such as tailing factor (K), relative retention time, plate number (N), resolution, and peak asymmetry of samples were investigated.

2.4.6. Robustness
Small adjustments in chromatographic settings such as flow (-) (0.45 mL/min), flow (+) (0.55 mL/min), organic phase (-) (18 O:82), and organic phase (+) (22 O:78) were used to test the method's robustness.

2.4.7. Specificity and selectivity
The absence of adjuvant interference during the application of the planned approach to the study of pharmaceutical formulations demonstrated its selectivity. The method's specificity was assessed in terms of interference caused by the occurrence of any additional placebos. Two dissimilar samples were administered and compared to their placebo counterparts.

2.5. Forced Degradation Studies
2.5.1. Peroxide degradation
The probable peaks and rates of asciminib degradation was assessed by weighing stock solution of 5 mL and transferring it into a volumetric flask of volume 50 mL. Then, it was subjected to forced degradation by adding 1mL of 30% H_2O_2; heating at 60 °C, and cooling to room temperature. After cooling, sample was diluted to volume with diluent and mixed. The samples were withdrawn at specific times (0, 6, 12, 18, and 24 hrs) intervals and subjected to UPLC runs.

2.5.2. Reduction degradation
Asciminib was tested for rate of degradation and potential degradation peaks. 5 mL of the stock solution was transferred into a fifty millilitres volumetric flask. Then, it was forcedly degraded by adding 1 mL of 30 % sodium bi sulphate and heated at 60 °C. Sample was diluted with diluent to volume after cooling, then mixed. Samples were taken out and processed through an UPLC at certain time intervals (0, 6, 12, 18, and 24 hours).

2.5.3. Acid degradation
Stock solution of 5 mL was weighed and put into a volumetric flask of 50 mL. Then, 1 millilitre of 1N HCl was added and the flask was heated for six hours and cooled to room temperature. After cooling, 1 mL of NaOH was added to neutralise the solution and sample was diluted with diluent and mixed. Samples were taken out and processed through an UPLC at certain time intervals (0, 6, 12, 18, and 24 hours).

2.5.4. Base degradation
The possible degradation peaks and rate of degradation of asciminib were assessed by weighing stock solution of 5 mL and transferring into a fifty

millilitres volumetric flask. Then, it was subjected to forced degradation. 1mL of 1N NaOH was added and heated at 60 °C and cooled to room temperature. After cooling, 1 mL of 1N HCl was added and diluted to volume with diluent. Samples were withdrawn at specific time (0, 6, 12, 18, and 24 hrs) intervals and subjected to UPLC runs.

2.5.5. Hydrolytic degradation

Asciminib was tested for rate of degradation and potential degradation peaks. 5 mL of the stock solution was transferred into a 50 mL volumetric flask. Then, it was forcedly degraded by adding 3 mL of HPLC grade water and heated at 60 °C for three hours. Sample was diluted with diluent to volume after cooling, then mixed. Samples were taken out and processed through an UPLC at certain time points (0, 6, 12, 18, and 24 hours).

2.5.6. Thermal degradation

Stock solution of 5 mL was weighed and shifted into a 50 millilitres volumetric flask. Diluents were added to this and sonicated for 15 min to dissolve the contents. This solution was heated for 48 hours. Samples were withdrawn at specific time (0, 6, 12, 18, and 24 hrs) points and subjected to UPLC runs to identify probable degradation chromatograms.

2.5.7. Photo stability degradation

The rate of degradation and possible degradation peaks of asciminib were assessed by weighing 250 mg of sample. The sample was placed in a photo stability chamber for 72 lux hours. 192 mg of the above sample was weighed and transferred to a 100 mL volumetric flask. Diluents were added to this and sonicated for 15 min to dissolve the contents. Further, from the above solution 5 mL was pipetted out into a volumetric flask of volume 50 mL and diluted to volume with diluent. Samples were withdrawn at specific time (0, 6, 12, 18, and 24 hrs) points and subjected to UPLC runs.

2.6. Assay of Asciminib

A total of 20 pills were weighed and ground to powder. Volumetric flask of volume 100 mL was filled with powder corresponding to 40 mg asciminib. 70 mL diluents were added, dissolved by sonication, diluted to volume using dilutants, and filtered by means of a 0.45 µm porosity membrane filter.

3. RESULTS AND DISCUSSION

3.1. Chromatographic Optimization

After a series of trials, the mobile phase of acetonitrile: ammonium dihydrogen phosphate buffer in the proportion of 20:80 had shown peak with good theoretical plate count, resolution, tailing factor. Hence this method was optimized and validated. Waters Acquity UPLC auto sampler enabled the elution, method development and validation of asciminib. The optimized chromatogram was shown in Figure 2.

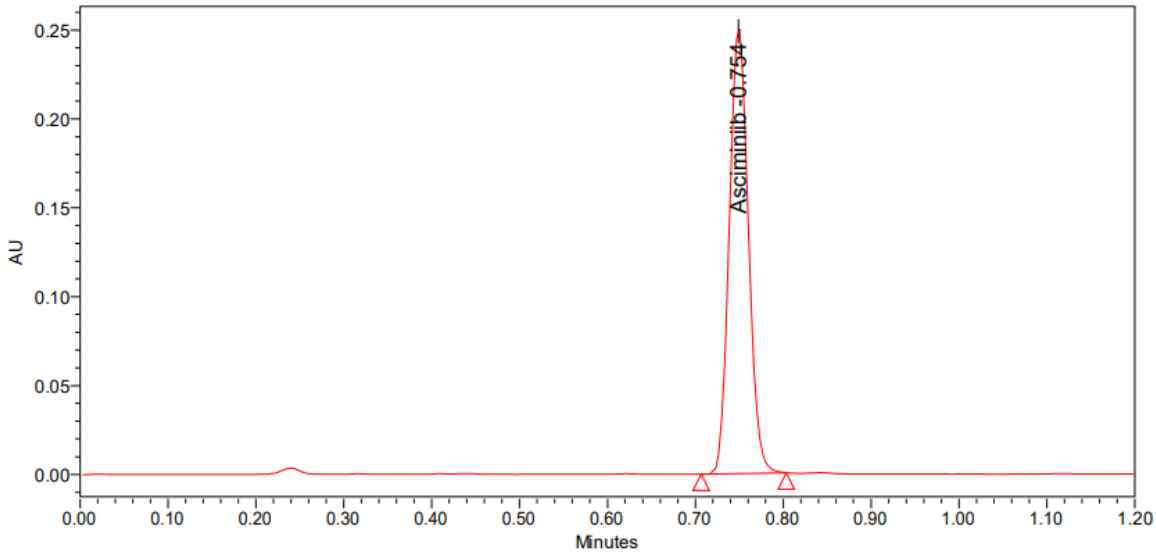

Figure 2: Optimized chromatogram of asciminib.

3.2. Method's Validation

3.2.1. Linearity

The analytical method's linearity was its capacity to produce test findings within a specified range that were directly proportional to the concentration of the analyte in the test sample (13). The regression line of analysis shows the relationship between concentration and peak area of asciminib. As a result, the findings revealed that the peak area and analyte concentration showed a strong correlation. The R high value indicated good linearity. The linearity of the analytical method was determined by seven concentration levels in the range of 4-60 µg/mL. The regression coefficient, y-intercept, and slope of regression line were calculated. The observed corelation coefficient value was 0.99982. The results were shown in Tables 1-2 and Figure 3.

3.2.2. Accuracy

The results of accuracy showed percentage recovery at all three levels in the range of 99.7–101.3%, and % RSD was 0.15 % as shown in Table 3. The percentage recovery and percent RSD values fell within the acceptable ranges of 98.0% to 102.0% and not more than 2.0%, respectively, demonstrating the method's suitability for routine drug analysis.

Table 1: Linearity studies of asciminib.

S. No	Concentration (µg/mL)	Peak area
1	4	326971
2	10	731459
3	20	1347935
4	30	2034756
5	40	2619390
6	50	3263458
7	60	3946340

Table 2: Optical characteristics of asciminib.

Parameters	Asciminib
Linearity (µg/mL)	4-60 µg/mL
Regression equation	y = 64712.07x + 46933.12
Slope	64712.07
Intercept	46933.12
Correlation coefficient (R)	0.99982

Table 3: Recovery studies of asciminib.

Recovery level	Amount Spiked (µg/mL)	Amount recovered (µg/mL)	% Recovery
50%	20	19.93	99.7
	20	20.26	101.3
	20	20.09	100.5
100%	40	40.09	100.2
	40	40.00	100.0
	40	40.26	100.7
150%	60	60.27	100.5
	60	60.27	100.5
	60	60.57	101.0
Mean			100.5
SD			0.2
RSD %			0.15

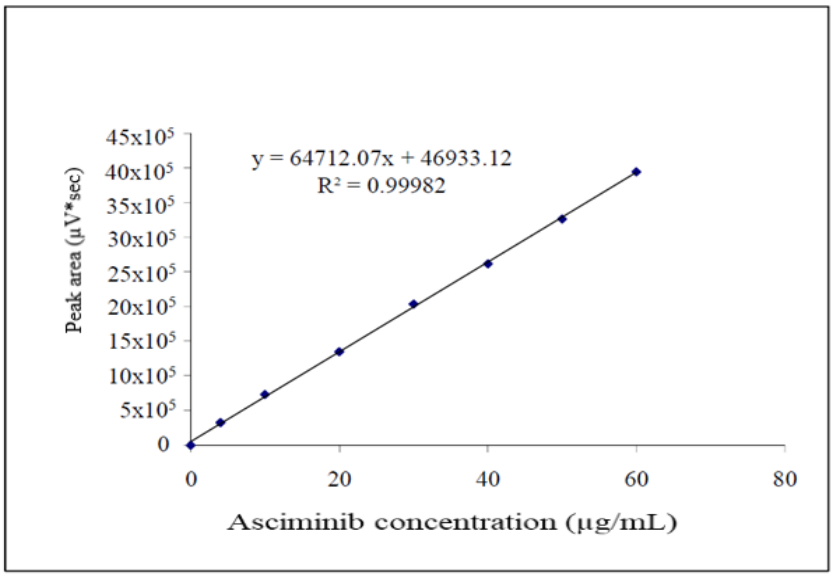

Figure 3: Calibration plot of asciminib.

3.2.3. Method precision

The degree of agreement between a set of measurements made using repeated samples of the same homogeneous material under the specified conditions was considered the precision of the method, and it was typically stated as relative standard deviation (13). The percent relative standard deviation value for method precision results of asciminib was found to be 0.38%. The percent relative standard deviation value for intermediate

precision results of asciminib was found to be 0.74%. The results were well under the usually accepted 2 percent limit. As a result, the new method's precision has been confirmed. The results were showed in Tables 4-5.

Table 4: Method precision studies of asciminib.

S. No	Area of asciminib
1.	2622418
2.	2611582
3.	2614570
4.	2628269
5.	2615321
6.	2637651
Mean	2621635
S.D	9920
RSD%	0.38

Table 5: Intermediate precision studies of asciminib.

S. No	Area of asciminib
1.	2653214
2.	2613206
3.	2615427
4.	2626539
5.	2600362
6.	2641488
Mean	2625039
S. D	19535
RSD%	0.74

3.2.4. Sensitivity

The limit of quantification (LOQ) was defined as the lowest quantity of analyte in a sample that was quantitatively identified with appropriate accuracy. The limit of detection (LOD) was defined as the lowest amount of analyte in a sample that was detected but not necessarily quantitated (13). The LOD and LOQ for asciminib were found to be 0.12 and 0.4 µg/mL respectively.

3.2.5. System suitability parameters

Analytical processes included testing for system compatibility. According to the ICH, a system suitability test was frequently used to assess a chromatographic system's resolution, column efficiency, and repeatability to ensure it was suitable for specific analysis. (13). The new approach was tuned to produce a symmetrical peak and high theoretical plates (N). The total number of theoretical plates was above 2000, which was deemed sufficient for the system suitability test. According to the standards, the tailing factor was within the specified limitations. These findings demonstrate that the proposed strategy can produce data of acceptable quality. The results were tabulated in Table 6.

Table 6: System suitability parameters for asciminib.

S. No	RT (min)	USP Plate Count	Tailing
1.	0.754	5634	1.08
2.	0.757	5623	1.12
3.	0.750	5580	1.10
4.	0.752	5600	1.11
5.	0.755	5558	1.09
6.	0.759	5567	1.09
Mean	0.755	5594	1.10

3.2.6. Robustness

The influence of slight alterations in chromatographic settings was used to determine the robustness of the analytical process. The percent RSD of assay of asciminib was less than 2.0 in all of the deliberately changed chromatographic settings. The system suitability parameters were not changed while varying the conditions, hence the method was robust. The results were showed in the Table 7.

3.2.7. Specificity and selectivity

The method's specificity and selectivity were tested by looking for interference peaks in the chromatograms of blank and placebo samples. In the retention time ranges, the UPLC chromatograms for the drug matrix (combination of the medicine and placebos) revealed nearly no interference peaks. As a result, the proposed UPLC approach in this study was selective. Figures 4 and 5 show the chromatograms of blank and working placebo solutions, respectively.

Table 7: Robustness studies of asciminib.

Condition	Retention time (min)	Peak tailing	Plate count	%RSD of assay of asciminib
Flow rate (-) 0.45 mL/min	0.925	1.12	6510	0.72
Flow rate (+) 0.55 mL/min	0.631	1.11	4361	0.21
Mobile phase (-) 18O:82B	0.903	1.14	5702	0.21
Mobile phase (+) 22O:78B	0.625	1.10	5588	0.21

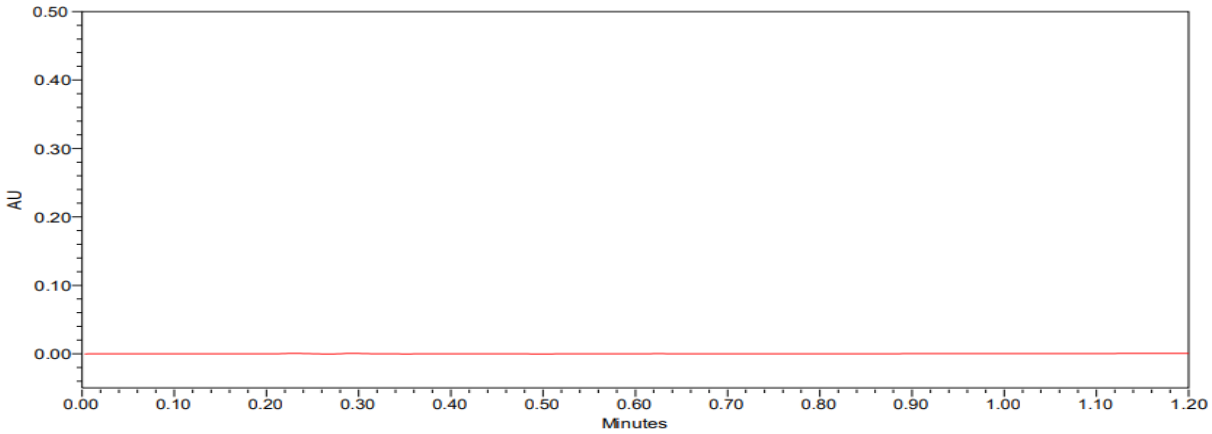

Figure 4: Chromatogram of blank.

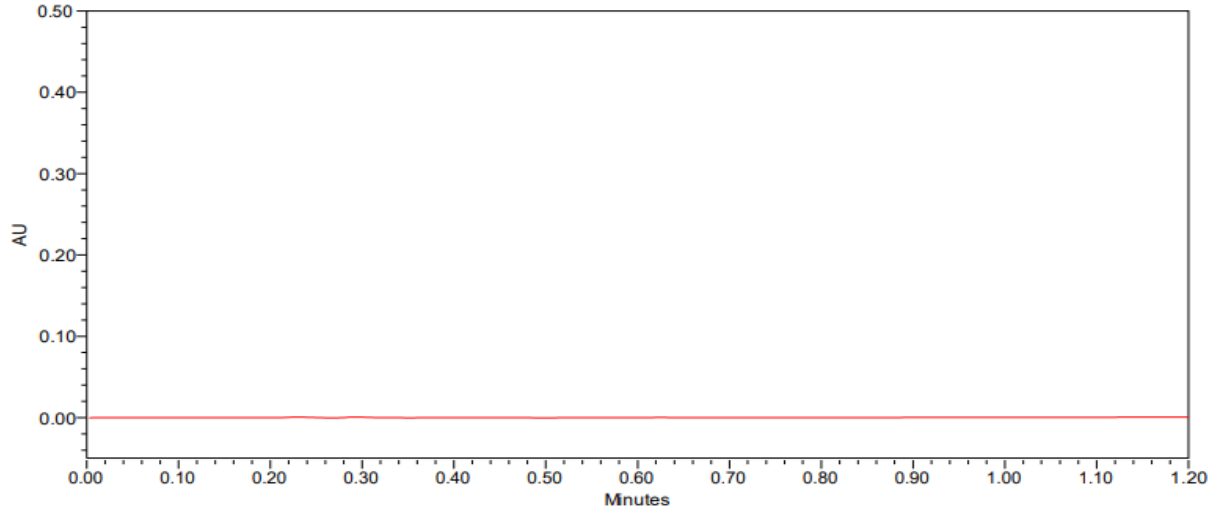

Figure 5: Chromatogram of placebo.

3.2.8. Forced degradation studies

Asciminib was subjected to a variety of stress conditions, which include hydrolysis, base, oxidative, acid, photo stability, and thermal degradation, as per ICH guidelines. The proposed UPLC approach was used to monitor degradation behaviour on a regular basis. The TUV detector results from the forced deterioration results revealed that the asciminib peaks were pure and homogenous in all of the stressful conditions studied. Also, the drug was more degraded in peroxide degradation and less degraded in hydrolysis degradation conditions. Degradant peaks were eluted in acid, thermal, peroxide and base conditions. All the results of stability studies were displayed in Tables 8-14. The chromatogram peaks of degradation studies were showed in Figures 6-11.

Table 8: Acid degradation studies of asciminib.

Time	Peak area	% Label claim	% Degraded	Purity angle	Purity threshold
Initial	2524786	96.4	3.6	18.137	72.185
6 hrs	2356301	90.0	10.0	18.133	72.184
12 hrs	2236589	85.4	14.6	18.139	72.185
18 hrs	2108547	80.5	19.5	18.901	72.554
24 hrs	1998549	76.3	23.7	18.905	72.505

Table 9: Base degradation studies of asciminib.

Time	Peak area	% Label claim	% Degraded	Purity angle	Purity threshold
Initial	2538564	96.9	3.1	18.134	72.186
6 hrs	2384154	91.0	9.0	18.142	72.187
12 hrs	2263052	86.4	13.6	18.131	72.179
18 hrs	2138547	81.7	18.3	18.133	72.175
24 hrs	2066953	78.9	21.1	18.656	72.763

Table 10: Peroxide degradation studies of asciminib.

Time	Peak area	% Label claim	% Degraded	Purity angle	Purity threshold
Initial	2510547	95.9	4.1	18.366	72.528
6 hrs	2330256	89.0	11.0	18.354	72.517
12 hrs	2228795	85.1	14.9	18.359	72.514
18 hrs	2058961	78.6	21.4	18.363	72.527
24 hrs	1975896	75.4	24.6	18.368	72.521

Table 11: Reduction degradation studies of asciminib.

Time	Peak area	% Label claim	% Degraded	Purity angle	Purity threshold
Initial	2548594	97.3	2.7	18.138	72.186
6 hrs	2406845	91.9	8.1	18.145	72.183
12 hrs	2279658	87.0	13.0	18.614	72.185
18 hrs	2175478	83.1	16.9	18.137	72.172
24 hrs	2120563	81.0	19.0	18.737	72.625

Table 12: Thermal degradation studies of asciminib.

Time	Peak area	% Label claim	% Degraded	Purity angle	Purity threshold
Initial	2566854	98.0	2.0	18.136	72.181
6 hrs	2500210	95.5	4.5	18.144	72.188
12 hrs	2360325	90.1	9.9	18.143	72.188
18 hrs	2285968	87.3	12.7	18.603	72.146
24 hrs	2245173	85.7	14.3	18.603	72.151

Table 13: Photolysis degradation studies of asciminib.

Time	Peak area	% Label claim	% Degraded	Purity angle	Purity threshold
Initial	2571578	98.2	1.8	18.133	72.152
6 hrs	2564587	97.9	2.1	18.158	72.167
12 hrs	2535214	96.8	3.2	18.172	72.149
18 hrs	2495896	95.3	4.7	18.129	72.151
24 hrs	2445716	93.4	6.6	18.734	72.667

Table 14: Hydrolysis degradation studies of asciminib.

Time	Peak area	% Label claim	% Degraded	Purity angle	Purity threshold
Initial	2585646	98.7	1.3	18.157	72.182
6 hrs	2554756	97.6	2.4	18.162	72.154
12 hrs	2543021	97.1	2.9	18.155	72.136
18 hrs	2521053	96.3	3.7	18.117	72.147
24 hrs	2505231	95.7	4.3	18.739	72.526

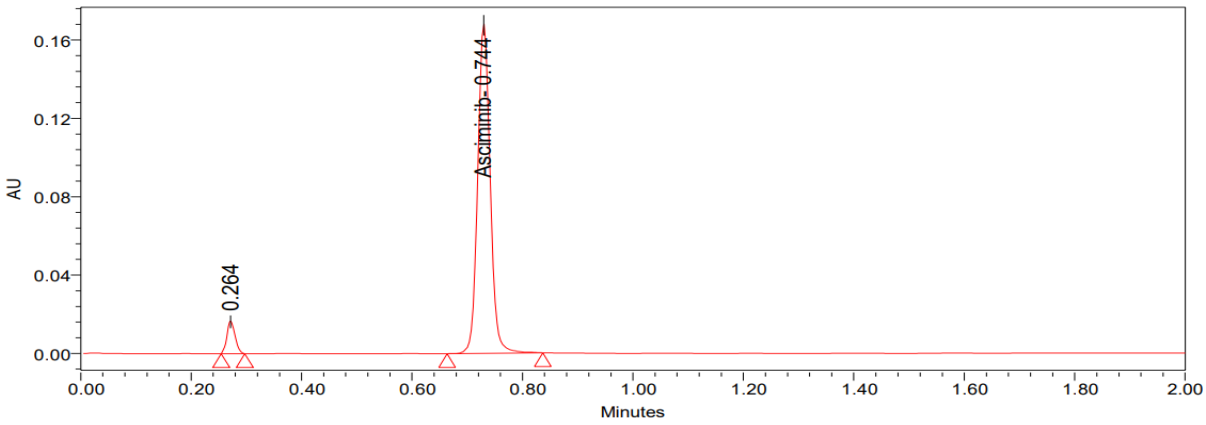

Figure 6: Acid degradation chromatogram.

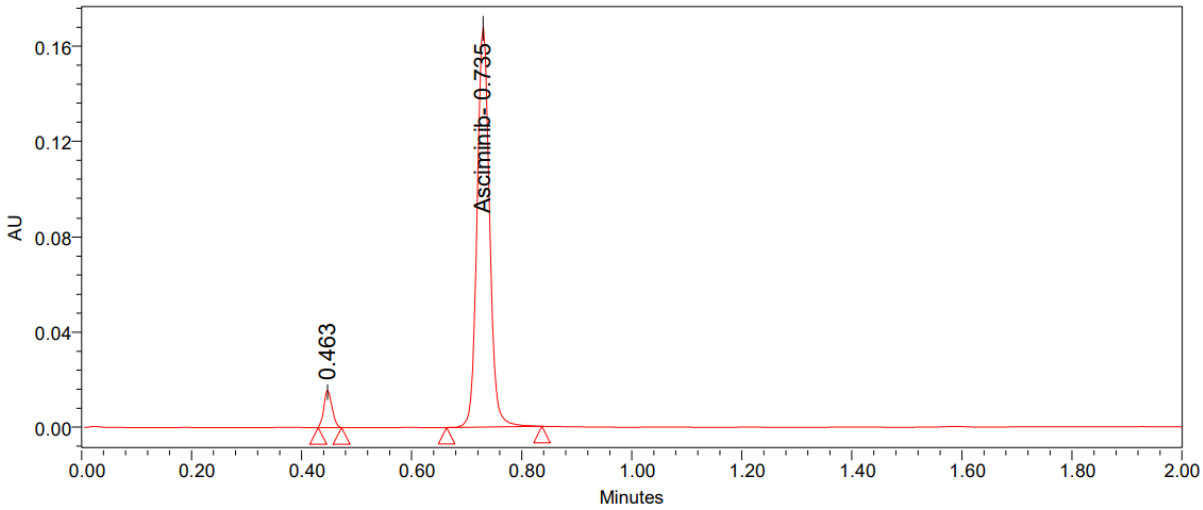

Figure 7: Base degradation chromatogram.

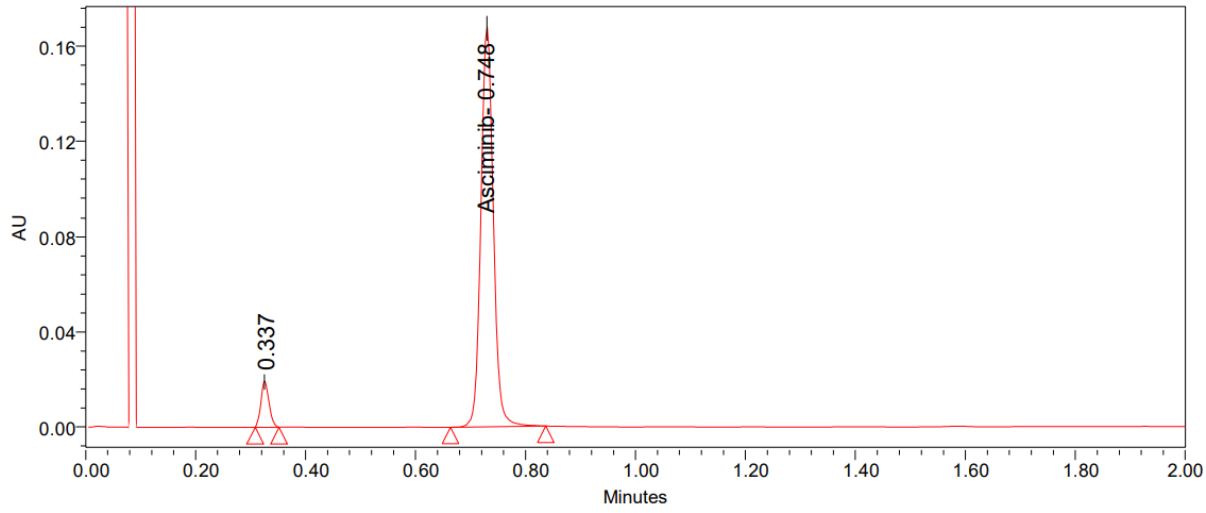

Figure 8: Peroxide degradation chromatogram.

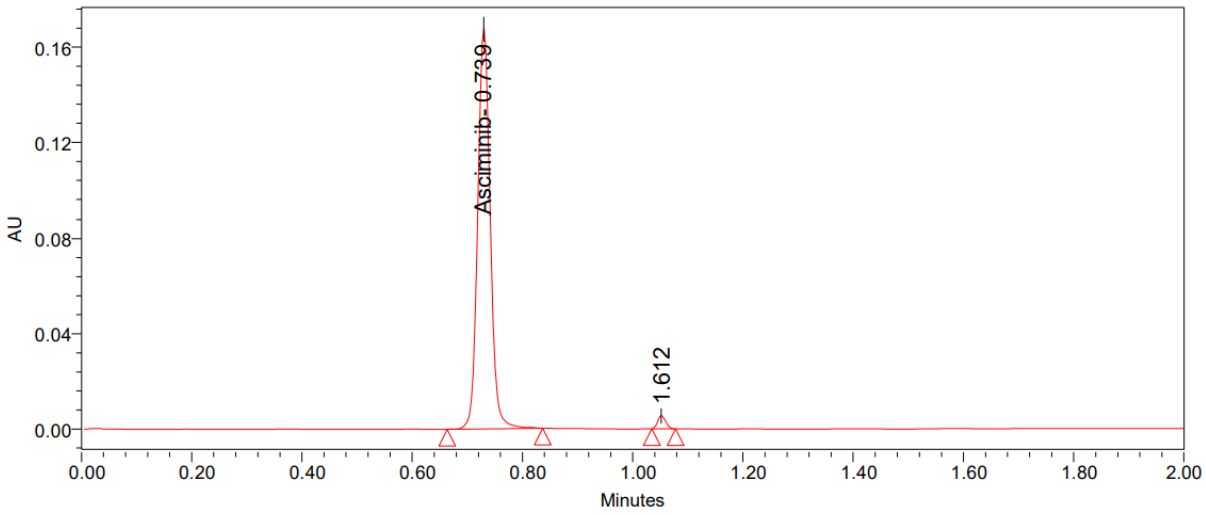

Figure 9: Thermal degradation chromatogram.

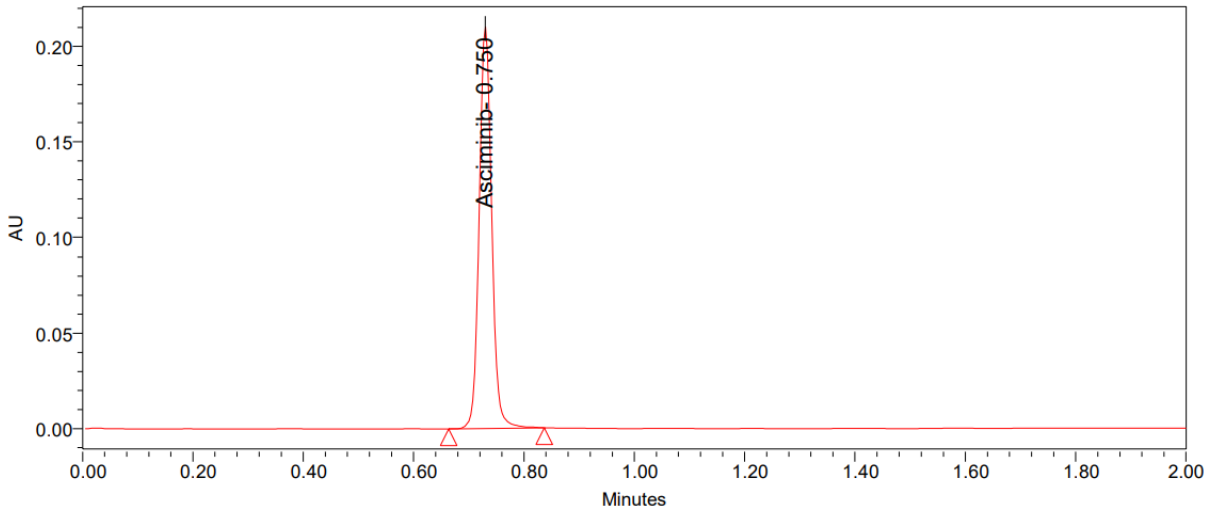

Figure 10: Photo degradation chromatogram.

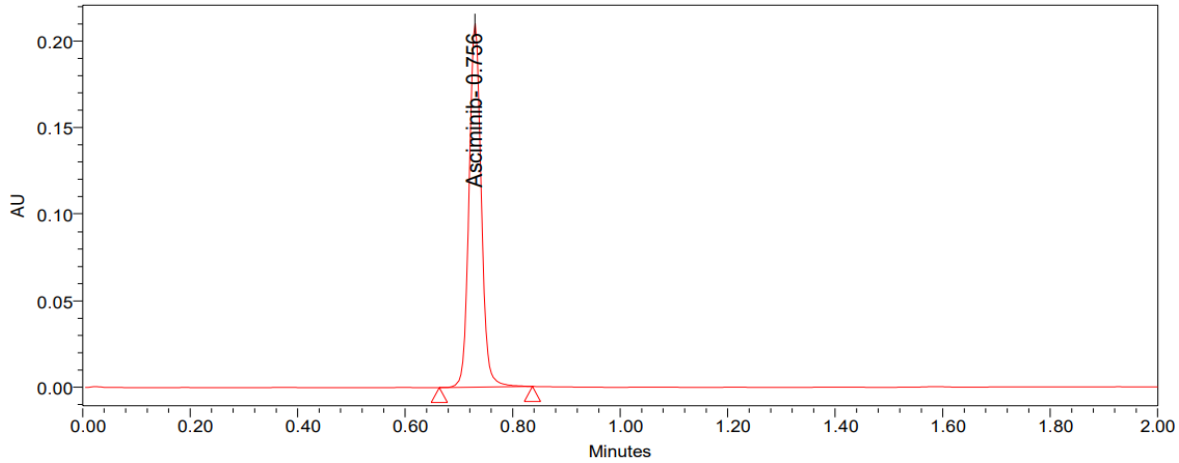

Figure 11: Hydrolytic degradation chromatogram.

3.3. Assay

The suggested method's application to the analysis of formulations is its key feature. Hence the market sample of asciminb was collected and analysed by employing the proposed method. According to the label claim, the drug content obtained from the values of sample solutions was found to be in the permissible range of 90–110 percent. The % assay of asciminib was found to be 40.08 mg/tablet. The study confirmed that the created UPLC method was accurate and easy enough to be used on a daily basis. The suggested assay method's high content results indicate that this technique can be engaged for quantitative regular quality control study of pharmaceutical dosage forms. The results were displayed in Table 15.

Table 15: Results of marketed formulation analysis.

Compound name	Brand name	Label claim (mg)	Assay (mg/tablet)
Asciminib	Scemblix	40	40.08

4. CONCLUSION

For the estimate of asciminib in tablet dose form, a simple, accurate, and specific approach was established. Asciminib had retention time of 0.754 minutes. The percent RSD of method precision and intermediate precision were found to be 0.38 % and 0.74 %. For asciminib, recovery was 100.5 %. The LOD and LOQ values for asciminib calculated from regression equations were 0.12 µg/mL and 0.4 µg/mL consecutively. Regression equation of asciminib was y = 64712.07x + 46933.12. There were some degradation peaks in acid, base, thermal and peroxide stressed conditions, according to the results of the forced degradation test. This drug was recently approved by FDA and there was no analytical method reported. This was the analytical method which has reduced retention time and run time. Hence, the method created was fast, short, simple, and economic, and it might be utilized in frequent quality control tests in industries.

5. CONFLICT OF INTEREST

The authors declare that there is no conflict of competing financial interests.

6. ACKNOWLEDGEMENTS

The authors are thankful to the management of GITAM (Deemed to be University), Visakhapatnam, Andhra Pradesh, India, for providing necessary facilities and M.V.V.S Murthi fellowship grants to carry out the research work.

7. REFERENCES

1. Patel M. Review Article: Chromatography Principle and Applications Mimansha. Int J Pharmacy&Pharmaceutical Res [Internet]. 2018;13(4):288–93. Available from: <URL>.

2. Priyadarshini R, Raj GM, Gopal Shewade D. Chromatography – The Essence of Bioanalysis. Eur J Biomed Pharm Sci [Internet]. 2016;3(1):366–77. Available from: <URL>.

3. Khan H, Ali J. UHPLC: Applications in Pharmaceutical Analysis. Asian J Pharm Anal [Internet]. 2017;7(2):124–31. Available from: <URL>.

4. Sri RS, Sri KB, Mounika C. A Review on Comparative study of HPLC and UPLC. Res J Pharm Technol [Internet]. 2020;13(3):1570–4. Available from: <URL>.

5. Srivastava B, Sharma BK, Baghel US, Yashwant, Sethi NK. Ultra Performance Liquid Chromatography (UPLC) : A Chromatography Technique. Int J Pharm Qual Assur [Internet]. 2010;2:19–25. Available from: <URL>.

6. Chandarana C, Manani L, Patel V, Prajapati P. UPLC: A Prominent Analytical Technique For Pharmaceuticals. Int J Pharm Sci Rev Res [Internet]. 2016;37(2):192–201. Available from: <URL>.

7. Roge AB, Firke SN, Dhane RM, Gunjkar VJ, Vadvalkar SM. Novel Achievement of HPLC: UPLC. Int J PharmTech Res [Internet]. 2011;3(3):1423–9. Available from: <URL>.

8. Gumustas M, Kurbanoglu S, Uslu B, Ozkan SA. UPLC versus HPLC on Drug Analysis: Advantageous, Applications and Their Validation Parameters. Chromatographia [Internet]. 2013 Nov 27;76(21–22):1365–427. Available from: <URL>.

9. Swartz ME, Murphy B. New Frontiers in Chromatography. Am Lab [Internet]. 2005 [cited 2023 May 13];22–7. Available from: <URL>.

10. Breccia M, Colafigli G, Scalzulli E, Martelli M. Asciminib: An investigational agent for the treatment of chronic myeloid leukemia. Expert Opin Investig Drugs [Internet]. 2021 Aug 3;30(8):803–11. Available from: <URL>.

11. Luna A, Pérez-Lamas L, Boque C, Giraldo P, Xicoy B, Ruiz Nuño C, et al. Real-life analysis on safety and efficacy of asciminib for ponatinib pretreated patients with chronic myeloid leukemia. Ann Hematol [Internet]. 2022 Oct 23;101(10):2263–70. Available from: <URL>.

12. Cortes JE, Hochhaus A, Takahashi N, Larson RA, Issa GC, Bombaci F, et al. Asciminib monotherapy for newly diagnosed chronic myeloid leukemia in chronic phase:Tthe ASC4FIRST phase III trial. Futur Oncol [Internet]. 2022 Dec;18(38):4161–70. Available from: <URL>.

13. Hubbard WK. International Conference on Harmonisation; Guideline on the Validation of Analytical Procedures: Methodology; Availability. Fed Regist [Internet]. 1997;62(96):27464–7. Available from: <URL>.

JOTCS A
Journal of the Turkish Chemical Society
Section: A
Chemistry
TURKISH CHEMICAL SOCIETY

Determination of Cefuroxime Axetil in Tablet by HPLC, UV and First-Order Derivative Spectroscopy Methods & Plasma by UV Spectroscopy Method

Atakan TURAN[1], Yucel KADIOGLU[2*]

[1]Çekirge State Hospital, Bursa, 16090, Turkey
[2]Ataturk University, Faculty of Pharmacy, Department of Analytical Chemistry, Erzurum, 25240, Turkey

Abstract: It was aimed to develop and validate the UV spectroscopic, the first-order derivative spectroscopy, and the HPLC method for determination of cefuroxime axetil in bulk and tablets and also in spiked human plasma samples by UV spectroscopy method. In the spectroscopic analyses, the maximum absorbance of cefuroxime axetil in acetonitrile was obtained at 277 nm wavelength in the spectra. In first-order derivative spectroscopy method, two peaks were observed in spectra, a maximum at 258 nm and a minimum at 298 nm. 298 nm wavelength was used in the study. In HPLC-UV study, parameters were chosen as follows: C18 column, 0.1% acetic acid-acetonitrile (30:70; v/v) for mobile phase, 1.0 mL/min of flow rate, 280 nm of wavelength, 10 µL of injection volume and etodolac (2.5 µg/mL) as internal standard. Accuracy, precision, recovery, linearity and sensitivity parameters were determined for each of the three methods. Developed and validated methods were successfully applied on 4 tablets which are named as Cefaks, Cefurol, Aksef ve Enfexia. As a result, it is claimed that proposed method is sensitive, precise, accurate, and successfully used in quality control studies in the drug industry.

Keywords: Cefuroxime axetil, UV spectroscopy, first-order derivative spectroscopy, HPLC, tablet.

Submitted: December 21, 2022. Accepted: April 28, 2023.

Cite this: Turan A, Kadıoglu Y. Determination of Cefuroxime Axetil in Tablet by HPLC, UV and First-Order Derivative Spectroscopy Methods & Plasma by UV Spectroscopy Method. JOTCSA. 2023;10(2):541-8.

DOI: https://doi.org/10.18596/jotcsa.1222357.

***Corresponding author. E-mail:** yucel@atauni.edu.tr

1. INTRODUCTION

Cefuroxime axetil (1-acetoxyethyl ester of cefuroxime, CFA), commonly used in therapy, is a prodrug of cefuroxime, CFA), cefuroxime axetil whose chemical formula is (1RS)-1-[(acetyl)oxy] ethyl (6R,7R)-3-[(amino carbonyl oxy) methyl]-7-[[(Z)-2-(furan-2-yl)-2- (methoxy imino) acetyl]amino]-8-oxo-5-thia-1-azabicyclo [4.2.0]oct-2-en-2-carboxylate (Figure 1), is a member of cephalosporins. Its closed formula is C20H22N4O10S and its molecular weight is 510.48 g. It has white, a bitter taste, and a powdery appearance in an amorphous structure. Cefuroxime axetil is very soluble in methanol, ethyl acetate, and acetone but it is sparingly soluble in water, ethanol (96%), and ether (1). Cefuroxime axetil is an antibiotic. Natural or chemical substances formed by fungi or similar microorganisms, which have the power to stop the growth of microorganisms and other living things, and even kill them, are called "antibiotics"(2). Cefuroxime axetil is a second-generation cephalosporin that is active against a wide range of gram-positive and gam-negative organisms and resistant to most β-lactamases. Cefuroxime axetil has a wide usage area due to its strong antibacterial effect. Cefuroxime axetil is indicated for the treatment of infections caused by sensitive bacteria (3).

Cefuroxime shows its effect by inhibiting bacterial cell wall synthesis and stimulating autolytic enzymes. Cefuroxime axetil, like other cephalosporin's, is highly resistant to β-lactamases

and especially shows good activity on Escherichia coli, Klebsiella spp., Proteus mirabilis, Moraxella subgenus, Branhamellacatarrhalis, Neisseria gonorrhaeae, Streptococcus spp., Staphylococcus spp. And Haemophil. In addition, it shows good activity against all strains, including ampicillin-resistant strains in generally (4,5). Cefuroxime is bound to plasma proteins up to 50% and dose adjustment is required in case of renal failure (6). Studies on the direct quantification of cefuroxime axetil are very limited. In the literature reviews of cefuroxime axetil, which has a wide area of use as an antibiotic, scientific studies have been reached in the determination of plasma and pharmaceutical preparations (7,8). These methods in pharmaceutical preparations: spectrofluorometric method (9), HPLC (10-13), thin-layer chromatography and densitometry (14), capillary zone electrophoresis (15) and spectroscopy methods (16-19).

In the studies based on spectroscopic analyses, cefuroxime axetil was derivatized by reacting with different reagents (1-nitroso-2 naphthol and sodium hydroxide; bromothymol blue) and analyzed by spectrophotometric method (16,17). Pritam et al. analyzed cefuroxime axetil in eye drops in HCl medium with spectrophotometer (18). Game et al., (19) on the other hand, developed a UV spectrophotometric method in 0.1 M HCl medium and a derivative spectrophotometric method in 0.1 M NaOH medium for the determination of cefuroxime axetil in tablets.

The aim of this study is to develop and validate UV spectroscopic, first-order derivative spectroscopy and HPLC methods for the determination of the active ingredient cefuroxime axetil in bulk and tablets, as well as UV spectroscopy methods for the determination of cefuroxime axetil in plasma. Quantitative determination of cefuroxime axetil in spectroscopy methods was performed without derivatization. This provides convenience in the determination method.

2. MATERIALS AND METHODS

2.1. Reagents and Chemicals

Cefuroxime axetil and etodolac was obtained from Nobel Ilac A.Ş. (Turkiye). Acetonitrile (HPLC grade), phosphoric acid (Merck), diethyl ether (Merck) and acetic acid (Fluka) were purchased. The deionized water was made fresh every day and filtered (0.45 m). 4 commercial tablets (Cefaks, Cefurol, Aksef and Enfexia) were obtained in the community pharmacy (Erzurum, Turkiye). Human plasma was obtained from Erzurum Kızılay Blood Bank.

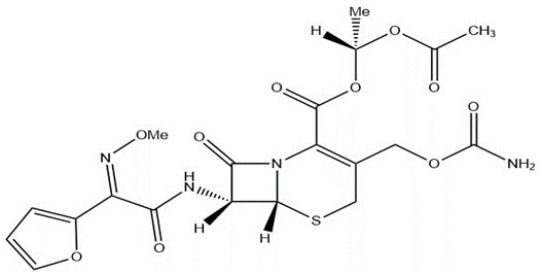

Figure 1: Chemical structure of cefuroxime axetil.

2.2. Apparatus and Method Conditions

A Thermospectronic double-beam UV-Visible spectrophotometer (HEλIOSβ) with a fixed slit width 2 nm and a data processing system was used. UV and first-order derivative spectra (N=6. Δλ=4.0 nm) of sample solutions were recorded in 1 cm quartz cells between wavelength ranges of 200-300 nm at a scan speed of 280 nm/min and derivation interval (Δλ) 21.0 nm. Maximum absorbance was observed at 277 nm and measurements were taken under these conditions. In first-order derivative spectroscopy methods, two peaks were observed in the spectrum, a maximum at 258 nm and a minimum at 298 nm.

HPLC System (Agilent Technologies 1200 Series), Degasser (Agilent Technologies), Pump (Agilent Technologies), Column (C18, 5µm, 250 x 4.6mm) (Phenomenex Bondolone USA), Auto Simpler (Agilent Technologies) and Computer (HP). HPLC conditions of work: UV detector (280 nm), deionized water (0.1% acetic acid): acetonitrile (30:70, v/v) of mobile phase, 25 °C of column temperature, 1.0 mL/min of flow rate and 10 µL of injection volume.

2.3. Preparation of Stock Solution, Standard Working Solutions, and Quality Control Solutions

The stock solution of cefuroxime axetil (100 µg/mL) was prepared by dissolving 10 mg of cefuroxime axetil in 100 mL of acetonitrile. The standard working solutions were prepared in 0.3, 0.5, 1.0, 3.0, 6.0, and 12. µg/mL concentrations for HPLC analysis and 1.0, 2.0, 4.0, 6.0, 8.0,10.0, 15.0, 20.0, 25.0, 30.0 and 35.0 µg/mL concentrations for spectroscopy methods from stock solution and also the quality control (QC) solutions were prepared at 0.4, 4.0, and 8.0 µg/mL concentrations for HPLC method and at 1.5, 4.5, 9.5, and 30.0 µg/mL concentrations for spectroscopic methods. The QC samples were analyzed for validation assessment.

In the HPLC study, etodolac (2.5 µg/mL) was used as the internal standard (IS).

2.4. Preparation of Plasma Samples

The plasma removed from -20 °C was allowed to dissolve at room temperature. An appropriate amount of cefuroxime axetil solutions at final concentrations of 1-30 µg/mL were spiked in 0.5 mL

of blank plasma and mixed and then extracted. After extraction, the plasma working solutions at 1.0, 2.0, 4.0, 6.0, 8.0, 10.0, and 30 µg/mL concentrations and the plasma quality control solutions at 1.5, 4.5, and 9.5 µg/mL concentrations were obtained.

2.5. Extraction Process of Cefuroxime Axetil from Plasma

0.5 mL of plasma was placed in centrifuge tubes and 0.5 mL of 1 M phosphoric acid was added to each of these tubes. Plasma was vortexed for one minute. 1 mL diethyl ether was added. Plasma was vortexed for three minutes and then centrifuged. The organic phase was taken. Evaporated under nitrogen gas at room conditions. Finally, it was dissolved in 4 mL of acetonitrile.

2.6. Preparation of Tablet Solutions

Application of the method to real samples was carried out by using 4 commercial tablets (Cefaks, Cefurol, Aksef and Enfexia) that contains cefuroxime axetil. In this study, 10 tablets from each formulation were weighed, mean values of them were recorded. Then, these tablets were grinded and blended until they became powder. A certain amount of this mixture was taken to be cefuroxime axetil weighing 1 tablet and put into a 100 mL volumetric flask. It was solved in acetonitrile and then its volume was completed to 100 mL. Final solutions were filtered, the new solutions at the concentrations of tablet samples to be used in the study were prepared and their concentrations were determined.

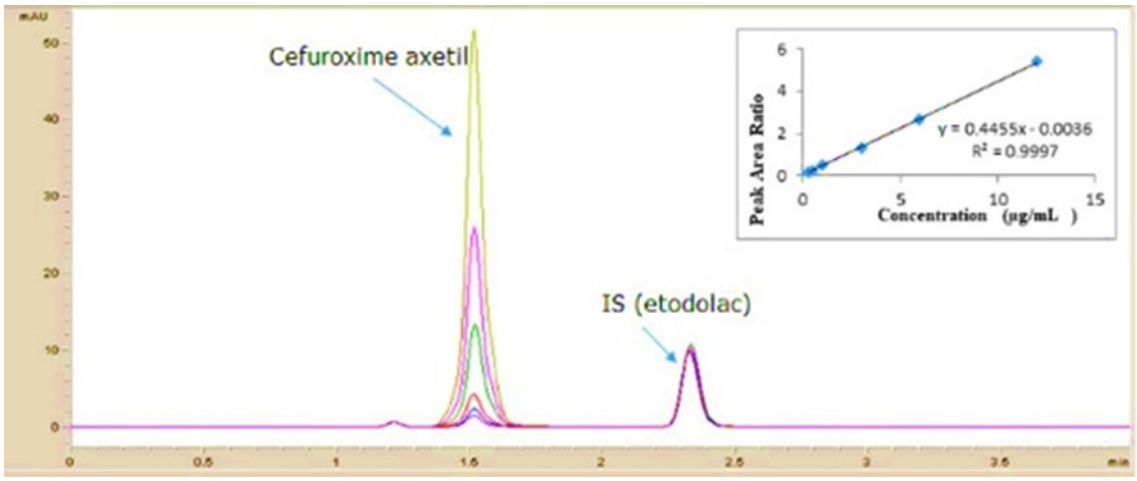

Figure 2: HPLC chromatogram of standard solutions (0.3, 0.5, 1.0, 3.0, 6.0, and 12 µg/mL) of cefuroxime axetil containing IS (etodolac:2.5 µg/mL).

3. RESULTS AND DISCUSSION

3.1. Results

3.1.1. Validation

To illustrate the applicability of the proposed analytical method, all three methods were validated according to the International Conference on Harmonization Conference (ICH) for approval of analytical procedures using several parameters (20). All statistical calculations were performed with excel functions and formulas.

3.1.2. Selectivity

When the chromatograms of standard solutions were examined, it was observed that the retention times of cefuroxime axetil and etodolac (IS) were 1.5 and 2.3 minutes, respectively. It was determined that the standard working solutions of cefuroxime axetil gave maximum absorbance at 280 nm for HPLC method (Figure 2) and at 277 nm for UV spectroscopic method (Figure 3). In first-order derivative spectroscopy method, two peaks were observed in the derivative spectrum: a maximum at 258 nm and minimum at 298 nm. In the study, the measurements were carried out at a wavelength of 298 nm (Figure 4). To obtain the calibration curve values for plasma study, the appropriate amounts of the previously prepared standard stock solution of cefuroxime axetil were spiked in 0.5 mL of human plasma and they were mixed and extracted. The spectra of the extracted solutions by UV spectroscopy method were taken and their absorbance value was read (Figure 5). When the spectrum and chromatogram of all three methods were examined, it was observed that there was no interfering substance.

3.1.3. Linearity and working range

Linearity was determined with 11 different standard solutions in the concentration range of 1.0-35.0 µg/mL for UV spectroscopy and first order derivative spectroscopy methods and with 6 different standard solutions in the concentration range of 0.3-12.0 µg/mL for HPLC method and also the linearity was determined 7 different extracted plasma solutions in the concentration range of 1.0 – 30.0 µg/mL for the UV spectroscopic method. The calibration curve was derived by plotting the absorbance values against

the solution concentrations in the spectroscopy methods. In the HPLC method, the calibration curve was derived by plotting the peak area ratios against the solution concentrations. Correlation coefficients and equations of the line were obtained by regression analysis of the calibration curves (Table 1).

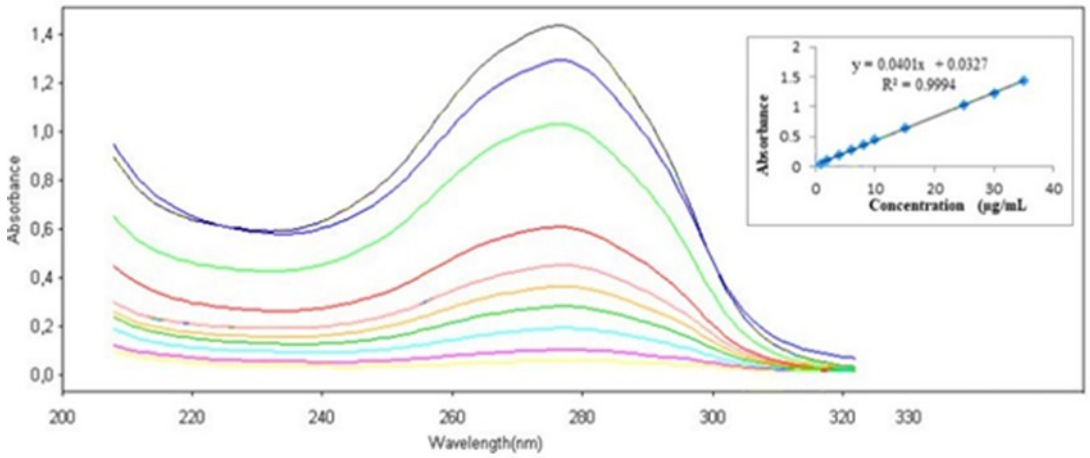

Figure 3: UV spectrum of standard solutions (1.0, 2.0, 4.0, 6.0, 8.0, 10.0, 15.0, 20.0, 25.0, 30.0, and 35.0 µg/mL) of cefuroxime axetil.

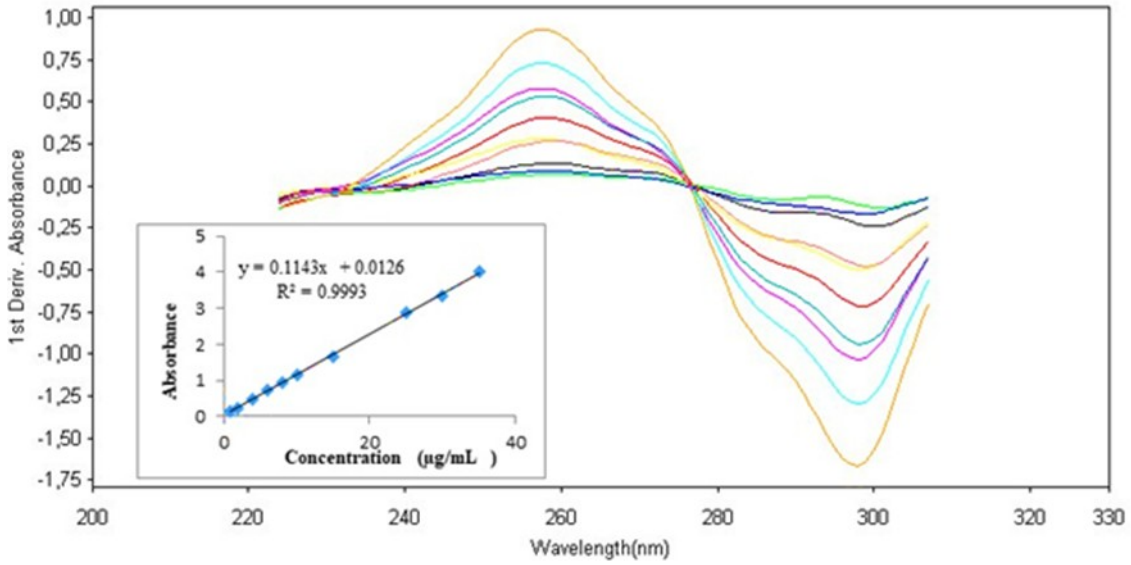

Figure 4: First-order derivative spectrum of standard solutions (1.0, 2.0, 4.0, 6.0, 8.0, 10.0, 15.0, 20.0, 25.0, 30.0, and 35.0 µg/mL) of cefuroxime axetil.

3.1.4. Precision and accuracy

Precision and accuracy were determined by intra-day and inter-day experimental. Intra-day precision and accuracy; QC solutions at 4 different concentrations (1.5, 4.5, 9.5, and 30.0 µg/mL) for UV and first-order derivative spectroscopy methods and 3 different concentrations (0.4, 4.0, and 8.0 µg/mL) for HPLC method were determined by measuring six replicates on the same day. Inter-day precision and accuracy were determined by analyzing the same samples over the 6 following days.

Intra-day and inter-day precision and accuracy were given with the relative standard deviation (RSD%) and the relative error (RE%), respectively. Obtained results for precision and accuracy were found to be acceptable (Table 2).

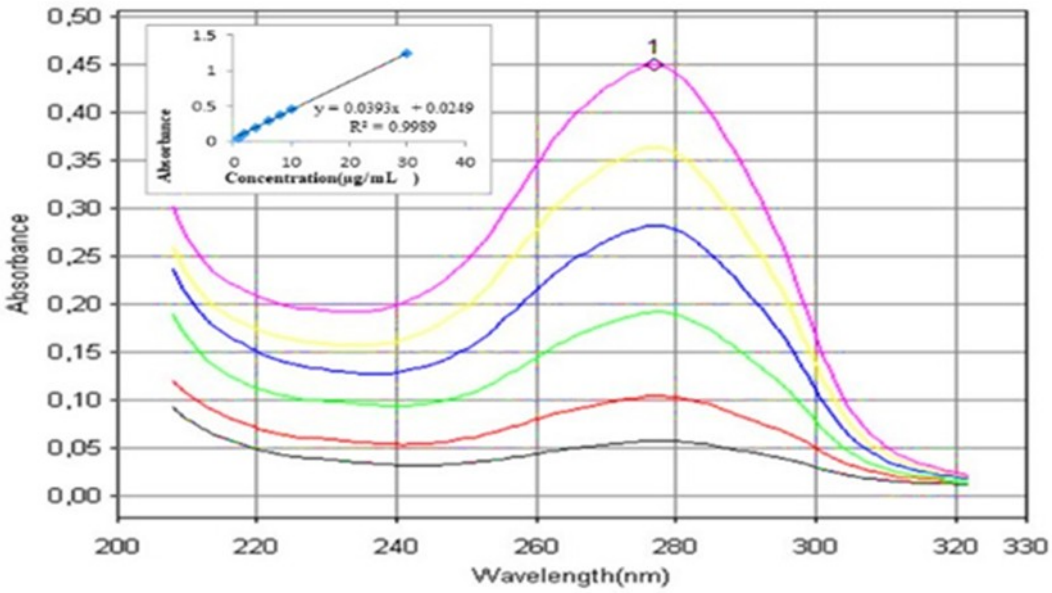

Figure 5: UV spectrum of extracted solutions (1.0, 2.0, 4.0, 6.0, 8.0, 10.0, and 30.0 µg/mL) from plasma of cefuroxime axetil.

Table 1: Statistical analysis values of calibration curves derived from cefuroxime axetil standard working solutions and plasma samples.

	HPLC method	**UV spectroscopic method**	**First-order derivative spectroscopy method**	**UV spectroscopic method for plasma**
Concentration (µg/mL)	0.3-12.0	1.0-35.0	1.0-35.0	1.0-30.0
λ (nm)	280	277	298	277
LRA[a]	0.4455x+0.0036	0.0401x + 0.0327	0.1143x + 0.0126	0.0393x + 0.0249
Sa	2.0 x 10^{-2}	2.4 x10^{-3}	3.9 x 10^{-4}	8.3 x10^{-4}
Sb	3.8 x 10^{-2}	8.3x10^{-2}	3.42 x 10^{-3}	7.3x10^{-3}
R^2	0.9998	0.9997	0.9996	0.9994

aBased on six calibration curves; λ: Wavelength, LRA: Regression Equation, Sa: Standard Error of Slope, Sb: Standard Error of Intercept, R2: Regression Coefficient.

Table 2: Precision and accuracy of the proposed methods (n=6).

Method	**λ (nm)**	**Added (µg/mL)**	**Intra-day**			**Inter-day**		
			Average± SD (µg/mL)	**Precision RSD%**	**Accuracy RE%**	**Average± SD (µg/mL)**	**Precision RSD%**	**Accuracy RE%**
UV spectroscopy	277	1.5	1.40±0.02	1.42	-6.66	1.41±0.02	1.42	-6.00
		4.5	4.37±0.02	0.46	-2.89	4.42±0.02	0.45	-1.78
		9.5	9.22±0.01	0.23	-2.95	9.43±0.02	0.21	-0.74
		30.0	31.02±0.09	0.30	3.40	30.10±0.09	0.30	0.33

First-order derivative spectroscopy	298	1.5	1.43±0.01	0.69	-4.67	1.45±0.01	0.41	-3.33
		4.5	4.37±0.01	0.23	-2.89	4.40±0.01	0.23	-2.22
		9.5	9.33±0.01	0.11	-1.79	9.43±0.01	0.11	-0.74
		30.0	29.38±0.02	0.07	-2.07	29.31±0.02	0.07	-2.30
UV spectroscopy in plasma	277	1.5	1.46±0.03	2.05	-2.67	1.51±0.05	3.31	0.67
		4.5	4.35±0.03	0.69	-0.03	4.36±0.03	0.69	-3.11
		9.5	9.48±0.03	0.32	-0.21	9.58±0.03	0.31	0.84
HPLC	280	0.4	0.41±0.01	2.43	2.50	0.42±0.01	2.38	5.00
		4.0	4.07±0.04	0.98	1.75	4.05±0.03	0.74	1.25
		8.0	8.26±0.01	0.12	3.25	8.28±0.06	0.72	3.50

λ: wavelength; RSD: Relative Standard Deviation; RE: Relative Error.

3.1.5. Limit of Detection (LOD) and Limit of Quantification (LOQ)

In UV and first-order derivative spectroscopy methods, a series of standard solutions were prepared at smaller concentrations than the smallest concentration on the calibration curve and the absorbance values of those solutions were monitored by six times. The RSD% values of these samples were determined. The concentration with a RSD% value less than 20% was defined as the LOD value, and the concentration value less than 10% was defined as the LOQ value. LOQ and LOD values of the proposed methods were 1.00 µg/mL and 0.40 µg/mL, respectively. For the plasma study, LOQ and LOD values of UV spectroscopy method were 1.01 µg/mL and 0.45 µg/mL, respectively.

In HPLC method, the lowest concentrations were assayed where the signal /noise ratio was at least 3, this concentration was described as LOD. The LOQ was defined as a signal/noise ratio of 10. Under these chromatographic conditions, LOQ and LOD values for proposed method were calculated as 0.10 and 0.03 µg/mL, respectively.

3.1.6. Recovery

Analytic recovery from the tablet formulations was carried out the standard addition method. For this purpose, the tablet solutions of Cefaks, Cefurol, Aksef ve Enfexia tablets as described in the Section 2.5 were prepared at a concentration of 10 µg/mL, and the absorbance of these tablet solutions was measured by the available spectroscopy methods. Then, the QC solutions in three different concentrations (1.5, 4.5 and 9.5 µg/mL) were added separately to the tablet solutions and the absorbance of these total solutions obtained by the present methods were measured again.

For HPLC method, the solutions of Cefaks, Cefurol, Aksef ve Enfexia tablets at a concentration of 2.5 µg/mL was prepared. The chromatogram was taken and the peak area was determined. Then, the QC solutions in 3 different concentrations (0.4, 4.0, and 8.0 µg/mL) were added separately in tablet solutions and the chromatograms of these solutions were taken by HPLC.

The analytical recovery values of proposed methods were calculated with the formula:

$$\frac{the\ value^{*}\ of\ total\ solutions - the\ value^{*}\ of\ tablet\ solution}{the\ value^{*}\ of\ added\ QC\ standard\ solutions}\ x\,100$$

value* = absorbance or peak area of our measurement

The average analytical recovery value of tablets (four different tablets) of UV spectroscopy, first-order derivative spectroscopy and HPLC methods was determined as 100.1, 100.3, and 99.9%, respectively.

In the recovery study in plasma samples, the certain concentrations of standard working solution of cefuroxime axetil were spiked to the

blank human plasma, they were mixed and extracted (according to Section 2.3). The absorbance of the obtained extracts was read at 277 nm. The percent recovery values were calculated by proportioning the absorbance value of the standard solution at the same concentration with the absorbance values of the extracted solution. The mean recovery value from plasma was determined as 99.8%.

3.2. Discussion

For an analytical method to be of value, it must be developed and validated by studying parameters such as accuracy, precision, reproducibility, selectivity, specificity, sensitivity and short analysis time. Before starting on work in an analytical study, it is necessary to conduct a good literature review about the study. Therefore, we conducted a good

literature review in our study. In the literature review, many studies were found about the cefuroxime axetil. In the current study, UV spectroscopy, first-order derivative spectroscopy and HPLC methods for determined of cefuroxime axetil in tablet formulations and plasma were developed and validated.

UV spectroscopy method is accepted as one of the preferred techniques for the quantification of pharmaceuticals in terms of high sensitivity, medium and high selectivity, high accuracy, certainty, facility, and comfortability (21). In spectroscopy methods, derivatization agents used in some other methods were not needed. A calibration curve with very good linearity was obtained without the need for any derivatization attempt, and a satisfactory study was observed based on the recovery values. In the UV spectroscopy study, cefuroxime axetil gave maximum absorbance at a wavelength of 277 nm. In first order derivative spectroscopic study; two peaks, a maximum at 258 nm and a minimum at 298 nm, were observed. Our study was carried out at a wavelength of 298 nm. It was observed that the proposed spectroscopic method was linear in the concentration range of 1.0-35.0 µg/mL. LOD and LOQ values proposed methods was found as 0.4 µg/mL, and 1.0 µg/mL. The intra-day and inter-day precision (RSD%) and accuracy (RE%) are lower than 1.5% and 7.0%, respectively. UV spectroscopy and first-order derivative methods was successfully applied to 4 commercial tablets for determination of cefuroxime axetil and the average analytical recovery values of UV spectroscopy and first-order derivative spectroscopy method were determined as 100.1% and 100.3%, respectively.

The amount of cefuroxime axetil in plasma was tried to be determined by UV spectroscopy method. It was observed that the method was linear in the concentration range of 1.0-35.0 µg/mL. LOD and LOQ values proposed method was determined as 0.45 µg/mL, and 1.0 µg/mL, respectively. The intra-day and inter-day precision and accuracy values were showed that lower than 3.5%. Recovery value from plasma was found as 99.8%.

Chromatography is widely used in the separation, identification and quantification of substances in a mixture (22). Between these methods; HPLC has more advantages such as accuracy, precision, repeatability, selectivity, sensitivity, recovery, having the opportunity for analysis with low-volume samples and getting results rapidly. For these reasons, HPLC has been used commonly in the drug industry for the quantification of tablets or the analysis of active substances in biological fluids. In this study, a new HPLC method was developed for determination of cefuroxime axetil in tablets. In the HPLC study, some parameters like temperature, column, mobile phase components and percentages may affect the run time. So, optimization of chromatographic conditions was needed to improve the distinction and acceptable results. In the study, the working parameters were optimized by trial-and-error method based on the literature. The reverse phase C18 column (5 µm, 250 x 4.6 mm) was used and different mobile phase mixtures (0.1% acetic acid-acetonitrile rate: 30:70, 20:80 and 10:90 v/v) tested. According to the results obtained, the value in which 0.1% acetic acid-acetonitrile rate (30:70, v/v) was determined as optimum. The column temperature, mobile phase flow rate, wavelength and injection volume were used as variable, 1.0 mL/ min, 280 nm and 10 µL, respectively, and also etodolac was used as IS (2.5 µg/mL). The concentration range of 0.3-12 µg/mL of HPLC method was determined to be linear. A calibration curve was obtained by plotting the ratio of the peak area of cefuroxime axetil to the peak area of IS (etadolac) against the concentration of each solution. The LOQ and LOD values of proposed method was found as 1.0 µg/mL and 0.3 µg/mL, respectively. The intra-day and inter-day precision (RSD%) and accuracy (RE%) were showed that lower than 2.5% and 5.0%, respectively. Average analytical recovery value from tablets was 99.9%.

The developed and validated methods were applied to determine the amount of active substance (cefuroxime axetil) in four different tablets (Cefaks, Cefurol, Aksef ve Enfexia tablets). The analysis time of our HPLC method is shorter than the others in the literature and it is a big superiority. Our method differs from the methods reported in the literature considering the chromatographic parameters used such as UV wavelength, column, temperature, detector, flow rate, preparation procedures of bulk and plasma samples.

4. CONCLUSION

In summary, UV spectroscopy, first-order derivative spectroscopy and HPLC methods were developed for the determination of the active substance of cefuroxime axetil in bulk and tablets. UV spectroscopy method was also developed and validated for the determination of cefuroxime axetil in plasma. Results showed that the methods are suitable for accuracy, precision, sensitivity, recovery, linearity, specificity, and selectivity parameters for determination of cefuroxime axetil. The methods can be applied for routine analysis of cefuroxime axetil in quality control assays and pharmaceutical preparations.

5. ACKNOWLEDGMENTS

The authors express their honest thanks Prof. Dr. Alptuğ ATILA and Assoc. Prof. Mehmet Emrah YAMAN and to Analytical Chemistry Department of Pharmacy Faculty in Atatürk University to benefit the research facilities.

6. REFERENCES

1. Powell DA, James NC, Ossi MJ, Nahata MC, Donn KH. Pharmacokinetics of cefuroxime axetil suspension in infants and children. Antimicrob Agents Chemother [Internet]. 1991 [cited 2023 May 30];35(10):2042–5. Available from: <URL>

2. Öner M. Genel Mikrobiyoloji. Ege Üniversitesi Fen Fakültesi Kitaplar Serisi. 2001; 992:231-245.

3. Bush K, Jacoby GA, Medeiros AA. A functional classification scheme for beta-lactamases and its correlation with molecular structure. Antimicrob Agents Chemother [Internet]. 1995 [cited 2023 May 30];39(6):1211–33. Available from: <URL>

4. Scott LJ, Ormrod D, Goa KL. Cefuroxime axetil: an updated review of its use in the management of bacterial infections. Drugs [Internet]. 2001 [cited 2023 May 30];61(10):1455–500. Available from: <URL>

5. Martindale W, Reynolds JEF. The Extra Pharmacopoeia. Pharmaceutical Press, 1 Lambeth Street, London, SEI 7JN, UK, 1999; 177.

6. Harding SM, Williams PEO, Ayrton J. Pharmacology of Cefuroxime as the 1-acetoxyethyl ester in volunteers. Antimicrob Agents Chemother [Internet]. 1984 [cited 2023 May 30];25(1):78–82. Available from: <URL>

7. Akalın HE. Antibiyotiklere Direnç Gelişmesi ve Antibiyotik Kullanımı. Klinik uygulamalarda antibiyotikler ve diğer antimikrobiyal ilaçlar. Baskı. Ankara, Güneş Kitabevi Ltd. Şti., 1994; 38–39.

8. Al-Said MS, Al-Khamis KI, Niazy EM, El-Sayed YM, Al-Rashood KA, Al-Bella S, et al. Bioequivalence evaluation of two brands of cefuroxime 500 mg tablets (Cefuzime and Zinnat) in healthy human volunteers. Biopharm Drug Dispos [Internet]. 2000 [cited 2023 May 30];21(6):205–10. Available from: <URL>

9. Murillo JA, Lemus JM, García LF. Spectrofluorimetric analysis of cefuroxime in pharmaceutical dosage forms. J Pharm Biomed Anal [Internet]. 1994 [cited 2023 May 30];12(7):875–81. Available from: <URL>

10. Elias B, Alfeen MA. Determination of Cefuroxime Axetil and Cefixime Trihydrate in Pharmaceutical Dosage Forms by RP-HPLC Method. Pharmaceutical Analytical Chemistry: Open Access [Internet]. 2016 [cited 2023 May 30];2(2):0–0. Available from: <URL>

11. (PDF) A Validated High performance liquid chromatography (HPLC) Method for the Estimation of Cefuroxime axetil [Internet]. [cited 2023 May 30]. Available from: <URL>

12. Alfeen M. New Development Method for Determination of Cefuroxime Axetil (CUA) and Cefprozil (CZ) in Pharmaceutical Drugs by RP-HPLC. Am J Biomed Sci Res. 2019 Jul 17;4(1):54–7. Available from: <DOI>

13. Patel N, Mehta I, Patel DrC, Patel DrMM. Development And Validation Of Rp-Hplc Method For Combination Of Cefuroxime Axetil And Linezolid In Pharmaceutical Dosage form. International Journal of Pharmaceutics and Drug Analysis [Internet]. 2017 Dec 4 [cited 2023 May 30];5:429–41. Available from: <URL>

14. Krzek J, Da ˛ Browska-Tylka / M. Simultaneous Determination of Cefuroxime Axetil and Cefuroxime in Pharmaceutical Preparations by Thin-Layer Chromatography and Densitometry. Chromatographia 2003 58:3 [Internet]. 2003 Aug [cited 2023 May 30];58(3):231–4. Available from: <URL>

15. Pajchel G, Tyski S. Adaptation of capillary electrophoresis to the determination of selected cephalosporins for injection. J Chromatogr A [Internet]. 2000 Oct 20 [cited 2023 May 30];895(1–2):27–31. Available from: <URL>

16. Shinde M, Pishawikar S, More H. Spectrophotometeric Determination of Cefuroxime Axetil from bulk and in its tablet dosage form. Indian J Pharm Sci [Internet]. 2008 Feb 1 [cited 2023 May 30];70(2):249. Available from: <URL>

17. Ramadan AA, Bakdash M. Direct Spectrophotometric Determination of Cefuroxime Axetil in Pure Form and Pharmaceutical Dosage Forms. JOURNAL OF ADVANCES IN CHEMISTRY [Internet]. 2018 Dec 1 [cited 2023 May 30];15(2):6282–95. Available from: <URL>

18. Pritam J, Manish P, Sanjay S. Development and validation of UV-Spectrophotometric method for determination of Cefuroxime Axetil in bulk and in Formulation "Development and validation of UV-Spectrophotometric method for determination of Cefuroxime Axetil in bulk and in Formulation." Int J Drug Dev & Res [Internet]. [cited 2023 May

30];3(4):318–22. Available from: <URL>

19. Validated spectrophotometric methods for the determination of Cefuroxime Axetil in bulk drug and tablets | Request PDF [Internet]. [cited 2023 May 30]. Available from: <URL>

20. International Conference On Harmonisatıon Of Technical Requirements For Registration Of Pharmaceuticals For Human Use Ich Harmonised Tripartite Guıdeline Validatıon Of Analytical Procedures: Text And Methodology Q2(R1). Available from: <URL>

21. Hladová M, Martinka J, Rantuch P, Nečas A. Review of Spectrophotometric Methods for Determination of Formaldehyde. Research Papers Faculty of Materials Science and Technology Slovak University of Technology. 2019 Jun 1;27(44):105–20. Available from: <DOI>

22. Hamilton RJ, Sewell PA. Introduction to high performance liquid chromatography. 1st ed. Chapman and Hall New York, 1982.

JOTCS A
Journal of the Turkish Chemical Society
Section: A
Chemistry
TURKISH CHEMICAL SOCIETY

Solvent-free Organic Reaction Techniques as an Approach for Green Chemistry

Ahmed Younis[1*], Ahmed O. Said[2]

[1]National Research Centre, Department of Green Chemistry, Cairo 12622, Egypt
[2]Greater Cairo Water Company, Senior researcher chemist, Cairo, Egypt

Abstract: Unfortunately, many toxic solvents are used in chemistry laboratories and in the manufacturing of materials, which poses a serious risk to process safety, the natural environment, and human health. In this review, different tools for solvent-free organic reactions have been surveyed as an approach for green chemistry, where many of the solvents are known to upset our ecosystems so an enormous research effort has been exerted during the last decade to avoid the utilization of hazardous solvents and the number of publications on solvent-free reactions has increased nearly exponentially. Obviously, this reflects the great interest in solventless reactions. In our survey, we will highlight the solvent-free organic reaction as an approach for green chemistry to cover work published up to nearly 2022.

Keywords: Solvent-free reactions, green chemistry, mechanochemistry, microwave assisted synthesis, ultrasound assisted green synthesis, photochemical reactions.

Submitted: October 16, 2022. **Accepted:** April 28, 2023.

Cite this: Younis A, Said AO. Solvent-free Organic Reaction Techniques as an Approach for Green Chemistry. JOTCSA. 2023;10(2):549–76.

DOI: https://doi.org/10.18596/jotcsa.1188983.

***Corresponding author. E-mail:** chem2you@gmail.com.

1. INTRODUCTION

We cannot deny that solvents play an important role in our life and are necessary for many applications such as cleaning, extraction, coatings, synthetic chemistry, separation of organic ingredients, etc. However, many of these solvents have a negative impact on our ecosystem because they cause ozone layer depletion, and contribute to tropospheric smog formation. In addition to the effect of these solvents on the human health, some of these solvents are neurotoxins, may cause sterility, or may cause cancer, so the utilization of these solvents is not accepted from environmental and health point of view (1–6).

We can say that there are no safe organic solvents, only more or less toxic ones. Table 1 shows the following: Aromatic hydrocarbons are the most dangerous solvents and most volatile organic compounds (VOC).

Solvents can harm the human body through the eyes, lungs, blood, skin, and kidneys. They are frequently between those (carcinogen, toxin, irritant, hepatotoxin, neurotoxin, and nephrotoxin). Therefore, different quality regulations force solvent producers to put well-known international labels on different solvents showing the extent of potential damage and how to handle, transport, and store different solvents (7). One of the major problems with using solvents is the time-consuming heating and recovery of the solvent after the reaction is complete (8).

In addition to the above, incorrect storage of solvents may cause fires or explosions. Most organic solvents have high flammability. Therefore, the pollution prevention Act of 1990 of environmental protection agency (U.S.EPA) encouraged the utilization of novel techniques to eliminate or reduce pollutants or waste and protect natural resources from depletion by increasing the efficiency of use.

Table 1: Some of the dangerous health effects resulting from solvents.

Health hazard	**Solvent and chemicals that create the hazard**
Carcinogen	Ethylene dichloride, methylene chloride, dioxin, chloroform, perchloroethane.
Toxic	Xylene, benzene, toluene
Irritant	Ammonium solution
Hepatotoxin	Dioxane, acetonitrile, carbon tetrachloride, phenol
Neurotoxin	Cresol, methylene chloride, xylene, carbon disulfide
Nephrotoxin	Ethylenediamine, chlorobenzene, dioxane, acetonitrile, Allyl alcohol, hexachloronaphthalene, phenol
Human organs that are harmed:	
1Blood	Nitrotoluene, benzene, cyanide, carbon monoxide
2Lung	Asbestos, silica, tars, dust
3Eyes or skin	Allyl alcohol, perchloroethane, ethyl butyl ketone, nitroethane, ethanolamine, propylene oxide.

As a result of the above-mentioned dangerous effect of solvents on human health and ecosystems, great efforts are made to find an innovative technique to eliminate or reduce the use of hazardous solvents or to use alternative safe solvents. From this approach, researchers worked to determine the role of alternative safe and green solvents like water, micellar medium, supercritical CO_2, ionic liquid in different chemical reactions (9). In addition to applied techniques (10) that reduce or prevent the use of solvents, such as solid-solid reaction (11,12), microwave assisted synthesis (13,14), and ultrasonic assisted reactions (15).

From the above aspects, we found the need for eliminating solvents in chemical reactions, so solvent less reactions are the key for solving all previously mentioned problems. Our review covers the recent advances of solvent-free organic reactions under different conditions as an approach to green chemistry.

Solvent-free reaction has many advantages (Fig.1) that are very important in industry:
1Reduced pollution (safe, nontoxic).
2Low costs.
3Simplicity in process (Renewable).
4Simplicity in handling (Easier to produce).
5Environmentally friendly.
6Reduced time.

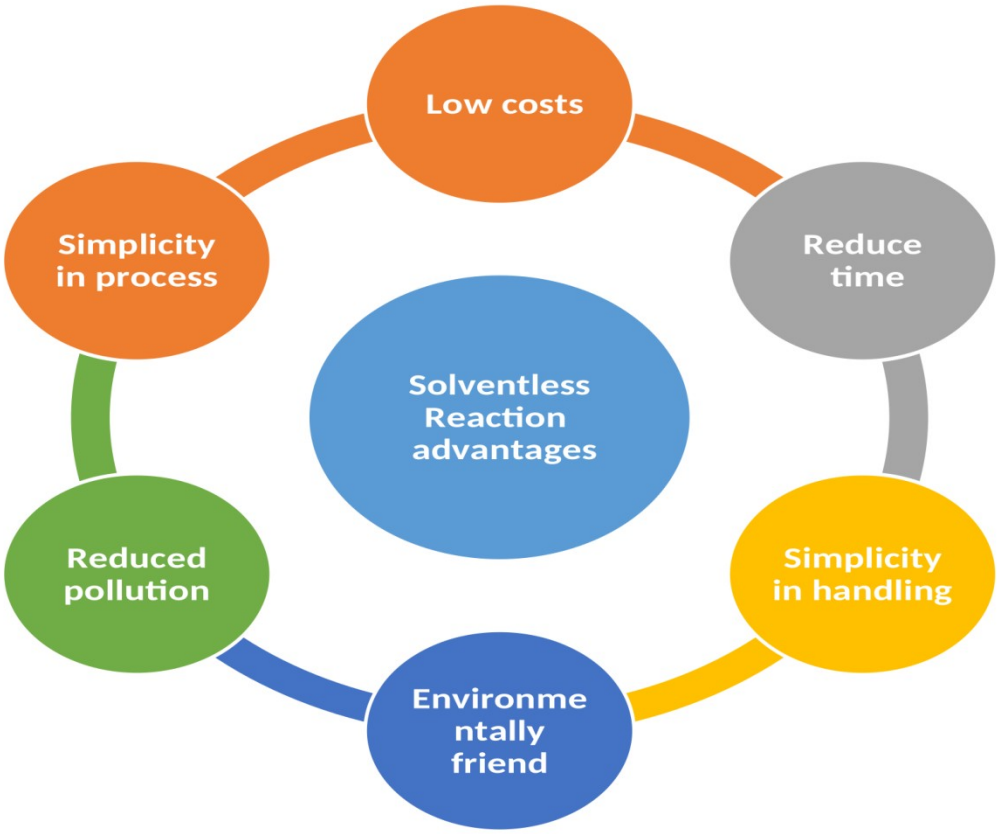

Figure 1: Advantages of solvent-free organic reactions.

2. APPLICATION OF ALTERNATIVE SOLVENTS

The process of replacing organic solvents with other systems is not easy, especially because most organic compounds are poorly soluble in natural solvents such as water, but there are many systems that are designed to skip the use of organic solvents, such as switchable solvents, supercritical fluids, ionic liquid systems, deep eutectic solvents (DES), and micellar systems.

2.1. Using Water as a Neutral Solvent

Water is an ideal alternative solvent in organic synthesis to verify some green chemistry principles (16–18) because water is safe from a health and environmental point of view. Unfortunately, the utilization of an aqueous medium instead of an organic solvent in organic synthesis is not a simple task. Many organic compounds are insoluble or sparingly soluble in water due to the high polarity of water, so many difficulties are faced.

2.2. Switchable Solvents

The liquids that can change their physical properties reversibly are defined as switchable solvents (19–21) where the reversible change between two different forms takes place by applying external stimulus (or trigger) such as changes in temperature and the addition or withdrawal of a gas (22, 23).

Although switchable solvents have many advantages, their use as reaction mediums is restricted to some specific reactions, such as the polymerization of styrene (24).

2.3. Supercritical Fluids

The most commonly used supercritical fluids are water and carbon dioxide, which are characterized by being inexpensive, nonflammable, and nonpoisonous, but the high cost of the used technology, especially for water, is because it needs to perform reactions at high temperature and pressure, which demand special equipment (25–28) .

2.4. Ionic Liquids

Ionic liquids' potential to take the place of common solvents as a reaction medium has been studied using a variety of organic processes. Ionic liquids are characterized by the catalytic activity of homogeneous transition-metal and the easy separation of the products of the reaction, but unfortunately, ionic liquids are not easily prepared, are expensive, and are sensitive to moisture, and some of them are hazardous (29–34).

2.5. Deep Eutectic Solvents

Deep eutectic solvents are considered a good alternative to ionic liquids because they have similar physicochemical properties. Deep eutectic

solvents are preferred over ionic liquids because they are biodegradable and much less expensive. Deep eutectic solvents (DES) were called "the organic reaction medium of the century" due to their simple, one-step purification-free production from readily available and renewable source chemicals. (35–39). But it is still uncommon and limited to some processes and reactions.

2.6 Micellar System

A micellar solution involves some aggregated surfactants, called micelles, in water as solvent. The micelle molecules have hydrophilic head and hydrophobic tail in aqueous solution. This system can perform internal reactions without resorting to organic solvents (40–42).

3. SOLVENTLESS ORGANIC REACTION TECHNIQUES

Many techniques have been exploited to go through chemical reactions without the need for solvents or using very small amounts compared to traditional methods (43). Grinding in a mortar (44) (mechanochemistry) is one of the oldest methods used to conduct reactions without solvents. Manual grinding has been developed into many automated methods that apply reactions by friction force, such as grinding by rotating mortar (45) and high-speed ball milling (46). Many other technologies have resorted to using energy to conduct reactions such as microwave-assisted reactions (47), reactions under ultrasonic waves (sonochemistry)(48), photochemistry, and electrochemistry (43), in addition to reactions that depend on microorganisms (biosynthesis)(49–51). In this section, we tried to shed light on the most important of these organic reactions that took place without harmful solvents as an approach to green chemistry.

3.1. Solventless Organic Reactions by Friction Force (Mechanochemistry)

The term “mechanochemistry” or “grindstone chemistry” is often used in a wide sense, covering the chemical reactions that depend on mechanical force as a source of energy (e.g., grinding, rotating mortar, and high-speed ball milling (52)).

Studying mechanochemistry became very important because it can assist the reactions quickly and quantitatively under solventless conditions (53–56). It is obvious that mechanochemical reactions are effective and advantageous, so we can say that mechanochemistry could in the future develop a more conventional techniques in addition to the unsustainable dependence on solvents, which are hazardous and problematic (57,58).

By grinding chromen-3-one derivatives **1** with various reagents, a quick, inexpensive, clean, and environmentally acceptable method to synthesize novel pyrazoles, pyrazolopyridazines, and condensed pyrimidines was devised. (59) (Scheme 1).

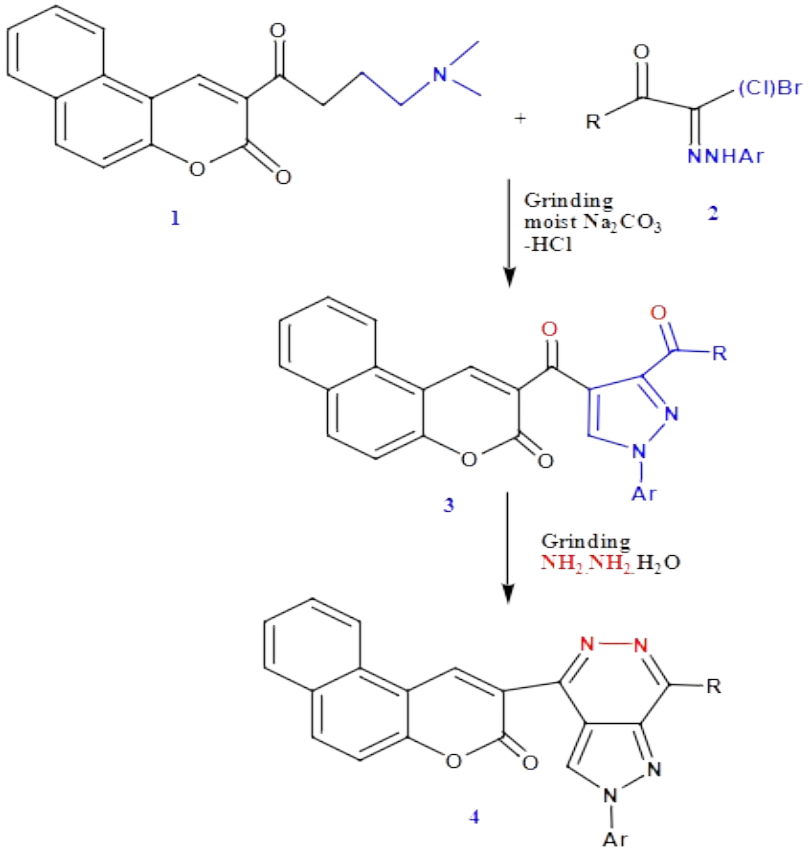

Scheme 1

Under solvent-free conditions, a quick and practical method for the mechanochemical oxidation of highly fluorinated anilines **5** to the corresponding symmetric azobenzene **6** was reported (60) (Scheme 2).

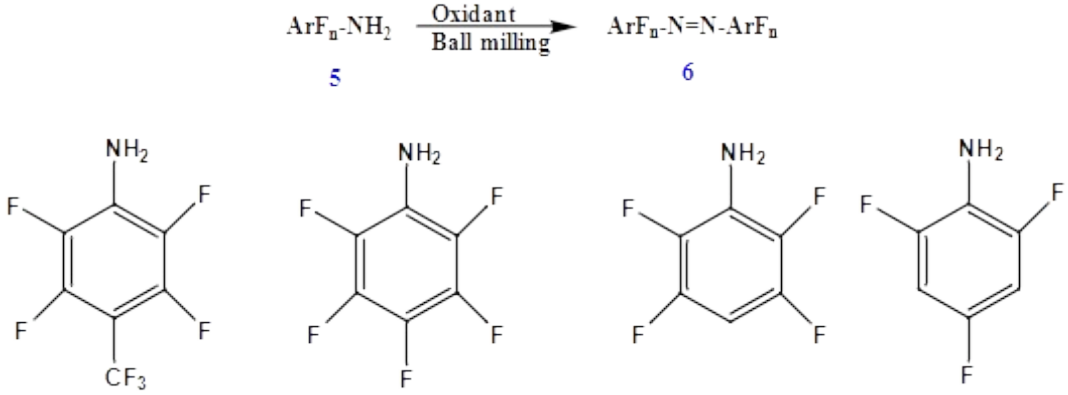

Scheme 2

The synthesis of physiologically active 2-amino-4*H*-benzo[b]pyrans **8**, a mild, ecofriendly green technique, has been established, using solid sodium ethoxide as the catalyst in solvent-free conditions at ambient temperature (61) (Scheme 3).

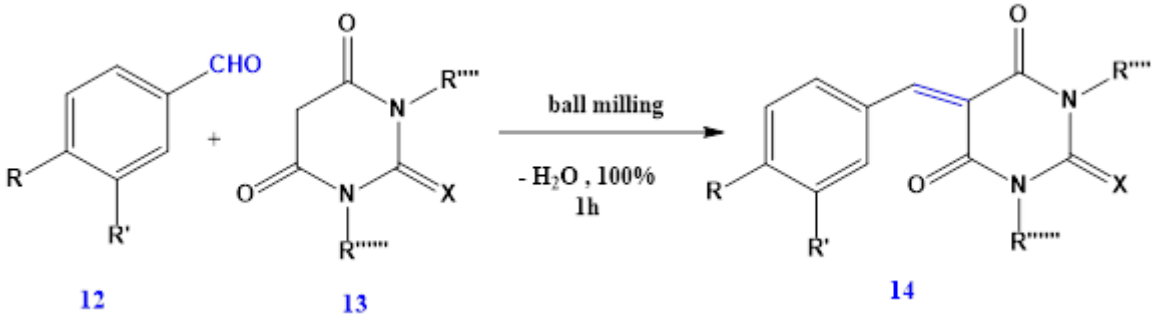

Scheme 3

By utilizing a grinding auxiliary, the mechanochemical fluorination of liquid β-ketoesters **9** has been accomplished. This led to good selectivity and good yields of mono- and difluorinated β-ketoesters **10,11** (62) (Scheme 4).

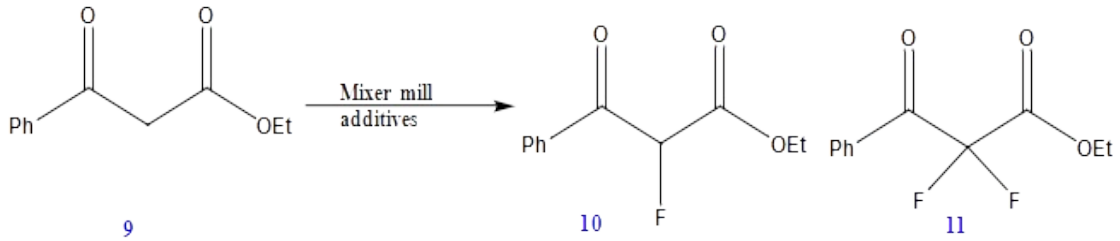

Scheme 4

The Knoevenagel condensation reaction is a significant C–C-bond forming **14**, produce α,β-unsaturated carbonyl organic compounds (63). A ball mill-based, solvent-free variant of this process was first introduced by Kaupp et al. He used the stoichiometric starting material amounts to produce the required results quantitatively. No work-up was necessary in this case, as well as in the alleged Michael additions, making these waste-free methods viable and environmentally friendly. (Scheme 5).

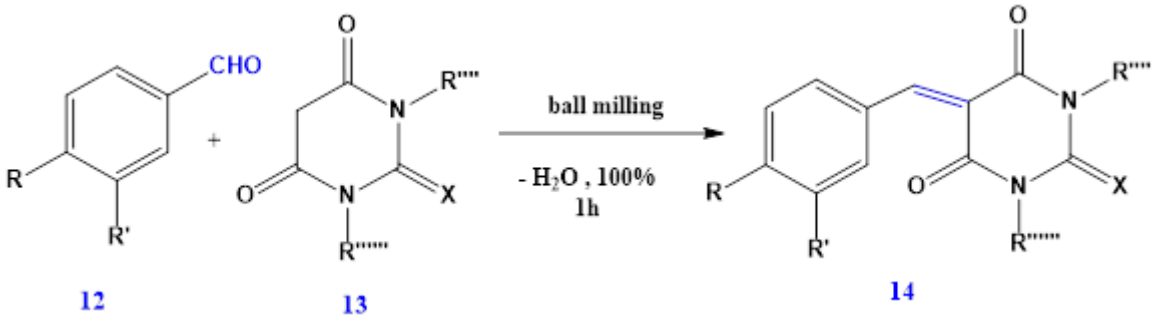

Scheme 5

Solvent-free synthesis of $[Cu(CH_3COO)_2(TMP)_2]$ and $[Ni(CH_3COO)_2(TMP)_2]$ **17** by ball milling of copper acetate dihydrate **15** and nickel acetate tetrahydrate with 5-(3,4,5-Trimethoxybenzyl)pyrimidine-2,4-diamine (Trimethoprim) **16** in the absence of solvent by ball-milling (64) (Scheme 6).

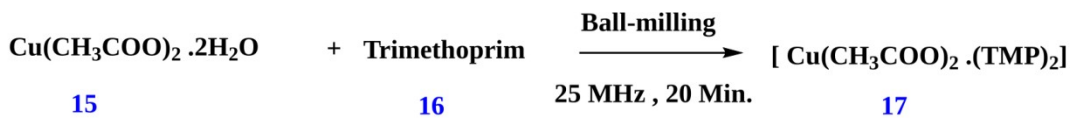

Scheme 6

1,5-diketones **20** were prepared by an efficient and ecofriendly method using mechanochemistry, where reactants are ground together in a mortar and pestle (65) (Scheme 7).

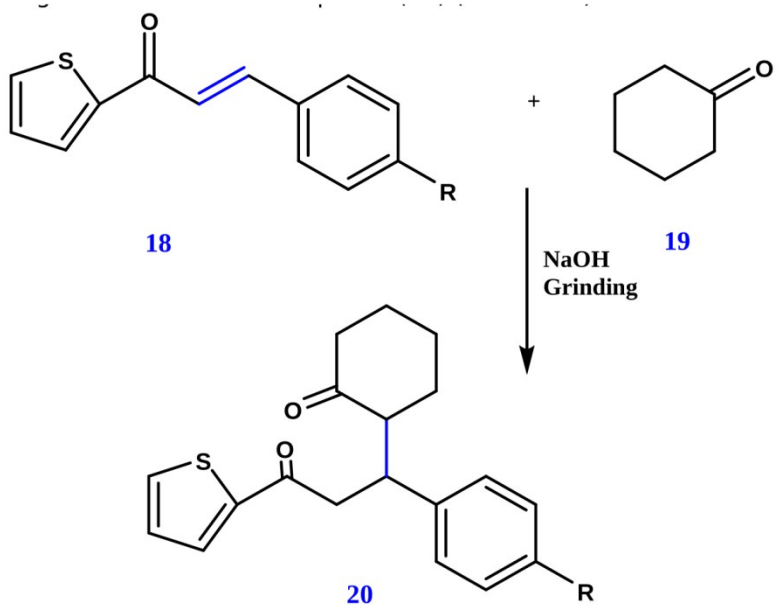

Scheme 7

Four π-π stacked arene-perfluoroarene co-crystals **23** made of naphthalene **22** or biphenyl, octafluoronaphthalene **21** or decafluorobiphenyl, and their mechanochemical synthesis are reported (66) (Scheme 8).

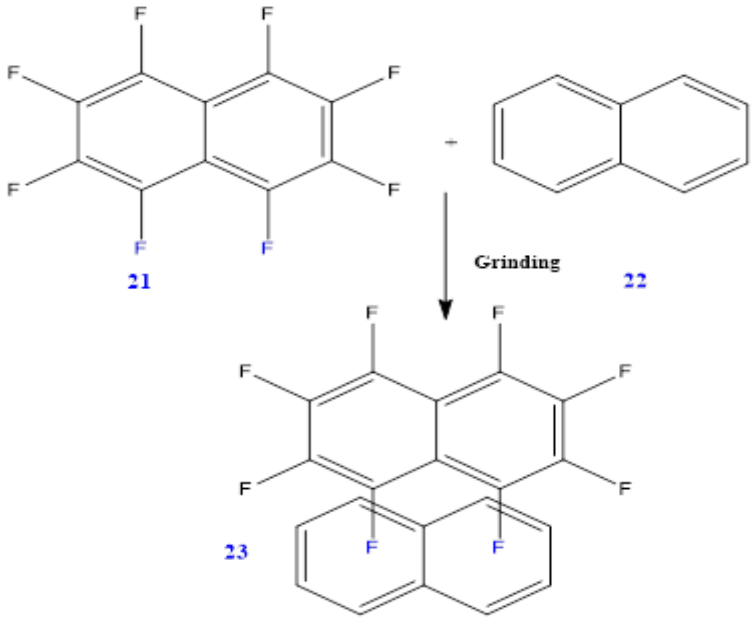

Scheme 8

The mechanochemical synthesis of benzil bis-hydrazones **27** occurred in two steps: the Schiff base reaction of 2-cyanoacetohydrazide **24** with benzil **25** in mole ratio 2:1, and the resulting grinding with benzaldehyde derivatives **26** (67). (Scheme 9).

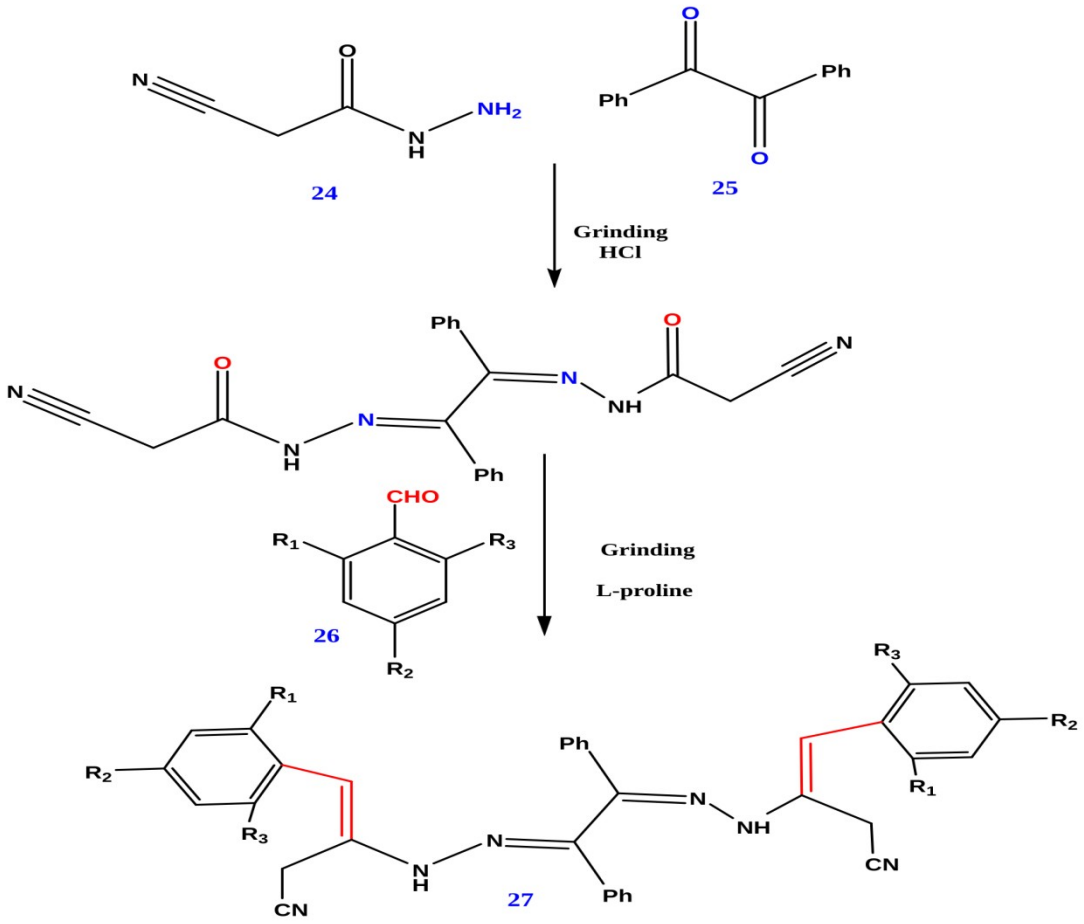

Scheme 9

Synthesis of benzimidazole **30** by grinding aromatic aldehyde **29** and ortho phenylenediamine **28** with very a high yield that reached 93% for forty-three substation samples in the percent of acetic acid (68) (Scheme 10).

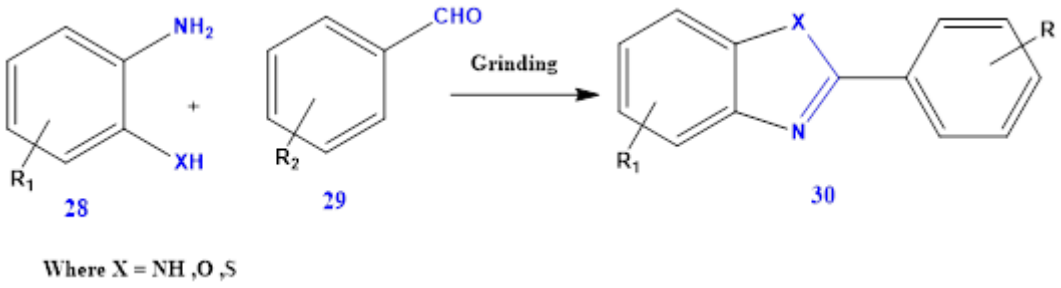

Scheme 10

High speed ball milling has been used to convert carbon-hydrogen bonding into amide **33** by the reaction of acyl azides **31** and different catalysts (69) (Scheme 11)

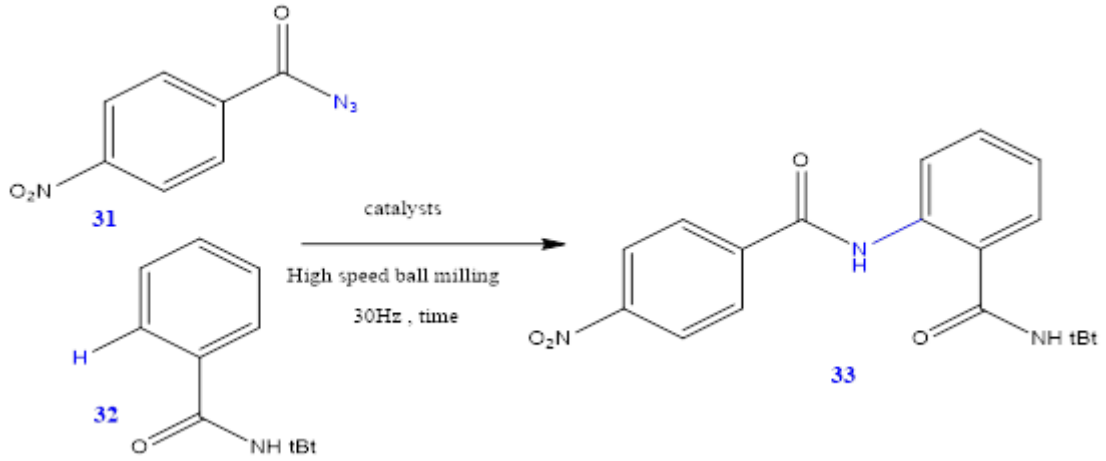

Scheme 11

Schiff base reaction of ketone or aldehyde and amine to form *N*-heterocyclic compounds **35, 37** have been developed by using solvent-less high-speed ball milling technique in the different forms of mechanism and present of manganese (III) acetate (70) (Scheme 12).

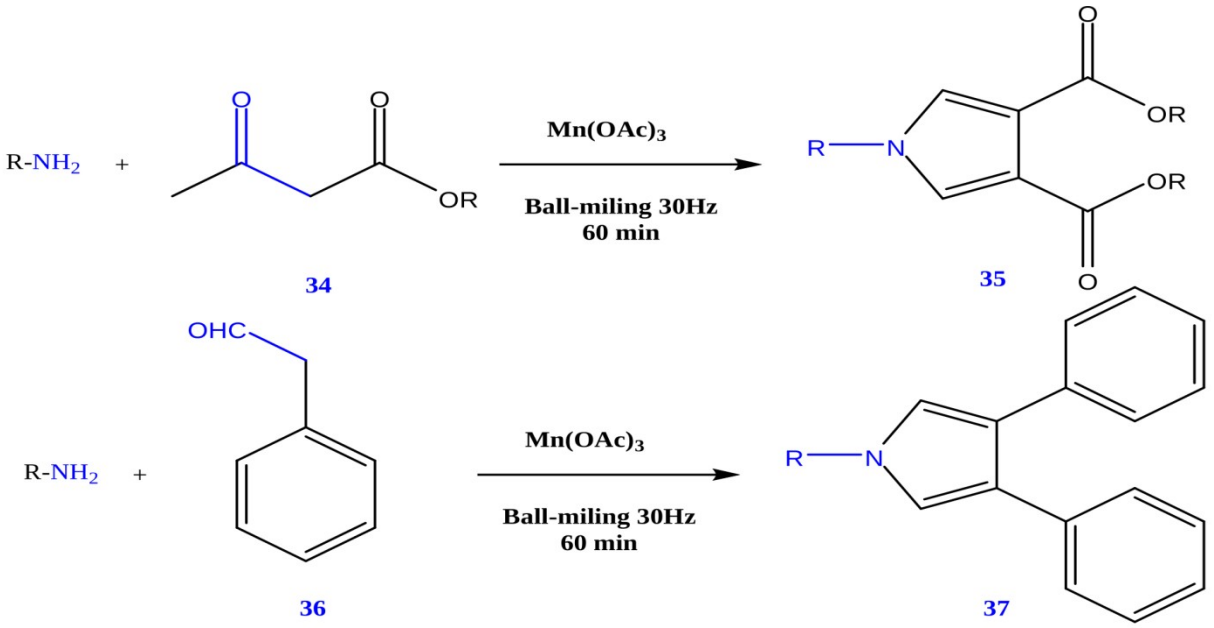

Scheme 12

3.2. Solventless organic reactions under microwave irradiation

Microwave-assisted organic synthesis (MAOS) has developed as a novel “approach” in solventless organic reactions. The process makes the synthesis of several organic compounds quick, easy, clean, effective, and affordable. Microwave assisted chemical reactions have become a new technique in the synthesis of organic compounds in recent years. The substantially increased reaction rate, faster reaction times, and improved product yield and quality are all significant benefits of this technique. The method used today is viewed as an important step toward green chemistry, especially with solventless reactions in industry (71–77).

High frequency electromagnetic waves can be used in microwave ovens to heat materials. The wave's electric field component interacts with the material's charge particles to produce the heating. There are two mechanisms for heating materials: dipolar Polarization and ionic conduction. The biggest difference between conventional heating and microwave is the even distribution of heat, in addition to the absence of solvents and the speed of production(78,79).

By conventional procedures, 3-(2-pyridyl) pyrazole (pypzH) **41** synthesis requires refluxing at high temperatures for more than 16 hours, but a microwave-assisted synthesis reduces this to two subsequent phases of 2 hours at 100 °C and 10 minutes at 50 °C. Additionally, with MW assistance, it coordinates as a chelating ligand **40** to the "fac-$ReIBr(CO)_3$" and "$RuII(bipy)_2$" fragments in 5 or 10 min, respectively (80) (Scheme 13).

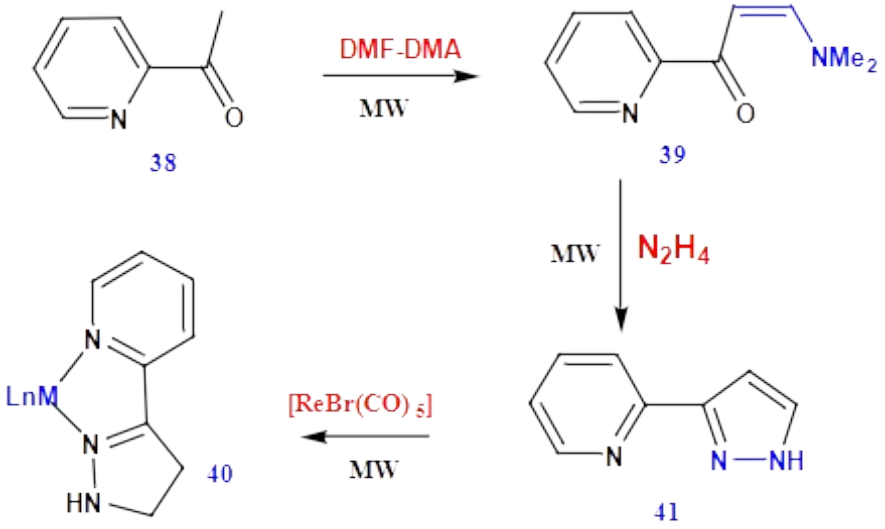

Scheme 13

Under catalyst- and solvent-free conditions, a microwave-assisted Fries rearrangement was employed to successfully create 2-fluoro-*N*-(3-methylsulfanyl-1*H*-1,2,4-triazol-5-yl) benzamide **45** from heterocyclic amide as a strategic intermediate (81) (Scheme 14).

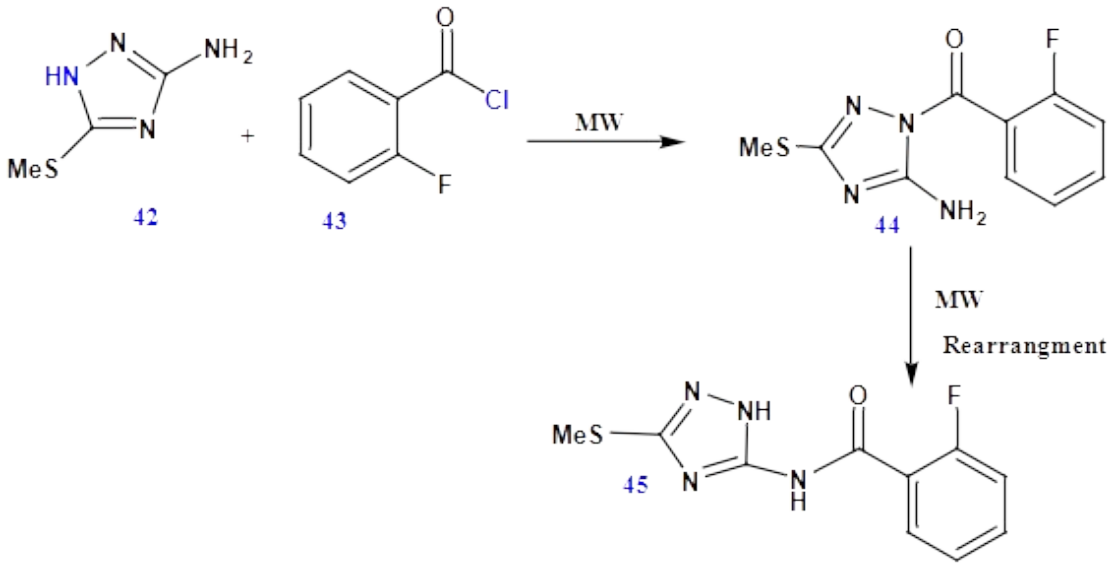

Scheme 14

A3-coupling and decarboxylative A3-coupling, chitosan-supported copper based heterogeneous catalysts have been studied. The established process uses minimal catalyst loading, a solventless environment, and a simple set-up to produce a variety of substituted propargylamines **49** (82) (Scheme 15).

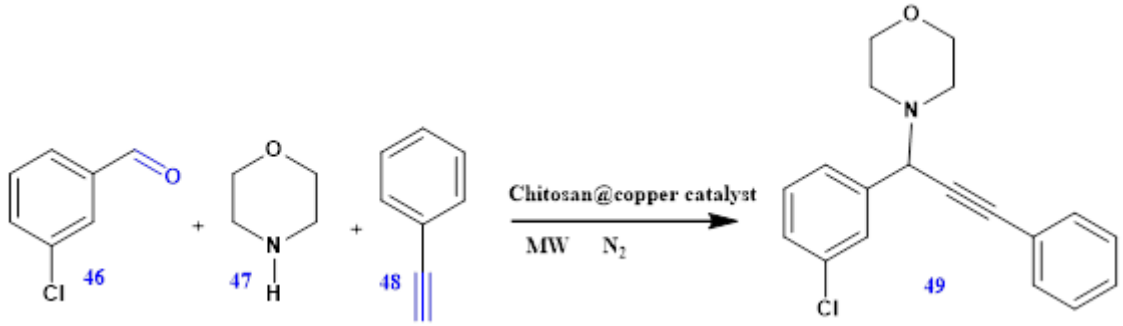

Scheme 15

Suzuki cross-coupling reactions are used to create twelve different biaryl compounds **52** using a microwave irradiation process that is safe, simple, and quick when a catalyst is present (83) (Scheme 16).

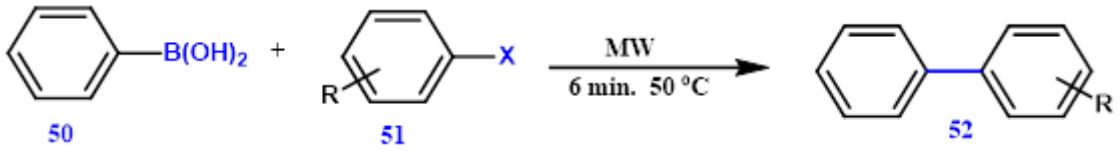

Scheme 16

For the synthesis of 12-aryl-8, 9, 10, and 12-tetrahydrobenzo[a]xanthen-11-one **56** derivatives, convenient and environmentally friendly processes have been reported. These involve multi-component condensation reactions of aromatic aldehydes **53** with naphthol **54** and cyclic 1, 3-dicarbonyl compounds, specifically dimedone and cyclohexane-1, 3-dione **55**. using microwaves to condense *p*-toluenesulfonic acid in a clean environment. The green approaches described here avoid the harsh conditions posed by the more traditional existing technologies and demonstrate efficiency in terms of high yields, ease of operation, simple set-up, and quick reaction times (84) (Scheme 17).

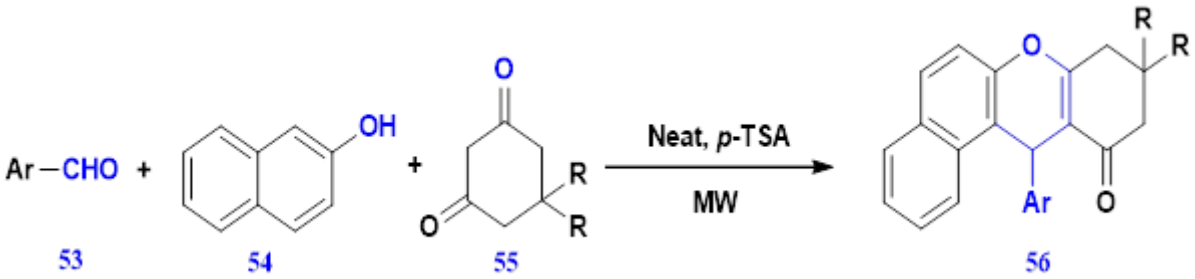

Ar = C_6H_5, 4-ClC_6H_4, 4-BrC_6H_4, 4-FC_6H_4, 4-$CH_3OC_6H_4$, 4-CH_3C_6
4-OHC_6H_4, 4-$NO_2C_6H_4$, 3-ClC_6H_4, 3-BrC_6H_4, 2-BrC_6H_4
R = H, CH_3

Scheme 17

Bandyopadhyay et al. (85) reported an easy and incredibly quick technique for the synthesis of 1,4-dihydropyridines **58** under solvent-free conditions by reacting various carbonyl compounds and 1,3-dicarbonyl **57** compounds using aromatic amine/ammonium acetate as an ammonia source in the occurrence of catalytic amounts of bismuth nitrate pentahydrate using microwave irradiation (Scheme 18).

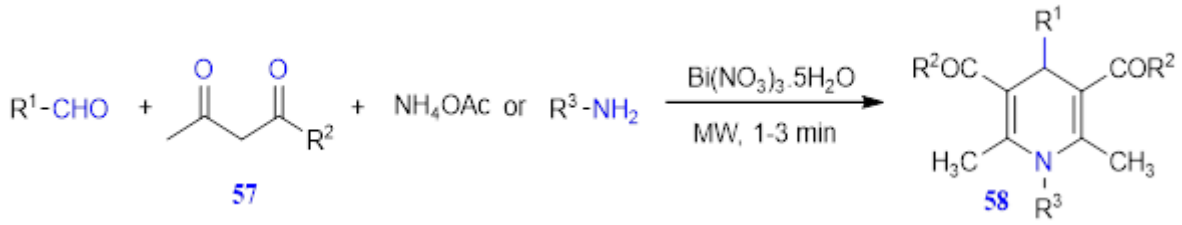

R1 = Aryl, Heteroaryl, Alkyl
R2 = Me, MeO, EtO
R3 = Aryl, Heteroaryl

Scheme 18

Under solvent-free conditions, TsOH effectively catalyzes a three-component reaction involving pyridin-2-amine **59**, 3-phenylpropiolaldehyde **60**, and alcohol to produce imidazo[1,2-a] pyridines **61** in good yields. High efficiency and good functional group tolerance are seen in the reactions. This method offers a practical procedure for making functionalized imidazo[1,2-a]pyridine derivatives (86) (Scheme 19).

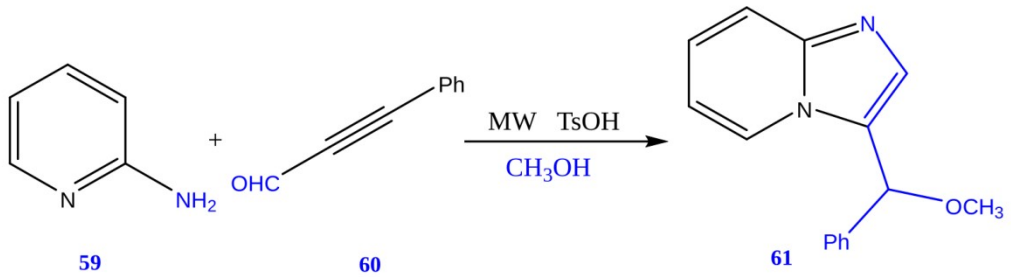

Scheme 19

P-substituted acetophenones **62** were reacted with thiourea **63** to produce 2-amino-4-arylthiazoles **64** in a single pot without the need for any solvents under microwave irradiation in the presence of iodine (87) (Scheme 20).

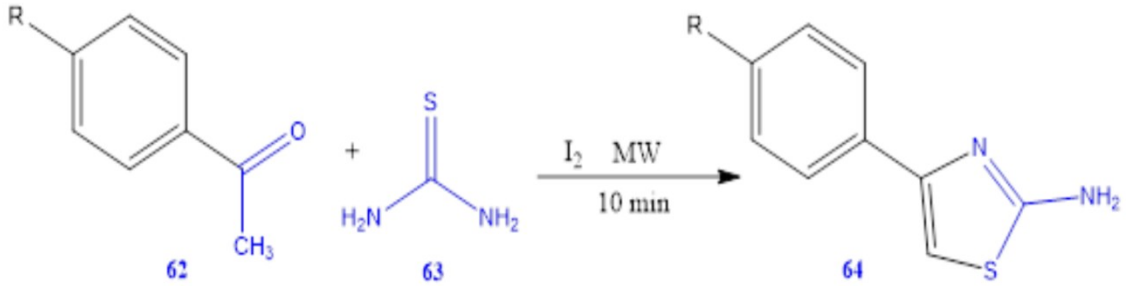

Scheme 20

Biginelli reaction employing aldehydes **62**, acetoacetates **65**, and thiourea **63** in the presence of iodine under solvent-free conditions has been successfully microwave-assisted to produce 3, 4-dihydropyrimidin-2-thiones **66** with good yields and purity without chromatographic separation (88) (Scheme 21).

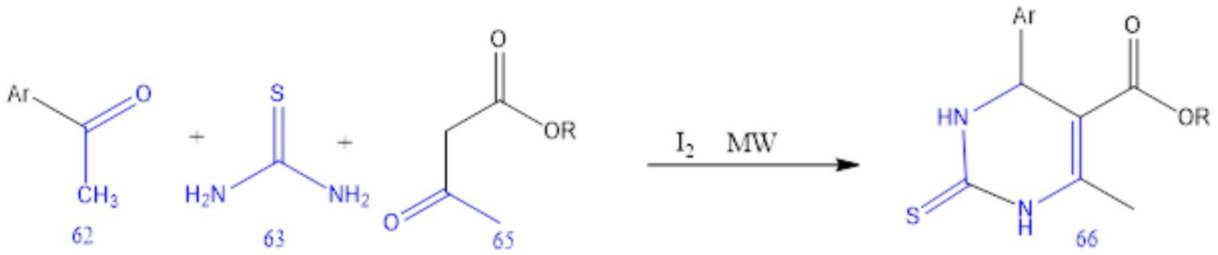

R = Me, Et
Ar = C_6H_5, 4-ClC_6H_4, 4-BrC_6H_4, 4-FC_6H_4, 4-$O_2NC_6H_4$, 3-$O_2NC_6H_4$, 2-$O_2NC_6H_4$, 4-$MeOC_6H_4$, 3-$MeOC_6H_4$, 4-OHC_6H_4, 4-OH-3-$MeOC_6H_3$

Scheme 21

Under microwave irradiation and solvent-free conditions, coumarin-3-carboxylic acids **69** have been produced in good to high yields from differently substituted Meldrum's acid **68** and 2-hydroxybenzaldehydes or 2-hydroxyacetophenones **67** as starting materials in the presence of catalyst $Yb(OTf)_3$ hydrate with a concentration of 5% mol (89) (Scheme 22).

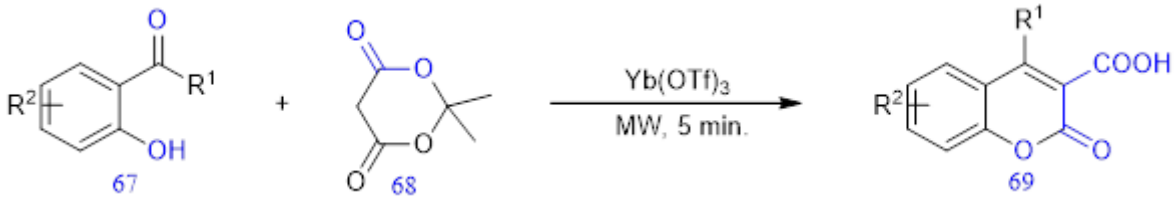

R1 = H, Me

Scheme 22

The Friedel-Crafts acylation of arenes containing electron-donating substituents employing aromatic carboxylic acids **70** as the acylating agents under microwave irradiation is shown to be boosted by the use of erbium trifluoromethane sulfonate as a catalyst. A variety of aryl ketones **71** can be prepared using an efficient, quick, and waste-free technique in good yields and with quick reaction times (90) (Scheme 23).

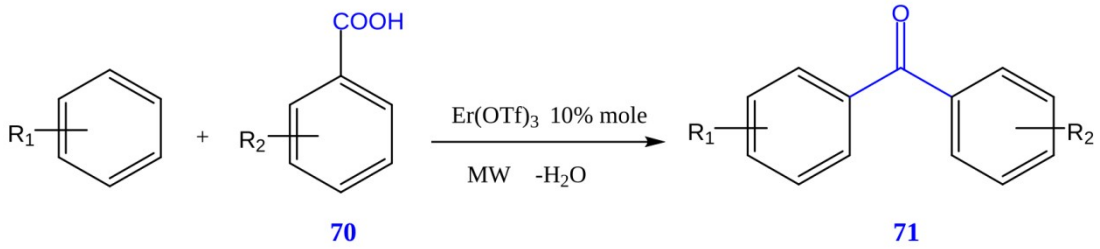

R_1 = Me, MeO, MeS, 1,2-di MeO, 1,3-di MeO, 1,4-di MeO
R_2 = H, 4-MeO, 2-MeO, 2-Cl, 2-F, 2-Br

Scheme 23

Under microwave irradiation and solvent-free conditions, pyrazol-3(2*H*)-one derivatives **75** were produced from 3-phenylisoxazole-5-carbaldehyde **72**, ethyl acetoacetate **73**, and (4-chlorophenyl) hydrazine **74**. Silicon oxide was discovered to have excellent catalytic activity and dispersancy for the condensation reaction. Environmentally friendly reaction conditions, straightforward operation, a wide substrate, satisfactory yields, and the ability to reuse silica are some of this method's benefits.(91) (Scheme 24).

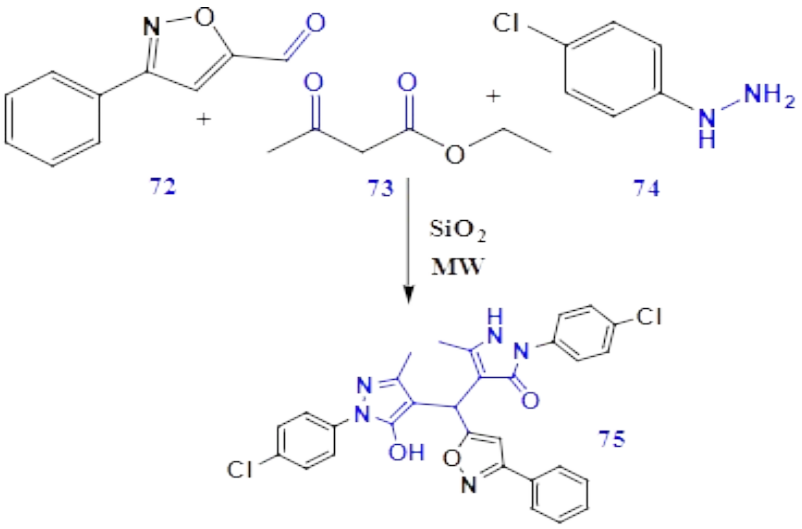

Scheme 24

Using fluoroboric acid supported on silica under solvent-free conditions in a microwave reactor, a number of naphthopyrans **77** were synthesized. To improve the reaction conditions, the catalytic influence of HBF_4-SiO_2 was thoroughly explored (92) (Scheme 25).

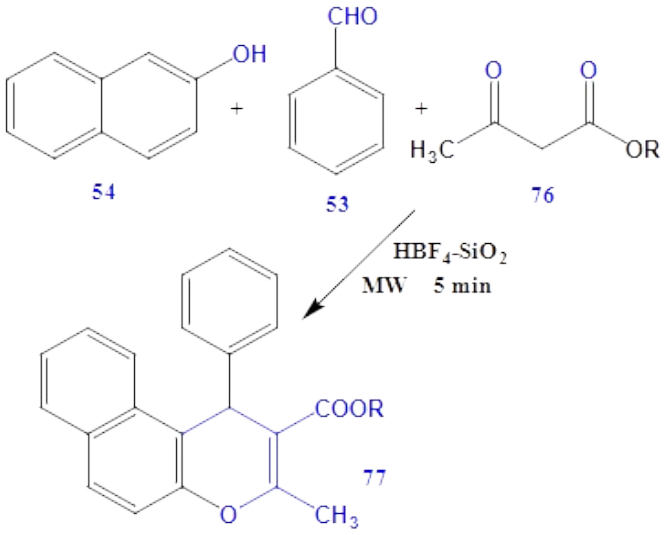

R = C_2H_5

Scheme 25

Using a one-pot, three-component reaction that involves acetophenones, 4-hydroxy-2*H*-chromen-2-one **78**, and aldehydes under microwave irradiation, to produce pyrano[3,2-c] chromen-5(4*H*)-ones **79** quickly and effectively. The current process has a number of benefits, including quick reaction times, straightforward operational procedures, avoiding hazardous solvents and catalysts, excellent product yields, and endurance of substrate diversity (93) (Scheme 26).

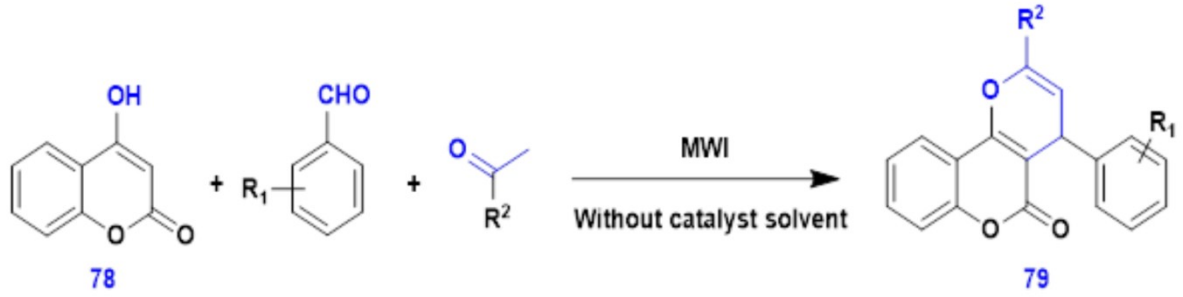

R_1 = 4-NO_2, 4-Cl, H
R_2 = 4-Me-C_6H_4, 4-MeO-C_6H_4, 2-Br-C_6H_4

Scheme 26

For the rapid synthesis of pyrimidine derivatives, microwave-induced cyclocondensation of methyl 2-(acetoxy(phenyl) methyl) acrylate **80** with 2-aminopyridine **59** has been accomplished. excellent yields of pyrimidin-2-one **81** with high selectivity and rapid reaction times (94) (Scheme 27).

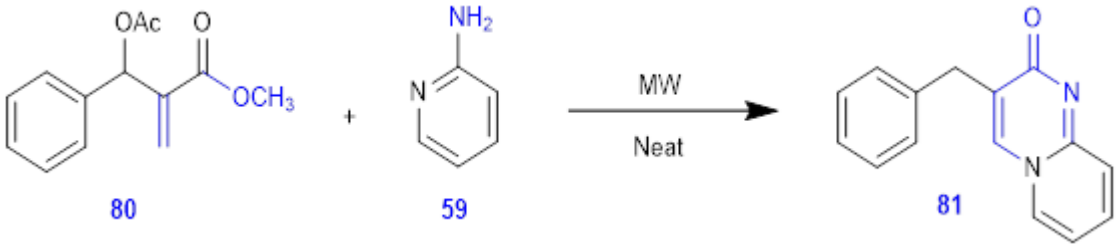

Scheme 27

Aza-Diels-Alder synthesis without a catalyst or solvent is reported. 1,3-dimethyluracil derivatives **82** combine with aldehyde and amine to quickly and efficiently produce dihydropyrido[4,3-d] pyrimidine derivatives **85** (95) (Scheme 28).

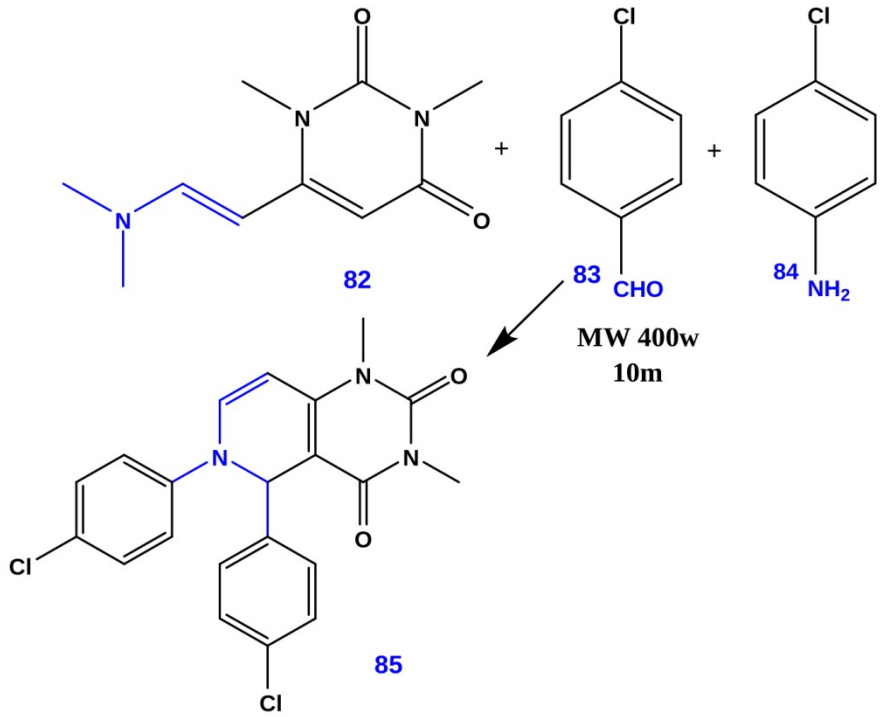

Scheme 28

Under microwave irradiation, hydrazines/hydrazides and diamines **88** can be quickly and easily combined with diketone **86** to produce pyrazoles and diazepines **87 ,89** in high yields without the use of a catalyst or reaction solvent (96) (Scheme 29).

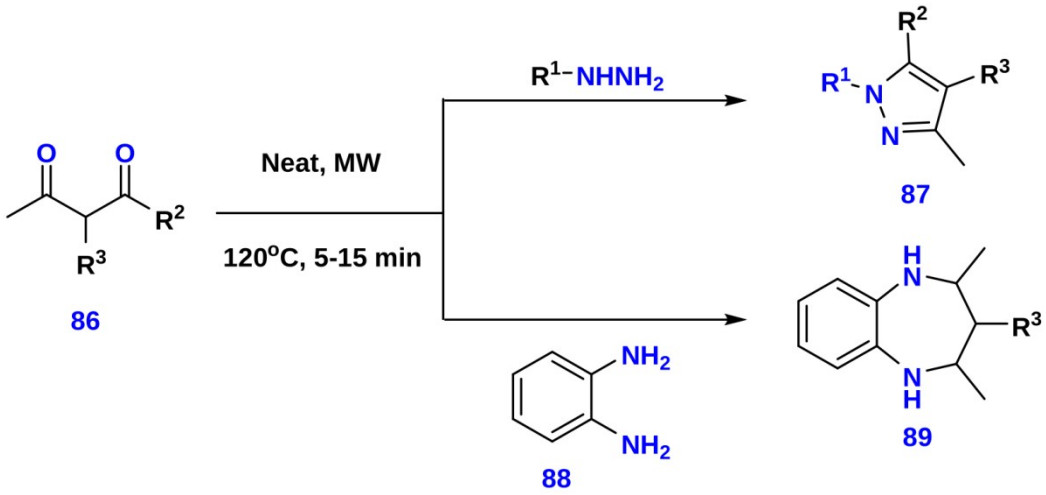

Scheme 29

1, 4-phenylenedithioureas **92** was prepared in solvent-free and catalyst-free conditions using microwave at 60 °C which exhibited the positive effect of microwave on yield and reaction time when compared to the traditional method (97) (Scheme 30).

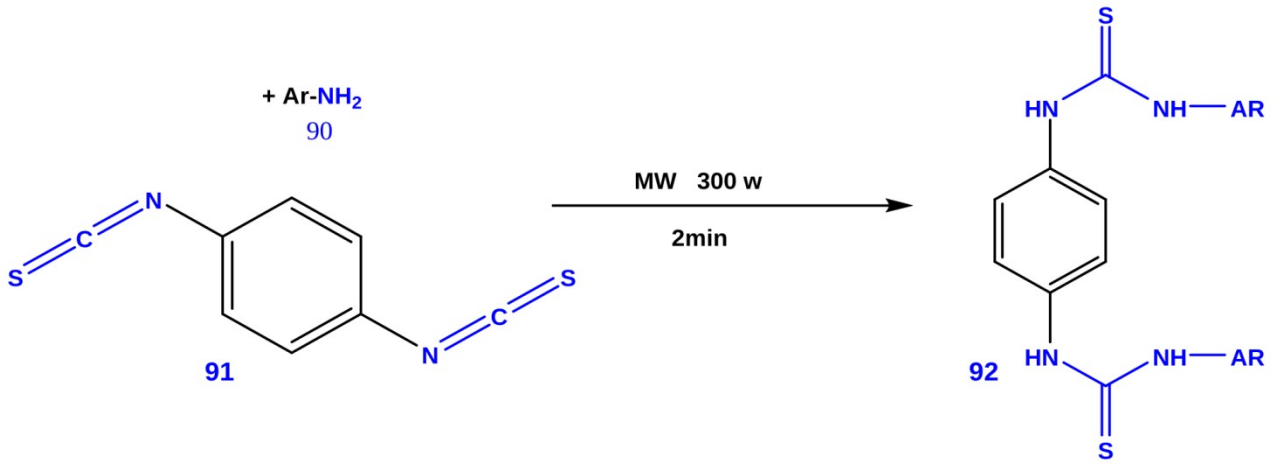

Scheme 30

When various aromatic aldehydes **93** were coupled with dimedone **94**, ethyl acetoacetate **95**, and ammonium acetate in the absence of a catalyst, under solvent-free, and microwave irradiation conditions, high yields of polyhydroquinolines **96** were produced (98) (Scheme 31).

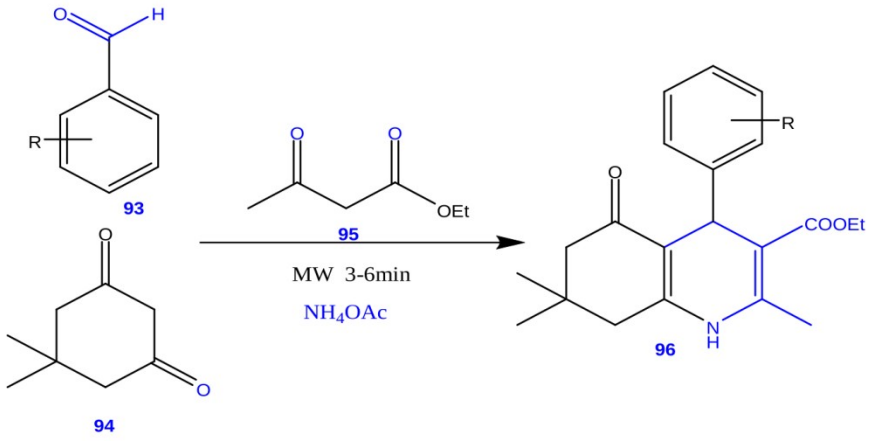

Scheme 31

Yin et al. studied the synthesis of a sequence of novel hydroxylated 2, 4, 6-trisubstituted pyridines using MW irradiation (99). Under ideal reaction conditions, 4-hydroxybenzaldehyde **97** and acetophenone **98** with ammonium acetate can be combined to form 4-(2, 6-Diphenylpyridin-4-yl) phenol **99** and its derivatives. in one pot**.** (Scheme 32).

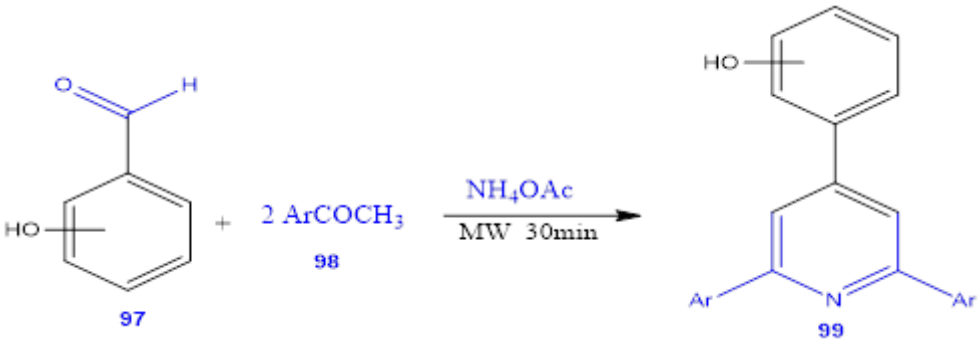

Scheme 32

Prajapati et al. developed the aza-Diels-Alder reaction under microwave irradiation by heating aldimines with 1,3-dimethyluracil **83** derivatives to produce pyrimidines **101** derivatives (100) (Scheme 33).

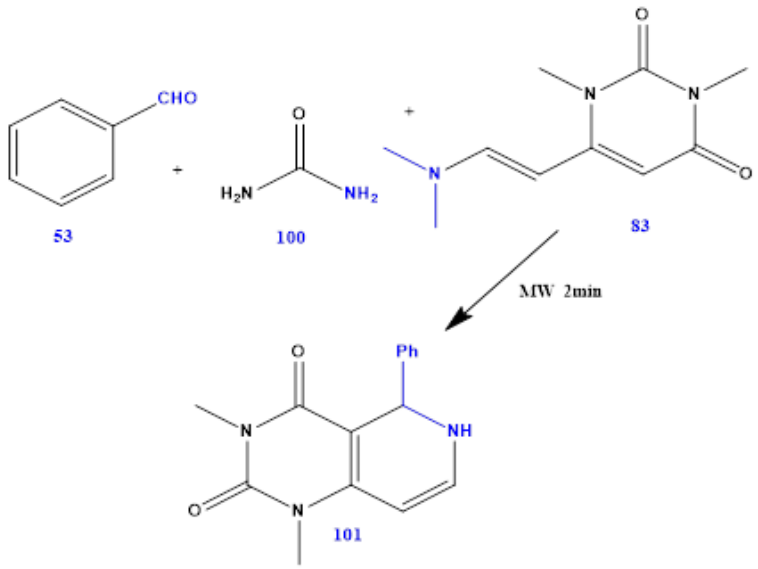

Scheme 33

Through a simple three-component condensation of 4-hydroxybenzaldehyde **97**, aldehyde **53**, and NH_4OAc **102**, a number of novel hydroxylated 2, 4, and 6-trisubstituted pyridines **103** were easily synthesized in high yield (83%) under MW irradiation (Scheme). Yin and his coworkers reported this work. (99) (Scheme 34).

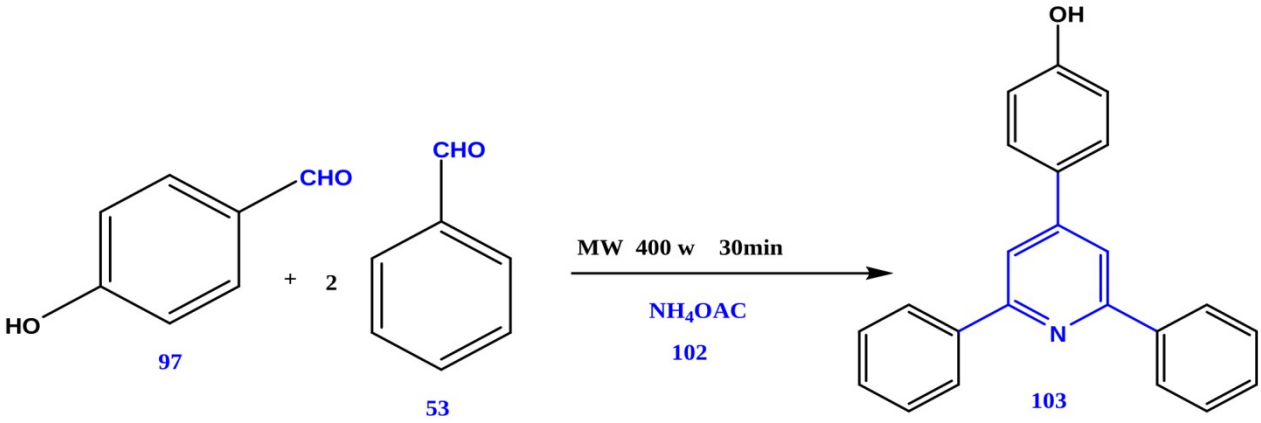

Scheme 34

Synthesis of a thioamides and thioester **106** under MW irradiation by reaction of esters and amides **104** with potassium thiocyanate **105** with yields in the range of 85-93% (101) (Scheme 35).

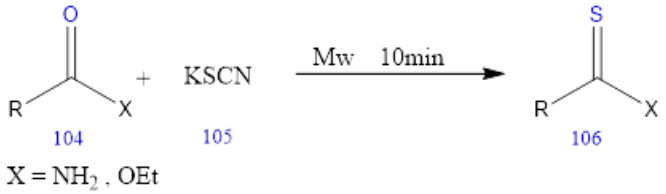

Scheme 35

3,4-disubstituted isoxazole **108** synthesis in a single pot with microwave irradiation in the presence of different catalysts such as potassium bromide (102,103) (Scheme 36).

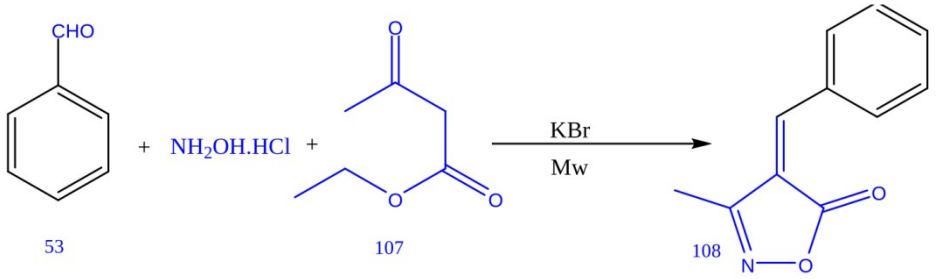

Scheme 36

3.3. Solventless Organic Reactions under Ultrasonic Waves

Recent years have seen a lot of interest in the use of ultrasound in organic synthesis, which affects a number of organic reactions (104–109). It has been noted that ultrasonic lowers the reaction temperature, allowing for faster reaction speeds in ambient settings. This section discusses some of the most recent advances in ultrasound-based organic synthesis. There have been a lot of literary reviews recently that have discussed this method and its significance. Many literary reviews shed light on this technique and its importance in recent times (110–112).

As an easy, effective, and environmentally friendly technique toward N-alkylated amines **111**, ultrasound-assisted solventless oxidation/reductive amination of benzyl halides **109** was developed. (113) (Scheme 37).

Scheme 37

Using an environmentally friendly ultrasonic process, a highly productive and active CuO nanoparticle decorated with phosphate functionalized graphene oxide (PGOCuO) nanocomposite was used as a catalyst in the Mannich reaction to synthesize β-amino carbonyl compounds **113** (114) (Scheme 38).

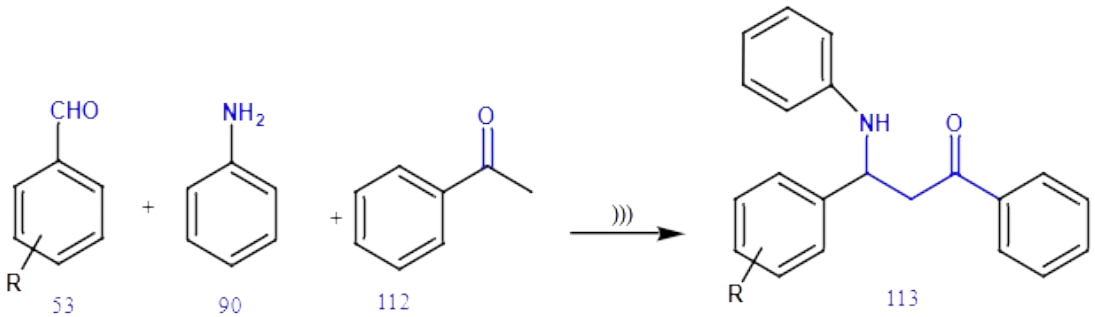

Scheme 38

MoO_3/Cu Schiff base complex nanocomposite (NMCS) was used to catalyze an atom-efficient and selective oxidation of alcohols **114** utilizing hydrogen peroxide under ultrasonic irradiation. Under solvent-free conditions, a structurally different set of alcohols was converted into the required aldehyde **53** and ketone products with high conversion and excellent selectivity. (115)(Scheme 39).

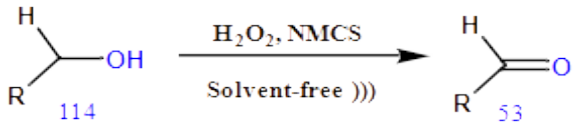

Scheme 39

Abdelkarim et al. used both microwave and ultrasonic techniques to synthesis 1 and 5 substituted-tetrazoles **116** under solvent free conditions (116) (Scheme 40).

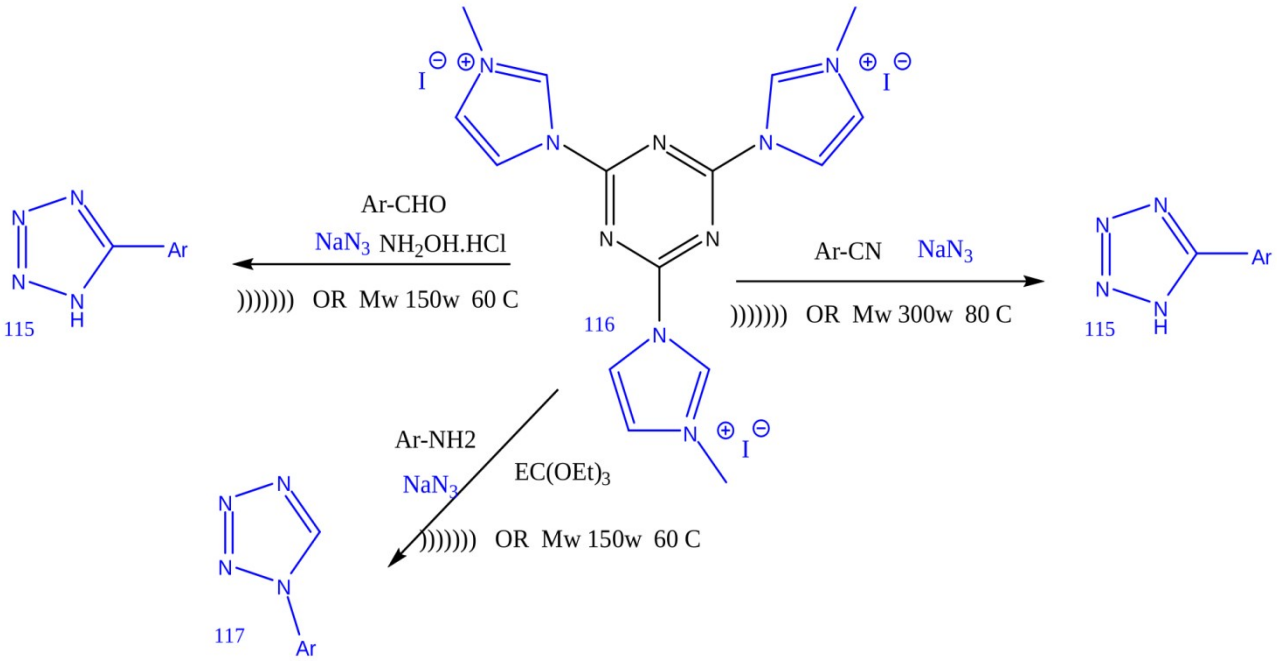

Scheme 40

3.4**Solventless Photochemical Organic Reactions**

Furthermore, numerous photochemical procedures have been carried out without the need for solvents. Currently, typical synthetic chemists who are interested in creating compounds with considerable biological or catalytic activity are less interested in these processes. However, it is anticipated that the significance of photochemical processes will increase over the next few decades, particularly if sunlight can be exploited to speed up the process. In addition, several processes that are straightforward in a photochemical pathway cannot be carried out thermally (117–121).

Many reactions can be carried out with only light and without the need for solvents, such as polymerization, dimerization, and cyclization reactions (117) (Scheme 41).

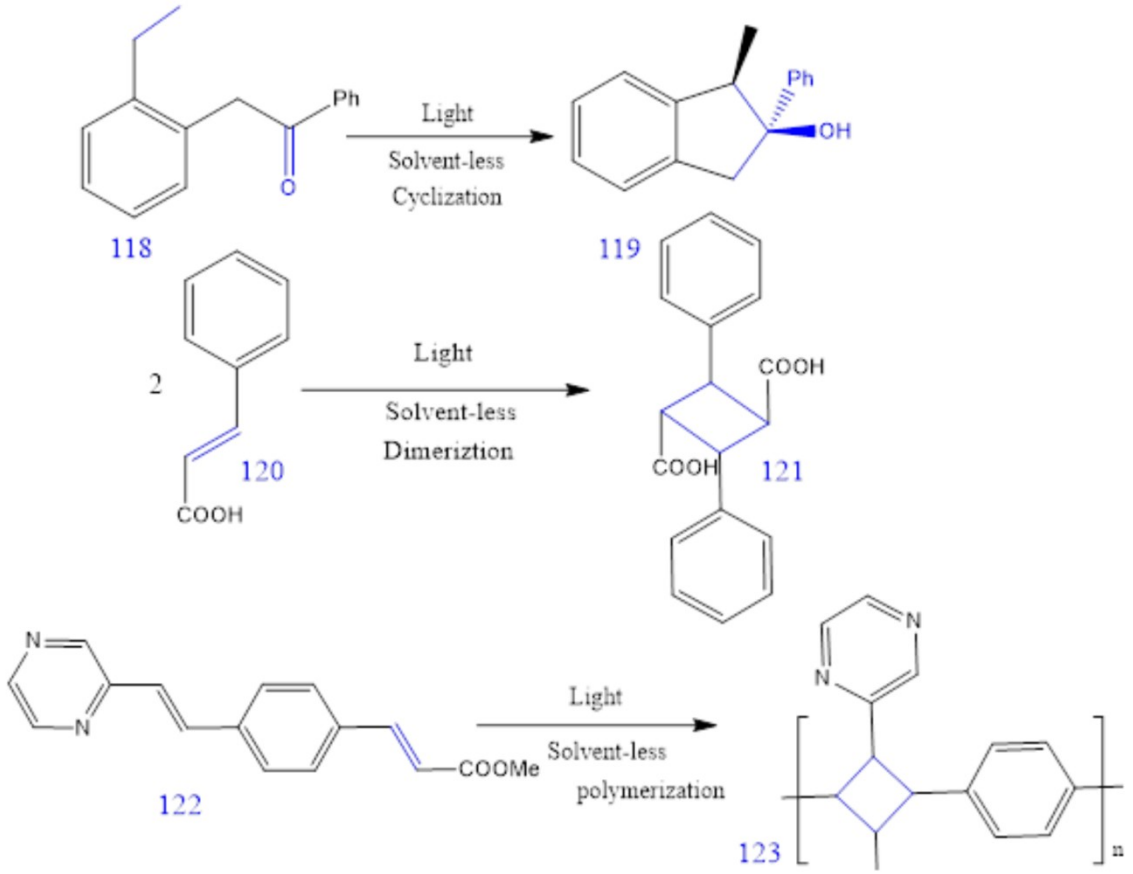

Scheme 41

Kei Ohkubo et al. (122) converted hydroquinone **124** function groups into di-hydroxide phenols **125** by xenon lamp in visible light (λ > 390 nm) with 99% conversion yield under solvent-free conditions (Scheme 42).

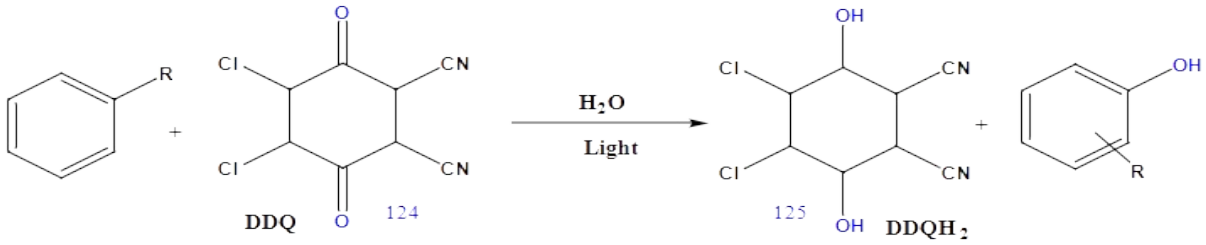

Scheme 42

Nazeef et al. (123) have developed a single pot, solvent-free photochemical reaction of aldehyde **53** and amine **90** in the presence of thioglycolic acid **126** to create thiazolidin-4-ones **127** ring without the use of a catalyst (Scheme 43).

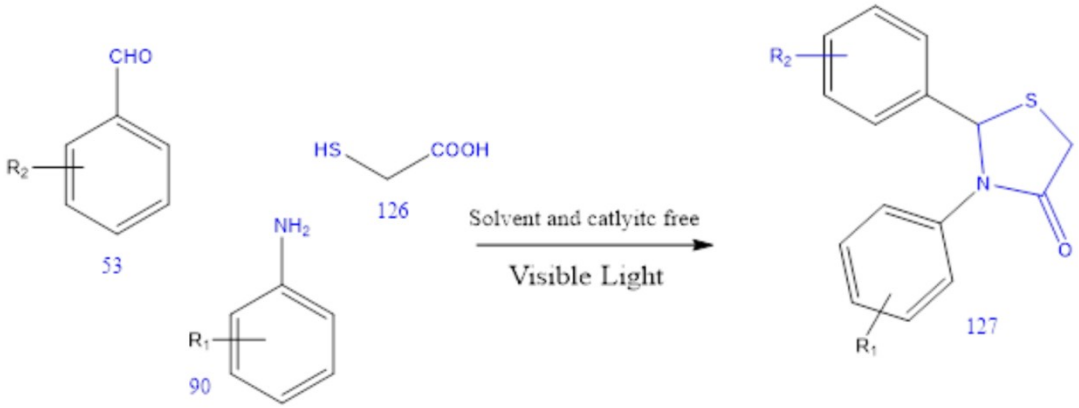

Scheme 43

4. CONCLUSIONS

The main goal of green chemistry is to reach materials and products without polluting the environment or human health. Therefore, the approach of not using solvents in chemistry reactions has become the first priority in all industries and products. This approach saves time and safety in addition to reducing costs and pollutants. The techniques used start with the use of alternative organic solvents that do not harm the environment and technologies that require energy, such as microwave assisted synthesis and ultrasound assisted synthesis, in addition to directly using natural renewable energy, such as solventless photochemical organic reactions. From our review information, we find that there are many researchers who have focused their work on microwave reactions because of their high and fast effectiveness and the availability of the required devices, but there is some shortcoming in the trend towards ultrasound interactions, and this may be due to the lack of ultrasound devices or difficulty of application at a larger scale in industries.

5. CONFLICT OF INTEREST

No potential conflict of interest was reported by the authors.

6. ACKNOWLEDGMENTS

The authors acknowledge and express their thanks, appreciation, and sincere gratitude to all staff members at the Department of Green Chemistry, the National Research Centre, and the laboratories and research sector of the Greater Cairo Water Company for their cooperation.

7. REFERENCES

1. Aquino T de, Zenkner FF, Ellwanger JH, Prá D, Rieger A. DNA damage and cytotoxicity in pathology laboratory technicians exposed to organic solvents. An Acad Bras Cienc. 2016 Feb 5;88(1):227–36. Available from: <URL>.

2. Niaz K, Bahadar H, Maqbool F, Abdollahi M. A review of environmental and occupational exposure to xylene and its health concerns. Available from: <URL>.

3. Tong R, Zhang L, Yang X, Liu J, Zhou P, Li J. Emission characteristics and probabilistic health risk of volatile organic compounds from solvents in wooden furniture manufacturing. J Clean Prod. 2019 Jan;208:1096–108. Available from: <URL>.

4. Ou R, Chang C, Zeng Y, Zhang X, Fu M, Fan L, et al. Emission characteristics and ozone formation potentials of VOCs from ultra-low-emission waterborne automotive painting. Chemosphere. 2022;305:135469. Available from: <URL>.

5. Zhang X, Zhao W, Nie L, Shao X, Dang H, Zhang W, et al. A new classification approach to enhance future VOCs emission policies: Taking solvent-consuming industry as an example. Environmental Pollution. 2021 Jan;268:115868. Available from: <URL>.

6. Vaudreuil M-A, Vo Duy S, Munoz G, Sauvé S. Pharmaceutical pollution of hospital effluents and municipal wastewaters of Eastern Canada. Science of The Total Environment. 2022 Nov;846:157353. Available from: <URL>.

7. Kuzmina O, Hartrick E, Marchant A, Edwards E, Brandt JR, Hoyle S. Chemical Management: Storage and Inventory in Research Laboratories. ACS Chemical Health & Safety. 2022;29(1):62–71. Available from: <URL>.

8. M. Hassan A, Heakal B, Said A, Aboulthana W, Abdelmoaz M. Comparative study for synthesis of novel Mn (II), Co (II), Ni (II), Cu (II), Zn (II) and Zr (IV)complexes under conventional methods and microwave irradiation and evaluation of their antimicrobial and Anticancer activity. Egypt J Chem. 2020 Jan 15;63(7):2533–50. Available from: <URL>.

9. Zangade S, Patil P. A Review on Solvent-free Methods in Organic Synthesis. Curr Org Chem. 2020 Jan 9;23(21):2295–318. Available from: <URL>.

10. Sahoo BM, Banik BK. Solvent-less reactions: Green and sustainable approaches in medicinal chemistry. In:

Green Approaches in Medicinal Chemistry for Sustainable Drug Design. Elsevier; 2020. p. 523–48. Available from: <URL>.

11. Rothenberg G, Downie AP, Raston CL, Scott JL. Understanding Solid/Solid Organic Reactions. J Am Chem Soc. 2001 Sep 1;123(36):8701–8. Available from: <URL>.

12. ben Othman A, Ayari F, Abidi R, Trabelsi Ayadi M. Hybrid nanocomposite by solid-solid reaction. Desalination Water Treat. 2019;152:185–96. Available from: <URL>.

13. Hassan AM, Heakal BH, Younis A, Abdelmoaz MA, Abdrabou MM. Conventional and Microwave-Assisted Synthesis, Antimicrobial and Antitumor Studies of Tridentate Schiff Base Derived from O-vanillin and Phenyl Urea and its Complexes. Advanced Journal of Chemistry-Section A. 2020;3(5):621–38.

14. Hassan AM, Said AO, Heakal BH, Younis A, Aboulthana WM, Mady MF. Green Synthesis, Characterization, Antimicrobial and Anticancer Screening of New Metal Complexes Incorporating Schiff Base. ACS Omega. 2022 Sep 13;7(36):32418–31. Available from: <URL>.

15. Karmakar R, Mukhopadhyay C. Ultrasonication under catalyst-free condition: an advanced synthetic technique toward the green synthesis of bioactive heterocycles. In: Green Synthetic Approaches for Biologically Relevant Heterocycles. Elsevier; 2021. p. 497–562. Available from: <URL>.

16. Akbaşlar D, Demirkol O, Giray S. Paal–Knorr Pyrrole Synthesis in Water. Synth Commun. 2014 May 3;44(9):1323–32. Available from: <URL>.

17. Simon M-O, Li C-J. Green chemistry oriented organic synthesis in water. Chem Soc Rev. 2012;41(4):1415–27. Available from: <URL>.

18. Faisal M. Water in Organic Synthesis as a Green Solvent. Industrial Applications of Green Solvents: Volume I. 2019;50:61–106. Available from: <URL>.

19. Jessop PG. Switchable solvents as media for synthesis and separations. Aldrichimica Acta. 2015;48(1):18–21. Available from: <URL>.

20. Lawley MD, Boon D, Stein LY, Sauvageau D. Switchable Solvents for the Reversible Dissolution of Poly(3-hydroxybutyrate). ACS Sustain Chem Eng. 2022 Feb 28;10(8):2602–8. Available from: <URL>.

21. Wolfs J, Nickisch R, Wanner L, Meier MAR. Sustainable One-Pot Cellulose Dissolution and Derivatization via a Tandem Reaction in the DMSO/DBU/CO 2 Switchable Solvent System. J Am Chem Soc. 2021 Nov 10;143(44):18693–702. Available from: <URL>.

22. Jessop PG, Heldebrant DJ, Li X, Eckert CA, Liotta CL. Reversible nonpolar-to-polar solvent. Nature. 2005;436(7054):1102. Available from: <URL>.

23. Mercer SM, Jessop PG. “Switchable water”: aqueous solutions of switchable ionic strength. ChemSusChem: Chemistry & Sustainability Energy & Materials. 2010;3(4):467–70. Available from: <URL>.

24. Phan L, Chiu D, Heldebrant DJ, Huttenhower H, John E, Li X, et al. Switchable solvents consisting of amidine/alcohol or guanidine/alcohol mixtures. Ind Eng Chem Res. 2008;47(3):539–45. Available from: <URL>.

25. Lopez-Periago AM, Portoles-Gil N, López-Domínguez P, Fraile J, Saurina J, Aliaga-Alcalde N, et al. Metal–organic frameworks precipitated by reactive crystallization in supercritical CO2. Cryst Growth Des. 2017;17(5):2864–72. Available from: <URL>.

26. Fedyaeva ON, Vostrikov AA, Shishkin A v, Dubov DY. Conjugated processes of black liquor mineral and organic components conversion in supercritical water. J Supercrit Fluids. 2019;143:191–7. Available from: <URL>.

27. Wei N, Xu D, Hao B, Guo S, Guo Y, Wang S. Chemical reactions of organic compounds in supercritical water gasification and oxidation. Water Res. 2021;190:116634. Available from: <URL>.

28. Chen J, Wang Q, Xu Z, Jiaqiang E, Leng E, Zhang F, et al. Process in supercritical water gasification of coal: A review of fundamentals, mechanisms, catalysts and element transformation. Energy Convers Manag. 2021;237:114122. Available from: <URL>.

29. Yang G-P, Wu X, Yu B, Hu C-W. Ionic liquid from vitamin B1 analogue and heteropolyacid: a recyclable heterogeneous catalyst for dehydrative coupling in organic carbonate. ACS Sustain Chem Eng. 2019;7(4):3727–32. Available from: <URL>.

30. Vekariya RL. A review of ionic liquids: Applications towards catalytic organic transformations. J Mol Liq. 2017;227:44–60. Available from: <URL>.

31. Gaikwad DS, Undale KA, Patil DB, Pore DM. Multi-functionalized ionic liquid with in situ-generated palladium nanoparticles for Suzuki, Heck coupling reaction: a comparison with deep eutectic solvents. Journal of the Iranian Chemical Society. 2019;16(2):253–61. Available from: <URL>.

32. Pei Y, Zhang Y, Ma J, Fan M, Zhang S, Wang J. Ionic liquids for advanced materials. Mater Today Nano. 2022;17:100159. <URL>.

33. de Jesus SS, Maciel Filho R. Are ionic liquids eco-friendly? Renewable and Sustainable Energy Reviews. 2022;157:112039. Available from: <URL>.

34. Curreri AM, Mitragotri S, Tanner EEL. Recent advances in ionic liquids in biomedicine. Advanced Science. 2021;8(17):2004819. Available from: <URL>.

35. Khandelwal S, Tailor YK, Kumar M. Deep eutectic solvents (DESs) as eco-friendly and sustainable solvent/catalyst systems in organic transformations. J Mol Liq. 2016;215:345–86. Available from: <URL>.

36. Yu F-L, Gu Y-L, Gao X, Liu Q-C, Xie C-X, Yu S-T. Alkylation of isobutane and isobutene catalyzed by trifluoromethanesulfonic acid-taurine deep eutectic solvents in polyethylene glycol. Chemical Communications. 2019;55(33):4833–6. Available from: <URL>.

37. Marset X, Torregrosa-Crespo J, Martínez-Espinosa RM, Guillena G, Ramón DJ. Multicomponent synthesis of sulfonamides from triarylbismuthines, nitro compounds and sodium metabisulfite in deep eutectic solvents.

Green Chemistry. 2019;21(15):4127–32. Available from: <URL>.

38. el Achkar T, Greige-Gerges H, Fourmentin S. Basics and properties of deep eutectic solvents: a review. Environ Chem Lett. 2021;19(4):3397–408. Available from: <URL>.

39. Cao J, Su E. Hydrophobic deep eutectic solvents: The new generation of green solvents for diversified and colorful applications in green chemistry. J Clean Prod. 2021;314:127965. Available from: <URL>.

40. Shen T, Zhou S, Ruan J, Chen X, Liu X, Ge X, et al. Recent advances on micellar catalysis in water. Adv Colloid Interface Sci. 2021;287:102299. Available from: <URL>.

41. Bose AL, Bhattacharjee D, Goswami D. Mixed micelles and bicontinuous microemulsions: Promising media for enzymatic reactions. Colloids Surf B Biointerfaces. 2022;209:112193. Available from: <URL>.

42. Abdel Hameed R, Abd el-kader MF, Qureshi M, al Elaimi M, Farghaly O. Green Synthesis for Nonionic Surfactants from Poly(etheleneterphthalate) Plastic Waste. Egypt J Chem. 2020 Nov 2;64(2):773–80. Available from: <URL>.

43. Clark JH, Macquarrie DJ. Handbook of green chemistry and technology. John Wiley & Sons; 2008. ISBN: 9781405172486.

44. Mukherjee N, Maity P, Ranu BC. Use of ball milling for the synthesis of biologically active heterocycles. In: Green Synthetic Approaches for Biologically Relevant Heterocycles. Elsevier; 2021. p. 167–87. Available from: <URL>.

45. Zhang P, Li S, Guo P, Zhang C. Seed-Assisted, OSDA-Free, Solvent-Free Synthesis of ZSM-5 Zeolite from Iron Ore Tailings. Waste Biomass Valorization. 2020 Aug 13;11(8):4381–91. Available from: <URL>.

46. Yoo K, Hong EJ, Huynh TQ, Kim B-S, Kim JG. Mechanochemical Regulation of Unstable Acyl Azide: Ir (III)-Catalyzed Nitrene Transfer C–H Amidation under Solvent-Free Ball Milling Conditions. ACS Sustain Chem Eng. 2021;9(26):8679–85. Available from: <URL>.

47. Hassan A, Heakal BH, Khamis H, Hassan GAN, Marzouk E, Abdelmoaz MA, et al. Design, Synthesis, DFT Studies and Anticancer Activity of Novel Metal Complexes Containing 1, 3, 5-triazino [1, 2-a] benzimidazole Moiety Using Microwave as an Approach for Green Chemistry. Egypt J Chem. 2021;64(1):323–40. Available from: <URL>.

48. Younis A, Awad G. Utilization of Ultrasonic as an Approach of Green Chemistry for Synthesis of Hydrazones and Bishydrazones as Potential Antimicrobial Agents. Egypt J Chem. 2019 Jul 2;63(2):599–610. Available from: <URL>.

49. Zhao W, Liu M, Shen C, Liu K, Liu H, Ou C, et al. Biosynthesis of plant-specific alkaloids tetrahydroprotoberberines in engineered Escherichia coli. Green Chemistry. 2021;23(16):5944–55. Available from: <URL>.

50. Jin X, Zhang W, Wang Y, Sheng J, Xu R, Li J, et al. Biosynthesis of non-animal chondroitin sulfate from methanol using genetically engineered Pichia pastoris. Green Chemistry. 2021;23(12):4365–74. Available from: <URL>.

51. Zhou X, Ji H, Hu G-H, Wang R, Zhang L. A solvent-less green synthetic route toward a sustainable bio-based elastomer: design, synthesis, and characterization of poly(dibutyl itaconate- co -butadiene). Polym Chem. 2019;10(45):6131–44. Available from: <URL>.

52. El-Sayed T, Aboelnaga A, El-Atawy M, Hagar M. Ball Milling Promoted N-Heterocycles Synthesis. Molecules. 2018 Jun 4;23(6):1348. Available from: <URL>.

53. Bose AK, Pednekar S, Ganguly SN, Chakraborty G, Manhas MS. A simplified green chemistry approach to the Biginelli reaction using 'Grindstone Chemistry.' Tetrahedron Lett. 2004;45(45):8351–3. Available from: <URL>.

54. Ghahremanzadeh R, Ahadi S, Shakibaei GI, Bazgir A. Grindstone chemistry: one-pot synthesis of spiro [diindenopyridine-indoline] triones and spiro [acenaphthylene-diindenopyridine] triones. Tetrahedron Lett. 2010;51(3):499–502. Available from: <URL>.

55. Saikia L, Baruah JM, Thakur AJ. A rapid, convenient, solventless green approach for the synthesis of oximes using grindstone chemistry. Org Med Chem Lett. 2011;1(1):1–6. Available from: <URL>.

56. Patel DS, Avalani JR, Raval DK. One-pot solvent-free rapid and green synthesis of 3, 4-dihydropyrano [c] chromenes using grindstone chemistry. Journal of Saudi Chemical Society. 2016;20:S401–5. Available from: <URL>.

57. Sheldon RA. Green solvents for sustainable organic synthesis: state of the art. Green Chemistry. 2005;7(5):267–78. Available from: <URL>.

58. Walsh PJ, Li H, de Parrodi CA. A green chemistry approach to asymmetric catalysis: solvent-free and highly concentrated reactions. Chem Rev. 2007;107(6):2503–45. Available from: <URL>.

59. Abdel-Aziem A, Rashdan HRM, Mohamed Ahmed E, Shabaan SN. Synthesis and cytotoxic activity of some novel benzocoumarin derivatives under solvent free conditions. Green Chem Lett Rev. 2019;12(1):9–18. Available from: <URL>.

60. Andreosso I, Papagni A, Vaghi L. Mechanochemical oxidation of fluorinated anilines to symmetric azobenzenes. J Fluor Chem. 2018;216:124–7. Available from: <URL>.

61. Thangamani A. Grindstone chemistry: an efficient and green synthesis of 2-amino-4H-benzo [b] pyrans. Journal of Applied and Advanced Research. 2017;2(2):78–85. Available from: <URL>.

62. Howard JL, Sagatov Y, Browne DL. Mechanochemical electrophilic fluorination of liquid beta-ketoesters. Tetrahedron. 2018;74(25):3118–23. Available from: <URL>.

63. Kaupp G, Naimi-Jamal MR, Schmeyers J. Solvent-free Knoevenagel condensations and Michael additions in the solid state and in the melt with quantitative yield.

Tetrahedron. 2003;59(21):3753–60. Available from: <URL>.

64. Tella AC, Eke UB, Owalude SO. Solvent-free mechanochemical synthesis and X-ray studies of Cu (II) and Ni (II) complexes of 5-(3, 4, 5-Trimethoxybenzyl) pyrimidine-2, 4-diamine (Trimethoprim) in a ball-mill. Journal of Saudi Chemical Society. 2016;20:S376–81. Available from: <URL>.

65. Mazimba O. Antimicrobial activities of heterocycles derived from thienylchalcones. Journal of King Saud University-Science. 2015;27(1):42–8. Available from: <URL>.

66. Owens AR, Saunders GC, Thomas HP, Wehr-Candler TT. Solvent-free mechanochemical syntheses and reactions of π–π stacked arene–perfluoroarene co-crystals. J Fluor Chem. 2015;175:139–44. Available from: <URL>.

67. Sayed AR, Gomha SM, Abd El-lateef HM, Abolibda TZ. L-proline catalyzed green synthesis and anticancer evaluation of novel bioactive benzil bis-hydrazones under grinding technique. Green Chem Lett Rev. 2021 Apr 3;14(2):180–9. Available from: <URL>.

68. Zhang P, Liu C, Yu L, Hou H, Sun W, Ke F. Synthesis of benzimidazole by mortar–pestle grinding method. Green Chem Lett Rev. 2021 Oct 2;14(4):612–9. Available from: <URL>.

69. Yoo K, Hong EJ, Huynh TQ, Kim B-S, Kim JG. Mechanochemical Regulation of Unstable Acyl Azide: Ir(III)-Catalyzed Nitrene Transfer C–H Amidation under Solvent-Free Ball Milling Conditions. ACS Sustain Chem Eng. 2021 Jul 5;9(26):8679–85. Available from: <URL>.

70. Zeng J-C, Xu H, Yu F, Zhang Z. Manganese (III) acetate mediated synthesis of polysubstituted pyrroles under solvent-free ball milling. Tetrahedron Lett. 2017 Feb;58(7):674–8. Available from: <URL>.

71. Martínez A v, Invernizzi F, Leal-Duaso A, Mayoral JA, García JI. Microwave-promoted solventless Mizoroki–Heck reactions catalysed by Pd nanoparticles supported on laponite clay. RSC Adv. 2015;5(14):10102–9. Available from: <URL>.

72. Princival C, Santos AA dos, Comasseto J v. Solventless and mild procedure to prepare organotellurium (IV) compounds under microwave irradiation. J Braz Chem Soc. 2015;26:832–6. Available from: <URL>.

73. Taher A, Nandi D, Islam RU, Choudhary M, Mallick K. Microwave assisted azide–alkyne cycloaddition reaction using polymer supported Cu (I) as a catalytic species: a solventless approach. RSC Adv. 2015;5(59):47275–83. Available from: <URL>.

74. Keshwal BS, Rajguru D, Acharya AD, Jain S. Microwave-Assisted Solventless Synthesis of 3, 5-Diaryl-2, 6-dicyanoanilines. Proceedings of the National Academy of Sciences, India Section A: Physical Sciences. 2016;86(1):1–5. Available from: <URL>.

75. Rout L, Kumar A, Chand PK, Achary LSK, Dash P. Microwave-Assisted Efficient One-Pot Multi-Component Synthesis of Octahydroquinazolinone Derivatives Catalyzed by Cu@ Ag Core-Shell Nanoparticle. ChemistrySelect. 2019;4(19):5696–706. Available from: <URL>.

76. Nain S, Singh R, Ravichandran S. Importance of Microwave Heating In Organic Synthesis. Advanced Journal of Chemistry-Section A. 2019 Jan 30;94–104.

77. Wahdan K, Zarie E, Elbialy Z., Wahba A, Heakal BH, Said A. Antimicrobial and antioxidant evaluation of newly synthesized nanomaterials of potential anticorrosion properties based on Co (II), Ni (II), Cu (II) and Zn (II) nano complexes of N-(p-methyl phenyl)-N-Benzoyl thiourea. Egypt J Chem. 2022 Jul 3;65(132):1253–68. Available from: <URL>.

78. Nüchter M, Ondruschka B, Bonrath W, Gum A. Microwave assisted synthesis–a critical technology overview. Green chemistry. 2004;6(3):128–41. Available from: <URL>.

79. Jha A. Microwave Assisted Synthesis of Organic Compounds and Nanomaterials. In: Nanofibers - Synthesis, Properties and Applications. IntechOpen; 2021. Available from: <URL>.

80. Merillas B, Cuéllar E, Diez-Varga A, Asensio-Bartolomé M, García-Herbosa G, Torroba T, et al. Whole microwave syntheses of pyridylpyrazole and of Re and Ru luminescent pyridylpyrazole complexes. Inorganica Chim Acta. 2019;484:1–7. Available from: <URL>.

81. Moreno-Fuquen R, Arango-Daraviña K, Becerra D, Castillo J-C, Kennedy AR, Macías MA. Catalyst-and solvent-free synthesis of 2-fluoro-N-(3-methylsulfanyl-1H-1, 2, 4-triazol-5-yl) benzamide through a microwave-assisted Fries rearrangement: X-ray structural and theoretical studies. Acta Crystallogr C Struct Chem. 2019;75(3):359–71. Available from: <URL>.

82. Kaur P, Kumar B, Kumar V, Kumar R. Chitosan-supported copper as an efficient and recyclable heterogeneous catalyst for A3/decarboxylative A3-coupling reaction. Tetrahedron Lett. 2018;59(21):1986–91. Available from: <URL>.

83. Baran NY. Fabrication and characterization of a novel easy recoverable and reusable Oligoazomethine-Pd (II) catalyst for Suzuki cross-coupling reactions. J Mol Struct. 2019;1176:266–74. Available from: <URL>.

84. Khurana JM, Lumb A, Pandey A, Magoo D. Green approaches for the synthesis of 12-aryl-8, 9, 10, 12-tetrahydrobenzo [a] xanthen-11-ones in aqueous media and under microwave irradiation in solventless conditions. Synth Commun. 2012;42(12):1796–803. Available from: <URL>.

85. Bandyopadhyay D, Maldonado S, Banik BK. A microwave-assisted bismuth nitrate-catalyzed unique route toward 1, 4-dihydropyridines. Molecules. 2012;17(3):2643–62. Available from: <URL>.

86. Zhang H, Jiang L. Microwave-assisted solvent-free synthesis of imidazo [1, 2-a] pyridines via a three-component reaction. Tetrahedron Lett. 2015;56(21):2777–9. Available from: <URL>.

87. Cáceres-Castillo D, Carballo RM, Tzec-Interián JA, Mena-Rejón GJ. Solvent-free synthesis of 2-amino-4-arylthiazoles under microwave irradiation. Tetrahedron Lett. 2012;53(30):3934–6. Available from: <URL>.

88. Liu Q, Pan N, Xu J, Zhang W, Kong F. Microwave-assisted and iodine-catalyzed synthesis of dihydropyrimidin-2-thiones via biginelli reaction under solvent-free conditions. Synth Commun. 2013;43(1):139–46. Available from: <URL>.

89. Fiorito S, Genovese S, Taddeo VA, Epifano F. Microwave-assisted synthesis of coumarin-3-carboxylic acids under ytterbium triflate catalysis. Tetrahedron Lett. 2015;56(19):2434–6. Available from: <URL>.

90. Tran PH, Hansen PE, Nguyen HT, Le TN. Erbium trifluoromethanesulfonate catalyzed Friedel–Crafts acylation using aromatic carboxylic acids as acylating agents under monomode-microwave irradiation. Tetrahedron Lett. 2015;56(4):612–8. Available from: <URL>.

91. Zhang D, Zhang Y, Zhao T, Li J, Hou Y, Gu Q. A rapid and efficient solvent-free microwave-assisted synthesis of pyrazolone derivatives containing substituted isoxazole ring. Tetrahedron. 2016;72(22):2979–87. Available from: <URL>.

92. Sharma S, Sharma K, Ojha R, Kumar D, Singh G, Nepali K, et al. Microwave assisted synthesis of naphthopyrans catalysed by silica supported fluoroboric acid as a new class of non purine xanthine oxidase inhibitors. Bioorg Med Chem Lett. 2014;24(2):495–500. Available from: <URL>.

93. Reddy MV, Kumar BS, Lim KT, Cho BG, Jeong YT. Microwave-promoted efficient synthesis of pyrano [3, 2-c] chromen-5 (4H)-ones under catalyst and solvent-free conditions. Tetrahedron Lett. 2016;57(4):476–8. Available from: <URL>.

94. Satyanarayana S, Kumar KP, Reddy PL, Narender R, Narasimhulu G, Reddy BVS. Microwave-assisted cyclocondensation: a rapid and solvent-free synthesis of 3-benzyl-2H-pyrido [1, 2-a] pyrimidin-2-one derivatives. Tetrahedron Lett. 2013;54(36):4892–5. Available from: <URL>.

95. Sarmah MM, Sarma R, Prajapati D, Hu W. Efficient synthesis of dihydropyrido [4, 3-d] pyrimidines by microwave-promoted three-component aza-Diels–Alder reaction. Tetrahedron Lett. 2013;54(3):267–71. Available from: <URL>.

96. Vaddula BR, Varma RS, Leazer J. Mixing with microwaves: Solvent-free and catalyst-free synthesis of pyrazoles and diazepines. Tetrahedron Lett. 2013;54(12):1538–41. Available from: <URL>.

97. Zhang L-P, Shang X-B, Wu Q-F, Zhang Y, Li J-P. Highly Efficient Method for the Synthesis of 1, 4-Phenylenedithioureas Under Solvent-and Catalyst-Free Conditions Promoted by Microwave Irridiation. Synth Commun. 2012;42(7):1045–52. Available from: <URL>.

98. Das S, Santra S, Roy A, Urinda S, Majee A, Hajra A. One-pot multicomponent synthesis of polyhydroquinolines under catalyst and solvent-free conditions. Green Chem Lett Rev. 2012;5(1):97–100. Available from: <URL>.

99. Yin G, Liu Q, Ma J, She N. Solvent-and catalyst-free synthesis of new hydroxylated trisubstituted pyridines under microwave irradiation. Green Chemistry. 2012;14(6):1796–8. Available from: <URL>.

100. Sarma R, Sarmah MM, Prajapati D. Microwave-promoted catalyst-and solvent-free aza-Diels–Alder reaction of aldimines with 6-[2-(dimethylamino) vinyl]-1, 3-dimethyluracil. J Org Chem. 2012;77(4):2018–23. Available from: <URL>.

101. D. D, L. Gaonkar S, S. Shetty N kumar. Synthesis of thioesters and thioamides using potassium thiocyanate under microwave irradiation. Rasayan Journal of Chemistry. 2022;15(01):288–91. Available from: <URL>.

102. Kulkarni P. An efficient solvent-free synthesis of 3,4-disubstituted isoxazole-5(4H)-ones using microwave irradiation. Journal of the Indian Chemical Society. 2021 Jan;98(1):100013. Available from: <URL>.

103. Rao DJ, Nagaraju K, Maddila S. Microwave irradiated mild, rapid, one-pot and multi-component synthesis of isoxazole-5(4H)-ones. Chemical Data Collections. 2021 Apr;32:100669. Available from: <URL>.

104. Kumar H, Parmar A. Ultrasound promoted ZrCl4 catalyzed rapid synthesis of substituted 1, 2, 3, 4-tetrahydropyrimidine-2-ones in solvent or dry media. Ultrason Sonochem. 2008;15(2):129–32. Available from: <URL>.

105. Upadhyaya DJ, Barge A, Stefania R, Cravotto G. Efficient, solventless N-Boc protection of amines carried out at room temperature using sulfamic acid as recyclable catalyst. Tetrahedron Lett. 2007;48(47):8318–22. Available from: <URL>.

106. He J-Y, Xin H-X, Yan H, Song X-Q, Zhong R-G. Convenient ultrasound-mediated synthesis of 1, 4-diazabutadienes under solvent-free conditions. Ultrason Sonochem. 2011;18(1):466–9. Available from: <URL>.

107. Chtourou M, Abdelhédi R, Frikha MH, Trabelsi M. Solvent free synthesis of 1, 3-diaryl-2-propenones catalyzed by commercial acid-clays under ultrasound irradiation. Ultrason Sonochem. 2010;17(1):246–9. Available from: <URL>.

108. Perozo-Rondón E, Martín-Aranda RM, Casal B, Durán-Valle CJ, Lau WN, Zhang XF, et al. Sonocatalysis in solvent free conditions: An efficient eco-friendly methodology to prepare chalcones using a new type of amino grafted zeolites. Catal Today. 2006;114(2–3):183–7. Available from: <URL>.

109. Estager J, Leveque J-M, Cravotto G, Boffa L, Bonrath W, Draye M. One-pot and solventless synthesis of ionic liquids under ultrasonic irradiation. Synlett. 2007;2007(13):2065–8. Available from: <URL>.

110. Puri S, Parmar A, Chopra HK. Ultrasound assisted reactions. In: Handbook of Greener Synthesis of Nanomaterials and Compounds. Elsevier; 2021. p. 177–246. Available from: <URL>.

111. Szabados M, Sipos P, Pálinkó I. Application of sonochemical activation in synthetic organic chemistry. In: Nontraditional Activation Methods in Green and Sustainable Applications. Elsevier; 2021. p. 137–70. Available from: <URL>.

112. Faisal M. Sonochemical protocol for solvent-free organic synthesis. In: Green Sustainable Process for Chemical and Environmental Engineering and Science. Elsevier; 2020. p. 113–39. Available from: <URL>.

113. Khumraksa B, Phakhodee W, Pattarawarapan M. Ultrasound-assisted solventless synthesis of amines by in situ oxidation/reductive amination of benzyl halides. RSC Adv. 2014;4(39):20454–8. Available from: <URL>.

114. Achary LSK, Nayak PS, Barik B, Kumar A, Dash P. Ultrasonic-assisted green synthesis of β-amino carbonyl compounds by copper oxide nanoparticles decorated phosphate functionalized graphene oxide via Mannich reaction. Catal Today. 2020;348:137–47. Available from: <URL>.

115. Naeimi A, Honarmand M, Sedri A. Ultrasonic assisted fabrication of first MoO3/copper complex bio-nanocomposite based on Sesbania sesban plant for green oxidation of alcohols. Ultrason Sonochem. 2019;50:331–8. Available from: <URL>.

116. Jasim SA, Tanjung FA, Sharma S, Mahmoud MZ, Kadhim SB, Kazemnejadi M. Ultrasound and microwave irradiated sustainable synthesis of 5- and 1-substituted tetrazoles in TAIm[I] ionic liquid. Research on Chemical Intermediates. 2022 Aug 15;48(8):3547–66. Available from: <URL>.

117. Kerton FM, Marriott R. Alternative solvents for green chemistry. Royal Society of chemistry; 2013. ISBN: 9781849735957.

118. Avila-Ortiz CG, Juaristi E. Novel methodologies for chemical activation in organic synthesis under solvent-free reaction conditions. Molecules. 2020;25(16):3579. Available from: <URL>.

119. Obst M, König B. Organic synthesis without conventional solvents. European J Org Chem. 2018;2018(31):4213–32. Available from: <URL>.

120. Cintas P, Tabasso S, Veselov V v, Cravotto G. Alternative reaction conditions: Enabling technologies in solvent-free protocols. Curr Opin Green Sustain Chem. 2020;21:44–9. Available from: <URL>.

121. Nagendrappa G. Organic synthesis under solvent-free condition: An environmentally benign procedure—I. Resonance. 2002;7(10):59–68. Available from: <URL>.

122. Ohkubo K, Hirose K, Fukuzumi S. Solvent-Free One-Step Photochemical Hydroxylation of Benzene Derivatives by the Singlet Excited State of 2,3-Dichloro-5,6-dicyano- p -benzoquinone Acting as a Super Oxidant. Chemistry - A European Journal. 2015 Feb 9;21(7):2855–61. Available from: <URL>.

123. Nazeef M, Shivhare KN, Ali S, Ansari K, Ansari MD, Tiwari SK, et al. Visible-light-promoted C N and C S bonds formation: A catalyst and solvent-free photochemical approach for the synthesis of 1,3-thiazolidin-4-ones. J Photochem Photobiol A Chem. 2020 Mar;390:112347. Available from: <URL>.